

A104 404

(15) DAAG29-79-M-0091

(6)

PROCEEDINGS OF THE

WORKSHOP ON

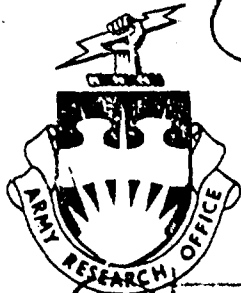
PRINTED CIRCUIT ANTENNA TECHNOLOGY

Held at Las Cruces, New Mexico on
17-19 October 1979

DAAG29-79-MOCT17N
for FORM SD

sponsored by

Accession For	
NTIS GRA&I	<input checked="" type="checkbox"/>
DTIC TAB	<input type="checkbox"/>
Unannounced	<input type="checkbox"/>
Justification	<i>on file</i>
By	ARO
Distribution/	
Availability Codes	
Dist	Avail and/or Special
A	21



(11) 1979

(12) 515



Physical Science
Laboratory

18) ARO

(19) 16626.1-EL

282450

9m

FOREWORD

This Proceedings is the first major volume to deal exclusively with the technology of printed circuit antennas, and will serve as a useful reference on microstrip and stripline radiators and arrays. The thirty-one papers herein have been contributed by forty-eight authors from universities, industrial research groups and governmental agencies in Belgium, England, France, Sweden, the United States and West Germany and are a permanent record of this first Workshop on Printed Circuit Antenna Technology. The intent of this workshop, which has been co-sponsored by the U. S. Army Research Office and the NMSU Physical Science Laboratory, has been to survey the state of printed circuit antenna technology as it exists at present and to focus on specific needs for future R&D emphasis.

Although the concept of printed circuit antennas dates to the early 1950's, there was no significant impetus to develop flight hardware until about 1970 when a governmental decision was made to move the rocket telemetry band from VHF to S-band, thus spurring the development of lightweight low-profile cylindrical arrays of printed circuit antenna elements. The success of this effort has been due in part to the simultaneous development by the materials industry of photo-etch techniques for copper-clad dielectric substrates with a wide range of dielectric constants, low loss tangents, and attractive thermal and mechanical properties. Since 1970, arrays of microstrip and stripline elements have been fabricated to meet a large variety of requirements for aircraft, missile and satellite antennas operating over the 500 MHz-30 GHz frequency range. In the past three years, there has arisen an intense interest among antenna theoreticians in the modeling of the properties of microstrip patches and printed-circuit dipoles. At the same time there has been a vigorous experimental effort made to determine methods of increasing the element bandwidth, of achieving dual-frequency and multiple-polarization operation, of characterizing mutual coupling, etc. All of this has resulted in a significant advancement in printed-circuit antenna technology.

Most of the advancement in this field is the result of the efforts of the authors and session chairmen for this workshop. This volume is evenly balanced between papers of an applied nature and those dealing with theoretical aspects; there are also two papers which describe the state of the substrate materials technology. In focusing on the need for future efforts, it is important that theoretical efforts should recognize the most critical problems faced by antenna development and production groups, e.g. the wide variety of gain, pattern shape, beam-pointing and polarization requirements faced from one application to the next coupled with the restrictions imposed by available substrates, the precision and repeatability of the dielectric constant, etc. It is also important that the antenna development and production community articulate its need for critical theoretical studies, although experience has shown that the experimental development by industry of novel microstrip and strip-line antenna arrays for varied customer requirements has generally outpaced the development of adequate and applicable theoretical models for both individual elements and efficient feed systems. This emphasizes the need for a continuing dialogue among the systems designer, the antenna development engineer, the materials technologist, and the theoretician. It is hoped that this Proceedings will encourage such a continuing dialogue.

Keith R. Carver
Technical Program Chairman
Physical Science Laboratory
New Mexico State University

TABLE OF CONTENTS

WEDNESDAY, OCTOBER 17, 1979

page

I. OPENING SESSION (9:00 - 9:30 a.m.), Chairman: K. R. Carver,
New Mexico State University, Physical Science Laboratory

Welcome to New Mexico State University - Harold R. Lawrence, Director,
Physical Science Laboratory, NMSU

"Challenges to Microstrip Antenna Technology Development," Robert J.
Mailloux, RADC, Hanscom AFB, Massachusetts

II. MICROSTRIP ANTENNA ELEMENTS (9:30 - 12:00), Chairman: John L. Kerr,
U. S. Army Combat Surveillance and Target Acquisition
Laboratory, Fort Monmouth, New Jersey

1. "Microstrip Antenna Research at the Royal Military College of Science," J. R. James, P. S. Hall, C. Wood, & A. Henderson, Dept. of Electrical & Electronic Engr., Royal Military College of Science, Shrivenham, Swindon, Wilts, England 1-1
2. "Measurement of Various Microstrip Parameters," H. D. Weinschel, Physical Science Laboratory, New Mexico State University, Las Cruces 2-1
3. "Microstrip Antenna Developments," John L. Kerr, U. S. Army Combat Surveillance and Target Acquisition Laboratory, Fort Monmouth, New Jersey 3-1
4. "Mutual Coupling between Microstrip Antennas," R. P. Jedlicka and K. R. Carver, Physical Science Laboratory, New Mexico State University, Las Cruces 4-1
5. "Some Conformal, Printed Circuit Antenna Designs," D. H. Schaubert and F. G. Farrar, Harry Diamond Laboratories, U. S. Army ERADCOM, Adelphi, Maryland 5-1
6. "Microstrip Antennas, Experimental Results," C. M. Kaloi, Pacific Missile Test Center, Point Mugu, California . . 6-1

III. MICROSTRIP ANTENNA THEORY, I (1:20 - 5:00), Chairman: C. L. Walter,
Electroscience Laboratory, The Ohio State University,
Columbus, Ohio

1. "Practical Analytical Techniques for the Microstrip Antenna," K. R. Carver, Physical Science Laboratory, New Mexico State University, Las Cruces 7-1
2. "Theory & Applications for Microstrip Antennas," W. F. Richards, Y. T. Lo, P. Simon & D. D. Harrison, Electromagnetics Laboratory, University of Illinois, Urbana 8-1
3. "Microstrip Analysis Technique," E. H. Newman & P. Tulyathan, Electroscience Laboratory, The Ohio State University, Columbus, 9-1
4. "A High Frequency Analysis Method for Open Microstrip Structures," T. Itoh, Dept. of Electrical Engr., The Univ. of Texas at Austin, & W. Menzel, Hochfrequenztechnik, AEG-Telefunken, Ulm, W. Germany 10-1
5. "Theoretical Investigations of Microstrip Antennas," A. R. Van de Capelle, K.U.L., Dept. of Electrical Engineering, Division Microwaves and Lasers, Leuven, Heverlee, Belgium 11-1
6. "Cavity Model of the Rectangular Microstrip Antenna," A. G. Derneryd, Telefon AB L M Ericsson, MI-Division, Moelndal, Sweden & A. G. Lind, Chalmers Univ. of Technology, Div. of Network Theory, Gothenburg, Sweden 12-1
7. "Analysis of a Coax-Fed Circular Microstrip Antenna," C. M. Butler, Dept. of Electrical Engineering, University of Mississippi, University, MS 13-1
8. "Theoretical Analysis of Printed-Circuit Antennas," L. C. Shen and S. A. Long, Dept. of Electrical Engineering, University of Houston, Houston, Texas 14-1

THURSDAY, OCTOBER 18, 1979

IV. MICROSTRIP ANTENNA ARRAYS (8:15 - 11:30), Chairman: R. E. Munson,
Ball Aerospace Systems Division, Boulder, Colorado

1. "An Extremely Lightweight Fuselage-Integrated Phased Array for Airborne Applications," J. S. Yee and W. J. Furlong, The Boeing Aerospace Co., Seattle, Washington 15-1
2. "Pattern Synthesis for Conformal Array," M. A. Huisjen, Ball Aerospace Systems Division, Boulder, Colo. and Lt. C. Nelson, Eglin AFB, Florida 16-1

3. "An Electrically Small Microstrip Dipole Planar Array," D. A. Huebner, Hughes Aircraft Co., Advanced Missile Systems Division, Canoga Park, California 17-1
4. "SEASAT and SIR-A Microstrip Antennas," L. R. Murphy, Ball Aerospace Systems Division, Boulder, Colorado . . 18-1
5. "A 7.5 GHz Microstrip Phased Array for Aircraft to Satellite Communications," F. W. Cipolla, Ball Aerospace Systems Division, Boulder, Colorado 19-1
6. "Microstrip Series Arrays," T. Metzler, Ball Aerospace Systems Division, Boulder, Colorado 20-1
7. "Printed Circuit Colinear Array," G. G. Sanford, Ball Aerospace Systems Division, Boulder, Colorado 21-1

V. PRINTED CIRCUIT ANTENNA SYSTEMS & MATERIALS (12:45 - 3:00), Chairman: Al Waterman, Physical Science Laboratory, New Mexico State University, Las Cruces, New Mexico

1. "Printed Circuit Antennas for Solving Various Instrumentation Problems," R. E. Wilton, Sounding Rocket Branch, Air Force Geophysical Laboratory, Hanscom AFB, Mass. . . . 22-1
2. "Stripline Antenna Development," A. Waterman, Physical Science Laboratory, New Mexico State University, Las Cruces, New Mexico 23-1
3. "UHF Coplanar-slot Antenna for Aircraft-to-Satellite Data Communications," R. W. Myhre, Communications Technology Branch, NASA Lewis Research Center, Cleveland, Ohio . . 24-1
4. "Variations on the Circular Microstrip Antenna Element," J. McIlvenna and N. Kernweis, Deputy for Electronic Technology, RADC/EEA, Hanscom AFB, Mass. 25-1
5. "Microwave Substrates Present and Future," T. E. Nowicki, 3M Electronic Products Division, St. Paul, Minnesota. . 26-1
6. "Clad Laminates of PTFE Composites for Microwave Antennas," G. R. Traut, Lurie Research & Development Center, Rogers Corporation, Rogers, Connecticut 27-1

FRIDAY, OCTOBER 19, 1979

VI. MICROSTRIP ANTENNA THEORY, II (8:15 - 10:30), Chairman: J. W. Mink, Army Research Office, Research Triangle Park, N. C.

VII. SUMMARY SESSION (10:30 - 12:00), Chairman: K. R. Carver, New Mexico State University, Physical Science Laboratory

PANEL MEMBERS

John Kerr, Ft. Monmouth, N. J.
Robert Maillicux, RADC, Hanscom AFB, Mass.
James Mink, Army Research Office, Durham, N. C.
Robert Munson, Ball Aerospace Systems Div., Boulder, Colo.
Daniel Schaubert, Harry Diamond Laboratories, Adelphi, Md.
Carlton Walter Ohio State University, Columbus, Ohio
Al Waterman, New Mexico State University, Las Cruces, NM

MICROSTRIP ANTENNA RESEARCH AT THE ROYAL MILITARY COLLEGE OF SCIENCE

J.R. JAMES, P.S. HALL, C. WOOD and A. HENDERSON
DEPARTMENT OF ELECTRICAL & ELECTRONIC ENG
ROYAL MILITARY COLLEGE OF SCIENCE, SHRIVENHAM,
SWINDON, WILTS, SN6 8LA ENGLAND

SUMMARY

The fundamental radiation mechanism occurring at an open-circuit discontinuity is initially discussed to reveal limitations on bandwidth, efficiency and sidelobe level control inherent in microstrip antennas. The presentation then summarises the performance that has actually been obtained from a wide variety of antenna types. These innovative designs include resonant and travelling wave arrays with integral triplate corporate feeds, frequency scanning arrays, variable polarisation arrays, very wideband circularly polarised elements, wideband integrated circuit elements and millimetre wave antennas. It is concluded that some improvement in performance can yet be obtained by increasing the precision of both the design methods and the manufacturing processes.

1.0 INTRODUCTION

In the past five years at RMCS we have considered many aspects of microstrip antennas and in this workshop paper an outline of our work is given. Our literature surveys [1] [2] on microstrip antennas have indicated a marked increase in worldwide research activity since about 1970 and particularly in the past two years. We do not intend to attempt to survey this literature here, particularly since a high proportion of the specialists are contributing to this workshop. It is interesting to note however that microstrip arrays were conceived as early as 1955 [3] and probably earlier references exist, yet viable devices did not appear until around 1970. The need for antennas that are compatible with integrated circuits and can be made conformal with missiles etc clearly provided an impetus to microstrip antenna development. Our initial studies [4], [5] commenced from the standpoint that an open-circuit termination could be

utilised as a radiating element and it was then evident that one way to overcome the intrinsic wave-trapping action of microstrip and release radiation in a controlled manner to create a designable array [6] [7] [8] [9] was the combine. Many other ideas were forthcoming but the sort of questions that were then becoming important concerned the choice of substrate material and geometry to achieve optimal performance e.g. efficiency, bandwidth and sidelobe level control. Detailed measurements and analysis [10] [11] [12] of an open circuit microstrip termination now give a good insight into these issues which are of fundamental importance to the designer.

2.0 RADIATION MECHANISM OF OPEN-CIRCUIT ELEMENT

Radiation takes place at a discontinuity in a microstrip line but even the simplest type of configuration presents profound analytical difficulties. The open-circuit termination Fig 1a has been analysed using a variational continuous mode matching technique and some degree of approximation [12]. The admittance Y seen by the quasi-TEM wave in the microstrip line at $z = 0$ is $G_r + G_s + jB$, Fig 1b where G_r and G_s are the conductance loading due to radiation loss and substrate surface waves and B is the susceptance due to evanescent fields. In static or quasi-static estimations only B is obtained by calculating the end capacity, commonly referred to as the end-effect $\Delta\ell = \{\text{arc tan } (BZ_m)\}/\beta_m$ where β_m and Z_m are the phase constant and impedance of the microstrip line respectively. The frequency dependence of Y is illustrated in Fig 2 where λ_0 , ϵ_0 and μ_0 are the free space wavelength, permittivity and permeability respectively. B is given by [12]

$$BZ_m = \frac{8}{h\omega\pi^2} \int_0^\infty \int_0^{\pi/2} \frac{f(A) \epsilon_r^{3/2} \mu_0 m k_y \gamma^2}{\cos(j\alpha) \epsilon_0 (gm \frac{\mu_0}{\epsilon_0} + |n|^2)} d\alpha dy \quad (1)$$

where $f(A)$ is comprised of $\frac{\sin x}{x}$ functions and m , g , n and $k_y \gamma$ are functions of α and γ . A similar integral relationship holds for G_r but this simplifies for h/λ_0 and $w_e/\lambda_0 \ll 1$ to

$$G_r Z_m \sim \frac{4\pi}{3} \left(\frac{h}{\lambda_0}\right) \left(\frac{w_e}{\lambda_0}\right) \frac{1}{(\epsilon_f)^{\frac{1}{2}}} \quad (2)$$

where w_e is the effective line width and ϵ_f the effective relative

permittivity. G_r and G_s are related by

$$\frac{G_r}{G_s} \sim \frac{\cos^2(k_{y2}h)\epsilon_r k_{y2}^2}{(\cos^2(k_{y2}h)\epsilon_r k_{y3}^2 + k_{y2}^2 h k_{y3})} \quad (3)$$

where k_{y2} and k_{y3} are eigenvalues. The components of \mathbf{Y} are in fact related by a transform pair [12], one of which is the Hilbert transform

$$B(\omega_1) = \frac{2\omega_1}{\pi} \int_0^\infty \frac{G(\omega) - G(\omega_1)}{\omega^2 - \omega_1^2} d\omega \quad (4)$$

where $G = G_r + G_s$ and $0 \leq \omega_1 \leq \infty$. At low frequency G_r is very small and G_s negligible (Fig 2) thus the termination is essentially an open circuit with end correction Δl ; any attempt to utilise the termination as a magnetic dipole antenna would result in a low radiation efficiency since the radiation loss will be comparable to the conductor loss of the line. At intermediate frequencies the efficiency increases with frequency but so does the ratio $(G_s/G_r) = S_L$ which means that a proportion of the incident line power is launched into the substrate and transported radially as a surface wave with nulls along the x-axis [12], [22]. The surface wave is a source of unwanted scattering and coupling within the printed assembly and S_L is a pessimistic measure of the degree of sidelobe control that can be exercised in a small array of elements. An example of the design curves that can be derived from these calculations is given in Fig 3 for a $\lambda/2$ microstrip resonator. The antenna efficiency n and Q factor Q_T are

$$n = \left(\frac{Q_c}{Q_c + Q_r} \right) \cdot 100\%; \frac{1}{Q_T} = \frac{1}{Q_c} + \frac{1}{Q_r} \quad (5)$$

where Q_c is based on typical conductor losses and Q_r is the radiation Q factor. These curves show the limitations imposed by the choice of substrate material. The required n and to some extent bandwidth sets the lower frequency of operation while S_L sets the upper frequency limit. A given substrate thus has a 'window' of frequencies over which useful antennas can be designed. The window can be translated in frequency by scaling h and w ; increasing ϵ_r narrows the window and the bandwidth obtainable but reduces S_L . The extension of these conclusions to large arrays of resonators appears to be reasonable for n and Q_T but the power launched into the

substrate will manifest itself as a leaky wave resulting in loss of pattern control at some angles. Existing analytical techniques for periodic structures are proving useful in this respect.

3.0 ANTENNA ARRAY STUDIES

The open-circuit terminations and appropriate feed arrangements are realised by connecting half-wavelength stubs to a central feeder. Neglecting radiation coupling and radiation from T junctions and steps, a network analysis [8] is used and the array manufactured using computer graphic and photo-etch methods. Both resonant and travelling-wave type arrays have been designed [8] and the photographic masks (not to scale) are shown in Fig 4 and Fig 5. A polyguide substrate with $\epsilon_r = 2.32$, $h = 0.794$ mm was found to give good design control at 17GHz and this is consistent with our more recent design data as in Fig 3. Even so over half the power is dissipated in the antenna due to both feeder losses and terminating loads. Fractional bandwidths of 0.4% and 3% were obtained for the resonant and travelling wave array respectively and sidelobe levels were typically 12 to 19dB. For many applications this performance is adequate and the arrays are very attractive low cost devices. Our aim however has been to push the performance to the limit and it was immediately apparent that both antennas were constrained by their microstrip corporate feeds which generate uncontrollable radiation. Continued research on the travelling wave antenna and a detailed analysis of a triplate corporate feed Fig 6, [13], [14] have produced the state-of-the-art performance summarised in Fig 7 with sidelobe levels 5-12dB better than the pessimistic limit of $S_L = -15$ dB and further improvements in this and the bandwidth (now 7%) will be obtained by tightening up the electrical and mechanical tolerances and including second order effects in the analysis. Tolerance effects are particularly important at higher frequencies but experiments [18] at 35GHz and 70GHz confirm that the performance of a scaled down version of the array using $h = 0.25$ mm is not noticeably impaired by these effects. Apart from the increased line loss, microstrip antennas may well be viable at 94GHz or higher. A frequency scanning array has been created by placing a thin slot in the stub elements of a combline [17] giving a beam scan of $\pm 8.5^\circ$ over a bandwidth of $\pm 2.5\%$ at 17GHz with sidelobe levels around -10dB. In the 'rampart' line Fig 8 mitred corners are taken as radiating

elements and with appropriate spacing [15] [16] three types of polarisation can be obtained. Performance figures so far are encouraging [15].

4.0 NOVEL WIDEBAND ELEMENT TECHNIQUES

Many useful narrow-band antennas can be created from resonant circular or rectangular patch antennas. A circularly polarised array of square patches Fig 10 has a bandwidth of 3% (7%) at 10.7GHz and 3dB (6dB) ellipticity. Other novel narrowband patch types having low angle radiation are under development [23]. A growing requirement is to integrate the microstrip antenna with printed circuits and active devices but this leads to a conflicting specification for the substrate material and thickness as Fig 3 indicates. We solve this by fixing sandwiches of polyguide resonators on an alumina substrate [19] [20]. Successful circularly polarised integrated packages Fig 11 have been built in this way having up to 16 times more bandwidth than that permitted by the alumina substrate alone, at the expense of some increase in the height of the assembly. To obtain a wide bandwidth with a single layer substrate assembly the resonator action must be avoided and a travelling-wave system has been adopted, based on spirals. The configurations of Fig 12 have been analysed and measured with good agreement [21] and the loss of radiation along a curved line predicted Fig 13. It is established that large spirals as in Fig 12a do not give good ellipticity results whereas the circular and curved line segment type Fig 12b and c respectively are viable antennas, Fig 14. The efficiency is dictated by the terminating load which is either connected from the rear of the substrate or a carbon track on the surface.

5.0 CONCLUSIONS

Analysis of the wave trapping behaviour of a microstrip open circuit line and the surrounding substrate reveals a window in the frequency range over which useful resonator microstrip antennas can be effectively designed. An investigation of numerous practical antennas and arrays confirms the overall limitations predicted by the fundamental studies but also indicates that greater design precision and tighter manufacturing tolerances can still yield improved performances. It is also apparent from the novel configurations presented that bandwidth, efficiency and aperture control can be traded against one another to a large extent; there is thus much scope for

innovative special purpose designs as evidenced by recent developments [24].

6.0 ACKNOWLEDGEMENTS

We thank Dr G.N. Taylor RSRE Malvern, Mr M. Sidford RAE Farnborough and SRC (UK) for continued support and encouragement.

7.0 REFERENCES

1. Hall, P.S. and James, J.R., Survey of design techniques for flat profile microwave antennas and arrays, Rad. and Electron Eng. Nov 1978 Vol 48 pp 549-565.
2. James, J.R., Hall, P.S. and Wood, C., Microstrip antennas, IEE Monograph (in preparation).
3. Gutton, H. and Baissinot, G., Flat aerial for ultra high frequencies, French Patent No 703113, 1955.
4. James, J.R. and Ladbroke, P.H., Surface wave phenomenon associated with open-circuited stripline terminations, Electron Lett., 1973, 9, pp 570-571.
5. James, J.R. and Wilson, G.J., Radiation characteristics of stripline antennas, Proc 4th Eur. Mic. Conf., Montreux, Sept 1974, pp 484-488.
6. James, J.R. and Wilson, G.J., New design techniques for microstrip antenna array, Proc 5th Eur. Mic. Conf., Hamburg, Sept 1975, pp 102-106.
7. James, J.R. and Wilson, G.J., Microstrip antennas and arrays, Pt 1 Fundamental action and limitations, IEE Jour MOA, Sept 1977, 1, pp 165-174.
8. James, J.R. and Hall, P.S., Microstrip antennas and arrays, Pt II New array-design techniques, IEE Jour. MOA, Sept 1977, 1, pp 175-181.
9. James, J.R. and Wilson, G.J., Combline antenna, UK Patent App. No 6691/75, 1975.
10. Wood, C., Hall, P.S. and James, J.R., Radiation conductance of open-circuit low dielectric constant microstrip, Electron. Lett, 1978, 14, pp 121-123.
11. Henderson, A. and James, J.R., Continuous eigenvalue mode spectrum analysis of microstrip open-circuit terminations, Proc. 8th Eur. Mic. Conf., Paris, 1978, pp 89-93.
12. James, J.R. and Henderson, A., High frequency behaviour of microstrip open-circuit terminations, IEE Jour. MOA, To be published Autumn 1979.

- *13. Hall, P.S. and James, J.R., Microstrip array antennas, Final report on Res. Agreement AT/2160/033RL, Dec 1978, 157 pages.
- 14. Hall, P.S. and James, J.R., Analysis and design of triplate corporate feeds at high frequencies, Proc. 9th Eur. Mic. Conf., Brighton, 1979.
- 15. Wood, C., Hall, P.S. and James, J.R., Design of wideband circularly polarised microstrip antennas and arrays, Proc IEE Int. Conf. on Ant. and Prop., London, Nov 1978, pp 312-316.
- 16. Hall, P.S., Rampart line antenna, UK Pat. App. No. 29460/78, 1978.
- 17. Aitken, J.E., Hall, P.S. and James, J.R., Swept frequency scanned antenna, UK Pat. App. No. 21195/78 (related to 6691/75), 1978.
- 18. Hall, P.S., Garrett, C., and James, J.R., Feasibility of designing millimetre wave microstrip planar antennas, Proc. AGARD Conf. on Millimetre and submillimetre wave Prop. and Cir., Munich, Sept 1978.
- 19. Hall, P.S., Wood, C., and Garrett, C., Wide bandwidth microstrip antennas for circuit integration, Electron Lett, July 1979.
- 20. Hall, P.S. and Wood, C., Wide band integrated antenna element, UK Pat. App. No. 7908621, 1979.
- 21. Wood, C., Curved microstrip lines as compact wideband circularly polarised antennas, IEE Jour. MOA, Jan 1^o79, pp 5-13.
- 22. James, J.R., and Ladbrooke, P.H., Surface wave inhibition, UK Pat. No. 1442383, 1973.
- *23. Wood, C. and James, J.R., Study of printed circuit antennas for aircraft radio systems, Prog. Reps on Res. Agreement D/DRLS/5/33/9 1978-1979.
- 24. Flat-Plate Antennas, Symposium 23rd May 1978, RSRE Malvern, England. (Chairman J.R. James Sec.G.N. Taylor) Sponsored by MOD(UK), Electronic Research Council.

*Internal Ministry of Defence Report.

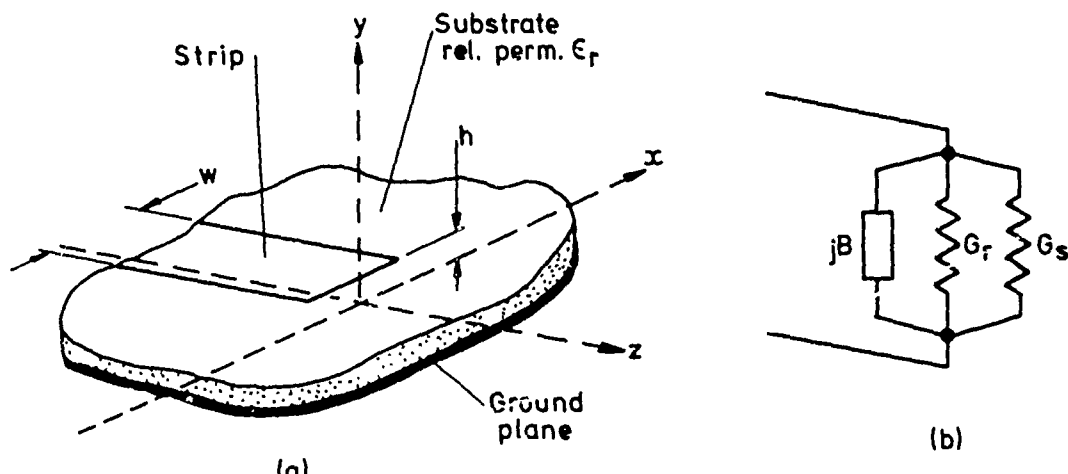


Fig. 1 OPEN - CIRCUIT MICROSTRIP TERMINATION

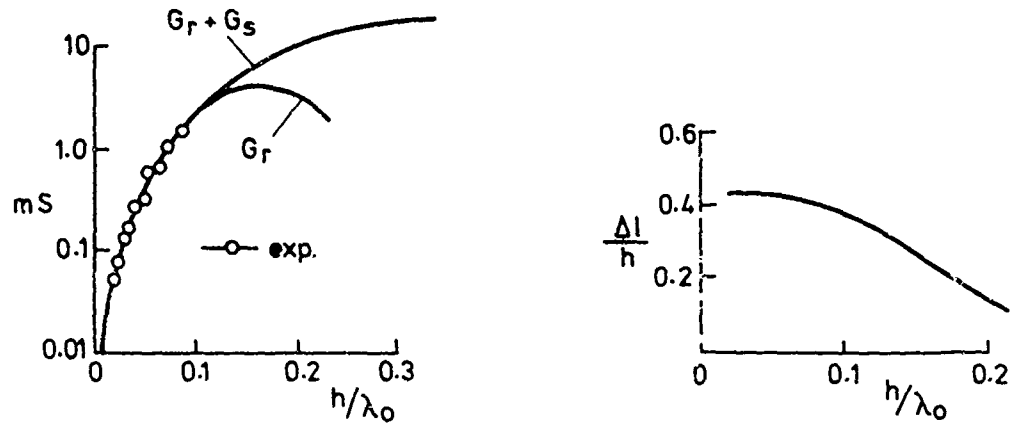


Fig. 2 ADMITTANCE FOR $w = 1.79h$, $\epsilon_r = 2.32$

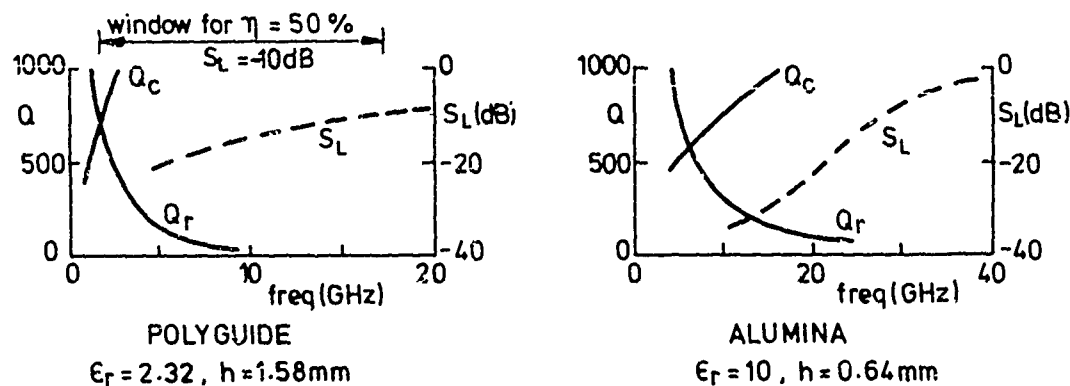


Fig. 3 DESIGN DATA FOR $\lambda_0/2$ RESONATOR ANTENNA $w \approx 1.79h$

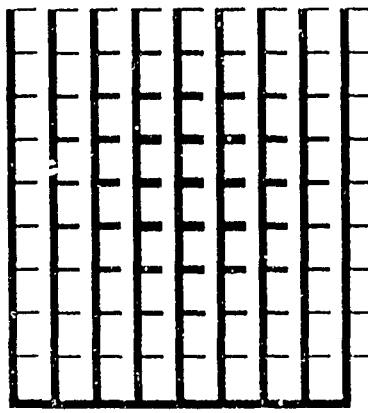


Fig.4 RESONANT ARRAY

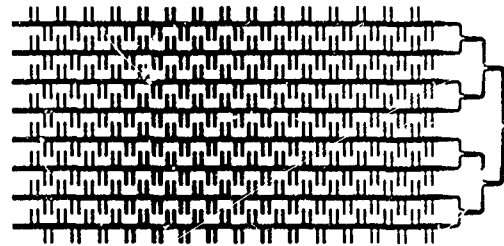


Fig.5 TRAVELLING - WAVE ARRAY

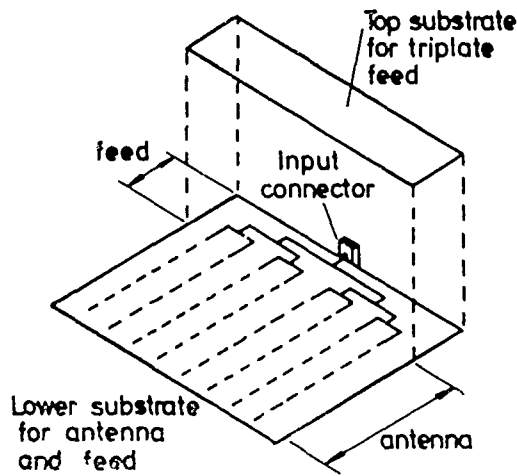


Fig.6 TRIPLET CORPORATE FEED

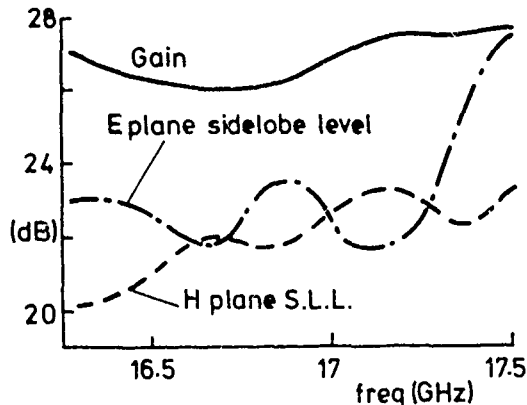


Fig.7 TYPICAL ARRAY PERFORMANCE

Efficiency = 22% Squint 0°-8°
VSWR = 1.5 : 1 Cross pol <-23dB

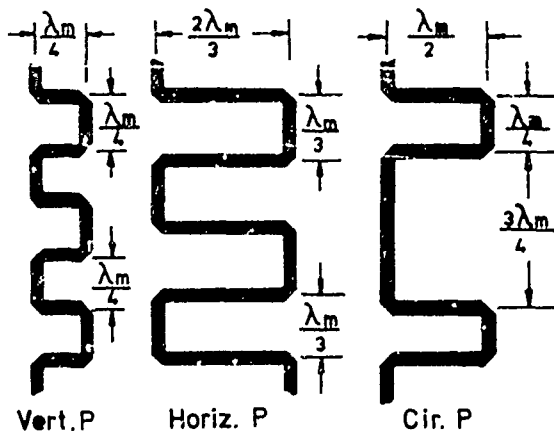


Fig.8 TYPES OF RAMPART LINE AND POLARISATION



Fig.9 MODIFIED COMBINER FOR FREQUENCY SCANNED ARRAY

MEASUREMENTS OF VARIOUS MICROSTRIP PARAMETERS

HENRY D. WEINSCHEL
PHYSICAL SCIENCE LABORATORY
NEW MEXICO STATE UNIVERSITY
LAS CRUCES, NEW MEXICO 88003

SUMMARY

The data presented in this paper is the result of a large number of impedance measurements on a rectangular microstrip antenna with a notched feed. It is presented in a form that should be of some aid in designing a microstrip antenna with a microstrip line feed. It is also shown to what extent the results from theoretically developed equations for the probe fed antenna can be applied to the line fed antenna. It appears that the equations would result in very good approximations if the S dimension is small.

The two primary parameters to be considered for the antenna design are the short side H of the rectangle to obtaining the desired resonant frequency and the depth N of the notch to obtain the desired input impedance. The long side W of the rectangle is not a primary impedance or frequency parameter but does effect the bandwidth and radiation resistance of the antenna. It was not possible to include that aspect of the antenna design in this paper. A reasonable dimension for W is approximately 0.9 of a wavelength in the dielectric.

1.0 INTRODUCTION

To aid in the design of rectangular microstrip antennas a large number of impedance measurements were made by Mr. Robert Lanphere at the Physical Science Laboratory. The measurements included variations of the patch dimensions and driving point positions. The data was then processed to obtain design curves and when possible the curves were compared with theoretical values calculated from the equations developed by Dr. Keith Carver.

2.0 GENERAL DESCRIPTION OF THE ANTENNAS

The microstrip patches were photoetched on printed circuit board K-6098 TYPE GT fabricated by the 3M Company. The boards consisted of a teflon/glass dielectric between two sheets of one mill thick copper which are bonded to the dielectric. According to the manufacturers specification the dielectric constant of the substrate generally varies between 2.45 and 2.55, but could be as high as 2.8.

The dimensions of the antenna were such that it would resonate in the S-Band region. The antenna and the nomenclature of the parameters are shown in Figure 1. All of the parameters were varied except the substrate thickness T which was constant at 0.152 cm (.060 inches).

The width of the feed line of length N was 0.32 cm (0.126 inches) which corresponds to a nominal 50 ohms characteristics impedance

3.0 OVERVIEW OF THE MEASUREMENTS

Five antenna parameters were varied. Impedance versus frequency curves were obtained for each configuration. These impedances were always measured at the edge of the rectangle as shown by the location of the feed connector in Figure 1. The reference short for the impedance measurements coincides with the top of the ground plane of the antenna.

For $N \neq 0$ the impedances were calculated at the driving point at the antenna which is displaced from the antenna edge by the length N , the depth of the notch.

The short side H of the antenna rectangle was varied from 3.81 cm (1.5 inches) to 4.572 cm (1.8 inches) in 0.254 cm (0.1 inches) increments. The long side W of the rectangle was varied from 3.048 cm (1.2 inches) to 6.858 cm (2.7 inches) in unequal increments and for two different values of N . The spacing S between the feed line and the antenna element was varied from 0.38 to 0.787 cm (0.015 to 0.310 inches) and the length of the notch N was varied from 0 to 1.257 cm (0 to 0.495 inches). The displacement D of the feed from the center line of the rectangle was varied from 0 to 2.553 cm (0 to 1.005 inches).

4.0 DISCUSSION OF THE INDIVIDUAL PARAMETERS

4.1 VARIATION OF THE SHORT SIDE H OF THE RECTANGLE

The dimension H was varied from 3.81 to 4.572 cm (1.5 to 1.8 inches) in 0.254 cm (0.1 inches) increments. The other dimensions were

$$W = 6.934 \text{ cm (2.73 in.)}$$

$$N = 0.762 \text{ cm (0.3 in.)}$$

$$S = 0.320 \text{ cm (0.126 in.)}$$

$$T = 0.152 \text{ cm (0.060 in.)}$$

$$D = 1/2 W, \text{ i.e., on the center line}$$

The H dimension is a primary frequency parameter as is illustrated in Figure 2. The 0.762 cm (0.3 inches) variation resulted in a 350 MHz frequency shift. Since the other dimensions were held constant, they varied in terms of wavelength and since the resonant frequency depends also on W the effect of its change is superimposed on the effect of the H variation. For example, when the dimensions are expressed in terms of wavelengths for H = 3.810 cm (1.5 inches), $f_0 = 2.4$. If ϵ is 2.456 then $H/\lambda_{0\epsilon} = 0.478$ and $W/\lambda_{0\epsilon} = 0.870$. For H = 4.572 cm (1.8 inches), $f_0 = 2.05$ GHz and $H/\lambda_{0\epsilon} = 0.490$ and $W/\lambda_{0\epsilon} = 0.743$. So that in terms of wavelengths W was decreased which would result in an increase of the resonant frequency as illustrated in Figure 4. The approximate increase is about 22 MHz which closely approximates the difference between the calculated and the measured value in Figure 2. The difficulty in calculating the antenna dimensions is in knowing the dielectric constant to three or preferably four significant figures. In the example above the dielectric constant was obtained by iterating the calculations until agreement was obtained between the calculated and the measured resonant frequency for a particular antenna and that dielectric constant was then used to calculate the resonant frequencies as a function of the H dimension.

The agreement between the calculated resonant resistances and the measured values is not as close as the one for the resonant frequencies. The curves are shown in Figure 3. It should be pointed out that the

theoretical derivations were developed by Dr. Carver for probe fed antennas and no attempt was made to include the effect of the notch. The calculated and measured impedances agree very well for probe fed antennas [1].

4.2 VARIATION OF THE LONG SIDE W OF THE RECTANGLE

The dimension W was varied from 3.81 to 6.858 cm (1.5 to 2.7 inches) with the other dimensions having the constant values listed below

$$H = 4.140 \text{ cm (1.63 in.)}$$

$$N = 0.762 \text{ cm (0.3 in.)}$$

$$S = 0.320 \text{ cm (0.126 in.)}$$

$$T = 0.152 \text{ cm (0.060 in.)}$$

$$D = 1/2 W, \text{ i.e., the feed on the center line}$$

The frequency and impedance dependence on the width are illustrated in Figures 4 and 5. A comparison of the curves in Figures 2 and 4 show that the H is a much more effective parameter for varying the resonant frequency than W. In the frequency range under discussion

$$\frac{\Delta f_0}{\Delta H} = 459 \text{ MHz/cm (1167 MHz/inch)}$$

and

$$\frac{\Delta f_0}{\Delta W} = 21 \text{ MHz/cm (55 MHz/inch)}$$

The resonant resistances vary more nearly at the same rate

$$\frac{\Delta R_0}{\Delta H} = 67 \text{ ohms/cm (170 ohms/inch)}$$

$$\frac{\Delta R_0}{\Delta W} = 50 \text{ ohms/cm (128 ohms/inch)}$$

The calculated and measured values do not agree very well for the resonant frequencies but agree quite well for the resonant resistances.

Again, this may be caused by the perturbation due to the notch which is not included in the calculations.

4.3 VARIATION OF THE NOTCH DEPTH N

The notch depth, i.e., the driving point location of the antenna has been most convenient to obtain the desired input impedance to the antenna. One can obtain a large impedance variation without a similarly large change in the resonant frequency.

$$\frac{\Delta R_0}{\Delta N} = 68 \text{ ohms/cm (173 ohms/inch)}$$

The frequency variation is shown in Figure 6. The curve is not monotonic and the frequency variation is about 23 MHz.

4.4 VARIATION OF THE SPACING S

The variation of S varies both the resonant frequency and impedance. The results are illustrated in Figures 8 and 9. The interesting part of the curve is that as S approaches zero the resonant frequency approaches the calculated resonant frequency of a probe fed antenna. A similar result can be seen in Figure 9 where the measured impedance approaches the calculated impedance as S approaches zero.

4.5 VARIATION OF THE DISPLACEMENT D

Displacing the feed from the center along the long edge of the rectangle has very little effect on either the resonant frequency or the impedance. No curves are presented for this parameter variation.

5.0 REMARKS ABOUT THE DETERMINATION OF THE RESONANT FREQUENCY

The resonant frequency was not defined as the frequency for which the reactive component of impedance is zero. The frequency was found as follows. The impedance versus frequency curve was plotted on a Smith chart. The center of the circle that most closely approximated the impedance curve was found graphically. The resonant frequency was then defined by the point on the impedance curve where the reactance curve that coincides with the center of the circle crosses the impedance curve.

This method gives a unique definition for resonant frequency even though the impedance curve may cross the real axis at more than one location.

6.0 REFERENCES

1. Carver, K. R. and E. L. Coffey, "Theoretical Investigation of the Microstrip Antenna", New Mexico State University, Physical Science Laboratory, Technical Report PT-00929, January 23, 1979.

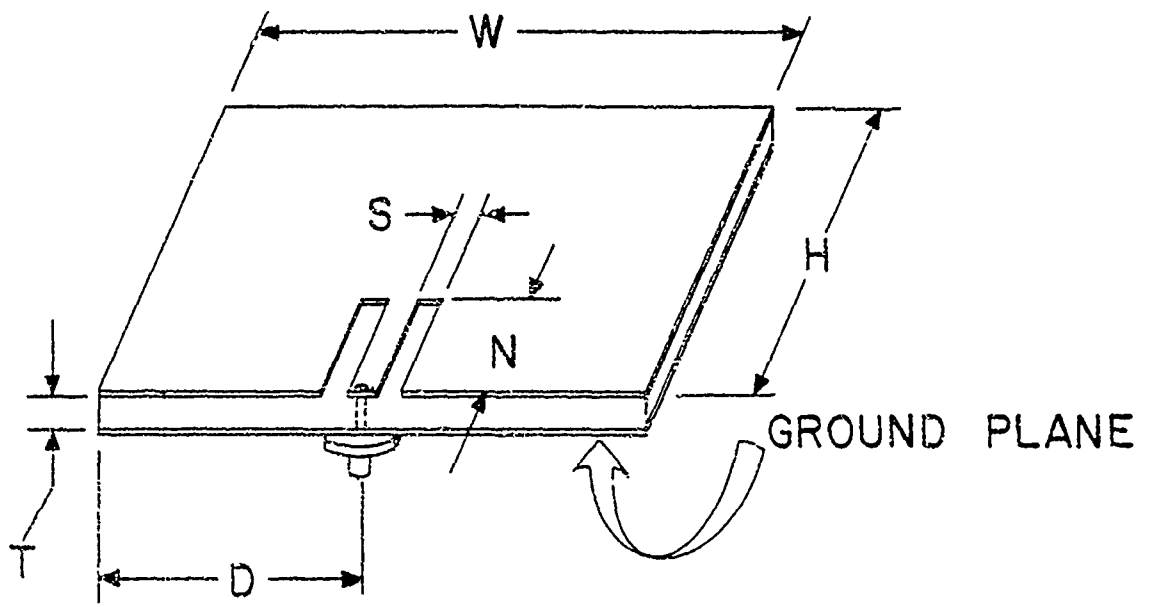


Fig. 1. Sketch of the antenna showing the various parameters.

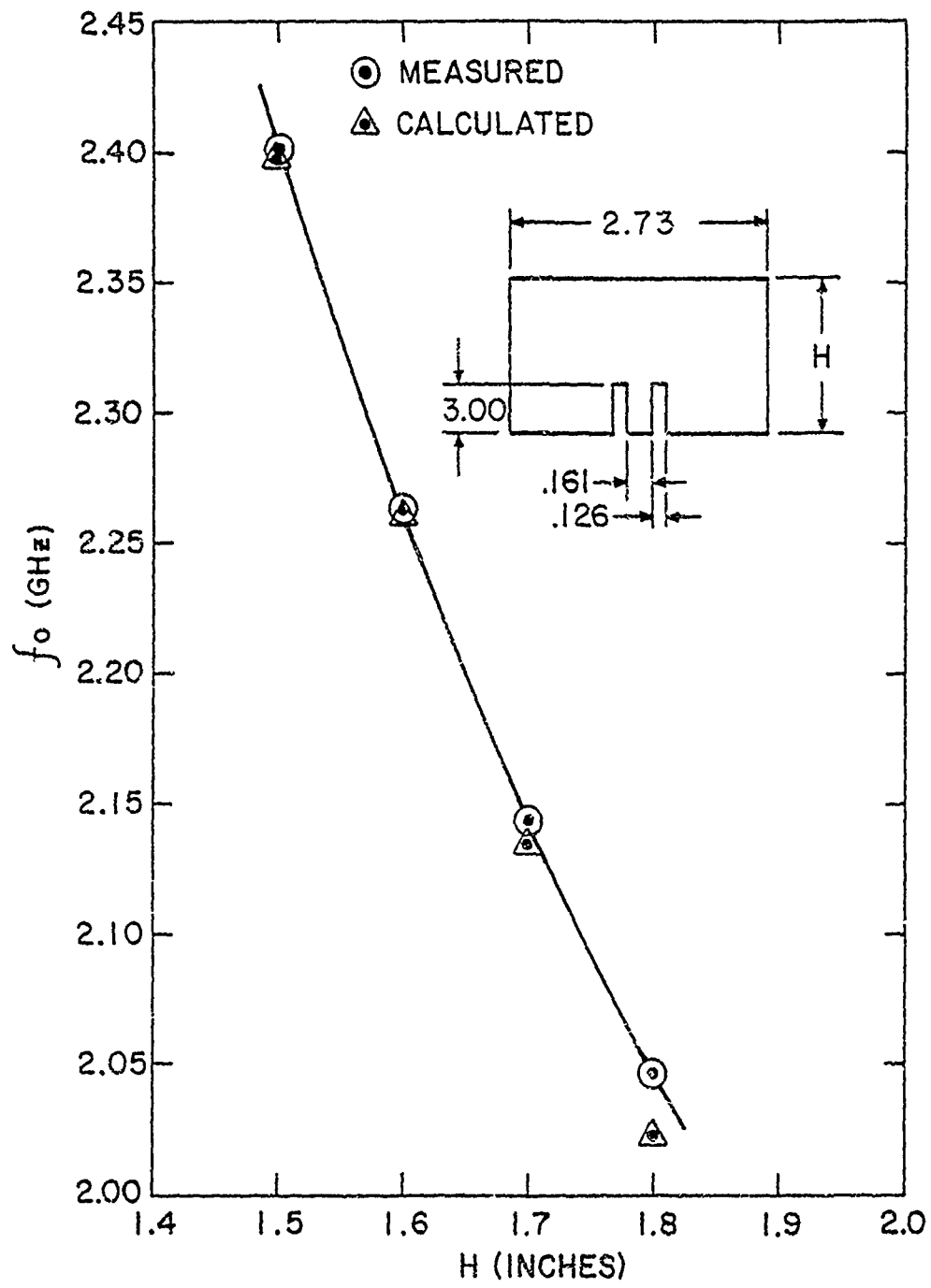


Fig. 2. Resonant frequency versus height curve. The values were calculated for a probe fed antenna with $\epsilon = 2.456$.

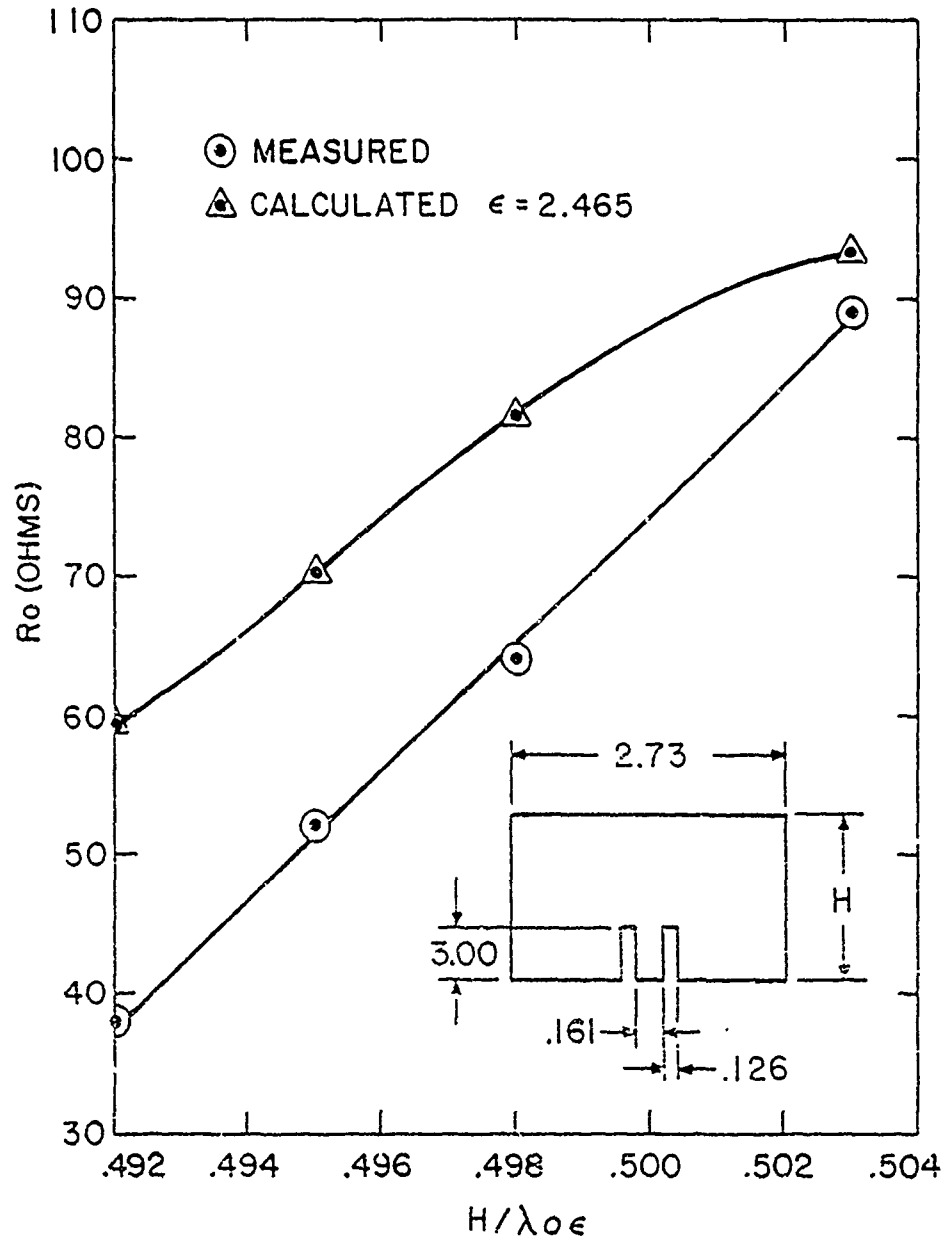


Fig. 3. Resonant resistance versus height curve. The values were calculated for a probe fed antenna with $\epsilon = 2.456$.

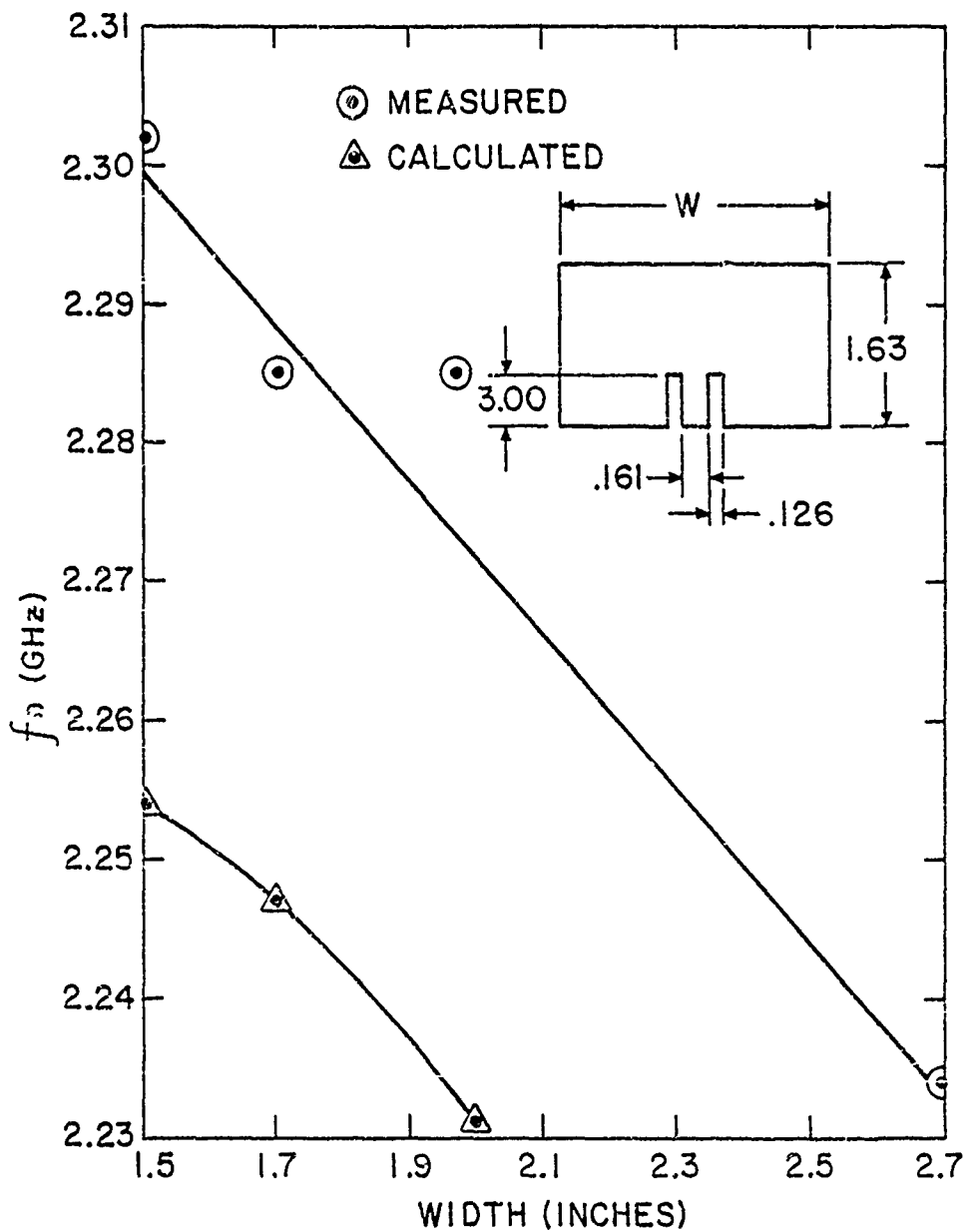


Fig. 4. Resonant frequency versus width curve. The values were calculated for a probe fed antenna with $\epsilon = 2.456$.

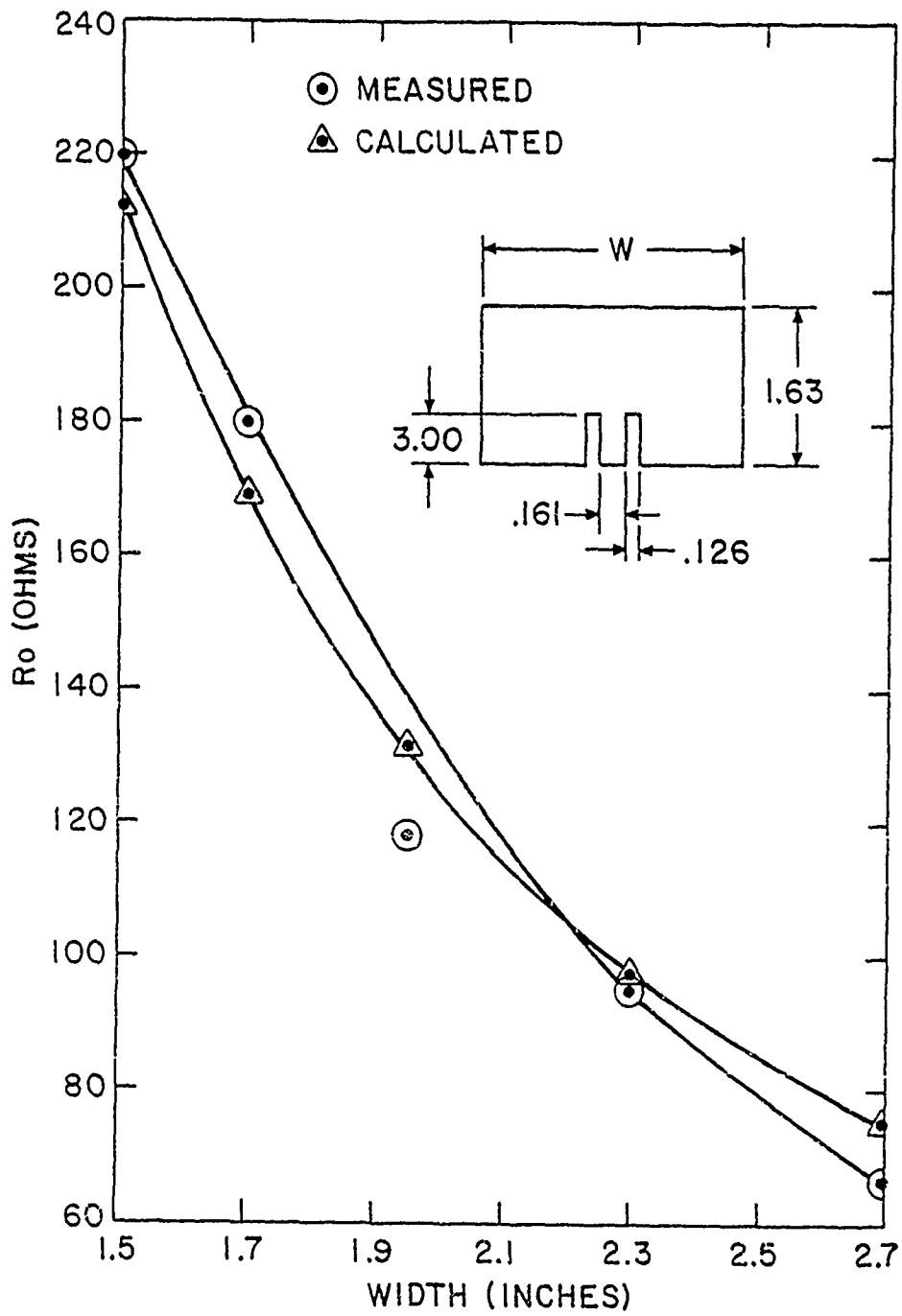


Fig. 5. Resonant resistance versus width curve. The values were calculated for a probe fed antenna with $\epsilon = 2.456$.

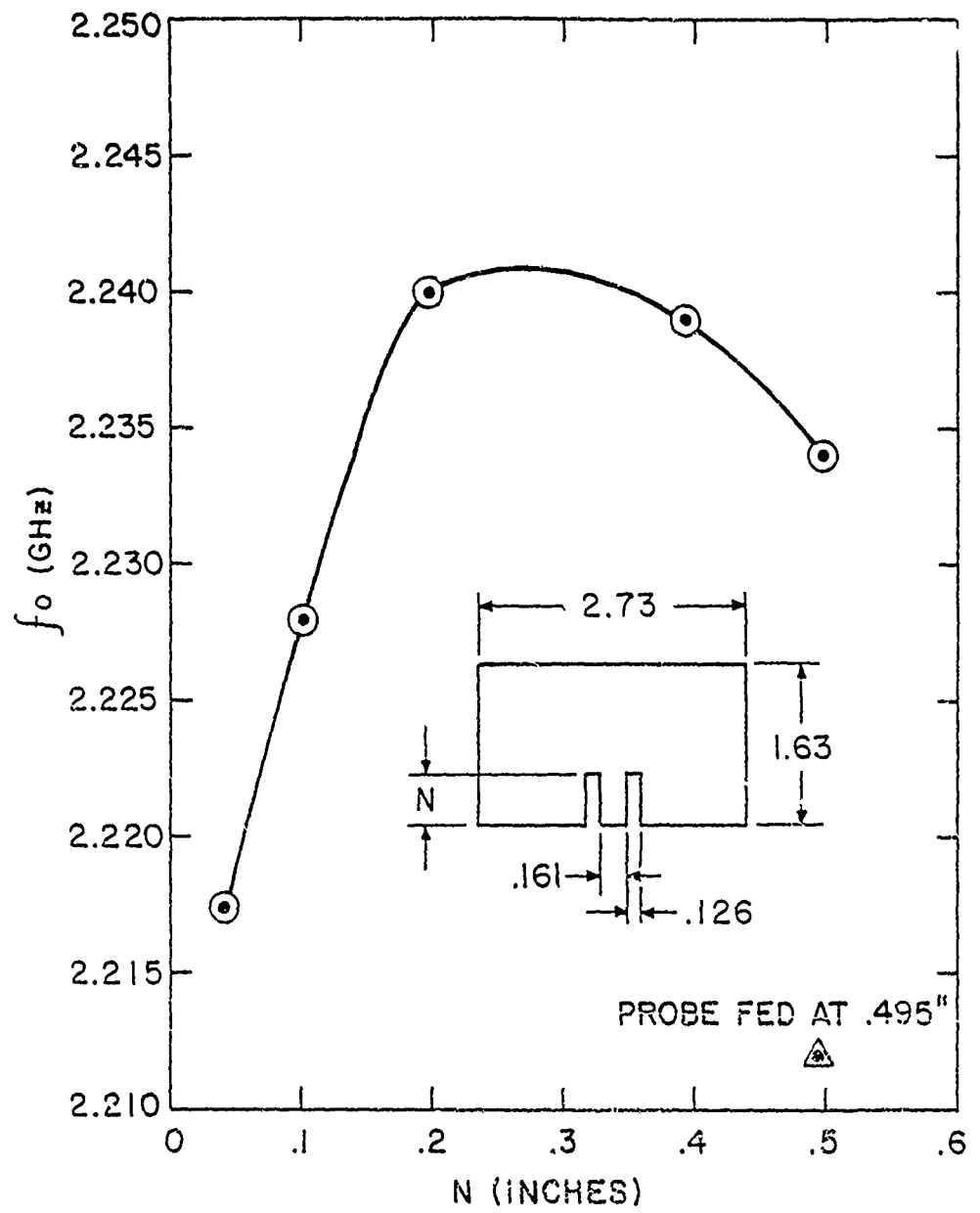


Fig. 6. Resonant frequency versus notch depth curve. The measured value for a probe fed antenna is shown in the lower right hand corner.

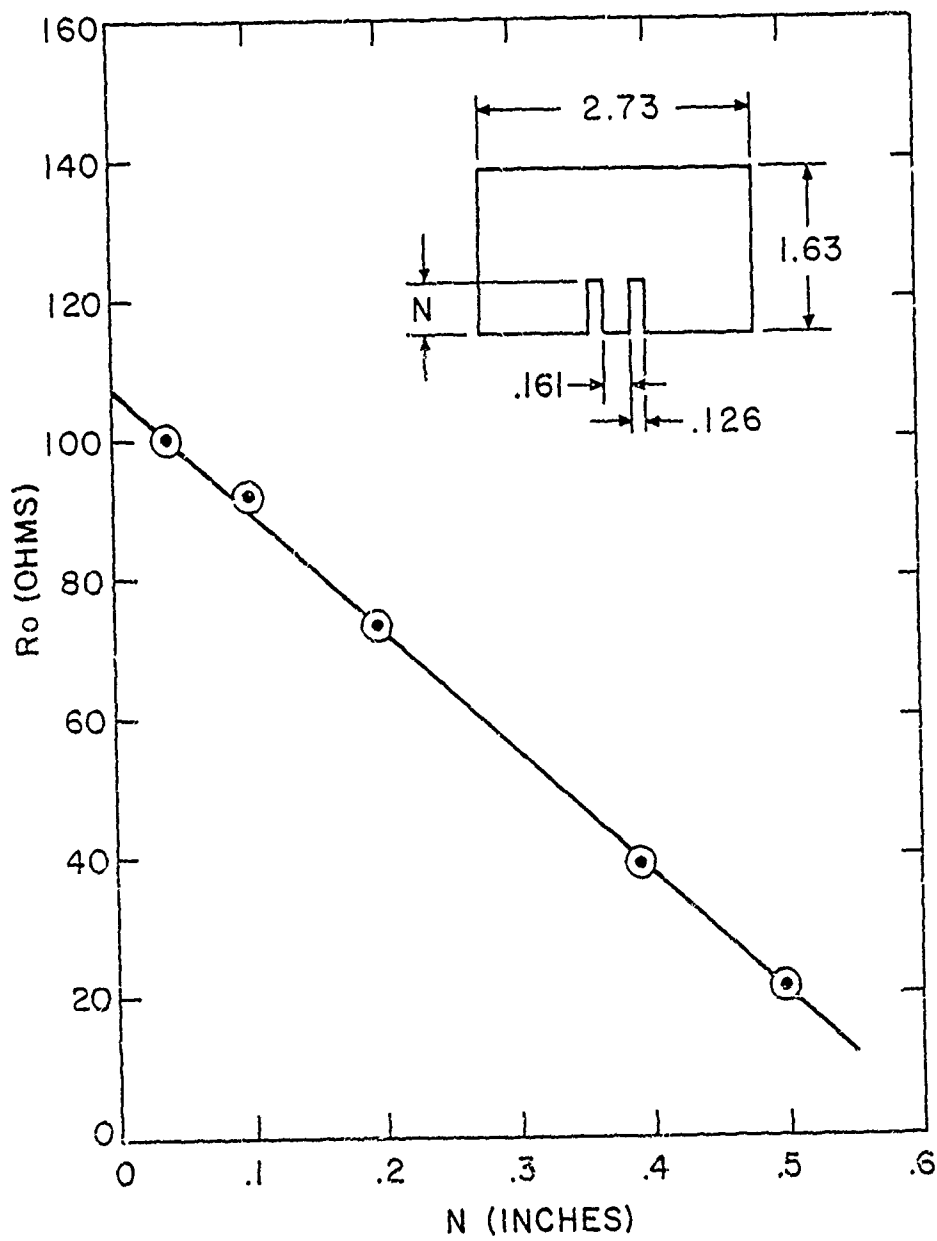


Fig. 7. Resonant resistance versus notch depth curve.

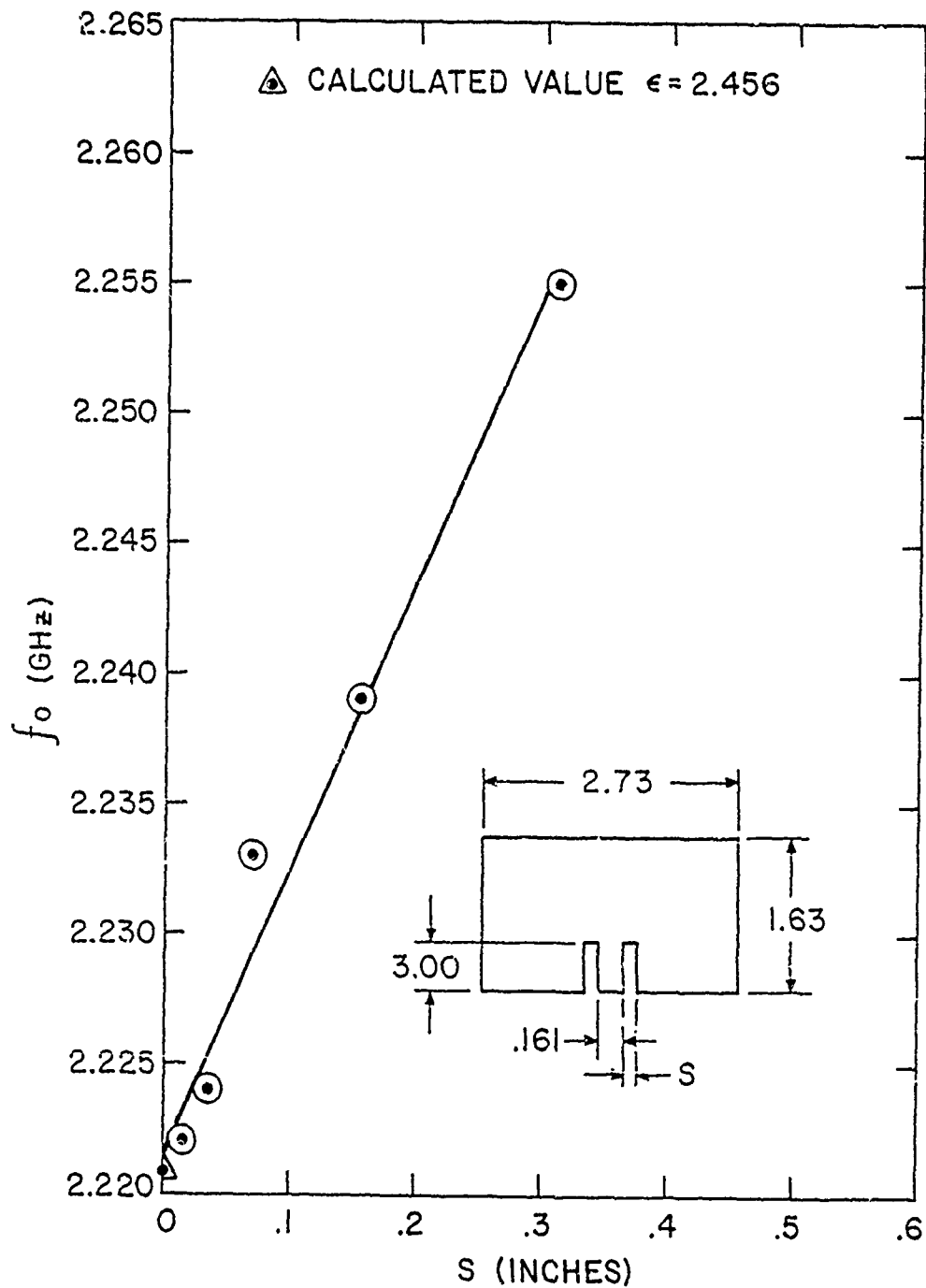


Fig. 8. Resonant frequency versus spacing curve. The calculated value for a probe fed antenna is shown in the lower left hand corner.

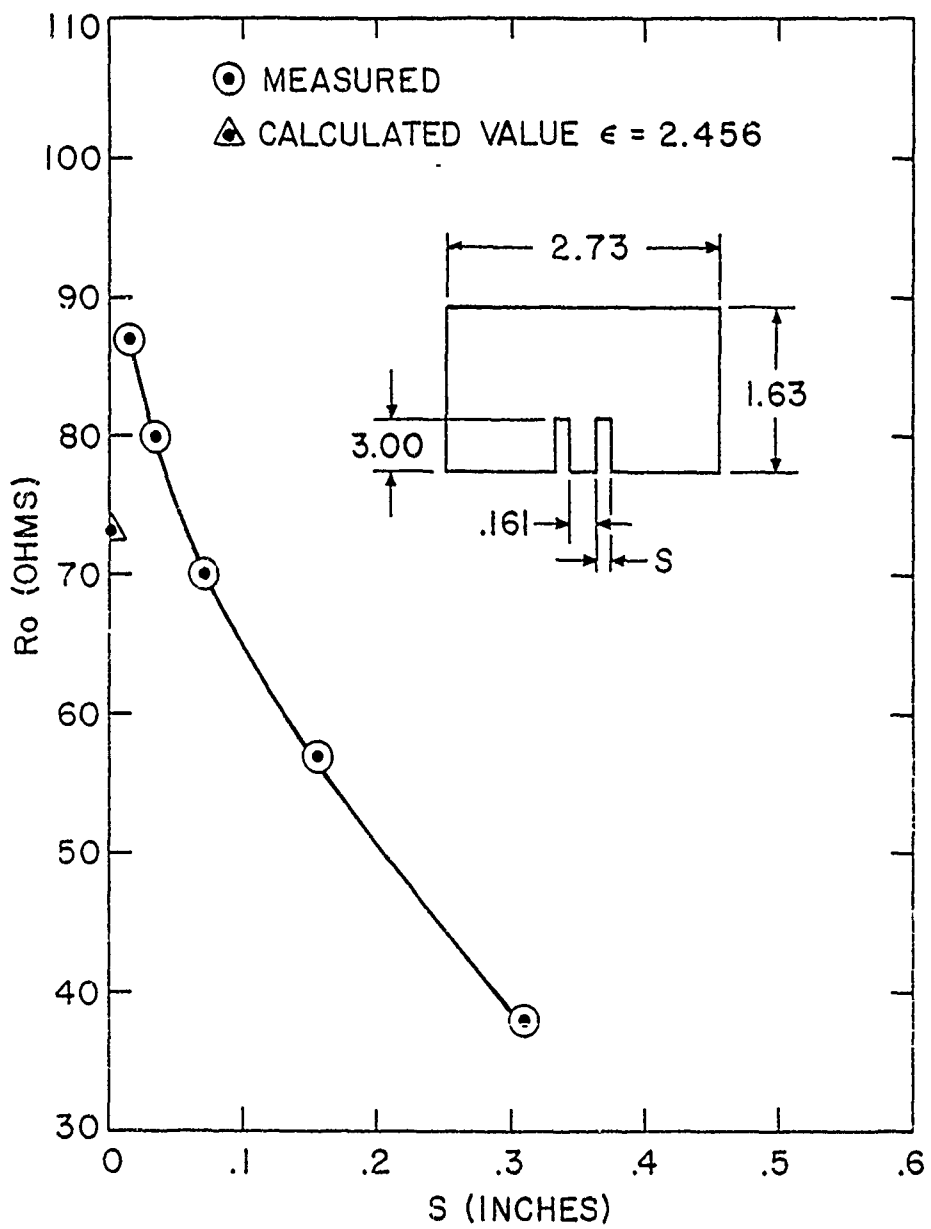


Fig. 9. Resonant resistance versus spacing. The calculated value for a probe fed antenna is shown at the center of the left hand side.

MICROSTRIP ANTENNA DEVELOPMENTS

JOHN L. KERR
US ARMY COMBAT SURVEILLANCE AND
TARGET ACQUISITION LABORATORY
DELCS-R-M
FORT MONMOUTH, NJ 07703

SUMMARY

The properties of the microstrip radiator as a feed element for various applications are evaluated. As a feed for parabolic reflectors, the small size of the microstrip element leads to good performance in reflectors which are on the order of half or less the size normally required for typical feeds. Both single and dual frequency versions are described. It is also shown that the microstrip radiator serves as a very simple, low cost, efficient feed for parasitic arrays.

A new method for generating circular polarization in microstrip antennas is presented. The technique uses symmetrical radiators and a single central feed the same as is commonly used on linearly polarized elements. In addition, the element size is always smaller than the linearly polarized counterpart.

Finally, a terminated version of the microstrip radiator is discussed. Results show that the usefulness of a given element can be increased by providing for frequency diversity in several different ways.

1.0 INTRODUCTION

The developments presented in this paper got under way in response to a need for a very small, simple, low cost L and radiator which could readily be added on to an existing 1.22m parabolic reflector with an X-band shepherd's crook feed. The feed was required to be exceptionally small since the reflector is only 5λ in diameter at 1250 MHz. L-band radiators and dual frequency feeds are, typically, none of the above so that a new approach was required. The properties of the microstrip radiator [1] [2] appeared to be appropriate provided that a hole could be cut through the center of the circuit board large enough to provide an opening through which the X-band feed horn might radiate. An experimental evaluation of the effects of providing such an opening through a microstrip radiator and the performance as part of a dual frequency feed was initiated.

2.0 EXPERIMENTAL RESULTS

The initial experiment consisted of removing a 2.54 cm square patch of metal from the center of the radiator side of a conventional rectangular microstrip antenna, followed by removal of the substrate and the metal of the ground plane side in the same area to provide the required hole through the circuit board. The major effect was a lowering of the resonant frequency of the radiator. The resonant frequency for the conventional case was 1375 MHz. When the square patch was removed, resonance was found to be at 1272 MHz and with the hole completely through the board it was 1250 MHz. Figure 1 shows the dual frequency feed with like polarization for the two radiators. Orthogonal polarization could not be implemented in this case since the X-band shepherd's crook seriously degraded the L-band E-plane pattern. Recorded performance of the dual frequency feed installed in the parabola is shown in Figure 2. Sidelobe levels on the order of -20dB at L-band are quite good considering the small size of the reflector. Some small differences in X-band sidelobe structure were noted due to the presence of the L-band card but with no measureable difference in gain. Measured gain at 1250 MHz was 21.5dB.

Orthogonal polarization of the two feeds was investigated by fabricating an X-band feed horn which could be supported at the focus with a typical tripod arrangement. Pattern results were comparable to those in Figure 2 with sidelobe levels at L-band again in the -18dB to -20dB range. Variations noted are most likely due to the differences in blockage by the shepherd's crook in the one case and the tripod support in the other.

Rather than remove an entire patch of metal from the central area of an L-band microstrip radiator, another dual frequency concept was implemented by etching an X-band microstrip element in that area. Models with like and orthogonal polarization were fabricated for evaluation. The model with orthogonal polarization is shown in Figure 3. A notch type of feed [3] was used in an effort to eliminate an X-band E-plane pattern problem which, at the time, was attributed to close spacing between an external transformer and the L-band radiator. An additional bonus due to that change was an 18% reduction in E-plane dimension resulting in increased spacing between radiators. The dual frequency etched models were tripod supported in the reflector and again L-band sidelobe levels were in the -18dB to -20dB range. The worst case X-band sidelobes were at -16dB in the E-plane for the orthogonally polarized version. Complete primary and secondary pattern performance may be found in [4].

2.1 OTHER APPLICATIONS

Parabolic reflector feeds are typically supported by a tripod or similar arrangement which adds to aperture blockage. Figure 4 shows a focal axis support which makes use of a central hole through an L-band circuit board. A flanged length of tubing is attached to the ground plane side of the radiator, passes through such a centrally located hole and on through the apex of the reflector. The rigid support tubing can serve as the outer conductor of a coaxial feed line or a smaller cable can be passed through the tubing as is the case in Figure 4. Radiation patterns for a 1250 MHz microstrip feed with focal axis support are shown in Figure 5. A significant improvement of 4-6dB in sidelobe level results as compared with patterns using a tripod support or the shepherd's crook feed support as shown in Figure 2.

It has also been shown that the microstrip radiator with a central patch removed can serve as a very simple, low cost, efficient feed for parasitic arrays. Figure 6 shows a 10-director microstrip-fed parasitic array. The pattern performance of that model is compared with that of the same array with a conventional feed in Figure 7. A substantial improvement is obtained and although the beamwidths in both planes are slightly wider with the microstrip-fed array, gain is somewhat more than 1dB greater. It is interesting to note that the impedance bandwidth is 50% greater than for the microstrip radiator alone.

3.0 MICROSTRIP POLARIZATION TECHNIQUES

Several methods for generating circular polarization [5] [6] in microstrip antennas have been devised. These rely on orthogonal feeds with external circuitry, asymmetrical radiators, off-set feeds and the like. During the developments described earlier, it was noted that if the patch of metal removed at the center of a microstrip radiator were not square or round but rather of an elongated form, then the effect on resonant frequency is a function of orientation with respect to the input axis. For example, a 6.8 cm square radiator had a resonant frequency of 1377 MHz. When a rectangular patch of metal 0.25×2.5 cm was removed at the center of the radiator where the long dimension was parallel with the input axis, little effect was noted with the resonant frequency being 1374 MHz. However, with the long dimension perpendicular to the input axis, the resonant frequency was found to be 1307 MHz. That finding has resulted in the development of circularly polarized microstrip radiators which are symmetrical, fed with a single input in the same manner as is commonly used for linearly polarized elements and, in addition, the radiator size is always smaller than that required for linear polarization at the same frequency.

Figure 8 shows a CP square microstrip radiator with a single input and with a rectangular polarizing patch oriented at an angle of 45° with respect to the input axis. That particular configuration results in RHC polarization. LHC is obtained by moving the feed to an adjacent side or by rotating the polarizing patch 90° . Figure 9 shows the radiation pattern recorded at

1358 MHz while using rotating linear illumination. Other designs such as circular and square as in Figure 8 but corner fed have been evaluated with similar results. In the latter case the polarizing patch is rotated 45° from that shown in Figure 8. A unique feature of this polarizing technique is that a given size radiator can be made circularly polarized at lower frequencies simply by increasing the size of the polarizing patch. The model of Figure 8 showed good results at 1358 MHz. That same size radiator has also shown similar results at 1220 MHz with a larger polarizing patch.

A square model similar to that of Figure 8 was developed for use at 1680 MHz. In that case it was shown that, if desired, the radiator can be fed coaxially at the appropriate point along the input axis with equally good results. Axial ratio performance of that model as a function of frequency was measured. At ± 5 MHz it was found to be 1.25 - 1.50dB, at ± 10 MHz, 3 - 3.5dB and at ± 20 MHz the result was 6.5 - 7dB.

Another circularly polarized microstrip radiator has also been developed which retains the desirable single central feed but relies on radiator asymmetry to obtain the desired results. That configuration resembles Figure 8 without the polarizing patch but with two diagonally opposite corners of the square radiator truncated. A model of that type, the same size as that of Figure 8 provided good results at 1385 MHz. In this case, the radiator is always slightly larger than that required for linear polarization. More complete details of models and performance may be found in [7].

4.0 TERMINATED MICROSTRIP ANTENNA

Figure 10 shows a terminated version of the microstrip antenna which can increase the usefulness of a given radiator by providing for frequency diversity [8] [9] in several ways. As shown in the photograph, the model was designed with an output terminal the same as the input with both fitted with SMA connectors.

When the output terminal of Figure 10 was short circuited, the resonant

frequency was found to be 1360 MHz, while for the open circuit condition it was 1410 MHz. A 2.54 cm length of coaxial line was then added to the output terminal and the short and open circuit experiment repeated. This time the resonant frequencies were 1312 MHz and 1382 MHz demonstrating that a means of frequency control exists.

Taking the short circuit resonance of 1312 MHz as the reference, another length of line equal to one-half wavelength at that frequency was added and the short circuit condition remeasured. As expected, a resonance again occurred at 1312 MHz but simultaneously another resonance was found at 1457 MHz. Thus a doubly resonant version is possible. The open circuit condition also produced two resonances, one at 1380 MHz and the other at 1780 MHz. The latter resonance is beyond the range where pattern performance is acceptable for this model. The upper limit is approximately 1500 MHz. Other dual resonances observed for various short circuited line lengths are shown in Table 1.

TABLE 1
DUAL RESONANCES

Freq 1	VSWR	Freq 2	VSWR
1232 MHz	1.50:1	1448 MHz	1.24:1
1260 MHz	1.58:1	1400 MHz	1.01:1
1330 MHz	1.35:1	1450 MHz	1.22:1
1352 MHz	1.14:1	1500 MHz	1.48:1

The foregoing results suggest a tunable version of the microstrip radiator. A variable short circuit was connected to the output port and adjusted for the best possible VSWR over a range of frequencies. It was found that the model could be tuned to a VSWR of 1.5:1 or better from 1275 MHz to 1500 MHz. That experiment was not pursued any further because of the poor arrangement of adapters required to connect the output port to the variable short.

The effect of reducing the length of the terminal line etched on the circuit board was next evaluated with the results shown in Table 2.

TABLE 2
EFFECT OF REDUCING TERMINAL LINE LENGTH

Line Length	Open Circuit				Short Circuit	
	Freq 1	VSWR	Freq 2	VSWR	Freq	VSWR
4.21 cm	1052 MHz	1.28:1	1440 MHz	1.22:1		
3.97 cm	1088 MHz	1.27:1	1452 MHz	1.32:1	1372 MHz	1.04:1
3.70 cm	1129 MHz	1.27:1	1468 MHz	1.45:1	1376 MHz	1.03:1
3.45 cm	1169 MHz	1.30:1	1486 MHz	1.66:1	1378 MHz	1.03:1
3.19 cm	1220 MHz	1.26:1	1504 MHz	2.00:1	1382 MHz	1.01:1
2.94 cm	1248 MHz	1.25:1			1384 MHz	1.02:1
2.69 cm	1276 MHz	1.20:1			1388 MHz	1.02:1
2.43 cm	1296 MHz	1.25:1			1392 MHz	1.04:1
2.18 cm	1312 MHz	1.20:1			1395 MHz	1.05:1
1.92 cm	1322 MHz	1.15:1			1399 MHz	1.05:1

When the output coaxial connector was removed and a short circuit placed at that point, the resonance which had been at 1360 MHz was then found to be at 1372 MHz which is very nearly the resonant frequency of an unterminated version of the same size. The short circuit resonance then moves very slowly upward as line length is reduced with the VSWR remaining very low throughout. For the open circuit condition, the resonance which had been at 1410 MHz was now found at 1440 MHz with the output connector removed. That resonance rapidly begins to fade out with reduced line length. At the same time, with the full length of line open circuited, another resonance was found at 1052 MHz. It is believed that resonance was below 1000 MHz with the coaxial connector in place and went undetected since only the 1000 - 2000 MHz range was being swept. That resonance steadily moves upward with reduced line length approaching the resonant frequency

of an unterminated version. Again the VSWR remains quite good throughout.

At the lower frequencies, bandwidth is reduced as compared with a conventional radiator. For example, at 1052 MHz it is 40%, at 1169 MHz it is 50% and at 1248 MHz which is still 125 MHz below the resonant frequency of the unterminated version, it is 70%. Figure 11 shows pattern performance over the range from 1052 MHz to 1500 MHz. Over that same band, gain varies from 5.5dB at the low end to 7.5dB at the higher frequencies.

5.0 CONCLUSIONS

The developments described in this paper have shown that the microstrip element can serve as a very simple, small, efficient feed in both single and dual frequency applications. The small size results in quite good sidelobe performance in parabolic reflectors much smaller than would normally be considered for typical feeds. Use of the microstrip element as a feed for parasitic arrays results in simplicity, improved pattern performance and efficiency.

A new method for generating circular polarization has been developed which provides such advantages as symmetrical radiators, a single central feed and, in addition, the element is always smaller than the linearly polarized counterpart. A unique feature is that a given size radiator can be made circularly polarized at lower frequencies simply by increasing the size of the polarizing patch.

A terminated version of the microstrip antenna has been described which can increase the usefulness of a given radiator by providing for frequency diversity in several different ways.

Since none of the developments presented in this paper have been investigated in any great detail, it is likely that there is much more to be learned and improvements to be made.

6.0 REFERENCES

1. Munson, R., Microstrip Phased Array Antennas, Twenty-second USAF Antenna Symposium, University of Illinois, October 1972,
2. Munson, R., Conformal Microstrip Antennas and Microstrip Phased Arrays, IEEE Transactions on Antennas and Propagation, Vol. AP22 pp. 74-78, January 1974.
3. Kaloi, C., Notch Fed Electric Microstrip Dipole Antenna, US Patent 3,947,850, March 1976.
4. Kerr, J., Other Microstrip Antenna Applications, Proceedings of the 1977 Antenna Applications Symposium, University of Illinois, April 1977.
5. Munson, R., Microstrip Antenna Structures and Arrays, US Patent 3,921,177, November 1975.
6. Weinschel, H., A Cylindrical Array of Circularly Polarized Microstrip Antennas, G-AP International Symposium Digest, pp. 177-180, June 1975.
7. Kerr, J., Microstrip Polarization Techniques, Proceedings of the 1978 Antenna Applications Symposium, University of Illinois, September 1978.
8. Derneryd, A., Microstrip Disc Antenna Covers Multiple Frequencies, Microwave Journal, Vol. 21, pp. 77-80, May 1978.
9. Kernweis, N., and McIlvenna, J., Dual Frequency Microstrip Disc Antenna Elements, RADC-TR-79-74, March 1979.

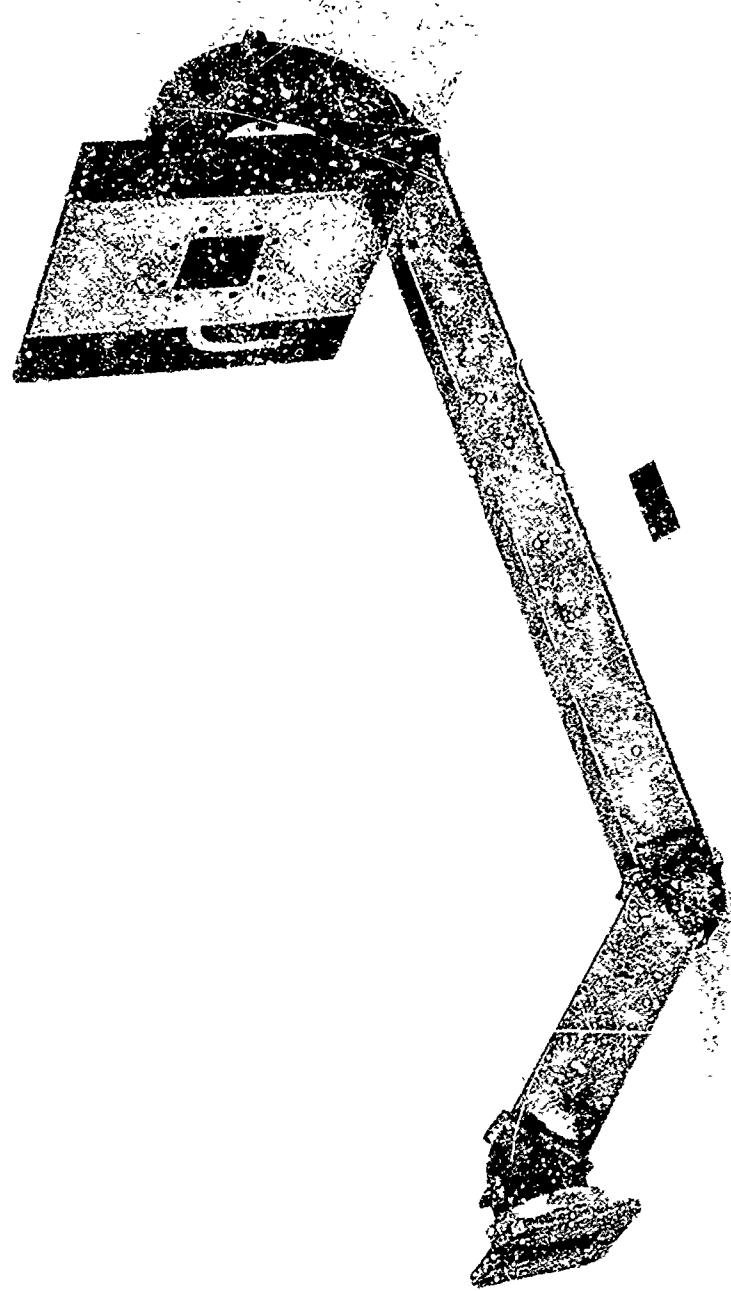


Figure 1. Dual Frequency Feed

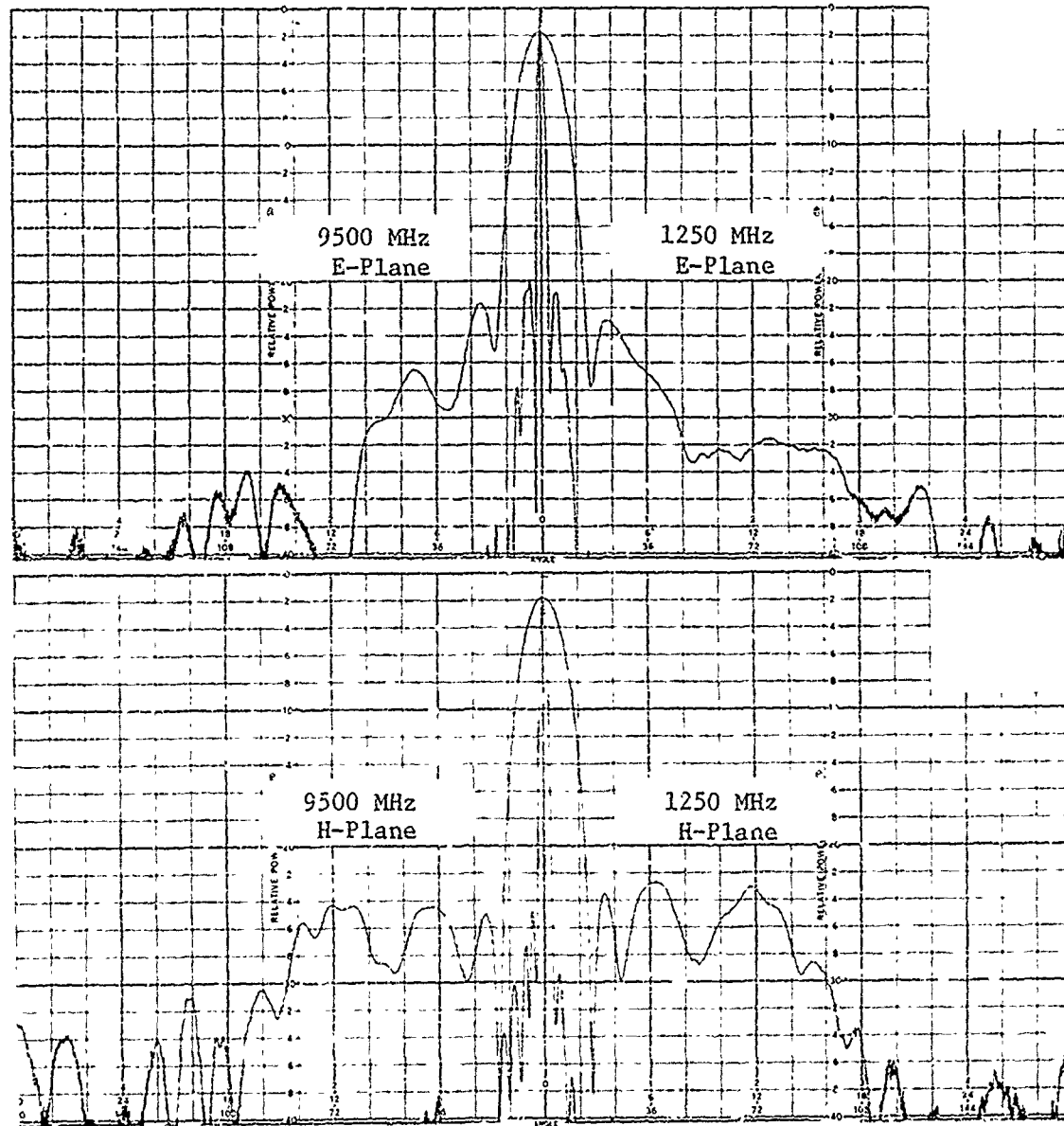
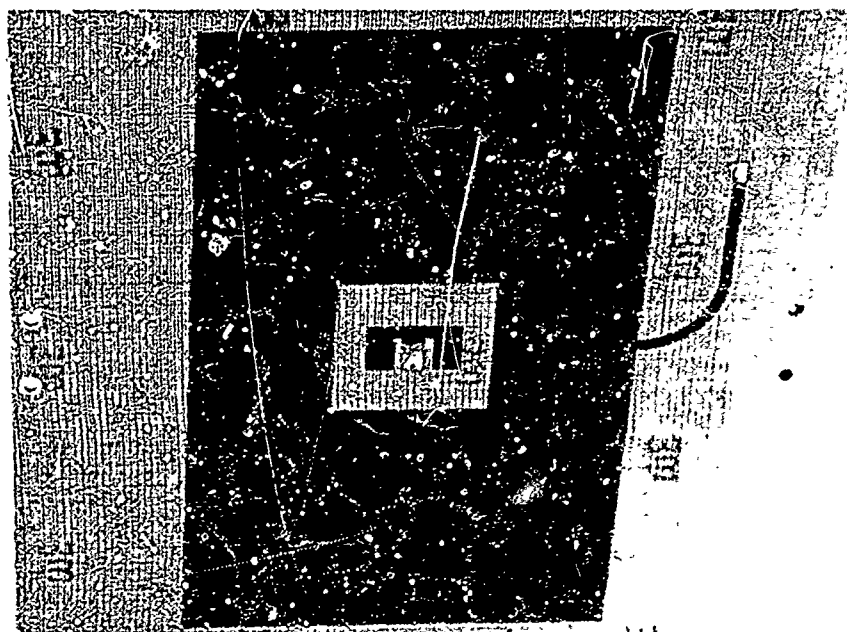


Figure 2. Dual Frequency Patterns

Figure 3. Dual Frequency Etched Antenna



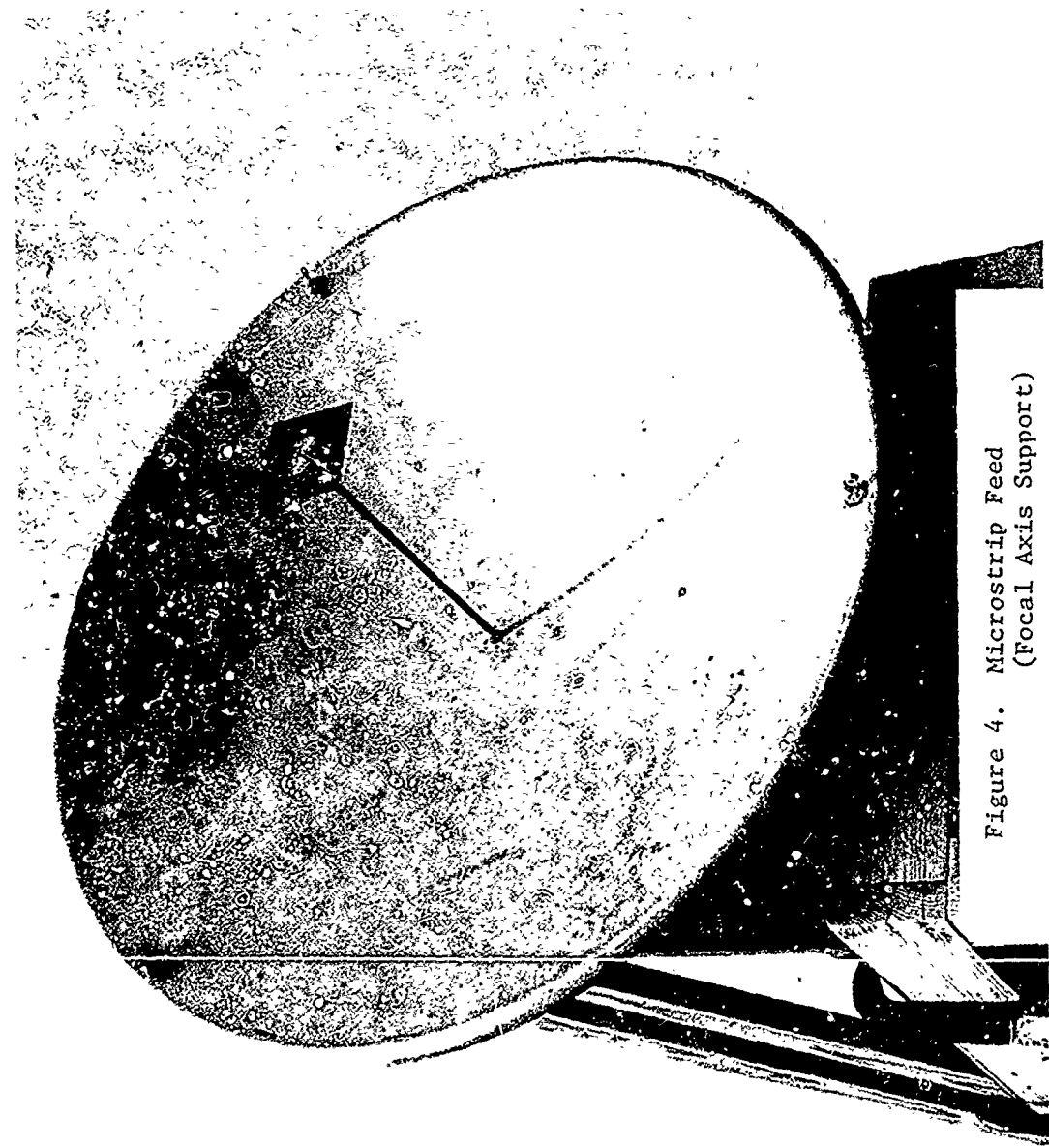


Figure 4. Microstrip Feed
(Focal Axis Support)

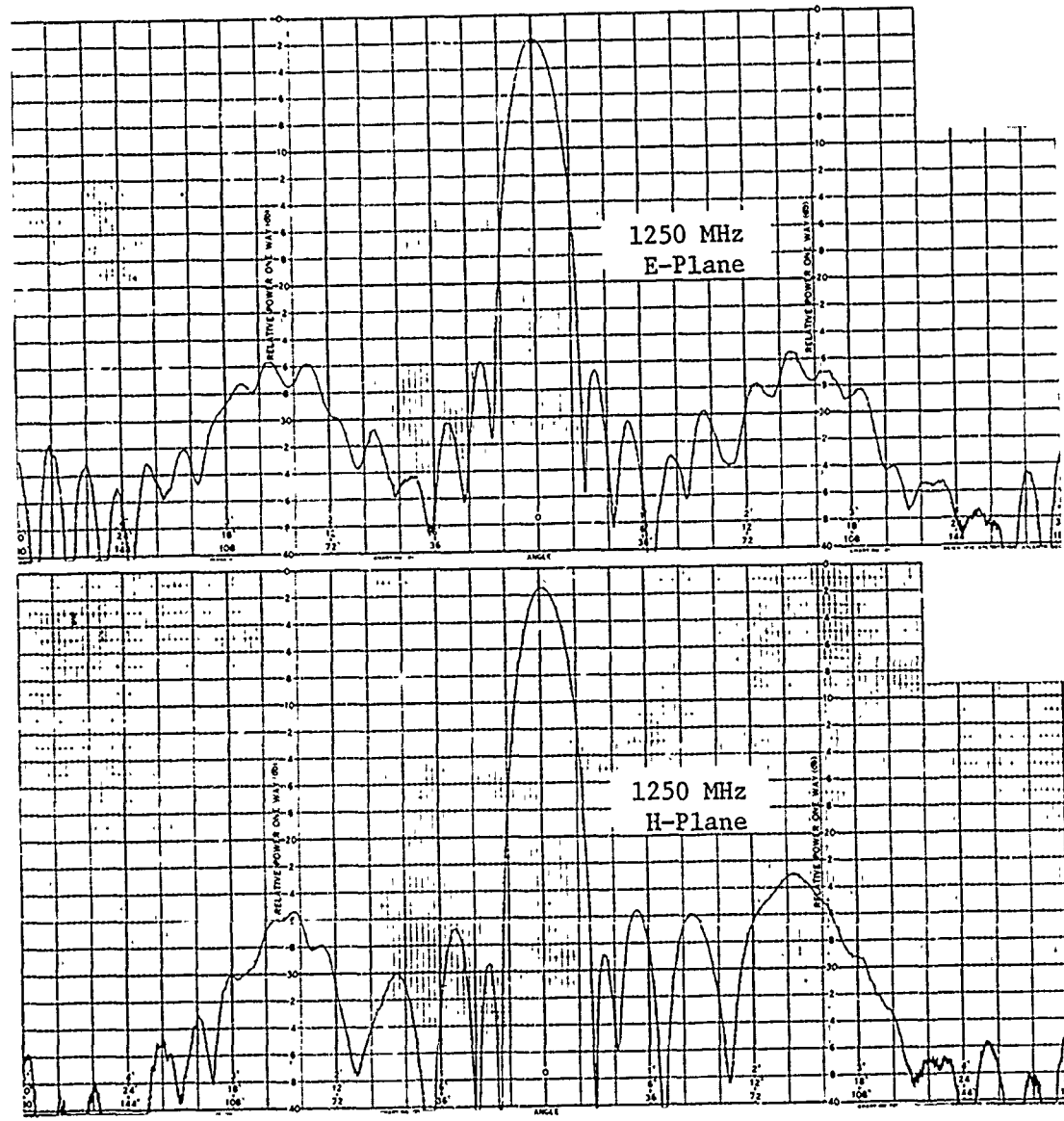
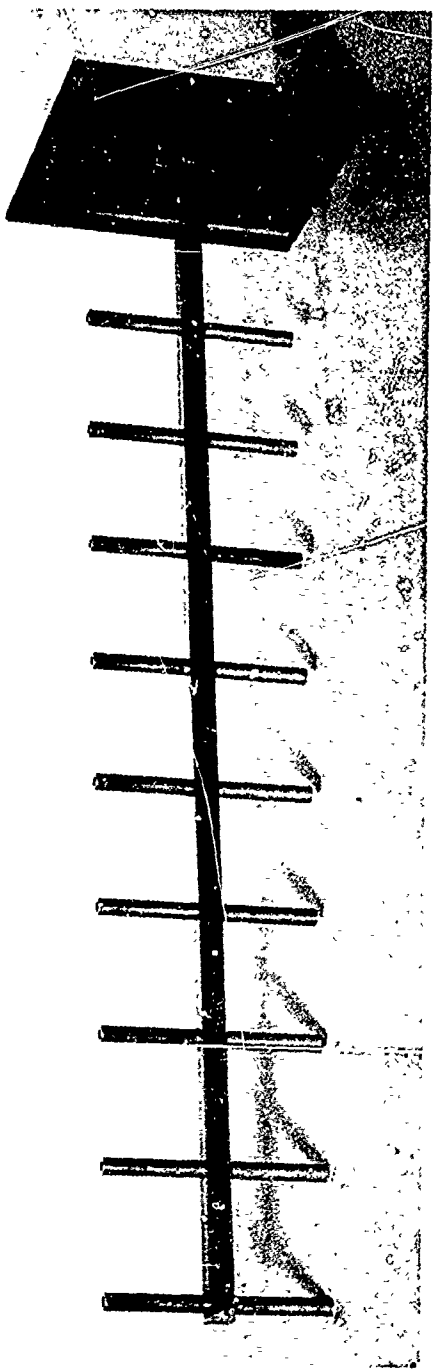


Figure 5. Radiation Patterns
(Focal Axis Support)

Figure 6. Microstrip-Fed Parasitic Array



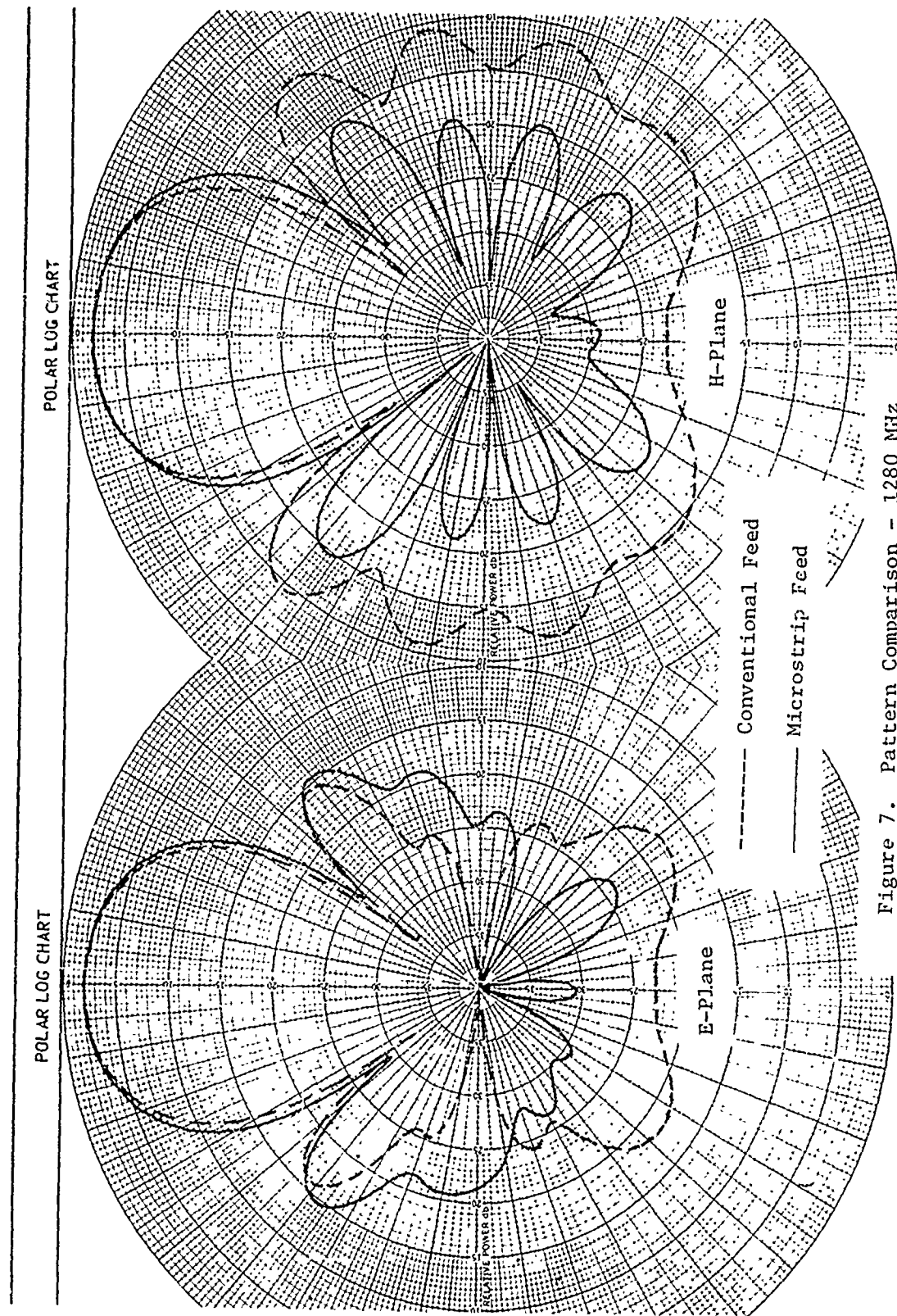
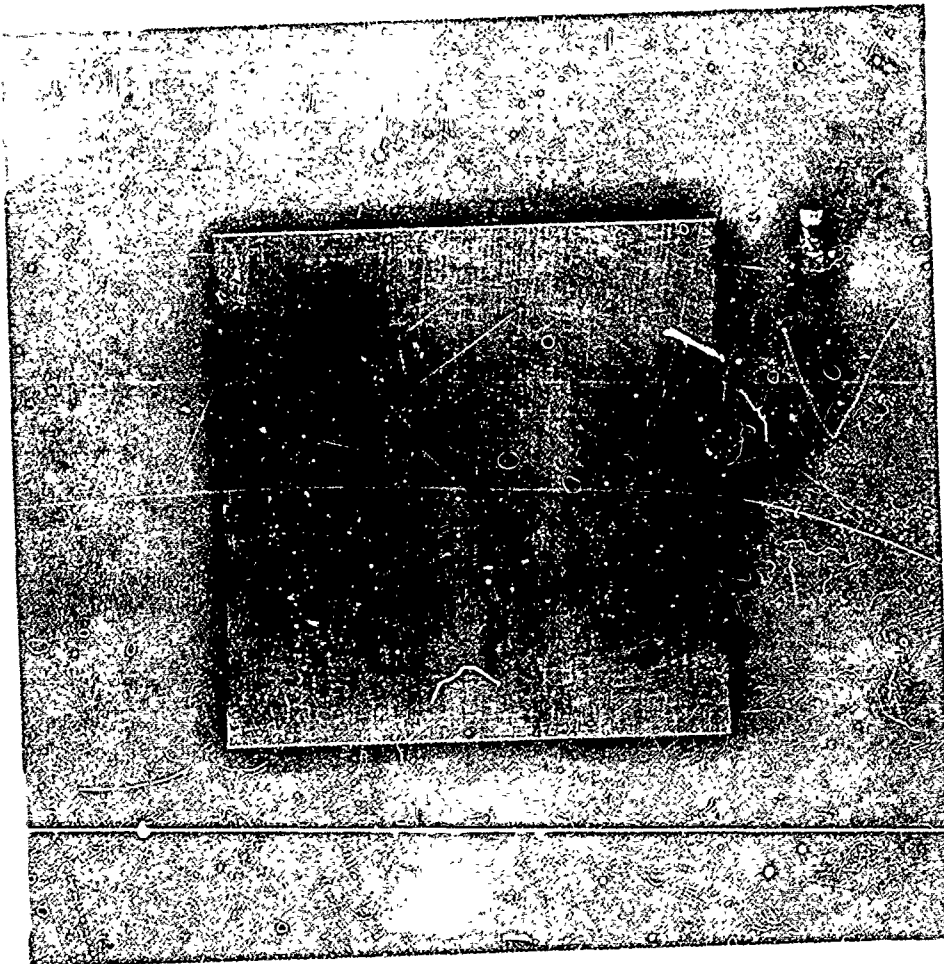


Figure 7. Pattern Comparison - 1.280 MHz

Figure 8. CP Square Microstrip Radiator



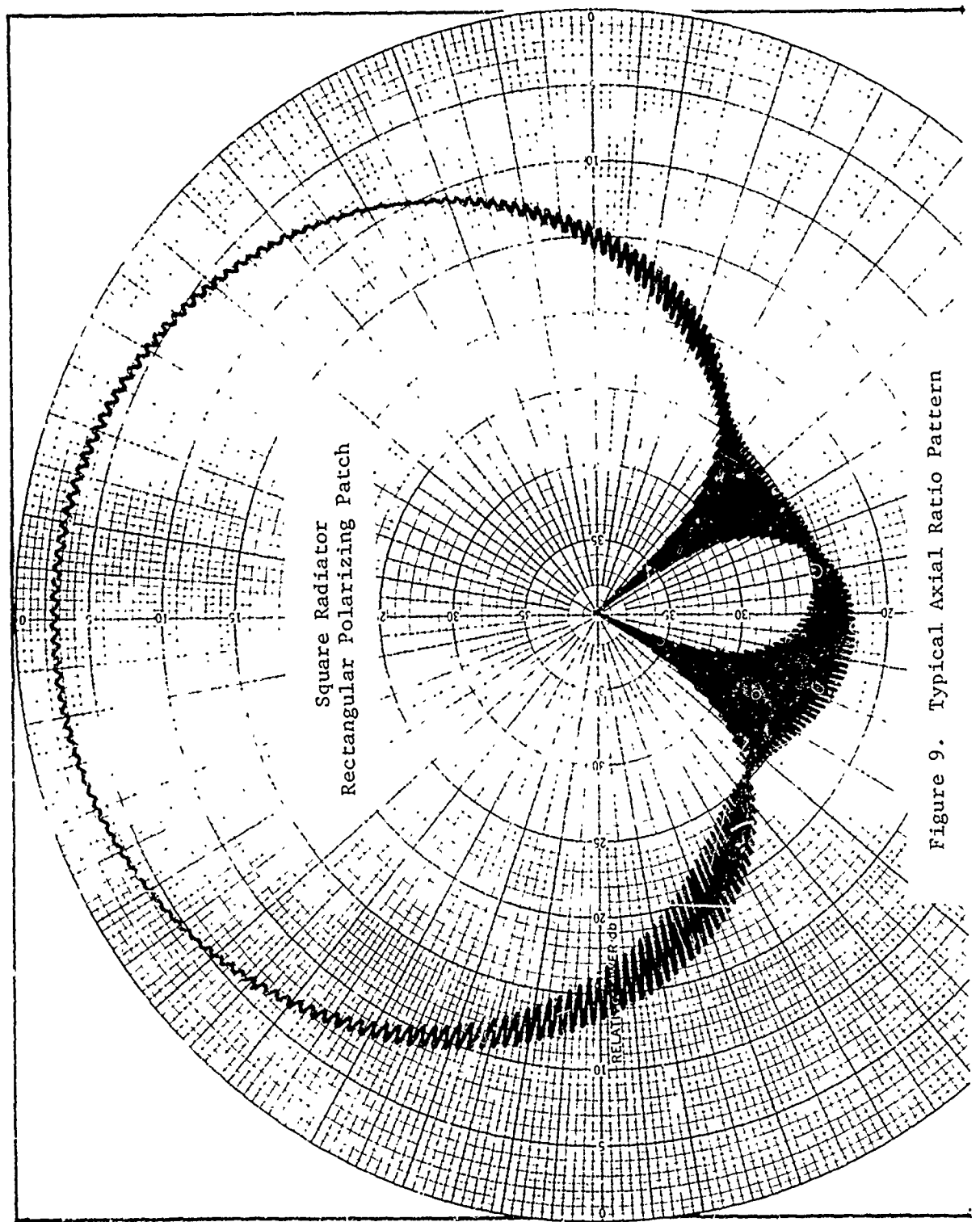


Figure 9. Typical Axial Ratio Pattern

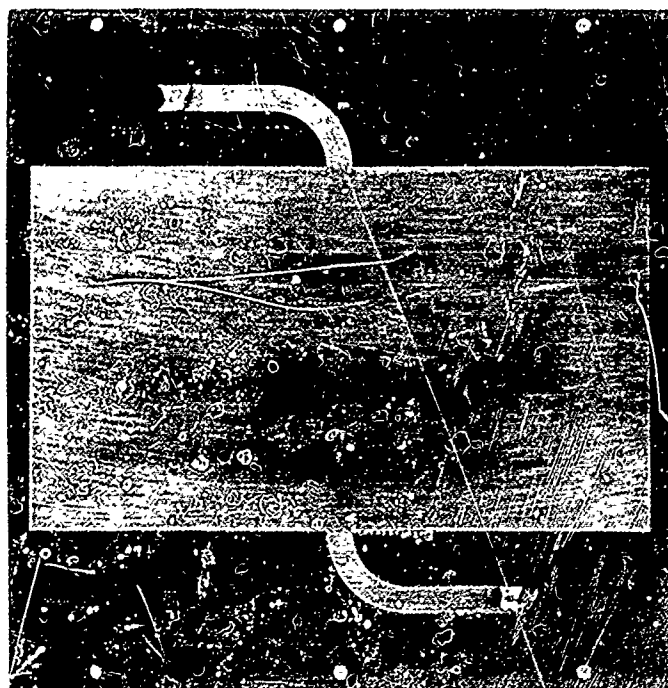


Figure 10. Terminated Microstrip Radiator

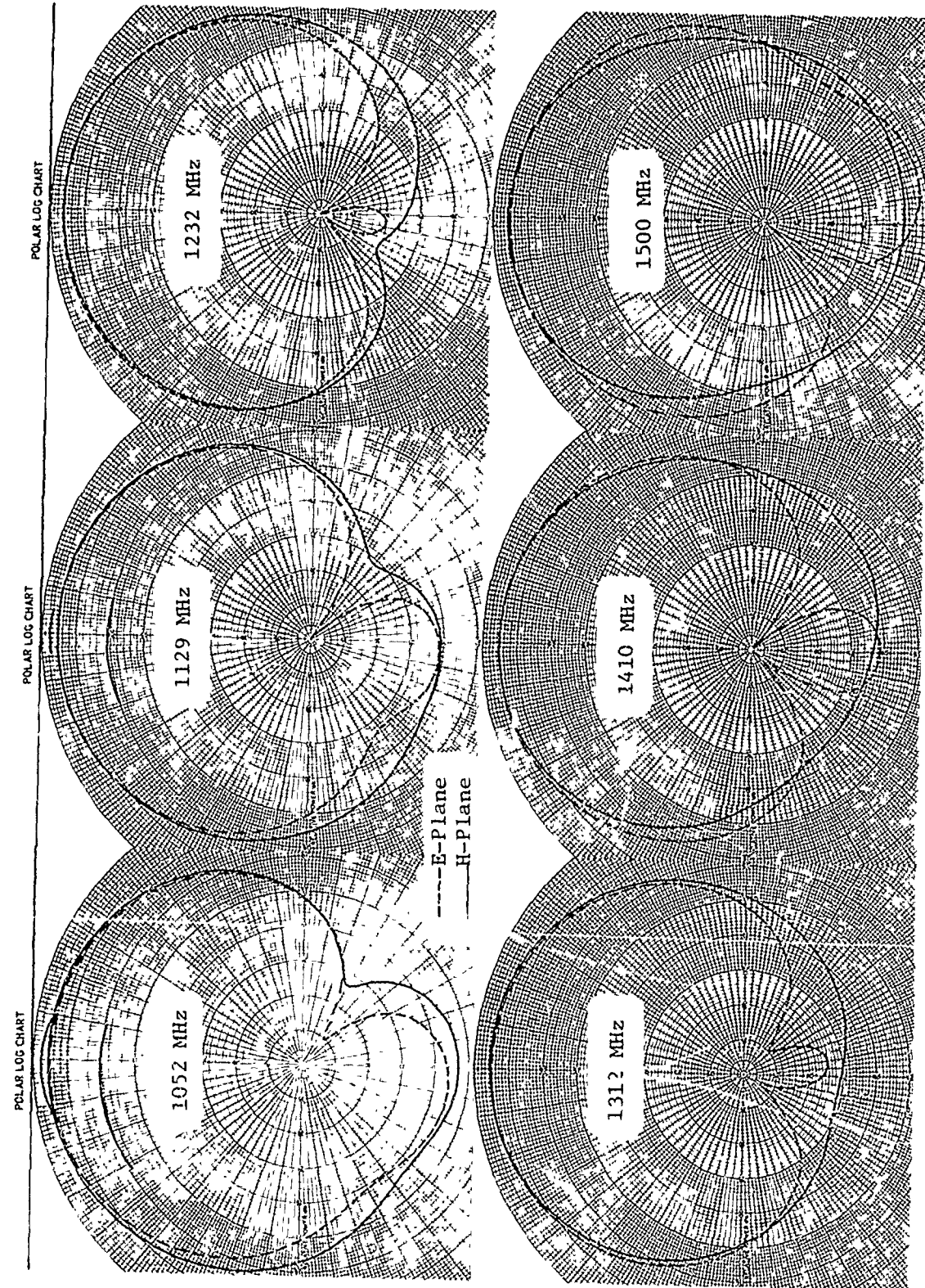


Figure 11. Representative Pattern Performance

MUTUAL COUPLING BETWEEN MICROSTRIP ANTENNAS

R. P. JEDLICKA and K. R. CARVER
PHYSICAL SCIENCE LABORATORY
NEW MEXICO STATE UNIVERSITY
LAS CRUCES, NEW MEXICO 88003

SUMMARY

Mutual coupling between microstrip antennas can have substantial effects on array performance. Reported herein are measured coupling values which are part of an ongoing empirical and theoretical study. For the L-Band microstrip elements considered, typical values of $|S_{12}|^2$ ranged from -20 dB to -50 dB. The effect of this coupling on the array patterns is demonstrated with two linear array examples.

1.0 INTRODUCTION

The properties of isolated microstrip radiating elements are well known [1]. Models have been developed for single rectangular or circular patches which predict the resonant frequency, bandwidth, and radiation resistance with good accuracy [2]. Arrays of microstrip elements have been used for a variety of applications where high gain and/or pattern shaping is required. In general, when a well-matched individual element is placed in an array environment its terminal properties will change as a result of mutual coupling effects. Sidelobe levels may increase (with a concomitant decrease in gain), nulls may fill in or be shifted and grating lobes may appear. When the antenna beam is electronically scanned the pattern may degrade as a function of scan angle; at some scan angles all the power may be reflected back into the feed network and array "blindness" may occur.

This paper describes the results obtained to date from an empirical investigation of the mutual coupling between rectangular and circular microstrip elements. A theoretical investigation is also under way, but is not described here.

The measured mutual coupling data is presented as a function of E-plane or H-plane element spacing, substrate thickness, patch size, etc. These measured values are then used in an array design example to demonstrate how the mutual coupling affects the far-field antenna pattern shape and gain.

2.0 S-PARAMETERS

2.1 S-PARAMETERS CHARACTERIZATION OF THE MUTUAL COUPLING PHENOMENA

It would be desirable to be able to characterize mutual coupling effects within a framework such that the measured values can be readily used to determine array performance. An S-parameter formulation represents the coupling effects in terms of the terminal quantities of the individual array elements, so that an N-element array is represented as an N-port network. For the case N=2, the usual S-parameter is as shown in Figure 1, with the extension to an N-port being obvious.

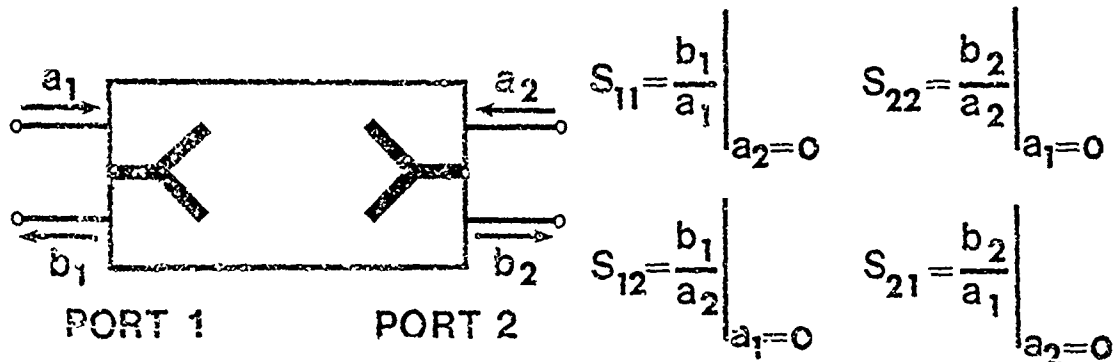


Figure 1 S-Parameter representation of a two-port network

Assuming that the S-parameters are measured with a network analyzer whose characteristic impedance is the same as that of the transmission lines connected to the array ports, then the measured quantities are exactly what are needed to determine the array excitation coefficients in the presence of mutual coupling. The signal flow graph shown in Figure 2 shows how the S-parameters are used to determine the change in the array excitation coefficients.

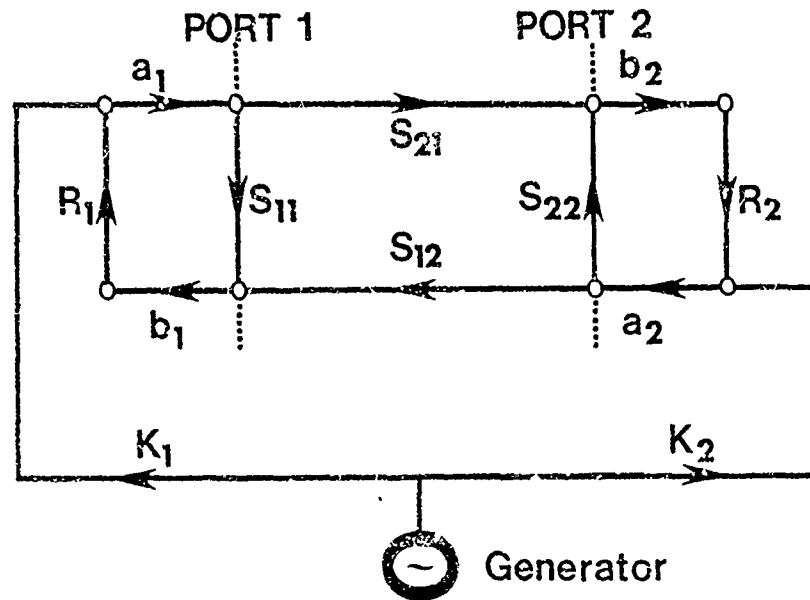


Figure 2 Signal flow graph of two-port network

It can be shown that the excitation coefficients are found by the following matrix equation [3]:

$$[a_m] = [I - [R_{mn}] [S_{mn}]]^{-1} [K_m] \quad (1)$$

where

$[a_m]$ is the array excitation coefficient vector

$[I]$ is the identity matrix

$[R_{mn}]$ is the diagonal matrix of reflection coefficients seen looking from each array port into the feed network

$[S_{mn}]$ is the scattering matrix

$[K_m]$ is the vector representing the ideal design relative currents at each element if the reflection coefficients were zero and if there was no mutual coupling

The array excitation coefficients are found via an iterative process since the $[R_{mn}]$ will change with each iteration. Thus, with a knowledge of the S-parameters and the form of the feed network, the array excitation coefficients may be found.

2.2 S-PARAMETER MEASUREMENT

The S-parameters were measured with a network analyzer system. The measurements were made on a two element array as a function of element spacing for several configurations. The self-impedance of the isolated elements was approximately 50Ω at resonance. The S_{ii} were measured as the reflection coefficient seen at one port while the other port was terminated in a 50Ω load. The S_{ij} , $i \neq j$, were measured as the transmission coefficient between the ports when a 50Ω source was connected at one port and a 50Ω detector was placed at the second port. The measurement configurations are shown in Figure 3.

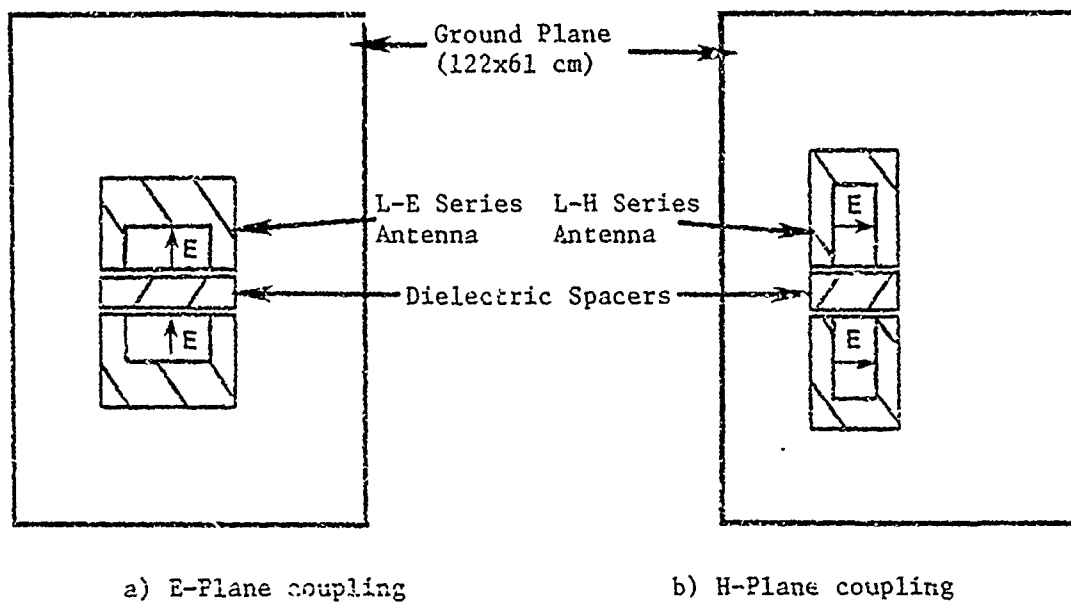
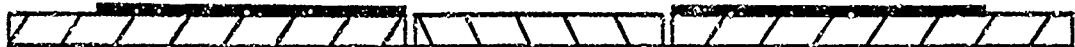


Figure 3 Measurement Configurations

Reference to Figure 3 shows that the dielectric material around each copper patch was cut at the two adjacent walls so that the coupling could be measured for small separations. An initial series of measurements were made to determine if this measurement procedure was characteristic of the "true" array environment. Since Parks and Bailey [4] had previously seen no difference between the measurement schemes in Figure 4 (b) and (c) it was decided to see if configuration (a) showed the same behavior as configuration (b) and by implication the same as configuration (c):



a) Measurement method utilized in this experiment



b) Microstrip elements with dielectric spacer



c) Linear array with continuous dielectric substrate

Figure 4 Measurement arrangements to determine the effects of dielectric spacers

(Figures 5-14 are included at the conclusion of the text material)

Figure 5 shows the results of this initial measurement series. The E-plane coupling for cases (a) and (b) is seen to fall on the same curve. The H-plane coupling shows good agreement down to -50 dB. Based upon these results it was decided to use measurements of the geometry shown in Figure 4(a) to represent the coupling in the array environment, i.e., Figure 4(c).

3.0 RESULTS

3.1 ANTENNAS MEASURED

L-Band rectangular patches were measured for two substrate thicknesses, nominally 0.15875 cm (1/16 in.) and 0.3175 cm (1/8 in.). L-Band circular patches were measured for the 0.15875 cm thickness. Additional measurements, not reported herein, are currently being carried out on 0.3175 cm thickness circular patches and for both thicknesses on a nearly-square element. The antennas measured thus far are shown in Figure 6.

3.2 MEASURED COUPLING DATA

Mutual coupling between microstrip patches may, in principle, be due to either surface waves or sky waves or both. The experimental procedure shown in Figure 7 and 9 was contrived to try to determine the effect of the surface wave. It is seen that with the dielectric spacers in place that the coupling is slightly higher for the thicker dielectric substrate. A slight difference is due to mismatch caused by the discontinuity in the dielectric, about .1 dB except for the L-E-1/L-E-2 series (c.f. Figure 6) where a difference of .5 dB is noted. This difference does not account entirely for the difference shown in the figures; thus, there is a small surface wave effect. Figure 9 indicates that the surface wave does increase with a thicker substrate but that the increase is small (for the case considered here).

It is also noted that the field configuration in the "radiating walls" of the two elements, L-E series with respect to L(1/8)-E series, will be slightly different due to the increased substrate thickness and this may cause a slight change in the sky wave magnitude.

Figure 10 demonstrates effects due to the length of the coupling edges (adjacent edges). In Figure 10(a) it is seen that the E-plane coupling for the rectangular element is greater than that for the disk (circular) element. This is readily explained by the fact that the radiating edge for the rectangular patch is considerably longer than that of the disk, a ratio of $.5\lambda_0$ to effectively $.3\lambda_0$.

In the H-plane case it is seen that the disk coupling exceeds that of rectangular coupling. In this case the coupling edges are effectively both about $0.3\lambda_0$. Thus, for the types of patches considered here, for the same length edge the coupling between the disk elements exceeds that of the rectangular in either the E-plane or H-plane.

Figure 11 shows E-plane as H-plane coupling for three situations. It is seen that in the first two cases that the E-plane coupling always exceeds that of the H-plane coupling while in the third case there is a crossover

of the two curves. This is due to the fact that in the latter case the E-plane and H-plane edges are effectively the same length, while in the former the E-plane edge is over 1.5 times longer than the H-plane edge and thus the E-plane coupling is elevated, causing the crossover.

These results confirm simple a priori models of the coupling mechanisms. It is now of interest to quantify the effects of the coupling on array performance.

4.0 ARRAY DESIGN EXAMPLES

4.1 ARRAY GEOMETRY

A hypothetical E-plane linear array and an H-plane linear array with nominally uniform distributions were chosen as examples to demonstrate the effects of mutual coupling. The array geometries are shown in Figure 12. The array excitation coefficients in each case were calculated using the method in Section 2.1. The results for both the broadside condition and with the beam scanned 20° off are shown for the H-plane and E-plane arrays in Figures 13, 14 and 15. Table 1 shows the ideal excitation coefficients and those achieved under the influence of coupling, a decrease in gain (with respect to the no-coupling case) due to coupling-induced mismatch is observed. An increase in sidelobe level with respect to the beam maximum is observed for both cases which include coupling. The coupling tends to bring up the level of the nulls and for the examples where the beam is scanned, a shifting of the null position is evident. With the levels of coupling reported and the array geometries given there were no scan angles of interest at which array blindness occurred.

5.0 CONCLUSIONS

For the L-Band microstrip antennas considered the mutual coupling was shown to be moderate and had small effects on the linear array design examples considered; however, for elevated values of net coupling (such as in a planar array), the effects on array performance are more severe.

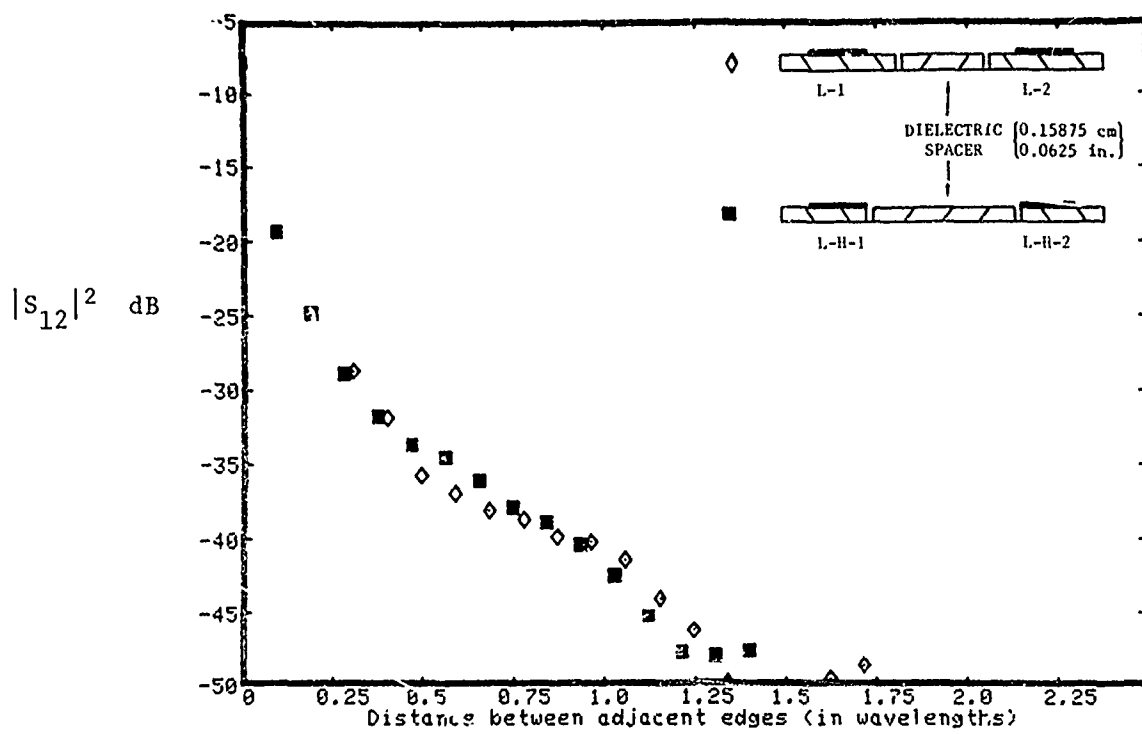
A simple method of calculating the actual array excitation coefficients has been presented (Equation 1, et. seq.) and this along with either measured or calculated S-parameters is helpful in predicting microstrip array performance. Both measurements and theoretical modeling efforts are continuing.

6.0 ACKNOWLEDGEMENTS

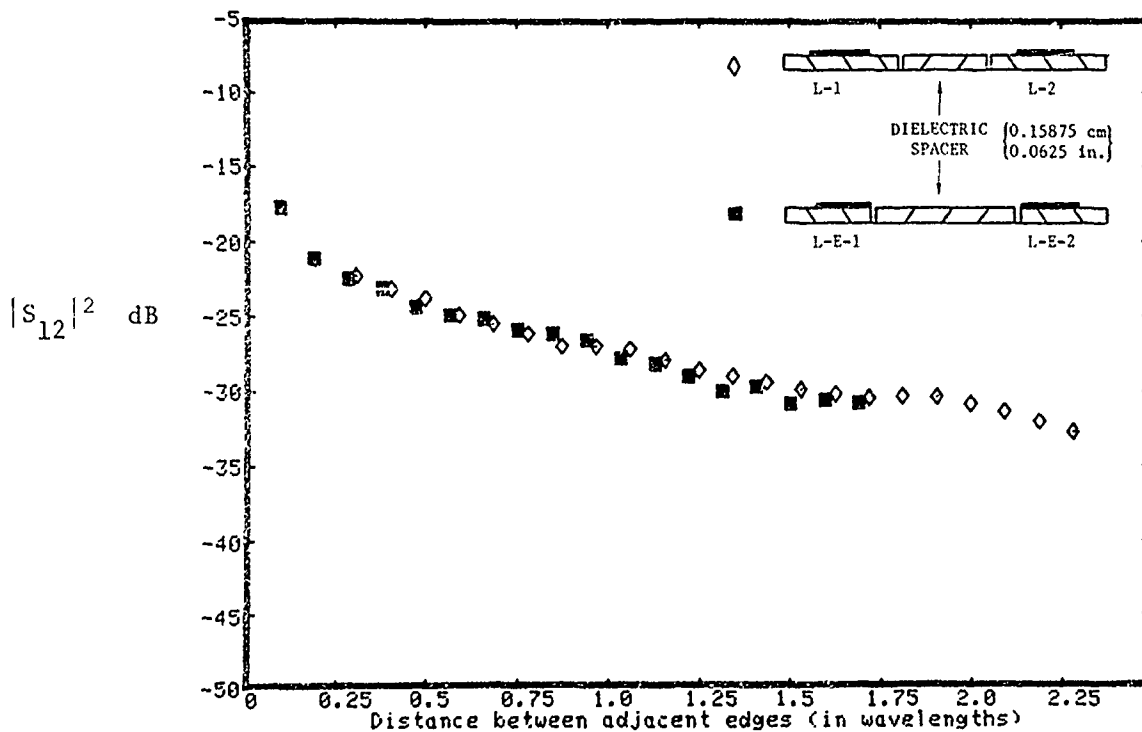
This work was supported by the Army Research Office, Research Triangle Park, NC.

7.0 REFERENCES

1. Munson, R. E., "Conformal Microstrip Antennas and Microstrip Phased Arrays," IEEE Transactions on Antennas and Propagation, Vol. AP-22, January 1974, pp. 74-78.
2. Carver, K. R., "Practical Analytical Techniques for the Microstrip Antenna," Proc. of Workshop on Printed Circuit Antenna Technology," Physical Science Laboratory, New Mexico State University, Oct. 17-19, 1979.
3. Carver, K. R., "Mathematical Modeling of Mutual Coupling Between Antennas," PSL Tech Note EM79-1, Physical Science Laboratory, New Mexico State University, Las Cruces, N.M.
4. Parks, F. G. and M. C. Bailey, "Mutual Coupling Between Microstrip Disk Antennas," AP-S International Symposium Digest, Oct. 11-15, 1976, pp. 399-400.

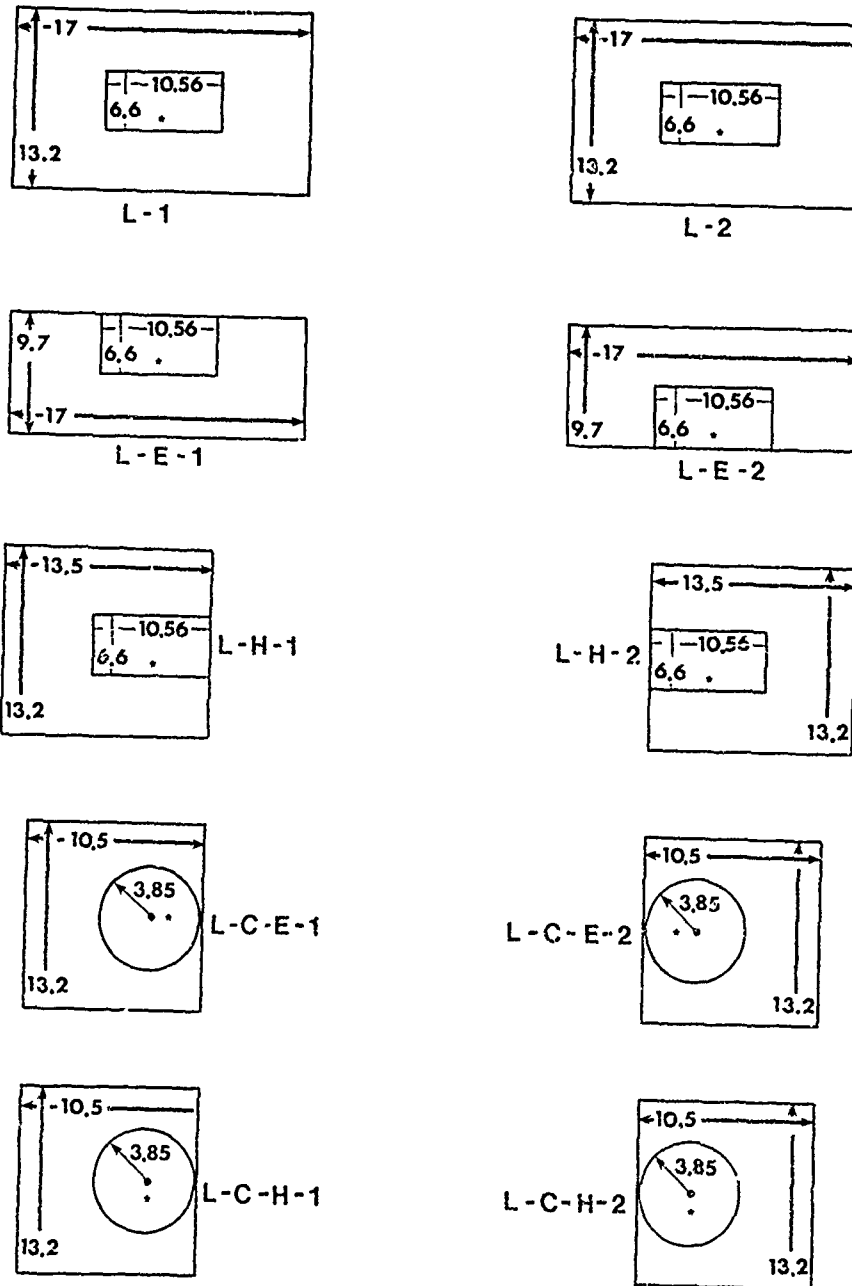


a) H-Plane



b) E-Plane

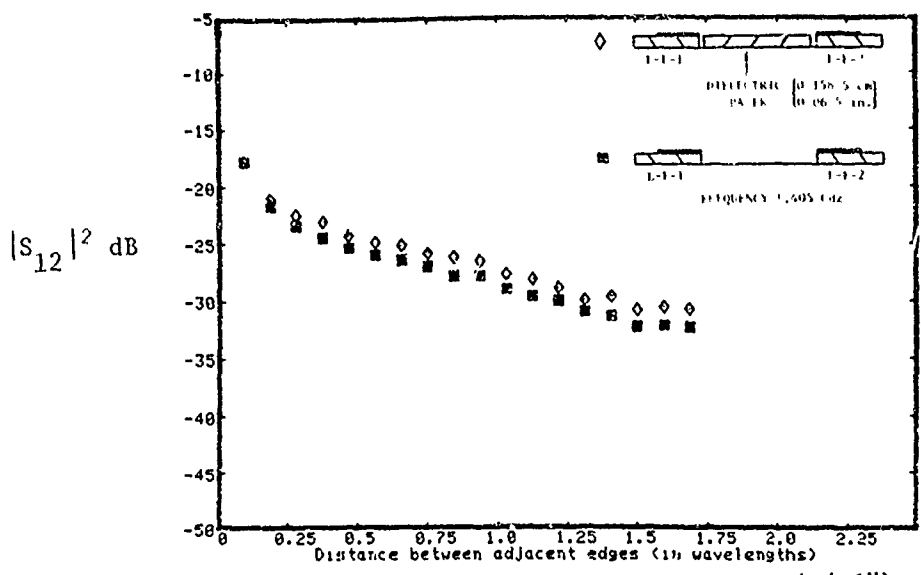
Figure 5 Dielectric spacer effects



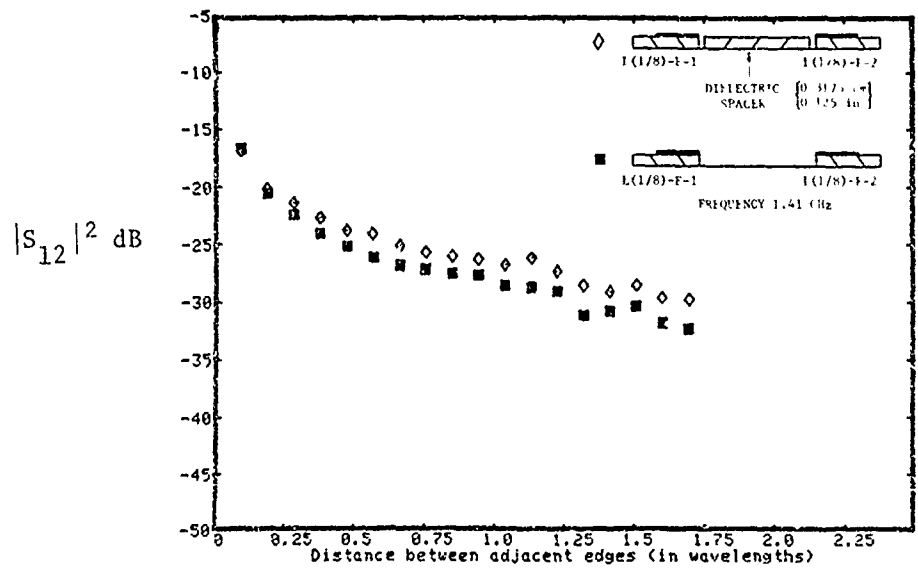
All dimensions are in centimeters

* Indicates the feedpoint location

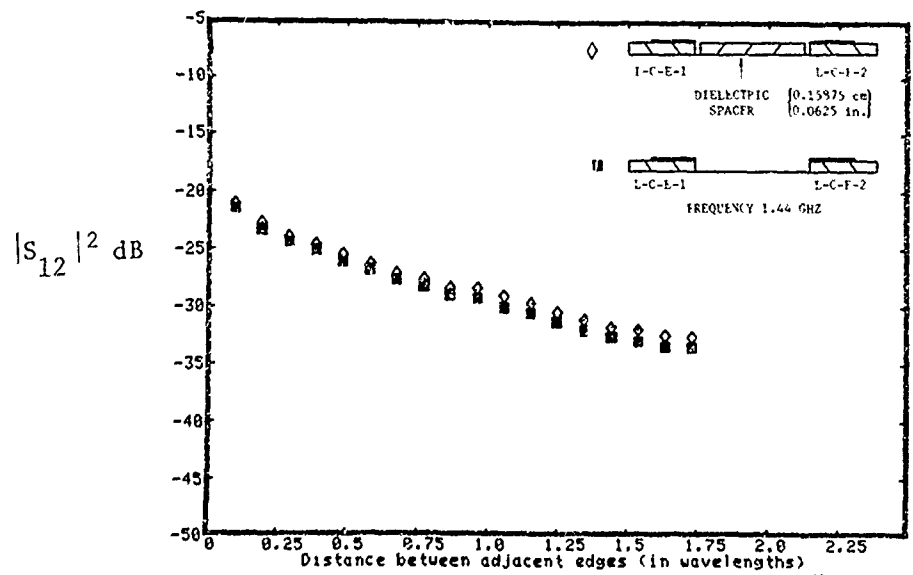
Figure 6 Measured antennas



a) L-Band rectangular patch (1/16")

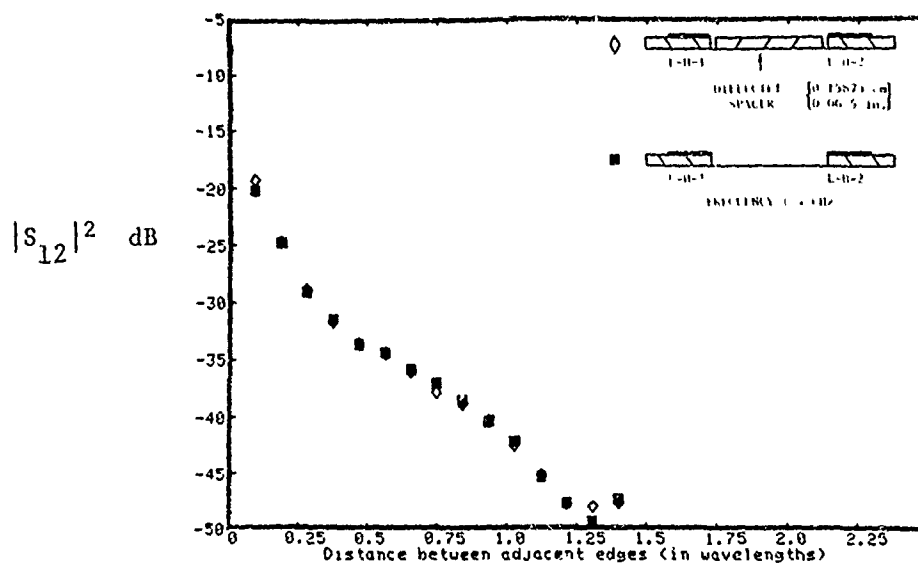


b) L-Band rectangular patch (1/8")

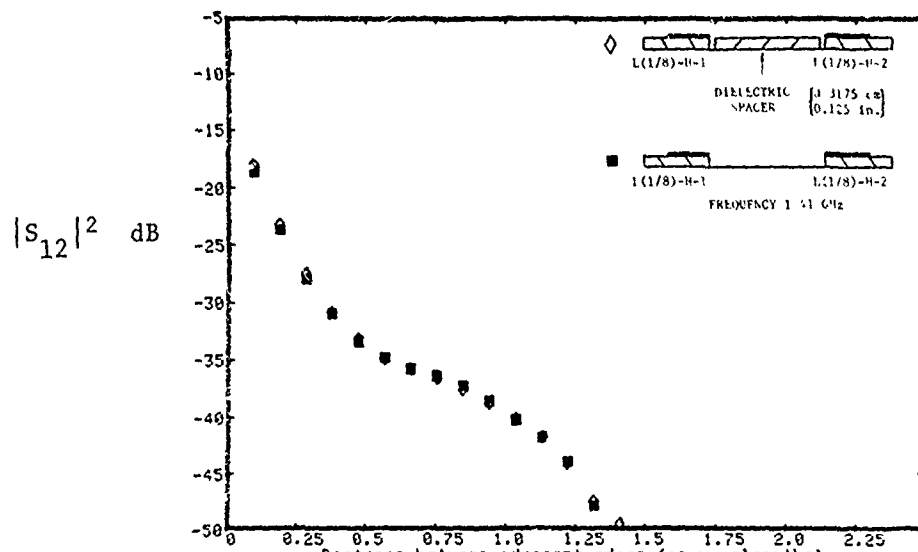


c) L-Band Circular patch (1/16")

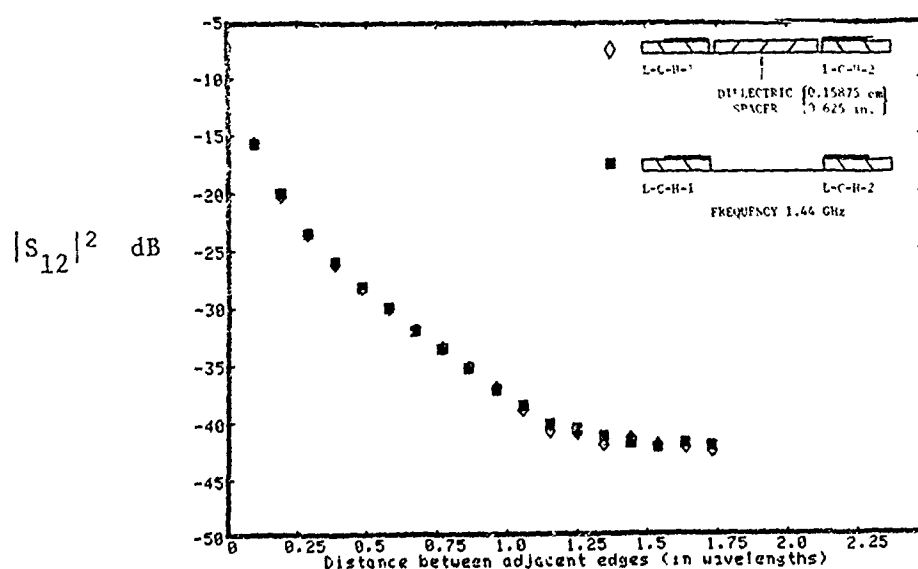
Figure 7 E-Plane dielectric spacer effects



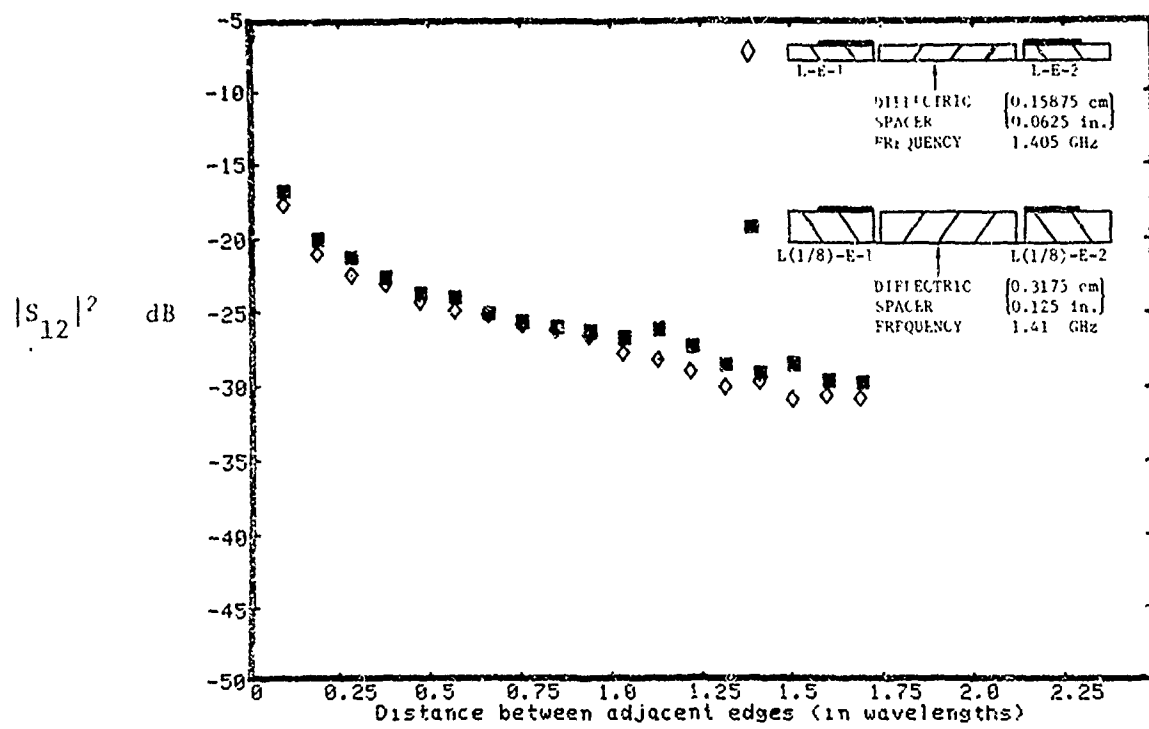
a) L-Band rectangular patch (1/16")



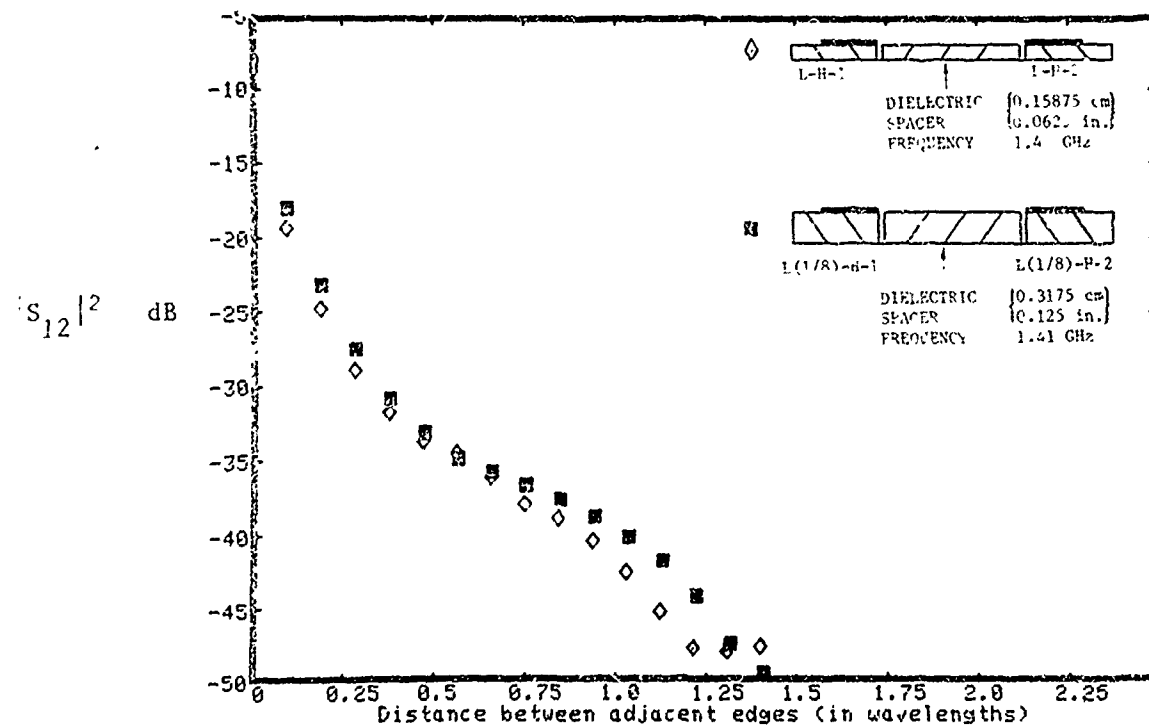
b) L-Band rectangular patch (1/8")



c) L-Band circular patch (1/16")
Figure 8 H-Plane dielectric spacer effects

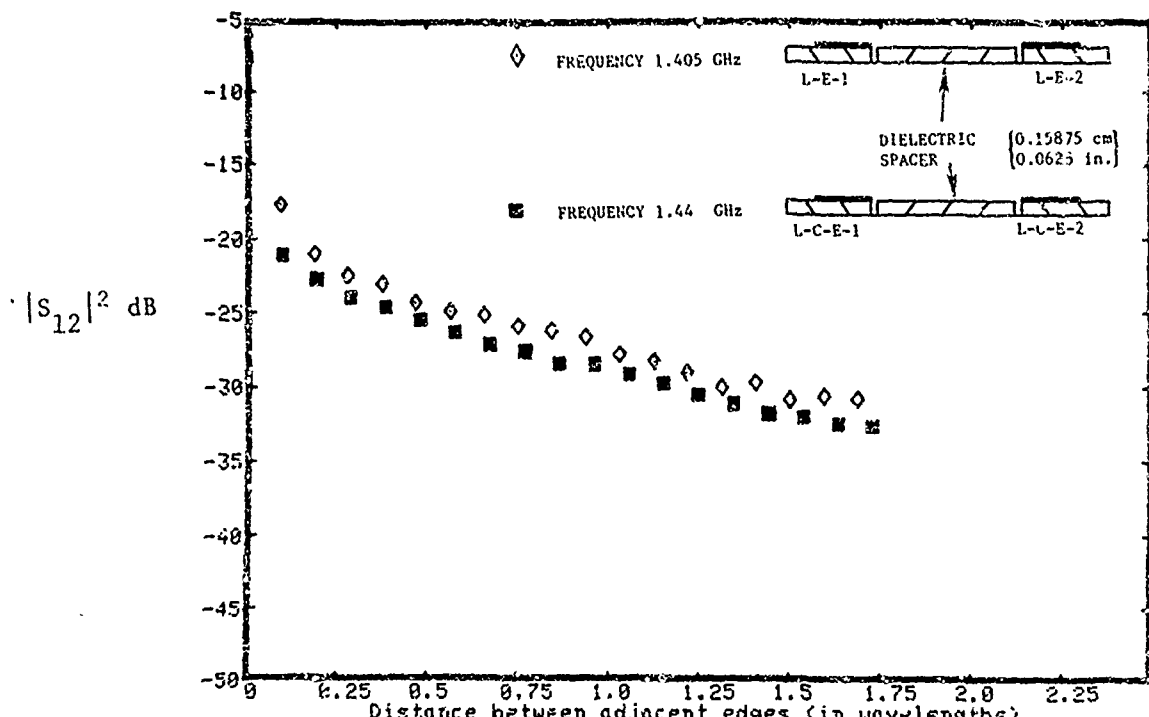


a) E-Plane

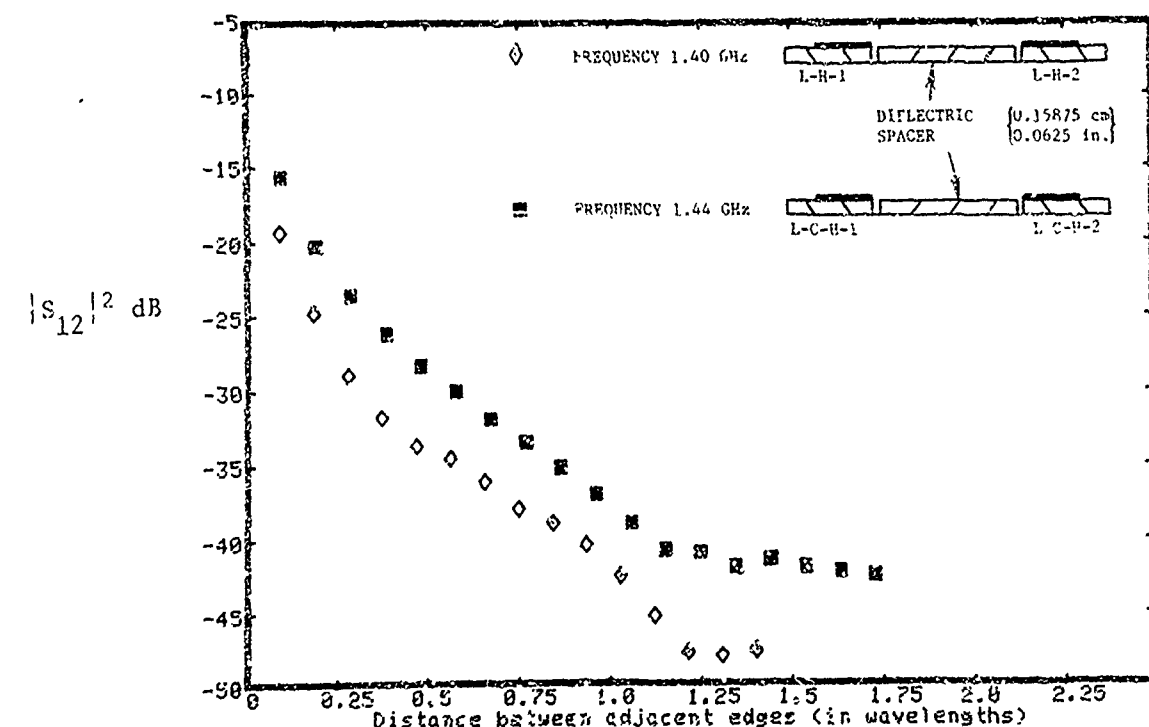


b) H-Plane

Figure 9 Coupling versus thickness

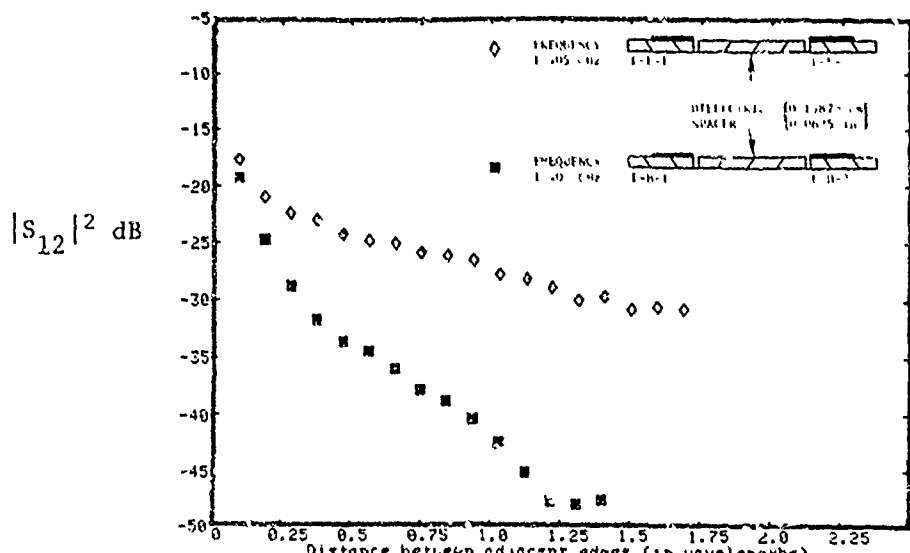


a) E-Plane

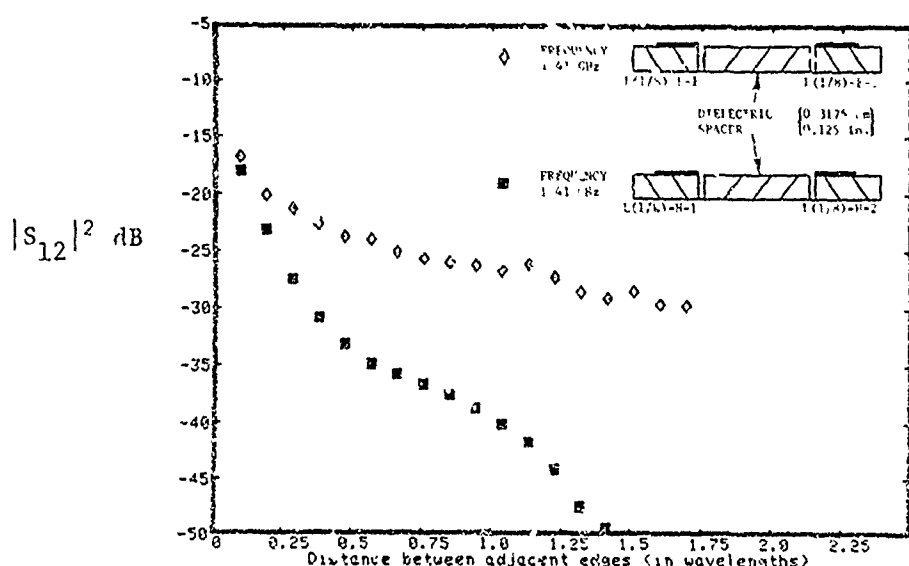


b) H-Plane

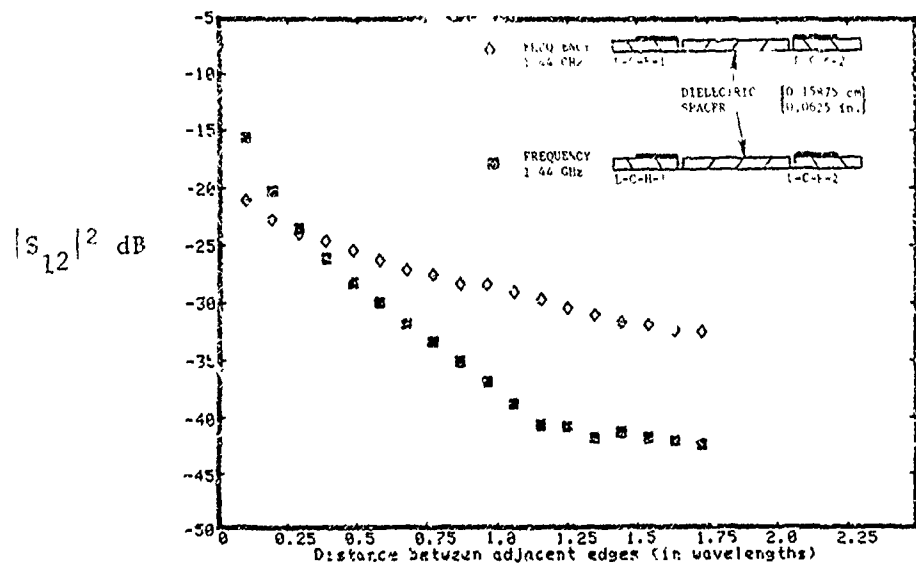
Figure 10 Rectangular versus circular coupling



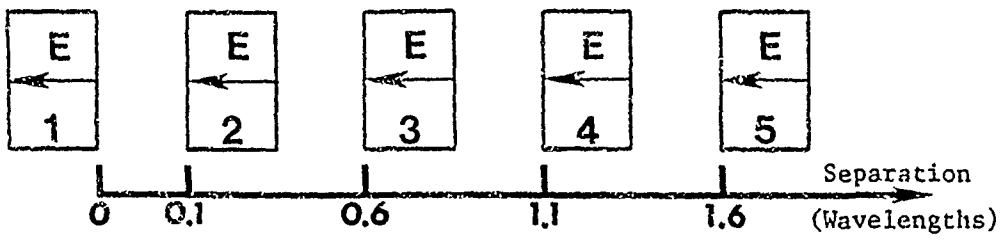
a) L-Band rectangular patches (1/16")



b) L-Band rectangular patches (1/8")

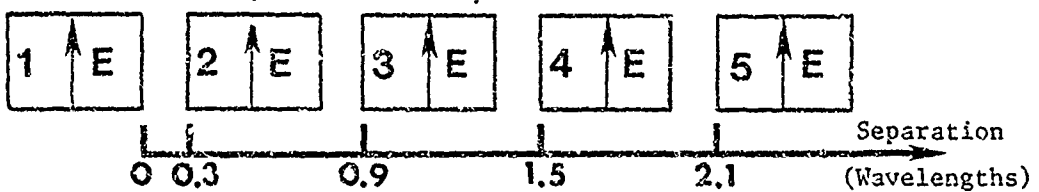


c) L-Band circular patches (1/16")
Figure 11 E-Plane versus H-Plane coupling



$$\begin{aligned}
 S_{11} = S_{22} = S_{33} = S_{44} = S_{55} &= -12.6 \angle 120^\circ \text{ dB} \\
 S_{12} = S_{21} = S_{23} = S_{32} = S_{34} = S_{43} = S_{45} = S_{54} &= -24.4 \angle 20^\circ \text{ dB} \\
 S_{13} = S_{31} = S_{24} = S_{42} = S_{35} = S_{53} &= -26.6 \angle -137.5^\circ \text{ dB} \\
 S_{14} = S_{41} = S_{25} = S_{52} &= -31.1 \angle -16.3^\circ \text{ dB} \\
 S_{15} = S_{51} &= -32.3 \angle 132.5^\circ \text{ dB}
 \end{aligned}$$

a) E-Plane Array



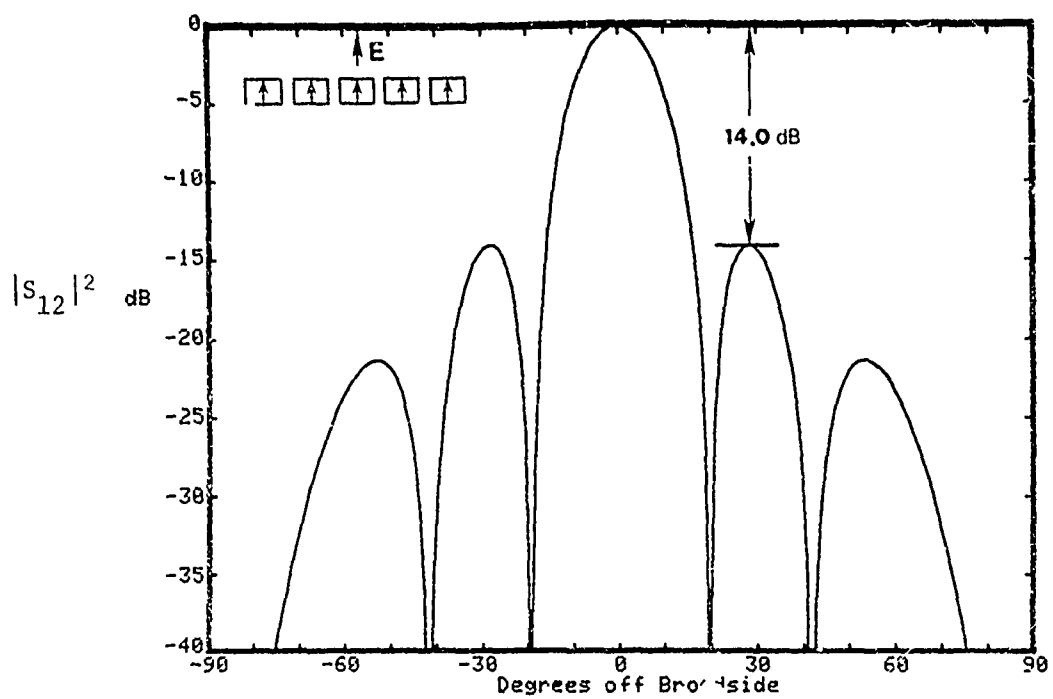
$$\begin{aligned}
 S_{11} = S_{22} = S_{33} = S_{44} = S_{55} &= -18 \angle 162^\circ \text{ dB} \\
 S_{12} = S_{21} = S_{23} = S_{32} = S_{34} = S_{43} = S_{45} = S_{54} &= -19.5 \angle 177.5^\circ \text{ dB} \\
 S_{13} = S_{31} = S_{24} = S_{42} = S_{35} = S_{53} &= -35 \angle -29.5^\circ \text{ dB} \\
 S_{14} = S_{41} = S_{25} = S_{52} &= -45 \angle 150^\circ \text{ dB} \\
 S_{15} = S_{51} &= -55 \angle -56^\circ \text{ dB}
 \end{aligned}$$

b) H-Plane Array

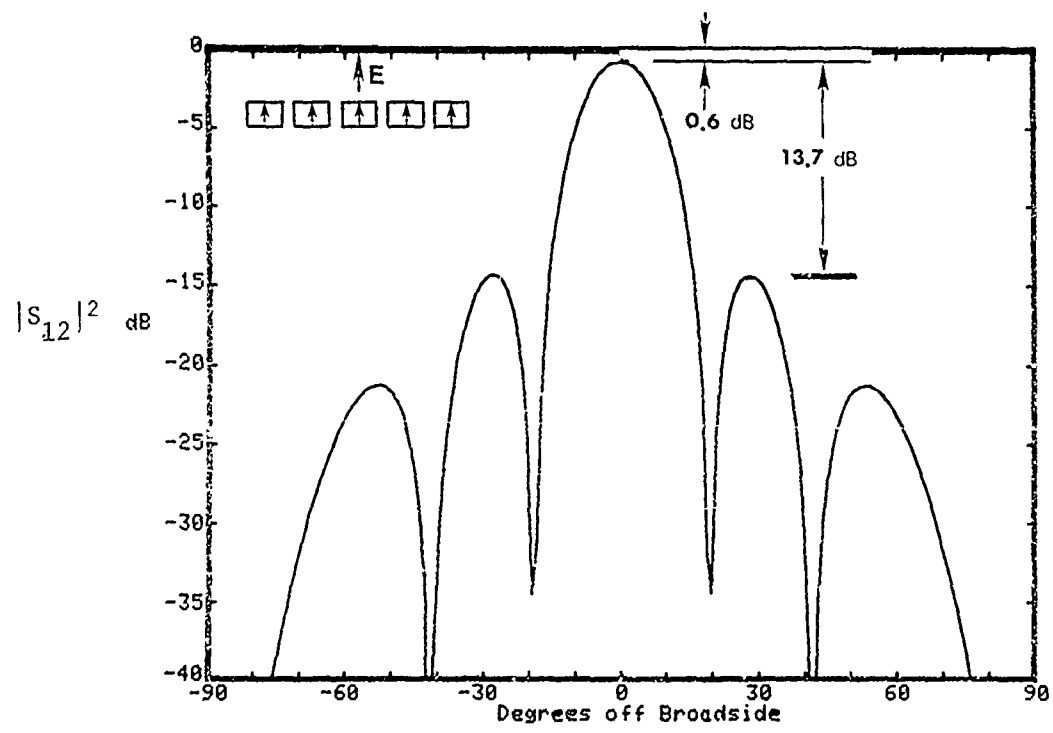
Figure 12 Array Geometries for the Design Examples

Table 1 Linear Array Excitation Coefficients [a_m]

	H-Plane		E-Plane	
	Ideal	With Coupling	Ideal	With Coupling
B	1	0.954 @ -1.1°	1	0.966 @ -1.9°
R	1	0.903 @ -1.6°	1	0.961 @ -0.2°
I	1	0.909 @ -1.3°	1	0.972 @ -1.5°
O	1	0.903 @ -1.6°	1	0.961 @ -0.2°
A	1	0.954 @ -1.1°	1	0.966 @ -1.9°
D	1 @ 0°	0.993 @ -2.7°	1 @ 0°	0.965 @ -2.7°
D	1 @ -73.9°	0.963 @ -74.8°	1 @ -73.9°	0.929 @ -76.5°
E	1 @ -147.8°	0.962 @ -149.1°	1 @ -147.8°	0.936 @ -148.4°
E	1 @ 138.4°	0.969 @ 137.1°	1 @ 138.4°	0.962 @ 136.8°
E	1 @ 64.5°	0.976 @ 65.4°	1 @ 64.5°	0.930 @ 61.7°

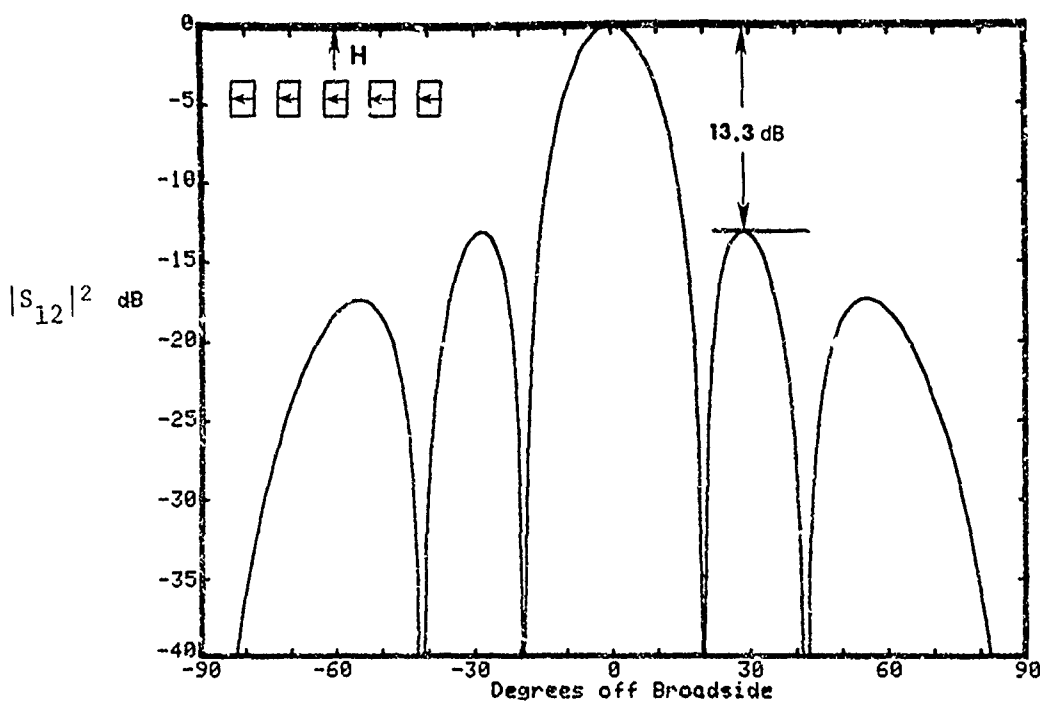


a) H-Plane pattern without coupling

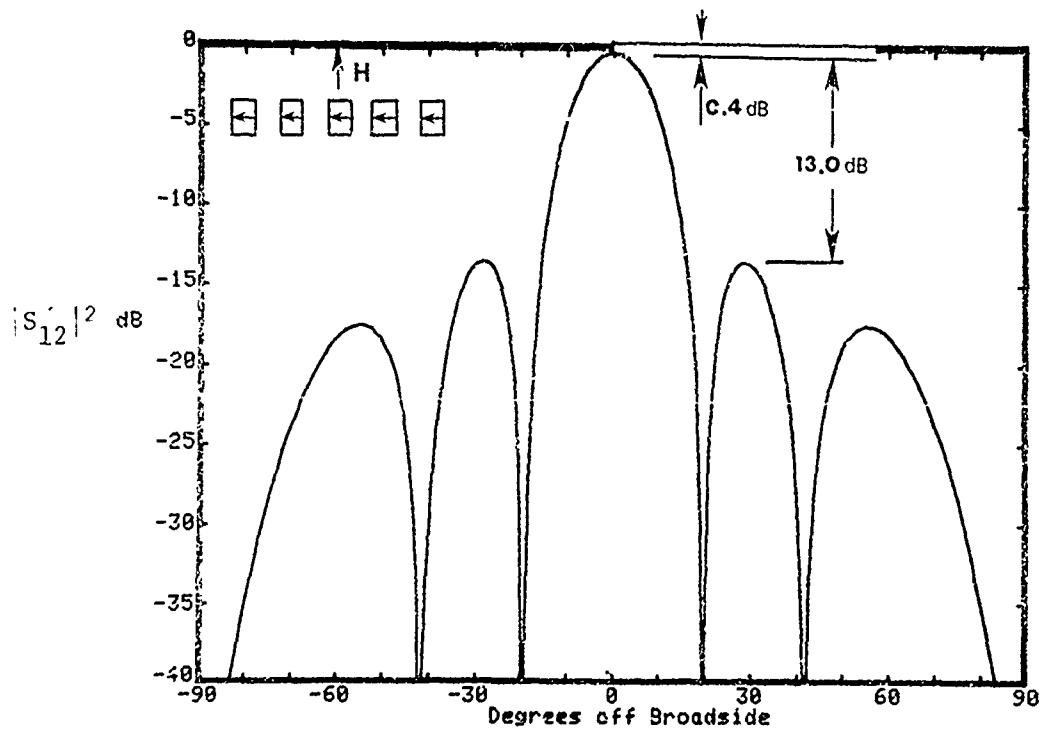


b) H-Plane pattern with coupling

Figure 13 H-Plane array (Broadside)

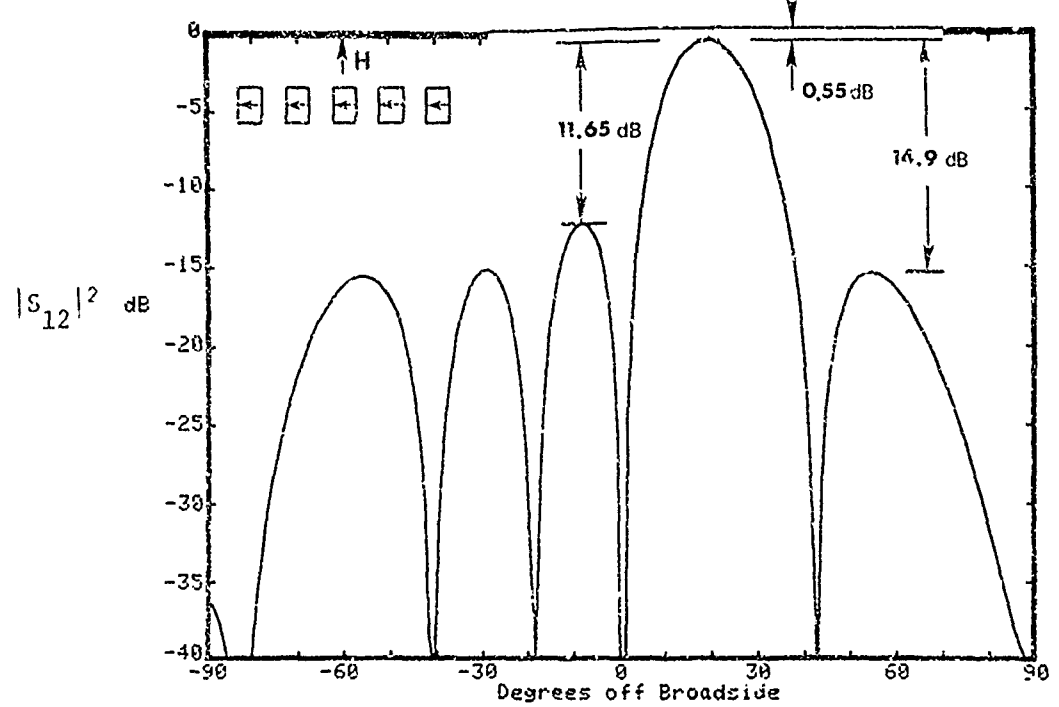


a) E-Plane pattern without coupling

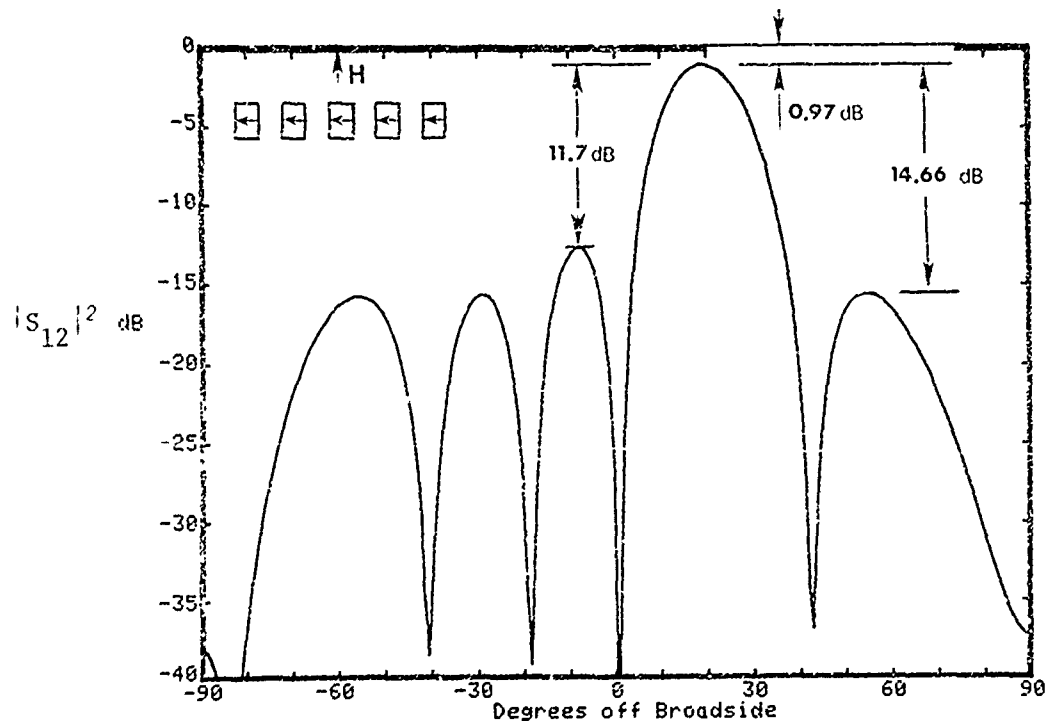


b) E-Plane pattern with coupling

Figure 14 E-Plane array (Broadside)



a) E-Plane pattern without coupling



b) E-Plane pattern with coupling

Figure 15 E-Plane array (20°)

SOME CONFORMAL, PRINTED CIRCUIT ANTENNA DESIGNS

D. H. SCHUBERT
F. G. FARRAR
HARRY DIAMOND LABORATORIES
US ARMY ERADCOM

SUMMARY

A variety of antennas that are based upon the radiating microstrip concept have been designed and tested. These antennas are conformally mounted on large and small bodies, and they are sometimes integrated into radomes. In all cases, the antennas are efficient radiators and they have a narrow, but adequate, operating bandwidth.

The SPIRAL-SLOT ANTENNA is an electrically small, microstrip radiator designed for small-diameter missile applications. High radiation efficiency is obtained by strongly coupling RF currents to the body of a missile and exciting the dipole mode of radiation. This mode of excitation is accomplished without dividing the body of the missile into two electrically insulated sections. When the antenna operates in the UHF band, an instantaneous bandwidth of approximately 2 percent is achieved. A means is provided for mechanically tuning the antenna over a narrow frequency range. The spiral-slot antenna produces an axially polarized radiation field and dipole radiation pattern with 0 dBi gain.

The DUAL-FREQUENCY PIGGYBACK ANTENNA is a microstrip antenna that allows two radiators to share a single aperture. The piggyback antenna consists of $\lambda/4$ or $\lambda/2$ radiators that are stacked. The upper element is somewhat smaller than the lower element, so that the lower element forms the ground plane for the upper one. Each antenna is fed from a coaxial line, with the outer conductor of the upper element's feed forming an inductive tuning post within the lower element. This tuning post aids in impedance matching the lower element.

The PARASITIC-TUNED MICROSTRIP ANTENNA utilizes narrow conducting strips adjacent to the driven radiator to alter its impedance and radiation

properties. These strips, which couple to the driven patch, can be used to improve the impedance match at a specific frequency or to increase the bandwidth of the antenna.

1.0 SPIRAL-SLOT ANTENNA

1.1 DESCRIPTION

The spiral-slot antenna [2] is ideally suited for applications that permit excitation of axial currents along a cylindrical body that is only a fraction of a wavelength in diameter. The antenna (Fig. 1) is fabricated from a tube of dielectric material that is copper-plated to form a ground plane on the interior surface and a spiral-shaped conductor on the exterior surface. The spiral conductor is connected to the ground plane at one end of the cylinder and is open circuited at the other end to form a $\lambda/4$ microstrip radiator. A coaxial probe feeds the antenna.

Three models of the spiral-slot antenna are shown in figure 2.

1.2 PERFORMANCE

The performance of the spiral-slot antenna is measured with the antenna mounted in a short (approximately $\lambda/4$), cylindrical test section as shown in figure 3. Since the antenna is designed to excite axial currents and the dipole mode of radiation, all tests for radiation pattern, gain, and input impedance match are conducted with the antenna in this simulated operating environment. Because it is electrically small, the antenna without a body is a very low efficiency radiator.

1.2.1 RADIATION PATTERN

The gain and the radiation pattern of the spiral-slot antenna are shown in figure 4. The electric field is polarized parallel to the axis of the cylinder. The $\phi = 0^\circ$ pattern is a cut through the axis in the plane of the inductive feed post. The $\phi = 90^\circ$ pattern is in the orthogonal plane. The roll plane pattern at $\theta = 90^\circ$, the plane orthogonal to the axis, shows less than a 1-dB deviation from a circle. The peak gain of approximately +1 dBi is just 1 dB less than the maximum

possible from a dipole antenna, indicating that the spiral-slot antenna is a highly efficient radiator. The cross-polarized field component is 10 to 15 dB below the principal component and is probably the main contributing factor to this 1-dB loss in gain.

1.2.2 BANDWIDTH

A plot of main-polarized and cross-polarized radiation-pattern gain over a narrow frequency range is given in figure 5. The spiral-slot antenna displays a 3-dB gain-bandwidth of 9 MHz or approximately 3 percent. The instantaneous impedance (2:1 VSWR) bandwidth is 4 MHz--about 2 percent. The cross-polarized field component is at least 9 dB down and decreases to about 14 dB down at the design center frequency of approximately 238 MHz.

1.2.3 INPUT IMPEDANCE

The plot of the input return loss in figure 6 shows the extremely good impedance match of the spiral-slot antenna at approximately 238 MHz. At the minimum return loss of 20 dB, the VSWR is 1.2:1. Also in figure 6 is a Smith Chart plot of the impedance locus as the input frequency is varied from 200 to 300 MHz. At very low frequencies, the impedance approaches zero. The real-axis crossing is at approximately 60 ohms at 237.4 MHz. The Q-factor of the antenna, based on the 3-dB input return loss, is a moderate 18, indicating that only small losses in gain can be expected from reactive stored energy.

1.2.4 TUNING

A technique exists for tuning the spiral-slot antenna over a small frequency range. By trimming away the conductor at T_1 or T_2 in figure 7, the resonant frequency can be increased or decreased. The effect of changes in these dimensions on the frequency is shown in figure 8. For each millimeter increase in T_1 , the resonant frequency increases 0.3 to 0.5 MHz, and the return loss is not changed appreciably. For each millimeter increase in T_2 , the resonant frequency decreases 1 MHz and the impedance match degrades.

Normally, the antennas are designed to resonate slightly below the desired frequency. During electrical testing, T_1 is trimmed as needed to raise the frequency and thus compensate for the detuning effects caused by variations in the conductor dimensions and the dielectric constant of the substrate. Trimming T_1 is preferred over trimming T_2 because of the smaller slope of the tuning curve and the smaller effect on the input impedance.

2.0 DUAL-FREQUENCY PIGGYBACK ANTENNA

The dual-frequency piggyback antenna [1] consists of two microstrip antennas that are stacked to share a common aperture, but are fed separately to allow radiation of two independent signals. The elements of the piggyback antenna (Fig. 9) may be either $\lambda/2$ (microstrip) or $\lambda/4$ (parallel plate) microstrip radiators. However, the lower element should be somewhat larger than the upper element in order to form a good ground plane for the upper element. The lower element is fed against the ground plane by means of a coaxial probe. The upper element is fed against the lower element by means of a second coaxial probe. The outer conductor of this coaxial feed line passes through the lower element and connects to the ground plane and the element. This forms an inductive post within the lower element that can be used to improve the impedance match of the element.

Figure 10 shows a model of the piggyback antenna. By using a $\lambda/2$ lower element and a $\lambda/4$ upper element, the antennas can operate at nearly the same frequency. Various combinations of $\lambda/2$ and $\lambda/4$ elements can be used to provide considerable freedom in the choice of operating frequencies. Also, the shape of the microstrip radiator (wedge, circle, rectangle, etc.) may be selected to fit the application. The radiation patterns of the antenna in figure 10 are shown in figure 11. The large amount of radiation in the lower hemisphere is due to diffraction around the relatively small ground plane on which the antenna is mounted.

The impedance match of the $\lambda/4$ element is controlled by the distance between the feed probe and the shorting wall. The impedance match of the $\lambda/2$ element is controlled by the location of the feed probe and its proximity to the inductive post formed by the coaxial feed of the upper element. The VSWR of the lower element in figure 10 is 1.33 and the 2:1 VSWR bandwidth is 0.5 percent. (The substrate thickness is 1.6 mm). The isolation between the elements is 20 dB at 990 MHz and 37 dB at 1140 MHz.

3.0 PARASITIC-TUNED MICROSTRIP ANTENNA

The parasitic-tuned microstrip antenna (Fig. 12) utilizes narrow conducting strips adjacent to the driven radiator in order to alter its impedance and radiation properties. These strips couple to the nonradiating edges of the antenna and significantly modify its impedance. A square, edge-fed microstrip antenna with $VSWR=4$ can be matched to $VSWR=1.2$ by using the parasitic strips.

The antenna works best when the parasitic strips are slightly longer than the patch. The performance of the antenna is strongly affected by the separation between the strips and the patch. The best performance has been obtained when the separation is 2.5 to 3 times the substrate thickness.

The interaction between the strips and the patch changes the resonant frequency of the patch a few percent. However, it is possible to broaden the impedance bandwidth of the antenna by stagger tuning the strips. Figure 13 shows the VSWR of the antenna in figure 12 before and after the strips were added. Radiation patterns of the parasitic-tuned antenna are shown in figure 14. The H-plane radiation pattern is slightly skewed by the asymmetry of stagger-tuned strips.

Another parasitic-tuned antenna was fabricated on 1.27-cm thick silicone fiberglass dielectric and was tuned to operate at 350 MHz. The dimensions of this antenna are shown in figure 15. The bandwidth of this antenna ($VSWR=2$) was 5 percent, and the measured VSWR

was unchanged by the addition of a 0.4-mm-thick window of silicone fiberglass.

4.0 CONCLUSION

The performance characteristics of three types of microstrip radiators have been investigated. The spiral-slot antenna is electrically small and is ideally suited for conformal mounting on small-diameter bodies. The piggyback antenna radiates two independent signals from a single aperture. The impedance and bandwidth properties of the parasitic-tuned microstrip antenna are controlled by conducting strips adjacent to the driven patch. All of these antennas are efficient radiators.

5.0 REFERENCES

1. Jones, H. S., Jr. F. G. Farrar, and D. H. Schaubert, "Dual-Frequency Piggyback Antenna," US Patent No. 4,162,499, 24 July 1979.
2. Schaubert, D. H., A. R. Sindoris, and F. G. Farrar, "The Spiral Slot--A Unique Microstrip Antenna," Proceedings of 1978 Antenna Applications Symposium, Univ. of Illinois, 1978.

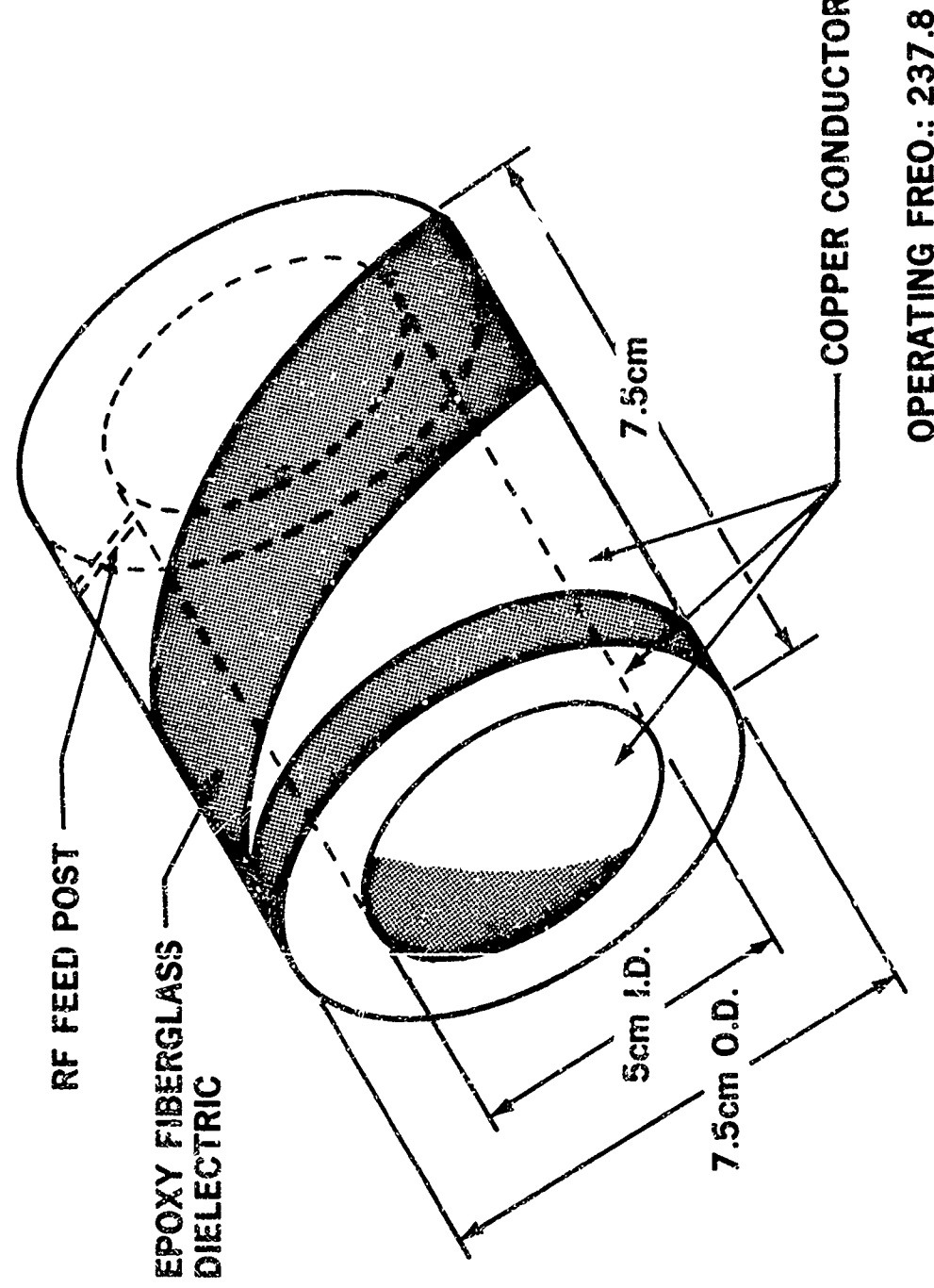


Figure 1. Drawing of typical spiral-slot antenna.

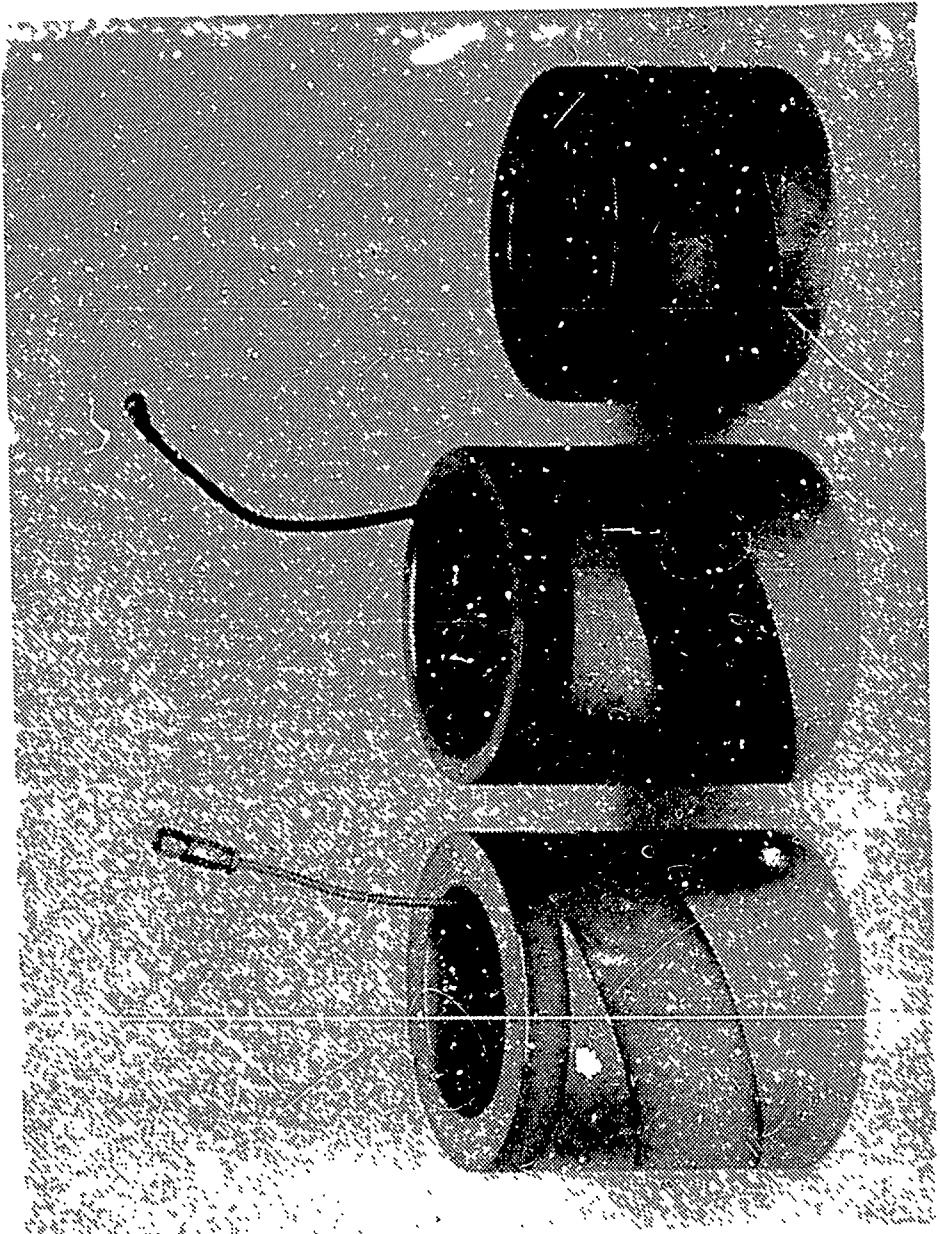


Figure 2. Prototype models of spiral-slot antenna.

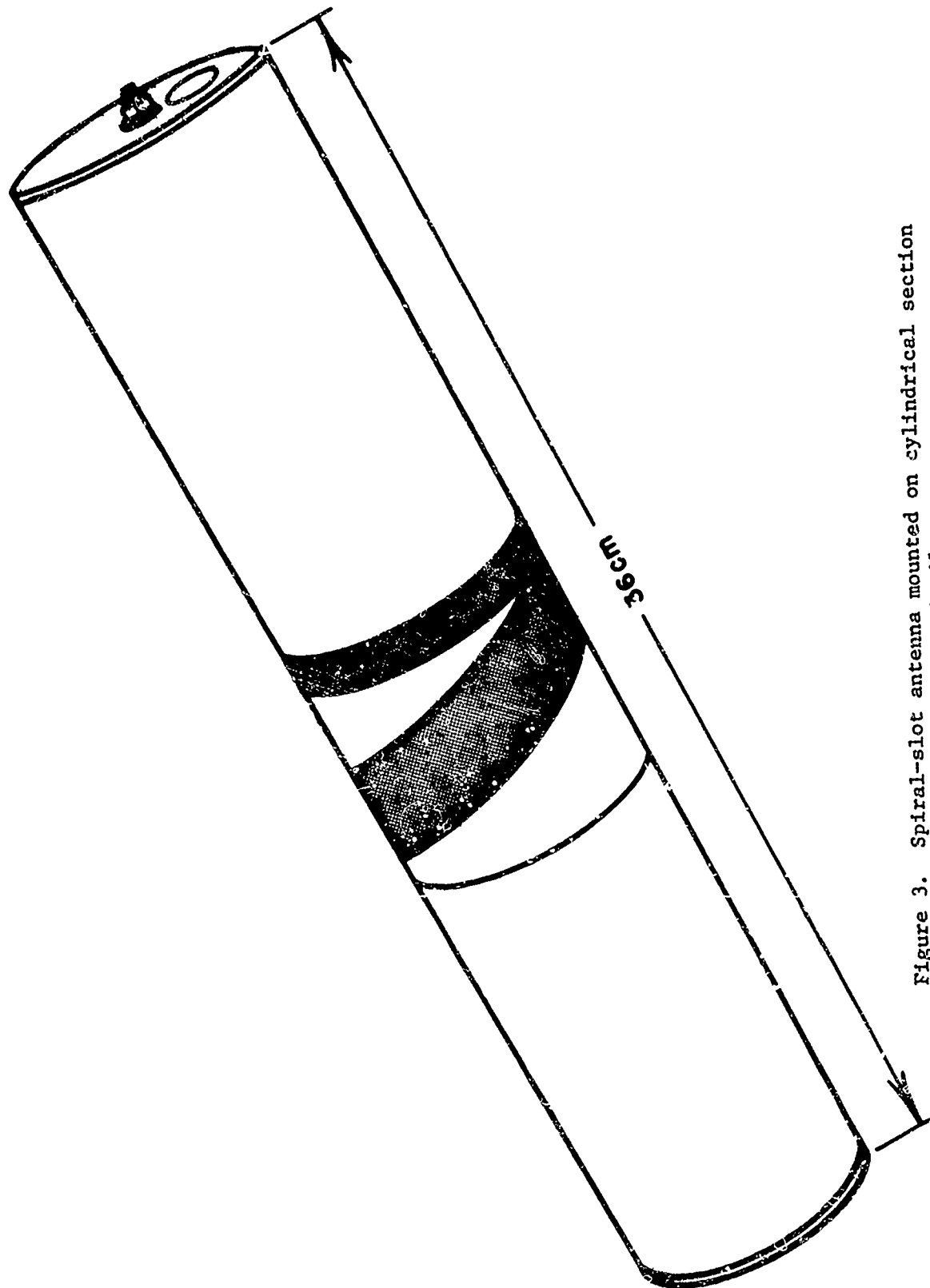


Figure 3. Spiral-slot antenna mounted on cylindrical section of small-diameter missile.

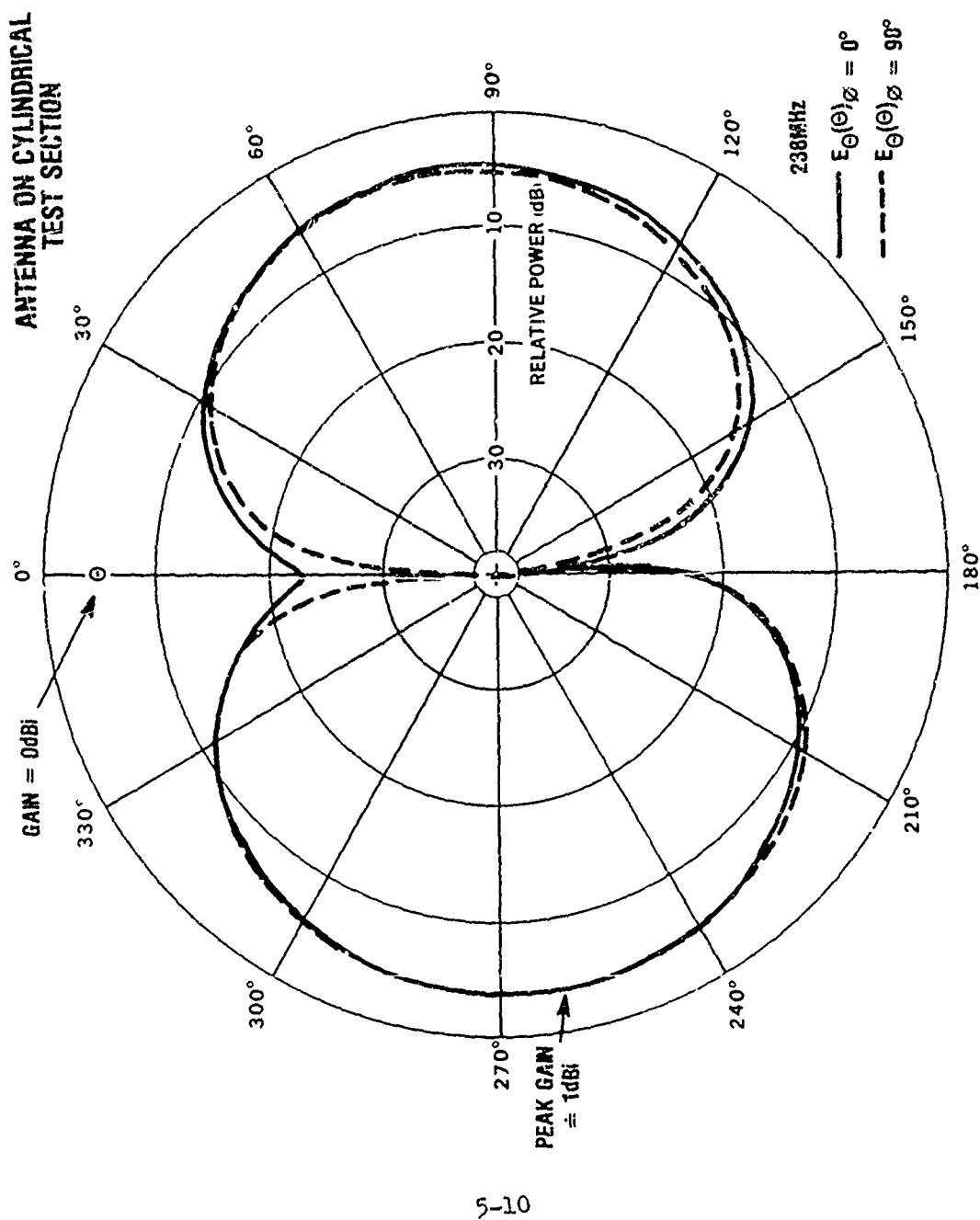


Figure 4. Radiation pattern of spiral-slot antenna mounted on cylinder.

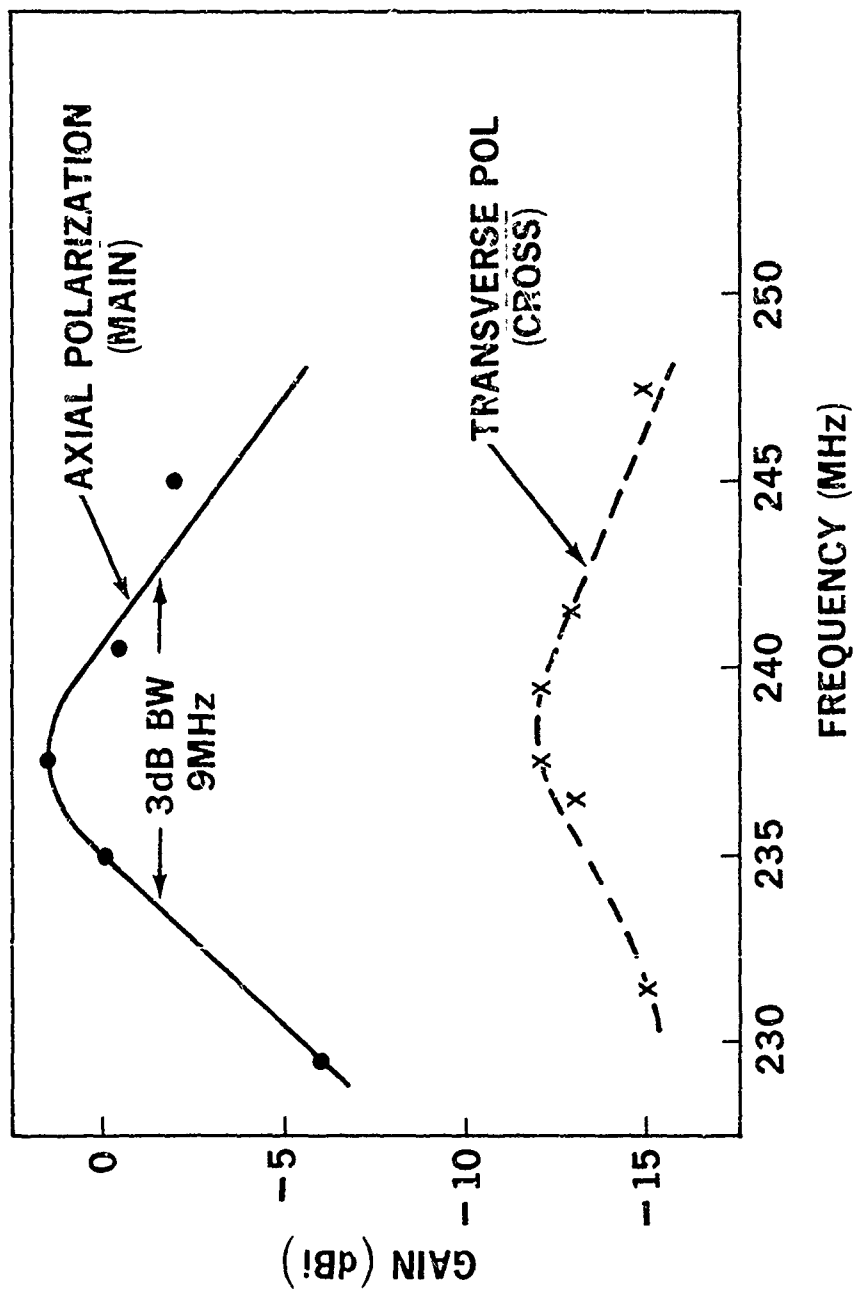


Figure 5. Gain-bandwidth of spiral-slot antenna.

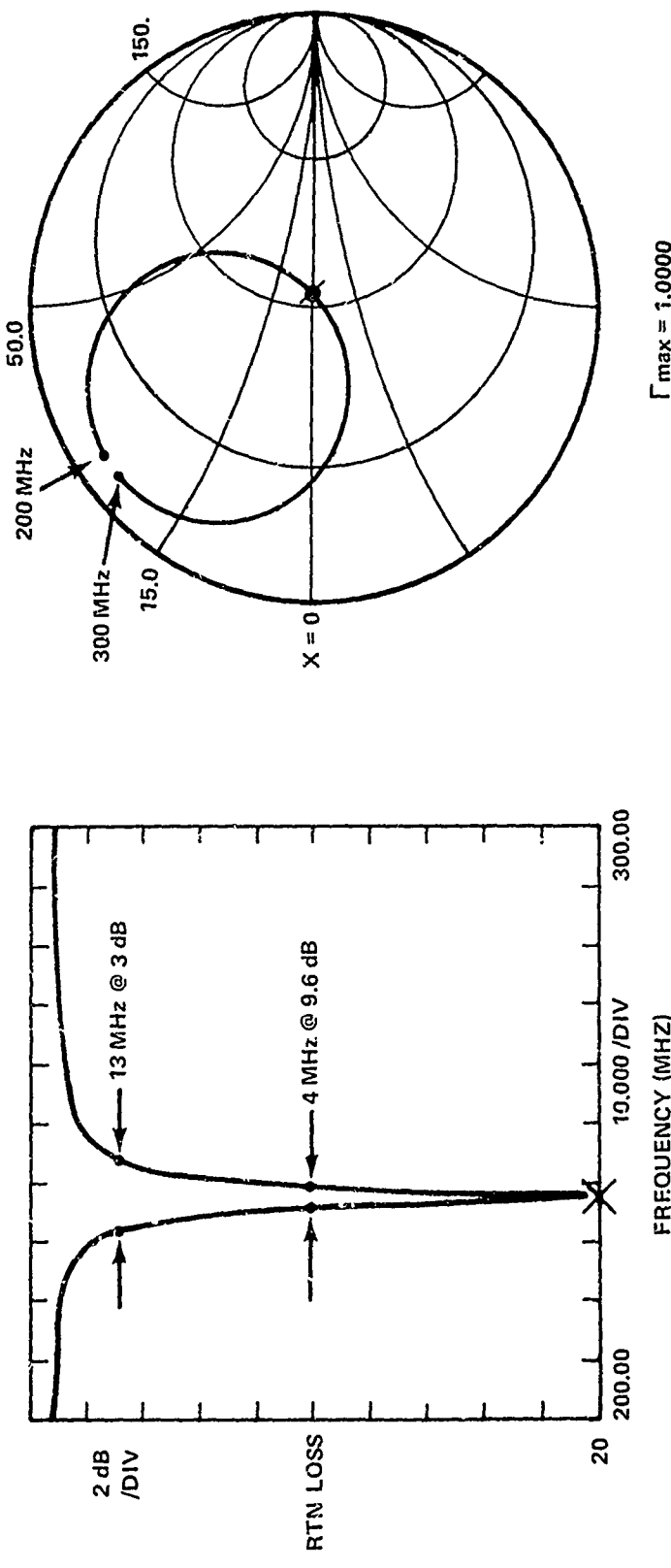


Figure 6. Input return loss and impedance of spiral-slot antenna on rocket.

IMPEDANCE

RETURN LOSS

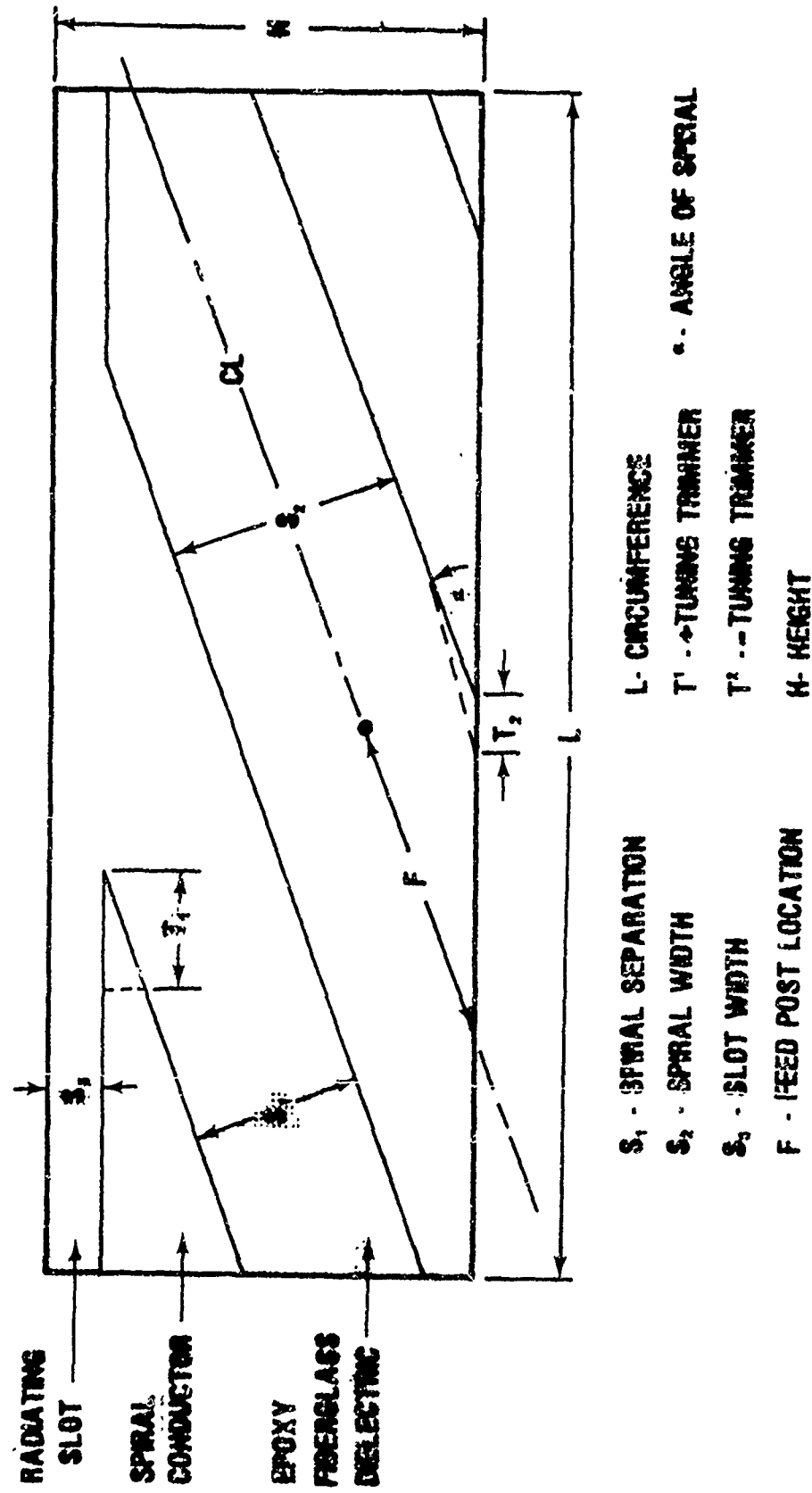


Figure 7. Planar view of spiral-slot antenna.

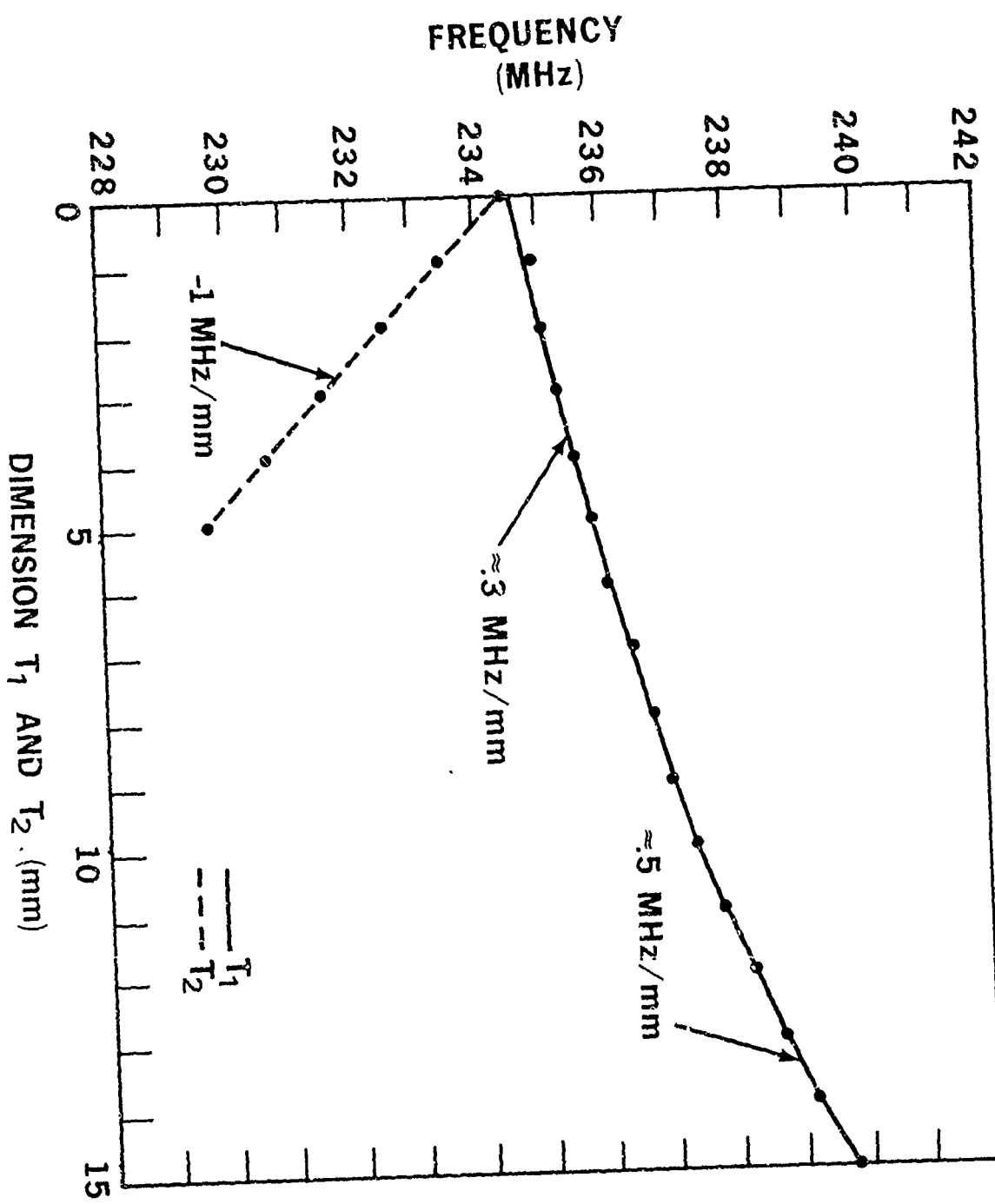


Figure 8. Tuning effects of T_1 and T_2 dimensions.

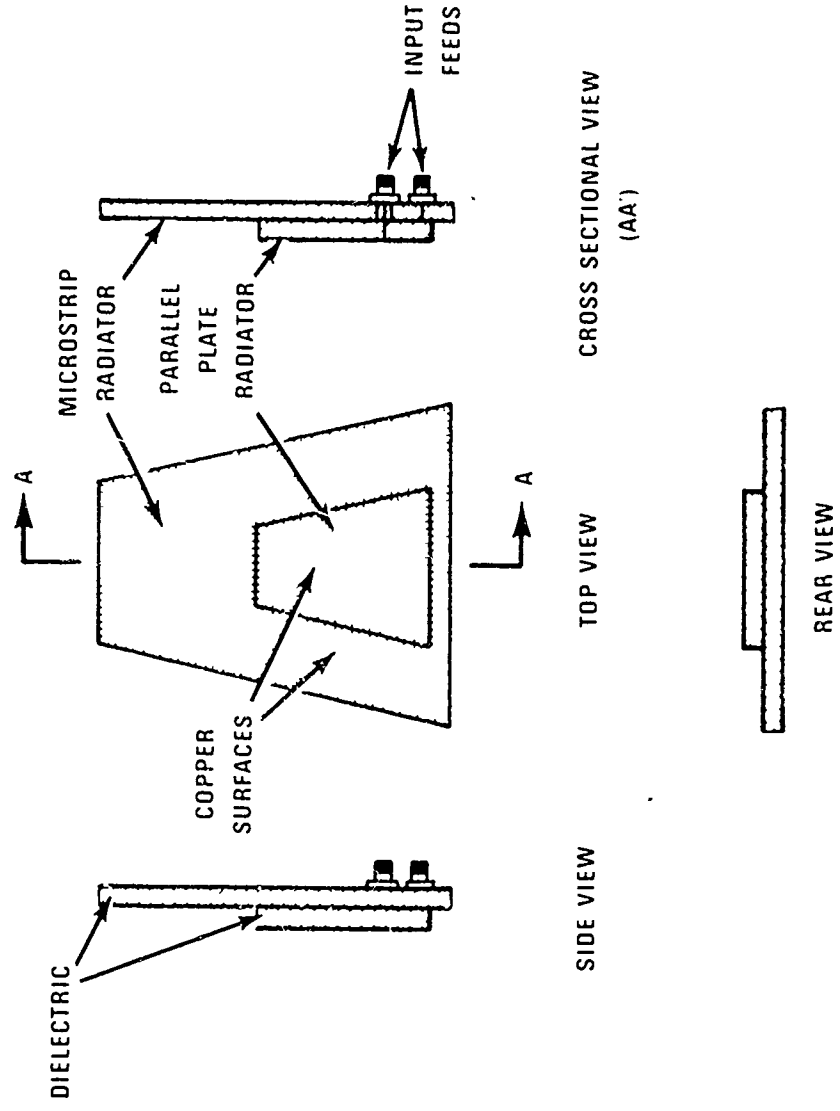
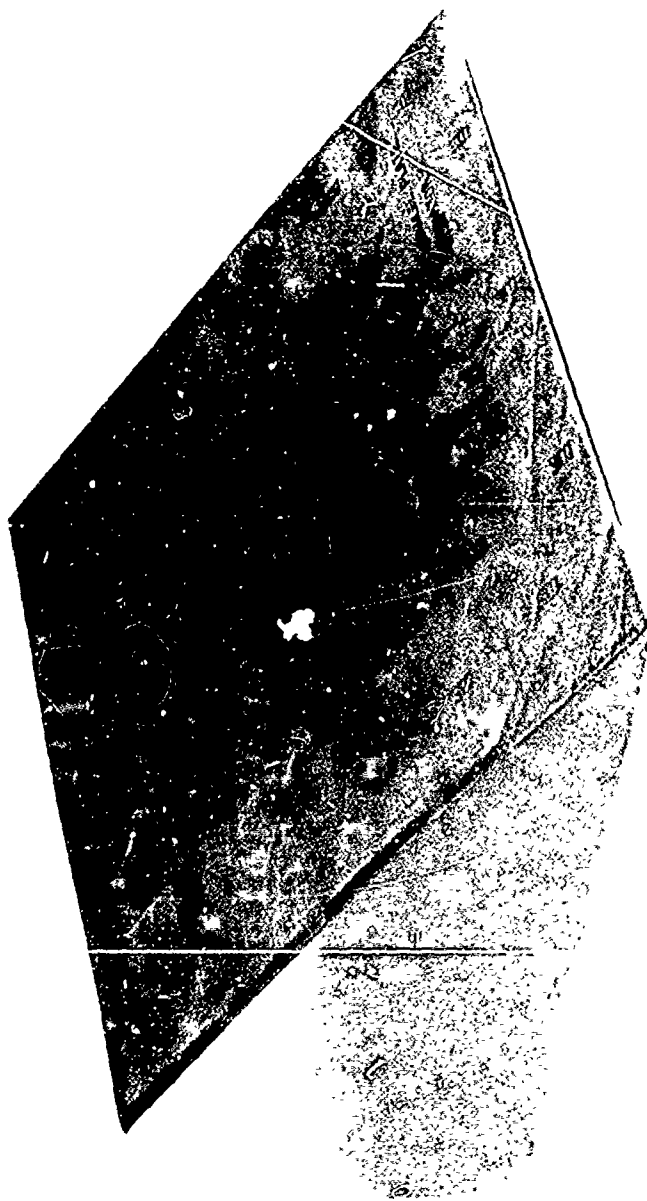


Figure 9. Piggyback microstrip antenna consisting of microstrip patch radiator ($\lambda/2$) and parallel plate radiator ($\lambda/4$).

Figure 10. Prototype model of piggyback microstrip antenna.



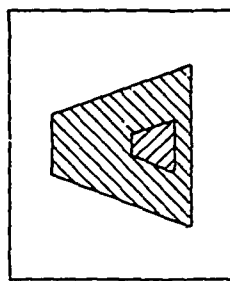
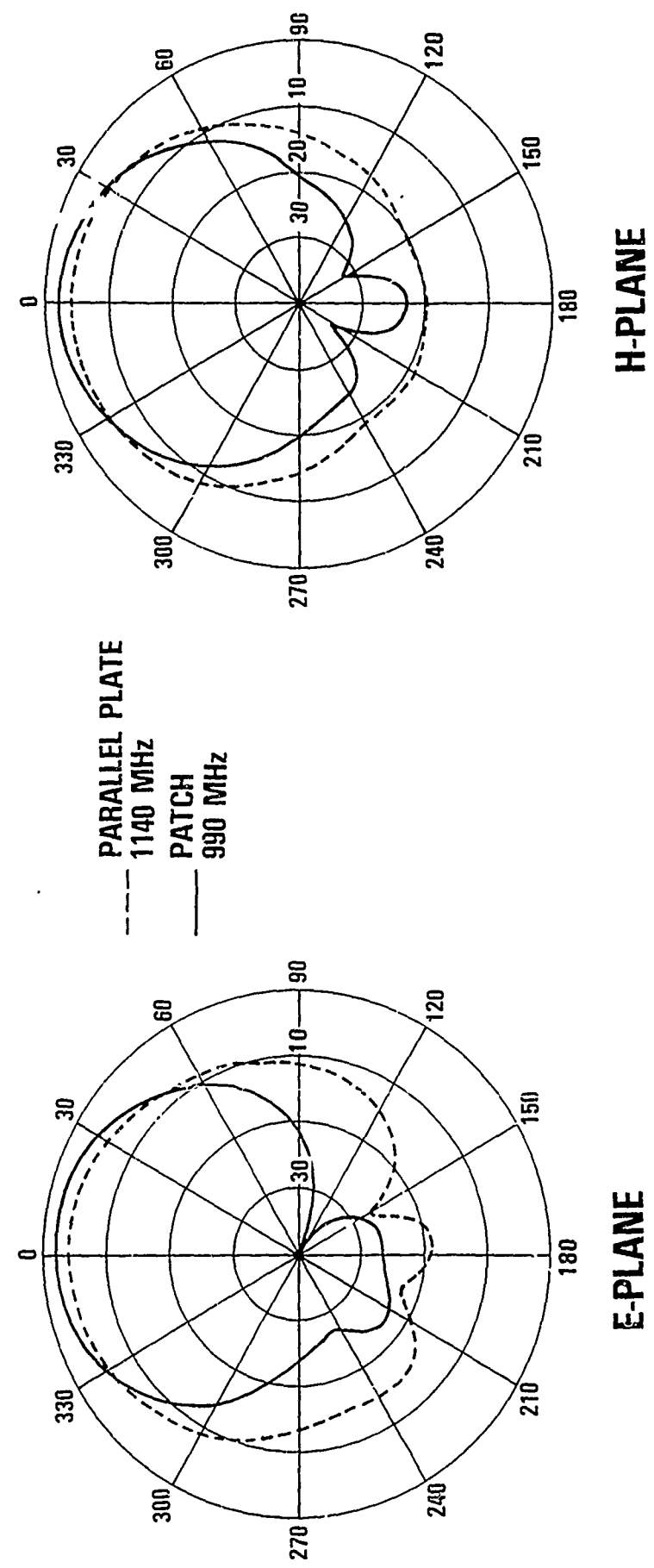


Figure 11. Radiation patterns of piggyback antenna. Patch gain = 3 dBi.
Parallel plate gain = 1 dBi.

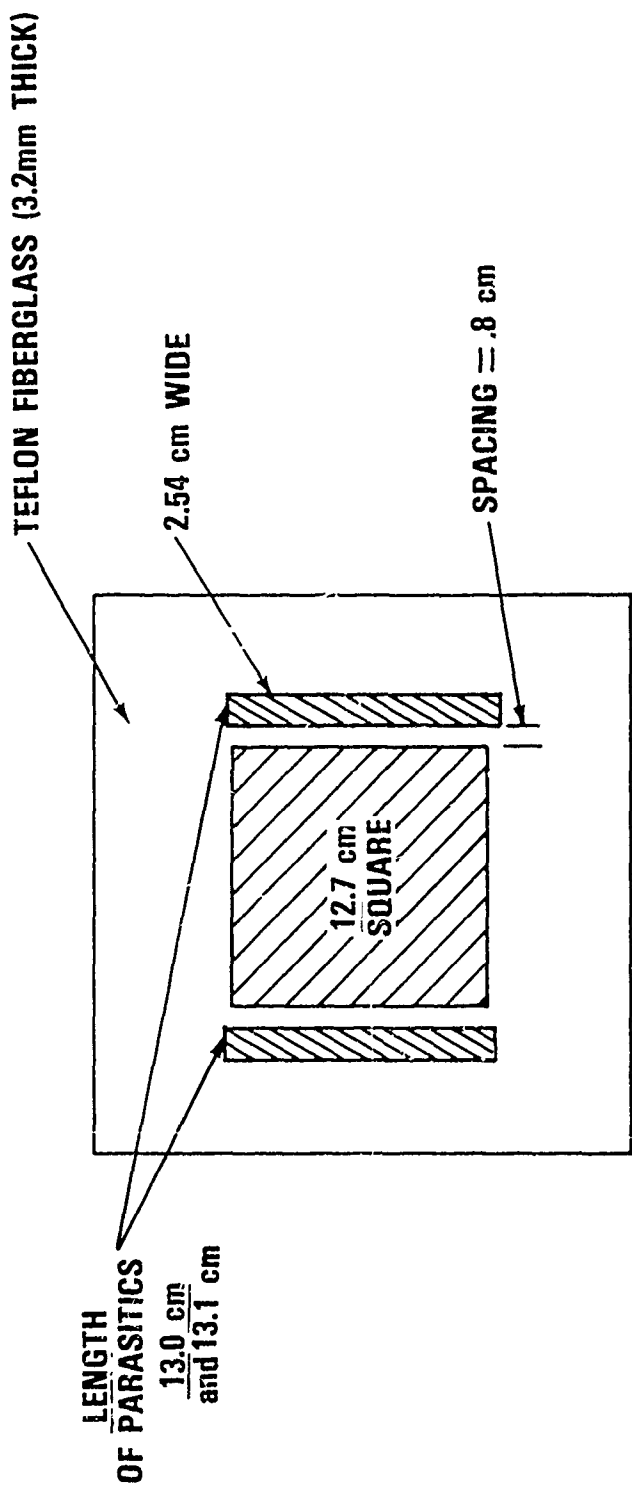


Figure 12. Typical parasitic-tuned microstrip antenna.

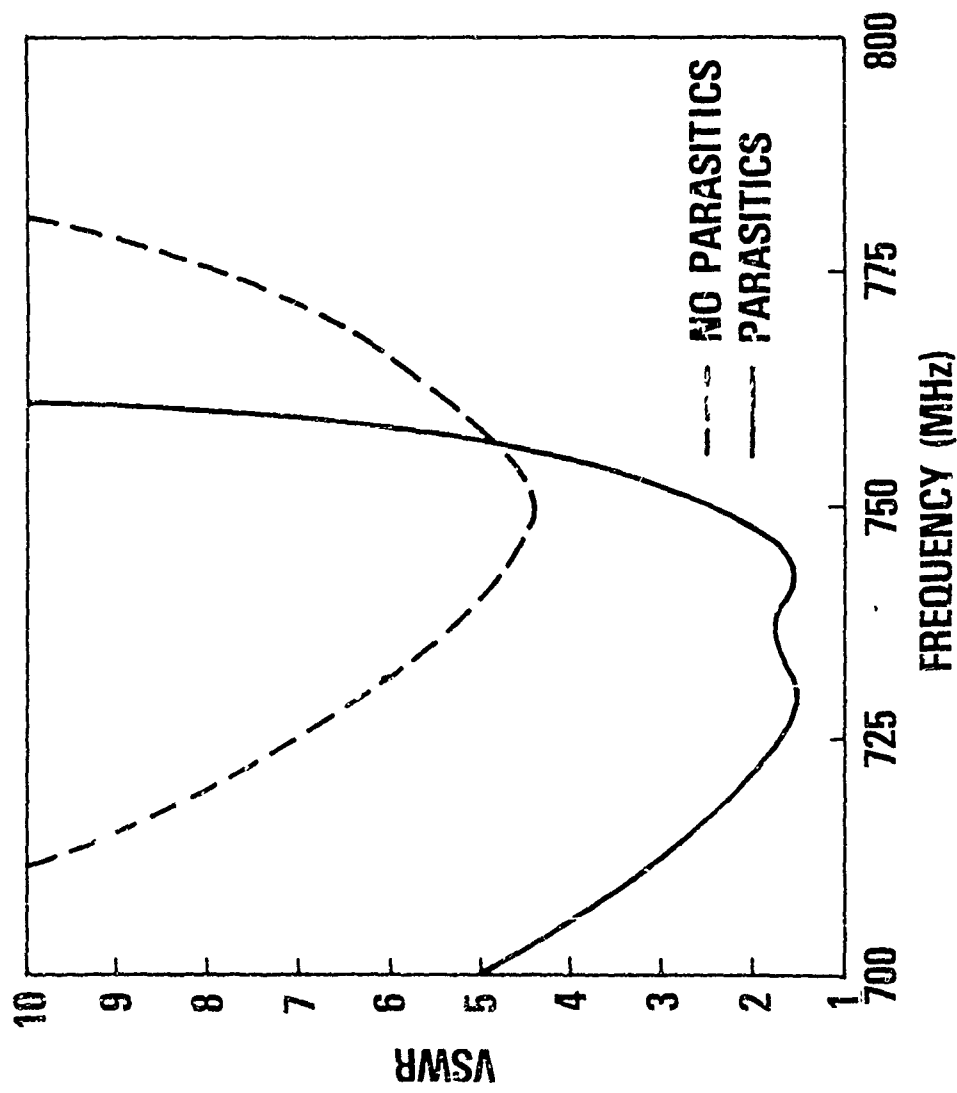
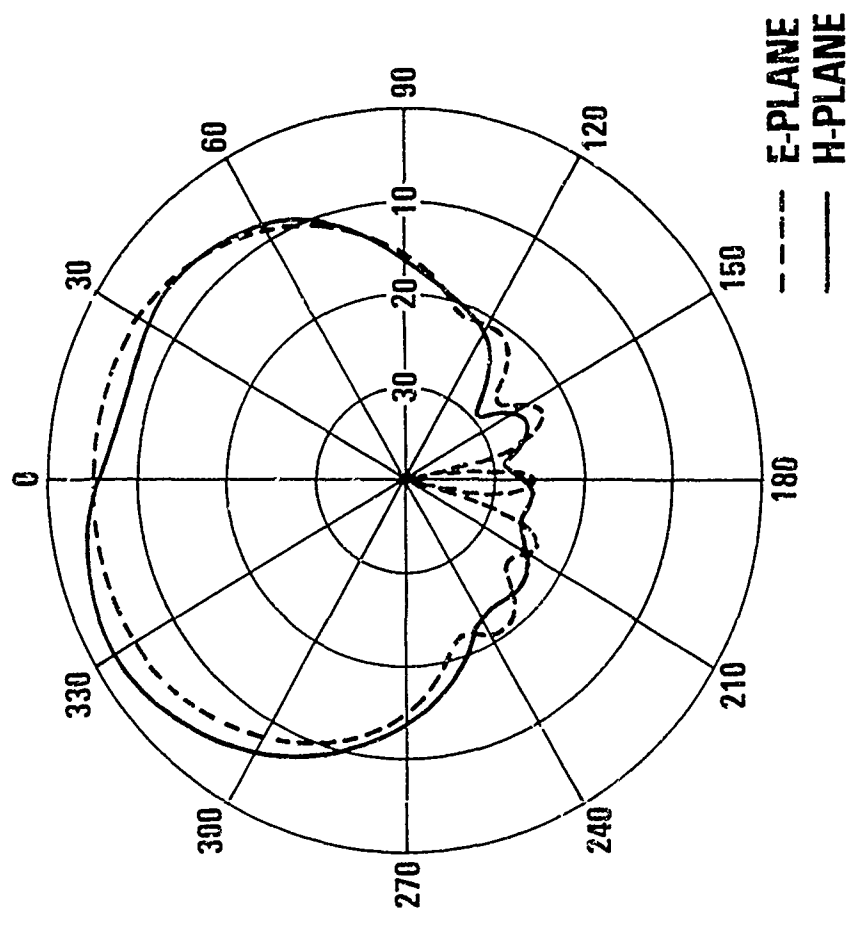


Figure 13. VSWR of microstrip patch with and without parasitics.



5-20

Figure 14. Radiation patterns of stagger-tuned antenna. E-plane
gain = 3 dBi.

1.27-cm-THICK SILICONE FIBERGLASS

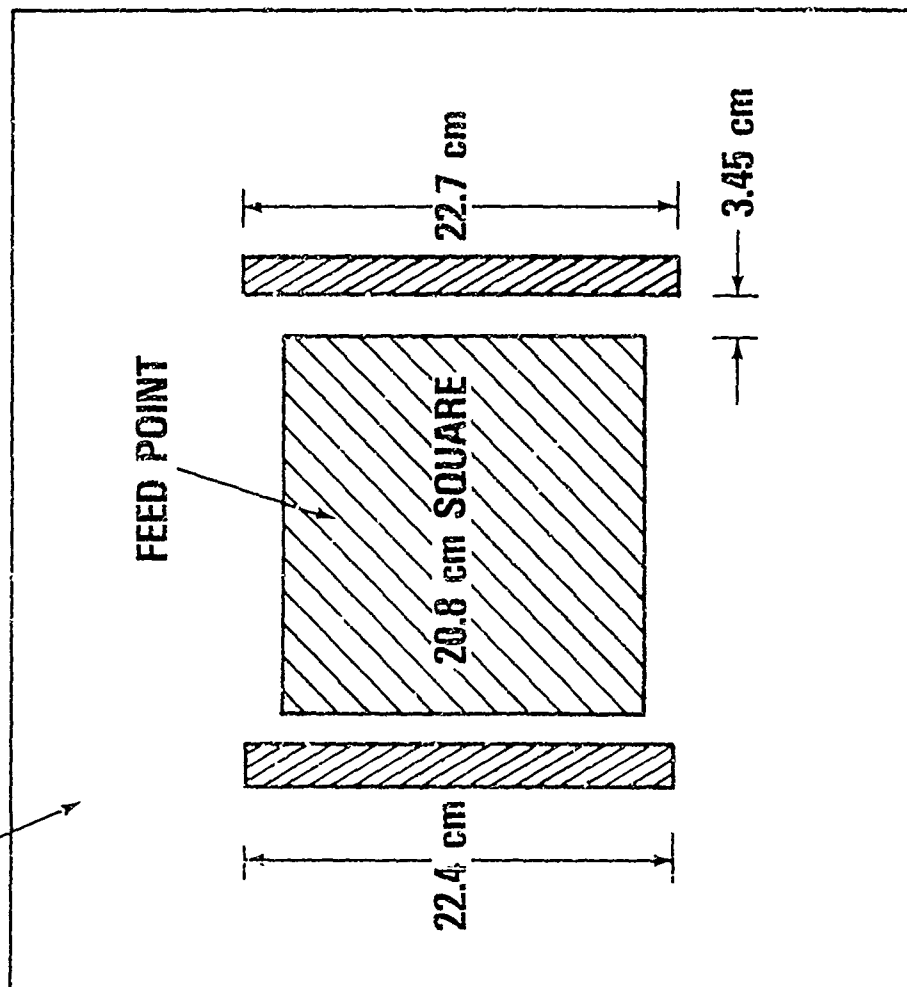


Figure 15. 350-MHz parasitic-tuned microstrip antenna.

ABSTRACT FOR THE NEW MEXICO STATE UNIVERSITY
MICROSTRIP ANTENNA WORKSHOP

Microstrip Antennas, Experimental Results

C. M. Kaloi

Pacific Missile Test Center

Point Mugu, California

ABSTRACT

A theoretical and experimental study has been made on two families of rectangular microstrip antenna elements. The first is the "Twin Electric Microstrip Antenna," where equally dimensioned thin electrically conducting rectangular shaped elements are formed on both sides of a dielectric substrate. Each of the elements act, in effect, as a ground plane for the other. The second incorporates the same element form factors but uses a larger ground plane.

The first family differs from the second in that both conducting strips and the appropriate slots are excited to radiate. In the second family, the ground plane being larger than the radiating element, could not be excited to radiate at the same resonant frequency as the smaller radiating element.

This paper very briefly outlines the analysis procedures for obtaining design equations and dwells mostly on presenting comparative results between experimental and theoretical studies and between the two families of microstrip antennas. These include results for the radiation resistance, center frequency, polarization characteristics (circular and linear), antenna gain, etc.

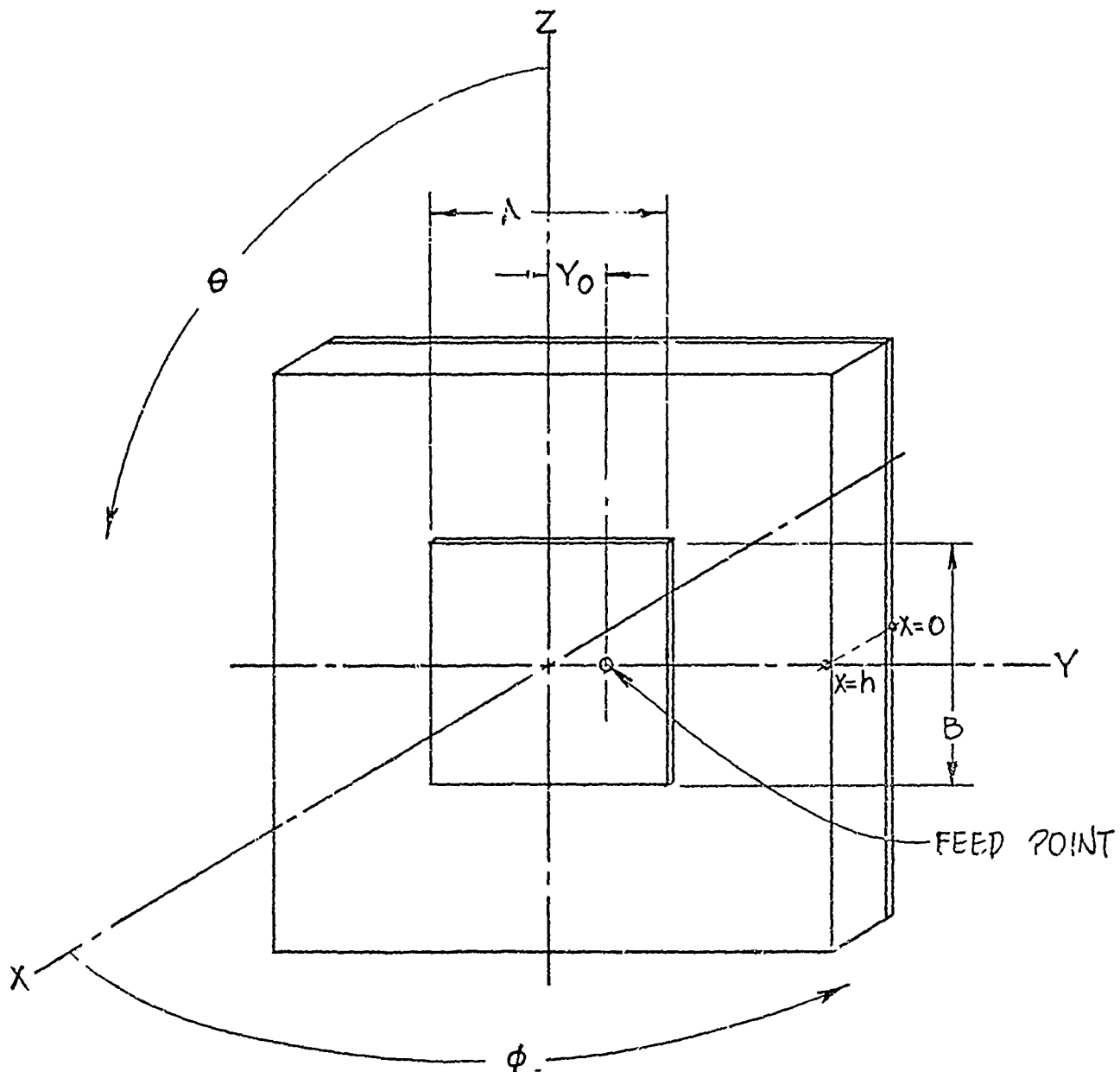
Introduction

This report presents data on three different types of microstrip antennas. The first is the "Twin Electric Microstrip Antenna," the second is the "Truncated Ground Electric Microstrip Antenna" and the third is the "Electric Microstrip Antenna." These antenna types are schematically shown in figure 1. The first type differs from the latter two in that the ground as well as the element is intentionally excited to radiate.

The purpose of this investigation is to determine the effects on the antenna design parameters when the dimensions of the ground plane is allowed to approach the dimensions of the antenna element. Specifically, to determine whether the design equations reported earlier (see Ref. (1), (2)) on the "Electric Microstrip Antenna" will apply to the "Truncated Ground Microstrip" and the "Twin Microstrip Antenna." Also determine if necessary what modifications to the earlier design equations would be required.

This paper will initially outline the analysis procedure for obtaining design equations for the microstrip rectangular element having linear polarization and zero ordered mode of excitation. The same analysis procedure can be used for other standard shaped elements having linear or elliptical polarization and higher order mode of excitation. Figure 2 shows the microstrip element in the coordinate system to be used in the analysis procedure. Note that the feed point is located at $X=0$, $Z=0$ and $y=y_0$. Therefore, one can only have current oscillation along the y axis if we further impose the conditions, $A < B$, $A \approx \lambda_g/2$,

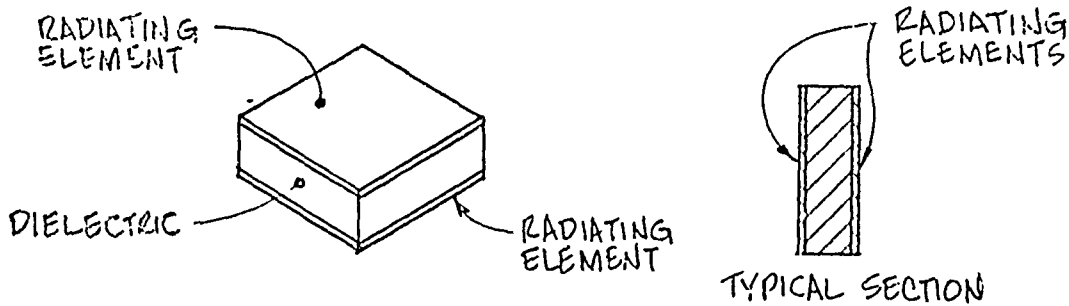
MICROSTRIP ANTENNAS



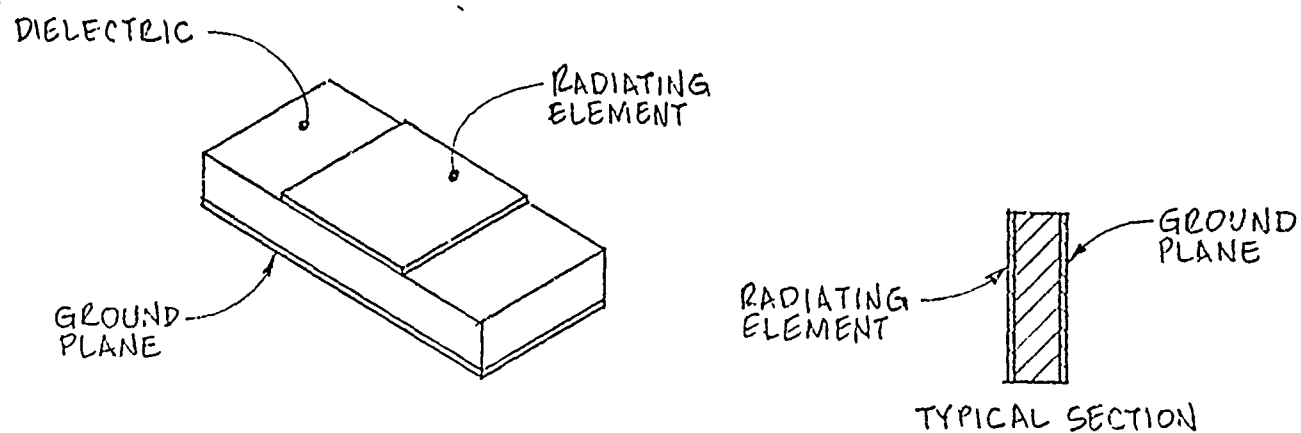
COORDINATE SYSTEM

FIG. 2

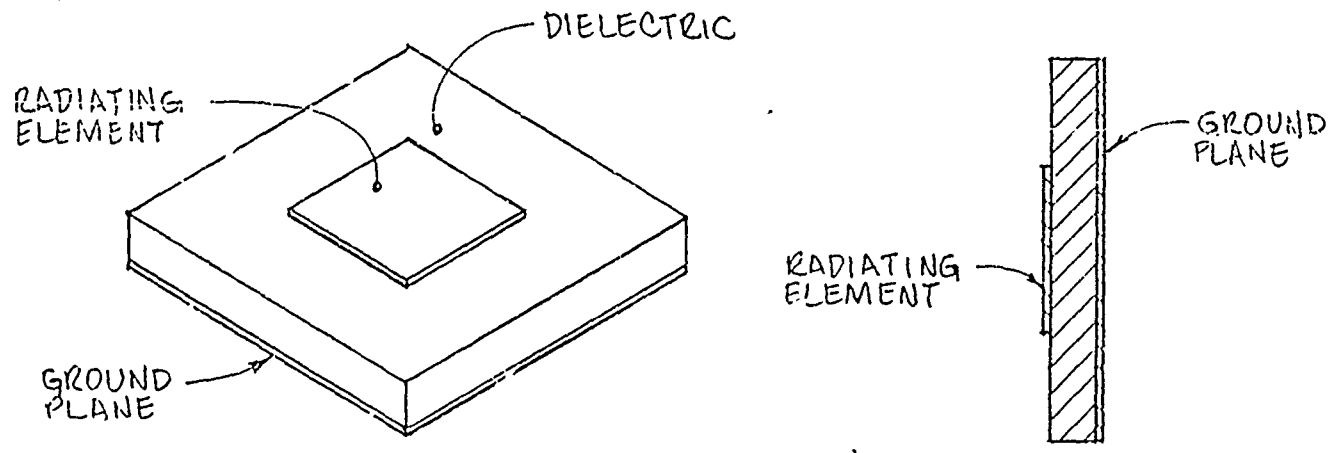
MICROSTRIP ANTENNAS



TWIN ELECTRIC MICROSTRIP ANTENNA



TRUNCATED GROUND ELECTRIC MICROSTRIP ANTENNA



ELECTRIC MICROSTRIP ANTENNA

FIG. 1

and $h \ll \lambda g/2$, where A is the element length, B the element width and h the substrate thickness.

Analysis Procedure

The analysis procedure in this paper is designed for the antenna element with physical properties shown in figure 2. An outline of the analysis procedure is as follows:

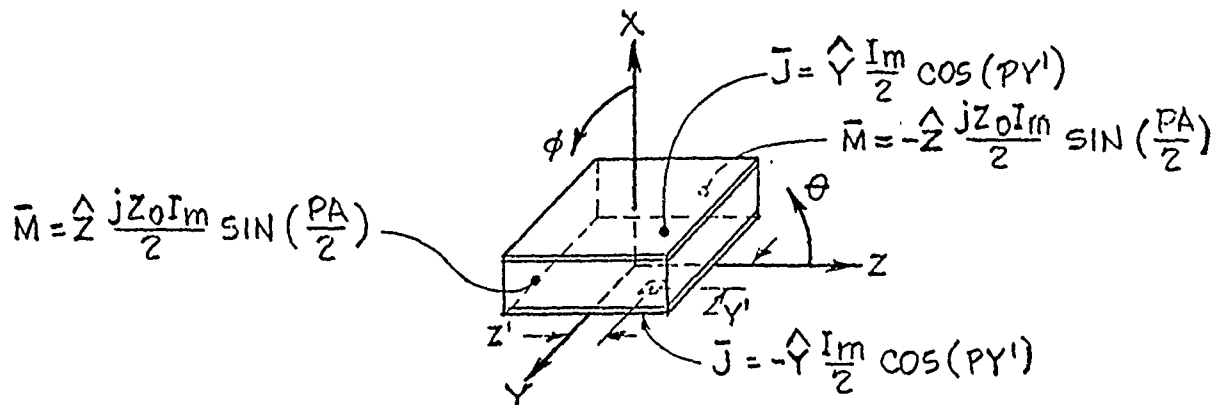
- a. Subdivide analysis of microstrip antenna into determining the Interior Non-radiation Fields, \bar{E}^I , \bar{H}^I and later the Exterior Radiating Fields, \bar{E} , \bar{H} .
- b. Use classical boundary-value problem technique to solve \bar{E}^I , \bar{H}^I for a resonator structure in figure 2. Assume propagation in the Y direction only and bounded by perfectly conducting planes in the X direction, therefore $E_{\text{tangential}} = 0$ and $H_{\text{normal}} = 0$ on the planes. The above cavity resonator problem is well documented in the literature (see Ref. (3), (4), and (5)).
- c. Examine the affects on \bar{E}^I , \bar{H}^I when the height, $h \ll \lambda/2$. It can be shown there is a frequency below which propagation ceases to occur in the first order or higher order modes and therefore only the zero ordered mode will exist.
- d. Examine the condition of \bar{E}^I , \bar{H}^I at various nodal and antinodal points. \bar{H}^I approaches a small number at the ENDS and whereas \bar{E}^I approaches a maximum at the ENDS. To meet these conditions, there must exist a forward traveling wave, \bar{E}^I , \bar{H}^I and a reflected wave, \bar{E}^R , \bar{H}^R , when combined appears as a standing wave. It should be mentioned that higher order mode of excitation due to the nodal and antinodal conditions can occur and may be determined at this point.
- e. Determine the tangential fields \bar{E}^I tangential, \bar{H}^I tangential.
- f. Invoke Schelkunoff Equivalence Theorem to couple the \bar{E}^I and \bar{H}^I fields to the external \bar{E} and \bar{H} fields, $\bar{J} = \hat{n}X\bar{H}^I$ tangential, $\bar{M} = -\hat{n}X\bar{E}^I$ tangential.
- g. Determine the vector potentials \bar{A} , \bar{F} .
- h. Determine far fields solution for E_ϕ .
- i. Determine a radiation resistance.
- j. Use transmission line techniques to compute the remaining design equations, where the computed radiation resistance is used as an equivalent transmission line lossy resistance.

Figure 3 shows schematically the locations of the electric currents, \bar{J} , and the magnetic currents, \bar{M} . For further discussions it is instructive to know that these currents are easily interchangeable to internal cavity fields.

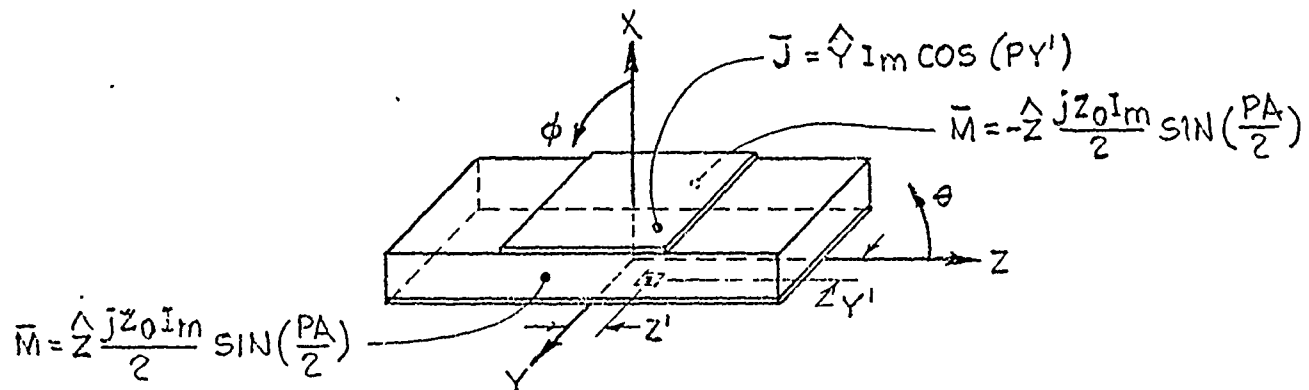
Radiation Patterns

Figure 4 shows radiation patterns of the three types of microstrip antenna. Note that the "Twin Electric" and the "Truncated Ground Electric" exhibit sizeable radiation on the ground plane side. In the case of the "Truncated

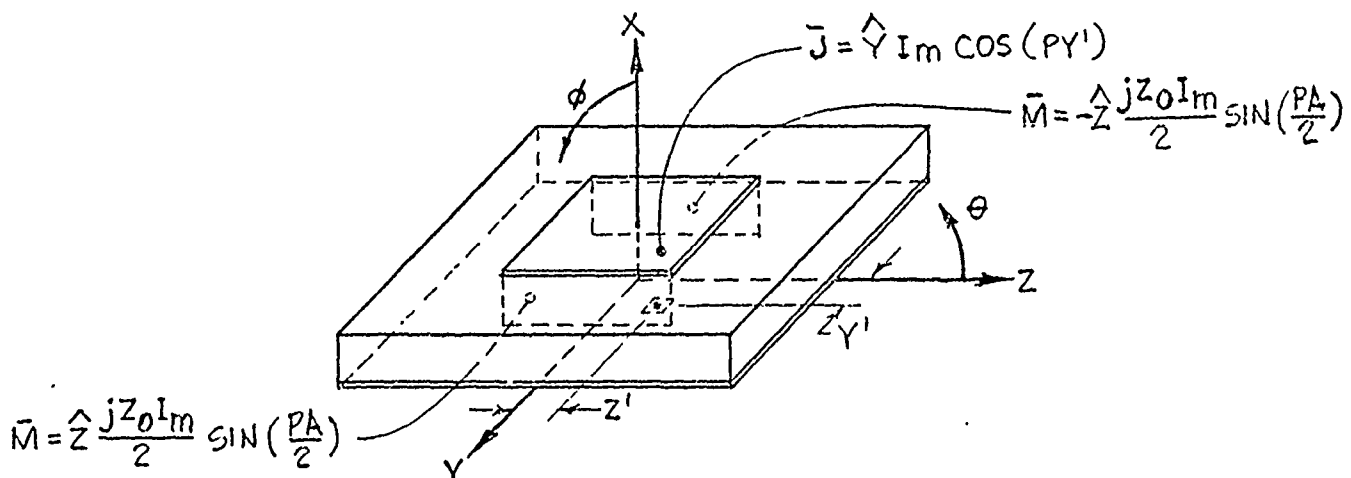
MICROSTRIP ANTENNAS



TWIN ELECTRIC MICROSTRIP ANTENNA



TRUNCATED GROUND ELECTRIC MICROSTRIP ANTENNA



ELECTRIC MICROSTRIP ANTENNA

FIG. 3

"Ground Electric," there is no ground along the length of the element to constrict radiation from the slots, therefore the fields overlap onto the ground plane side. In the case of the "Twin Electric," the radiation emanates from the ground plane.

Antenna Parameters (Measured vs Calculated)

Table 1 shows comparison between measured antenna parameters using the foregoing analysis method. A is the length, B is the width, h is the substrate thickness, f_0 is the center frequency, R_{af} is the radiation resistance due to the slots, R_{aA} is the radiation resistance due to the elements, R_a is the combine radiation resistance due to the slots and elements, Δf is the bandwidth with Y_0 is the dimension from the center of the element to the feedpoint giving a 50Ω match.

Antenna Parameters (Measured)

Table 2 shows comparison of measured data between the three microstrip antenna types. Note that in all cases the dielectric substrate was left to extend beyond the microstrip radiating element. Comparing the "Electric Microstrip" with the "Truncated Ground Microstrip," one observes a noticeable shift in both the center frequency and the feedpoint location. Comparing the "Truncated Ground Microstrip" with the "Twin Microstrip" one notes a further shifting of the center frequency but a shifting back of the feedpoint towards the location for the "Electric Microstrip." The reason is that the fringing fields on the ENDS affect the "effective element length," whereas the fringing fields on the SIDES affects the "characteristic impedance" as well as the "effective element width." Removal of the ground causes a foreshortening effect on the elements, and as was shown in earlier reports, one will observe feedpoint shifts as shown in Table 2.

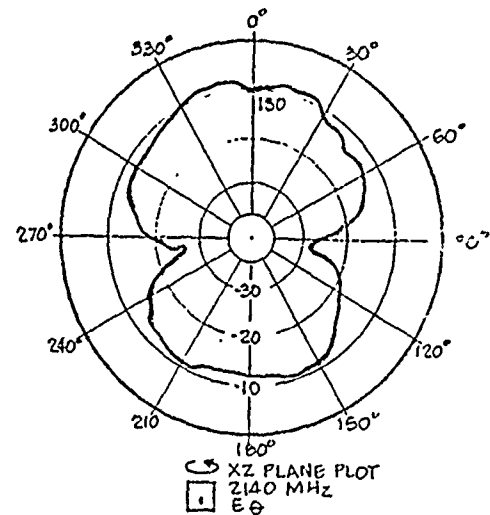
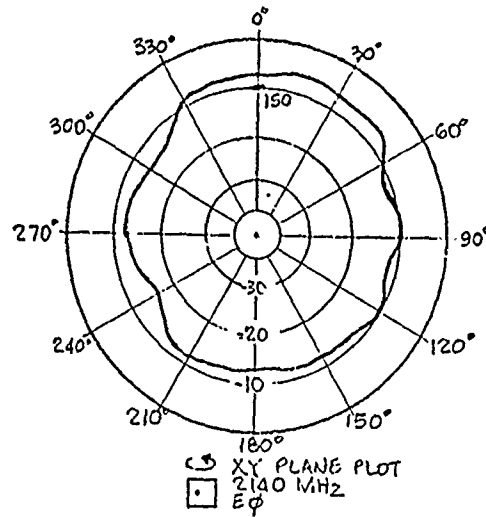
Table 3 shows comparison of measured data between the three microstrip antenna types. Note that in this case the dielectric substrate is also removed everywhere the ground is removed. As one can deduce the changes in the parameters are somewhat more drastic than those shown in Table 2.

Conclusion

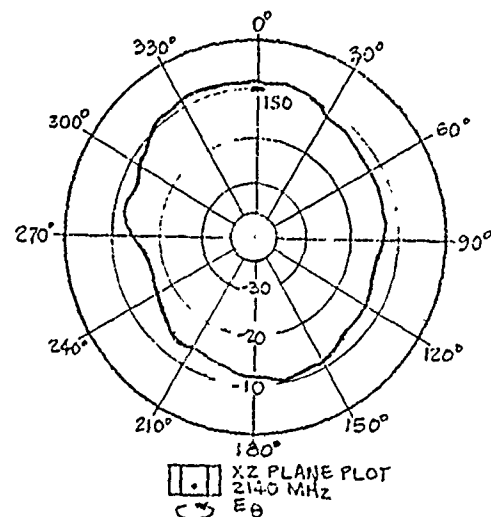
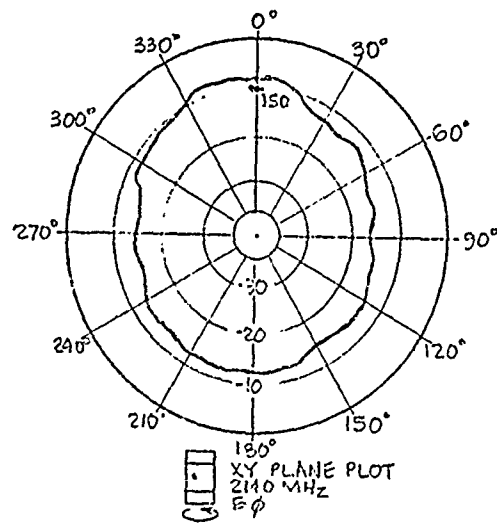
The experimental results shown that a strong field exists within the cavity. If the dielectric substrate is extended beyond the element only small changes in the antenna parameters are observed. Other than the center frequency, the same design equations referred to in earlier reports gave good results for the "Twin Electric Microstrip Antenna." A corrected "effective length" and "effective width" for both the "Twin Electric Microstrip" and the "Truncated Ground Microstrip" would immensely improve on the design equations.

A new "effective length" and "effective width" incorporating the affects of a reduced fringing field has been found and will be reported later. Studying all three antenna types appears to provide a better insight to understanding the radiation mechanism from the microstrip antennas.

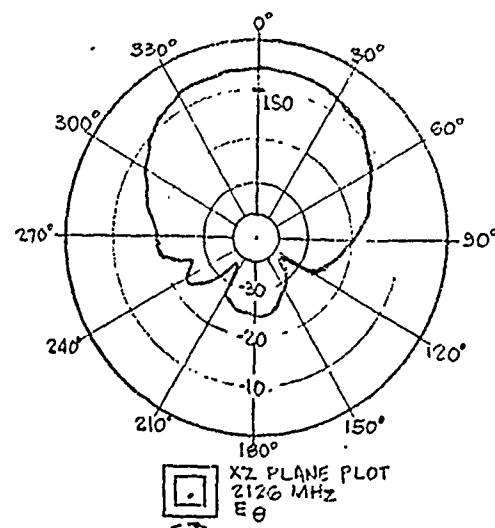
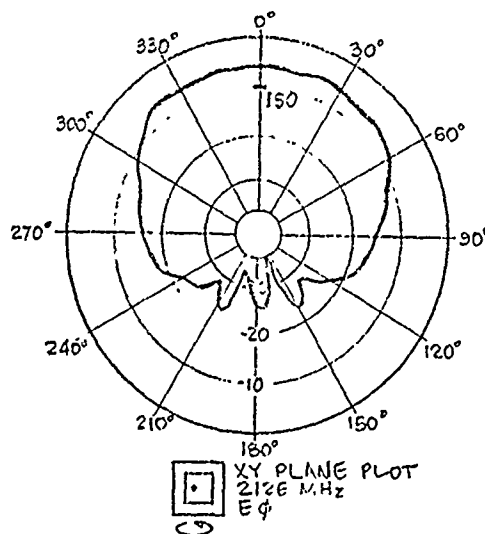
MICROSTRIP ANTENNAS



TWIN ELECTRIC MICROSTRIP ANTENNA



TRUNCATED GROUND ELECTRIC MICROSTRIP ANTENNA



ELECTRIC MICROSTRIP ANTENNA

FIG. 4

ELECTRIC MICROSTRIP ANTENNA PARAMETERS
 (MEASURED VS CALCULATED)

ANTENNA SAMPLES	ANT #1	ANT #2	ANT #3	ANT #4	ANT #5	ANT #6	ANT #7
INPUT PARAMETERS	A	0.93	0.93	1.75	1.75	3	3
	B	0.93	0.465	1.75	0.875	3	1.5
	\hbar	0.031	0.031	0.062	0.062	0.062	0.031
	ϵ	10	10	2.35	2.35	2.35	2.35
MEASURED VALUES	f_o (MHz)	1968	2010	2126	2144	1229	1276
	Δf (MHz)	45	35	102	80		
	R_a (ohms)	0.040	0.044	0.350	0.402	0.213	0.261
	Y_o (inches)	0.130	0.100	0.185	0.145		
CALCULATED VALUES	f_o (MHz)	1962	2029	2112	2155	1247	1274
	Δf (MHz)	46	38	110	89		
	R_a (ohms)	0.0378	0.0439	0.2915	0.362	0.178	0.228
	Y_o (inches)	0.110	0.090	0.210	0.185		

MICROSTRIP ANTENNA PARAMETERS
(MEASURED VALUES)

ANTENNA SAMPLES	ANT #1	ANT #2	ANT #3	ANT #4	ANT #5	ANT #6	ANT #7
INPUT PARAMETERS	A	0.93	0.93	1.75	1.75	3	3
	B	0.93	0.465	1.75	0.875	3	1.5
	h	0.031	0.031	0.062	0.062	0.062	0.062
	ϵ	10	10	2.35	2.35	2.35	2.35
ELECTRIC MICROSTRIP	f_o (MHZ)	1968	2010	2126	2144	1229	1276
	Δf (MHZ)	45	35	102	80		
	R_a (OHMS)	0.040	0.044	0.350	0.402	0.213	0.261
	Y_o (INCHES)	0.130	0.100	0.185	0.145		
TRUNCATED GROUND ELECTRIC MICROSTRIP (EXTENDED DIELECTRIC)	f_o (MHZ)	1976	2018	2150	2165	1241	1289
	Δf (MHZ)	45	35	102	80		
	R_a (OHMS)	.030		0.221			
	Y_o (INCHES)	0.110	0.080	0.145	0.105		
TWIN ELECTRIC MICROSTRIP (EXTENDED DIELECTRIC)	f_c (MHZ)	1982	2024	2175	2180	1250	1299
	Δf (MHZ)	45	35	102	80		
	R_a (OHMS)	0.036		0.292			
	Y_o (INCHES)	0.120	0.090	0.165	0.125		

MICROSTRIP ANTENNA PARAMETERS
(MEASURED VALUES)

ANTENNA SAMPLES	ANT #1	ANT #2	ANT #3	ANT #4	ANT #5	ANT #6	ANT #7
INPUT PARAMETERS	A	0.93	0.93	1.75	1.75	3	3
	B	0.93	0.465	1.75	0.875	3	1.5
	\hbar	0.031	0.031	0.062	0.062	0.062	0.062
	ϵ	10	10	2.35	2.35	2.35	2.35
ELECTRIC MICROSTRIP	f_o (MHz)	1968	2010	2126	2144	1223	1276
	Δf (MHz)	45	35	102	30	.	.
	R_a (ohms)	0.040	0.044	0.350	0.402	0.213	0.261
	Y_o (inches)	0.130	0.100	0.185	0.145	.	.
TRUNCATED GROUND MICROSTRIP (DIELECTRIC REMOVED FROM ENDS)	f_o (MHz)	2004	2049	2177	2193	1273	1324
	Δf (MHz)	46	35	103	81	.	.
	R_a (ohms)
	Y_o (inches)
TWIN MICROSTRIP (DIELECTRIC REMOVED FROM ENDS AND EDGES)	f_o (MHz)	2055	2105	2206	2224	1305	1347
	Δf (MHz)	46	36	104	31	.	.
	R_a (ohms)
	Y_o (inches)

References

- (1) Kaloi, C. M. ASSEMTRICALLY FED ELECTRIC MICROSTRIP DIPOLE ANTENNA, Pacific Missile Test Center, Point Mugu, CA, Technical Report TP-75-03, January 1975
- (2) Kaloi, C. M. MICROSTRIP ANTENNAS, DESIGN EQUATIONS, Presented at 1979 APS Symposium, Seattle, Washington
- (3) Wolff, E. A. ANTENNA ANALYSIS, John Wiley & Sons, Inc. 1966
- (4) Ramo & Whinnery, FIELDS AND WAVES IN MODERN RADIO, John Wiley & Sons, Inc. 1960
- (5) Jones, D. S. THE THEORY OF ELECTROMAGNETISM, The Macmillan Company, 1964

PRACTICAL ANALYTICAL TECHNIQUES FOR THE MICROSTRIP ANTENNA

K. R. CARVER
PHYSICAL SCIENCE LABORATORY
NEW MEXICO STATE UNIVERSITY
LAS CRUCES, NEW MEXICO 88003

SUMMARY

This paper presents a series of design equations which accurately describe the input impedance, resonant frequency, bandwidth, efficiency and polarization for rectangular or circular microstrip antennas. These relations are based on the modal expansion technique wherein the field under the microstrip patch is expanded in a Fourier series with the radiation and near-field stored energy represented by an impedance boundary condition at the radiating edges. This leads to complex eigenvalues from which the real resonant frequencies and Qs of the modes may be predicted. Although this is a problem of considerable interest to theoreticians, the intent of this paper is to phrase the equations and procedures for design in a form which is directly usable by the practicing antenna design engineer who may not be familiar with the nuances of mathematical boundary-value problems involving leaky cavities. All of the equations and procedures presented in this paper can be implemented on hand-held programmable calculators. The theory presented here leads to resonant frequencies which are typically within 0.5% of measured results and resonant input resistances which are typically within 10% of measured results.

1.0 INTRODUCTION

A theory for microstrip antennas should begin by clearly recognizing and stating its motivation. This theory is addressed to the determination of equations, procedures, etc. which are of direct use to the practicing antenna engineer designing both single patches and arrays of microstrip patches of either rectangular or circular shape. This theoretical work has been strongly motivated by nearly a decade of practical printed circuit

antenna design and development experience at the Physical Science Laboratory which has resulted in dozens of microstrip and stripline array designs for both planar and cylindrical geometries. The antenna engineer with a requirement for a microstrip array begins with a design frequency and bandwidth, polarization, pattern shape and gain in mind, along with geometrical and weight constraints such as a missile diameter or planar array dimensions. Depending on the pattern shape and polarization(s) desired, an array geometry can then be chosen along with either a rectangular or circular patch shape. Since the microstrip patch has an intrinsic bandwidth of at most a few percent, the patch size and substrate must be carefully chosen to produce the desired input impedance and bandwidth. The crucial theoretical problem is to relate the in situ input impedance to the following parameters:

1. Patch shape and size
2. Feedpoint type and location
3. Substrate dielectric constant and loss tangent
4. Substrate thickness and material stability
5. Mutual coupling to adjacent elements

Since the mutual coupling problem is described elsewhere in this Proceedings [1], it will not be further discussed in this paper and attention will be directed to the properties of a single patch.

In the context discussed above, an adequate theory must not only predict accurate input impedances, etc. but it must also be presented in a fashion which makes it of practical value to the design engineer. The transmission line theory for a simple rectangular patch as presented in [2,3] is a good example of a simple understandable theory which has been used with success. This theory has some notable deficiencies, in that the predicted resonant frequencies for rectangular patches are several percent on the high side of measured resonant frequencies, in that it does not predict the exterior near-field structure and that it is not adaptable to circular patches. Nonetheless, the combination of this simple analytical approach expressed in a few equations along with a few cut-and-try experimental iterations is often quite adequate for the practical design process.

In the past two years work has been reported by this author [4,5] and workers at the University of Illinois [6,7] on a modal expansion theory for microstrip antennas, which may be viewed as a second stage in the evolution of better theories. This approach, which treats the patch as a thin TM cavity with leaky magnetic walls, is slightly more complicated than the earlier transmission-line models, but gives a much more accurate description of the input impedance, resonant frequency, etc. for both rectangular and circular patches. It is not completely rigorous in that the boundary conditions for the radiating magnetic walls are not based on a rigorous solution to the exterior radiation problem. However, it produces accurate design relations which are of direct use to the engineer.

These remarks are not meant to suggest that better theories are not needed. Certainly, more work is needed on accurate models for the feedpoint (either coaxial or microstrip) as well as better representations for the near-field distribution and surface waves immediately exterior to the patch. However, such design theories must ultimately be in either step-by-step equation or nomograph form if they are to be of value to the hardware design community.

2.0 BASIC THEORY FOR RECTANGULAR AND CIRCULAR MICROSTRIP PATCHES

Since most arrays of microstrip elements use either rectangular or circular patches, the theory presented here is confined to these shapes; other polygonal microstrip patches have been treated in a separate report [4].

2.1 RECTANGULAR PATCHES : DESIGN EQUATIONS

Fig. 1 shows a rectangular conducting patch of size $a \times b$, which is separated from a large ground plane by a substrate with relative permittivity ϵ_r and thickness t . Unless either dimension a or b is small with respect to a wavelength, the region under the patch may be modeled as a thin cavity with leaking magnetic sidewalls. Such a cavity will support quasi-discrete modes which are TM_{mn} to z where m is the mode number associated with the y -direction and n is the mode number associated with the x -direction. The dominant rf mode which is of most

practical interest is the TM_{10} mode which would be obtained if the dimension $b \approx \lambda_d/2$ (where λ_d is the wavelength in the dielectric), the dimension a is chosen between b and $2b$, and with the feedpoint at location (x_0, y_0) . The total electric field in the interior is assumed to be z -directed and can be expressed as the sum of the fields associated with each mode:

$$E_z = \sum_m \sum_n A_{mn} e_{mn} \quad (1)$$

where the A_{mn} are the mode coefficients and the e_{mn} are the orthonormalized mode vectors given by

$$e_{mn} = \frac{x_{mn}}{\sqrt{\epsilon_a b t}} \cos k_x x \cos k_y y \quad (2)$$

Similarly,

$$\bar{h}_{mn} = \frac{1}{j\omega\mu} \frac{x_{mn}}{\sqrt{\epsilon_a b t}} \left\{ \begin{array}{l} \hat{x} k_y \cos k_x x \sin k_y y \\ - \hat{y} k_x \sin k_x x \cos k_y y \end{array} \right\} \quad (3)$$

where

$$\begin{aligned} x_{mo} &= x_{on} = \sqrt{2} \quad (m \neq 0, n \neq 0) \\ x_{mn} &\approx 2 \quad (m \neq 0, n \neq 0) \end{aligned} \quad (4)$$

The mode vectors all satisfy the wave equation and the eigenvalues k_x and k_y satisfy the separation condition

$$k^2 = \omega^2 \mu \epsilon = k_x^2 + k_y^2 \quad (5)$$

It is at this point in the development that some means of connecting the interior fields to the exterior fields must be devised, if a radiating microstrip cavity is to be considered. This can be done by artificially making the cavity slightly longer or through the incorporation of an effective loss tangent as has been carried out by the Illinois group [6,7]. The approach taken here is to lump all of the external stored and radiated energy effects through a complex wall admittance for each wall which amounts to the imposition of an impedance boundary condition at each of the four walls. This leads to the following coupled transcendental equations for the eigenvalues k_x , k_y :

$$\tan k_x a = \frac{2 k_x \alpha_x}{k_x^2 - \alpha_x^2} \quad (6)$$

$$\tan k_y b = \frac{2 k_y \alpha_y}{k_y^2 - \alpha_y^2} \quad (7)$$

where

$$\alpha_x = j \frac{2\pi Z_0}{\lambda_0} \frac{t}{b} Y_{wx} F_x(b/a) \quad (8)$$

$$\alpha_y = j \frac{2\pi Z_0}{\lambda_0} \frac{t}{a} Y_{wy} F_y(a/b) \quad (9)$$

and where

Y_{wx} = wall admittance for $x = 0$, $x = a$ walls

Y_{wy} = wall admittance for $y = 0$, $y = a$ walls

Z_0 = 376 Ω

λ_0 = free-space wavelength

The factors F_x and F_y in (8) and (9) are included to represent the effect of the aspect ratio (a/b) on the degree to which the actual field distribution on the radiating edges matches the modal forms given in (2). These factors are approximately unity; for the TM_{10} mode,

$$F_y = .7747 + .5977(\frac{a}{b} - 1) - .1638(\frac{a}{b} - 1)^2 \quad (10)$$

Rigorous solutions for the wall admittances Y_w for the microstrip antenna have not yet been obtained. However, in the work to date, an approximation based on the wall conductance of a TEM parallel-plate waveguide radiating into a half-space and the wall susceptance of a uniform microstrip transmission line has been used [4] which leads to the following formulas:

$$Y_w = G_w + j B_w \quad (11)$$

where

$$G_w = 0.00836 \frac{a}{\lambda_0} \quad (12)$$

$$B_w = 0.01668 \frac{\Delta\ell}{t} \frac{a}{\lambda_0} \epsilon_e \quad (13)$$

and where the susceptance formula is based on Hammerstad's result [8] that

$$\frac{\Delta\ell}{t} = 0.412 \left[\frac{\epsilon_e + .300}{\epsilon_e - .258} \right] \left[\frac{\frac{a}{t} + .262}{\frac{a}{t} + .813} \right] \quad (14)$$

and where the effective dielectric constant ϵ_e is given by Schneider's formula [9]

$$\epsilon_e = \frac{\epsilon_r + 1}{2} + \frac{\epsilon_r - 1}{2} \left[1 + \frac{10 t}{a} \right]^{-1/2} \quad (15)$$

2.1.1 CALCULATION OF THE RESONANT FREQUENCY

The first problem of practical interest is the calculation of the resonant frequency for the dominant rf TM_{10} mode. A rough approximation may be obtained by assuming that the radiating walls at $y = 0$, $y = b$ are open circuited with zero tangential magnetic field (perfect magnetic walls), i.e. $Y_w = 0$. This would give $\alpha_y = 0$ so that the first non-zero root of (7) is $k_y = \pi/b$, i.e. $b = \lambda_0/2\sqrt{\epsilon_r}$; this corresponds to a resonant frequency for the dominant mode given by $f_r = c/(2b\sqrt{\epsilon_r})$ where c is the speed of light in vacuum. Unfortunately, this predicts a resonant frequency which is a few percent too high and does not incorporate the patch aspect ratio and substrate thickness into the formulation.

A much more accurate result may be obtained by solving the transcendental equation (7) for the eigenvalue k_y . For electrically thin substrates, this eigenvalue is typically 1%-5% less than π/b . The following definitions are helpful:

$$\Delta = \pi - k_y b \quad (16)$$

and

$$\kappa = \alpha_y b \quad (17)$$

so that (7) becomes

$$\tan \Delta = \frac{2\kappa(\pi - \Delta)}{\kappa^2 + 2\Delta\pi - \Delta^2 - \pi^2} \quad (18)$$

Since Δ is small, we may approximate the tangent function by the first two terms of its series expansion and use an iterative process to solve (18) which is given by the following algorithm:

$$\Delta_{p+1} = \frac{2\kappa(\pi - \Delta_p)}{\kappa^2 + 2\Delta_p\pi - \Delta_p^2 - \pi^2} - \frac{\Delta_p^3}{3} \quad (p = 0, 1, 2, 3) \quad (19)$$

It has been found that the root Δ_4 obtained after four iterations of (19) satisfies (18) to an accuracy of five decimal places. The seed value $\Delta_0 = 0$ was used for a variety of microstrip patches from 1.5 GHz to 5.0 GHz along with (19) to produce a very rapid convergence toward the complex eigenvalue which is then given by

$$k_y = \frac{\pi}{b} - \frac{\Delta_4}{b} \quad (20)$$

Assuming the TM_{10} condition that $k_x = 0$, the complex resonant radian frequency may be found from (5), i.e.

$$\omega_r + j \omega_i = \frac{c}{\sqrt{\epsilon_r(1 - j \tan \delta)}} k_y \quad (21)$$

where $\tan \delta$ is the substrate loss tangent, usually a very small number. The resonant frequency for the rectangular microstrip patch is found by

$$f_r = \omega_r / 2\pi \quad (22)$$

2.1.2 CALCULATION OF THE RESONANT INPUT RESISTANCE

It has been shown by this author [4] and others that the equivalent circuit for a single spectrally-isolated resonant mode of the microstrip antenna can be represented by a parallel RLC lossy resonant circuit which is then in series with an inductive term representing both the effect of the feed and also the residual net magnetic energy associated with all the higher-order modes. The capacitance C of the TM_{10} mode is given by

$$C = \frac{\epsilon_e \epsilon_0 a b}{2 t} \cos^{-2}(\pi y_0/b) \quad (23)$$

The inductance is given by

$$L = \frac{1}{C \omega_r^2} \quad (24)$$

and the resonant resistance is given by

$$R = \frac{Q}{\omega_r C} \quad (25)$$

where Q is the quality factor associated with system losses including radiation out the walls, heat loss in both the dielectric and copper, and surface waves. Thus, assuming the surface wave power is small,

$$R = R_{rad} + R_{cu} + R_{di} \quad (26)$$

where the three terms represent the radiation resistance, the equivalent resistance of the copper loss and the equivalent resistance of the dielectric loss. It may be shown [4] that these last two may be calculated by

$$R_{cu} = 0.00027 \sqrt{f(\text{GHz})} \frac{b}{a} Q_r^2 \quad (\Omega) \quad (27)$$

$$R_{di} = 30 \frac{\tan \delta}{\epsilon_r} \frac{t \lambda_0}{ab} Q_r^2 \quad (\Omega) \quad (28)$$

The term Q_r associated with the radiation resistance may be obtained from the complex eigenvalue or complex radian resonant frequency by

$$\omega_r + j \omega_i = \omega_{10} \sqrt{1 + (j/Q_r)} \quad (29)$$

and where ω_{10} is the real radian resonant frequency which is well-approximated by ω_r , if $\omega_r \gg \omega_i$. Under this assumption, which holds well for thin substrates,

$$Q_r = \frac{\omega_r}{2\omega_i} \quad (30)$$

from which

$$R_{rad} = \frac{Q_r}{\omega_r C} \quad (31)$$

Thus the resonant resistance may be calculated from (26) using (31), (27) and (28).

2.1.3 CALCULATION OF THE BANDWIDTH

The bandwidth of the microstrip antenna is found from the Q as

$$\Delta f = f_r/Q \quad (32)$$

where f_r is found from (22) and Q is found from (25).

2.1.4 CALCULATION OF INPUT IMPEDANCE

The input impedance is found in the modal expansion method by calculating the modal amplitudes A_{mn} in (1) which are in turn related to the excitation method. Microstrip patches are fed either by a coaxial probe or by a microstrip transmission line. For a patch fed at position (x_0, y_0) by either a probe or a microstrip line, the input impedance is given by [4]

$$Z_{in} = -j \frac{t\omega}{\epsilon_{ab}} \sum_{m=0}^{\infty} \sum_{n=0}^{\infty} \frac{x_{mn}^2 \cos^2(m\pi y_0/b) \cos^2(n\pi x_0/a)}{\omega^2 - \tilde{\omega}_{mn}^2} G_{mn} \quad (33)$$

where $\tilde{\omega}_{mn}$ is the complex radian resonant frequency for the TM_{mn} mode, which to an excellent approximation is given by the real value $\tilde{\omega}_{mn} = (1/\sqrt{\mu\epsilon})k_{mn}$ where $k_{mn}^2 = (m\pi/b)^2 + (n\pi/a)^2$ except for the lowest-order rf mode(s) where the resonant frequency should be calculated from eqn. (21). The factor G_{mn} in the series of (33) accounts for the finite width of either the coaxial probe wire or the width of the microstrip transmission line, and to a very good approximation is given by

$$G_{mn} = \frac{\sin(m\pi d_x/2a)}{m\pi d_x/2a} \frac{\sin(n\pi d_y/2b)}{n\pi d_y/2b} \quad (34)$$

where d_x is the width of the feed in the x-direction and d_y is the width of the feed in the y-direction. For microstrip feed lines connected to one edge of the patch (e.g. dimension a) the feedwidth dimension perpendicular to that edge is set equal to zero (e.g. $d_y = 0$). For coaxially-fed patches, $d_x = d_y$ = probe diameter. The factor (34) causes the series (33) to converge because of the finite feed width or diameter; for filamentary probes, $G_{mn} = 1$ and the reactive portion of the input impedance becomes infinite. Unfortunately, even with the

factor (34), the series converges slowly and the evaluation of (33) is cumbersome with a hand-held calculator. For a rectangular patch supporting only the dominant rf mode, an excellent approximation to the infinite series (33) may be obtained by considering only the $m=1$, $n=0$ term in the series and lumping all the remaining terms together as a single lumped inductance, i.e.

$$Z_{in} = j X_L + \frac{j (\omega/C)}{\omega^2 - j(\omega_r + j \omega_i)^2} \quad (35)$$

where X_L is modeled as the inductive reactance of a coaxial probe feed of length t with a short at the position where the feed-wire is connected to the patch, i.e.

$$X_L = \frac{376}{\sqrt{\epsilon_r}} \tan \frac{2\pi t}{\lambda_0} \quad (\Omega) \quad (36)$$

and where C is the dominant-mode patch capacitance given by (23). The complex resonant radian frequency is calculated from (21). The use of (35) will give accurate values of the input impedance near the resonant frequency and slightly less accurate values as the frequency departs from resonance.

2.1.5 CALCULATION OF THE ANTENNA EFFICIENCY

The antenna efficiency, which is defined as the ratio of radiated power to input power, may be calculated from the radiation resistance R_{rad} , the copper loss resistance R_{cu} and the dielectric loss resistance R_{di} from the relation

$$\eta = 1 - \frac{R_{cu} + R_{di}}{R_{rad} + R_{cu} + R_{di}} \quad (37)$$

where the terms R_{rad} , R_{cu} and R_{di} are calculated from (31), (27) & (28). Antenna engineers more frequently refer to this efficiency as an "antenna loss" L_a expressed in dB, i.e.

$$L_a (\text{dB}) = 10 \log(1/\eta) \quad (38)$$

2.2 COMPARISON OF THEORETICAL PREDICTIONS WITH EXPERIMENTAL RESULTS FOR A RECTANGULAR MICROSTRIP PATCH

Measurements of the input impedance vs. frequency for microstrip patches for various sizes and thicknesses have been made; the agreement between theory and measured results is good and will be illustrated by a set of experimental data for an S-band rectangular microstrip antenna with dimensions listed in Table 1.

TABLE 1
DIMENSIONS OF EXPERIMENTAL MICROSTRIP ANTENNA

Parameter	Value
Height (b)	4.140 cm
Width (a) : Model 1	4.100 cm
Model 2	6.858 cm
Model 3	10.800 cm
Substrate thickness (t)	0.1524 cm
Dielectric constant	2.50 (nominal)
Substrate type	3-M K-6098 GT
Feed type	Coaxial (type SMA connector)
Feed location	$x_0 = a/2$ $y_0 = 0$

One of the greatest practical design problems relates to the ± 0.05 typical tolerance for the dielectric constant for these materials. This uncertainty in the exact dielectric constant would cause a resonant frequency uncertainty of ± 22 MHz in the above S-band model. This uncertainty due to the dielectric constant is thus of at least as much concern as the exact theoretical approach to formulating a mathematical model for the microstrip antenna. To put this in another way, it is necessary to begin with a substrate dielectric constant which is known to at least two significant figures. It turns out that for the above S-band model, the true dielectric constant was equal to the nominal value. However, in a more general case, it would be desirable to separately measure the constant using either a cavity or transmission-line jig.

2.2.1 NUMERICAL CALCULATIONS FOR S-BAND RECTANGULAR PATCH

In order to illustrate the use of the analysis formulas (1) - (38), the S-band rectangular patch of Table 1 with $a = 6.858$ cm will be considered, in a step-by-step procedure:

1. Calculate effective dielectric constant from (15): $\epsilon_e = 2.428$
2. Calculate extension parameter from (14): $\Delta\ell/t = 0.5117$
3. Calculate wall susceptance from (13): $B_w = 0.010450$ mhos
4. Calculate wall conductance from (12): $G_w = 0.004215$ mhos
5. Estimate resonant wavelength $\lambda_0 = 2.1 \sqrt{\epsilon_r} = 13.6$ cm
6. Calculate aspect factor from (10): $F_y = 1.0965$
7. Use (9) and (11) to calculate the impedance parameter (17):
 $\kappa = \alpha_y b = -0.183120 + j 0.073862$
8. Calculate the eigenvalue shift factor from (19), using $\Delta_0 = 0$
 $\Delta_1 = 0.116780 - j0.047477$
 $\Delta_2 = 0.120217 - j0.050638$
 $\Delta_3 = 0.120293 - j0.050744$
 $\Delta_4 = 0.120295 - j0.050747$
9. Calculate the complex eigenvalue for the TM_{10} mode:
 $k_y = (\pi - \Delta_4)/b = 0.729782 + j .0122577 \text{ cm}^{-1}$
10. Calculate the complex resonant radian frequency from (21):
 $\tilde{\omega}_{10} = \omega_r + j \omega_i = 1.38466 \times 10^{10} + j 2.32570 \times 10^8 \text{ rad s}^{-1}$
11. Calculate the real resonant frequency from (22): $f_r = 2203.8$ MHz
12. Calculate the radiation Q_r from (30): $Q_r = 29.8$
13. Calculate the patch dominant mode capacitance from (23): $C = 20.02$ pF
14. Calculate the radiation resistance referred to the input
from (31): $R_{rad} = 107.5 \Omega$
15. Calculate the copper resistance from (27): $R_{cu} = 0.22 \Omega$
16. Calculate the dielectric loss resistance from (28) using $\tan \delta = 0.001$: $R_{di} = 0.78 \Omega$
17. Calculate the input resistance at resonance: $R_{in} = 108.4 \Omega$
18. Calculate the total Q from (25): $Q = 30.0$
19. Calculate the bandwidth from (32): $\Delta f = 73$ MHz

20. Assuming a coaxially-fed patch with probe location at $y_0 = 0$, $x_0 = a/2$, calculate the input impedance vs. frequency, using (35) and (36). From (36), the series inductive reactance is 16.8Ω , and from step 13 the capacitance is 20.02 pF ; the complex resonant radian frequency is found in step 10. Thus, (35) may be used to predict the Smith Chart impedance trace. A more accurate trace may be found by measuring the probe diameter and using (33) and (34).

The values calculated in steps (11) and (17) are compared to measured values in Table 2.

TABLE 2
COMPARISON OF THEORETICAL AND MEASURED VALUES

Patch Dimensions	Resonant Frequency	Resonant Resistance
a = 4.10 cm b = 4.14 cm	2232 MHz (theory) 2228 MHz (exper.)	284 Ω (theory) 280 Ω (exper.)
a = 6.858 cm b = 4.14 cm	2204 MHz (theory) 2200 MHz (exper.)	108 Ω (theory) 115 Ω (exper.)
a = 10.800 cm b = 4.14 cm	2180 MHz (theory) 2181 MHz (exper.)	53 Ω (theory) 65 Ω (exper.)
a = 11.049 cm b = 6.909 cm	1342 MHz (theory) 1344 MHz (exper.)	116 Ω (theory) 102 Ω (exper.)

The agreement between theoretical and experimental values of the resonant frequency is typically within 0.5%; for the resonant resistance the agreement is typically 10%. A better prediction of the resonant resistance is tied to (1) a more precise knowledge of the dielectric constant and (2) better models for the wall conductance than the one presented in eqn. (12).

2.3 CIRCULAR PATCHES: DESIGN EQUATIONS

Consider a circular microstrip cavity of radius a and substrate thickness t , assumed to be electrically small so that only TM_z mode vectors are supported. The total electric field in the interior can then be expanded in terms of the fields associated with each mode:

$$E_z = \sum_n \sum_r A_{nr} e_{nr}(r, \phi) \quad (39)$$

where A_{nr} are the mode coefficients and the e_{nr} are the ortho-normalized mode vectors given by [4]

$$e_{nr} = \frac{x_n}{a\sqrt{2\pi t} B_{nr}} J_n(k'_{nr} \frac{r}{a}) \cos n\phi \quad (40)$$

and where

$$x_n = \begin{cases} \sqrt{2} & (n = 0) \\ 2 & (n \neq 0) \end{cases} \quad (41)$$

$$B_{nr} = \begin{cases} J_0(k'_{nr}) & (n = 0) \\ \frac{1}{k'_{nr}} \left[\sum_{p=0}^{\infty} (n+1+2p) J_{n+1+2p}^2(k'_{nr}) \right]^{1/2} & (n \neq 0) \end{cases} \quad (42)$$

and where, except for the dominant rf TM_{10} mode, the eigenvalues k'_{nr} may be calculated by the Neumann condition $J'_n(k'_{nr}) = 0$, i.e. $k'_{20} = 3.05424$, $k'_{01} = 3.83170$, etc. For the dominant rf mode with a zero field at the patch center, and fed at the edge, the eigenvalue becomes complex and may be found from the transcendental equation

$$k'_{10} J_0(k'_{10}) = (1 - \alpha a) J_1(k'_{10}) \quad (43)$$

where

$$\alpha a = j \frac{Z_0 t}{\lambda_0} (G_w + j B_w) \quad (44)$$

In order to solve (43), the Bessel functions are expanded in terms of the asymptotic polynomials [10] :

$$J_0(x) = 1 - 2.2499997(x/3)^2 + 1.2656208(x/3)^4 - .3163866(x/3)^6 + .0444479(x/3)^8 - .0039444(x/3)^{10}$$

$$J_1(x) = x(0.5 - .56249985(x/3)^2 + .21093573(x/3)^4 - .03954289(x/3)^6 + .00443319(x/3)^8 - .00031761(x/3)^{10}) \quad (45)$$

For the case of a perfect open-circuit at the patch edge, the Neumann boundary condition gives the eigenvalue $k_{10}' = 1.84118$. When the wall admittance factor (44) is introduced, the eigenvalue is reduced to a complex value having a real part slightly less than 1.84118, i.e. the resonant frequency is less than the Neumann value. For the moment, make the substitution $x = k_{10}'$ so that (43) becomes

$$x = (1 - \alpha a) \frac{J_1(x)}{J_0(x)} \quad (46)$$

Since the expected value of the eigenvalue (real part) is in the range 1.7 to 1.84, the Bessel function ratio in (46) may be expanded in the first three terms of a power series to give

$$\frac{J_1(x)}{J_0(x)} \approx 9.3648618 - 11.499148 x + 4.0260952 x^2 \quad (47)$$

(1.7 < x < 1.84)

Next define the parameter

$$\Delta = 1.84118 - x \quad (48)$$

and substitute this and (47) into (46) to arrive at the following iterative algorithm for circular patches:

$$\Delta_{p+1} = \frac{1.8410969 + 4.0260952 \frac{\Delta_p^2}{a^2} (1 - \alpha a) - 1.84118}{3.3263839(1 - \alpha a) - 1} \quad (49)$$

along with the "seed" value $\Delta_0 = 0$. This will ordinarily converge to five significant figure accuracy after five iterations. Thus, the complex eigenvalue is given by

$$k_{10}' = 1.84118 - \Delta_5 = \operatorname{Re}(k_{10}') + j \operatorname{Im}(k_{10}') \quad (50)$$

The resonant frequency can then be found from

$$f_r = \frac{c \operatorname{Re}(k_{10}')}{2\pi a \sqrt{\epsilon_r}} \quad (51)$$

The accuracy of the complex root $k'_{01} = x_5$ is dependent on the wall conductance G_w and wall susceptance B_w ; unfortunately, a rigorous solution to this problem is not known to this author. However, empirically-determined expressions have been found which are based primarily on the analog between the circular patch and its rectangular cousin; these formulas are

$$G_w = 0.01254 \frac{\pi a}{\lambda_0} \text{ (mhos)} \quad (52)$$

$$B_w = 0.00834 \frac{\pi a}{\lambda_0} \epsilon_r \text{ (mhos)} \quad (53)$$

It can be shown that the capacitance for an edge-fed dominant-mode patch is given by

$$C_e = \frac{\epsilon_r \epsilon_0 a^2}{2.775 t} \quad (54)$$

As in the case of the rectangular patch, the radiation Q_r is given by

$$Q_r = \frac{\operatorname{Re}(k'_{10})}{2 \operatorname{Im}(k'_{10})} \quad (55)$$

so that the radiation resistance referred to a feed-point at $\rho = \rho_0$ (see Fig. 2) is given by

$$R_{\text{rad}} = \frac{Q_r}{\omega_r C_e} J_1^2 \left(\operatorname{Re}(k'_{10}) \frac{\rho_0}{a} \right) \quad (56)$$

Expressions have not yet been derived for the copper loss and dielectric loss resistance for the circular patch, but a reasonable approximation may be obtained by using the loss resistance values for a square patch of the same area as the circular patch.

It may be shown [4] that in the vicinity of dominant-mode resonance for a circular patch, the input impedance is given to a good approximation by the relation

$$Z_{\text{in}} = j X_L - \frac{j(\omega/C_e)}{\omega^2 - (\omega_r + j \omega_i)^2} J_1^2 \left(\operatorname{Re}(k'_{10}) \frac{\rho_0}{a} \right) \quad (57)$$

where the complex resonant radian frequency may be obtained by multiplying (51) by 2π and where the patch capacitance is given by (54). The series inductive reactance may be calculated from (36). This formula produces good agreement with measurements, although better and more rigorous forms may be derived considering the probe diameter or width such that a relation similar to (33) or (34) is obtained.

2.3.1 CALCULATIONS FOR A UHF CIRCULAR MICROSTRIP PATCH

A circular microstrip patch fed at the edge will normally have a resonant resistance of several hundred ohms and is thus poorly matched to lower-impedance feedlines. In order to insure that the dominant TM_{10} rf mode is excited (with zero E field at the center), a shorting pin is normally placed at the patch center. In order to produce lower resonant resistance, the patch may be fed coaxially at a point inset from the edge, denoted by the radius ρ_0 . Such a patch was constructed using 3-M 7098 GX board with a radius $a = 3.80$ cm and a thickness $t = 0.1524$ cm; the dielectric constant was $\epsilon_r = 2.49$ and the feedpoint was set at $\rho_0 = 1.17$ cm.

This set of geometrical parameters will be used to illustrate the use of formulas (39) - (57).

1. From (52), $G_w = .007374$ mhos
2. From (53), $B_w = .012017$ mhos
3. From (44), $1 - \alpha a = 1.033921 - j0.020814$
4. From (49), $\Delta_5 = 0.026811 - j0.014949$
5. From (50), $k_{10}^t = 1.814369 + j 0.014949$
6. From (51), $f_r = 1444.7$ MHz
7. From (55), $Q_r = 60.7$
8. From (54), $C_e = 7.52$ pF
9. From (56), $R_{rad} = 64 \Omega$
10. $R_{in} = R_{rad} + R_{di} + R_{cu} \approx 65 \Omega$

These calculated values are compared with measured values in Table 3.

TABLE 2
COMPARISON OF THEORETICAL AND MEASURED VALUES

Patch Dimensions	Resonant Frequency	Resonant Resistance
$a = 3.80 \text{ cm}$ $p_0 = 1.17 \text{ cm}$ $t = 0.1524 \text{ cm}$ $\epsilon_r = 2.49$	1445 MHz (theory) 1443 MHz (exper.)	64 Ω (theory) 66 Ω (exper.)

It is seen that the agreement in resonant frequency is to about 0.1% and the agreement in resonant resistance is to about 3%.

3.0 CONCLUSIONS

This paper has presented a series of engineer-usable design equations for both rectangular and circular microstrip antennas, based on the modal expansion theory. The accuracy of these relations is tied directly to the accuracy of the wall conductance and wall susceptance expressions used, which are based on the solutions for geometries similar to the microstrip antenna; rigorous solutions are not yet available and theoretical work should continue to find better forms. The accuracy of the resonant frequencies calculated was typically 0.5% for the models tested and the accuracy of the resonant resistances was typically 10%. Although these relations have been tested against specific experimental models designed for L-band and S-band, they have not yet been compared to results for C-band and X-band patches where electrically thicker substrates are encountered. In order to use this theory (or any other), it is necessary to know the substrate dielectric constant to at least two significant figures, i.e. to better precision than the data supplied by printed-circuit board manufacturers.

4.0 ACKNOWLEDGEMENT

This work was supported by the Army Research Office, Research Triangle Park, N. C.

5.0 REFERENCES

1. Jedlicka, R. P. and K. R. Carver, "Mutual coupling between microstrip antennas," Proc. of Workshop on Printed Circuit Antenna Technology, New Mexico State University, Physical Science Laboratory, October 17-19, 1979.
2. Munson, R. E., "Conformal microstrip antennas and microstrip phased arrays," IEEE Trans. Ant. & Prop., Jan., 1974, pp. 74-78.
3. Derneryd, A. G., "Linearly polarized microstrip antennas," IEEE Trans. Ant. & Prop., Nov., 1976, pp. 846-851.
4. Carver, K. R. and E. L. Coffey, "Theoretical Investigation of the Microstrip Antenna," New Mexico State University, Physical Science Laboratory Technical Report PT-00929, Jan. 23., 1979.
5. Carver, K. R., "A modal expansion theory for the microstrip antenna," Digest IEEE International Symposium on Antennas & Propagation, Seattle, Washington, June, 1979, pp. 101-104.
6. Lo, Y. T., D. Solomon, F. R. Cre, D. D. Harrison, and G. A. Deschamps, "Study of microstrip antennas, microstrip phased arrays and microstrip feed networks," Univ. of Illinois, Dept. of Electrical Engineering, report RADC-TR-77-406, October 21, 1977.
7. W. F. Richards, Y. T. Lo, "An Improved Theory for Microstrip Antennas and Applications," Digest IEEE International Symposium on Antennas & Propagation, June, 1979, pp. 109-112.
8. Hammerstad, E. O., "Equations for microstrip circuit design," 5th European Microwave Conference, Sept., 1975, pp. 268-272.
9. Schneider, M. V., "Microstrip dispersion," Proc. IEEE, 60, No. 1, Jan., 1972, pp. 144-146.
10. Abramowitz, M. and I. A. Stegun (eds.) Handbook of Mathematical Functions, NBS Applied Mathematics Series 55, U. S. GPO, Washington, D. C., June, 1964.

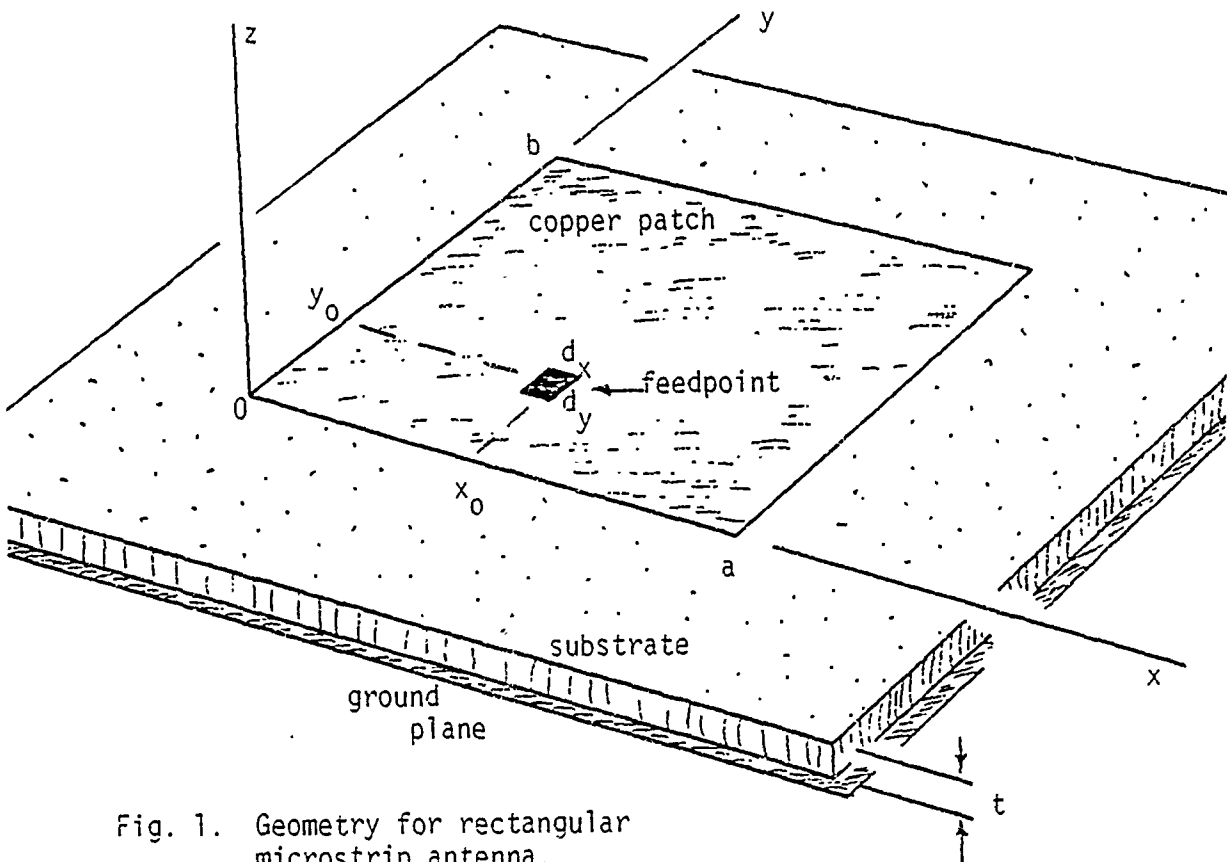


Fig. 1. Geometry for rectangular microstrip antenna.

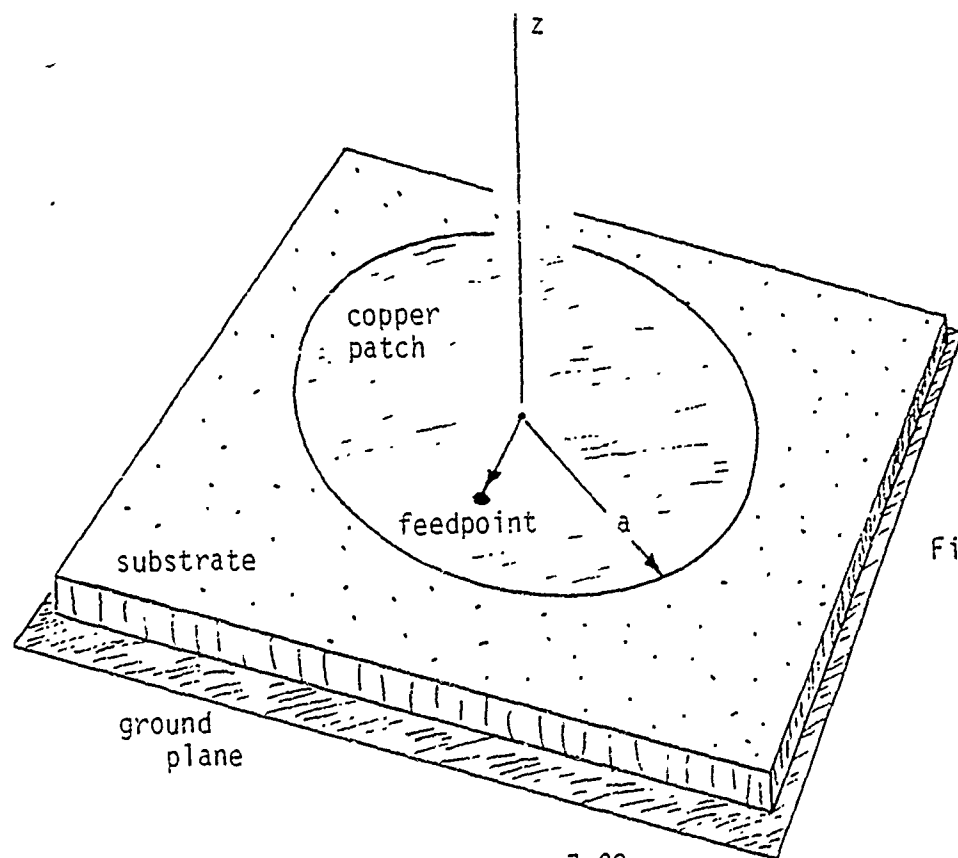


Fig. 2. Geometry for circular microstrip antenna.

THEORY AND APPLICATIONS FOR MICROSTRIP ANTENNAS

W. F. RICHARDS, Y. T. LO, P. SIMON, D. D. HARRISON
ELECTROMAGNETICS LABORATORY
UNIVERSITY OF ILLINOIS
URBANA, IL 61801

SUMMARY

A method described in a number of previous papers and symposiums [1]-[4] for the analysis of thin microstrip antennas is reviewed. The method consists of treating the microstrip antenna, for the purpose of obtaining an approximation to the internal field structure, initially as a cavity bounded on the perimeter of the patch by a magnetic wall. From these approximate fields, a "quality factor" for the antenna can be computed, and from this, a correction to the internal field structure made. The process is *iterative*, but requires in the usual case no more than a single iteration. The essence of the "correction" is to account for the power loss due to radiation in the space and surface waves. The change in resonant frequency due to fringing is easily taken into account by extending the edge of the patch and appropriately scaling all other dimensions. The simple, albeit approximate, expressions provided by this method readily lend themselves to some useful applications including multiport analysis and design of circularly polarized antennas, both of which are discussed below. Results are presented which show that this method of treating thin microstrip antennas is very accurate. As the thickness of the microstrip increases, the theory begins to lose accuracy although the precise limits of applicability are not yet known. One difficulty that seems to be important for the thicker antennas is an adequate modelling of its feed. This is a very difficult problem to analyze for most antennas. A discussion of a canonical feed problem for applications to microstrip antennas is also included.

1.0 THEORY

For the sake of illustration of the theory, the case of the rectangular microstrip antenna is developed. All other separable geometries (which encompass the most widely used microstrip antennas) can be analyzed by the same procedure. Non-separable geometries can also be analyzed, but the modes associated with them must be determined numerically (for instance as

in [5])

1.1 CAVITY APPROXIMATION

When a microstrip antenna is very thin compared to a wavelength, (the *typical* case of many practical applications), the structure, from one point of view, can be considered as a truncated parallel plate waveguide. Fields within the antenna that vary in a direction perpendicular to the patch, the z direction, evanesce away from the feed and the patch boundary leaving only fields which are z-independent in most regions of the antenna. The patch boundary approaches, with increasing accuracy, an open circuit to these transverse electromagnetic fields as the thickness of the microstrip approaches zero. Thus, a reasonable assumption with which to begin is that the fields within the microstrip are all z-independent, and the magnetic field vanishes tangentially at the patch boundary. Actually, the fringing of the fields at the boundary makes it more accurate to assume that the tangential magnetic fields vanish a small distance exterior to the physical patch. This "edge correction" has been estimated for rectangular geometries [6]-[7] and for circular geometries [8]. The assumptions made as far as the field inside the antenna is concerned are equivalent to treating the microstrip antenna as a cavity whose patch and ground plane are joined at the patch boundary by an enclosing magnetic wall.

1.1.1. FEED MODELING

The feed must also be idealized if the solution to the problem is to retain a practical level of simplicity. There are two types of feeds commonly employed, the coaxial feed and the stripline feed. In the former case, one would, upon application of Huygen's principle, represent the feed by removing the coaxial cable, closing the electric wall on the ground plane at the feed by an electric conductor, and impressing a cylindrical band of electric current flowing from the bottom to the top conductors encircled by an annular ribbon of magnetic current on the ground plane. Further simplification involves neglecting the contribution due to the magnetic current and assuming that the electric current is uniform over the cylinder with total current of 1 A. A final idealization which makes the computation especially convenient is to replace the current cylinder by a uniform current ribbon of some "effective feed width," d, centered on the cylinder and oriented, say in the x direction. If more than one port is present, each would be treated in the same manner as shown in Fig. 1. The choice of the effective width is discussed later. For the case of a stripline feed, Huygen's principle reduces the problem to modelling the feed by a strip of z directed electric current backed by a magnetic wall. Of course, with thin microstrips, this current will be small everywhere on the patch boundary except in the immediate vicinity of the feed. The obvious form of idealization of this source is simply to assume a uniform current

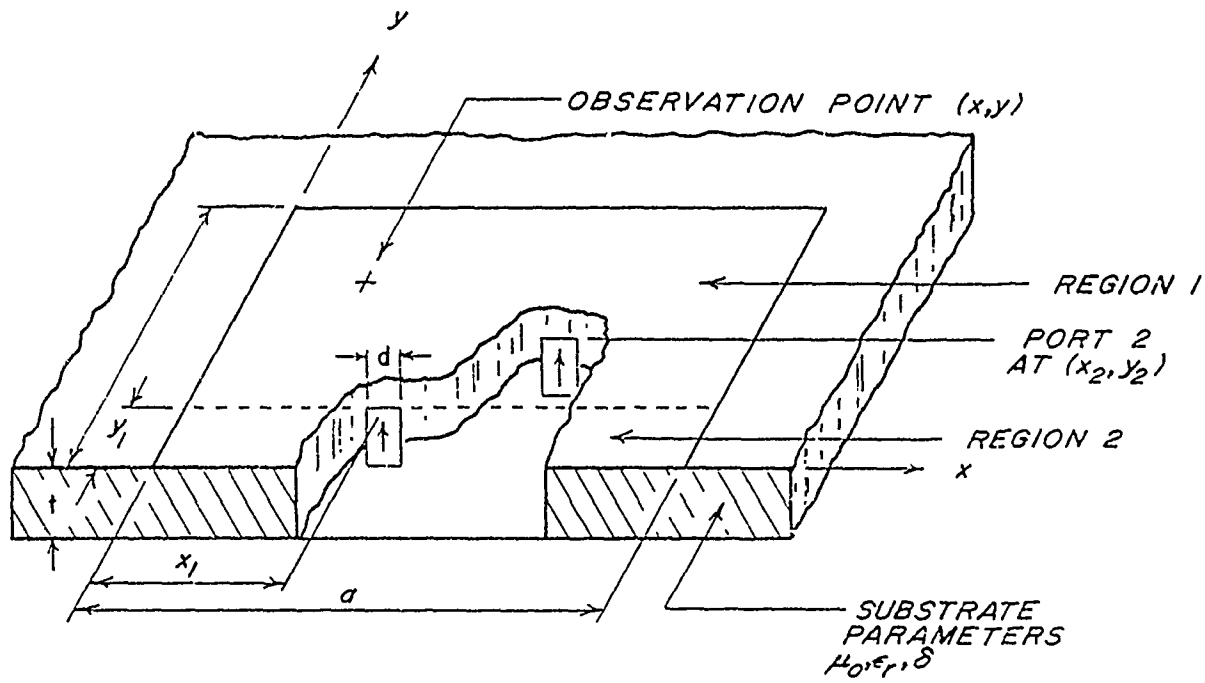


Figure 1. Geometry and idealized feed for a rectangular microstrip antenna.

ribbon of total current, I A, as in Fig. 1 but at the patch boundary. The width, due to fringing, may not be exactly the physical width of the stripline, but some "effective width." Thus, both types of feeds are idealized to the same type of model. It will be seen later that the effect of the feed is to "shift" an amount of the impedance locus of the microstrip antenna into the inductive portion of the Smith Chart.

1.1.2. CAVITY FIELDS

Having thus idealized both the feed and antenna, the fields within the "cavity" can be computed conveniently by either of two well-known equivalent methods. The first method, herein called modal expansion, results in the following expression for the electric field, $E = \hat{z}E'(x,y)$,

$$E = -jk_0\eta_0 \sum_{m=0}^{\infty} \sum_{n=0}^{\infty} \frac{\phi_{mn}(x,y) \phi_{mn}(x_1,y_1)}{k^2 - k_{mn}^2} j_0\left(\frac{m\pi d}{2a}\right). \quad (1)$$

where

$$k^2 = \epsilon_r(1-j\delta)k_0^2,$$

$$k_0 = \omega/\nu,$$

$$\nu = \text{speed of light}.$$

f = frequency, $\omega = 2\pi f$,

ϵ_r = relative dielectric constant of substrate.

δ = the loss tangent of the substrate.

$\eta_0 = 377 \Omega$,

$$k_{mn}^2 = \left(\frac{m\pi}{a} \right)^2 + \left(\frac{n\pi}{b} \right)^2,$$

$$j_0(x) = \frac{\sin(x)}{x},$$

$$\phi_{mn}(x,y) = \left(\frac{\epsilon_0 \epsilon_{0n}}{ab} \right)^{1/2} \cos(m\pi x/a) \cos(n\pi y/b),$$

$\epsilon_{0n} = 1$ for $m=0$ and 2 for $m \neq 0$, and

d = the "effective feed width."

An alternative approach, termed "mode matching," involves finding modal solutions in the two regions shown in Fig. 1, each of which satisfies the wave equation and the conditions on those parts of the patch boundary within their respective regions. The appropriate continuity conditions, including the excitation, are applied at the intersection of the regions to determine the unknown modal coefficients. Under this approach, the electric field has the representation

$$v = -jk_0 \eta_0 i \sum_{m=0}^{\infty} \frac{\epsilon_{0m}}{a} \frac{\cos(p_m y_<) \cos(p_m(b-y_>)) \cos\left(\frac{m\pi x_1}{a}\right) \cos\left(\frac{m\pi x}{a}\right)}{p_m \sin(p_m b)} j_0\left(\frac{m\pi d}{2a}\right) \quad (2)$$

where $y_<$ and $y_>$ are the smaller and the greater of y and y_1 , respectively, and $p_m = [k^2 - (m\pi/a)^2]$. In fact, equation (2) follows directly from (1) by simply summing the inner series of (1). Computationally, equation (2) is more convenient than (1) in most instances. However, (1) provides some physical insight not afforded by (2) into a number of phenomena including circular polarization.

1.2 CORRECTION OF ANTENNA FIELDS

As it stands, equations (1) and (2) *cannot* represent the internal fields of the microstrip antenna adequately. Clearly this is so, since (for a *practical* antenna at least) the *major* component of energy given up by the source is due to radiation whose effect is absent in (1) and (2). The effect of loss is seen in the *complex* poles (in the ω plane) of the terms in equation (1). The structure will "ring down" at a number of frequencies corresponding to the real part of the poles at rates dependent on the imaginary part of the poles. The magnitudes of the latter are directly related to the losses in the system. Therefore, the imaginary parts of the poles in (1) must be modified in order to account for this loss.

The manner in which this is done has been discussed in previous reports [2]-[3]. Briefly, it amounts to estimating the radiated power, P_{rad} , surface wave loss, P_{sw} , the dielectric loss, P_d , and the copper loss, P_{Cu} , of the antenna from the cavity fields computed in (2). The radiation pattern is computed by considering the cavity electric field at the boundary of the patch, through Huygen's principle and subsequent approximations, as its source. The surface wave is similarly considered as being due to an equivalent magnetic current at the boundary of the patch and computed as the residue of a pole in the spectral representation of the field. In the case of a surface wave, an equivalent electric current component, which is the current induced on the free-space side of the patch, is ignored. The dielectric loss is computed by

$$P_d = \omega \epsilon_0 \delta / \int \int |E|^2 dx dy = 2\omega W_E ,$$

where W_E is the electric stored energy. The copper loss is computed by the usual perturbation method and is given by

$$P_{\text{Cu}} = 2 \frac{\Delta}{t} \omega W_H ,$$

where W_H is the magnetic stored energy, $\Delta = \left(\frac{2}{\sigma k_0 \eta_0} \right)^{1/2}$ is the skin depth of the conductor, and σ is the conductivity of the material. (Actually, σ is the "effective conductivity" of the conductor since surface finish can reduce the conductivity of the pure conductor. The estimation of σ is discussed in section 2.0). In the vicinity of resonance, $W_H \approx W_E$; thus, P_{Cu} and P_d are simply related by

$$\frac{P_{\text{Cu}}}{P_d} \approx \frac{\Delta}{t \delta} . \quad (3)$$

Thus, P_{Cu} is determined from P_d for these z -independent cavity fields.

It is important from a numerical point of view to recognize that all these loss expressions depend mainly upon one term of equation (1), the dominant mode. All other terms are relatively small compared to this term. The same statement holds for the total stored energy, $W_E + W_H \approx 2W_E$. The factor in each of these terms that makes them "dominant" is the factor, $1/k^2 - k_{\text{res}}^2$, where k_{res} is the wave number of the resonant mode. Initially, only the dielectric loss is accounted for in this factor. However, when forming the ratio,

$$Q = 2\omega \frac{W_E}{P_{\text{rad}} + P_{\text{sw}} + P_d + P_{\text{Cu}}} .$$

this factor is approximately cancelled leaving a relatively accurate estimate for Q . Once Q is obtained, the poles of (1) are modified by lumping all the losses into an "effective dielectric loss tangent," δ_{eff} . Thus, a new wave number is defined such that $k^2 = k_{\text{eff}}^2 = k_0^2 \epsilon_r (1 - j\delta_{\text{eff}})$ and is used in equations (1) and (2). The whole process described above can be repeated in an

iterative sequence. However, the sequence has been found to essentially converge after a single iteration.

1.3 VOLTAGE AT THE FEED

The voltage at the feed as in all antennas can be defined in a variety of ways. For instance, one may take it as the microstrip thickness, t , times the electric field at the feed strip center. One might also average the field over the strip and multiply by t . The authors have, for simplicity, chosen the latter definition which is found to be useful in comparing the theoretical and experimental impedance characteristics. The voltage becomes

$$v = -jk_0\eta_0 t \sum_{m=0}^{\infty} \sum_{n=0}^{\infty} \frac{\phi_{mn}(x_1, y_1)^2}{k^2 - k_{mn}^2} j_0^2\left(\frac{m\pi d}{2a}\right) \quad (4)$$

or

$$v = -jk_0\eta_0 t \sum_{m=0}^{\infty} \frac{\epsilon_{0m}}{a} \frac{\cos(p_m y_1) \cos(p_m(b-y_1))}{p_m \sin(p_m b)} \cos^2\left(\frac{m\pi x_1}{a}\right) j_0^2\left(\frac{m\pi d}{2a}\right). \quad (5)$$

Since the input current was assumed to be 1 A, the driving point impedance, Z , is simply taken to be the voltage, v .

1.4 NUMERICAL CONSIDERATIONS

The summand in equation (5) has the asymptotic form of

$$\frac{jk_0\eta_0 t}{\pi^3} \left(\frac{a}{d}\right)^2 \frac{\cos^2(m\pi x_1/a) \sin^2(m\pi d/2a)}{m^3} \quad (6)$$

for $0 < y_1 < b$. (For $y_1 = 0$ or $y_1 = b$, (6) is multiplied by a factor of two). The sum of the series associated with (6) is

$$S(x_1, y_1, d) = \frac{jk_0\eta_0 t}{\pi^3} \left(\frac{a}{d}\right)^2 \times \\ \left\{ F\left(\frac{2\pi x_1}{a}\right) - \frac{1}{2} F\left(\frac{2\pi}{a}(x_1 + \frac{d}{2})\right) - \frac{1}{2} F\left(\frac{2\pi}{a}(x_1 - \frac{d}{2})\right) - F\left(\frac{\pi d}{a}\right) \right\}$$

where

$$F(x) = x^2[\frac{1}{2}\ln(x) - \frac{3}{4} - 2G(x)]$$

and $G(x)$ is a smooth and bounded function conveniently expressed and evaluated in terms of Tchebyshev polynomials. Clearly, as $d \rightarrow 0$, $S(x_1, y_1, d)$ grows as $-\ln(d)$. Moreover, $S(x_1, y_1, d)$ is a positive imaginary number. Therefore, it is quite clear that probes with smaller and smaller diameters become increasingly inductive as expected. It should be noted that an inductive shift also occurs for a stripline feed. With $S(x_1, y_1, d)$ computed as above, the series of equation (5)

can be easily accelerated by a Kummer's transformation.

1.5 NETWORK REPRESENTATION

Writing equation (4) as

$$Z = j\omega \frac{\mu_0 t \nu^2}{\epsilon_r} \sum_{m,n=0}^{\infty} \frac{\phi_{mn}^2(x_1, y_1) j_0^2\left(\frac{m\pi d}{2a}\right)}{\omega_{mn}^2 - (1 - j\delta_{eff})\omega^2} = \sum_{m,n=0}^{\infty} \frac{1}{j\omega C_{mn} - j\frac{1}{\omega L_{mn}} + G_{mn}(\omega)} \quad (7)$$

where

$$G_{mn}(\omega) = \omega\delta_{eff}/\alpha_{mn}, \quad L_{mn} = \alpha_{mn}/\omega_{mn}^2, \quad C_{mn} = 1/\alpha_{mn},$$

and

$$\alpha_{mn} = \frac{\mu_0 t \nu^2}{\epsilon_r} \phi_{mn}^2(x_1, y_1) j_0^2\left(\frac{m\pi d}{2a}\right), \quad \omega_{mn} = \nu k_{mn}/\epsilon_r^{1/2},$$

leads to the network representation as shown in Fig. 2a. For all sufficiently higher-order modes, each of the corresponding R-L-C networks can be replaced by the inductance, L_{mn} , since the latter approaches zero as the mode indices go to infinity as seen in equation (7). If

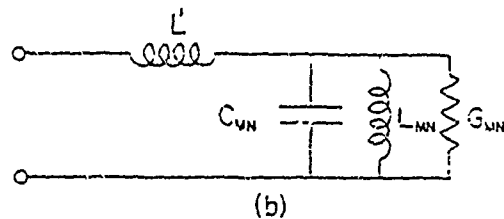
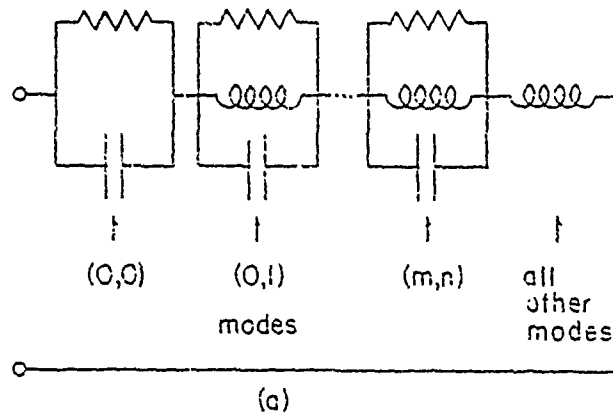


Figure 2. (a) General network model of the microstrip antenna.
 (b) Network model over a narrow band about an isolated mode.

the microstrip is to be characterized over a limited range of frequencies centered about an isolated resonance ($\omega_{l,V}$) of the antenna, the network representation of Fig. 2b is applicable where

$$L' = \sum_{\substack{m,n=0 \\ (m,n) \neq (M,N)}}^{\infty} \frac{\alpha_{mn}}{\omega_{mn}^2 - \omega_{l,V}^2} .$$

1.6 THE FEED PROBLEM

An idealized feed model was presented in Section 1.1.1. This model required the specification of an "effective feed width," d . This parameter can be determined empirically so as to give the best fit of the calculated-to-measured impedance locus at a given feed point and mode. The authors have found that, once this parameter has been so determined, it can be used successfully at any feed location and frequency except when the feed is on the patch boundary. For the latter case, it is believed that the more complicated fringing of the fields at the patch boundary changes d from the value it takes within the interior of the antenna. For the rectangular antenna, an effective width of five times the diameter of the center conductor of a coaxial feed has been found to give good results with thin rectangular microstrip antennas.

For the thicker microstrips, the effective width becomes a more critical parameter which has prompted the authors to study this problem in detail for a canonical geometry. The geometry of Fig. 3 is analyzed by the method of moments. This geometry was chosen for its simplicity since all the fields are axially symmetric. However, it is believed that useful conclusions can be drawn for a coaxial feed located *anywhere* (except at the patch boundary) within a microstrip antenna.

The integral equation that an equivalent magnetic current, $K = \hat{p} K$, must satisfy is

$$(G_1 + G_2) K > = \phi_0$$

where

$$G_1 = \sum_{m=0}^{\infty} Y_{0m} \coth(\gamma_m t) \psi_m > < \psi_m ,$$

$$G_2 = \sum_{m=1}^{\infty} Y_{0m} \phi_m > < \phi_m ,$$

$$\gamma_m = (\xi_m - k_f^2)^{1/2} .$$

The ψ 's and the ϕ 's are the normalized p components of the electric field waveguide modes in coaxial waveguides 1 and 2, respectively. The eigenvalue of waveguide 1 is ξ_m . The respective wave admittances are Y_{0m} and Y_{1m} . Bracket notation is used to simplify the expressions.

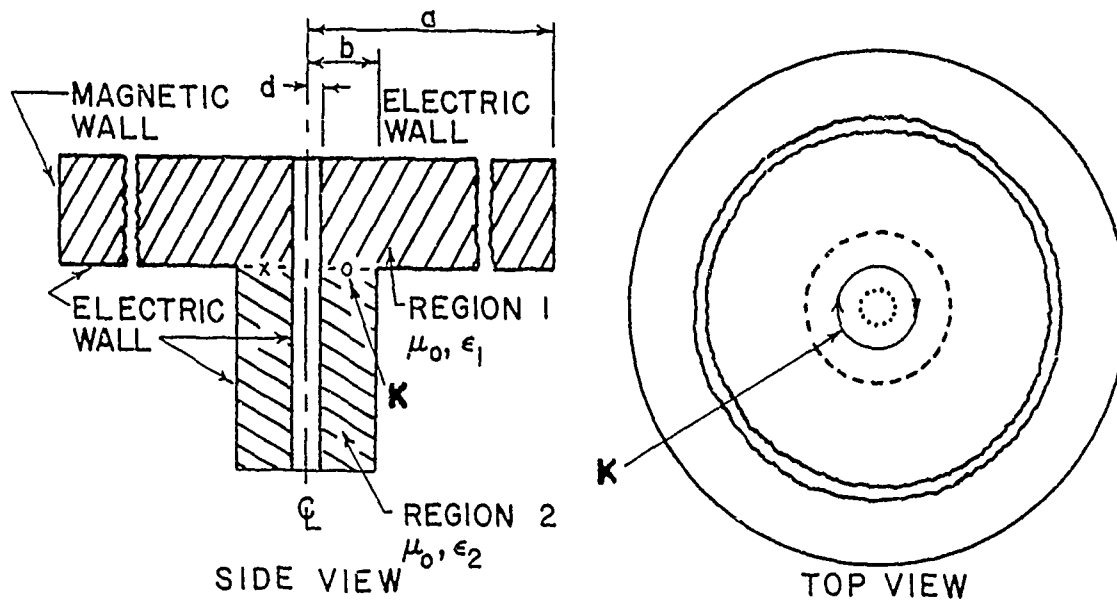


Figure 3. Geometry for a canonical feed problem.

(Juxtaposition of a "bra," $\langle u,$ and a "ket," $v \rangle$, implies the integration, $\int_d^b \rho u(\rho) v(\rho) d\rho$). This equation is solved by Galerkin's method using a basis set of

$$\{K_m\} = [\rho^{m-2}(b-\rho)^{-\mu}], \quad m = 1, 2, 3, \dots,$$

where μ is chosen to make K_m satisfy the edge condition at $\rho = b$ [9]. (Programming of the solution is not completed and numerical results were not available at the time of writing of this report). From K , the field distribution in the vicinity of the feed can be found, and from this, a more accurate idealization of the feed can be deduced. and from this, it is hoped that a more accurate idealization of the feed current distribution can be deduced.

2.0 LOSS TANGENT AND CONDUCTIVITY ESTIMATES

Although radiation from the typical microstrip antenna accounts for the major contribution of the power supplied by the source, the power consumed in the dielectric and the metallic parts of the antenna cannot be neglected except in the thickest microstrips. It has been the experience of the authors that the published values of loss tangent for printed circuit board and conductivity for pure conductor are not always adequate. The following very simple scheme has been successfully used to estimate the loss characteristics of the materials employed.

The first step is to take a sample of the double-clad printed circuit (PC) board from which the antenna is to be constructed and form from it a *bona fide* cavity by soldering copper foil between the two conducting plates. A feed is attached to this cavity, and its quality factor, Q_1 , is measured at a mode corresponding to the frequency of the antenna to be constructed. A second cavity with patch dimensions the same as the first is made by joining two identically shaped samples of the PC board together to form a cavity of twice the thickness of the first. The quality factor, Q_2 , of this second cavity is measured. The only two types of loss in this structure are the dielectric loss and loss in the upper and lower plates of the microstrip and the relatively smaller loss in the copper foil. Neglecting the latter, and using equation (3), one has for the two cavities

$$\frac{1}{Q_1} = \frac{\Delta}{t} + \delta$$

$$\frac{1}{Q_2} = \frac{\Delta}{2t} + \delta$$

where t is the thickness of cavity 1. These two equations are straight lines in the (Δ, δ) plane whose intersection should yield the actual loss tangent, δ , and the skin depth, Δ , of the PC board. For thin microstrips, say $\frac{1}{16}$ inch Rexolite 2200, the Q is relatively low and can be determined with adequate consistency from measurement to measurement. For thicker microstrips, the Q is larger and less accurate to measure. However, for these thicknesses, the antenna is also more efficient and the loss estimates can therefore be cruder without affecting the overall accuracy of the impedance calculations. It is interesting to note that the conductivity has been measured as low as one half that of the pure metal.

3.0 APPLICATIONS

Two easily implemented applications of this theory are the analysis of multiport elements and the design of single feed, circularly polarized antennas. The multiport analysis has important applications to array design, and to adaptive and tunable elements. For example, one could use the multiport analysis to predict the required tuning range for a capacitively loaded two-port to give two senses of circular polarization.

3.1 MULTIPORT ANALYSIS

Once the antenna has been replaced by an ideal cavity with the appropriate loss tangent, it becomes a relatively simple matter to perform multiport analysis. Consider the rectangular microstrip in Fig. 1 with two feed points of coordinates (x_1, y_1) and (x_2, y_2) for ports 1 and 2,

respectively. The z parameters for the two-port are simply

$$Z_{11} = V_1 \Big| \begin{array}{l} I_1=1 \text{ A.} \\ \text{port 2 open} \end{array}, \quad Z_{22} = V_2 \Big| \begin{array}{l} I_2=1 \text{ A.} \\ \text{port 1 open} \end{array}$$

$$Z_{12} = Z_{21} = V_2 \Big| \begin{array}{l} I_1=1 \text{ A.} \\ \text{port 2 open} \end{array}.$$

Thus, Z_{11} and Z_{22} are computed in precisely the same way as was the input impedance for the one port discussed earlier. The mutual impedance, Z_{12} , is computed using

$$Z_{12} = -j\omega\mu_0 t \sum_{m,n} \frac{\phi_{mn}(x_1, y_1)\phi_{mn}(x_2, y_2)}{k^2 - k_{mn}^2} j_0^2\left(\frac{m\pi d}{2a}\right)$$

or

$$Z_{12} = -jk_0\eta_0 t \sum_{m=0}^{\infty} \frac{\epsilon_{0m}}{a} \cos\left(\frac{m\pi x_1}{a}\right) \cos\left(\frac{m\pi x_2}{a}\right) j_0^2\left(\frac{m\pi d}{2a}\right) \times$$

$$\frac{\cos(p_m(b-y_2))\cos(p_m y_1)}{p_m \sin(p_m b)},$$

where it is assumed without loss of generality that $y_1 \leq y_2$. From the z parameters, the s parameters can be easily computed and compared with measured results as shown in Fig. 4 for the case of a rectangular microstrip. The agreement is excellent.

For some applications it is of interest to find the input impedance at one port while the other is loaded. This would provide a means for tuning, matching, modifying patterns, and formation of arrays. In particular, when port 2 is shorted, the input impedance at port 1 can be computed from the following formula

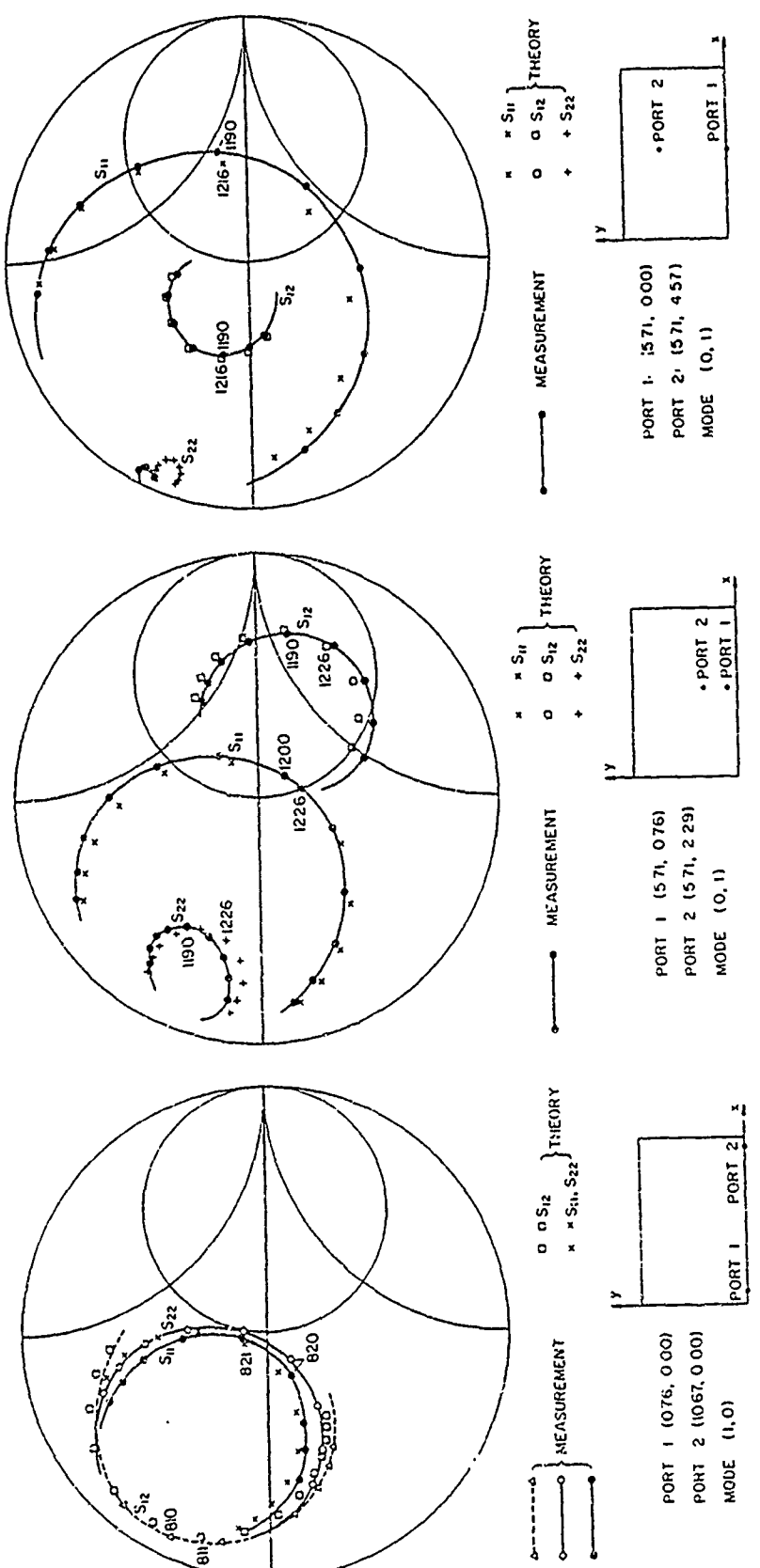
$$Z_{in} = Z_{11} - \frac{Z_{11}^2}{Z_{22}}. \quad (8)$$

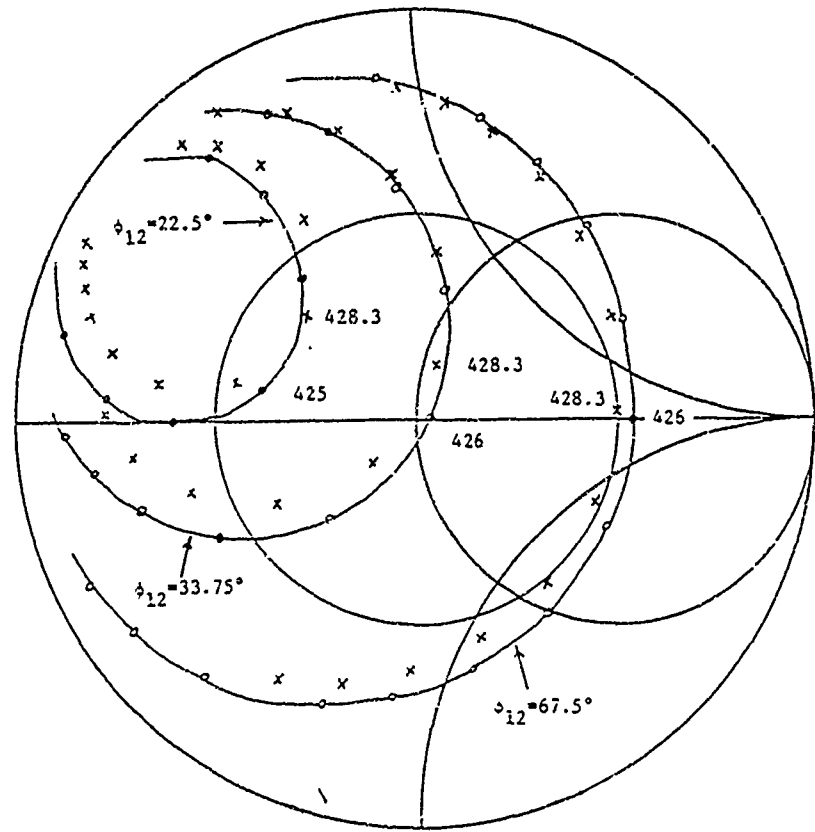
An application of this theory is made to a circular disk microstrip antenna fed along the edge. Due to circular symmetry, the input impedance will be independent of the feed location as long as it is on the circumference. Now if a short-circuiting pin is placed at some point on the circumference, the input impedance at the feed will vary according to its relative position to the short. The computed Z_{in} loci from equation (8) for various angles, ϕ_{12} , between the short and the feed are shown with the experimental results in Fig. 5. Once again, the close agreement between the two supports the validity of the theory. This analysis can obviously be extended to any number of ports for more complex array structures and even for systems with adaptive elements.

Another very useful application is the construction of circularly polarized microstrip antennas formed by appropriately loading one of its ports. An example of this application is discussed in the next section. The input impedance to such an antenna as well as the current in the loaded

Figure 4. Comparison of computed and measured scattering parameters for a rectangular microstrip two-port.

FREQUENCY INCREMENT : 10 MHz





RADIUS = 12.68 cm
 THICKNESS = 0.15 cm
 $\epsilon_r = 2.62$
 $\delta = 0.00083$
 $\sigma = 368 \text{ KV/cm}$

COMPUTED POINTS
 MEASURED LOCUS
 FREQUENCY INCREMENT = 1 MHz

Figure 5. Comparison of computed and measured impedance loci for a short-loaded two-port disk microstrip antenna.

port is computed from circuit analysis using the z parameters (as for the case of the short). To find the pattern, the current in the loaded port is treated as a secondary source which yields a pattern through the method described in section 1.2 which is then superposed on the pattern computed for the 1 A source in the driven port.

3.2 CIRCULAR POLARIZATION

Circular polarization (CP) has been reported in a variety of microstrip antennas [10]-[12]. Experimental work was reported last year [10] on a class of CP antennas derived from disk and

square microstrip antennas by cutting slots in their interiors or corners off their perimeters. In all these antennas, the current theory provides an explanation for the mechanism of antenna operation, and in some cases, provides a means for predicting the necessary dimension needed for CP operation. This is important because CP operation is possible only for a very narrow band of frequency and, without a theoretical prediction, it would take many painstaking cut-and-trials to reach the correct dimensions.

Consider, as a first example, a *nearly square* microstrip of dimensions $a \times b$ as shown in Fig. 6a. If $b+c=a$ where $c/b \ll 1$, then the resonant wave numbers of the mode $(0,1)$, k_{01} , and of the mode $(1,0)$, k_{10} , will be very close to one another. In fact, they will be close enough to assume that the effective loss tangent is the same for each of the two modes. Feeding the antenna at point 1 will excite the ϕ_{10} mode but not the ϕ_{01} . Feeding at point 3 will excite ϕ_{01} but not ϕ_{10} . Feeding at point 2 or on the diagonal drawn in Fig. 6a will excite a dominant field proportional to $\psi_+ = \phi_{01} + \phi_{10}$. With a feed at point 4, the excited field will be proportional to $\psi_- = \phi_{01} - \phi_{10}$. In the far field, in the direction perpendicular to the plane of the microstrip, the electric fields produced by ϕ_{01} and ϕ_{10} are polarized in the x and y directions, respectively, and can be written for appropriate choice of input current magnitude and phase as

$$E_x \approx \frac{\cos(\pi x_1/a)}{k^2 - k_{10}^2}, \quad E_y \approx \frac{\cos(\pi y_1/b)}{k^2 - k_{01}^2}. \quad (9)$$

The contributions of the non-resonant modes are ignored in (9) for frequencies near the resonances of the two modes. To obtain CP in the direction of the zenith, the ratio of E_y to E_x

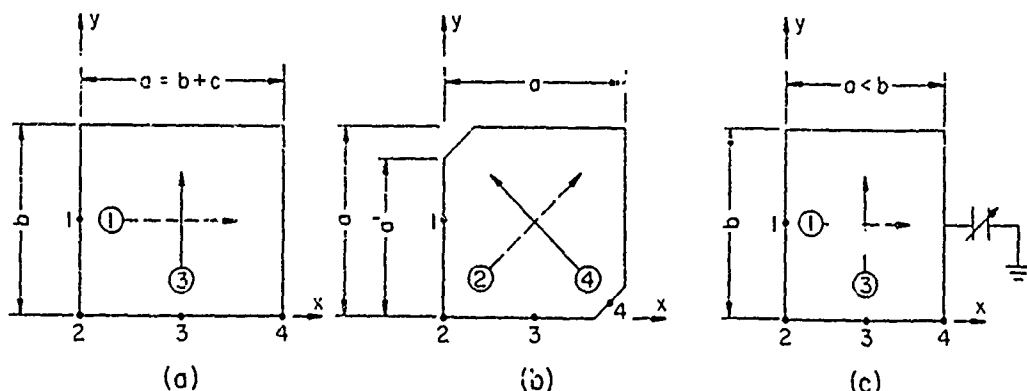


Figure 6. Geometries of three microstrip antennas capable of supporting circular polarization.

should be $e^{\pm j\pi/2}$. Define $A = \cos(\pi y_1/b)/\cos(\pi x_1/a)$. Then

$$\frac{E_y}{E_x} \approx A \frac{k^2 - k_{10}^2}{k^2 - k_{01}^2} \approx A \frac{k - k_{10}}{k - k_{01}} . \quad (10)$$

It is particularly illuminating to plot k , k_{01} , and k_{10} in the complex k plane as was done in Fig. 7. For E_y/E_x to be $e^{j\pi/2}$, equation (10) requires that

$$\Delta k = k_{01} - k_{10} = L(A + \frac{1}{A}) . \quad (11)$$

But

$$\frac{L}{k} \approx \frac{1}{2}\delta_{\text{eff}} = \frac{1}{2Q} , \quad (12a)$$

$$k_{01} - k_{10} = \frac{\pi}{b} - \frac{\pi}{a} = \frac{\pi}{b} - \frac{\pi}{b+c} \approx \frac{\pi c}{b^2} . \quad (12b)$$

$$\bar{k}b \approx \pi . \quad (12c)$$

(The parameters \bar{k} and L are defined in Fig. 7.) Thus, combining (11) with (12),

$$\frac{\Delta k}{\bar{k}} = \frac{k_{01} - k_{10}}{\bar{k}} \approx \frac{c}{b} \approx \frac{A + \frac{1}{A}}{2Q} .$$

For the case of the feed point taken on the diagonal of the microstrip, $A=1$ and, therefore,

$$\frac{a}{b} = 1 + \frac{1}{Q} .$$

The sense of rotation of the CP wave produced by the antenna fed at point 2 will be left-hand

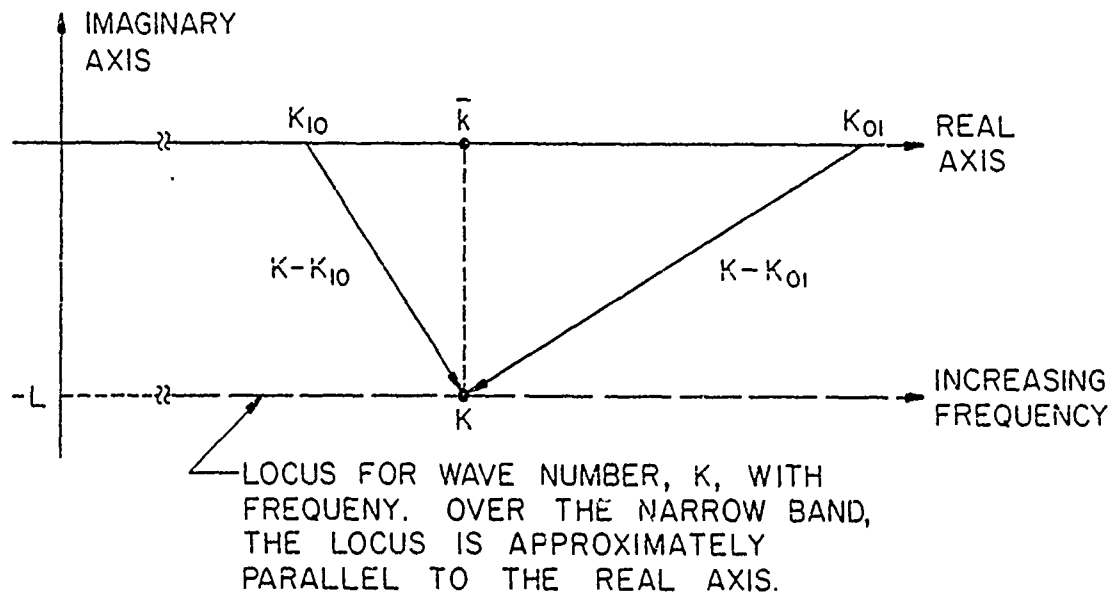


Figure 7. Wave number and its poles in the complex k plane.

circularly polarized. By simply feeding at point 4 instead, the sense is reversed. Figure 8 shows the far-field pattern of the nearly square antenna taken with a rotating dipole. The quality of the CP is very good broadside to the antenna and, as expected, degrades to linear polarization on the horizon.

For the antenna of Fig. 6b, the analysis follows along the same lines as that for Fig. 6a. However, in this case, rather than using ϕ_{10} and ϕ_{01} modes, ψ_+ and ψ_- are used with corresponding wave numbers k_+ and k_- . Of course, if the corners of the square microstrip are not trimmed off, then $k_+ = k_-$. However, by trimming the corners, k_- is increased while k_+ stays nearly constant. The precise amount of this shift has been estimated using a perturbation formula [13]:

$$\frac{k_- - k_+}{k} \approx \frac{2(a-a')}{\pi a} \sin[\pi(a-a')/a]$$

This formula is based on the assumption that the boundary condition along the perimeter of the microstrip is that of a perfect magnetic wall. Although this assumption has proven reasonably applicable to the analysis of most aspects of microstrip antennas, it is not entirely adequate to predict the shift in poles in this critical application. It is believed that the complicated fringing fields at the corners where the perturbation formula is applied make the approximation of insufficient accuracy in this application. However, one can *experimentally* refine the proper dimensions by simply measuring the resonant frequencies corresponding to k_+ and k_- by feeding at ports 2 and 4, respectively.

The antenna in Fig. 6c operates by the same mechanism as that in 6a. In this case, however, the pole k_{10} can be varied by simply adjusting the capacitance attached to the antenna. (Since the capacitor is located at $y=b/2$, a null of the ϕ_{01} mode, k_{01} , is unaffected by the capacitor.) If the range of capacity is large enough, and $a < b$, one is able to adjust the antenna to produce fields of practically any polarization and sense. Thus the antenna can be at one moment left-hand CP, linear at the next, and right-hand CP at some other time by simply changing the capacitance (or the bias on a varactor diode). However, since only one pole is affected by the capacitor, the frequency of operation shifts as the capacitance is varied. It should be noted that the capacitor could just as well have been located in the corner of the antenna, in which case, one would feed at points 1 or 3 to achieve CP operation.

Other single-feed CP microstrip antennas can be explained in the same way as the rectangular A disk microstrip antenna was designed on the basis of this theory. A capacitor to the ground plane was attached to the circumference of the disk. When fed at an angle of forty-five degrees from the capacitor, CP operation was also obtained.

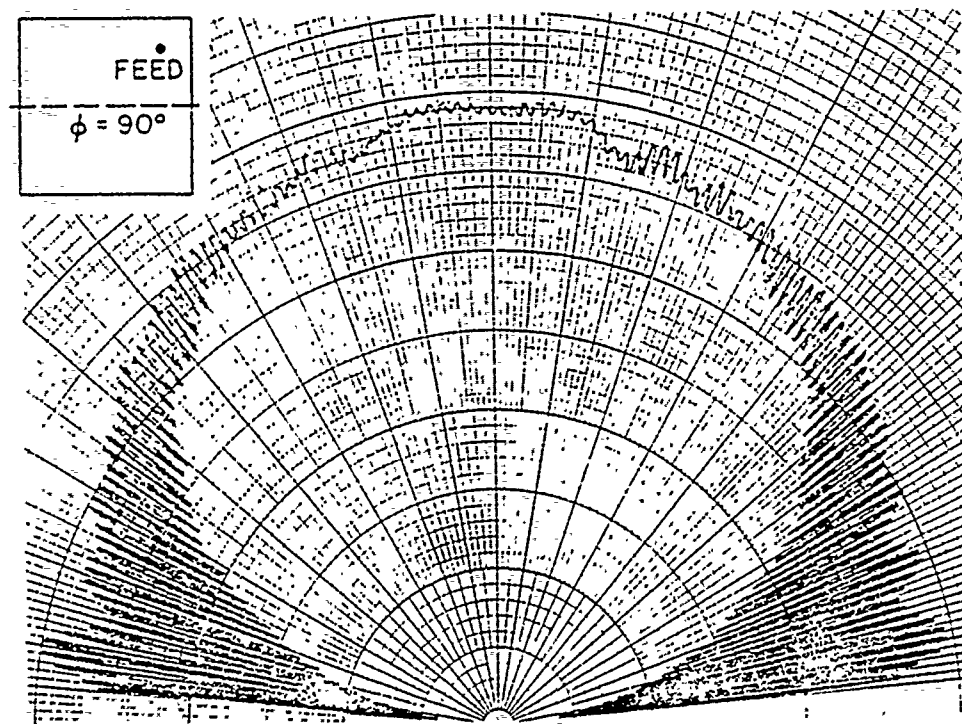
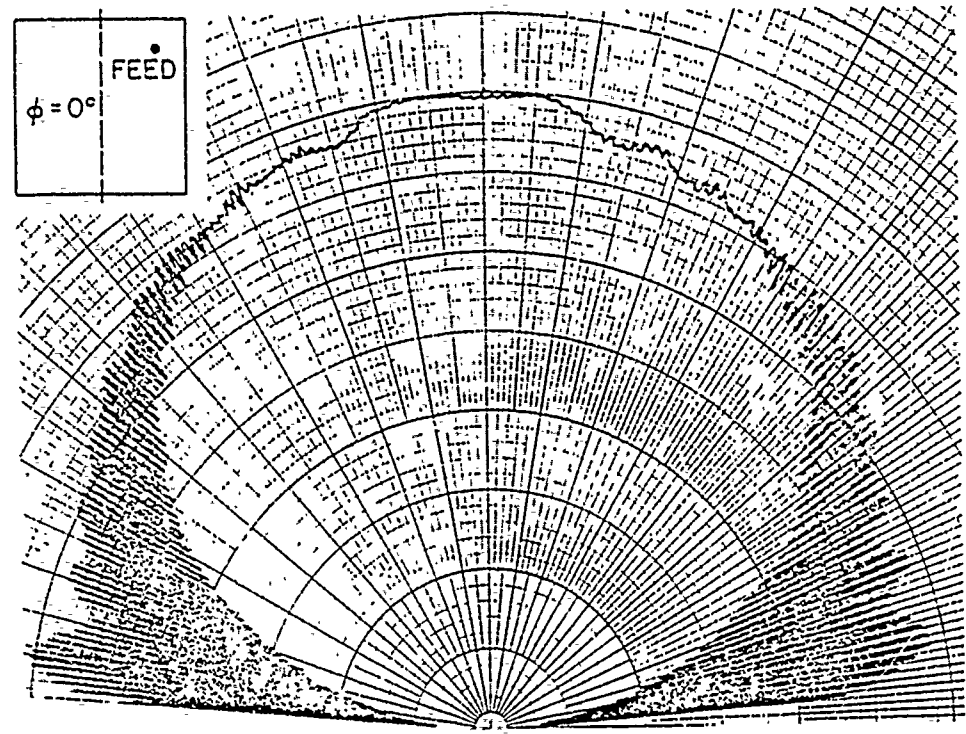


Figure 8. Elevation patterns taken with rotating dipoles for a nearly square microstrip antenna.

Figure 9 shows a square microstrip antenna loaded by two independently biased varactor diodes. The varactors are located on the nodal lines of the ϕ_{10} and ϕ_{01} modes. The biasing arrangement shown in the figure ensures RF and DC isolation between bias supplies and antenna. The location of the varactors allows independent adjustment of the poles k_{01} and k_{10} . By this scheme, the difference in the poles $k_{01} - k_{10}$ can be adjusted while keeping their mean, \bar{k} , fixed. Thus, for operation at a fixed frequency, virtually any polarization can be achieved simply by adjusting the varactor biases. Figures 10 and 11 show the impedance and radiation patterns of this antenna for the various polarizations. The asymmetry in the patterns is probably due to the asymmetrical placement of the diodes. It is conjectured that using two

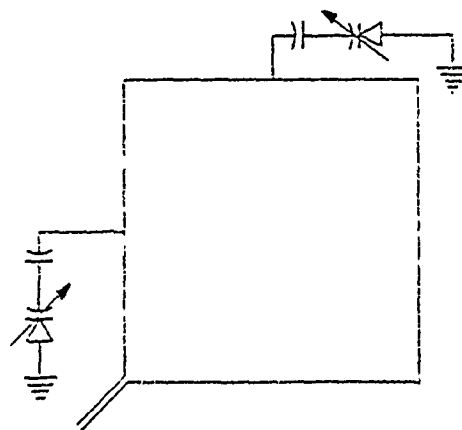
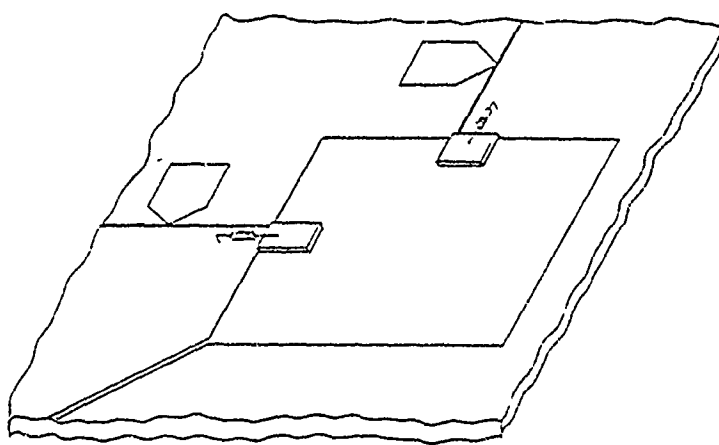


Figure 9. Double-tuned antenna.

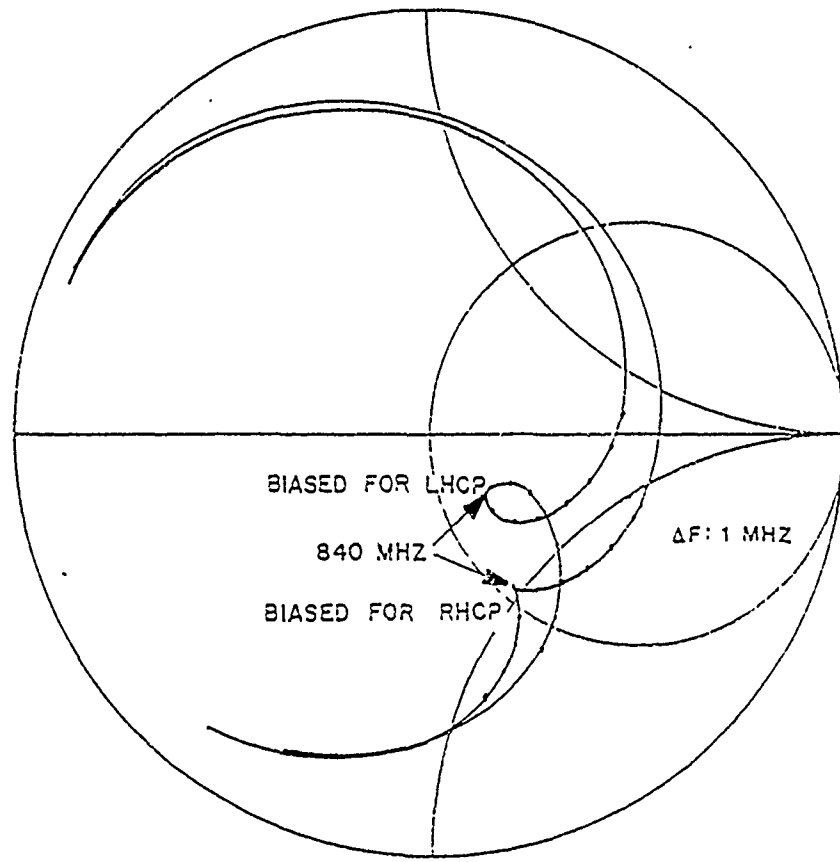


Figure 10. Impedance locus for the double-tuned antenna.

pairs of matched diodes on opposite sides of the antenna would minimize this effect.

Using the double-tuned antenna of Fig. 9, it is also possible to vary the frequency of operation without interfering with the state of polarization. The double-tuned antenna constructed by the authors is tunable from 800 MHz to 840 MHz while still maintaining quite good CP. Obviously, the tuning bandwidth is dependent on the quality of varactors used.

Although all these antennas are able to produce good CP without requiring an external phase-shifter and power divider, a distinct advantage, it is clear from the theory given above that their CP operation is *extremely narrow band*. Figure 12 shows the predicted degradation in axial ratio

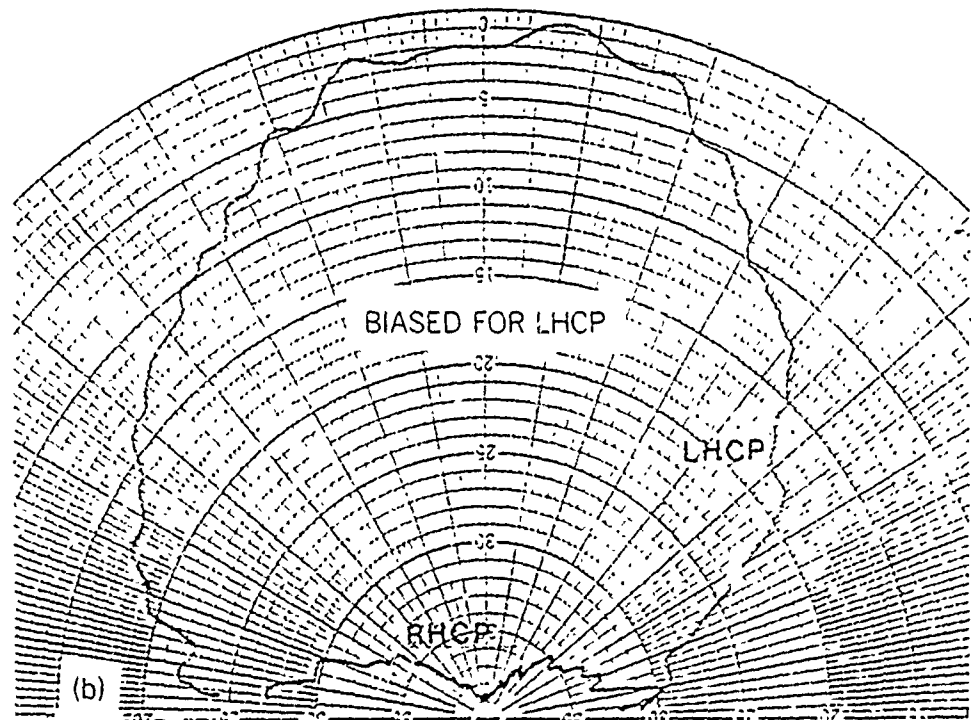
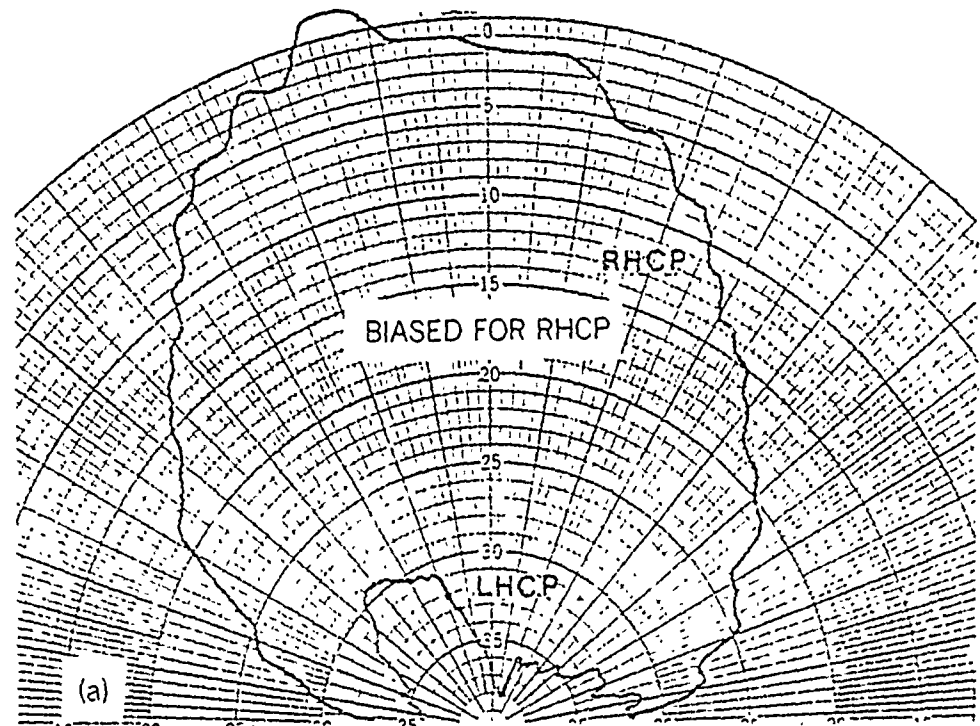


Figure 11. Left and right hand CP patterns of the double-tuned antenna biased for (a) RHCP and (b) LHCP.

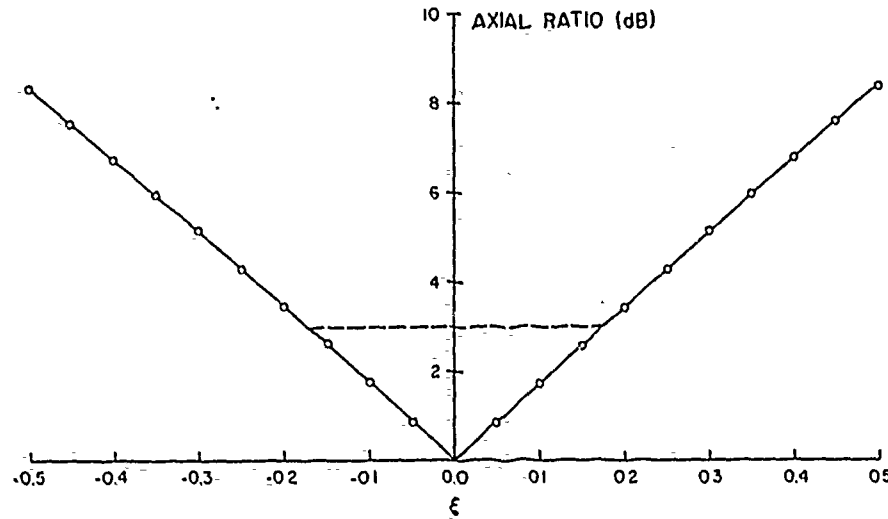


Figure 12. Axial ratio vs. normalized frequency of a circularly polarized microstrip antenna.

with normalized frequency defined as

$$\xi = \frac{f - \bar{f}}{f_{01} - f_{10}} \quad \text{where } \bar{f} = \frac{v\bar{k}}{2\pi}, \quad f_{01} = \frac{v\epsilon_r^{-1/2}}{2b}, \quad f_{10} = \frac{v\epsilon_r^{-1/2}}{2a}.$$

Thus, for an axial ratio within 3 dB (at zenith) which would produce a polarization mismatch loss of less than 1/4 dB with respect to CP, one is limited to a bandwidth of about 35% of the frequency difference between the two dominant poles or about 35/Q percent bandwidth. Figure 12 applies to any CP microstrip whose feed excites both of the near degenerate modes equally. A more general set of curves for less symmetrically located feeds can easily be constructed. The close agreement between theory and experiment is shown in Fig. 13 where axial ratio as a function of frequency is plotted for the nearly square antenna.

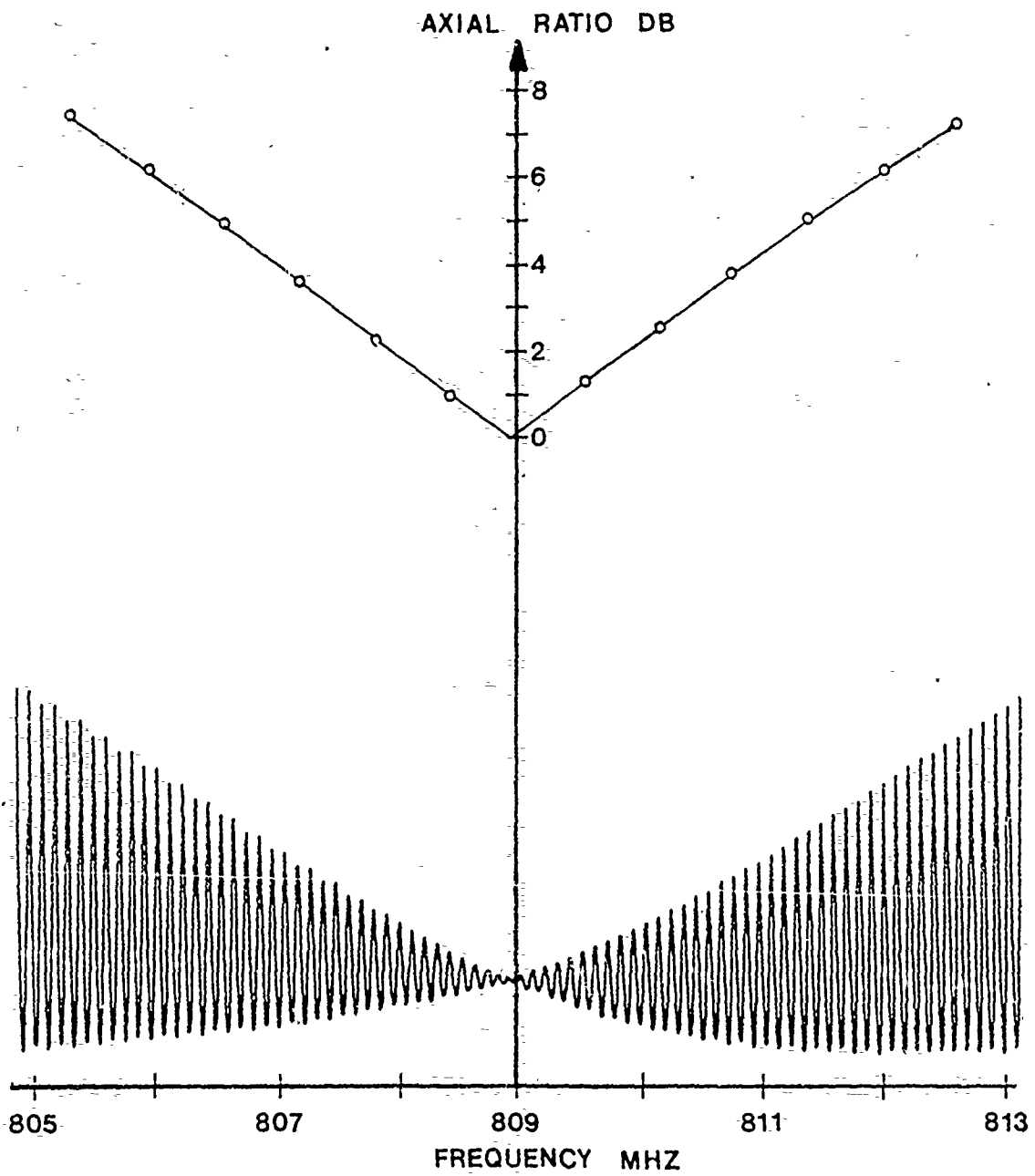


Figure 13. Measured response of a rotating dipole to and a plot of axial ratio for the nearly square antenna.

4.0 CONCLUSION

A simple and efficient theory is established to analyze the behavior of microstrip antennas with remarkable accuracy even if the dominant mode is not strongly excited. Several important applications which require a theory of high accuracy are presented. The input antenna impedance can be varied over a wide range for matching purposes simply by changing the feed location. The confidence in the theory is particularly strengthened when it predicted correctly the extremely critical antenna dimensions for producing circular polarizations. The theory is also applied to multiport antenna configurations. For nearly all the cases considered, theoretical and experimental results are found in remarkably good agreement.

5.0 ACKNOWLEDGEMENT

This work is supported by Rome Air Development Center, Deputy for Electronic Technology.

6.0 REFERENCES

1. Y. T. Lo, D. Solomon, W. F. Richards, "Theory and Experiment on Microstrip Antennas," *IEEE Trans. Antennas Propagat.*, vol. 27, pp. 137-145, March 1979
2. W. F. Richards, Y. T. Lo, D. D. Harrison, "Improved Theory for Microstrip Antennas," *Electronics Letters*, Vol. 15, No. 2, pp. 42-44, 18 January 1978.
3. W. F. Richards, Y. T. Lo, "An Improved Theory For Microstrip Antennas and Applications," *IEEE AP-S International Symposium Digest*, pp. 113-116, June 1979.
4. W. F. Richards, Y. T. Lo, P. Simon, "Design and Theory of Circularly Polarized Microstrip Antennas," *IEEE AP-S International Symposium Digest*, pp. 109-112, June 1979.
5. K. R. Carver and E. L. Coffey, "Theoretical Investigation of the Microstrip Antenna," *Technical Report PT-00929*, Physical Science Laboratory, Las Cruces, New Mexico, 1979.
6. Hammerstad, "Equations for microstrip circuit design," *Proc. 5th European Microwave Conference*, pp. 268-272.
7. Y. T. Lo, D. Solomon, F. R. Ore, D. D. Harrison, G. A. Deschamps, "Study of Microstrip Antennas, Microstrip Phased Arrays, and Microstrip Feed Networks," *Final Report for Period 2 February 1976 - 9 September 1977, Contract No. AF19628-76-C-0140*, (Prepared for Rome Air Development Center), 21 October 1977.
8. S. A. Long and L. C. Shen, "The Circular Disc, Printed Circuit Antenna," *IEEE AP-S International Symposium Digest*, pp. 100-103, June 1977.
9. J. Meixner, "The Behavior of Electromagnetic Fields at Edges," *Inst. Math. Sci. Rept. EM-72*, New York University, N.Y., December, 1954.
10. J. L. Kerr, "Microstrip polarization techniques," *Proceedings of the 1978 Antenna Applications Symposium* (Sponsored by Electromagnetics Laboratory, University of Illinois, Urbana, IL 61801)
11. R. E. Munson, "Microstrip Antenna Structures and Arrays," U.S. Patent 3,921,177, November 1975.
12. H. D. Weinschel, "A cylindrical array of circularly polarized microstrip antennas," *IEEE AP-S International Symposium Digest*, pp. 175-180, June 1975.
13. C. C. Johnson, *Field and Wave Electrodynamics*, pp. 229-232, McGraw-Hill, 1965.

MICROSTRIP ANALYSIS TECHNIQUE

E. H. NEWMAN AND P. TULYATHAN
THE OHIO STATE UNIVERSITY
ELECTROSCIENCE LABORATORY
1320 KINNEAR ROAD
COLUMBUS, OHIO 43212

SUMMARY

A technique for analyzing microstrip antennas involving surface patch modeling and a transmission line model is presented. The surface patch model is used to determine an aperture admittance which is then used in the transmission line model.

1.0 DISCUSSION

1.1 INTRODUCTION

The method of moments using surface patch modeling [3] and transmission line models [2] are two potential techniques for analyzing microstrip antennas. It is felt that a major limitation of the transmission line model is the difficulty of accurately determining the radiating aperture admittance used as loads at either end of the transmission line. Its greatest advantages are ease, speed, and simplicity of computation.

Surface patch modeling can be used to accurately model the air dielectric microstrip antenna. Unfortunately, the computer code is time consuming to run if considerable design data is needed. Also, incorporating the dielectric slab in a computationally efficient manner is a challenging problem. Here, we present a method which combines the surface patch and transmission line models, to best employ their respective advantages, while avoiding their disadvantages.

Here the method is applied only to rectangular microstrips. Application to trapezoidal shaped patches would require non-uniform transmission lines and non-rectangular surface patch modeling, and is avoided for simplicity.

1.2 SURFACE PATCH MODEL

Fig. 1a shows a coax fed microstrip with air dielectric. In Fig. 1b image theory has been used to remove the ground plane. Fig. 1c shows a side-view of the antenna plus image indicating five modes used to describe the current in the surface patch moment method solution [3]. Mode 1 is a wire mode, modes 2 and 3 are surface patch modes, and modes 4 and 5 are attachment modes. Since from symmetry mode 2 equals mode 3 and mode 4 equals mode 5, this model involves only three unknowns. Using standard moment method procedures, the current on the antenna is determined, and the input impedance or patterns can then be found. Although no real effort has yet been made to reduce the computation time, typically a few minutes of computer time are required to find the currents and impedance at one frequency. This large amount of computer time for only five modes is a result of the extreme accuracy required in the evaluation of certain critical terms in the impedance matrix.

1.3 TRANSMISSION LINE MODEL

Fig. 2 shows a transmission line model of the microstrip antenna shown in Fig. 1a, except that now a dielectric slab of permittivity ϵ_r covers the ground plane, between it and the microstrip patch. The characteristic impedance, Z_0 , and propagation constant, β , of the transmission line can be easily evaluated [4,5]. Each end of the transmission line is terminated in the aperture admittance of the radiating wall (of width W) of the antenna. Approximate expressions for this admittance, $Y_A = G_A + jB_A$, are [1,2]

$$G_A = 0.00836W \sqrt{\epsilon_e} / \lambda_0 \quad (1)$$

where λ_0 is the free space wavelength, and

$$B_A = 0.01668 \frac{\Delta L}{T} \frac{W}{\lambda_0} \epsilon_e \quad (2)$$

where

$$\Delta L = 0.412 \frac{(\epsilon_e + .300)}{(\epsilon_e - .258)} \frac{\left(\frac{W}{T} + .262\right)}{\left(\frac{W}{T} + .813\right)} \quad (3)$$

$$\epsilon_e = \frac{\epsilon_r + 1}{2} + \frac{\epsilon_r - 1}{2} \left[1 + \left(\frac{10T}{W} \right) \right]^{-1/2}. \quad (4)$$

Thus, the input impedance is the parallel combination of Y_A transformed a distance L_1 and Y_A transformed a distance L_2 ,

$$Y_i = \frac{1}{Z_i} = Y_0 \frac{Z_0 C_1 + j Z_A S_1}{Z_A C_1 + j Z_0 S_1} + Y_0 \frac{Z_0 C_2 + j Z_A S_2}{Z_A C_2 + j Z_0 S_2} \quad (5)$$

where $Z_0 = 1/Y_0$, $Z_A = 1/Y_A$, and $C_1 = \cos \beta L_1$, $S_1 = \sin \beta L_1$, $C_2 = \cos \beta L_2$, and $S_2 = \sin \beta L_2$.

The effects of the probe are included by placing a lumped inductive reactance [1]

$$X_L = \frac{376}{\sqrt{\epsilon_r}} \tan \frac{2\pi \sqrt{\epsilon_r} T}{\lambda_0} \quad (6)$$

in series with Z_i . Thus, the input impedance seen at the coax aperture in Fig. 1a is

$$Z_{in} = Z_i + j X_L \quad (7)$$

1.4 COMBINED SURFACE PATCH AND TRANSMISSION LINE MODEL

The combined surface patch and transmission line model is identical to the transmission line model of Section 1.3, except that the surface patch model is used in conjunction with Eqs. (1) and (2) to find the aperture admittance. The procedure is outlined below.

Although the microstrip antenna of interest probably involves a dielectric slab with $\epsilon_r > 1$, the first step is to determine the input impedance of the air-dielectric microstrip antenna at frequency f^0 using surface patch modeling. Next, Eq. (5) is used to solve for the air dielectric aperture admittance. This yields

$$Z_A = \frac{1}{Y_A} = \frac{B \pm \sqrt{B^2 - 4AC}}{2A} \quad (8)$$

where

$$A = Y_i C_1 C_2 - j Y_0 (S_1 C_2 + C_1 S_2) \quad (9)$$

$$B = -2(C_1 C_2 - S_1 S_2) + j Y_i Z_0 (S_1 C_2 + C_1 S_2) \quad (10)$$

$$C = -Y_i Z_0^2 S_1 S_2 - j Z_0 (C_1 S_2 + S_1 C_2) \quad (11)$$

In Eq. (8) the root with capacitive reactance is chosen. The frequency f^0 is chosen near the resonance of the air dielectric microstrip antenna.

The next step will be to determine the aperture admittance of the dielectric slab microstrip at a frequency near its resonance, f^d , from the aperture admittance of the air dielectric antenna at frequency f^0 . This is done by using the functional form of Eqs. (1) and (2). Thus,

$$G_A^d = \frac{f^d}{f^0} \sqrt{\epsilon_e} G_A^0 \quad (12)$$

$$B_A^d = \frac{\Delta L^d}{\Delta L^0} \frac{f^d}{f^0} \epsilon_e B_A^0 \quad (13)$$

In Eqs. (12) and (13) the superscript 0 refers to a quantity computed for the air dielectric at frequency f^0 , while the superscript d refers to a quantity computed for the dielectric loaded case at frequency f^d . Note that although the quantities in Eq. (8) or Eqs. (12) and (13) have been referred to as an aperture admittance, it is probably more descriptive to refer to them as the value of aperture admittance which, when used in conjunction with the transmission line model, yields accurate input impedance.

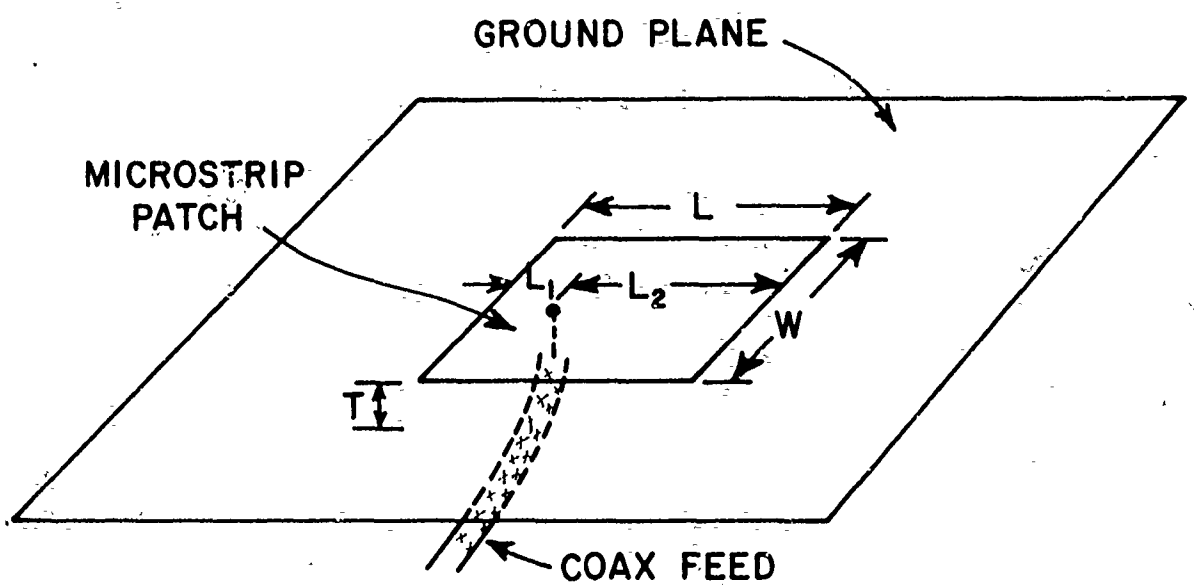
2.0 RESULTS

Fig. 3 shows the measured and computed input impedance of a microstrip antenna with $L = 15$ cm., $W = 7.5$ cm., $T = 0.32$ cm., $L_1 = 6$ cm., and $\epsilon_r = 2.56$. The computed data shows less than a 2% resonance shift, and an increase in impedance level. The resonance shift can be explained

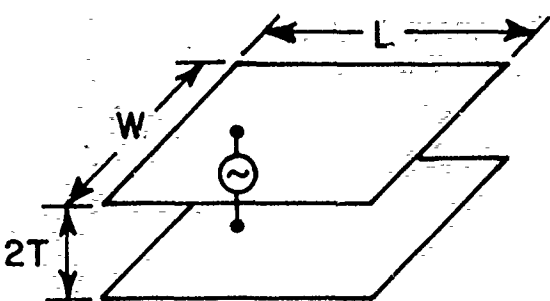
in terms of tolerances. For example, while the dielectric is nominal $\epsilon_r = 2.56$, if the actual $\epsilon_r = 2.48$ the resonant shift would be entirely eliminated. The increase in impedance level may be due to the relatively simple way the wire to plate attachment is handled. A more sophisticated attachment mode is currently being investigated.

3.0 REFERENCES

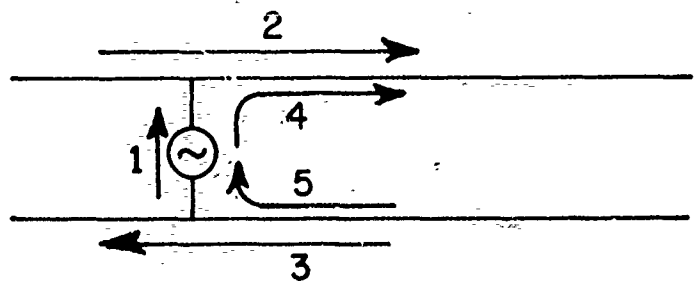
1. Carver, R. C. and Coffey, E. L., "Theoretical Investigations of the Microstrip Antenna," Tech. Report PT-00929, Physical Science Laboratory, New Mexico State Univ., Box 3-PSL, Las Cruces, New Mexico, 88003, Jan. 1979.
2. Derneryd, A. G., "Linearly Polarized Microstrip Antennas," IEEE Trans. on Ant. and Prop., Vol. AP-24, No. 6, Nov. 1976, pp. 846-851.
3. Newman, E. H. and Pozar, D. M., "Electromagnetic Modeling of Composite Wire and Surface Geometries," IEEE Trans. on Ants. and Prop., Vol. AP-26, No. 6, Nov. 1978, pp. 784-789.
4. Schneider, M. V., "Microstrip Lines for Microwave Integrated Circuits," Bell System Tech. Journal, May-June 1969, pp. 1421-1444.
5. Wheeler, H. A., "Transmission-Line Properties of a Strip on a Dielectric Sheet on a Plane," IEEE Trans. Microwave Theory and Tech., Vol. MTT-25, No. 8, Aug. 1977, pp. 631-647.



(a)



(b)



(c)

Fig. 1. The microstrip patch antenna (a) over a ground plane, (b) with ground plane removed and image inserted, (c) showing modal layout.

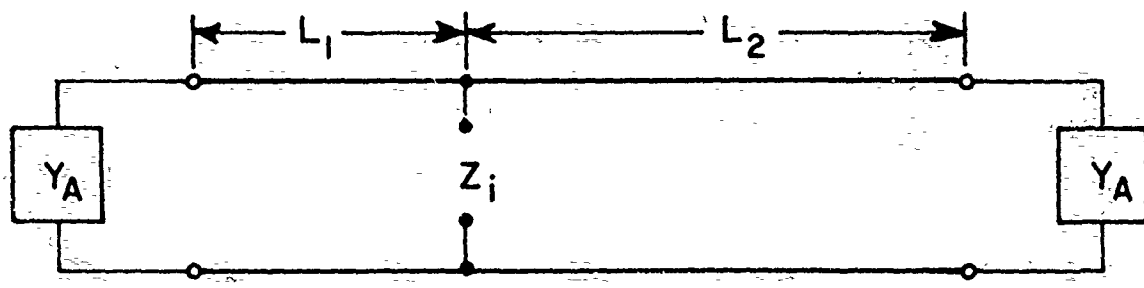
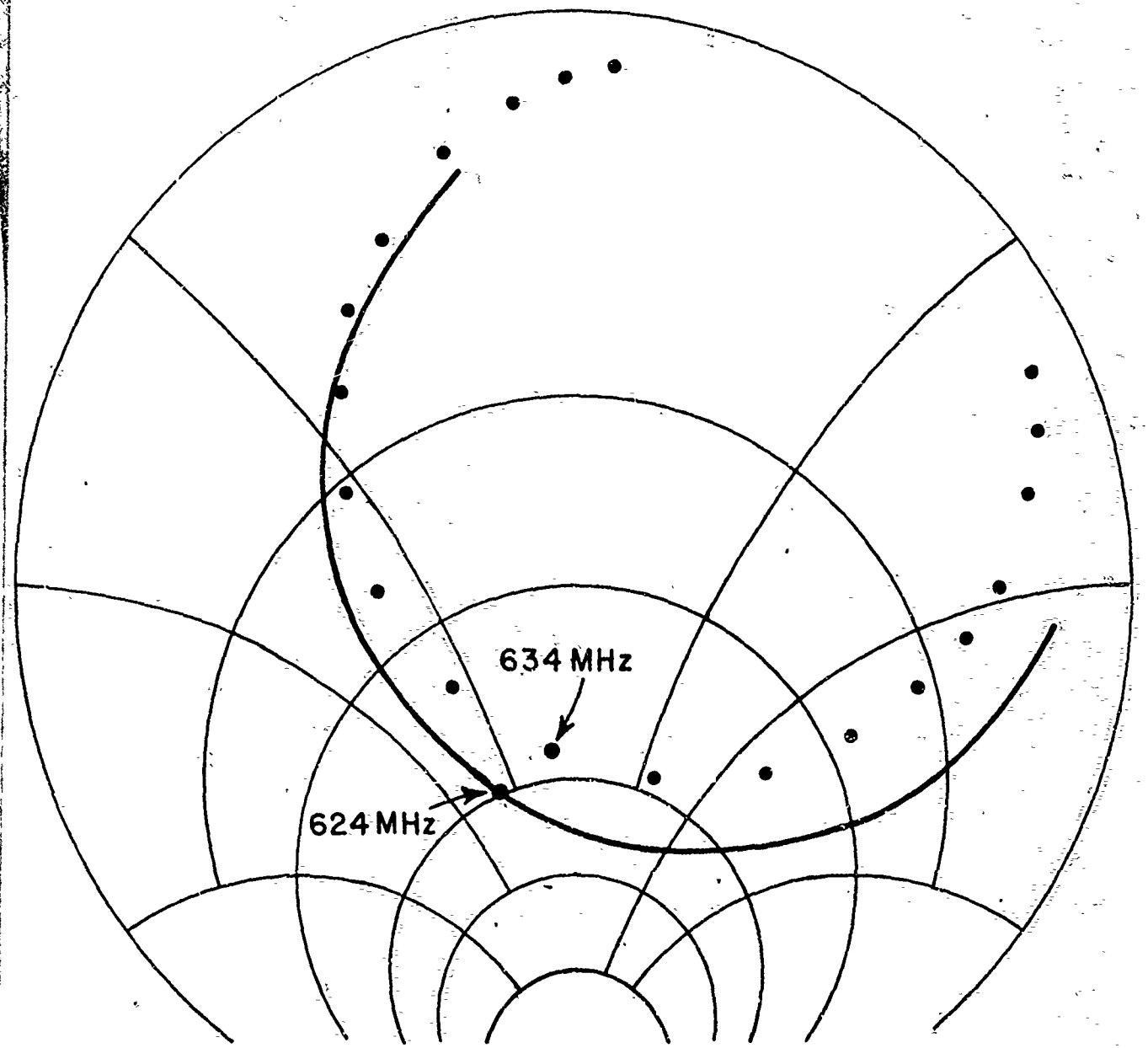


Fig. 2. Transmission line model of microstrip antenna.



————— CALCULATED
 • • • MEASURED HDL

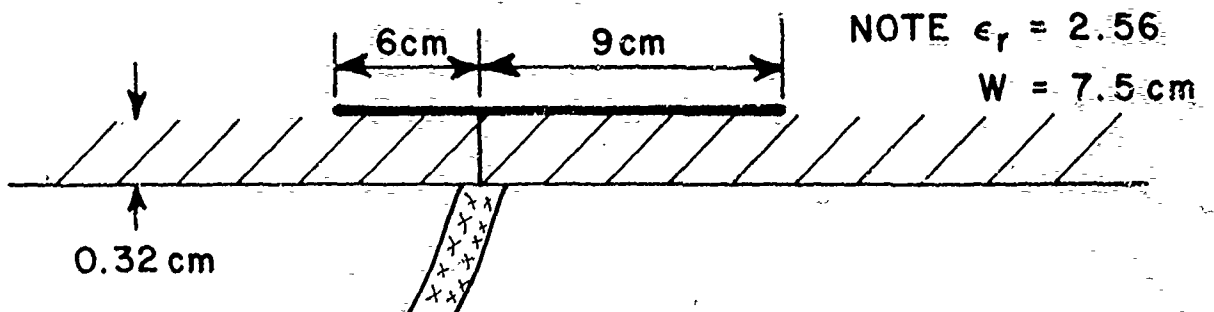


Fig. 3. A comparison of measured and computed input impedance for a microstrip antenna. Note: impedance is referenced to a point 0.01 free space meters below the ground plane.

A HIGH FREQUENCY ANALYSIS METHOD
FOR
OPEN MICROSTRIP STRUCTURES.

TATSUO ITOH
DEPT. OF ELECTRICAL ENGINEERING
THE UNIVERSITY OF TEXAS
AUSTIN, TEXAS 78712

AND

WOLFGANG MENZEL
HOCHFREQUENZTECHNIK
AEG-TELEFUNKEN
D-7900 ULM, W. GERMANY

SUMMARY

A method for analyzing characteristics of open microstrip disk structures is presented. The method is based on the spectral domain immittance matrix approach and all the wave phenomena associated with the structures are incorporated. The method provides a number of unique and convenient features both in analytical and numerical phases. A numerical example illustrating the usefulness of the method is included.

1.0 INTRODUCTION

A number of theoretical analyses of printed circuit antenna structures appeared recently (for example [1]). Most of these analyses are based on the quasi-static model of printed circuit structures. One typically computes the resonant

frequency of the hypothetical closed resonator devived from the actual structure by placing a magnetic side wall extending from the microstrip to the ground plane.

Magnetic current components computed from this resonator model are used to calculate the radiation patterns. The results so obtained indicate good agreement with experimental data, and hence the theory seems quite useful.

Independent of the efforts on antennas, microstrip and other printed circuit structures have been used in microwave and millimeter-wave integrated circuits. As the frequency of operation is increased, it has been realized and now it is widely known that the quasi-static analyses of microstrip circuit elements are not accurate enough and a more rigorous full-wave analysis is required. For instance, as for the analysis of microstrip disc resonators, a number of improved theoretical analyses appeared in the past [2, 3, 4]. It has been reported that the results by the full-wave analysis agree extremely well with results measured at high frequencies [4].

This paper presents a full wave analysis of the open printed circuit structures such as those encountered in microstrip antennas. Since all the wave phenomena are incorporated in the analysis, it is believed useful for microstrip type antenna applications at higher frequencies. The method is based on the spectral domain immittance matrix approach developed recently [5]. In the formulation process the directions parallel to the substrate surface are completely separated from the normal direction by the use of the equivalent network for spectral waves. As we will see shortly, the formulation process is so simple that it may be accomplished almost by inspection. The method is quite versatile and may be applied to almost

any type of printed structures including coplanar, slot and microstrip-slot resonators. Additionally, since we solve the problem for the Fourier Transforms of unknown current distributions on the strip or aperture electric fields on the substrate, the far field radiation patterns may be simply extracted.

2.0 FORMULATION OF THE PROBLEM

Although the method may be applied to other printed circuit structures, we will use a simple rectangular open microstrip disk in Fig. 1 for the formulation. In conventional analysis we would derive coupled homogeneous integral equations for current distributions $J_x(x, z)$, $J_z(x, z)$

$$\iint [\sum_{xx} (x-x', z-z') J_x(x', z') + \sum_{xz} (x-x', z-z') J_z(x', z')] dx' dz' = 0 \quad (1)$$

$$\iint [\sum_{zx} (x-x', z-z') J_x(x', z') + \sum_{zz} (x-x', z-z') J_z(x', z')] dx' dz' = 0 \quad (2)$$

where the integrations are over the strip and the equations are valid for (X, Z) on the strip. As is well known, (1) and (2) state that E_x and E_z are zero on the strip. These equations can be solved for the resonant frequency and J_x and J_z provided all the dyadic Green's function components Z_{xx} , $Z_{xz} = Z_{zx}$ and Z_{zz} are available which are functions of the frequency. In the radiating structure, this resonant

frequency becomes complex and its imaginary part accounts for the energy loss due to radiation.

In the spectral domain method, we use Fourier transforms of (1) and (2) and deal with algebraic equations instead of convolution integrals in (1) and (2):

$$\widehat{Z}_{xx}(\alpha, \beta) \widehat{J}_x(\alpha, \beta) + \widehat{Z}_{xz}(\alpha, \beta) \widehat{J}_z(\alpha, \beta) = \widehat{E}_x(\alpha, \beta, d) \quad (3)$$

$$\widehat{Z}_{zx}(\alpha, \beta) \widehat{J}_x(\alpha, \beta) + \widehat{Z}_{zz}(\alpha, \beta) \widehat{J}_z(\alpha, \beta) = \widehat{E}_z(\alpha, \beta, d) \quad (4)$$

where the Fourier transform is defined via

$$\widehat{\phi}(\alpha, \beta) = \int_{-\infty}^{\infty} \int_{-\infty}^{\infty} \phi(x, z) e^{j(\alpha x + \beta z)} dx dz \quad (5)$$

Notice also that the right hand sides of (3) and (4) are no longer zero because they are the Fourier transforms of E_x and E_z on the substrate surface which are obviously non-zero except on the strip. Although (3) and (4) contain four unknown, \widehat{J}_x , \widehat{J}_z , \widehat{E}_x and \widehat{E}_z , two of them, \widehat{E}_x and \widehat{E}_z may be eliminated later in the solution process, and we can derive a homogeneous set of equations which can be solved for the complex resonant frequency.

The recently proposed spectral domain immittance method is a simple visual approach to the derivation of \widehat{Z}_{xx} , \widehat{Z}_{xz}

and \tilde{Z}_{zz} . These quantities are actually impedance matrix elements that relate \tilde{J}_x and \tilde{J}_z with \tilde{E}_x and \tilde{E}_z . We will make use of equivalent transmission lines for the derivation. To this end, we first recognize that, from the definition of the inverse Fourier transform.

$$\phi(x, z) = \frac{1}{(2\pi)^2} \iint_{-\infty}^{\infty} \tilde{\phi}(\alpha, \beta) e^{-j(\alpha x + \beta z)} d\alpha d\beta \quad (6)$$

all the field components are superpositions over α and β of inhomogeneous (in y) waves propagating in the direction θ from the z axis where $\theta = \cos^{-1}(\beta/\gamma)$, $\gamma = \sqrt{\alpha^2 + \beta^2}$. For each ϕ , the waves may be decomposed into TM to y (\tilde{E}_y , \tilde{E}_v , \tilde{H}_u) and TE to y (\tilde{H}_y , \tilde{E}_u , \tilde{H}_v) where the coordinates v and u are as shown in Fig. 2 and related with (x, z) via

$$u = z \sin \phi - x \cos \phi \quad (7)$$

$$v = z \cos \phi + x \sin \phi \quad (8)$$

Next, we recognize that, if there were a current component \tilde{J}_v , it generates only the TM fields and only the TE fields are generated by \tilde{J}_u . Hence, it is possible to draw equivalent circuits for the TM and TE fields as shown in Fig. 3. The wave admittances in each region are

$$Y_{TMi} = \frac{\tilde{H}_u}{\tilde{E}_v} = \frac{j\omega \epsilon_0 \epsilon_i}{\gamma_i}, \quad i=1, 2 \quad (9)$$

$$Y_{TEi} = -\frac{\tilde{H}_u}{\tilde{E}_u} = \frac{\gamma_i}{j\omega \mu}, \quad i=1, 2 \quad (10)$$

where $\gamma_i = \sqrt{\alpha^2 + \beta^2 - \epsilon_i k^2}$ is the propagation constant in the y direction in the i -th region. γ_i is real for decaying wave and is imaginary for wave propagating in the y direction. All the boundary conditions which these TE and TM waves are required to satisfy are incorporated in the equivalent circuits. Specifically, the electric conductor boundary at $y=0$ is represented by the short circuit conditions in the equivalent circuits whereas the radiation condition at $y \rightarrow \infty$ corresponds to infinitely long transmission lines for $y > d$. The continuity condition of tangential electric fields at $y=d$ can be seen from the fact that the voltages on both sides of the junction $y=d$ are equal while the discontinuity of the magnetic field on both sides of the strip is represented by the equivalent current sources \tilde{J}_v and \tilde{J}_u for the spectral wave. In these equivalent circuits, the voltages, \tilde{E}_v and \tilde{E}_u at $y=d$ are related to the current sources via

$$\tilde{E}_v(\alpha, \beta, d) = \tilde{Z}_d^e(\alpha, \beta) \tilde{J}_v(d, \beta) \quad (11)$$

$$\tilde{E}_u(\alpha, \beta, d) = \tilde{Z}_d^h(\alpha, \beta) \tilde{J}_u(d, \beta) \quad (12)$$

It is easy to see that \tilde{Z}_d^e and \tilde{Z}_d^h are input impedances looking into the equivalent circuits at $y=d$ and, hence, are expressed as

$$\tilde{Z}_d^e = \frac{1}{Y_1^e + Y_2^e} \quad (13)$$

$$\tilde{Z}_d^h = \frac{1}{Y_1^h + Y_2^h} \quad (14)$$

where Y_1^e and Y_2^e are input admittances looking down and up at $y = d$ in the TM equivalent circuit, and Y_1^h and Y_2^h are corresponding quantities in the TE circuit:

$$Y_1^e = Y_{TM1} \coth \gamma_1 d, \quad Y_2^e = Y_{TM2} \quad (15)$$

$$Y_1^h = Y_{TE1} \coth \gamma_1 d, \quad Y_2^h = Y_{TE2} \quad (16)$$

The final step of the formulation consists of the mapping from the u, v coordinate to the x, z coordinate for spectral waves corresponding to each ϕ . Because of the coordinate transform relations (7) and (8), \hat{E}_x and \hat{E}_z are linearly related to \hat{E}_u and \hat{E}_v . Similarly, \hat{J}_x and \hat{J}_z are superposition of \hat{J}_u and \hat{J}_v . When these relations are used, the impedance matrix elements in (3) and (4) are given by

$$\tilde{Z}_{xx}(\alpha, \beta) = N_x^2 \tilde{Z}_d^e + N_z^2 \tilde{Z}_d^h \quad (17)$$

$$\tilde{Z}_{xz}(\alpha, \beta) = N_x N_z (-\tilde{Z}_d^e + \tilde{Z}_d^h) \quad (18)$$

$$\tilde{Z}_{zz}(\alpha, \beta) = N_z^2 \tilde{Z}_d^e + N_x^2 \tilde{Z}_d^h \quad (19)$$

where N_x and N_z are transforming ratios given by

$$N_x = \frac{\alpha}{\sqrt{\alpha^2 + \beta^2}} = \sin \phi, \quad N_z = \frac{\beta}{\sqrt{\alpha^2 + \beta^2}} = \cos \phi \quad (20)$$

Notice that \hat{Z}_x^e and \hat{Z}_z^h are functions of $\alpha^2 + \beta^2$ and the ratio of α to β enters only through N_x and N_z .

3.0 DERIVATION OF THE EIGENVALUE EQUATION

We now have two ways to solve the original open microstrip problem. The first one is use of the integral equations (1) and (2). In such instances, it is necessary to take inverse Fourier transforms of the spectral impedance matrix elements given in (17), (18) and (19). Another approach is the direct use of algebraic equations (3) and (4) as all the necessary quantities have been derived in the previous chapter. As discussed earlier, (3) and (4) contain four unknowns. Two of them, \hat{E}_x and \hat{E}_z , however, are eliminated in the solution process based on the Galerkin's method.

To this end, the unknown spectral current components \hat{J}_x and \hat{J}_z are expanded in terms of linear combinations of known basis functions

$$\hat{J}_x(\alpha, \beta) = \sum_{m=1}^M c_m \hat{J}_{xm}(\alpha, \beta) \quad (21)$$

$$\hat{J}_z(\alpha, \beta) = \sum_{n=1}^N d_n \hat{J}_{zn}(\alpha, \beta) \quad (22)$$

In selecting basis functions, we ensure that they are Fourier transforms of functions with finite support. That is, \hat{J}_{xm} and \hat{J}_{zn} are Fourier transforms of $J_{xm}(x, z)$ and $J_{zn}(x, z)$ which are nonzero only on the strip. Let us now

substitute (21) and (22) into (3) and (4) and take the inner products of the resulting equations with each of basis function as the standard Galerkin's procedure calls for. The result is the following homogeneous matrix equation

$$\sum_{m=1}^M K_{pm}^{xx} c_m + \sum_{n=1}^N K_{pn}^{xz} d_n = 0, \quad p=1, 2, \dots, M$$

$$\sum_{m=1}^M K_{qm}^{zx} c_m + \sum_{n=1}^N K_{qn}^{zz} d_n = 0, \quad q=1, 2, \dots, N \quad (23)$$

where the typical matrix element is given by

$$K_{pn}^{xz} = \int_{-\infty}^{\infty} \int_{-\infty}^{\infty} \hat{J}_{xp}(\alpha, \beta) \hat{J}_{xz}(\alpha, \beta) \hat{J}_{zn}(\alpha, \beta) d\alpha d\beta \quad (24)$$

Since K_{pn}^{xz} etc. are functions of a frequency, a non-trivial solution of (23) is by seeking a complex frequency that makes the determinant of the coefficient matrix of (23) zero. The corresponding eigenvector (c_m, d_n) specifies the current distributions on the stri,

Notice that the right hand side of (23) is zero. This is explained by writing a more specific process in the Galerkin's procedure. When a basis function is multiplied with (3) or (4), we typically have

$$\iint_{-\infty}^{\infty} \hat{J}_{xp}(\alpha, \beta) \hat{E}_x(\alpha, \beta, d) d\alpha d\beta = (2\pi)^2 \iint_{-\infty}^{\infty} \hat{J}_{xp}(x, z) E_x(x, z, d) dx dz \quad (25)$$

by virtue of the Parseval's relation. The right hand side

vanishes because J_x and E_x are nonzero only over regions of (x, z) complementary to each other, that is, J_x is zero outside the strip and E_x is zero on the strip.

Equation (23) is exact if $M = N \rightarrow \infty$. However, in practice, M and N must be finite, and such truncation introduces an approximation. If individual basis functions \tilde{J}_{xm} and \tilde{J}_{zm} are chosen such that their inverse Fourier transforms include qualitative natures of the true unknown current distributions, it is possible to use only a few basis functions to obtain good results, and the computation time can be reduced. Another important feature for time saving is to choose the basis functions which are expressed in closed forms. Therefore, one may use $J_{xm}(x, z)$ and $J_{zm}(x, z)$ which reasonably represent qualitative natures of the true current components and still whose Fourier transforms are analytically obtainable. One possible choice for J_{xm} and J_{zm} is

$$J_{xm}(x, z) = \frac{\cos[(r-1)\pi \frac{2x}{w}]}{\sqrt{(\frac{w}{2})^2 - x^2}} \frac{\cos[(2s-1)\pi \frac{z}{\ell}]}{\sqrt{(\frac{\ell}{2})^2 - z^2}} \quad (26)$$

$$J_{zm}(x, z) = \frac{\sin[2r\pi \frac{x}{w}]}{\sqrt{(\frac{w}{2})^2 - x^2}} \frac{\sin[(2s-1)\pi \frac{z}{\ell}]}{\sqrt{(\frac{\ell}{2})^2 - z^2}} \quad (27)$$

where m is given by a combination of r and s . For instance, $m = 1$ if $r = s = 1$ and so on. The Fourier transforms of (26) and (27) are readily available as combinations of the Bessel function of order zero. Notice also that the correct singularities of the current distribution at the edges are incorporated in (26) and (27). The current becomes singular

of order $1/\sqrt{R}$ at the edges parallel to the current and zero of \sqrt{R} at the edges normal to it, where R is the distance from the edge.

4.0 FEATURES OF THE METHOD

The present method incorporates a number of unique features. Let us describe numerical aspects first, and then go to more important analytical aspects. It has been proven in a number of papers on microstrip and other printed line structures that the spectral domain method is numerically quite efficient [4, 5]. For instance, accurate solutions are obtained by using a relatively small size matrix (23) such as $M = N = 1$ or 2. In contrast, many space domain analyses which typically deal with the coupled integral equations (1) and (2), the size of the matrix to be inverted is quite large, if for instance the point matching is used. On the other hand, if Galerkin type procedures are used in the space domain, it is necessary first to perform the inverse Fourier transforms, which are extremely time consuming, to get the Green's functions and then to carry out the convolution integrals.

The time saving feature of the spectral domain method are caused essentially by two elements. First, it is possible to use basis functions which incorporate certain qualitative natures of the true current distributions such as the edge condition. This eliminates use of a large number of basis functions to accurately represent unknown current distributions. Second, in the spectral domain approach, we deal with algebraic rather than integral equations. It is not necessary to carry out the convolution integrals and the spectral domain impedance functions are given in closed forms. Of course, the price we have to pay for such features is that the inner products to compute matrix elements K_{pm}^{xx} etc. are infinite integrals. However, the integrands of these integrals

decay as fast as α^{-2} and β^{-2} when the basis functions like those obtained from (26) and (27) are used, and hence the inner products can be computed without much difficulty.

Let us now turn our attention to more analytical features of the method. We go back to (17), (18) and (19) and study their construction. We recognize that \widehat{Z}_d^e and \widehat{Z}_d^h are obtained from the equivalent circuits which extend in the y direction. The information in the x and z direction come in \widehat{Z}_{xx} , \widehat{Z}_{xz} and \widehat{Z}_{zz} only through the transforming ratios N_x and N_z . Also the information on the microstrip is contained only in the basis functions. This is not special at all because \widehat{Z}_{xx} etc. are the Fourier transform of the Green's functions which are independent of the source shapes and related only to the location and the direction of the source.

Wave phenomena associated with an externally excited open microstrip structure (antenna problem) may be studied easily from the equivalent circuits in Fig. 3. When the transverse resonances occur, the denominator of \widehat{Z}_d^e or \widehat{Z}_d^h becomes zero as a surface wave pole is encountered. The radiation phenomena are associated with the imaginary part of γ_2 . Therefore, the visible region ($\alpha^2 + \beta^2 < k^2$) of the $\alpha\beta$ plane is responsible for radiation, and the surface wave poles occur on circles with radius $\sqrt{\alpha^2 + \beta^2}$ between $\sqrt{\epsilon_1}k$ and $\sqrt{\epsilon_2}k$. The invisible region $\alpha^2 + \beta^2 > k^2$ is responsible for the stored energy in the near region. The equivalent circuits do not however tell any directional information in the XZ plane. Such is provided by the "weighting" functions \widehat{J}_x and \widehat{J}_z .

What is presented in the previous paragraph is rather well known. In the present eigenvalue problem, it is necessary to consider complex k 's because only the complex

frequency can satisfy the system which loses energy by radiation. In the computation, we keep α and β to be real. Therefore surface wave poles are not crossed. However since they are located near the integration surface, their effects are contained in the formulation.

Once the problem is solved the far field radiation patterns are given from \hat{E}_x and \hat{E}_z as they are Fourier transforms of the electric field:

$$E_\theta(\phi, \theta) \propto \sin \phi \cdot \hat{E}_z(\alpha, \beta)$$

$$E_\phi(\phi, \theta) \propto \cos \phi \cos \theta \hat{E}_z(\alpha, \beta) + \sin \theta \hat{E}_x(\alpha, \beta) \quad (28)$$

with

$$\alpha = k \sin \theta \cos \phi$$

(29)

$$\beta = k \cos \theta$$

and \hat{E}_x , \hat{E}_z given by (3), (4) and (21), (22).

In the E-plane ($\phi = \pi/2$)

$$E_\theta \propto \sum_n d_n \hat{Z}_{zz}(0, k \cos \theta) \hat{J}_{zn}(0, k \cos \theta) \quad (30)$$

and in the H-plane ($\theta = \pi/2$)

$$E_\theta \propto \sin \phi \sum_n d_n \hat{Z}_{zz}(k \cos \phi, 0) \hat{J}_{zn}(k \cos \phi, 0) \quad (31)$$

It is clear that the cross polarization is caused by the \hat{J}_x component of the strip current.

5.0 NUMERICAL RESULTS

A FORTRAN-program has been made to perform the calculations described above. The integration over the α - β -plane has to

be done numerically. As $\widehat{J}_z \propto 1/\sqrt{\alpha\beta^3}$ and $\widehat{Z}_{zz} \propto \beta^2/\sqrt{\alpha^2+\beta^2}$ for large arguments α and β (and similar relations are valid for \widehat{J}_x , \widehat{Z}_{xx} and \widehat{Z}_{xz}) the integration converges with $1/(\alpha\beta\sqrt{\alpha^2+\beta^2})$. As a first example, a rectangular microstrip patch resonator of width $W = 15$ mm and length $l = 10$ mm was calculated (substrate height $d = 0,158$ mm, $\epsilon_r = 2.32$) taking into account one basis function for \widehat{J}_z .

Fig. 4 shows the E- and H-plane radiation pattern (resonant frequency 8,19 GHz) of this microstrip resonator. The H-plane radiation pattern is comparable to those of earlier calculations based on a quasi-static approach. The E-plane radiation pattern, however, shows a somewhat different behaviour. Especially close to the substrate plane, the field decreases considerably. This fact agrees well with experimental results, e.g. in [1], where a discrepancy between the quasi-static theory and experiment at small angles (and near 180°) has been stated. It is, therefore, believed that the present method provides much more realistic data.

6.0 CONCLUSIONS

We have presented a full-wave method for analyzing open printed circuit structures. The formulation is based on the spectral domain imittance matrix derived from the spectral domain equivalent circuits. In the solution process, a Galerkin's method is used. The method contains several attractive features from both analytical and numerical points of view. Although a microstrip structure is treated in the paper, the method itself is quite general and is applicable to other types of printed structures such as the coplanar and slot lines. Also, it is quite straightforward to extend the method to structures involving stratified substrates, several radiating elements and even those containing conductor elements at different interfaces of stratified substrate [5].

7.0 ACKNOWLEDGMENT

This work was in part supported by a US Army Research Office Grant DAAG29-78-G-0145. The authors thank Dr. B. Rembold of AEG-TELEFUNKEN, for his giving the opportunity to complete the present work.

8.0 REFERNECES

1. James, J.R. and Wilson, G.J., "Microstrip antennas and arrays. Pt. 1-Fundamental action and limitations", IEE J. Microwaves, Optics and Acoustics, 1, 5, 157-164, September 1977.
2. Itoh, T. and Mittra, R., "Analysis of a microstrip disk resonator", Archiv für Elektronik und Übertragungs-technik, 27, 11, 456-458, November 1973.
3. Wolff, J. and Knoppik, N., "Rectangular and circular microstrip disk capacitors and resonators", IEEE Trans. Microwave Theory and Techniques, MTT-22, 10, 857-864, October 1974.
4. Itoh, T., "Analysis of microstrip resonators", IEEE Trans. Microwave Theory and Techniques, MTT-22, 11, 946-952, November 1974.
5. Itoh, T., "Spectral domain immittance approach for dispersion characteristics of shielded microstrips with tuning septums", 9th European Microwave Conference, Brighton, England, September 17-21, 1979.

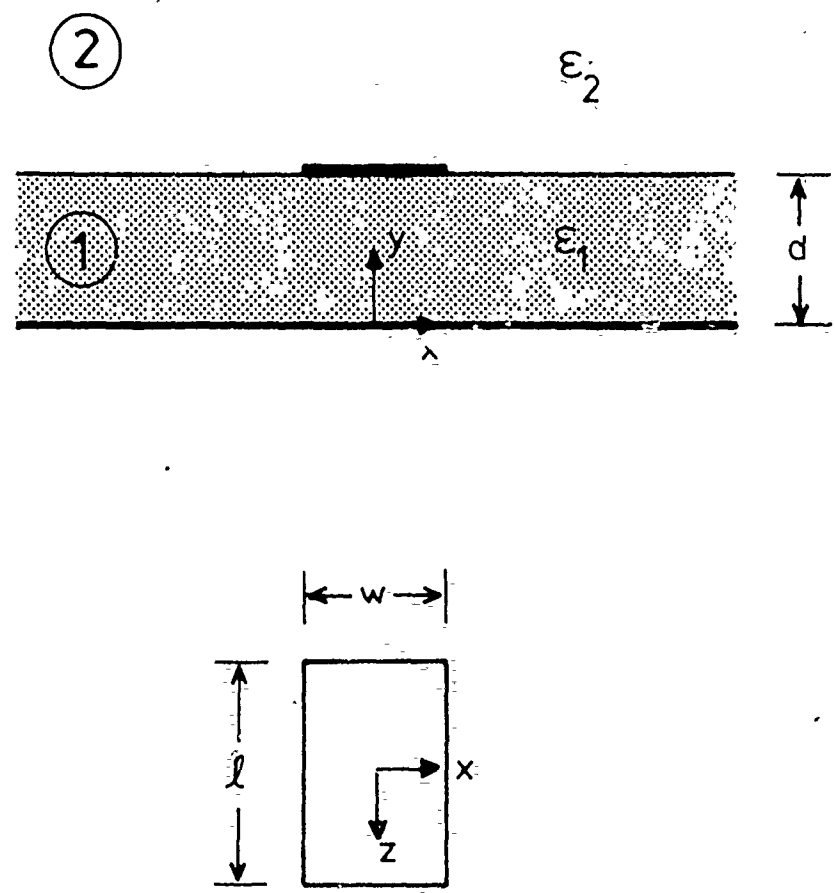


Fig. 1 Open microstrip resonant structure

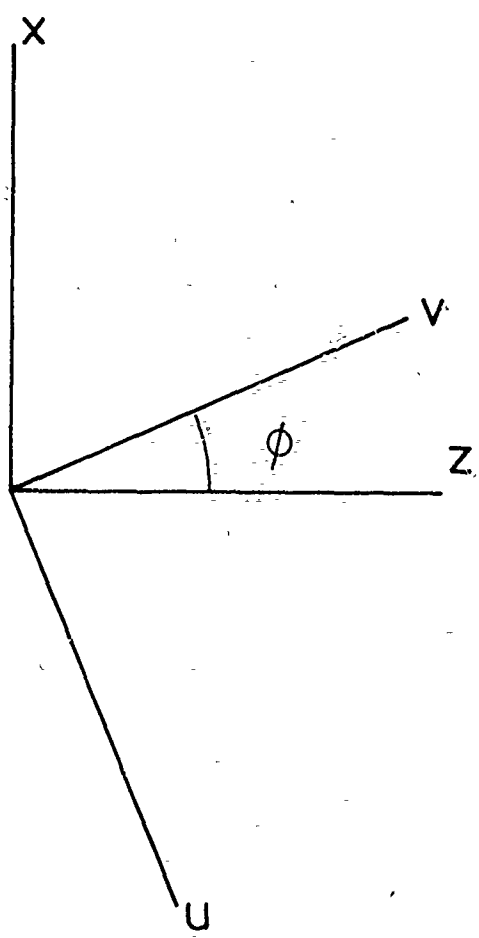


Fig. 2 Coordinate transformation

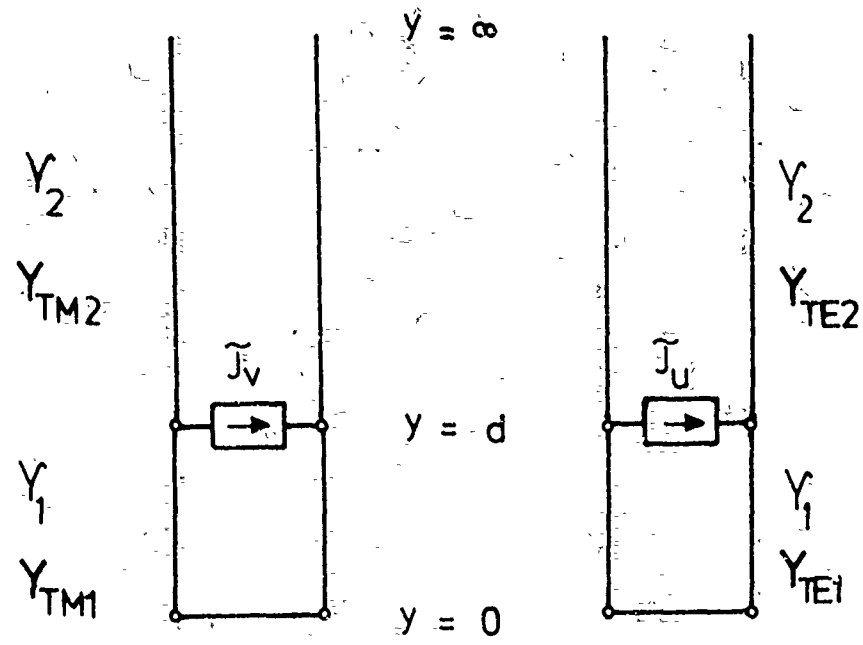
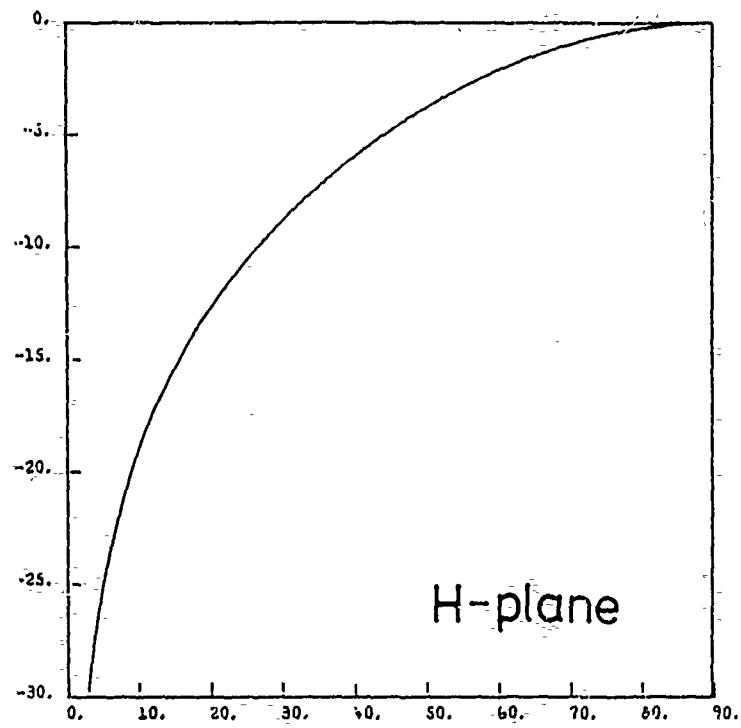
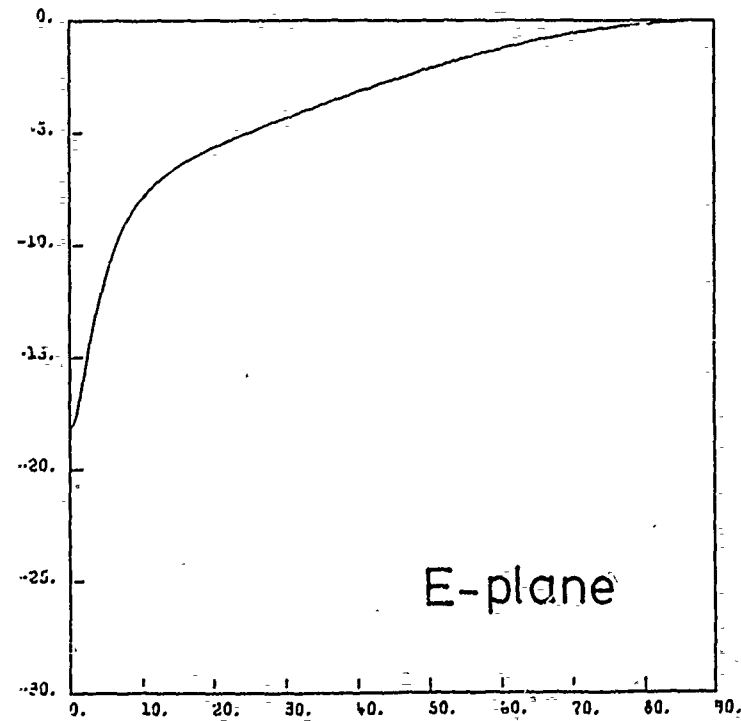


Fig. 3 Spectral domain equivalent circuits

RELATIVE AMPLITUDE (dB)



H-plane



E-plane

θ (degree)

Fig. 4 Radiation patterns of the microstrip resonator

THEORETICAL INVESTIGATIONS OF MICROSTRIP ANTENNAS

ANTOINE R. VAN DE CAPELLE
K.U.L., DEPT. OF ELECTRICAL ENGINEERING
DIVISION MICROWAVES AND LASERS
KARDINAAL MERCIERLAAN 94
B-3030 LEUVEN - HEVERLEE, BELGIUM

SUMMARY

This paper gives a review of some recent investigations concerning microstrip resonator antennas and microstrip slot antennas performed in our antenna research group.

1.0. MICROSTRIP RESONATOR ANTENNA

1.1. ANALYSIS MODEL

Starting from the equivalence principle, an aperture model has been developed, enabling to analyse the antenna characteristics for the fundamental as well as for the higher order modes.

The antenna configuration considered in this paper consists of an infinite dielectric substrate coated on one side with a perfect-conducting ground plane and on the other side with a perfect-conducting overlay S, Fig. 1. The contour of S determines the form of the resonator. The theory has been applied for a rectangle [1], as well , for a circular contour [5] .

The calculation of the radiation field is based on the equivalence principle : the field in the half space $z > 0$ is completely determined by the tangential component \bar{E}_t of the electric field in the plane $z = 0$.

The variation of \bar{E}_t in the plane $z = 0$ and along directions perpendicular to the edge of S has no important influence on the radiation field.

Therefore one can approximate the field $|\bar{E}_t|$ with a constant E_a over a certain distance from the edge of the resonator, and outside this area one can suppose $\bar{E}_t = 0$. The value of E_a should correspond with the z-

This research program has been sponsored by the Belgian National Science Foundation.

component of the electric field in the dielectric at the edge of the surface S. The variation of E_z along the edge of S is calculated by approximating the open resonator with a closed-resonator model.

Finally, we obtain the following "aperture model" for the antenna : "an infinite conducting plane at $z = 0$ with slots around the surface S excited by an electric field E_a ". This aperture model refers to the theory of aperture antennas which are solved with the spatial Fourier transform of the aperture field. The further calculations are straightforward.

1.2. DESIGN METHOD

In order to perform a design method, different models have been compared : a design model based on the microstrip resonator theory of Wolff and Knoppik [11], the transmission line model proposed by Munson [2] and a new combined design model.

This new model [10] supposes the resonator loaded with an impedance $Z(S)$, so that :

$$\bar{E}_t = \bar{H}_t \times \bar{n} \cdot Z(S) \quad (1)$$

For simplicity $Z(S)$ has been assumed constant over each of the 4 bounds of the rectangular resonator, and zero on the conducting surfaces.

After solving Maxwell's equations with the specified boundary conditions, one obtains the following equations, assuming the resonator symmetrically loaded :

$$\tan(k_x W_x + (N_x - \delta_x) \pi/2) = - k_x Z_x / (j\omega\mu) \quad (2)$$

$$\tan(k_y W_y + (N_y - \delta_y) \pi/2) = - k_y Z_y / (j\omega\mu) \quad (3)$$

$$k_x^2 + k_y^2 = \omega^2 \mu \epsilon \quad (4)$$

where :

W_x and W_y means the length of the resonator respectively in the x- and the y- direction.

The loading impedance Z has to be chosen equal to the radiation impedance of a rectangular slot adjacent to the upper surface of the resonator, because the field produced by those antennas can be explained by the radiation of a narrow slot surrounding the upper surface of the structure.

If we simplify those equations, neglecting the real part of the radiation impedance, it gives already sufficient agreement with experiments. The higher order modes are, as measured, in general lower than those found by Wolff and Knoppik.

1.3. BROADBAND MICROSTRIP RESONATOR ANTENNAS

A design procedure has been developed [3] to increase the bandwidth, combining two or more radiators with different resonance frequencies. The idea is the following, each resonator has its own resonance frequency. Depending upon the momentary frequency, the feed network will supply power (in the transmitting case) to the appropriate radiator. Therefore, the radiation pattern of the array is the same as the pattern of each of the radiating elements, because in principle only one resonator is radiating at any frequency of the bandwidth. In practice, the array-effect occurs anyhow, and (as an advantage) increases the gain of the antenna with respect to one radiator. Nevertheless, the optimized design procedure of the feed network makes it possible to diminish the array-effect to an admissible level and to point the direction of the main beam in broadside direction, independent of the momentary frequency.

The bandwidth of a configuration consisting of two radiators is about twice the bandwidth of a single resonator.

1.4. CIRCULARLY POLARISED MICROSTRIP RESONATOR ANTENNA

A study is going on to obtain a microstrip resonator antenna with circular polarisation [9]. It is the aim of this study to develop an antenna meeting the C.C.I.R. recommendations for private receiving of T.V. broadcast satellites. For the same purpose, a study has been made of printed circuit spiral antennas [6].

1.5. ANALYSIS MODEL FOR RECTANGULAR MICROSTRIP RESONATORS

A new analysis model [4] has been developed for open rectangular micro-

strip resonators. The length of the resonator has been assumed to be large in comparison with the width. The model is based on the analysis method of the discrete mode spectrum of open microstrip transmission lines introduced in the past [7].

The analysis of the resonator enables to calculate the complete field distribution for the fundamental as well as for the higher order modes. It is very well suited to be used with the aperture model mentioned in section 1.1. of this paper.

2.0. MICROSTRIP SLOT ANTENNA

The configuration considered in this section is shown in Fig. 2. It consists of a microstrip feedline terminated in a matched load and a radiating slot at the other side of the substrate. The scope of the present study is limited to narrow slots positioned symmetrically with respect to the microstripline.

Applying the Lorentz reciprocity theorem an equivalent circuit, Fig. 3 has been developed [8], containing one parameter R which is a function of the field in the slot, of the magnetic field along the microstrip feedline and of the radiation conductance of the slot.

The magnetic field along the microstripline has been calculated in function of the current distribution [7] on the stripconductor. Normalization of the field components has been carried out by application of Parsevals formula.

The radiation conductance G_r has been determined in function of the tangential electric field distribution in the radiating slot. In order to obtain a convenient approximation for the field distribution in the slot different functions has been considered. Antenna parameters has been calculated for any assumed slot distribution function. The antenna parameters has been measured very carefully and compared with the different calculated results. In this way an appropriate field distribution in the radiating slot has been selected.

Although the model described above is conceived for the use of a single slot, it can easily be applied to several slots fed by the same microstrip line.

3.0. ACKNOWLEDGEMENT

The author should like to thank all the persons who participated in this research program and who contributed to a large extent to the achieved results. There are too numerous to listen their names, but there are mentionned as co-author of the different papers given in the references.

4.0. REFERENCES

1. Hammer, P., Van Bouchaute, D., Verschraeven, D., Van de Capelle, A., A Model for Calculating the Radiation Field of Microstrip Antennas, I.E.E.E. Trans. on A.&P., Vol. AP-27, n° 2, March 1979, pp. 267-270.
2. Munson, R., Conformal Microstrip Antennas and Microstrip Phased Arrays, I.E.E.E. Trans. on A.P., Vol. A.P.-22, January 1974, pp. 74-78.
3. Pues, H., Vandensande, J., Van de Capelle, A., Broadband Microstrip Resonator Antennas, Proceedings of the I.E.E.E. Int. Symp. on A. & P., Washington, D.C., 1978, pp. 268-271.
4. Thijs, J., Luypaert, P., Van de Capelle, A., Analysis Model for Rectangular Microstrip Resonators, accepted for presentation at SPACECAD '79, to be held at Bologna, Italy, September 19-21, 1979.
5. Van de Capelle, A., Van den Mooter, B., Verbiest, H., Vandensande, J., Analysis and Design of Circular Microstrip Resonator Antennas, accepted for presentation at the 1979 Antenna Applications Symposium, Monticello, Illinois, September 1979.
6. Van de Capelle, A., De Bruyne, J., Verstraete, M., Pues, H., Vandensande, J., Microstrip Spiral Antennas, Proceedings of the I.E.E.E. Int. Symp. on A. & P., Seattle, 1979, pp. 383-386.
7. Van de Capelle, A., Luypaert, P., A Complete Analysis of the Discrete Mode Spectrum of Open Microstrip Transmission Lines,

Proceedings of the I.E.E.E. Int. Symp. on M.T.T., Ottawa,
1978, pp. 413-415.

8. Van de Capelle, A., Amandt, D., Hermans, J., Analysis Model for the Microstrip Slot Antenna, Proceedings of the 8th European Microwave Conference, Paris, September 1978, pp. 312-316.
9. Vandensande, J., Pues, H., Van Lil, E., Van de Capelle, A., A Circularly Polarised Microstrip Resonator Antenna, Proceedings of the National Radio Science Meeting, Seattle, June 1979, pp. 116.
10. Van Lil, E., Van Loock, R., Van de Capelle, A., Design Models for Rectangular Microstrip Resonator Antennas, Proc. of the I.E.E.E. Int. Symp. on Ant. & Prop., Washington, D.C., 1978, pp. 264-267.
11. Wolff, I., Knoppik, N., Rectangular and Circular Microstrip Disc Capacitors and Resonators, I.E.E.E. Trans. on M.T.T., Vol. M.T.T.-22, October 1974, pp. 857-864.

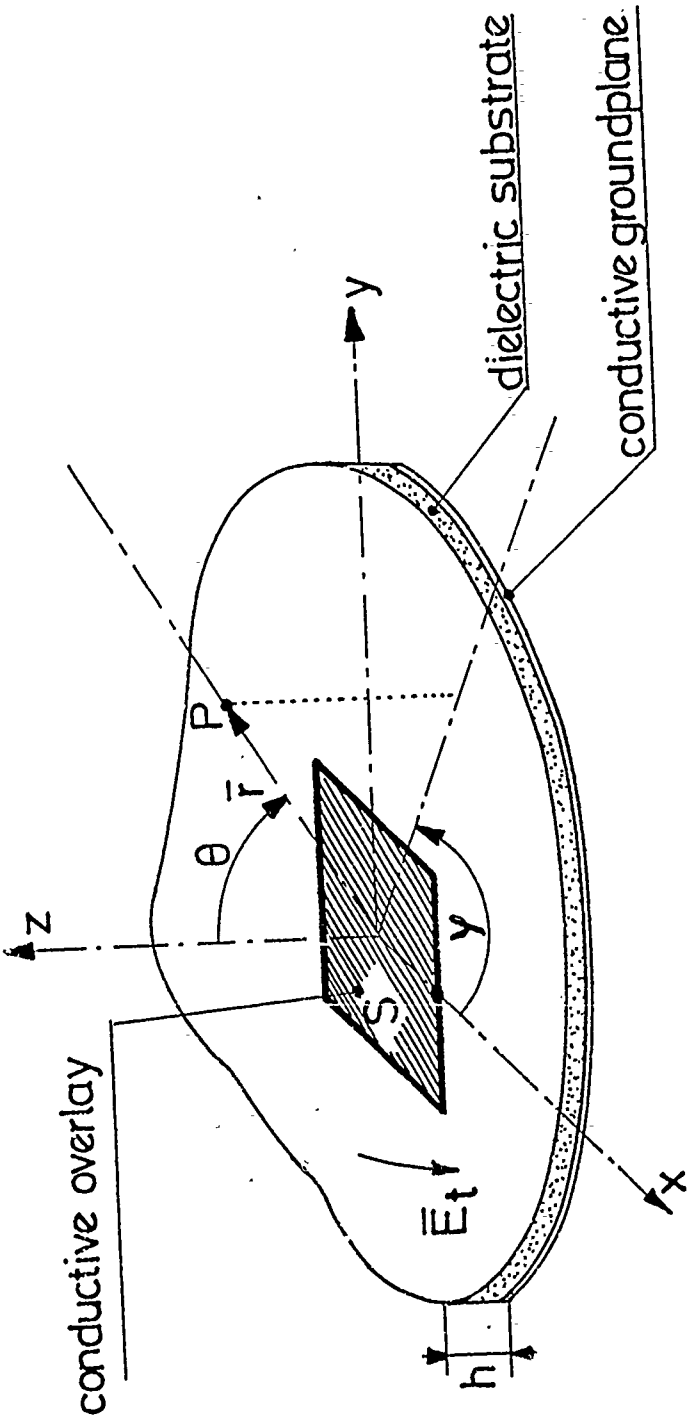


Fig. 1.- Microstrip resonator antenna configuration with rectangular overlay S.

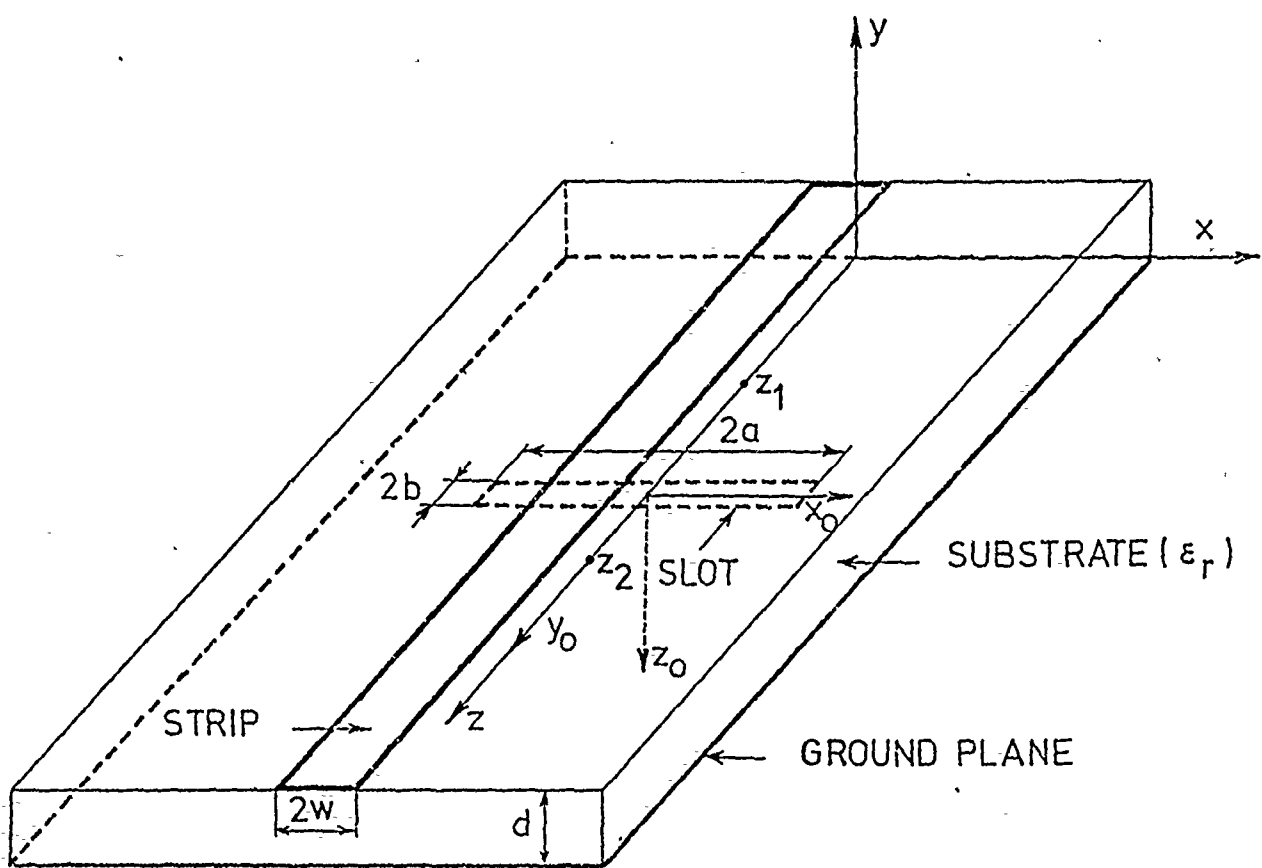
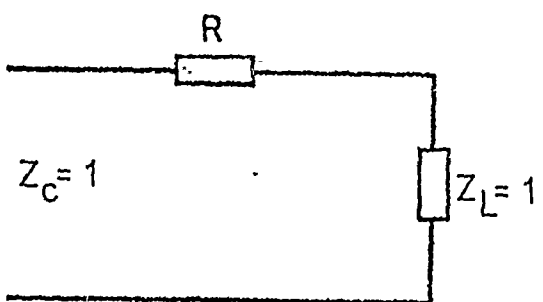


Fig. 2.- The microstrip slot antenna.



R = equivalent resistance; the power dissipation in R is equal to the power radiated by the slot

Z_C = normalized characteristic impedance of the microstrip line

Z_L = normalized load impedance

Fig. 3.- Equivalent transmission line circuit for the microstrip slot antenna.

CAVITY MODEL OF THE RECTANGULAR MICROSTRIP ANTENNA

ANDERS G. DERNERYD
TELEFON AB L M ERICSSON
MI-DIVISION
431 20 MOELNDAL
SWEDEN

ANDERS G. LIND
CHALMERS UNIV. OF TECHNOLOGY
DIVISION OF NETWORK THEORY
412 96 GOTHENBURG
SWEDEN

SUMMARY

The simple and very useful cavity model is used to analyze and predict the fundamental properties of the rectangular microstrip antenna element. Radiation from all four edges of the element as well as ohmic and dielectric losses within the cavity are considered. The resonant frequency is predicted within a few percent by introducing effective length and width to account for the influence of the fringing field.

The antenna input conductance at resonance consists of three parts, namely equivalent conductances arising from radiation, ohmic loss, and dielectric loss. Since the losses usually are some tenth's of a dB, they are calculated using a perturbation technique based on the lossfree fields within the cavity. An expression for the bandwidth is derived based on the quality factor of narrow-banded devices. With a proper choice of parameters, (e.g. thickness greater than one tenth of a wavelength) bandwidths of more than ten percent is achieved for a VSWR less than two with standard laminates.

1. INTRODUCTION

In recent years, the interest in microstrip antennas has increased dramatically. This type of antenna element has found use in a wide variety of planar and conformal arrays because of its low profile and light weight.

Microstrip antennas have been described by several authors. A transmission-line model was first developed for the basic rectangular micro-

strip element [11]. However, only fundamental and simple higher order modes can be analyzed with this line model since the element is treated as two independent radiating slots [3, 8]. More generally, microstrip elements can be modeled as resonant cavities but only elements of simple shapes can be treated [2, 6, 10]. Recently, model expansion methods have been presented that are adopted to simple multi-mode structures [1, 9]. A general theory for microstrip antennas of arbitrary shapes appears to be very involved.

In this paper the simple and useful cavity model is further developed to analyze the rectangular microstrip resonator antennas. Although all calculations are limited to the fundamental mode of operation, this model can easily be extended to higher-order resonance modes [4].

2. CAVITY MODEL

The antenna element considered in this paper consists of a rectangular conducting plate separated from an infinite groundplane by a thin layer of a dielectric sheet as shown in Figure 1.

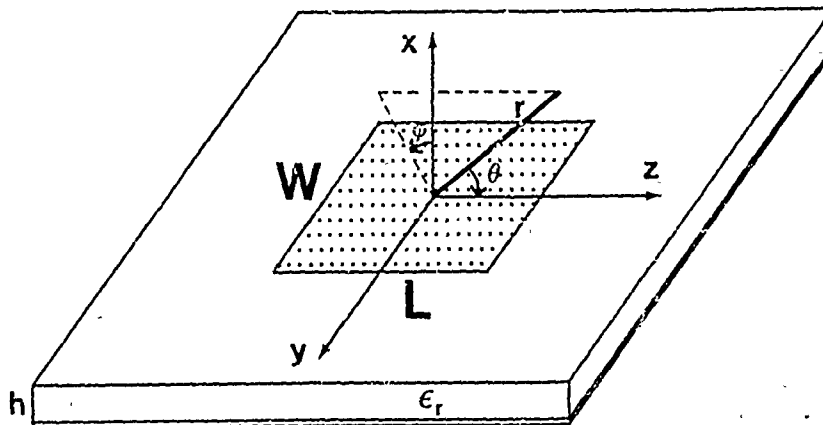


Figure 1 Rectangular microstrip antenna element

As the thickness of the dielectric is much less than one wavelength, it is assumed that the E-field has an x-component only and also that the variation of the field along the x-direction is negligible. On the basis

of these assumptions, the field between the patch and the groundplane is determined by modeling the microstrip resonator as a rectangular cavity with electric walls at top and bottom and magnetic walls along the sides. Once this field is known the induced magnetic current in the magnetic sidewalls are immediately found and the radiated field in the half-space above the patch is calculated using image theory, i.e. the magnetic currents are doubled while the conductors are removed.

3. FUNDAMENTAL RESONANT FREQUENCY

In the immediate vicinity of the resonator edges there are fringing fields making the cavity acting larger than the physical size. This effect is considered by introducing a normalized extension of a microstrip line [7].

$$\frac{\Delta L}{h} = 0.412 \frac{\epsilon_{eo} + 0.300 \frac{w}{h} + 0.262}{\epsilon_{eo} - 0.258 \cdot \frac{w}{h} + 0.813} \quad (1)$$

where ϵ_{eo} is the effective dielectric constant at zero frequency to account for non-ideal TEM-propagation. At higher frequencies, the effective dielectric constant of a microstrip line begins to change due to propagation of hybrid modes. Analytical expression for dispersion is given by [5].

$$\epsilon_e = \epsilon_r - \frac{\epsilon_r - \epsilon_{eo}}{1 + \frac{f^2}{f_p^2}} \quad (2)$$

where

$$f_p = \frac{Z_0}{8 \cdot \pi \cdot h}$$

Here frequency is in GHz and substrate thickness in cm.

The fundamental resonant frequency of a rectangular microstrip antenna is then

$$f_o = \frac{c}{2\sqrt{\epsilon_r}(L + 2z + \Delta L)} \quad (3)$$

where c is the speed of light in vacuum. This equation predicts the resonant frequency with less than 3.5 percent error as seen in Table 1.

TABLE 1
PREDICTED AND MEASURED RESONANT FREQUENCY

Predicted (GHz)	Measured (GHz)	Δf (%)
2.995	2.940	- 1.9
3.078	2.985	- 3.2
3.150	3.089	- 2.0
5.325	5.377	+ 1.0
5.435	5.250	- 3.5
5.650	5.471	- 3.3
8.950	8.767	- 2.1
8.930	8.716	- 2.4

4. RADIATION FIELD

In the fundamental mode of operation a standing wave is excited in the z -direction when a voltage V_o is applied at $z = - L/2$. However, most of the radiation takes place along the sides at $z = \pm L/2$ where the E-field is uniform. The far electric field of the fundamental mode is obtained with image theory.

$$\left\{ \begin{array}{l} E_\theta = -j \frac{e^{-jk_0 r}}{\pi r} V_o \frac{\sin(kh \sin\theta \cos\varphi) \sin(k_o \frac{W}{2} \sin\theta \sin\varphi)}{kh \sin^2\theta \sin\varphi} \cos(k_o \frac{L}{2} \cos\theta) \\ E_\varphi = j \frac{e^{-jk_0 r}}{r} V_o \frac{\sin(kh \sin\theta \cos\varphi) \sin(k_o \frac{W}{2} \sin\theta \sin\varphi)}{kh \sin^2\theta \cos\varphi} \\ \cdot \cos(k_o \frac{L}{2} \cos\theta) \cos\theta \frac{\epsilon_e - 1}{\epsilon_e - \cos^2\theta} \end{array} \right. \quad (4)$$

where $k = k_o \sqrt{\epsilon_r}$.

To account for fringing effects the equivalent length and width are employed. The length extension is given in (1) while the equivalent width, W_{eq} , is defined as the width of a parallel plate line having an impedance level, Z_o , equal to that of the microstrip line.

$$W_{eq} = \frac{120 \cdot \pi \cdot h}{Z_o \cdot \sqrt{\epsilon_{eo}}} \quad (5)$$

5. RESONANT CONDUCTANCE

The input conductance at resonance is equal to the sum of conductances due to power lost within the resonator and from radiation. In general the radiation conductance is the dominant part.

A radiation conductance is determined from the total radiated power while a conductance due to finite conductivity, σ , is given by integrating the loss-free field over the conductor surfaces at $x = 0$ and $x = h$. This equivalent conductance at the fundamental mode resonance is

$$G_c = \frac{\pi^2 \cdot W \cdot (\pi \cdot f_o \cdot \mu_o)^{-3/2}}{4 \cdot L \cdot h^2 \cdot \sqrt{\sigma}} \quad (6)$$

As can be seen the ohmic loss decreases for a thick and narrow microstrip resonator.

An equivalent conductance due to loss in the supporting dielectric is found in a similar way

$$G_d = \frac{\pi \cdot W \cdot \tan\delta}{4 \cdot \mu_0 \cdot h \cdot f_0} \quad (7)$$

The dielectric loss decreases also for a thick and narrow resonator.

6. BANDWIDTH

In the vicinity of the resonant frequency, say $f = f_0 + \Delta f$, the input admittance of a high-Q device may be expressed as

$$Y = G \left(1 + j \cdot 2 \cdot Q \cdot \frac{\Delta f}{f_0} \right) \quad (8)$$

The bandwidth of an antenna is usually defined using the voltage standing wave ratio. This ratio is closely related to the input admittance and the bandwidth of a narrow-banded device can, therefore, be expressed in terms of the Q-factor. Thus, the bandwidth for a voltage standing wave ratio less than two can be expressed as

$$BW = \frac{1}{\sqrt{2} \cdot Q} \quad (9)$$

7. EXPERIMENTAL VERIFICATION

A great number of microstrip antennas with various resonant frequency, thickness, and feed method have been fabricated using DiClad with a relative permittivity of 2.52 and a loss tangent of 0.001.

The measurements presented in this paper are made on quadratic antennas for different resonant frequencies ranging from one to ten GHz and with laminate thicknesses of $1/8"$, $1/16"$ and $1/32"$.

Typical radiation patterns including cross polarization levels of a quadratic microstrip antenna with both length and width equal to 16.2 mm are shown in Figures 2 and 3.

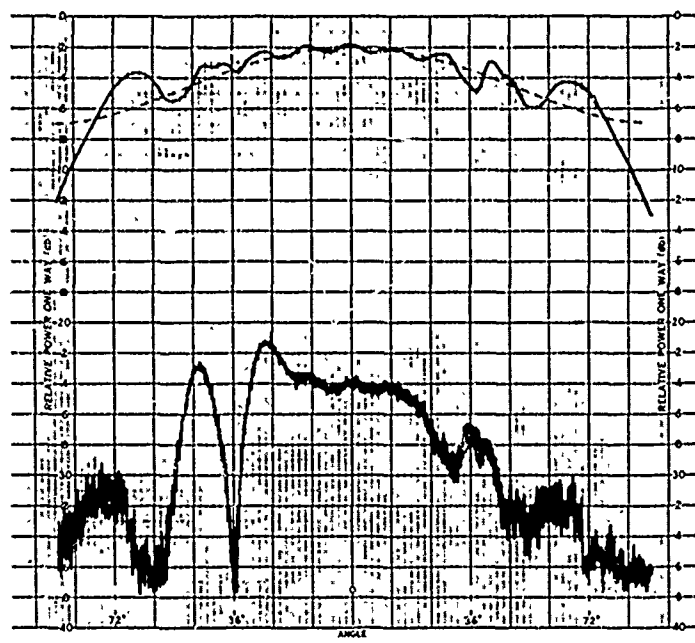


Figure 2 Radiation and crosspolarization pattern, E-plane
 —: Measured, --- : theoretical

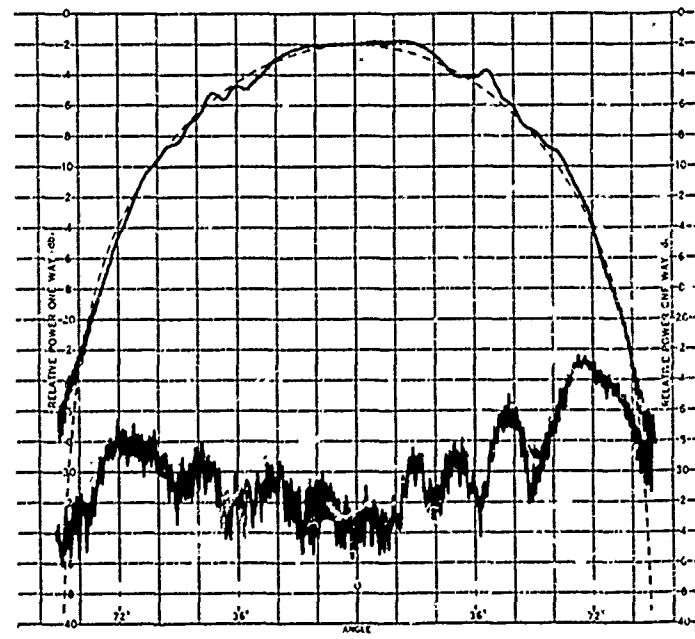


Figure 3 Radiation and crosspolarization pattern, H-plane
 —: Measured, --- : theoretical

The measured resonant frequency was 5.25 GHz on a 1/16" laminate. The oscillatory nature of the recorded pattern in the E-plane is due to the finite groundplane (in this case 8.5 wavelengths). The theoretical patterns are also shown in the figures and as can be seen the agreement is very good. The presented theory is not suitable for handling the crosspolarization content of the radiation pattern and theoretically no crosspolarization is expected in the main planes. No effort has been made to minimize the crosspolarization level on the experimental models, but it ought to be possible to reduce it below the measured -20 dB level (e.g. with two symmetrical feedpoints). The measured gain of this antenna was about 7 dBi.

In Figure 4 the total input conductance referred to the edge of the radiator is shown as a function of the thickness(h)-to-guidewavelength (λ_g) ratio, together with measured results.

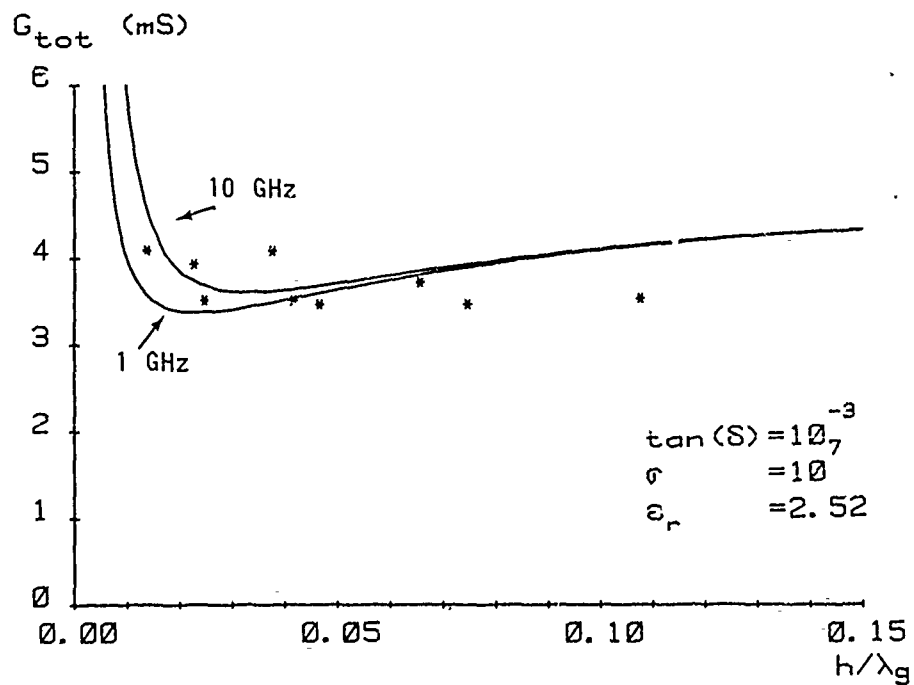


Figure 4 Total input conductance at resonance.

— : Theoretical, * : measured

Up to now published bandwidth of microstrip antennas has been in the order of a few percent, for VSWR less than two. However, in Figure 5 it is seen that bandwidths of at least 15 percent is achievable with

standard laminates. Also here the measurement have been made on quadratic antenna elements designed for a number of resonant frequencies between one and ten GHz. The bandwidth can be further increased by increasing the width-to-length ratio or by decreasing the dielectric constant.

Bandwidth (%)

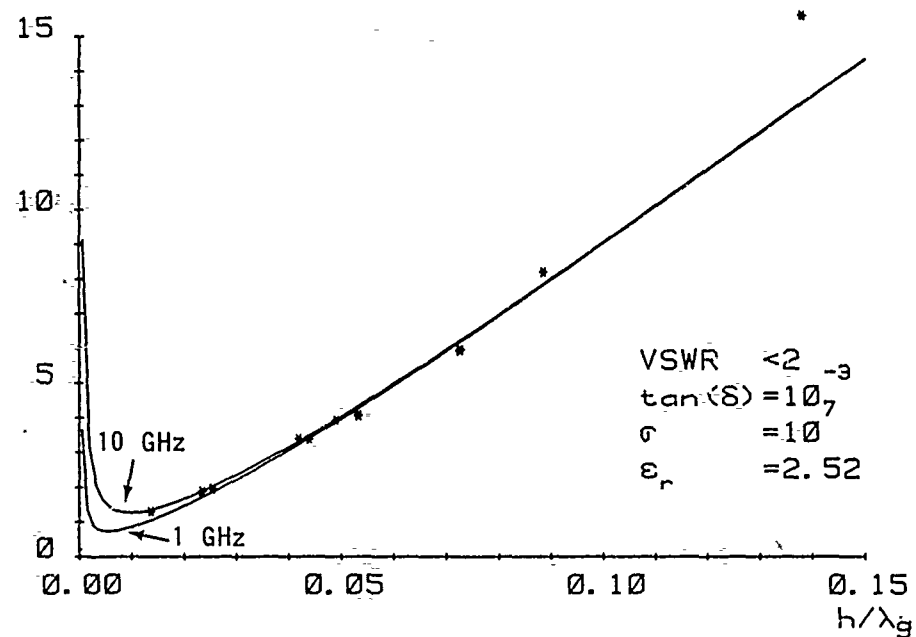


Figure 5 Bandwidth. — : Theoretical, * : measured

The losses which consist of conductor and dielectric losses are usually very small for microstrip antennas. They are plotted in Figure 6 and theoretically shown to be typically some tenth's of a dB for well designed antennas.

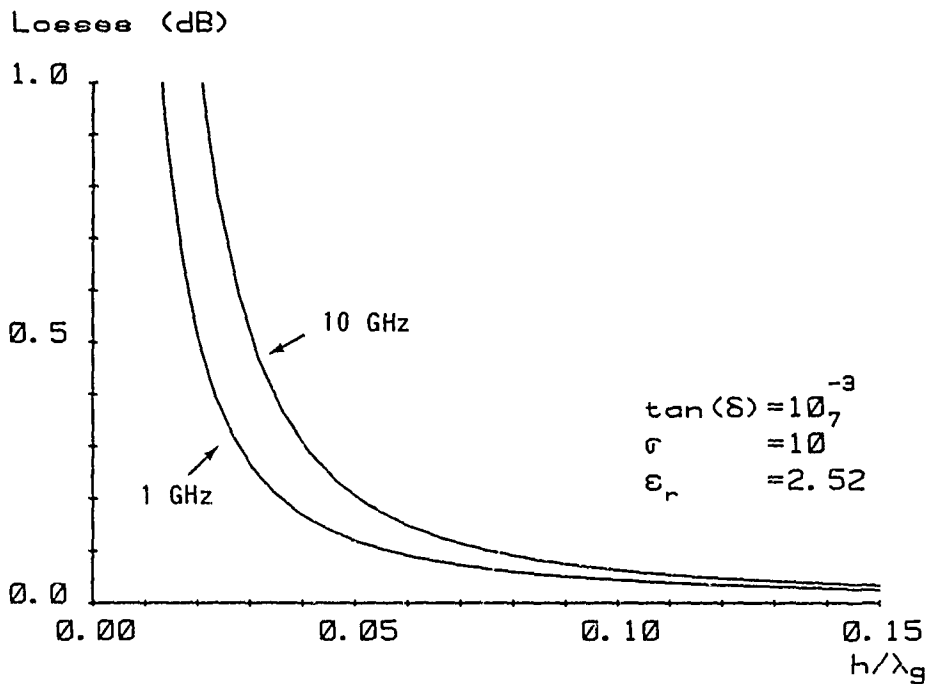


Figure 6 Losses at resonance

REFERENCES

- [1] Cauer, K. R., "A model expansion theory for the microstrip antenna", IEEE AP-S, Int. Symp. Digest, pp. 101-104, June 1979
- [2] Cuhaci, M. and James, D. S., "Radiation from triangular and circular resonator in microstrip", Proc. IEEE MTT-S Microwave Symp., pp. 438-441, June 1977
- [3] Derneryd, A. G., "A theoretical investigation of the rectangular microstrip antenna element", IEEE Trans. Antennas Propagat., vol. AP-26, pp. 532-535, July 1978
- [4] Derneryd, A. G. and Lind, A. G., "Extended analysis of rectangular microstrip resonator antennas", to be published in the IEEE Trans. Antennas Propagat., Nov. 1979
- [5] Getsinger, W. J., "Microstrip dispersion model", IEEE Trans. Microwave Theory Techniques, vol. MTT-21, pp. 34-39, Jan. 1973

- [6] Hammer, P. et. al., "A model for calculating the radiation field of microstrip antennas", IEEE Trans. Antennas Propagat., vol. AP-27, pp. 267-270, March 1979
- [7] Hammerstad, E. O., "Equations for microstrip circuit design", Proc 5th European Microwave Conference, pp. 268-272, Sept. 1975
- [8] James, J. R. and Wilson, G. J., "Microstrip antennas and arrays. Pt. 1-Fundamental action and limitations", IEE Journal Microwaves, Optics & Acoustics, vol. MOA-1, pp. 165-174, Sept. 1977
- [9] Lo, Y. T. et. al., "Theory and experiment on microstrip antennas", IEEE Trans. Antennas Propagat., vol. AP-27, pp. 137-145, March 1979
- [10] Long, S. A. et. al., "Theory of the circular-disc printed-circuit antenna", Proc. IEE, vol. 125, pp. 925-928, Oct. 1978
- [11] Munson, R. E., "Conformal microstrip antennas and microstrip phased arrays", IEEE Trans. Antennas Propagat., vol. AP-22, pp. 74-78, Jan. 1974

ANALYSIS OF A COAX-FED CIRCULAR MICROSTRIP ANTENNA

CHALMERS M. BUTLER
DEPARTMENT OF ELECTRICAL ENGINEERING
UNIVERSITY OF MISSISSIPPI
UNIVERSITY, MS 38677

SUMMARY

The purposes of this paper are to develop an accurate theoretical model of a microstrip antenna, to analyze the model, and to carefully identify the antenna's radiation mechanism, at least, insofar as the selected model is concerned. A circular microstrip antenna, fed at its center by a coaxial waveguide, is chosen for the present investigation, and it is viewed as a coax-driven radial waveguide terminated in an aperture. An integral equation is formulated and subsequently solved numerically for the aperture electric field. From knowledge of the aperture electric field, the load on the coax-to-radial-guide junction can be computed as can the field radiated by the structure. Data characterizing the behavior of the radial waveguide are presented.

1.0 INTRODUCTION

In Fig. 1 is illustrated the fundamental problem of interest in this paper. Here one sees a slotted radial guide fed by a coaxial line. For this structure to be applicable to the microstrip antenna problem, the guide height h is restricted to be much smaller than the wavelength, and the slot width ($b-a$) is made very very large - ideally, infinite. With $h/\lambda \ll 1$, the higher order modes at the coax-to-radial-guide junction and at the slot are of significance only in the very near vicinity of these two discontinuities. Outside these two localities, the radial guide can be looked upon as a radial transmission line on which only the TEM mode exists. Thus, one can view the problem of Fig. 1 as that of the coax-to-radial-guide junction and that of the slotted section of guide with the two joined by a section of TEM radial line. This point of view is suggested in Fig. 2. Such a partitioning allows one to solve individually the two major boundary value problems, the coax-to-radial-guide junction

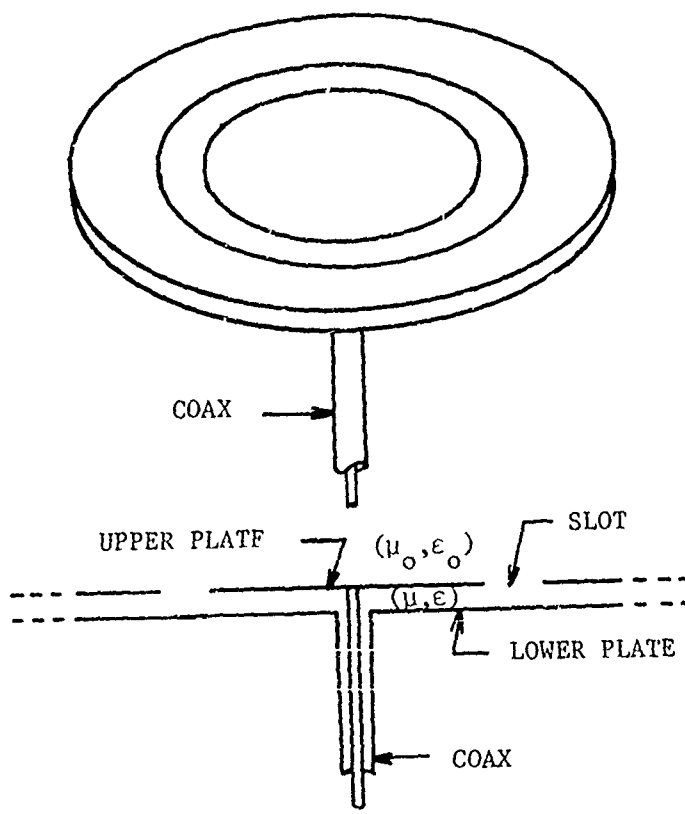
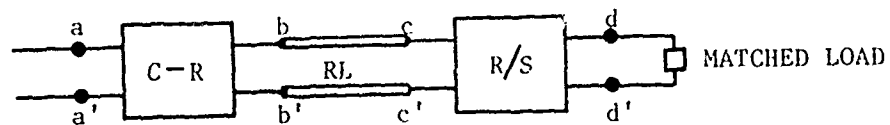


Fig. 1. Coax-Fed Radial Guide with Slot



C-R COAX-TO-RADIAL-GUIDE JUNCTION
 R/S SECTION OF SLOTTED RADIAL GUIDE
 RL SECTION OF RADIAL GUIDE

Fig. 2. Microwave Circuit Representation of Coax-Fed, Radial Guide with Slot

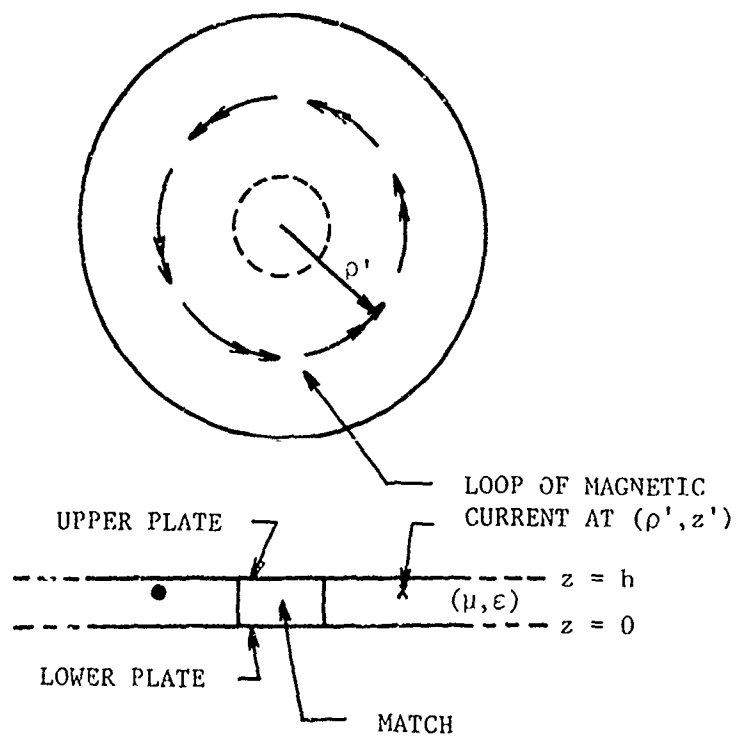


Fig. 3. Fundamental Green's Function Problem

and the slotted section, and then to study the original structure of Fig. 1 by means of microwave circuit techniques.

In this paper, attention is limited to the slotted section of radial parallel-plate guide, while the coax-to-radial-guide junction problem is to be investigated in a subsequent paper. Below, an integral equation is derived for the unknown electric field E_p^A in the annular slot under the assumption that a known TEM wave exists in the region $\rho < a$ and is incident upon the slotted section of guide. Beyond the slot $\rho > b$, the guide extends to infinity. The integral equation is solved numerically for E_p^A and the TEM reflection and transmission coefficients are determined. Also, from E_p^A the radiated field is computed. The structure of Fig. 1 is, of course, representative of a microstrip antenna only for the case of a very wide slot.

2.0 FORMULATION OF INTEGRAL EQUATION

In this section an integral equation is derived for the unknown electric field E_p^A in the annular slot cut in the upper plate of the radial, parallel-plate waveguide. The guide extends to infinity in the radial direction and the slot is made sufficiently wide to ensure that there is no coupling to the portion of the guide beyond the slot. The excitation is a known TEM, outwardly propagation wave in the region between the slot and coax junction. With the slotted section under investigation, the details of the exact structure of the coax junction are unimportant. In fact, one can place a reflectionless termination in the central locale of the junction insofar as the analysis of the slotted guide is concerned. The integral equation for E_p^A is derived by expressing the magnetic field in the region above the upper plate and that in the region between the plates in terms of E_p^A and subsequently requiring the total magnetic field to be continuous along any path through the slot. This formulation is based upon aperture theory [1-3] and draws heavily upon equivalent models involving equivalent magnetic surface currents placed on conducting surfaces [1-4].

2.1 FUNDAMENTAL GREEN'S FUNCTION

As an aid in the formulation of desired integral equations, the Green's function problem

$$\left(\frac{\partial^2}{\partial \rho^2} + \frac{1}{\rho} \frac{\partial}{\partial \rho} + [k^2 - \frac{1}{\rho^2}] + \frac{\partial^2}{\partial z^2} \right) g = j\omega\epsilon \delta(\rho-\rho')\delta(z-z') \quad (1)$$

is solved subject to the conditions that

$$\frac{\partial}{\partial z} g = 0 \text{ at } z=0 \text{ and at } z=h \quad (2)$$

and that g represent a wave traveling away from $\rho=\rho'$ both for $\rho<\rho'$ and for $\rho>\rho'$. In (1) and (2), $\delta(\cdot)$ is the delta function, ω is the angular frequency, h is the guide height, (μ,ϵ) characterizes the material in the guide and $k^2 = \omega^2\mu\epsilon$. Physically, g can be interpreted as the magnetic field H_ϕ due to a filamentary loop of magnetic current which is between two perfectly conducting parallel plates as illustrated in Fig. 3. For $\rho>\rho'$ there is no reflected wave traveling in the negative ρ direction because the parallel-plate guide extends to infinity, while the ideal reflectionless termination prohibits a wave traveling in the positive ρ direction for $\rho<\rho'$. The Green's function g is represented by the series

$$g(\rho, z; \rho', z') = \frac{1}{2} a_0(\rho; \rho') + \sum_{q=1}^{\infty} a_q(\rho; \rho', z') \cos \frac{q\pi}{h} z \quad (3)$$

which satisfies (2). Substitution of (3) into (1) and utilization of the orthogonality of the set $\{\cos \frac{q\pi}{h} z\}$ enable one to show that the coefficients satisfy

$$\left(\frac{\partial^2}{\partial \rho^2} + \frac{1}{\rho} \frac{\partial}{\partial \rho} + [k^2 - \frac{1}{\rho^2}] \right) a_0 = j \frac{2\omega\epsilon}{h} \delta(\rho-\rho') \quad (4)$$

and

$$\left(\frac{\partial^2}{\partial \rho^2} + \frac{1}{\rho} \frac{\partial}{\partial \rho} + [\gamma_q^2 - \frac{1}{\rho^2}] \right) a_q = j \frac{2\omega\varepsilon}{h} \cos \frac{q\pi}{h} z' \delta(\rho-\rho') \quad (5)$$

where

$$\gamma_q^2 = k^2 - \left(\frac{q\pi}{h} \right)^2, \quad q=1, 2, \dots \quad (6)$$

Eqs. (4) and (5) are inhomogeneous Bessel equations so we construct the following solutions

$$a_0 = \begin{cases} C_0 H_1^{(1)}(k\rho') H_1^{(2)}(k\rho), & \rho > \rho' \\ C_0 H_1^{(2)}(k\rho') H_1^{(1)}(k\rho), & \rho < \rho' \end{cases} \quad (7)$$

and

$$a_q = \begin{cases} C_q H_1^{(1)}(\gamma_q \rho') H_1^{(2)}(\gamma_q \rho), & \rho > \rho' \\ C_q H_1^{(2)}(\gamma_q \rho') H_1^{(1)}(\gamma_q \rho), & \rho < \rho' \end{cases} \quad (8)$$

which are continuous at $\rho=\rho'$ and which obey the outward wave condition.
 $H_n^{(1)}$ and $H_n^{(2)}$ are the first and second kind Hankel functions of order n.
In addition, a_0 and a_q must exhibit the following "jump" properties:

$$\frac{\partial}{\partial \rho} a_0 \Big|_{\rho=\rho',+} - \frac{\partial}{\partial \rho} a_0 \Big|_{\rho=\rho',-} = j \frac{2\omega\varepsilon}{h} \quad (9a)$$

and

$$\frac{\partial}{\partial \rho} a_q \Big|_{\rho=\rho',+} - \frac{\partial}{\partial \rho} a_q \Big|_{\rho=\rho',-} = j \frac{2\omega\varepsilon}{h} \cos \frac{q\pi}{h} z'. \quad (9b)$$

Enforcing (9), one can show from (7) and (8) that

$$C_0 = - \frac{\pi}{2} \frac{\omega\epsilon}{h} \rho' \quad (10a)$$

and

$$C_q = - \frac{\pi}{2} \frac{\omega\epsilon}{h} \rho' \cos \frac{q\pi}{h} z' \quad (10b)$$

from which expressions for a_0 and a_q are readily obtained. Therefore, the desired Green's function is

$$g(\rho, z; \rho', z') = \begin{cases} g^+(\rho, z; \rho', z') & , \rho > \rho' \\ g^-(\rho, z; \rho', z') & , \rho < \rho' \end{cases} \quad (11a)$$

where

$$\begin{aligned} g^+ &= - \frac{\pi}{4} \frac{k}{\eta h} \rho' H_1^{(1)}(k\rho') H_1^{(2)}(k\rho) \\ &\quad - \frac{\pi}{2} \frac{k}{\eta h} \rho' \sum_{q=1}^{\infty} H_1^{(1)}(\gamma_q \rho') H_1^{(2)}(\gamma_q \rho) \cos \frac{q\pi}{h} z' \cos \frac{q\pi}{h} z, \quad \rho > \rho' \end{aligned} \quad (11b)$$

and

$$\begin{aligned} g^- &= - \frac{\pi}{4} \frac{k}{\eta h} \rho' H_1^{(2)}(k\rho') H_1^{(1)}(k\rho) \\ &\quad - \frac{\pi}{2} \frac{k}{\eta h} \rho' \sum_{q=1}^{\infty} H_1^{(2)}(\gamma_q \rho') H_1^{(1)}(\gamma_q \rho) \cos \frac{q\pi}{h} z' \cos \frac{q\pi}{h} z, \quad \rho < \rho' \end{aligned} \quad (11c)$$

in which $\eta = \sqrt{\mu/\epsilon}$ and

$$\gamma_q = \begin{cases} \sqrt{k^2 - \left(\frac{q\pi}{h}\right)^2}, & k^2 > \left(\frac{q\pi}{h}\right)^2 \\ -j\sqrt{\left(\frac{q\pi}{h}\right)^2 - k^2}, & k^2 < \left(\frac{q\pi}{h}\right)^2 \end{cases} \quad (11d)$$

2.2 INTERIOR MAGNETIC FIELD

With the Green's function g of (11) available, one can formulate an expression for the total magnetic field in the region between the parallel plates. For present purposes, the TEM field propagating in the positive ρ direction in the region between the matched load and the slot is the specified excitation. The electric and magnetic field components of such an excitation are [4]

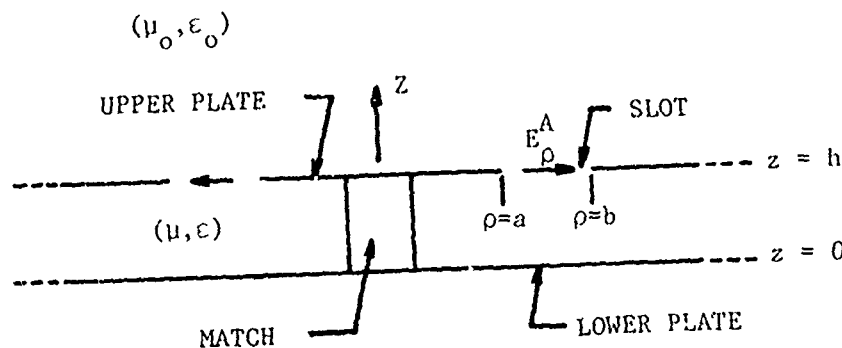
$$E_z^{sc} = E_0^+ H_0^{(2)}(k\rho) \quad (12a)$$

and

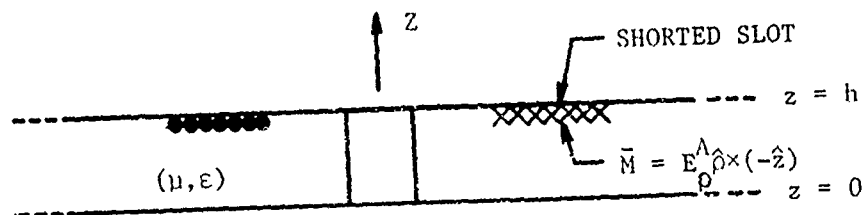
$$H_\phi^{sc} = j \frac{1}{\eta} E_0^+ H_1^{(2)}(k\rho) \quad (12b)$$

where E_0^+ is a known complex constant. If no slot were present, only the field of (12) would exist in the infinite parallel-plate guide.

To compute H_ϕ , the total magnetic field in the interior region, one appeals to the equivalent model of Fig. 4. In Fig. 4a is depicted the radial guide with slot and in Fig. 4b is seen an equivalent model valid for $0 < z < h$. The surface magnetic current M_ϕ of value $M_\phi = E_0^+ \rho$ is placed over the short-circuited slot, and it causes the ρ component of electric field to approach E_∞^A as z approaches h from the guide interior. Since $g(\rho, z; \rho', z')$ of (11) is the magnetic field due to a filament of magnetic current, one can compute the interior magnetic field due to E_ρ^A (or due to M_ϕ) by integration of $M_\phi(\rho') g(\rho, z; \rho', h)$ over $\rho' \epsilon(a, b)$. To the magnetic field due to M_ϕ must be added H_ϕ^{sc} to obtain the total magnetic field H_ϕ . That is,



(a) Original Problem (Valid Everywhere)



(b) Equivalent Model (Valid $0 < z < h$)

Fig. 4. Interior Region Equivalent Model

$$H_\phi = H_\phi^{sc} + L(M_\phi) \quad , \quad 0 < z < h \quad (13)$$

where H_ϕ^{sc} is given in (12b) and where

$$L(M_\phi) = \begin{cases} \int_a^b E_\rho^A(\rho') g^-(\rho, z; \rho', h) d\rho' \quad , \quad \rho < a \\ \int_a^0 E_\rho^A(\rho') g^+(\rho, z; \rho', h) d\rho' + \int_p^b E_\rho^A(\rho') g^-(\rho, z; \rho', h) d\rho' \quad , \quad a < \rho < b \\ \int_a^b E_\rho^A(\rho') g^+(\rho, z; \rho', h) d\rho' \quad , \quad \rho > b . \end{cases} \quad (14)$$

2.3 EXTERIOR MAGNETIC FIELD

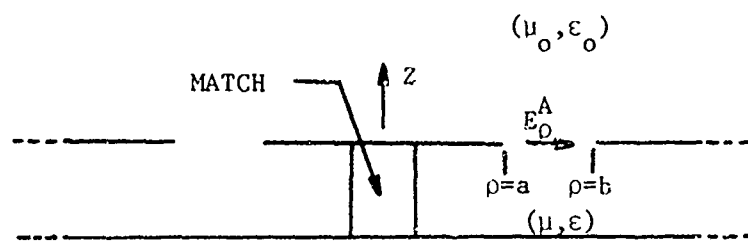
The equivalent model valid in the exterior region is presented in Fig. 5b. Based on image theory, the model of Fig. 5c is valid for $z > h$, and, with this equivalence in which $-M_\phi$ plus its image ($= -2M_\phi$) radiates in open space characterized by (μ_0, ϵ_0) , one readily computes the exterior magnetic field H_ϕ^0 in the form

$$H_\phi^0 = -j \omega F_\phi \quad (15a)$$

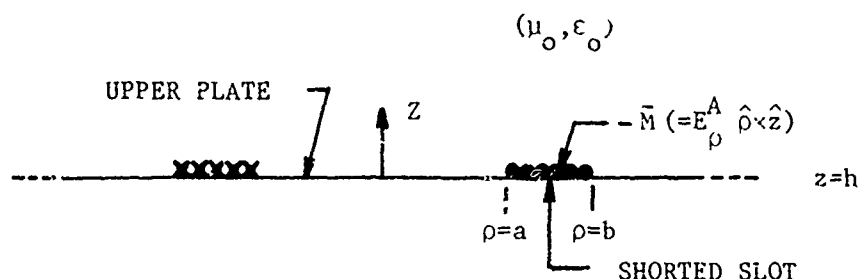
where the electric vector potential F_ϕ is

$$F_\phi(\rho, z) = -\frac{\epsilon_0}{2\pi} \int_a^b \rho' E_\rho^A(\rho') \int_{-\pi}^{\pi} \cos\phi' \frac{e^{-jk_c[(z-h)^2 + R^2]^{1/2}}}{[(z-h)^2 + R^2]^{1/2}} d\phi' d\rho' \quad (15b)$$

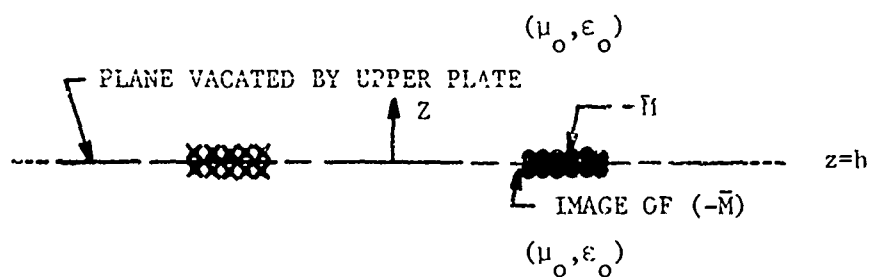
with $k_c = \sqrt{\mu_0/\epsilon_0}$ and with



(a) Original Problem (Valid Everywhere)



(b) Equivalent Model (Valid $z>h$)



(c) Equivalent Model (Valid $z>h$)

Fig. 5. Exterior Region Equivalent Models

$$R = [\rho^2 + \rho'^2 - 2\rho\rho' \cos\phi']^{1/2}. \quad (15c)$$

2.4 INTEGRAL EQUATION FOR E_ρ^A

The interior and exterior magnetic fields H_ϕ and H_ϕ^0 , with their companion electric fields, satisfy the conditions of electromagnetics in their respective regions. These fields must be coupled through the slot which is achieved by requiring

$$\lim_{z \downarrow h} H_\phi(\rho, z) = \lim_{z \downarrow h} H_\phi^0(\rho, z), \quad \rho \in (a, b). \quad (16)$$

Since expressions for H_ϕ and H_ϕ^0 are formulated in terms of E_ρ^A in (a, b) , the tangential electric field is automatically continuous along any path through the slot. Thus, all conditions of electromagnetics are satisfied.

Enforcement of (16) in terms of Eqs. (13), (14), and (15) leads to the integral equation below for the unknown E_ρ^A :

$$\begin{aligned} j \frac{1}{\pi} \frac{k_o}{\eta_o} \int_a^b \rho' E_\rho^A(\rho') \int_0^\pi \cos\phi' \frac{e^{-jk_o R}}{R} d\phi' d\rho' - \int_a^b E_\rho^A(\rho') g^+(\rho, h; \rho', h) d\rho' \\ - \int_\rho^b E_\rho^A(\rho') g^-(\rho, h; \rho', h) d\rho' = j \frac{1}{\eta} E_0^+ H_1^{(2)}(k\rho), \quad \rho \in (a, b). \end{aligned} \quad (17)$$

The known forcing function on the right hand side of (17) above is H_ϕ^{sc} . The solution of this integral equation is the sought electric field E_ρ^A in the slot. Eq. (17) is valid for any width slot.

3.0 REFLECTION AND TRANSMISSION COEFFICIENTS

The TEM electric field reflection coefficient Γ at a reference $\rho = P_1$ is defined

$$\Gamma = \frac{\text{Reflected } E_z^{\text{TEM}} \text{ at } P_1}{\text{Incident } E_z^{\text{TEM}} \text{ at } P_1}$$

while the transmission coefficient is

$$T = \frac{\text{Transmitted } E_z^{\text{TEM}} \text{ at } P_2}{\text{Incident } E_z^{\text{TEM}} \text{ at } P_1}$$

where $\rho = P_2$ is another reference [$P_1 < a$, $P_2 > b$]. These coefficients are found to be

$$\Gamma = j \frac{\pi}{4} \frac{k}{h} \frac{H_0^{(1)}(kP_1)}{H_0^{(2)}(kP_1)} \frac{1}{E_0^+} \int_a^b E_p^A(\rho') H_1^{(2)}(k\rho') \rho' d\rho' \quad (18)$$

and

$$T = \frac{H_0^{(2)}(kP_2)}{H_0^{(2)}(kP_1)} \left\{ 1 + j \frac{\pi}{4} \frac{k}{h} \frac{1}{E_0^+} \int_a^b E_p^A(\rho') H_1^{(1)}(k\rho') \rho' d\rho' \right\}. \quad (19)$$

4.0 RADIATED FIELD

From (15), one can readily show that the far magnetic field due to radiation from the slot is

$$H_\phi^0 = j \frac{1}{\pi} \frac{k_o}{n_o} \frac{e^{-jk_o r}}{r} \int_a^b \rho' E_p^A(\rho') \int_0^\pi \cos\phi' e^{jk_o \rho' \sin\theta \cos\phi'} d\phi' d\rho', \quad (20a)$$

$r >> b$

where θ is the polar angle from the z axis and where

$$r = [x^2 + y^2 + (z-h)^2]^{1/2} = [\rho^2 + (z-h)^2]^{1/2} \quad (20b)$$

is the distance from the center of the upper plate to the field point. In view of the integral representation of $J_1(\cdot)$, the first order Bessel function, (20) can be written simply as

$$H_{\phi}^0 \doteq - \frac{k_o}{\eta_o} \frac{e^{-jk_o r}}{r} \int_a^b E_p^A(\rho') J_1(k_o \rho' \sin \theta) \rho' d\rho', \quad r \gg b. \quad (21)$$

5.0 RESULTS

In Figs. 6 and 7 is displayed the aperture electric field E_p^A for different guide heights h and slot widths $(b-a)$. In each case, $a/\lambda = 0.5$ and the material inside and outside the guide is free space. In order to relate the data to a TEM voltage reference, we set $E_0^+ = V/h$. Notice the manifestation of the edge condition and the rapid decay of the aperture field as a function of ρ in the slot. With a sufficiently wide slot, further increases in width do not appreciably affect E_p^A as can be seen in Figs. 6 and 7. The small value of E_p^A for $\rho \rightarrow b$ means that the coupling to the radial guide beyond the slot is very small. This implication of small coupling is corroborated by the values of transmission coefficient T in Table 1. Observe also the small change in Γ and T for increased slot widths.

TABLE 1
REFLECTION AND TRANSMISSION COEFFICIENTS

h/λ	a/λ	b/λ	Γ/N_r	T/N_t
0.1	0.5	1.5	$0.522 + j 0.232$	$0.115 + j 0.072$
0.1	0.5	2.0	$0.538 + j 0.199$	$0.085 + j 0.054$
0.1	0.5	2.5	$0.550 + j 0.174$	$0.067 + j 0.045$
0.05	0.5	1.0	$0.533 + j 0.511$	$0.099 + j 0.046$
0.05	0.5	1.5	$0.562 + j 0.484$	$0.066 + j 0.022$
0.05	0.5	2.0	$0.584 + j 0.463$	$0.050 + j 0.013$

$$N_r = H_0^{(1)}(kP_1)/H_0^{(2)}(kP_1); \quad N_t = H_0^{(2)}(kP_2)/H_0^{(2)}(kP_1)$$

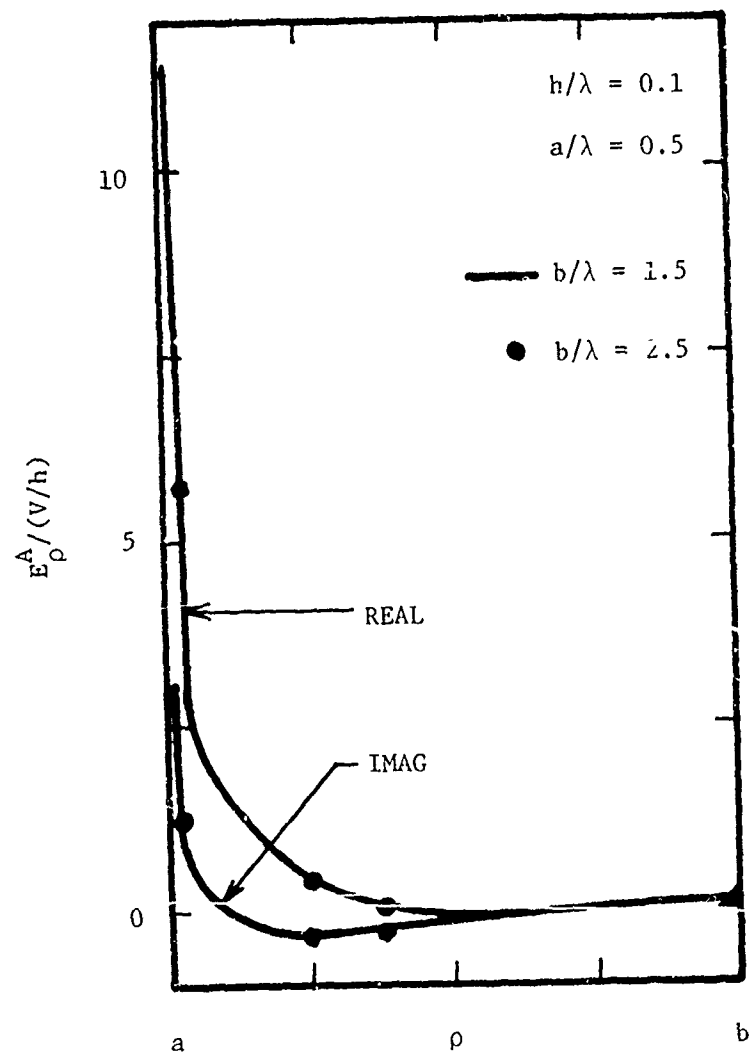


Fig. 6. Electric Field in Slot

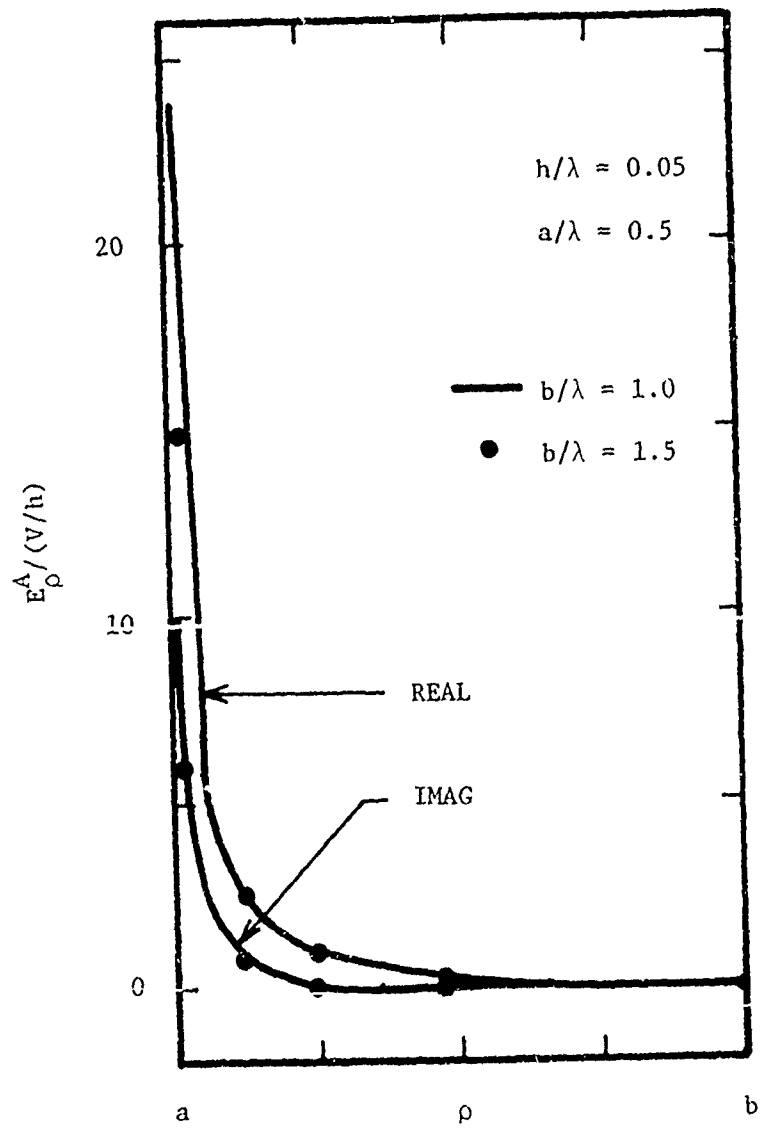


Fig. 7. Electric Field in Slot

6.0 ACKNOWLEDGEMENTS

The work reported in this paper was supported in part by the U.S. Army Research Office under Grant DAAG-29-G-0285. Mr. T. L. Keshavamurthy wrote the computer program to solve Eq. (17).

7.0 REFERENCES

1. Butler, C. M., Y. Rahmat-Samii, and R. Mittra, "Electromagnetic Penetration through Apertures in Conducting Surfaces," Joint Special EMP Issue of IEEE Trans. Ant. and Prop. & IEEE Trans. EMC, Vol. AP-26, No. 1, pp. 82-93; Jan., 1978.
2. Butler, C. M., and E. Yung, "Analysis of a Terminated, Parallel-Plate Waveguide with a Slot in its Upper Plate," to appear in Annales des Télécommunications.
3. Van Bladel, J., and C. M. Butler, "Aperture Problems," in Theoretical Methods for Determining the Interaction of Electromagnetic Waves with Structure, Sijthoff and Noordhoff International Publishers, Alphen aan den Rijn, Netherlands, 1980.
4. Harrington, R. F., Time-Harmonic Electromagnetic Fields, McGraw-Hill Book Co., New York, 1961.

THEORETICAL ANALYSIS OF PRINTED-CIRCUIT ANTENNAS

LIANG C. SHEN AND STUART A. LONG
DEPARTMENT OF ELECTRICAL ENGINEERING
UNIVERSITY OF HOUSTON
HOUSTON, TEXAS 77004

SUMMARY

Both circular and elliptical printed-circuit antennas were analyzed theoretically with the side walls of the cavity modeled as finite impedance walls. This surface impedance was determined from the effects of both the power radiated and that in the fringing fields.

1.0 INTRODUCTION

In previous investigations analytical formulas for the electromagnetic fields in the region between the radiator and the ground plane of a printed-circuit antenna have been derived using a resonant cavity model. The upper and lower boundaries were assumed to be perfect conductors while the sides were modeled by perfect magnetic walls. This model allows the radiated fields to be calculated in analytical form for simple geometrical shapes; however, difficulties are encountered in calculating the input impedance at resonance and in applying this method to structures which are not extremely thin, as compared to a wavelength. In the present investigation, the side walls of the cavity are modeled as finite impedance walls rather than as perfect magnetic conductors. The surface impedance is determined by calculating the effects of both the radiated power and the fringing field. Using this more realistic model, the input impedance can be calculated directly from basic principles. Values obtained from this model are found to correlate more accurately with experimental data than previous theoretical results, particularly for antennas of moderate thickness. This new formulation also enables the relative intensity to be found for the internal field of the dominant mode as compared to other modes as the operating frequency is varied.

2.0 CIRCULAR-DISC, PRINTED-CIRCUIT ANTENNA

The fields inside the cylindrical cavity formed between the circular disc

and the ground plane can be represented by a suitable combination of Bessel functions for an arbitrary feed point position. Using these internal fields and imposing the boundary condition of a constant admittance surface at the edge of the disc, the internal fields can be calculated analytically. The real part of the surface admittance is found from the total radiated power, while the imaginary portion is calculated from the effect of the fringing field on the apparent radius of the disc. (It should be noted that both of these calculated quantities are functions of the thickness of the antenna.) This allows the input impedance to be calculated as a function of all the parameters of the antenna including the position of the feed. In addition the magnitudes of the internal fields can be found for each mode to check the dominance of the $n=1$ mode for a variety of feed positions.

3.0 ELLIPTICAL PRINTED-CIRCUIT ANTENNA

A similar analytical technique was also applied to elliptically shaped discs. The radiated fields can then be expressed in terms of tabulated functions. It is found that for the proper selection of both the driving-point position and the eccentricity of the ellipse, the antenna will radiate circularly polarized waves. A detailed experimental investigation has also been undertaken and has confirmed the presence of quite good circular polarization with only a single simple coaxial feed.

4.0 CONCLUSIONS

The inclusion of the impedance wall in the boundary conditions is seen to improve the accuracy of the theoretical predictions, especially for the cases of antennas which are not extremely thin with respect to a wavelength. In addition the technique has also been used for a more complicated shape to predict the existence of circularly polarized waves.

5.0 ACKNOWLEDGMENT

This work was supported in part by the U. S. Army Research Office under Grant DAAG29-78-G-0198.

AN EXTREMELY LIGHTWEIGHT FUSELAGE-INTEGRATED
PHASED ARRAY FOR AIRBORNE APPLICATIONS

JAMES S. YEE AND WILLIAM J. FURLONG
THE BOEING AEROSPACE COMPANY
SEATTLE, WASHINGTON 98124

SUMMARY

A design of a lightweight, low-volume electronically-scanned antenna is described. This antenna, besides being the radiating aperture, serves as a load-sharing fuselage panel in a small weight-sensitive remotely piloted vehicle (RPV). A demonstration array incorporating the micro-strip radiating elements, stripline feed circuit, and microstrip diode phase shifters was assembled to evaluate the electrical characteristics and scanning capabilities of the array. The demonstration array was tested on the antenna range and operated successfully as part of a radar/communication subsystem demonstration. An eight-element lightweight section of the demonstration array was subsequently designed and fabricated in a modern production facility utilizing numerically-controlled machines and state-of-the-art printed circuit board etching and plating equipment. Successful operation of this lightweight section sufficiently demonstrated that a lightweight and low volume electronically steerable phased array antenna can be fabricated and integrated into a structural panel in production quantities.

1.0 INTRODUCTION

Lightweight, low volume, low cost, and high performance are familiar requirements for airborne antenna systems. Technological advances in lightweight, low volume radiating element designs and advances in lightweight, high density packaging techniques for r.f. components and devices in microstrips and striplines make phased array designs possible. The

unique feature of this design is the application and integration of these technologies to achieve an antenna/fuselage panel which serves as the antenna aperture and load-sharing structure in a small, weight-sensitive RPV. This paper discusses the critical electrical and mechanical design concepts necessary to achieve the desired weight and performance characteristics.

2.0 DESCRIPTION OF ANTENNA

The phased array antenna has 32 elements arranged in 2 x 16 element lattice to form a rectangular aperture of 1 ft x 8 ft. It is designed to operate at 970 MHz. The elements are spaced $\lambda/2$ apart, and are fed uniformly in power by a corporate 16-way stripline power divider. The azimuth beam is scanned electronically by microstrip diode phase shifters. A schematic of the phased array and the feed components is shown in Figure 1.

3.0 WEIGHT AND SPACE SAVING FEATURES IN THE DESIGN

In the RPV fuselage-integrated antenna, a number of weight and space saving features are noted. These are enumerated as follows:

1. The use of lightweight and low volume microstrip radiating elements.
2. The use of stripline circuits for antenna feed components and microstrip circuits for diode phase shifters.
3. The use of a multi-layer board construction to save space and the use of plated-through holes to make electrical connections to save electrical connectors and thus to save weight.
4. The routing out of excessive substrate material not essential to the feed circuit in the stripline circuit board to save additional weight.
5. The laminating of lightweight and load-bearing honeycomb structure with epoxy fiberglass skins to the antenna to form the RPV structural fuselage member.

An exploded view of the antenna/fuselage assembly depicting the design and weight saving features is shown in Figure 2.

4.0 DEMONSTRATION ARRAY

Prior to any detailed production and packaging considerations, it was deemed necessary to design an array using microstrip radiating elements and stripline feed components to evaluate the electrical characteristics. The experimental array assembly, the stripline feed, and phase-shifters are shown in Figure 3.

Overall antenna performance was evaluated on the antenna range. The antenna was scanned to various beam positions by means of a beam steering controller which sets the 4-bit phase shifters to the proper element incremental phases. A series of beam-scanned patterns is shown in Figure 4. Quite evident in the pattern is the expected decrease in main beam gain and the expected increase in the 3 dB main beam width as the antenna is scanned from broadside to + 60 degrees. It should be noted that the patterns hold up well even toward the endfire direction, which is an indication that the mutual coupling effects are not too serious in this instance. This is further substantiated by driving-point impedance measurements of an element in the presence of one, two, and three identical elements under the various termination conditions, such as open circuited, short circuited, and matched load conditions.

5.0 RADIATING ELEMENT DESIGN

The microstrip radiating element design was based on the work of John Q. Howell [1]. The element is a conducting disk supported by a thin layer of low-loss dielectric substrate which rests on a conducting ground plane. The essential parts of the element are shown in Figure 5. Also shown is the element E-plane radiation pattern and the network analyzer setup used to determine the resonant dimensions and the impedance in the element design. The disk diameter for resonance is primarily determined by the dielectric constant of the substrate material beneath the disk and the resonance mode which is excited inside the disk. Howell based his resonant diameter determination on the TM_{11} mode of a circular resonant structure in microstrip [2]. Generally, this initial diameter dimension is a good starting point, but the determination of the exact resonant diameter requires additional fine trimming in the laboratory with the setup shown in Figure 5. It was found that the dia-

meter for resonance is also a function of probe offset, substrate thickness, and the disk physical environment, such as the substrate material extending beyond the top conducting disk and the size of the ground plane.

The feed point offset distance from the disk center determines primarily the impedance match at resonance. Since the disk is fed with a 50 ohm line, Howell [1] suggested an initial offset distance of approximately one-third of the radius from the center for a substrate material whose dielectric constant is 2.6. Final offset distance trimming is required to achieve good impedance match. Since the effect on resonance and on impedance match due to the above two dimensions is generally predictable, a little laboratory experience on the behavior of the element provides a workable design fairly rapidly.

A very desirable feature of this radiating element design is the ease of achieving radiation in the orthogonal polarization. This can be accomplished by locating the feed point at the same offset position 90^0 away from the original feed point. Circular polarization radiation is easily achievable by exciting the two orthogonal feeds simultaneously with a 90^0 3 dB hybrid. A typical spinning linearly polarized radiation pattern for an element excited to give circular polarization is shown in Figure 6. The pattern performance quality (axial ratio) is determined by the excursion of the pattern trace. Since the excursion is less than 1 dB over a wide angular portion of the pattern, the radiation pattern is considered nearly circularly polarized.

6.0 LIGHTWEIGHT SECTION OF DEMONSTRATION ARRAY

A quarter-sized lightweight section of the demonstration array was fabricated in the Boeing manufacturing facilities to demonstrate that a lightweight version of the array can be produced in quantities with state-of-the-art manufacturing and processing techniques. The lightweight design would incorporate the ideas and concepts that were presented in an earlier section on weight and space saving features. The dimensions of the section were 1' x 2'. It contained eight elements in a lattice of two rows and four columns. The original weight allocation for the whole array (1' x 8'

in a 2×16 lattice of 32 elements) was 10 lbs. Hence, the quarter-sized section would have a target weight of 2.5 lbs. The assembled section as shown in Figure 7, including the r.f. feed circuits and cover, had an overall weight of 2.8 lbs.

The eight-element lightweight section performed as expected the first time it was tested on the antenna range. A series of beam-scanned patterns are shown in Figure 8. A small amount of element loading due to the thin fiberglass cover was noted. The best frequency of operation in terms of antenna gain for the section was 955 MHz instead of 970 MHz, the original design frequency. This loading effect can be easily compensated in the design by resizing the element diameter for resonance with the thin cover on.

7.0 SUMMARY OF PERFORMANCES

The performances of the 2×16 32-element demonstration array and the 2×4 8-element lightweight section are summarized in Table 1.

TABLE 1
PERFORMANCE SUMMARY

PARAMETERS	ESTIMATED	ACHIEVED
<u>(2 X 16 32-ELEMENT DEMONSTRATION ARRAY)</u>		
• Frequency:	970 mHz (Specified)	970 mHz
• Electronic Steerability	$\pm 90^\circ$ from broadside	$\pm 60^\circ$ from broadside Some endfire coverage
• Half-power beamwidths		
• Azimuth:	6.5° nominal	7° at broadside
• Elevation:	51.5° nominal	35° at broadside
• Gain:	16.4 db nominal (3.5 db loss included)	16.5 db at broadside
• Sidelobe/mainlobe ratio:	-13.2 db nominal	-13.5 db nominal
• Polarization:	Horizontal	Horizontal
<u>(2 X 4 8-ELEMENT LIGHTWEIGHT ARRAY)</u>		
• Frequency:	970 mHz	955 mHz
• Electronic Steerability	$\pm 90^\circ$ from broadside	$\pm 60^\circ$ from broadside Some endfire coverage
• Half-power beamwidth		
• Azimuth:	25.8° nominal	27° at broadside
• Elevation:	51.5° nominal	35° at broadside
• Gain:	10.4 db nominal (3.5 db loss included)	10 db at broadside
• Sidelobe/mainlobe ratio:	-13.2 db nominal	-14 db at broadside
• Polarization:	Horizontal	Horizontal
• Weight:	2.5 LB	2.8 LB

8.0 ANTENNA/VEHICLE INTEGRATION

Figure 9 illustrates the integration of the antenna with the fuselage of a small remotely piloted vehicle (RPV). In this case, the total vehicle requirements together with the antenna requirements were considered in the basic configuration. The sides of the vehicle are straight and the arrays are part of the structure. The straight side configuration not only allows for ease of array fabrication, but also for overall ease of vehicle fabrication and equipment installation resulting in low weight, volume, and cost.

9.0 GROWTH FEATURES OF THE ANTENNA SYSTEM

One desirable growth feature of the antenna system is to further reduce the existing sidelobe level relative to the peak of the main beam. The radiation patterns in Figure 4 show a sidelobe level of -13.5 dB, which is to be expected from an array of uniformly excited elements. A reduction to -25 dB has been achieved by developing and incorporating an amplitude-tapered distribution function in the antenna feed design. A feed design using microstrip lines to achieve a -28 dB sidelobe level in a 6-element Dolph-Chebyshev array has been demonstrated [3].

Another desirable growth feature of this antenna system is to achieve some forward coverage when an array is mounted on each side of the RPV fuselage. This requirement means that each array must provide a usable endfire beam. This endfire coverage is usually very difficult to attain in an electronically-scanned phased array because: 1) there is negligible energy in the endfire direction in the element radiation pattern, and 2) mutual coupling between elements in the array. In this case, the microstrip element radiates some energy in the endfire direction, as can be observed in the single element E-plane radiation pattern shown in Figure 5. The array produces a recognizable endfire beam when it is set to scan in that direction, as shown in Figure 4. The dual endfire lobes shown in the pattern occur because the elements are spaced $\lambda/2$ apart. To favor the forward lobe, a straight-forward solution is to arrange the element spacing to be less than $\lambda/2$ to eliminate the second (back) principal lobe. Another 3 dB enhancement of the radiation in the forward direction can be

achieved by combining the radiation from each array when the two are simultaneously scanned in the endfire direction. However, due to potential vehicle body-antenna interaction effects, the level of achievement in the forward coverage must only be assessed through testing of the arrays actually mounted on the sides of a vehicle.

10.0 CONCLUSION

Feasible weight and space saving ideas have been proposed for the fabrication of a lightweight fuselage-integrated phased array. These concepts are essential to make it possible for an extremely weight-sensitive and space-limited RPV to carry a high performance antenna system. The electrical characteristics of the array of microstrip radiating elements together with the associated stripline feed and microstrip diode phase shifters have been adequately evaluated in the demonstration array. The experience in the design and fabrication of a lightweight section of the demonstration array in a production facility provided sufficient confidence that a lightweight and low volume electronically steerable phased array antenna can be fabricated, integrated into a structural panel, and produced at low cost in production quantities. The achievement of a workable vehicle antenna configuration is an example of the close working relationship between the mechanical designer and the antenna designer. Additional growth features can be designed into the existing array.

11.0 ACKNOWLEDGEMENT

The authors wish to acknowledge Mr. Fred Lightfoot, Manager of Avionics Preliminary Design for the encouragement and support during the course of this work.

12.0 REFERENCES

1. Howell, John Q., Microstrip Antennas, IEEE Transactions on Antennas and Propagation, January 1975, pp. 90-93.
2. Watkins, J., Circular Resonant Structures in Microstrips, Electronics Letters, October 16, 1969, Vol. 5, No. 21, pp. 524-525.
3. Gupta, Chimmoy Das, Build An Integrated Dolph-Chebyshev Array, Microwaves, November 1976, pp. 54-58.

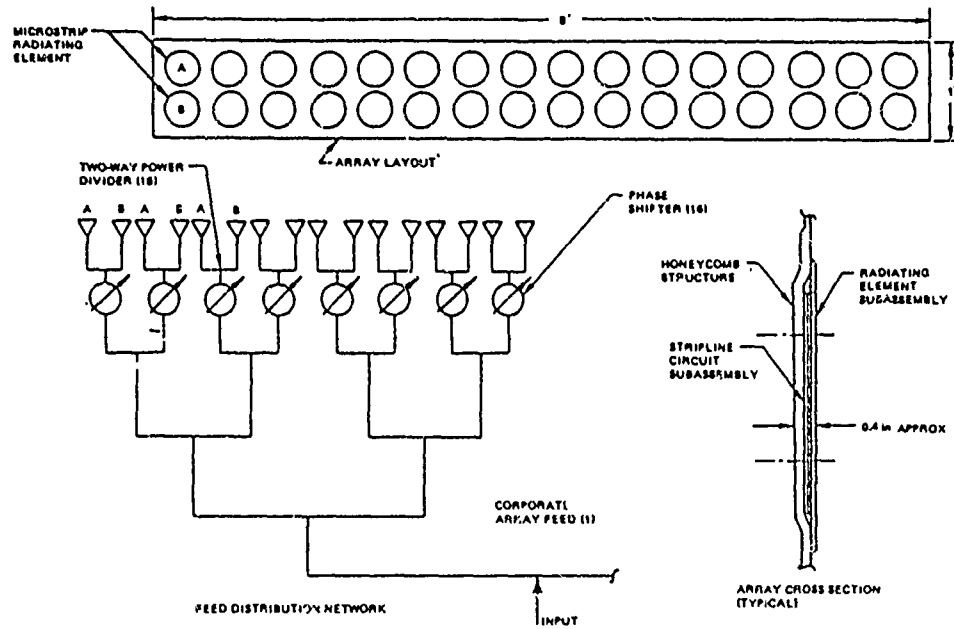


FIGURE 1 ARRAY LAYOUT AND FEED DISTRIBUTION NETWORK

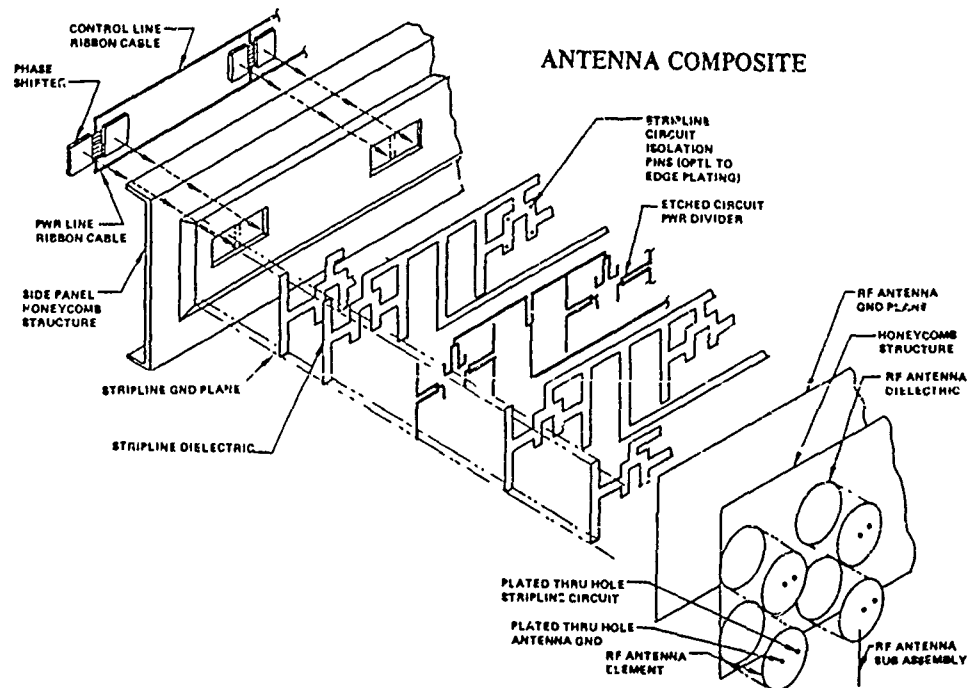


FIGURE 2 COMPOSITE LIGHTWEIGHT ANTENNA DESIGN

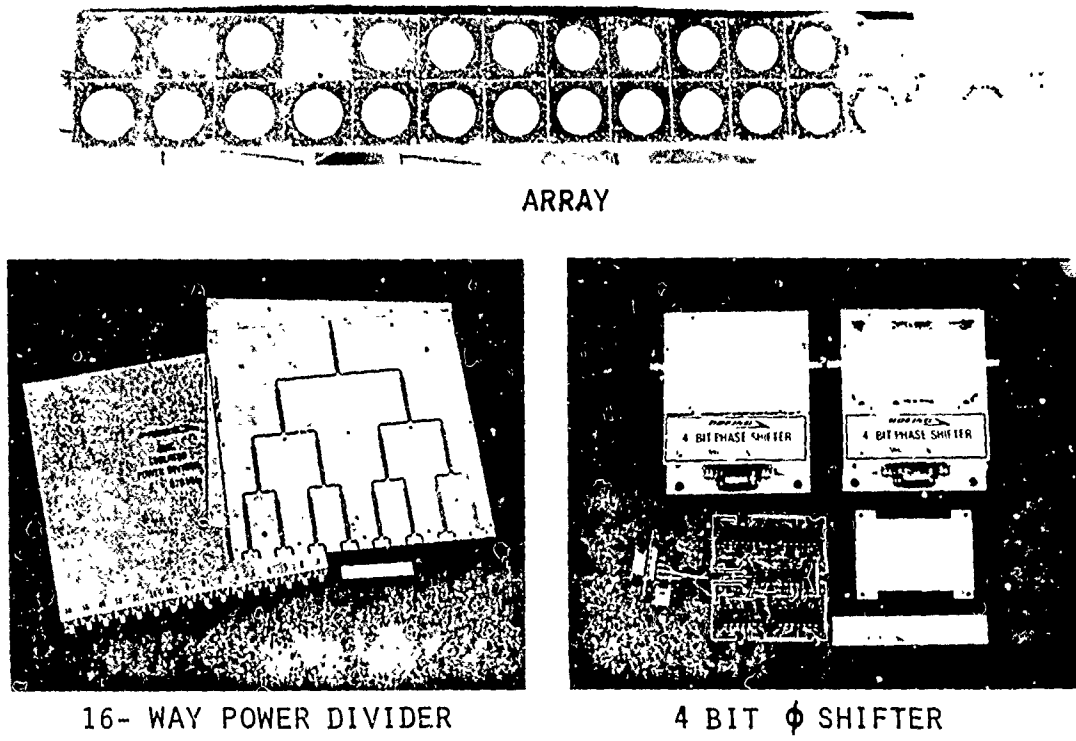


FIGURE 3 PHOTO OF ARRAY HARDWARE

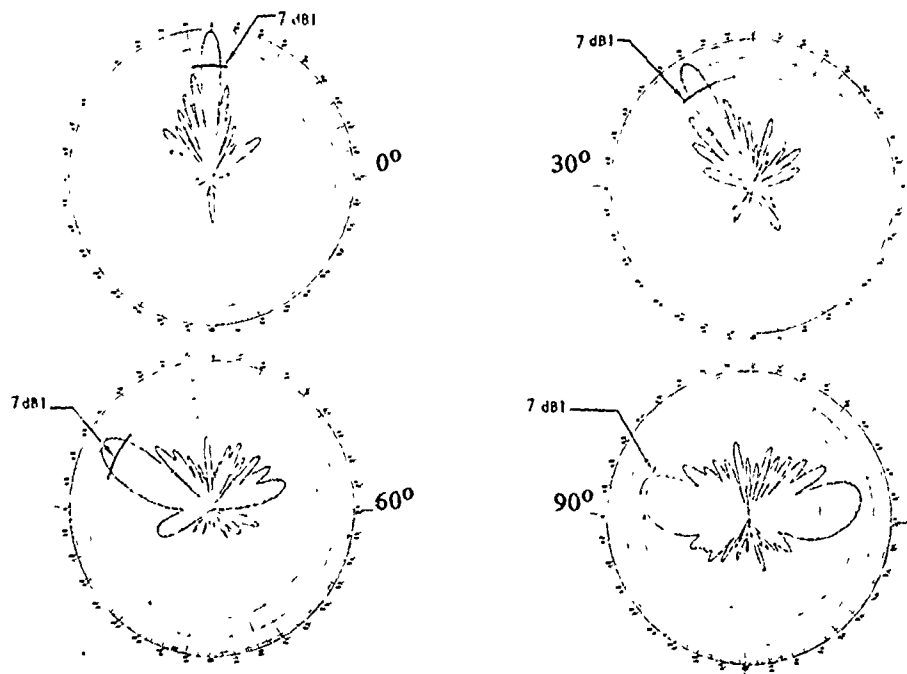
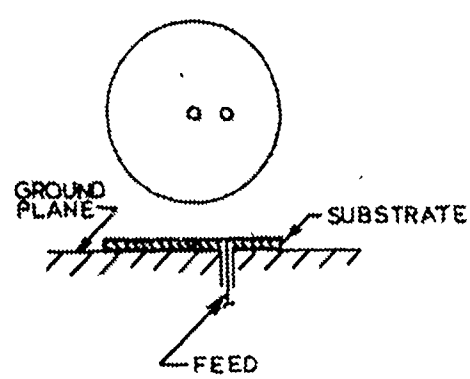
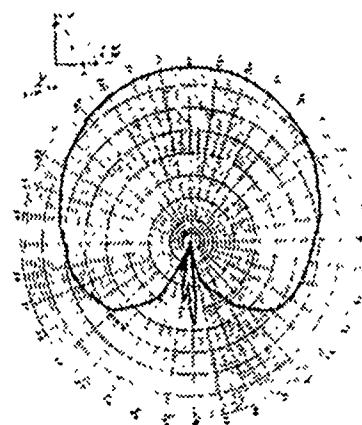


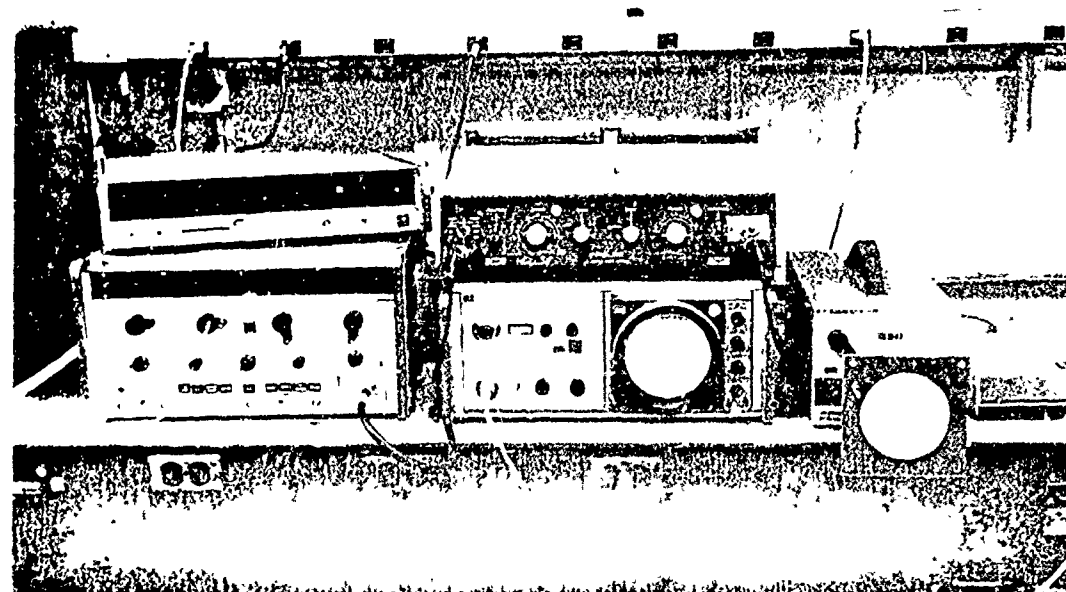
FIGURE 4 SCANNED PATTERNS 970 MHz
(2 x 16 ELEMENTS DEMONSTRATION ARRAY)



CIRCULAR DISK
MICROSTRIP ELEMENT



E-PLANE PATTERN



IMPEDANCE MEASUREMENT SETUP

FIGURE 5 RADIATING ELEMENT, RADIATION PATTERN, AND MEASUREMENT SETUP

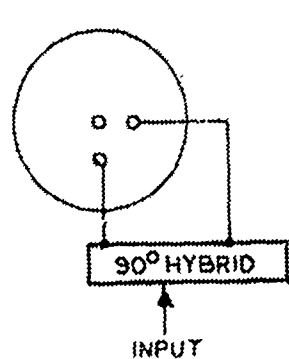
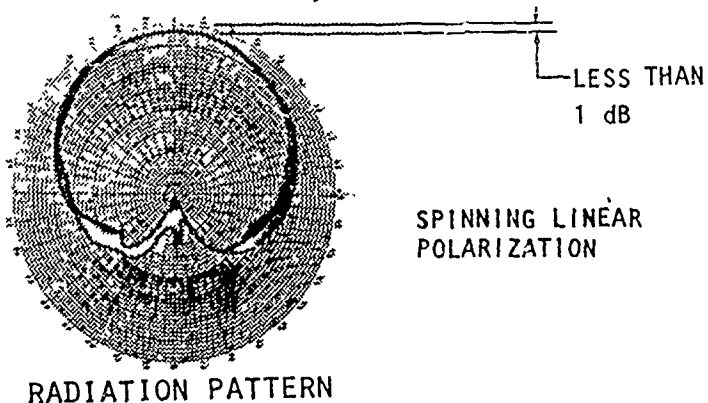
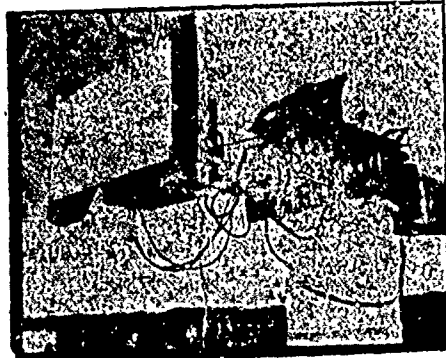


FIGURE 6 CIRCULAR POLARIZATION PERFORMANCE

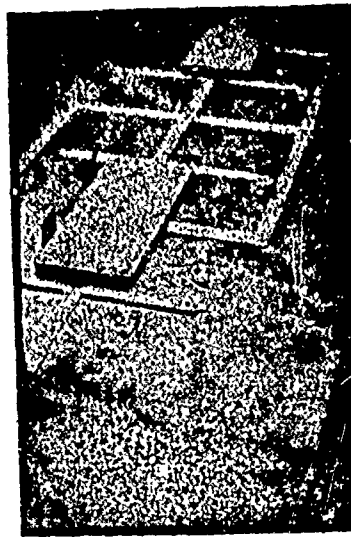


RADIATION PATTERN

SPINNING LINEAR
POLARIZATION



FRONT



BACK

FIGURE 7 PHOTO OF LIGHTWEIGHT SECTION

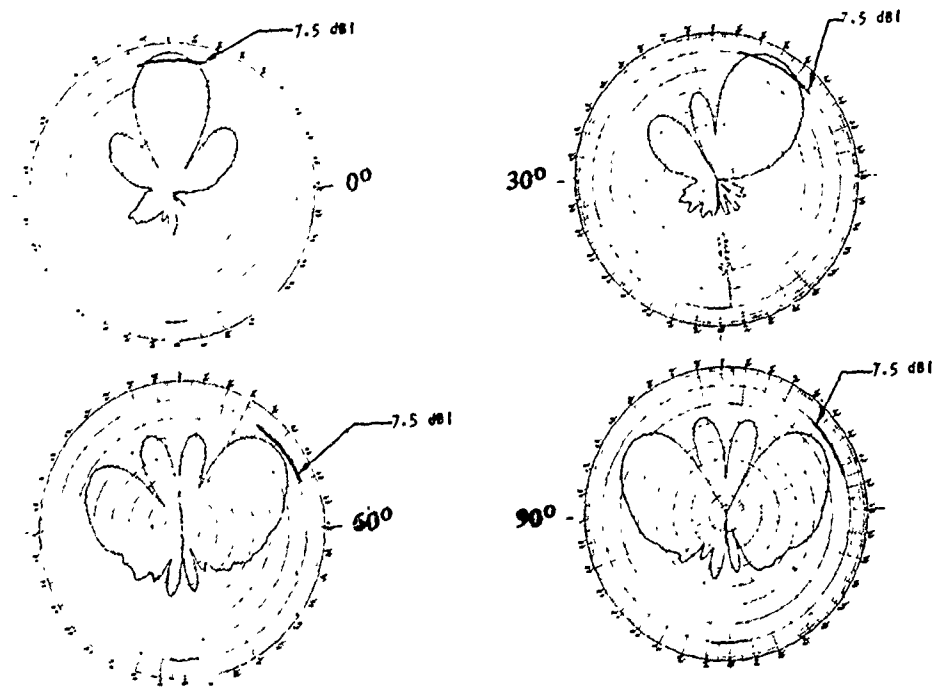


FIGURE 8 SCANNED PATTERNS 955 MHz
(2 x 4 ELEMENTS LIGHTWEIGHT ARRAY)

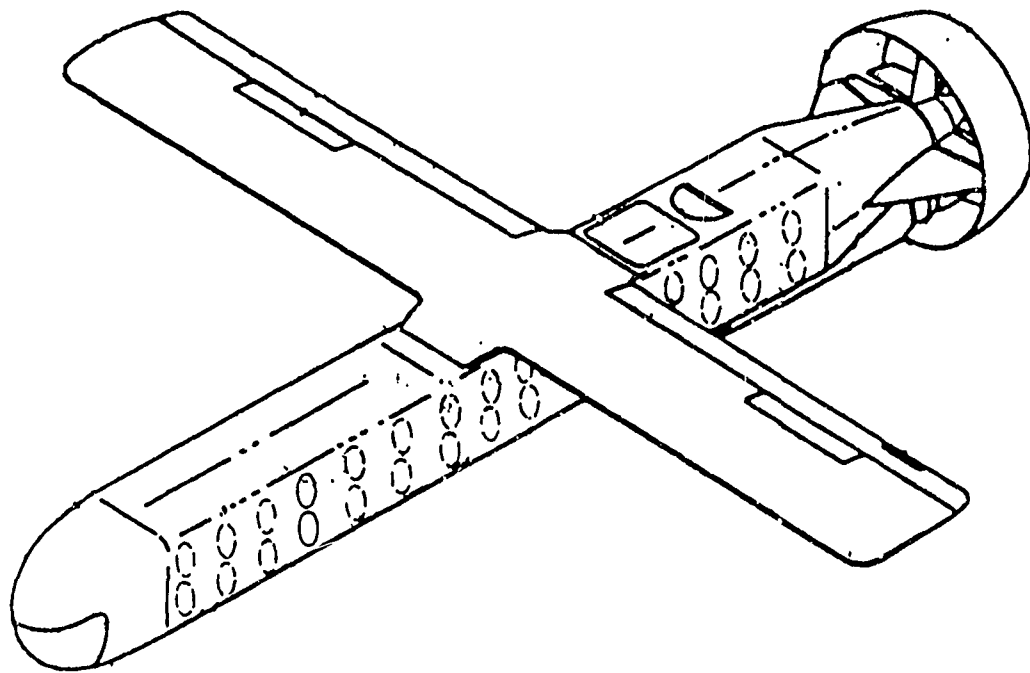


FIGURE 9 FUSELAGE-INTEGRATED ANTENNA IN SMALL RPV

PATTERN SYNTHESIS FOR CONFORMAL ARRAY

MARTIN A. HUISJEN
BALL AEROSPACE SYSTEMS DIVISION
PO BOX 1062
BOULDER, COLORADO 80306

LT. CHRIS NELSON
AFATL/DLMM
EGLIN AFB, FLORIDA 32542

SUMMARY

The synthesis of a desired antenna pattern from an array of elements conformal to a non-planar surface is quite different from that for a planar array. This paper describes an adaptive array technique for synthesizing conformal array patterns. In this technique, angular regions of desired and undesired coverage are defined; signal and jammer covariance matrices are then set up; and a generalized eigenvalue problem is solved to find the element weights corresponding to the maximum signal-to-jam power ratio. Applying these weights (amplitude and phase) to the elements gives the desired pattern.

Examples which apply this technique to cylindrical arrays are presented.

1.0 INTRODUCTION

Printed circuit antenna technology is well suited for constructing conformal non-planar antenna arrays. While such arrays can have obvious configurational advantages over planar arrays, they also present a different set of problems in synthesizing desired patterns. The difference can be seen by considering the pattern equations for linear and circular arrays. For a linear array the pattern can be written

$$F(\theta) = L(\theta) \sum_m W_m Z^m; Z \equiv e^{-j \frac{2\pi}{\lambda} d \sin \theta} \quad (1)$$

where θ is the angle measured from array broadside; $L(\theta)$ is the single element pattern; d is the element spacing; W_m is the complex weight applied to the m th element; λ is the signal wavelength; and the sum is over all array elements. It is seen that the pattern is factorable into an element pattern times an array factor, and the array factor is expressed as a polynomial of a normalized parameter. In contrast, the pattern of a circular array is written

$$F(\theta) = \sum_m L(\theta - \theta_m) W_m e^{-j \frac{2\pi}{\lambda} R [\cos \theta - \cos(\theta - \theta_m)]} \quad (2)$$

where R is the radius of the circle and θ_m is the angular position of the m th element. The element pattern cannot be factored, and there is no polynomial of a normalized parameter. As a result, the synthesis techniques which have been developed for linear arrays (and are appropriate for planar arrays) do not apply to circular and other shapes of arrays representative of conformal antennas.

This paper describes a conformal array pattern synthesis procedure which makes use of adaptive array theory. The procedure is an extension of a technique described elsewhere (1, 2) which is appropriate for situations in which there is a desired signal arriving from one direction and there are undesired (jamming) signals arriving from many directions. The procedure described here is appropriate for situations in which both the desired and undesired signals are arriving from many directions. An example of the latter would be a situation in which one desires communication with a satellite which could be anywhere

within a large overhead cone. To synthesize a broad pattern which would cover this cone, one would treat this situation as though uncorrelated signals were arriving from all directions within the cone. This will be described further in Section 3.0.

2.0 MATHEMATICAL FORMULATION

The purpose of the pattern synthesis procedure is to determine the complex weights (amplitude and phase) which should be applied to the elements of an array in order to synthesize a desired pattern. The desired pattern is described in terms of regions of desired and undesired signals.

Let $E_m(\theta_j)$ be the signal voltage received by the m th array element from a direction θ_j , and let W_m be the weight applied to the m th element in the antenna combining network. (E_m and W_m are complex numbers.) The signal voltage at the array output due to a signal from θ_j is

$$v(\theta_j) = \sum_m W_m E_m(\theta_j) \quad (3)$$

where the sum is over all array elements. If there are signals arriving from several directions, the output voltage becomes

$$v_T = \sum_m \sum_j S_j W_m E_m(\theta_j) \quad (4)$$

where the sum over j is for all signal directions, and S_j represents the phase and amplitude of the j th signal. The time averaged output signal power of the array is

$$\bar{P}_s = \overline{|v_T|^2} = \overline{\sum_m W_m^* \sum_j S_j^* E_m^*(\theta_j) \sum_n W_n \sum_i S_i E_n(\theta_i)} \quad (5)$$

where the overhead bar means time averaged.

If the signal sources are uncorrelated, then

$$\overline{s_i s_j^*} = |s_j|^2 \delta_{ij} \quad (6)$$

where δ_{ij} is the Kronecker delta. The signal power becomes

$$P_s = \sum_m \sum_n w_m^* w_n \sum_j |s_j|^2 E_m^*(\theta_j) E_n(\theta_j) \quad (7)$$

Generalizing to a continuum of signal sources this becomes

$$P_s = \sum_m \sum_n w_m^* w_n \int |s(\theta)|^2 E_m^*(\theta) E_n(\theta) d\theta \quad (8)$$

where the integral is over the angular distribution of signal sources.

This can be rewritten in matrix form as

$$P_s = \langle W | S | W \rangle \quad (9)$$

where $|W\rangle$ is the column vector $(w_1, w_2, \dots w_n)$, $\langle W|$ is the conjugate transpose of $|W\rangle$, and S is the covariance matrix with ij component =

$$S_{ij} = \int |s(\theta)|^2 E_i^*(\theta) E_j(\theta) d\theta \quad (10)$$

In exactly the same way, the received power due to a continuum of jammer sources can be written

$$P_j = \langle W | J | W \rangle \quad (11)$$

where

$$J_{ij} = \int |j(\theta)|^2 E_i^*(\theta) E_j(\theta) d\theta \quad (12)$$

and the integration is over the angular distribution of jammer sources.

Now the ratio of signal to jammer power can be written

$$\frac{P_s}{P_j} = \frac{\langle W | S | W \rangle}{\langle W | J | W \rangle} \quad (13)$$

Since $S_{ij} = S_{ji}^*$, $J_{ij} = J_{ji}^*$, and P_s and P_j are both positive real numbers, both S and J are positive definite Hermitian matrices. This means that there are real eigenvalues λ and the corresponding eigenvectors $|W\rangle$ of the generalized eigenvalue problem

$$S|W\rangle = \lambda J|W\rangle \quad (14)$$

For eigenvectors $|W\rangle$ which satisfy (14), equation (13) becomes

$$\frac{P_s}{P_j} = \frac{\langle W | \lambda J | W \rangle}{\langle W | J | W \rangle} = \lambda \quad (15)$$

so that among the eigenvectors $|W\rangle$ satisfying equation (14), the one corresponding to the largest eigenvalue λ_{\max} gives the maximum signal-to-jam ratio. It is shown in the appendix that this eigenvector gives the maximum possible signal-to-jam ratio for given signal and jam covariance matrices S and J .

The procedure described thus far optimizes signal-to-jam ratio. Receiver noise can also be included. If the receiver noise power is N , the ratio of signal power to total noise power can be written

$$\frac{P_s}{P_N} = \frac{\langle W | S | W \rangle}{\langle W | J | W \rangle + N} = \frac{\langle W | S | W \rangle}{\langle W | J + NI | W \rangle} \quad (16)$$

where I is the identity matrix and it is understood that $\langle W | W \rangle = 1$.

The maximum possible signal to total noise ratio is given by the eigenvector $|W\rangle$ corresponding to the maximum eigenvalue of the equation

$$S|W\rangle = \lambda (J + NI)|W\rangle \quad (17)$$

Summarizing the procedure, one first defines angular regions of desired and undesired coverage. Then the signal and jammer matrices are set up as defined by equations (10) and (12). The functions $|S(\theta)|^2$ and $|J(\theta)|^2$ can be nonuniformly weighted to emphasize or de-emphasize particular regions of interest. The generalized eigenvalue problem given by equation (14) is then solved, and the desired element weights are given by the eigenvector $|w\rangle$ corresponding to the maximum eigenvalue λ . When it is desired to keep the coverage in the signal region above a minimum level, it may be useful to include receiver noise in the procedure. In this case, one adds a constant noise term to the diagonal elements of the jammer matrix and proceeds to solve the eigenvalue problem given by equation (17). The procedure will be further described by examples given in the next section.

3.0 CYLINDRICAL EXAMPLES

Suppose one wishes to synthesize patterns in a plane perpendicular to the axis of a cylindrical array (roll plane pattern). Let there be eight elements at positions θ_m ($m = 1$ to 8) on the circumference of the cylinder. Then

$$E_m(\theta) = L(\theta - \theta_m) e^{-j \frac{2\pi R}{\lambda} [\cos \theta - \cos (\theta - \theta_m)]} \quad (18)$$

where $L(\theta)$ is the radiation pattern of the individual element on the cylinder, R is the radius of the cylinder, λ is the signal wavelength, and θ_m is the angular position of element m on the cylinder. The ij element of the signal matrix becomes

$$S_{ij} = \int_{\theta_i}^{\theta_2} |S(\theta)|^2 L^*(\theta - \theta_i) L(\theta - \theta_j) e^{j \frac{2\pi R}{\lambda} [\cos(\theta - \theta_j) - \cos(\theta - \theta_i)]} \quad (19)$$

where θ_1 and θ_2 define the region of desired coverage and $|S(\theta)|^2$ defines the desired coverage distribution in that region. (It would equal 1 for uniform coverage.) For an eight element array, S would be an 8×8 matrix. The matrix elements can be found by numerical integration of (19) using for $L(\theta)$ the element pattern actually measured on the cylinder. To find the jammer matrix elements, $|S(\theta)|^2$ is replaced by $|J(\theta)|^2$ and the integration limits are changed to define the desired area of low sidelobes.

After the matrices have been set up by performing the numerical integrations, the generalized eigenvalue problem is solved by computer using a general purpose library subroutine. For an 8-element array, the entire process of setting up the matrices and solving the eigenvalue problem takes less than five seconds CPU time on a CDC 6600.

The patterns shown in the remainder of this section were synthesized for a case of eight elements spaced 0.58λ around the circumference of a cylinder with radius $4/3\lambda$. The roll plane pattern of a single element on this cylinder is shown in Figure 1. Figure 2 is the pattern resulting from specifying uniform signal power from -70° to 70° , uniform jammer power from 90° to 270° , and no receiver noise. When receiver noise is included, the tendency is toward broader coverage and higher sidelobes. Figure 3 is the pattern resulting from specifying uniform signal power from -70° to 70° , uniform jammer power from 85° to 95° and from -95° to -85° , and some receiver noise. The amount of added receiver noise is somewhat heuristic and was chosen here to achieve some balance between coverage width and sidelobe levels.

These examples indicate that the technique described in this paper is a very powerful one for synthesizing conformal array patterns. The examples shown are for cases of uniform signal and jammer distributions over given angular regions. Another tool available to the designer is the use of non-uniform distributions to emphasize a particular coverage area or to further reduce sidelobes in a particular jammer area.

Figure 1 Roll Pattern of Single Element on Cylinder

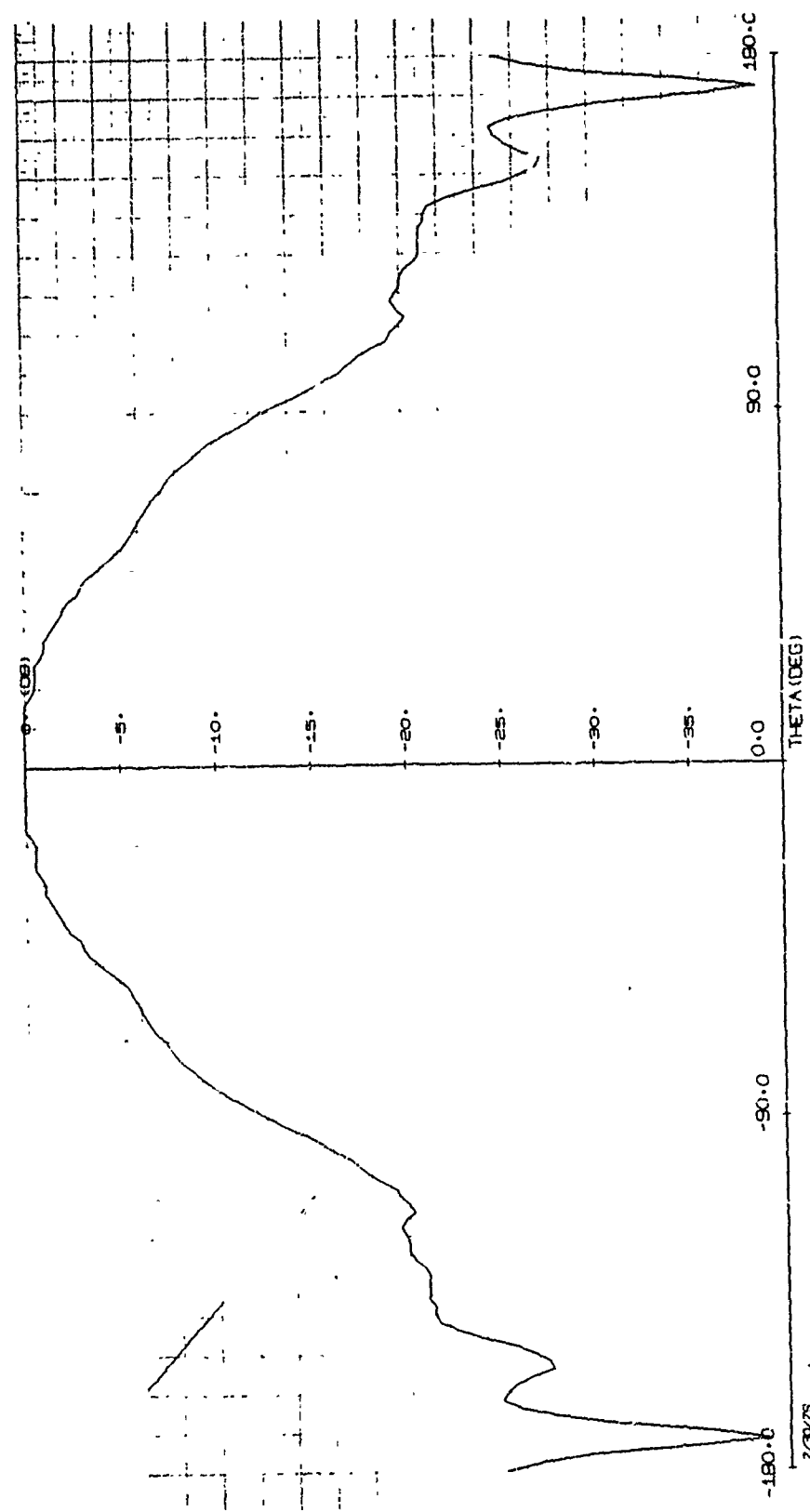


Figure 2 Signal from -70° to 70°
Jammers from 90° to 270°

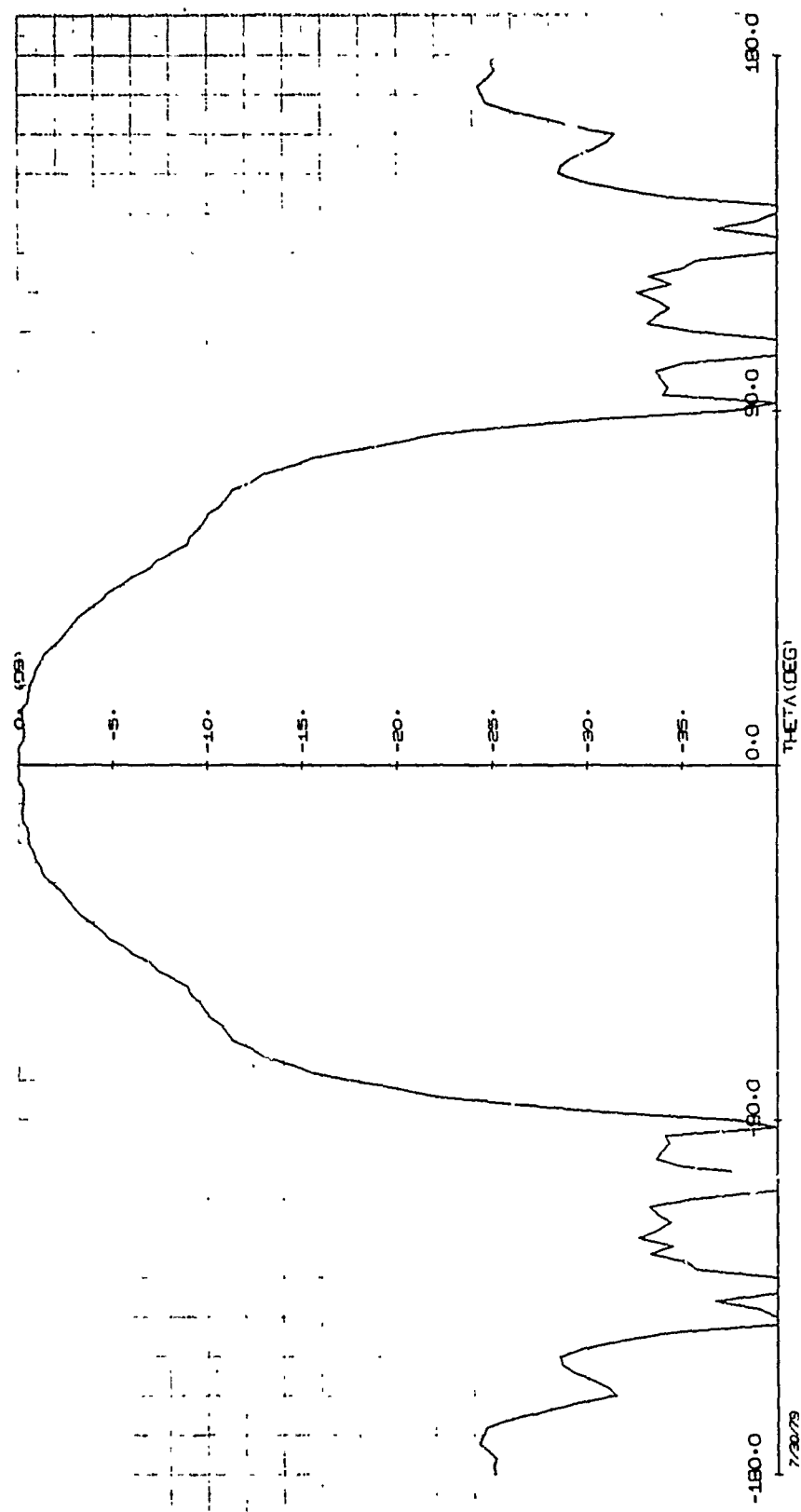
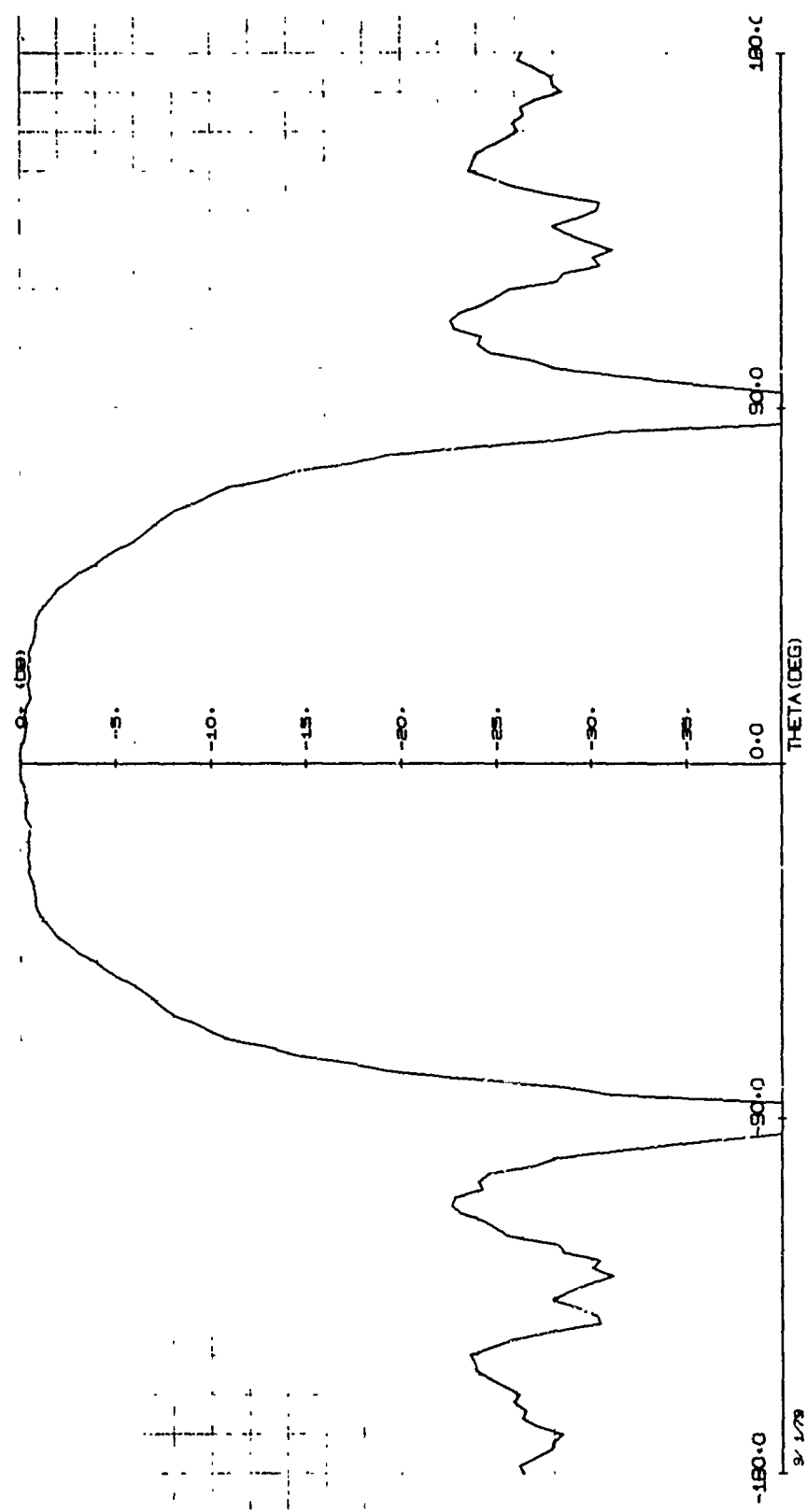


Figure 3 Signal -70° to 70°
Jammers 85° to 95° and -95° to -85°



4.0 APPENDIX

In this appendix it is proved that for positive definite Hermitian matrices S and J, the maximum value of

$$R = \frac{\langle W|S|W\rangle}{\langle W|J|W\rangle} \quad (20)$$

is given by the vector $|W\rangle$ corresponding to the maximum eigenvalue λ of the equation

$$S|W\rangle = \lambda J|W\rangle \quad (21)$$

Since J is a Hermitian positive definite matrix, there exists a matrix A such that

$$A^* JA = I \quad (22)$$

where A^* means the conjugate transpose of A. Make the transformation

$$|W\rangle = A|U\rangle \quad (23)$$

Then equation (20) becomes

$$R = \frac{\langle U|A^*SA|U\rangle}{\langle U|A^*JA|U\rangle} = \frac{\langle U|A^*SA|U\rangle}{|U|^2} \quad (24)$$

The Cauchy-Schwarz inequality states that the inner product of two vectors is less than or equal to the product of the magnitudes of the vectors.

Therefore,

$$R \leq \frac{|U| |A^*SAU|}{|U|^2} \quad (25)$$

The equality holds when the vectors are colinear, or in other words when

$$A^* S A |U\rangle = \lambda |U\rangle \quad (26)$$

There are generally several values of λ which satisfy (26). Obviously the maximum λ gives the maximum possible value of R. Using equation (23), (26) can be rewritten

$$A^* S |W\rangle = \lambda A^{-1} |W\rangle \quad (27)$$

and then substituting from equation (22),

$$S|W\rangle = \lambda A^{*-1} A^{-1} |W\rangle = \lambda J|W\rangle \quad (28)$$

Thus, the $|W\rangle$ corresponding to the maximum eigenvalue λ_{\max} of (28) gives the maximum possible value of R. This maximum possible value is λ_{\max} .

5.0 REFERENCES

1. L. E. Brennan, "Design and Adaptive Control of Conformal Arrays", in Proceeding of the Array Antenna Conference held at San Diego in February 1972.
2. K. J. Keeping and J. C. Sureau, "Control of Sidelobes in Cylindrical Arrays", Lincoln Laboratory Technical Note 1978-22.

AN ELECTRICALLY SMALL MICROSTRIP DIPOLE
PLANAR ARRAY

DONALD A. HUEBNER
HUGHES AIRCRAFT COMPANY
ADVANCED MISSILE SYSTEMS DIVISION
CANOGA PARK, CALIF. 91304

SUMMARY

An efficient electrically small planar antenna consisting of an array of printed circuit elements is described. The element itself is a microstrip dipole which is electromagnetically coupled to a strip transmission line imbedded in the substrate [1]. The small area occupied by the dipole along with the location of the feed line on a different level allows freedom in element placement unmatched with either strip-fed slots or conventional patch-type microstrip radiators. The particular antenna discussed is a 3.5λ diameter X-band monopulse array consisting of 24 elements. Both theoretical and experimental results are presented and compared. Errors in the aperture distribution were assessed utilizing both liquid crystal and near-field probing diagnostic techniques. The results of these investigations are presented.

1.0 INTRODUCTION

During the past decade, most printed-circuit antenna research has centered on the patch-type microstrip radiator. In contrast, such efforts in the Advanced Missile Systems Division of Hughes Aircraft Company have emphasized an antenna which is configured quite differently: the electromagnetically-excited microstrip dipole. This radiator offers numerous advantages, foremost among them being its small size. This is especially advantageous in electrically small arrays where high element density is required to achieve a reasonable aperture distribution.

In this paper, both the nature of the element and its application in an electrically small array will be discussed. The characteristics and

theory of operation of the microstrip dipole are presented in Section 2.0. An array where the radiator is used to advantage is then discussed in Section 3.0. Finally, some conclusions are presented in Section 4.0.

2.0 THE MICROSTRIP DIPOLE

The configuration of the microstrip dipole is shown in Figure 1. The element is seen to consist of a resonant printed-circuit dipole located on the top surface of a microstrip substrate. The dipole is fed from a strip transmission line which is imbedded within the dielectric. As the two are not in physical contact, the energy is electromagnetically coupled from the feed to the radiator. The actual overlap of the two strips is a function of their vertical spacing and is chosen to produce a match to the feed line. Optimum performance has been found to occur when the overlap region encompasses approximately one-half of the dipole length, and this thus determines the desired vertical spacing. This overlap corresponds to maximum dipole-feed coupling.

The actual effect of varying the feed-dipole spacing is shown for a particular geometry in Figure 2. It is seen that a vertical separation between the dipole and feed which is too great will fail to yield a match at any frequency. As the separation is decreased, a critical spacing is reached where the radiator exhibits a single matched resonance. This corresponds to the dipole-feed overlap of one-half the dipole length mentioned above. For vertical spacings less than this value, the antenna exhibits two matched resonances. This results from the fact that closer spacings require the overlap region to be changed to lower the resultant overcoupling. This can be done by reducing the region of overlap and producing capacitive coupling, or by increasing the region and yielding inductive coupling. Either choice will produce a match, but the resultant resonant frequencies will differ as shown by the figure.

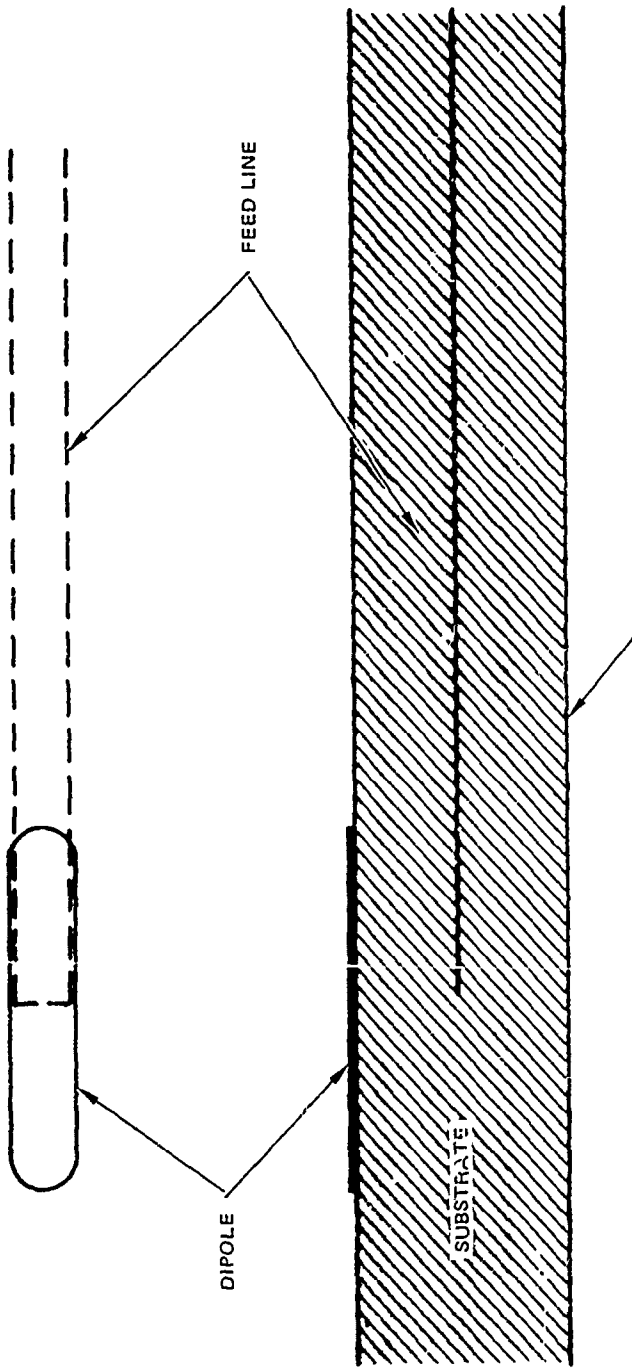
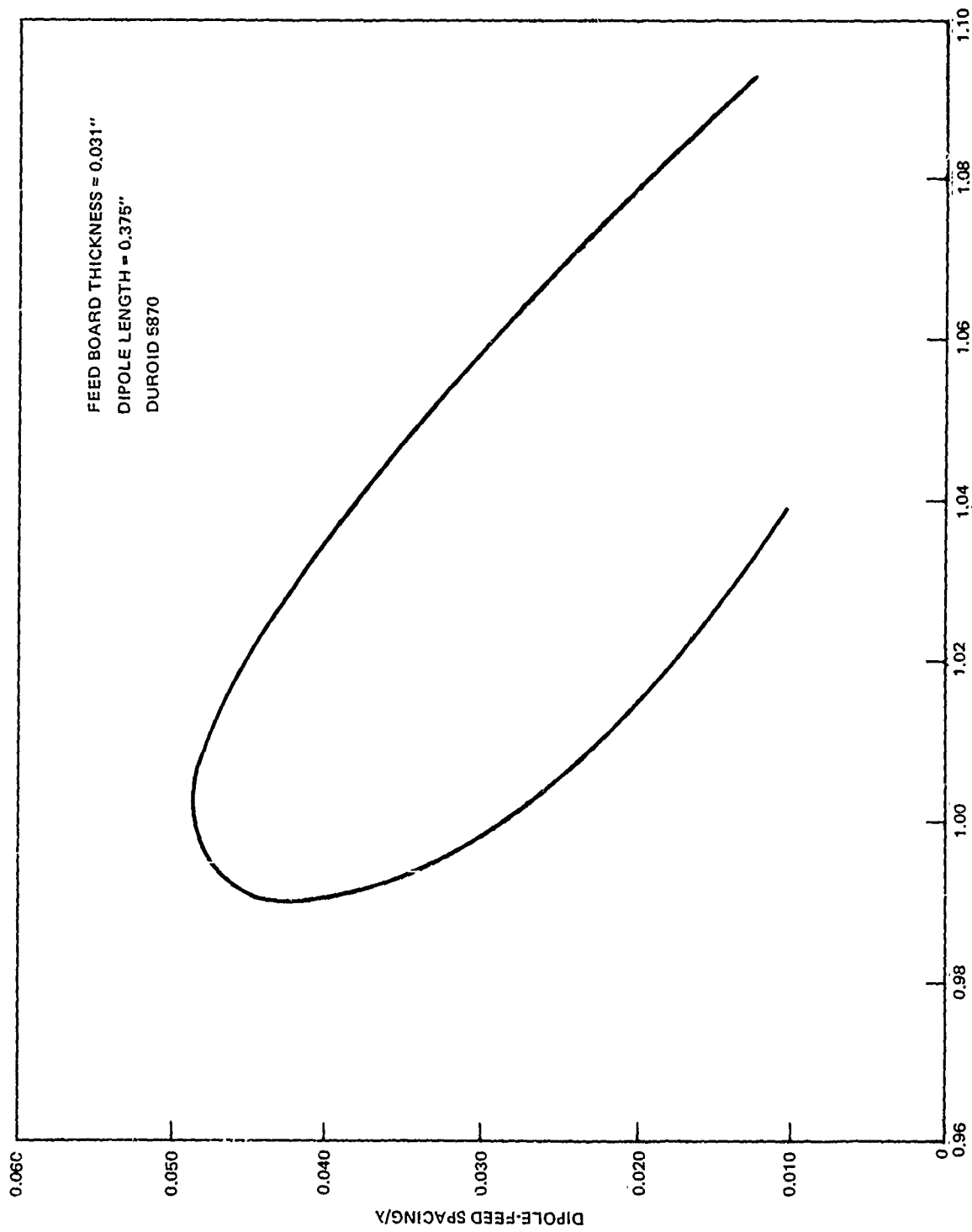


Figure 1. Geometry of the Element and Its Feed



17-4

Figure 2. Dipole-Feed Spacing Vs. Frequency for a Match at Resonance

The measured principal plane radiation patterns of the microstrip dipole are shown in Figures 3 and 4. The H-plane pattern (Figure 4) is seen to possess the expected shape of a dipole over a ground plane. In contrast, the E-plane pattern (Figure 3) deviates substantially from that expected for a simple dipole placed above a ground plane. The pattern is seen to be much broader, to radiate significant energy along the ground plane, and to exhibit substantial scalloping. A slight asymmetry is also apparent. In fact, the microstrip dipole radiation pattern resembles the pattern of a conventional microstrip patch much more than that of a dipole above a ground plane. The reason for this, surprisingly, is that the microstrip dipole is in reality just a narrow microstrip patch.

The above assertion has been verified by liquid crystal tests which demonstrate the prime radiation regions of the microstrip dipole to be at its two ends. Further tests where the dipole has been sequentially widened until it has a square shape have all exhibited the same radiation regions. This, then explains the basic pattern shape. The E-plane scalloping is due to diffraction of the substantial radiation directed along the ground plane from the edges of the finite backing plate, while the slight asymmetry is due to the presence of the feed line.

As is well known, reduction of the width of the two radiation regions lowers their equivalent radiation conductances [2]. For structures as narrow as the microstrip dipole, these conductances are so low that conventional feeding and impedance matching techniques which are used with ordinary microstrip patches are ineffective. However, the use of electromagnetic coupling provides a very effective impedance transformation technique. This method of feeding allows the low input impedance of the microstrip dipole to be matched where other techniques would fail. It is of interest to note that the equivalent circuit of the dipole-feed coupling region is actually given by a transformer plus a series open-circuited stub [3]. When the coupling region is a quarter-wave in length, the stub effectively disappears. This corresponds to the configuration of maximum coupling mentioned earlier.

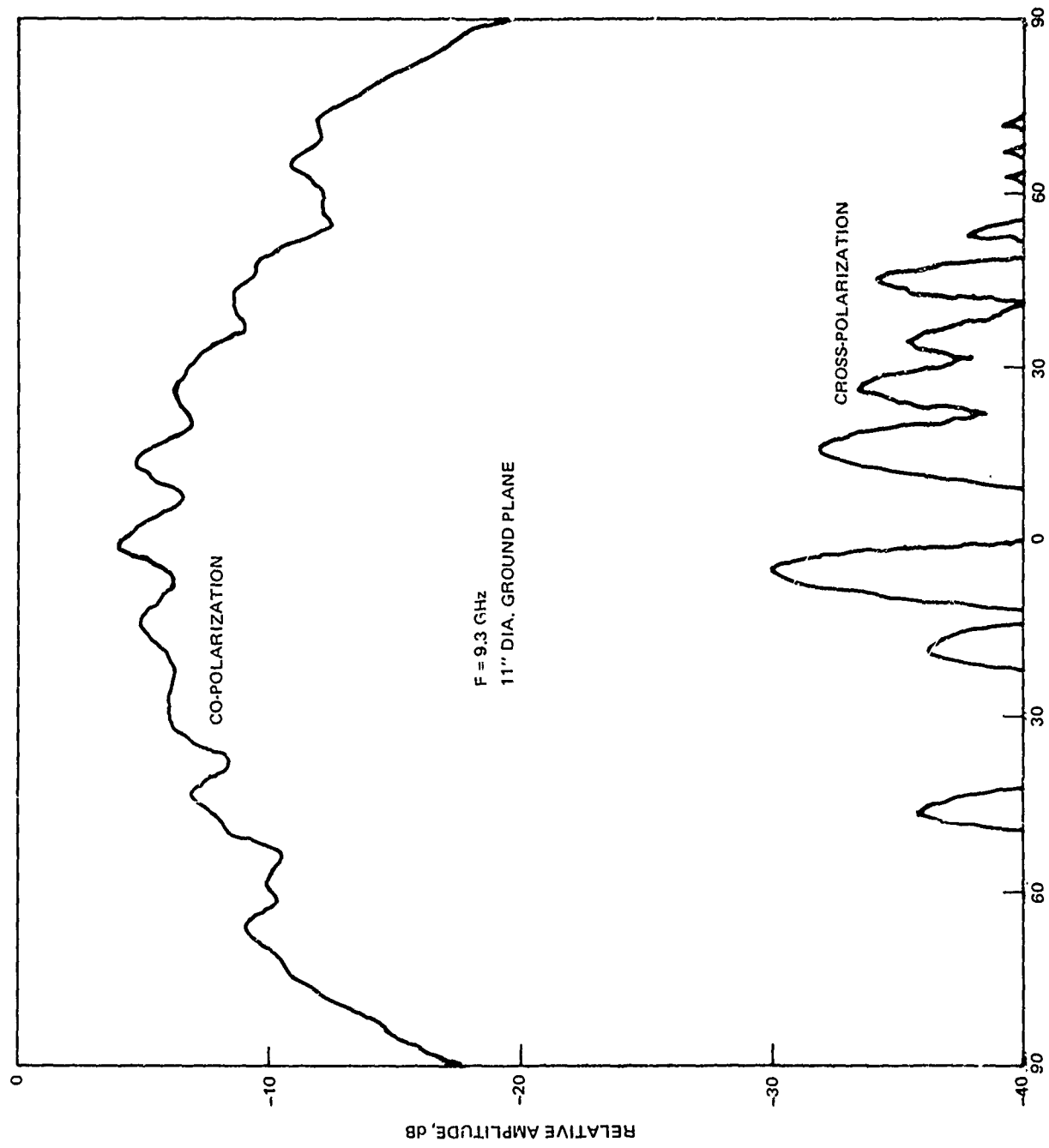


Figure 3. Measured Element E-Plane Pattern

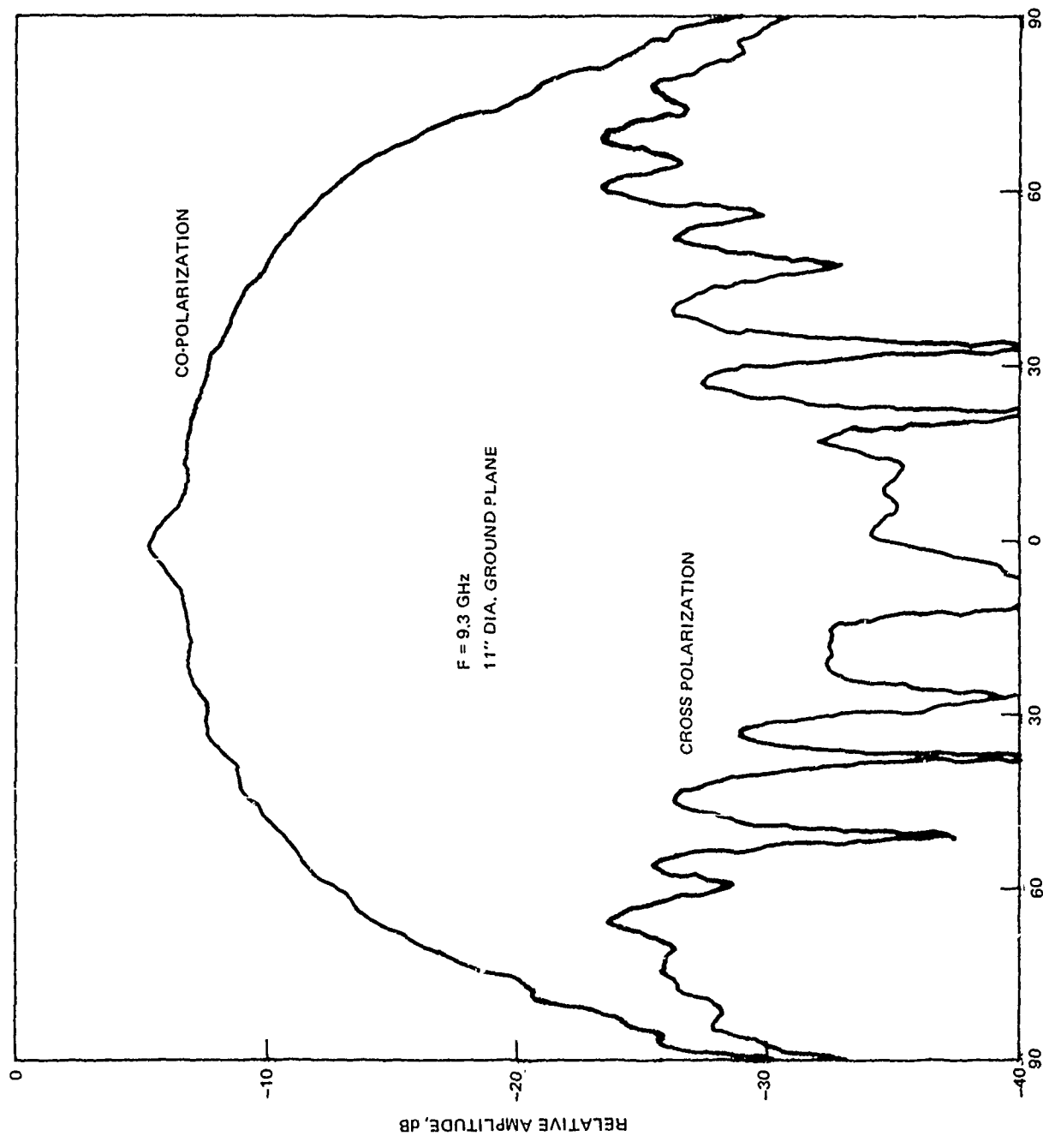


Figure 4. Measured Element H-Plane Pattern

As with the microstrip patch, a complete theoretical solution for the microstrip dipole is very complicated. The situation is in fact somewhat worse for the latter due to the nature of the feed. Since a full solution using the pertinent Green's functions was considered too difficult, it was decided to analyze a simplified model in order to particularly gain some insight into the feed-dipole coupling. To this end, a model which ignores the dielectric boundary and assumes filamentary currents (instead of strips) was examined. Such a geometry can be analyzed in a straight forward manner using the moment method.

The results from this study verified the shape and nature of the coupling curve in Figure 2. Figure 5 displays the resultant feed line and dipole current distributions which were calculated for the case of optimum coupling. As the overlap or feed-dipole spacing is varied from this configuration, calculations show the dipole current amplitude is reduced while standing waves begin to appear on the feed line. This, of course, is exactly as expected.

3.0 A MICROSTRIP DIPOLE ARRAY

A 3.5λ diameter X-band monopulse array consisting of 24 elements distributed equally among 4 quadrants was constructed using the above described microstrip dipole. A picture of the array is shown in Figure 6. Since the antenna was constructed from polystyrene (Rexolite), it is sufficiently transparent to allow both the dipoles and their underlying feed network to be viewed.

The 24 elements are seen to be distributed among three rings. The rings themselves have been slightly distorted in shape to provide the optimum theoretical radiation pattern. A separate corporate feed is used to excite each quadrant. The feed is seen to consist of an input three-way power divider followed by three binary power dividers. All power dividers are designed to give equal power division. Ideally, all dipoles are thus excited with equal phase and amplitude. Since a peak sidelobe level below that achievable with a uniform aperture distribution was desired, the dipole positions were chosen to yield the lowest possible sidelobe level compatible with uniform excitation coefficients.

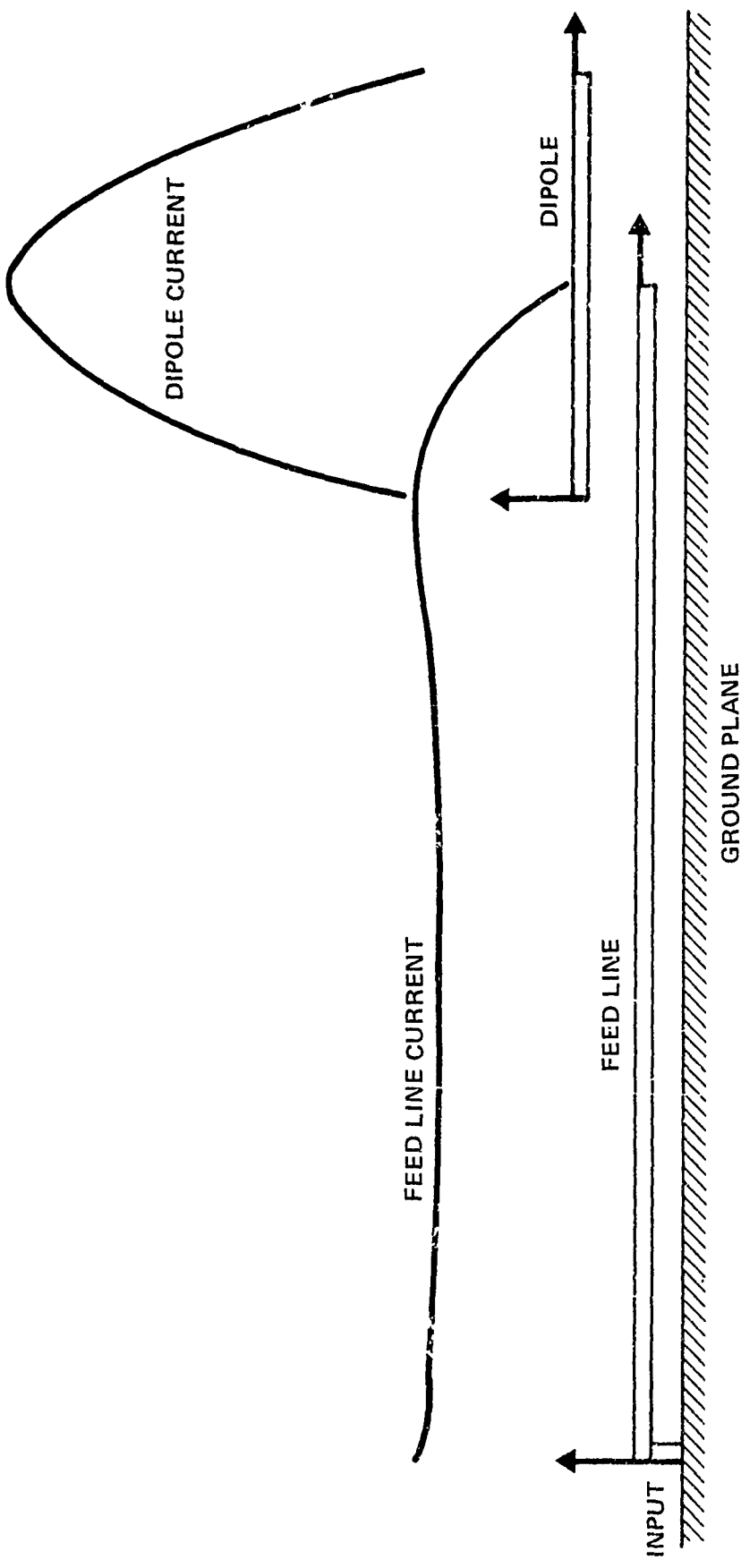


Figure 5 Current Distribution for Matched Resonant Dipole Excitation

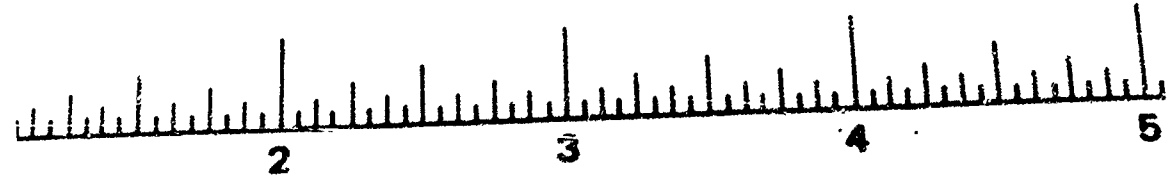
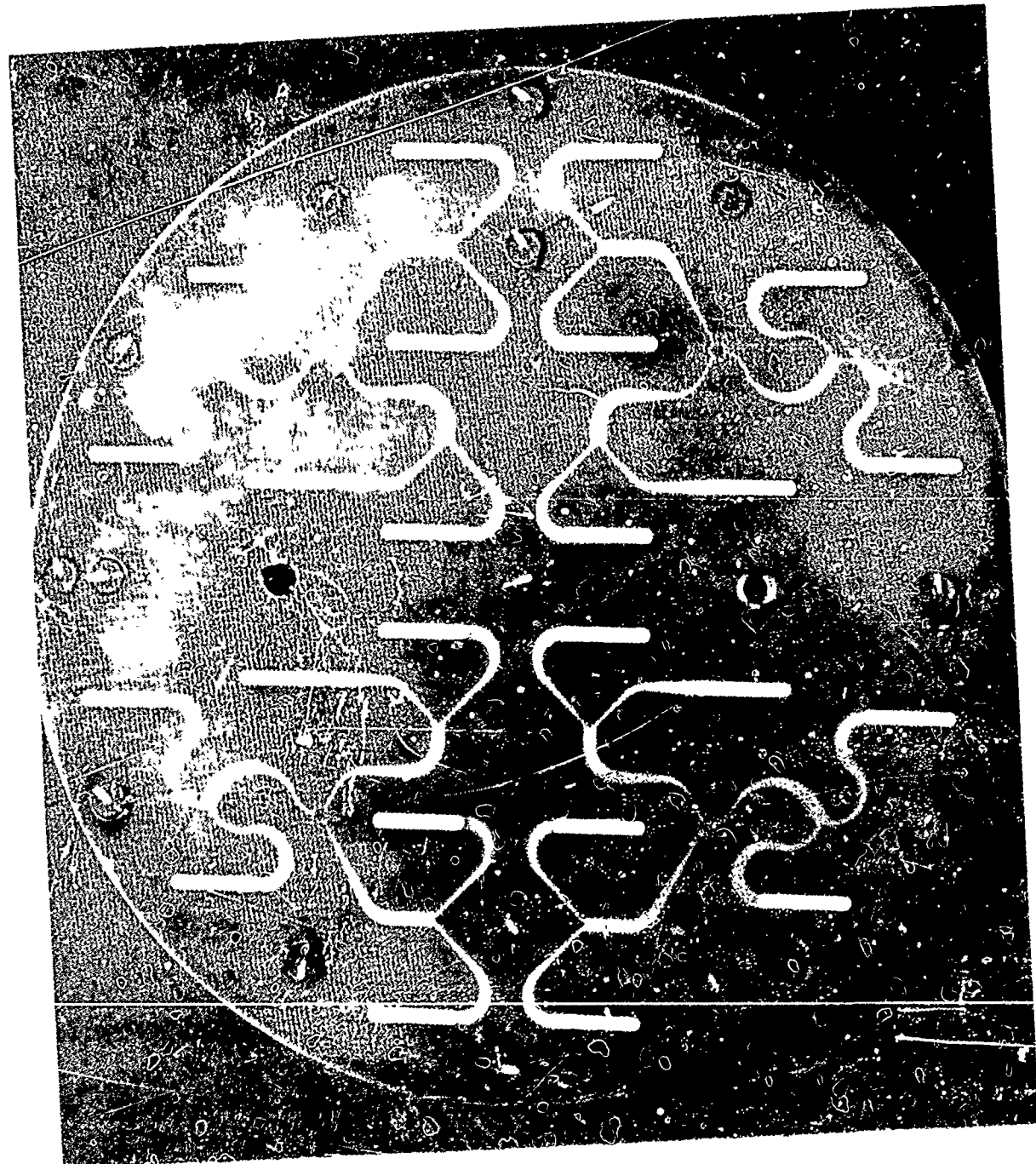


Figure 6. The 24-Element Microstrip Dipole Array

The resultant optimum theoretical radiation pattern is shown in Figure 7. Both the directivity and sidelobe level are seen to be better than 20 dB, exceeding the design goal of 19 dB for each.

Measured principal plane patterns from one of several such antennas constructed are shown in Figures 8 and 9. These patterns are average, being neither the best nor worse measured. The peak sidelobe level is approximately the same in both planes, being about 17.5 dB. Since this is what is expected from a uniformly illuminated aperture, it is apparent that the desired excitation coefficients were not achieved. Pattern integrity is satisfactory in both planes; however, a sum-and-difference network asymmetry is apparent in the H-plane pattern. The measured gain was found to be 19.7 dB, corresponding to an aperture efficiency of 77 percent.

While the gain exceeded the design goal, the sidelobe level failed to meet it. A diagnostic program including both experimental and computer simulation aspects was thus undertaken. Liquid crystal experiments involving the entire array were somewhat disappointing. The H-plane quadrant excitation asymmetry was verified, as was the fact that the dipoles were not uniformly excited. However, consistent results of comparative dipole excitations did not agree from quadrant to quadrant. Since all quadrant corporate feeds were identical, this appeared to be an anomalous result.

Detailed measurement of the array excitation coefficients were then made using a near-field probe facility. The results were averaged for corresponding dipoles over the four quadrants to suppress comparator network errors. The resultant excitation coefficients for a typical quadrant are shown in Figure 10. Significant errors are shown to be present in the aperture distribution. Although some of the error is attributable to the probe itself, computer simulation of the patterns using the probe-derived excitation coefficients verifies the measured pattern shapes and relative sidelobe levels.

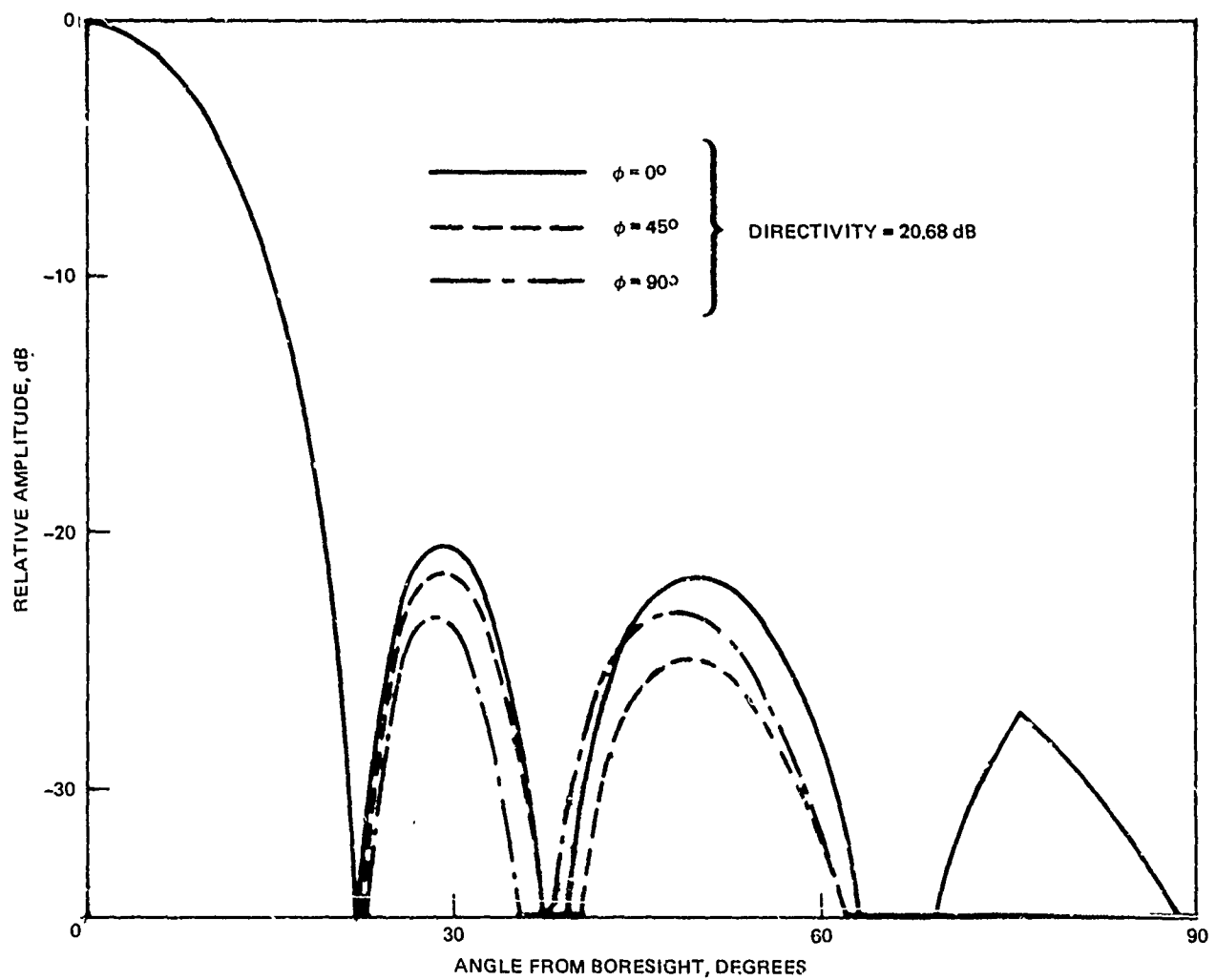


Figure 7. Theoretical Radiation Patterns of the 24-Element Array

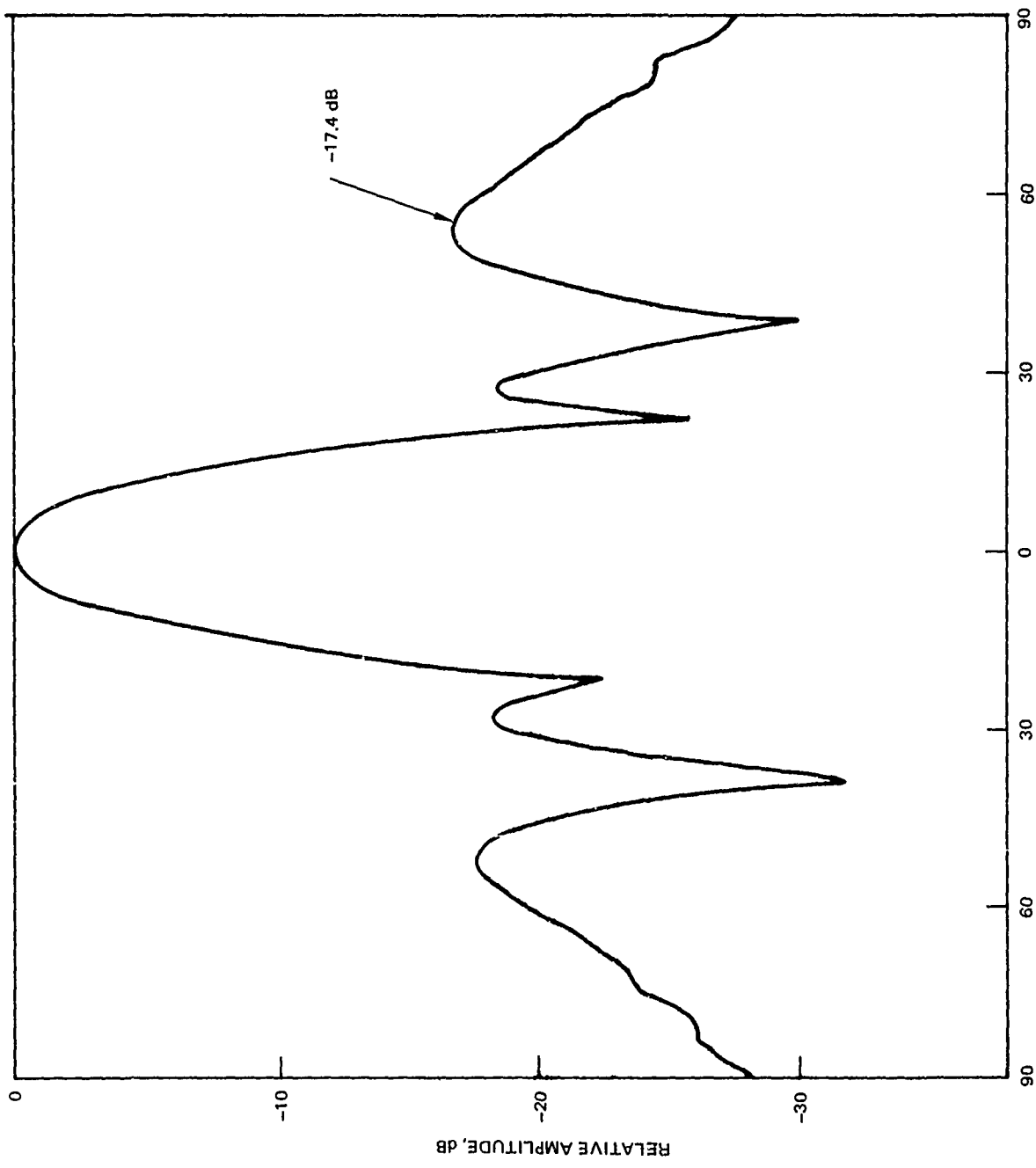


Figure 8. Measured Array E-Plane Pattern

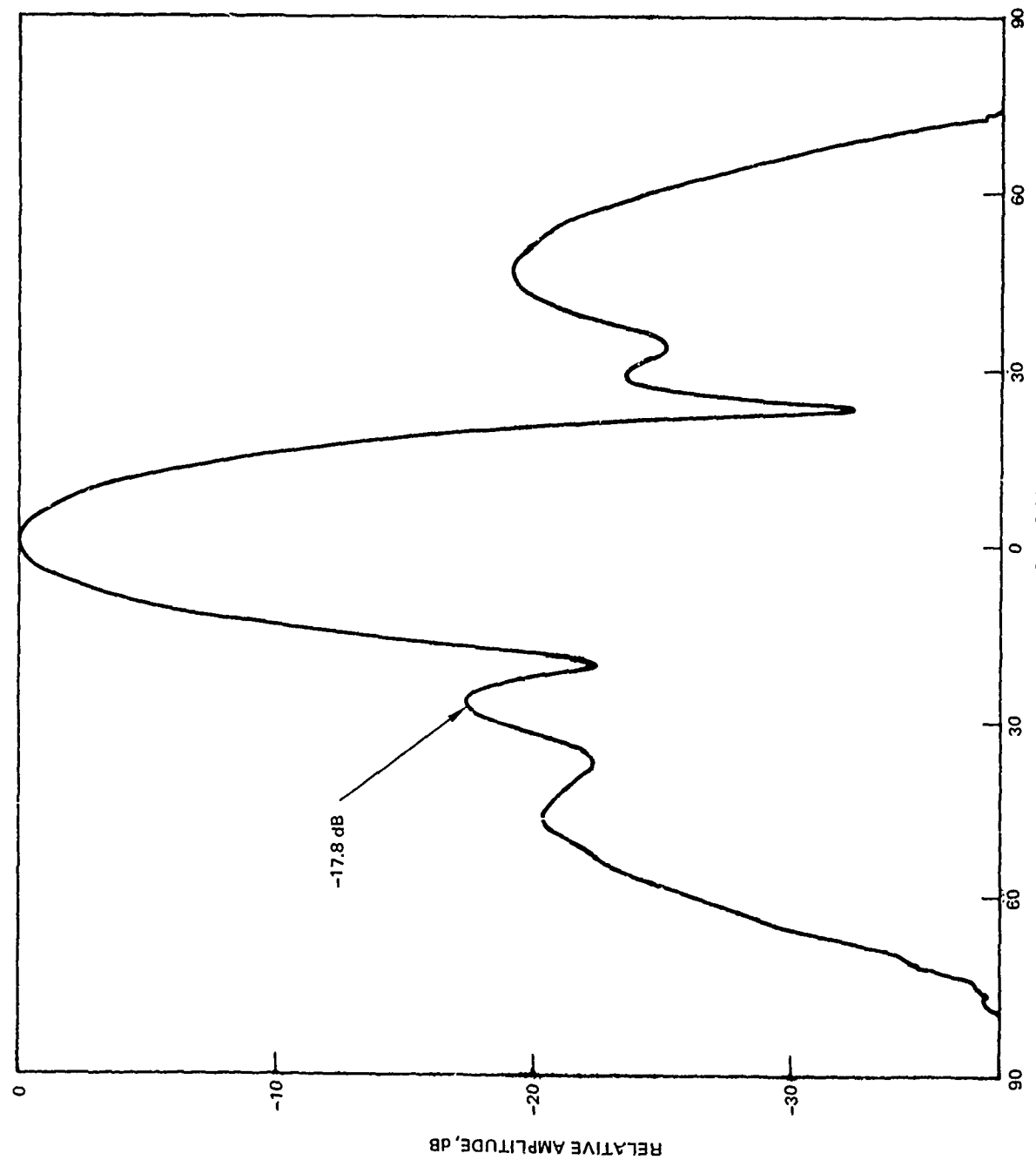


Figure 9. Measured Array H-Plane Pattern

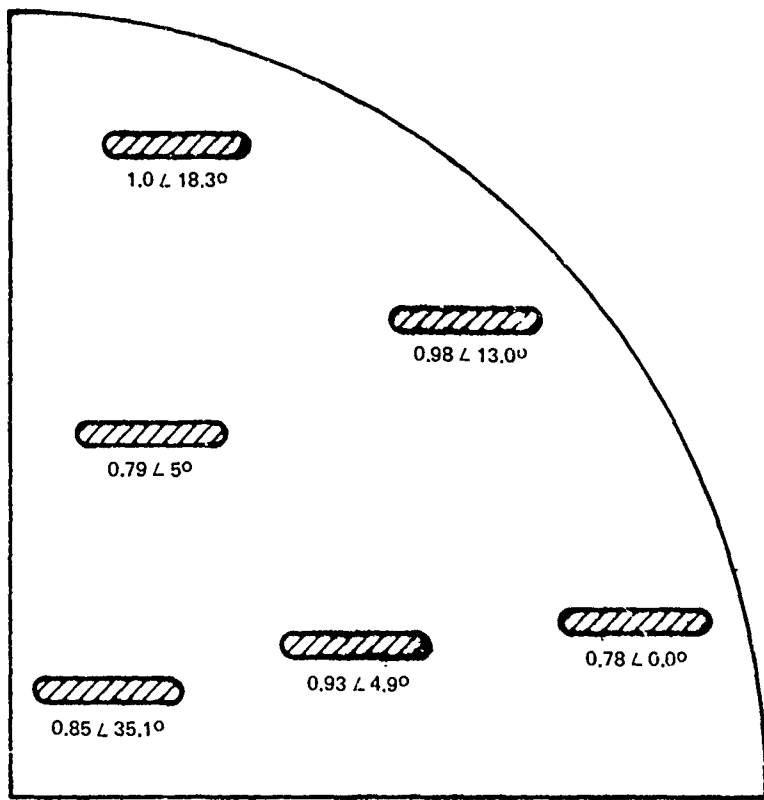


Figure 10. Dipole Excitation Coefficients Derived from Near-Field Probe

It is felt that mutual coupling, which was not compensated for in this design, plays a significant role in the pattern degradation. Since the array is quite small, none of the averaging of its effects which occur in large arrays will happen. Subsequent measurements of inter-element mutual coupling has verified the necessity to include it in the design of small arrays of microstrip dipoles.

4.0 CONCLUSIONS

The microstrip dipole has been shown to be a useful printed circuit radiator, particularly suited for those applications where small size is at a premium. When antenna diameters drop below about 4.0λ , very few high performance, low profile candidates exist. Slotted waveguides must be loaded, and even then have not yielded good results. Short backfire arrays have comparable gain and better sidelobes for the same size, but their thickness is a half wavelength. The microstrip dipole array thus is an excellent choice for this application. Of course, the versatility provided by the electromagnetic coupled feed opens the door to a number of other applications.

5.0 ACKNOWLEDGEMENTS

The Author wishes to thank George Oltman, inventor of the EM-coupled microstrip dipole and long time advocate of the element for his help and encouragement through many years. Thanks also go to Al Clavin and the antenna staff of the Microwave Department for providing many enlightening discussions and important experimental results.

6.0 BIBLIOGRAPHY

1. Oltman, Jr., H. G., U.S. Patent 4,054,874, Oct. 18, 1977.
2. Derneryd, Anders G., Trans. IEEE, Vol. AP-24, pp. 846-851, Nov. 1976.
3. Matthaei, G. L. et. al., Design of Microwave Filters, Impedance-Matching Networks, And Coupling Structures, Vol. I, AD402852, January 1963.

SEASAT AND SIR-A MICROSTRIP ANTENNAS

L. R. MURPHY
BALL AEROSPACE SYSTEMS DIVISION
BOULDER, COLORADO 80306

SUMMARY

The SEASAT and SIR-A antennas are parts of a space-borne imaging radar system used for ocean and land surveillance. Both are L-band and planar arrays using microstrip patch elements. The SEASAT antenna, the largest array ever flown in space, was launched in June, 1978 and operated successfully until spacecraft failure in October, 1978. The SIR-A antenna is scheduled to fly aboard the second space shuttle flight.

The design and fabrication of these antennas was the combined effort of many different engineering disciplines. The fabrication of the antennas was different for their individual mission requirements.

This paper will discuss the mission requirement differences of the antennas, the fabrication differences of the antennas, the performance of the two antennas, and the techniques used to accomplish the antenna gain and sidelobe performance.

This paper presents the results of one phase of research carried out by the Jet Propulsion Laboratory, California Institute of Technology (SEASAT) and by the NASA Johnson Space Center (SIR-A).

1.0 DESCRIPTION OF SEASAT AND SIR-A ANTENNAS

The SEASAT and Shuttle Imaging Radar (SIR-A) antennas are large planar arrays which are a part of the Synthetic Aperture Radars (SAR) of the SEASAT-A satellite and OSTA-1 instrument sets. These instruments are capable of generating imagery of the ocean and land surface with

resolution of 25m and 40m respectively. This resolution can be obtained by processing of the received reflected signals in a manner such that a large effective or synthetic aperture is obtained.

The operational missions of the SEASAT and SIR-A antennas are quite different. The SEASAT antenna was required to be stowed in a folded configuration during the satellite launch and deployed in orbit.^[1] The SIR-A antenna is to be launched in a deployed configuration within the bay of the Space Shuttle. Both antennas, therefore, were required to be low-weight, low-volume, high-efficiency radiators; but with the capability to withstand entirely different structural loads.

The SEASAT and SIR-A antennas are among the largest arrays to be designed to be flown in space. The deployed radiating surface of the SEASAT antenna is 10.74m x 2.16m and the measured gain at 1,275 MHz is 34.9 dB. The SIR-A antenna radiating surface is 9.4m x 2.16m and the measured gain at 1,278 MHz was 33.8 dB. These antennas were both fabricated from 2.16m x 1.25m x 0.6cm antenna panels, with 128 microstrip elements per panel. The SEASAT antenna consisted of eight panels supported on an extendable graphite epoxy structure. The SIR-A antenna consisted of seven panels supported by an aluminum tube truss structure.^[3]

The basic electrical schematic of both the SEASAT and SIR-A antennas is a large corporate feed system feeding individual antenna panels of 128 corporately-fed microstrip radiating elements. The actual corporate feed and individual antenna panels of the two antennas are different in order to accommodate the difference in the required missions. This paper will describe the difference between the antennas, list the achieved performance, and discuss the unique design and fabrication techniques used to meet the performance requirements.

2.0 SYSTEM REQUIREMENTS

The system mechanical requirements of both the SEASAT and SIR-A were quite extensive. However, because this paper is being presented at a printed circuit antenna technology workshop, the system mechanical requirements will be presented in brevity to flavor the effects and requirements upon the antenna electrical design.^[2]

The SEASAT antenna had a folded dimensional envelope of 258cm x 163cm x 22cm. This volume included:

1. The launch restraint mechanism
2. Biaxial deployment mechanism
3. Deployment interface coaxial cable
4. Extendable support structure (ESS)
5. Microstrip panels
6. Corporate feed network
7. Antenna thermal blankets

Figure 1, a back view of the antenna before thermal blanket installation, shows these components on the extended antenna. The outstanding feature of this mechanical design was the fact that the above small volume, upon completion of the seven-minute antenna extension, was deployed to provide 10.74m x 2.16m array flat to within $\pm 0.23\text{cm}$. Figure 2 shows the SEASAT antenna folded.

The SIR-A antenna panels are mounted on an antenna truss of aluminum tubing which is mounted on a pallet truss designed for mounting directly to a single European Space Agency (ESA) shuttle payload pallet structure. The antenna will be positioned 2.8 meters above the pallet floor and will, upon opening of the shuttle bay doors, have an unobstructed field-of-view.

The SIR-A antenna mechanical structure has been designed to withstand the dynamic performance of the space shuttle while providing an antenna surface flatness in orbit of $\pm 0.1\text{cm}$. It is planned that this antenna can, with minor refurbishment, be used on additional shuttle flights.

Table 1 lists the antenna performance requirements and achievements of both antennas. The particular parameters which required the most design effort were the antenna gain and power handling capability. The antenna gain required the development of a unique low-loss substrate material which would provide a highly efficient antenna panel. Additionally, it would be required that the developed technique produce antenna panels which could be repeatedly fabricated such as to obtain the required phase and amplitude of the large-spaced seven and eight-element panel arrays.

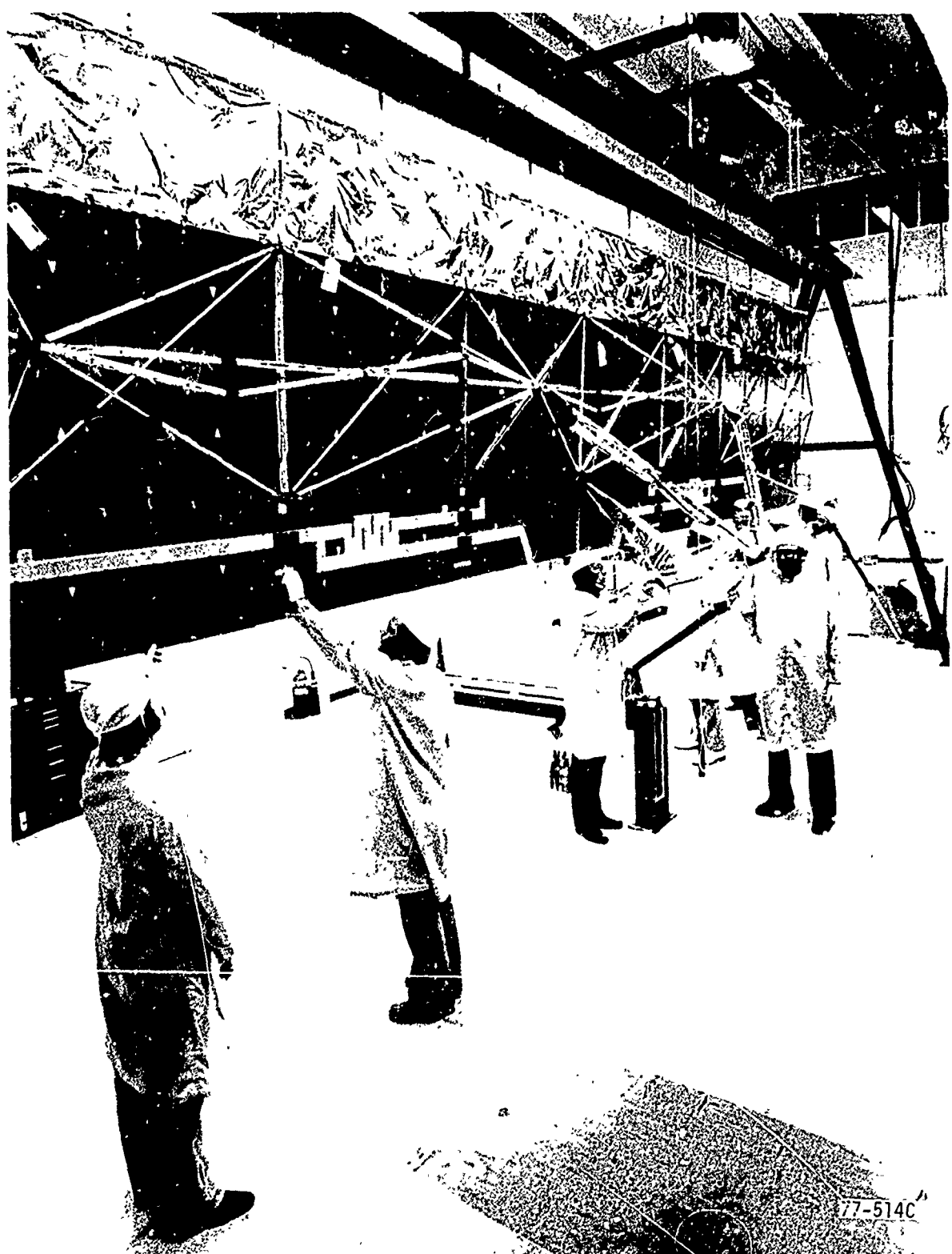


Figure 1 SEASAT Antenna Before Thermal Blanket Installation
(View from Back of Antenna)

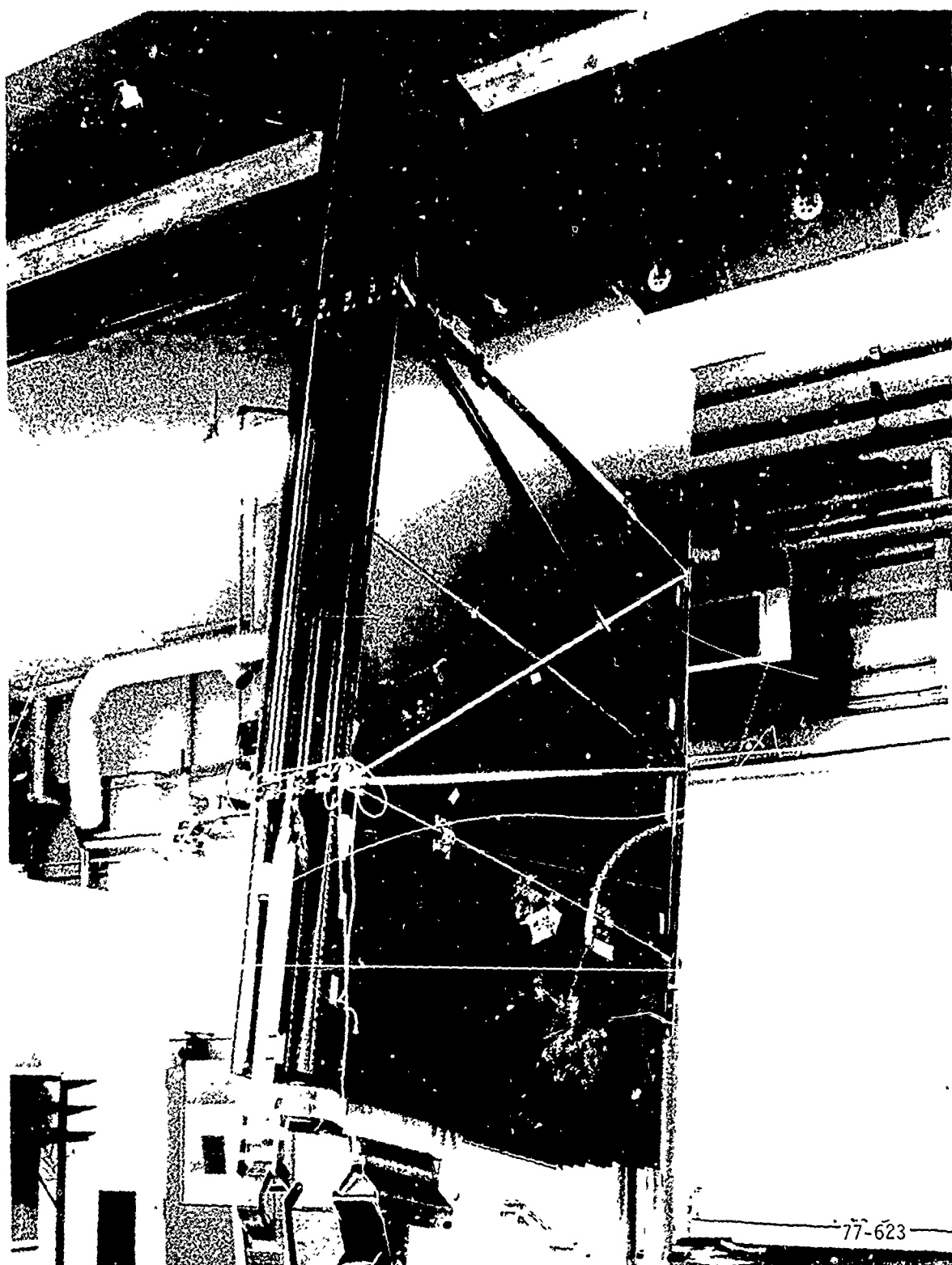


Figure 2 Folded SEASAT Antenna

TABLE 1
SAR ANTENNA PERFORMANCE PARAMETERS

Parameter	SEASAT		SIR-A	
	Specification	Achieved	Specification	Achieved
Operating Frequency, MHz	1,275 MHz	1,275 MHz	1,278 MHz	1,278 MHz
Bandwidth, MHz	± 11 MHz	± 11 MHz	± 4 MHz	± 4 MHz
Gain, dB	34.9 dB	34.9 dB	≥ 33.0 dB	33.85 dB
VSWR	1.5:1	<1.5:1	1.5:1	<1.5:1
Beamwidth E-plane (-8 dB point), degrees	$1.2^\circ \leq \text{BW}$ $\leq 1.73^\circ$	1.7°	$1.4^\circ \leq \text{BW}$ $\leq 2.2^\circ$	1.99°
Beamwidth H-plane (-2, -4 dB points), degrees	$6.2 \pm 0.1^\circ$	6.2°	$6.2 \pm 0.1^\circ$	6.03°
Polarization purity, dB	<-20	-25.7	<-20	<-31
Sidelobes E-plane, dB	<-12.5	-12.8	First SL ≤ -14.5 dB Others to $40^\circ \leq -16$	-12, -18 dB ≤ -18.5 dB
Sidelobes H-plane, dB	<-12.5	-17.1	First SL ≤ -14.5 dB Others to $40^\circ \leq -16$	≤ -17.5 ≤ -21
Peak Power	1,500W	3,000W	3 dB above 950W	3 dB above 950W
Weight, kg	<107	103	<220	184

The design of the corporate feed structure required that the feed cable provide low-loss and the capability of withstanding of relatively high power levels without multipacting. This specification required special venting of all coaxial connectors and power dividers. The type of 7/8-inch coaxial cable used in the high power leads of the SIR-A antenna was selected to match the coax center conductor construction with the antenna thermal environment. The SEASAT antenna required the development of unique suspended substrate feed system with an even more unique technique of providing a flexible suspended substrate for the folding of the antenna.

3.0 PANEL AND FEED CONSTRUCTION/DESCRIPTION

The substrate material for the SAR antennas had to be light-weight, structurally strong, and provide a low-loss, highly efficient and repeatable antenna panel. The honeycomb structure construction shown in Figure 3 was selected because it provided the required structural strength and, while the loss tangents of the epoxy fiberglass sheets and honeycomb material is relatively high, the substrate loss is small because of the large percentage of voids in the honeycomb. The relative dielectric constant of the SIR-A substrate was measured to be 1.18. Therefore, small percentage changes of dielectric constant would not greatly effect the panel-to-panel antenna repeatability.

Figure 3 shows a cut-away view of both the SEASAT and SIR-A antennas. The final antenna panel constructions were different to conform with the different antenna mission requirements. Table 2 lists the antenna fabrication differences between the SEASAT and SIR-A panels.

The corporate feed network of the two SAR antennas were also quite different; again, to satisfy different mission requirements. Figures 1 and 4 are versions of the back side of the SIR-A and SEASAT antennas. The SIR-A antenna feed network incorporated 7/8 and 1/2-inch coaxial cable in a seven-way power divider which provided an amplitude taper to the outside panels. The actual coaxial cable selected was chosen for the dielectric support material and center conductor construction for thermal dissipation. The individual components and the total flight system were power/altitude tested for peak power handling capability.

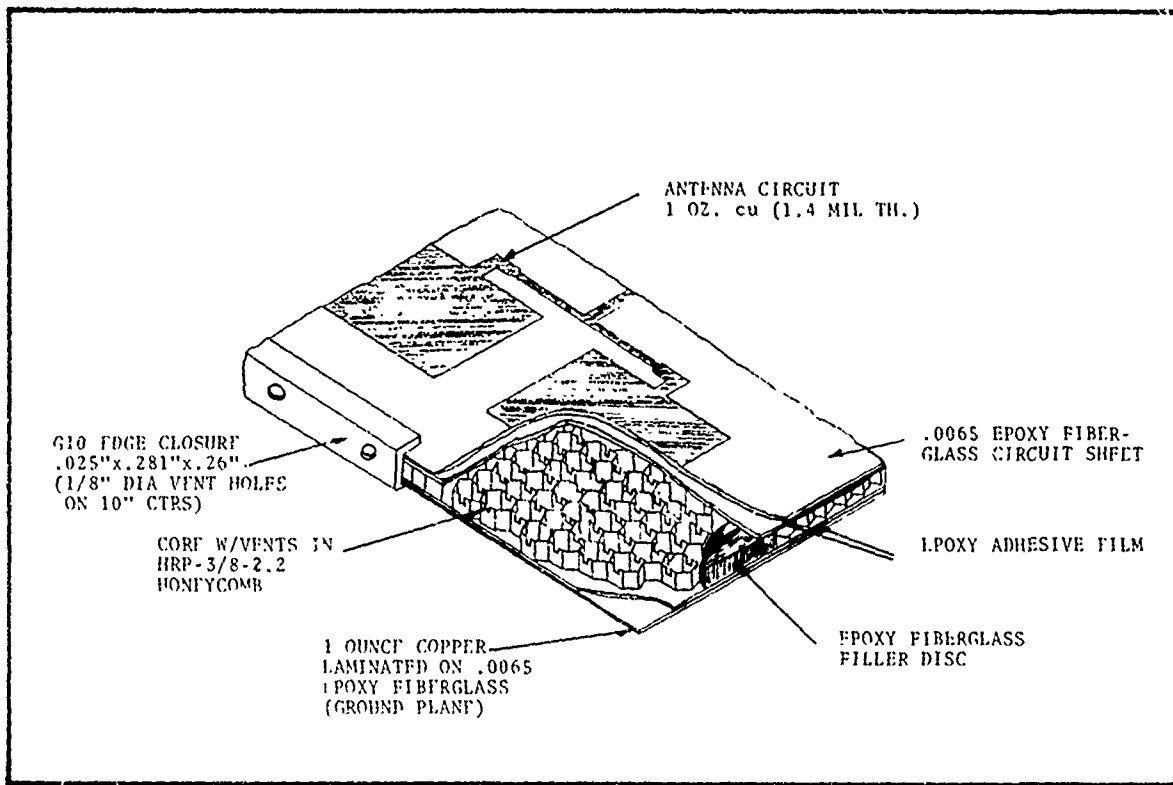


Figure 3a SIR-A Antenna Panel

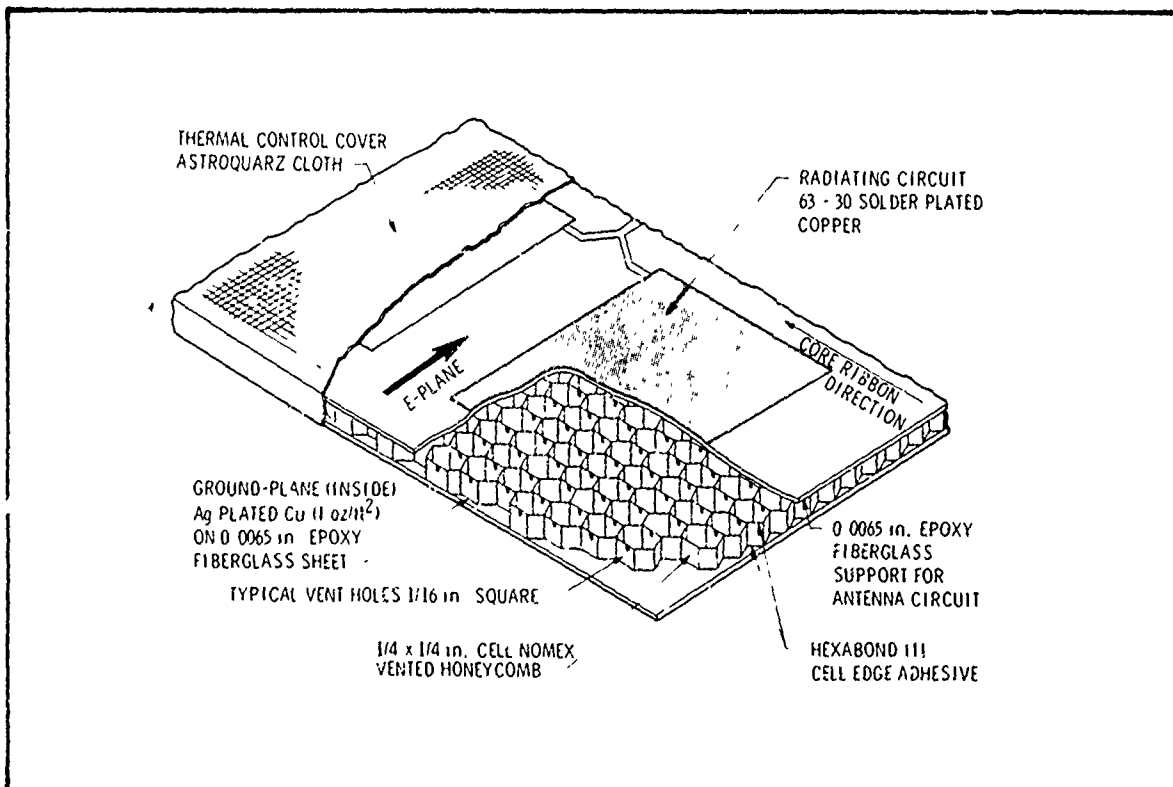


Figure 3b SEASAT Antenna Panel

TABLE 2
SEASAT AND SIR-A DIFFERENCES

SEASAT		SIR-A	
	Panel Advantages		Panel Advantages
Coax feed at 4x4 level	Gain	Full microstrip	Strength
Mounting plates glued to back of antenna	Truss Fabrication	Internally bonded G-10 inserts	Truss Fabrication
Ground plane silver-plated and bonded on honeycomb side	Gain	Copper ground plane outward facing	Strength
Side feed element	Gain	End feed element	----
Astroquartz glass thermo cover	----	Beta cloth cover w/element standoffs	Thermal Control
Honeycomb edge dip adhesive	Gain	Epoxy adhesive film	Strength
Open panel edges	Weight	G-10 edge closure	Strength
1/4 x 1/4-inch cell Nomex honeycomb	Gain	1/4 x 3/8-inch cell HRP honeycomb	----

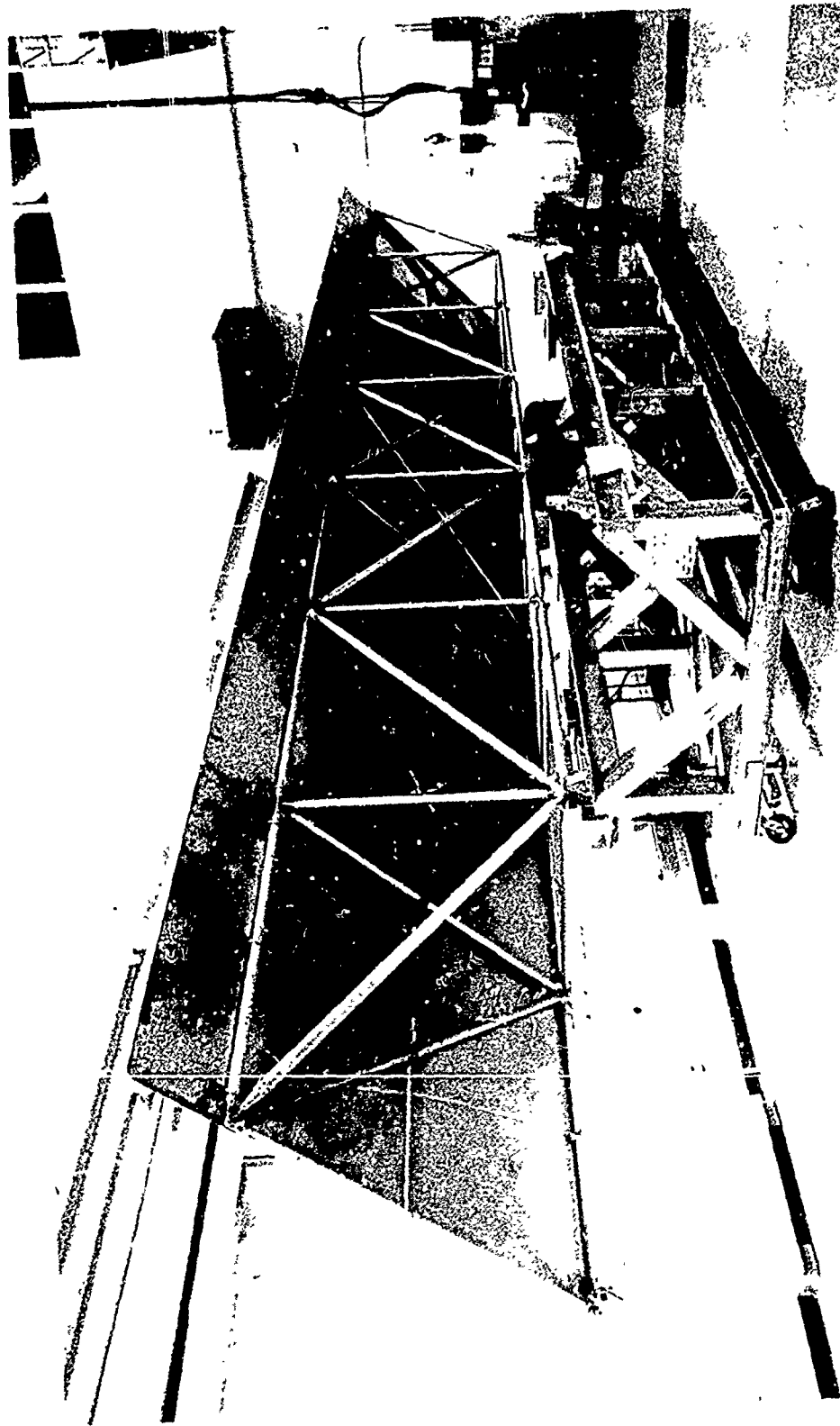
The SEASAT feed network requirements specified a feed system with low-loss, low folded volume, and the capability to obtain the flexible 180° bends in the folded condition.^[4] The selection of suspended substrate feed lines provided an optimum design which satisfied both the mechanical and electrical requirements.

4.0 DESIGN AND CONSTRUCTION TO MEET REQUIREMENTS

The previous sections of this paper have attempted to present an overview of the SAR antenna requirements and design approaches. This section will discuss some of the unique techniques and approaches to solve the problems of antenna gain and sidelobes.

4.1 GAIN

The antenna gain specifically for the SEASAT was a very critical parameter. The antenna gain of an antenna of this size is simply a direct



78-593C

Figure 4 SIR-A Antenna Before Thermal Blanket

18-10

function of the feed network and panel feed line losses. The original SEASAT panel construction was quite similar to that of the SIR-A antenna (Figure 5) with full microstrip construction. The gain of this panel was, however, approximately 1 dB below the expected value. In order to correct for this deficiency, three design modifications were made:

1. Reduction of feed coupling
2. Reduction of microstrip loss
3. Design of suspended substrate flexible joints

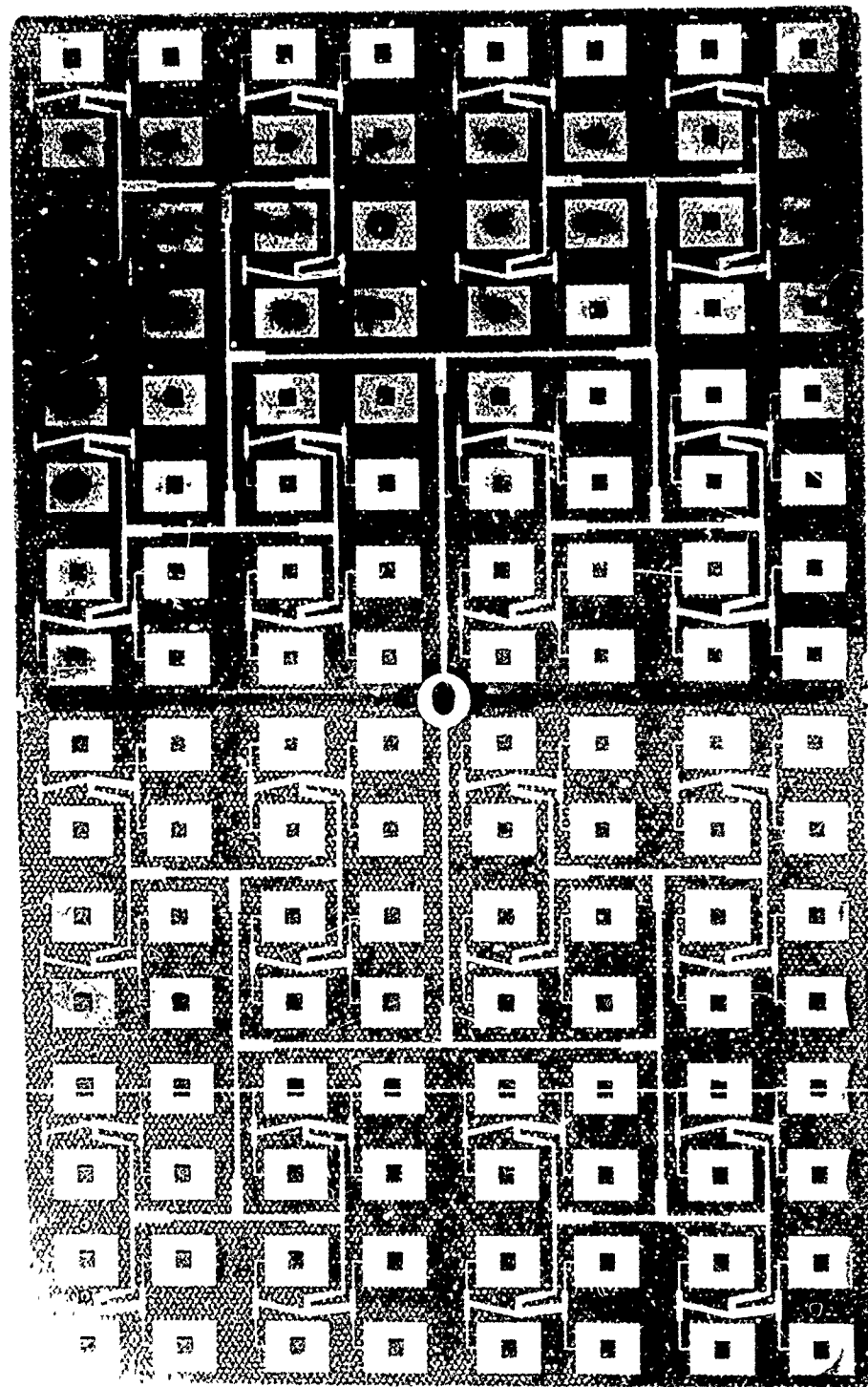
The coupling between the microstrip feed lines and the microstrip radiators on the antenna panels is of the order of -20 dB. However, some of the feed lines would carry 64 times the power of an individual radiator. The coupled energy from the high power feed lines tended to distort the antenna aperture distribution. The feed line sections to the antenna 4 x 4 element subarrays was, therefore, replaced with 0.6cm coaxial cable as shown in Figure 6.

In order to further reduce the loss of the honeycomb microstrip substrate four modifications of the SEASAT substrates were made:

1. Reversal of the ground plane to place the ground plane dielectric support outside of the substrate material
2. Silver plating of the copper ground plane
3. Replacement of the HRP honeycomb (fiberglass) by Nomex (nylon paper) honeycomb
4. Replacement of film adhesive bonding film by cell edge adhesive

These modifications of the microstrip substrate reduced the mechanical strength of the antenna panel in relation to original SIR-A-type construction. However, the mechanical strength was ample for the SEASAT mission.

The resultant effect of the antenna panels changes was to increase the gain of the antenna panel by 0.7 dB.



78-599C

Figure 5 SIR-A Antenna Panel

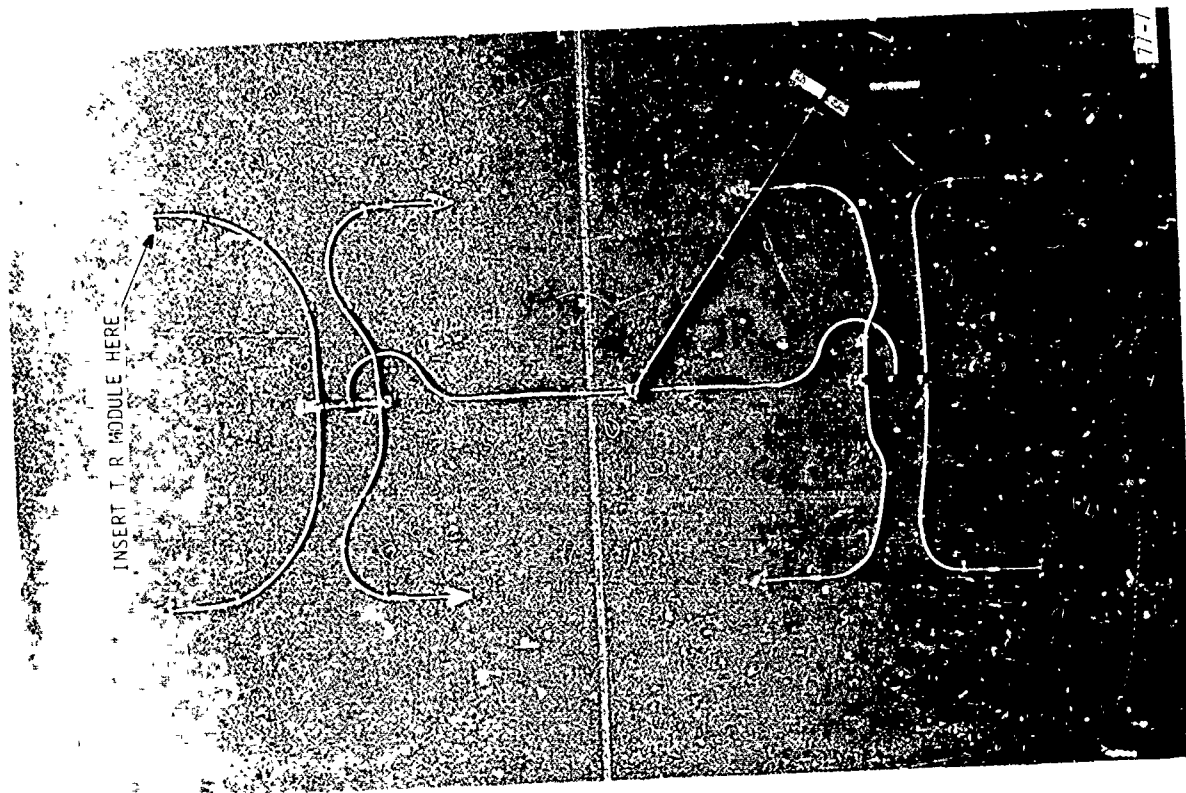
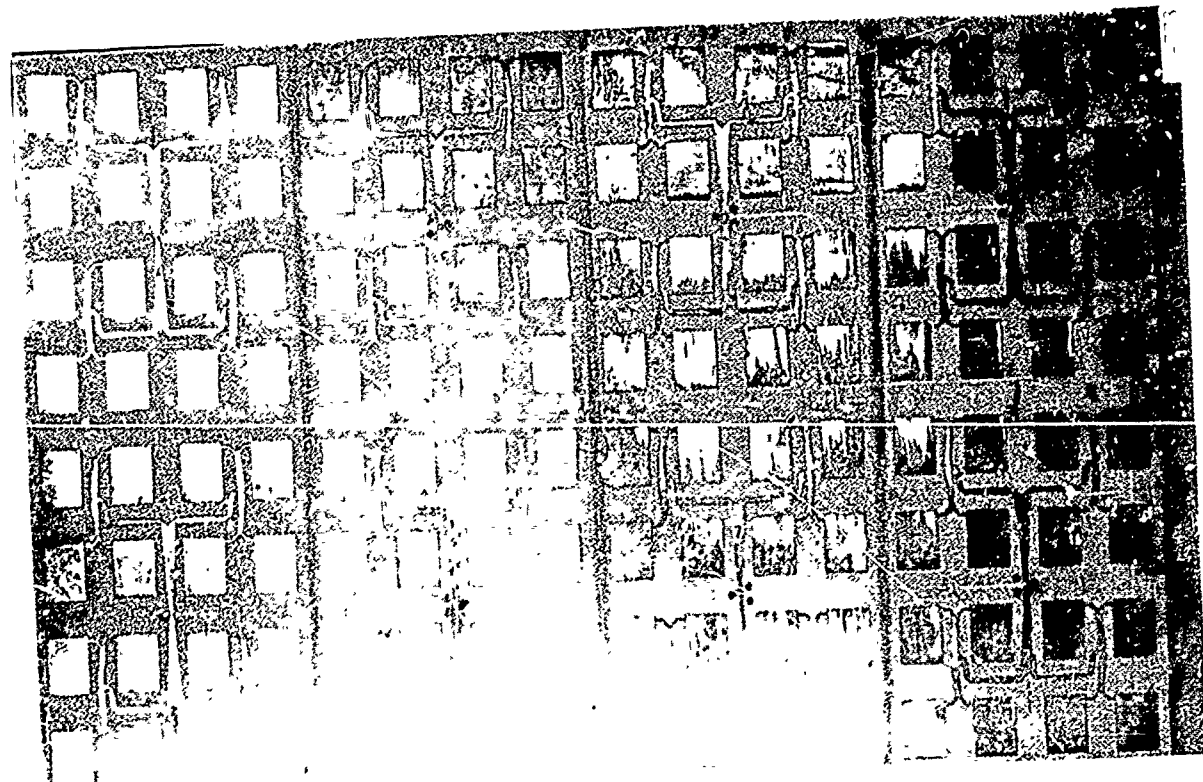


Figure 6 SEASAT Antenna Panel 1



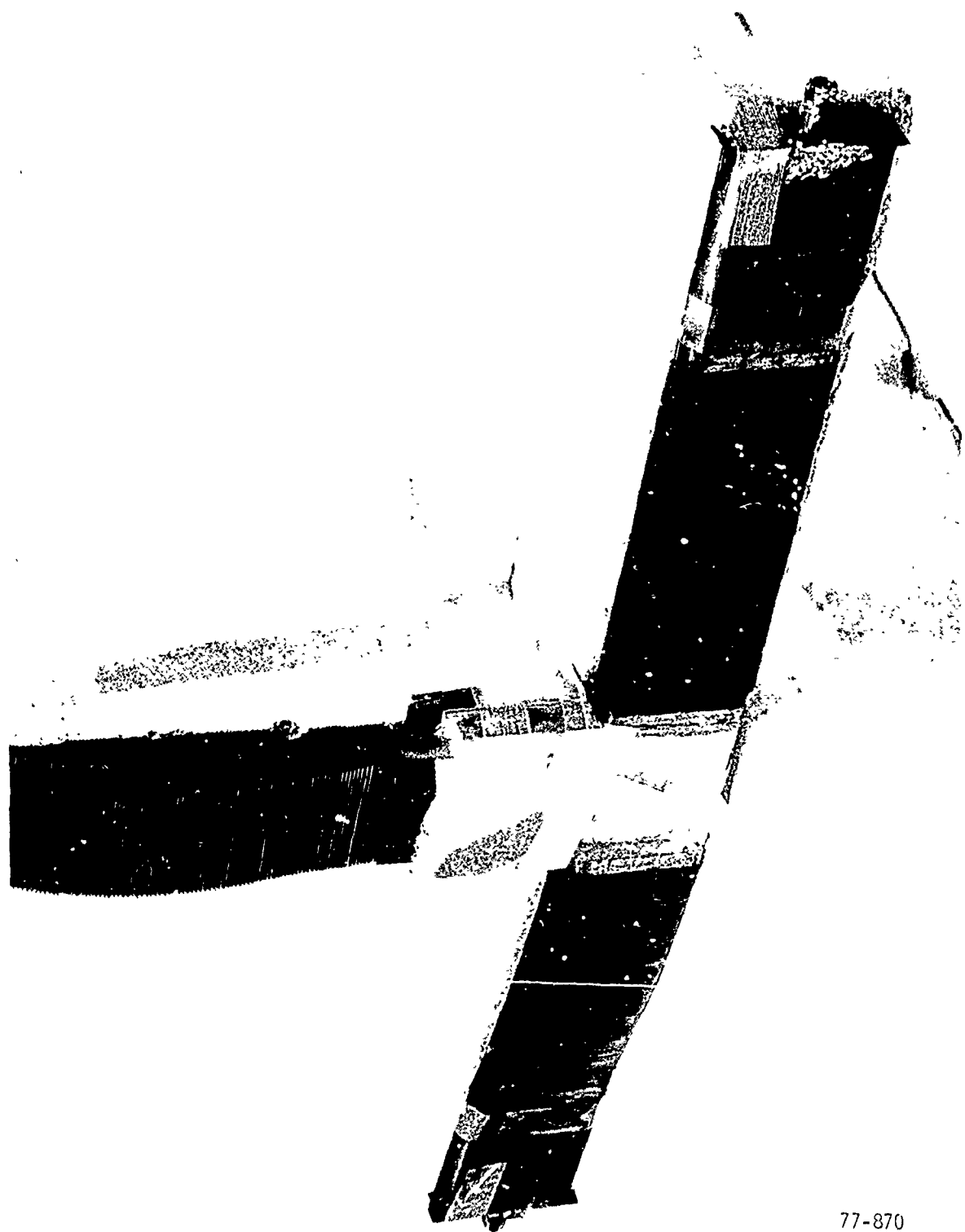
The original SEASAT antenna design was to have used flexible coaxial cable at the antenna fold joints. The tradeoff of small-sized coax for mechanical flexibility and cable loss was a large concern in the design of the SEASAT feed network. The solution to this problem was to create a flexible suspended substrate. Figure 7 shows a power divider with flexible suspended substrate or bellows inputs. The feed line was fabricated by bonding small wires between bellowed ground planes with center attachment to center suspended substrate. This arrangement provided a flexible feed system with connections only at the input and output ports and very low loss. The design goal for the loss of the feed network was 0.9 dB and the measured loss was only 0.6 dB.

4.2 SIDELOBES

The H-plane dimensions (2.16m) of both SAR antennas is larger than that required for antenna beamwidth. The H-plane was, therefore, amplitude tapered for beamwidth and sidelobe suppression. This task was accomplished by a four-step Taylor distribution with two types of unequal microstrip power dividers. The two halves of a panel are mirror images; all of the 4 x 4 element arrays within a panel are identical with an unequal power division within the 4 x 4; and an unequal power divider H-plane feeds the halves of a half-panel.

This process reduces the artwork design of the antenna to a 2 x 2 element block, two unequal power dividers, and the microstrip feed lines necessary to build up the panel. This process greatly enhances the repeatable antenna fabrication. The SEASAT antenna fabrication was different in that the power dividers combining the 4 x 4 element arrays was on the antenna backside. The H-plane sidelobes of both SAR antennas were less than -17 dB.

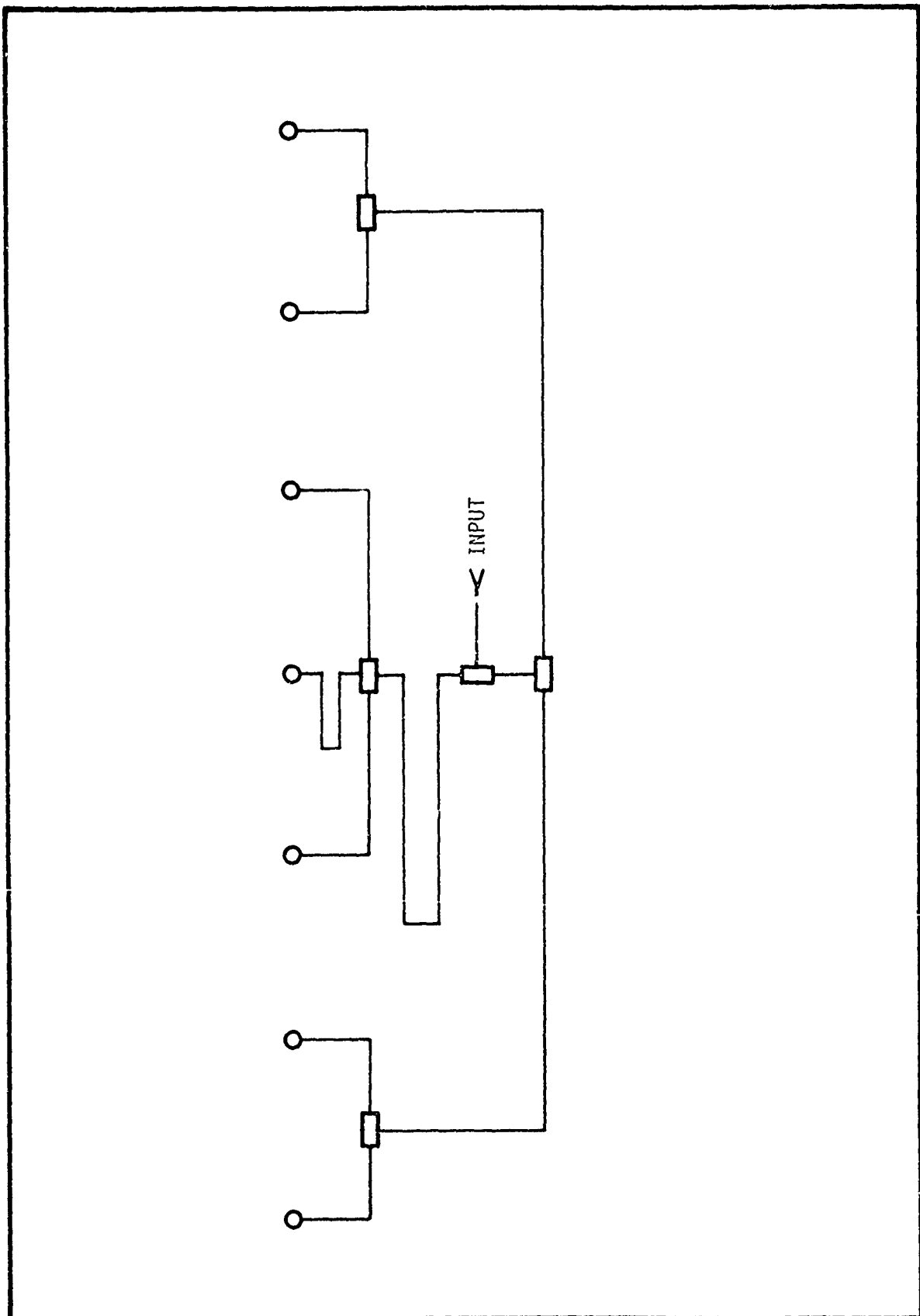
The SEASAT antenna had uniform E-plane (10.74m) distribution with -12.8 dB sidelobes. The SIR-A had a seven-way corporate power division (Figure 8) which should have provided E-plane sidelobes of less than -14.5 dB. The measured first sidelobes were, however, unbalanced -12 and -18 dB.



77-870

Figure 7 Suspended Substrate Power Divider with Bellows Input

Figure 8 SIR-A 7-Way Corporate Feed



The insertion phase through the SIR-A antenna was measured by a near field probe and is shown in Table 3. Two of the antenna panels showed a phase delta of greater than -14° from the average of the other panels. The insertion phase of the flight feed system had been measured to be within $\pm 3^\circ$. Careful investigation of the material used in the fabrication of these panels showed that these panels had been made with an adhesive of density 0.18 kg/m^2 (0.039 lb/ft^2) instead of 0.15 kg/m^2 (0.030 lb/ft^2). This small change caused a less than one percent change in the substrate dielectric constant which, when coupled with the $2,600^\circ$ plus phase length within a panel, caused the phase delta. If the panel distribution of Table 3 were modified, the sidelobe unbalance could have been corrected; however, since the integrated sidelobe level of the antenna did not disturb the antennas SAR capability, this modification was not made.

TABLE 3
MEASURED INSERTION PHASES OF SIR-A PANELS

Panel Position	Insertion Phase
1	$+2^\circ$
2	-12°
3	-14°
4	0°
5	$+4^\circ$
6	$+3^\circ$
7	$+4^\circ$

5.0 CONCLUSIONS

The SEASAT and SIR-A SAR antennas are two applications of printed circuit microstrip antenna for large space antennas. The important technologies developed during these programs, such as low loss substrate and flexible high power suspended substrate, have greatly expanded the field of application of microstrip antennas and shown the capability of the antenna to meet varying environmental requirements.

Figures 9 and 10 show the completed SEASAT and SIR-A antennas.

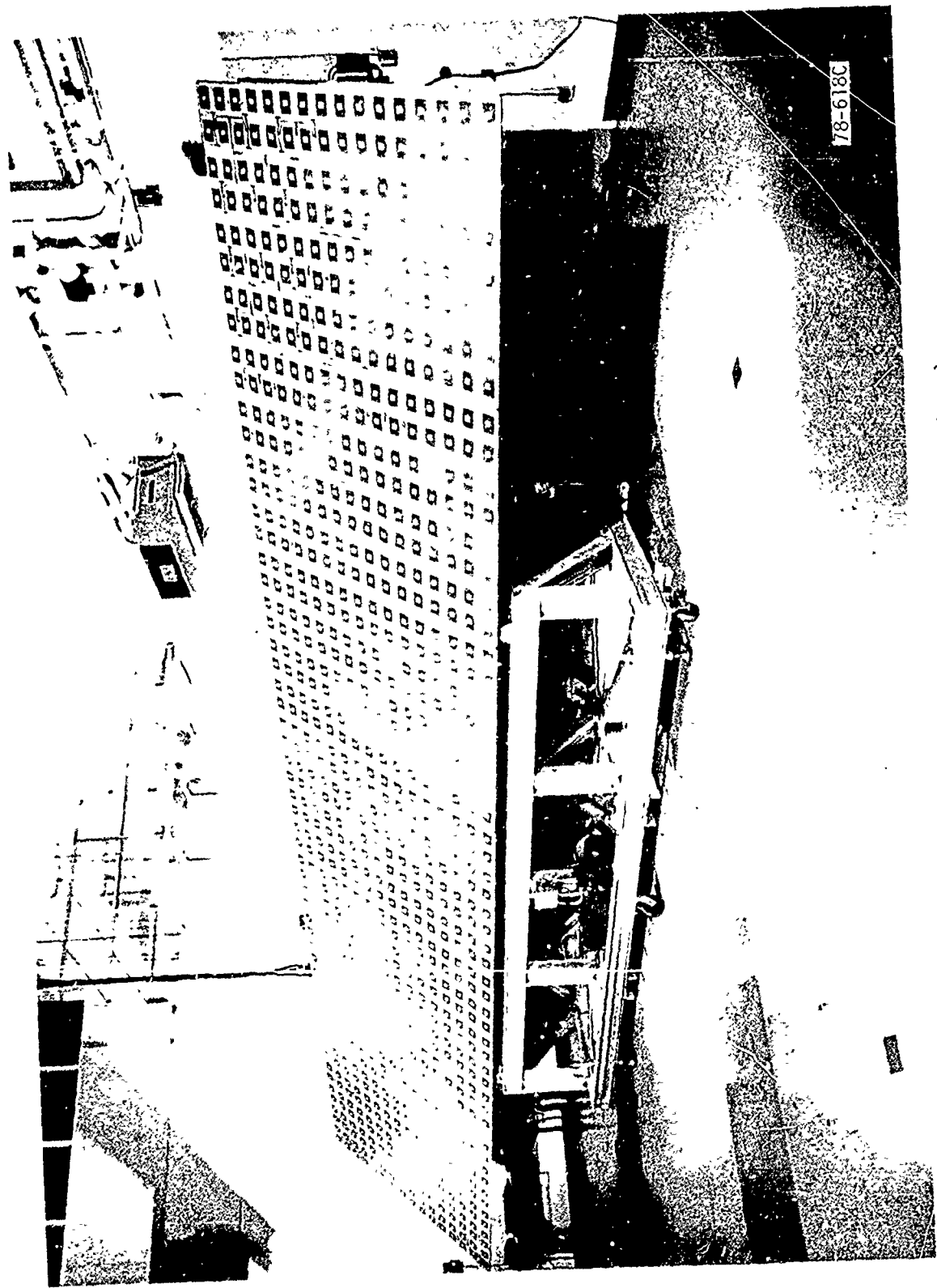


Figure 9 SIR-A Antenna (Before Thermal Blankets)

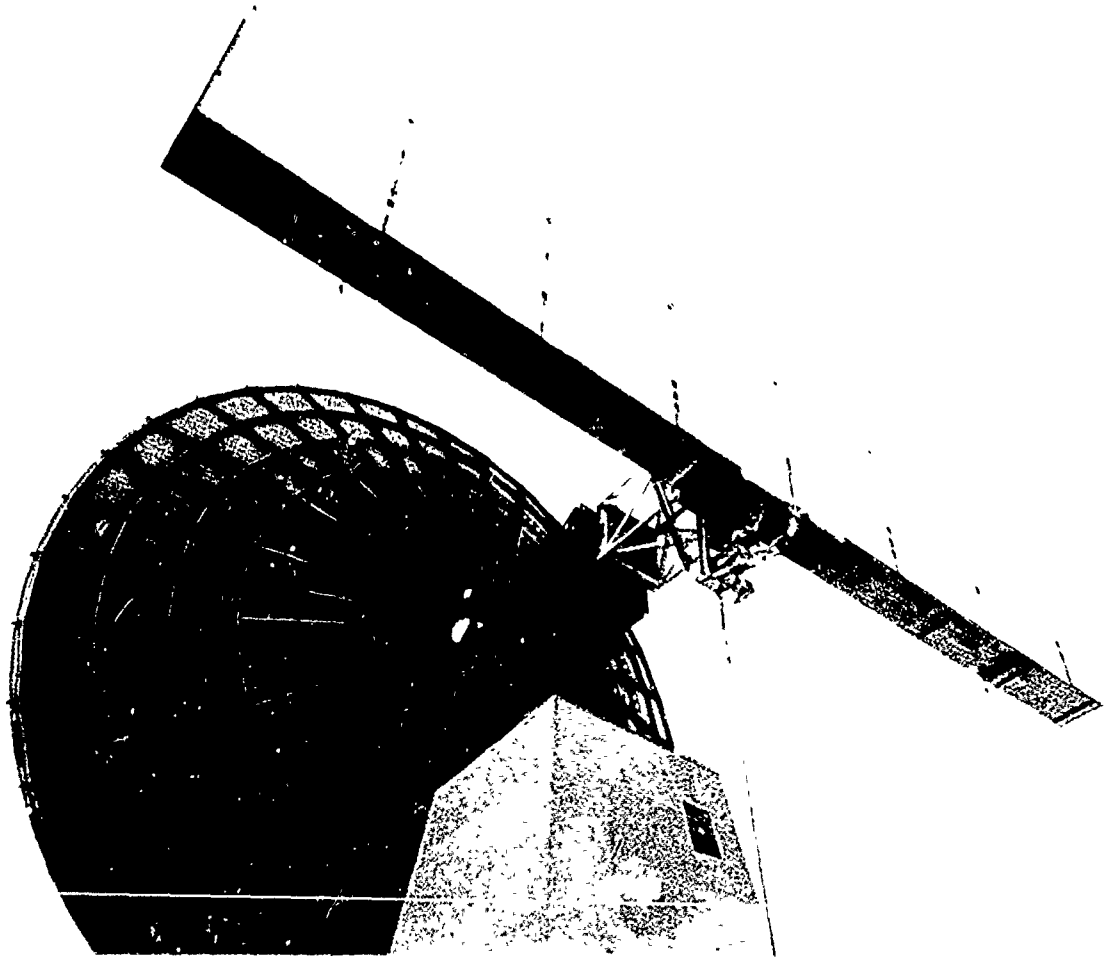


Figure 10 SEASAT Antenna on Positioner

6.0 REFERENCES

1. Brejcha, A. G., Keeler, L. H., and Sanford, G. G., "The SEASAT-A Synthetic Aperture Radar Antenna", SAR Technology Conference, March, 1978
2. Hawkins, W. C., "An Eleven-Meter Deployable Truss for the SEASAT Radar Antenna, Twelfth Aerospace Mechanism Symposium", Ames Research Center, April, 1978
3. Huisjen, M. A., "Prediction of Antenna Array Performance from Subarray Measurements", SAR Technology Conference, March, 1978
4. Schiavone, F. J., "High-Efficiency, Flexible, Light-weight Corporate RF System for SAR Antenna Application", SAR Technology Conference, March, 1978

A 7.5 GHz MICROSTRIP PHASED ARRAY
FOR
AIRCRAFT TO SATELLITE COMMUNICATION*

Frank W. Cipolla
BALL AEROSPACE SYSTEMS DIVISION
Boulder, Colorado 80306

SUMMARY

The demand for high gain full hemisphere coverage for aircraft to satellite communications is ever increasing. Many approaches to this problem have been investigated; including, a parabolic dish under a radome and the more conformal hybrid-scan array under a radome¹. Both are heavy and protrude a significant distance from the aircraft skin.

An ideal solution to the problem may be a completely conformal lightweight microstrip phased array. Ball Aerospace Systems Division (BASD) has developed a unique technology in building this type of phased array.

1.0 INTRODUCTION

This paper reports results of a research and development program conducted at BASD under a contract with Rome Air Development Center to investigate, design, and fabricate a microstrip phased array for the SHF SATCOM communications systems. A 7.5 GHz receive only microstrip phased array has been developed which achieved a gain of 19.8 dBic for the broadside beam. It is left-hand circularly polarized and has 3-bit digital PIN diode phase shifters for steering the beam. A microprocessor based beam steering controller was also provided for calculating the phase shifter settings for each beam position. The entire array including radiating elements, qua-

* This work was supported by the Air Force Systems Command, Rome Air Development Center, Griffiss AFB, New York, under the direction of Tom Treadway, Contract No. F30602-78-C-0329.

drature hybrid, phase shifters, corporate feed, R.F. chokes and D.C. bias is in microstrip medium. Some requirements of this phased array are:

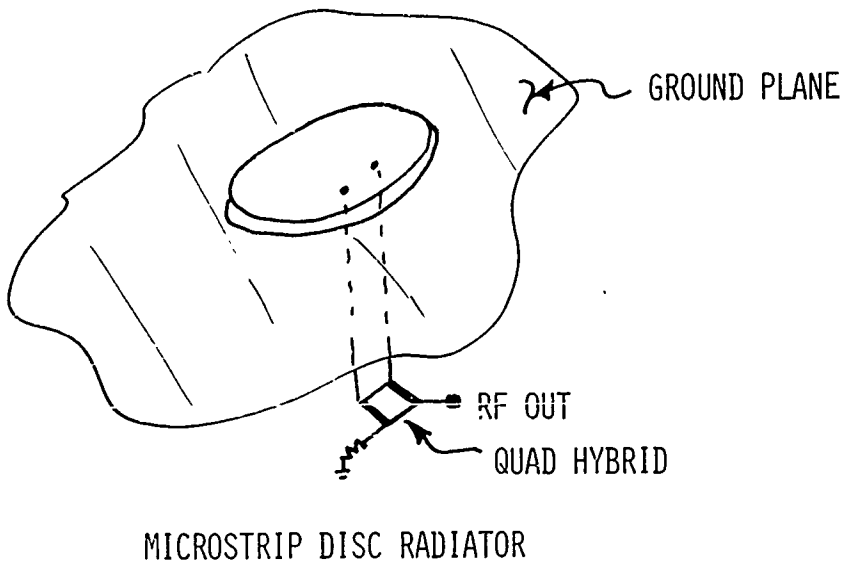
Frequency	7.5 GHz (Receive Only)
Bandwidth	500 MHz
Gain	20 dBic
Polarization	Left Hand Circular
Efficiency	50%
Scan Volume	$\theta = \pm 45^\circ$ $\phi = 0^\circ$ or 180° $\theta = \pm 60^\circ$ $\phi = 90^\circ$ or 270°
Beam Steering Control	Microprocessor - Based System

In order to achieve these goals, these requirements were put on each subsystem of the microstrip phased array.

2.0 MICROSTRIP RADIATING ELEMENT

The two major factors put on the microstrip radiating element of this phased array are the bandwidth of 7% and the element's beamwidth. To achieve the bandwidth at this frequency, a 0.794 mm (.03125 in) thick substrate material was used. The substrate material is woven teflon-fiberglass. This thickness gave the needed bandwidth requirement. The beamwidth is a function of the type of element used. That is, the half-wave microstrip patch, quarterwave patch, microstrip crossed-slot, or the circular disk element. Since circular polarization is a requirement, the quarter-wave element could not be used. Due to manufacturability, the microstrip crossed-slot was eliminated. And finally, the half-wave patch was eliminated due to the packing factor or closeness of the elements in the array lattice. Therefore, the disk radiating element was chosen.

To achieve circular polarization, the disk element is fed in phase quadrature at the appropriate locations to excite orthogonal modes. This was done with a branch-line hybrid as depicted in Figure 1.



BANDWIDTH - OVER 500 MHz ON 1/32" THICK DIELECTRIC
BEAMWIDTH - ~120°
AXIAL RATIO - 0 - 4 dB OVER THE BAND
SIZE - ~ $.35\lambda_0$ DIAMETER
MANUFACTURABILITY - SIMPLE PHOTOETCH PROCESS; HIGH REPEATABILITY

FIGURE 1 MICROSTRIP DISK RADIATOR

This element achieved a bandwidth of over 500 MHz under a 2:1 VSWR, a beamwidth of 110° and an axial ratio of 0 to 4 dB over the entire band within the 3 dB points. The element is easy to manufacture using a photo-etch process.

3.0 MICROSTRIP DIGITAL PHASE SHIFTER

A 3-bit digital phase shifter was specified for use in steering the beam of this phased array. This gives eight possible phase positions that are multiples of 45° at each element. A switched line type phase shifter was used for the 180° and 90° bits and a loaded-line type was used for the 45° bit. Thus, a total of 10 PIN diodes is required for each phase shifter. The entire phase shifter including R.F. chokes is in microstrip on a .508 mm (.020 in) thick Duroid type substrate. It is shown in Figure 2. The final version achieved an insertion loss of $1.2 \pm .3$ dB.

4.0 MICROSTRIP CORPORATE FEED

The corporate feed provides a uniform amplitude distribution to the radiating elements. Therefore all power divisions are equal. It is accomplished entirely in microstrip on the same substrate as the phase shifters as shown in Figure 3. The module shown is an 8x8 element array. This is the basic module size. Larger arrays can be constructed by arraying these modules and using another lower-loss type medium to feed the modules, such as waveguide or low-loss coax. The basic 8x8 array module is $\sim 17.9 \times 16.3$ cm (7.1 x 6.45 in) in size and only 1.8 mm (.071 in) thick.

5.0 ARRAY CONFIGURATION

The basic module has 64 elements in an 8x8 rectangular lattice. The element spacing is $\sim .51\lambda$ in the 60° scan plane and $\sim .56\lambda$ in the 45° scan plane at center frequency. This is based on the maximum spacing before the appearance of a grating lobe at the highest frequency of operation. Figure 4 shows the element layout of a module.

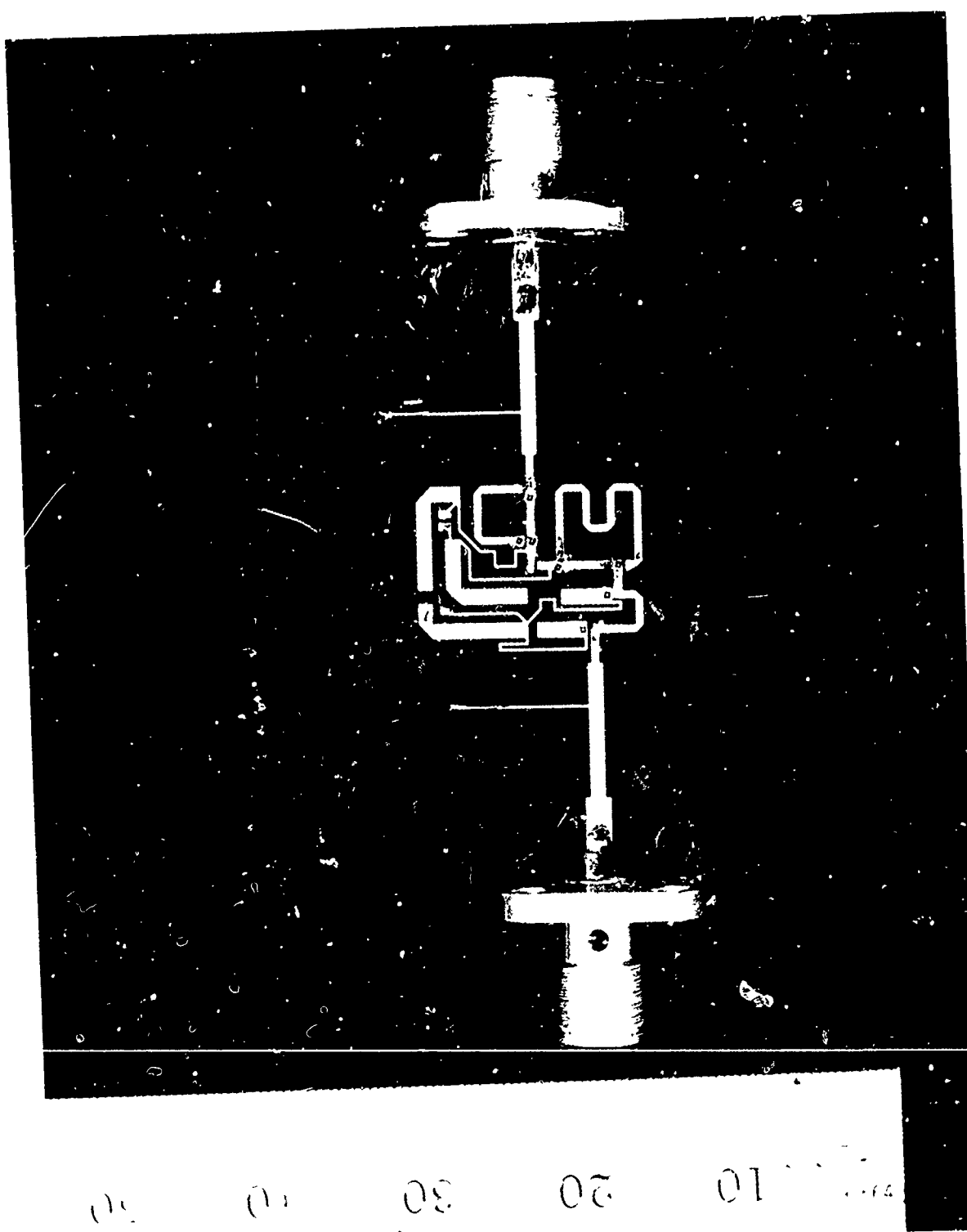
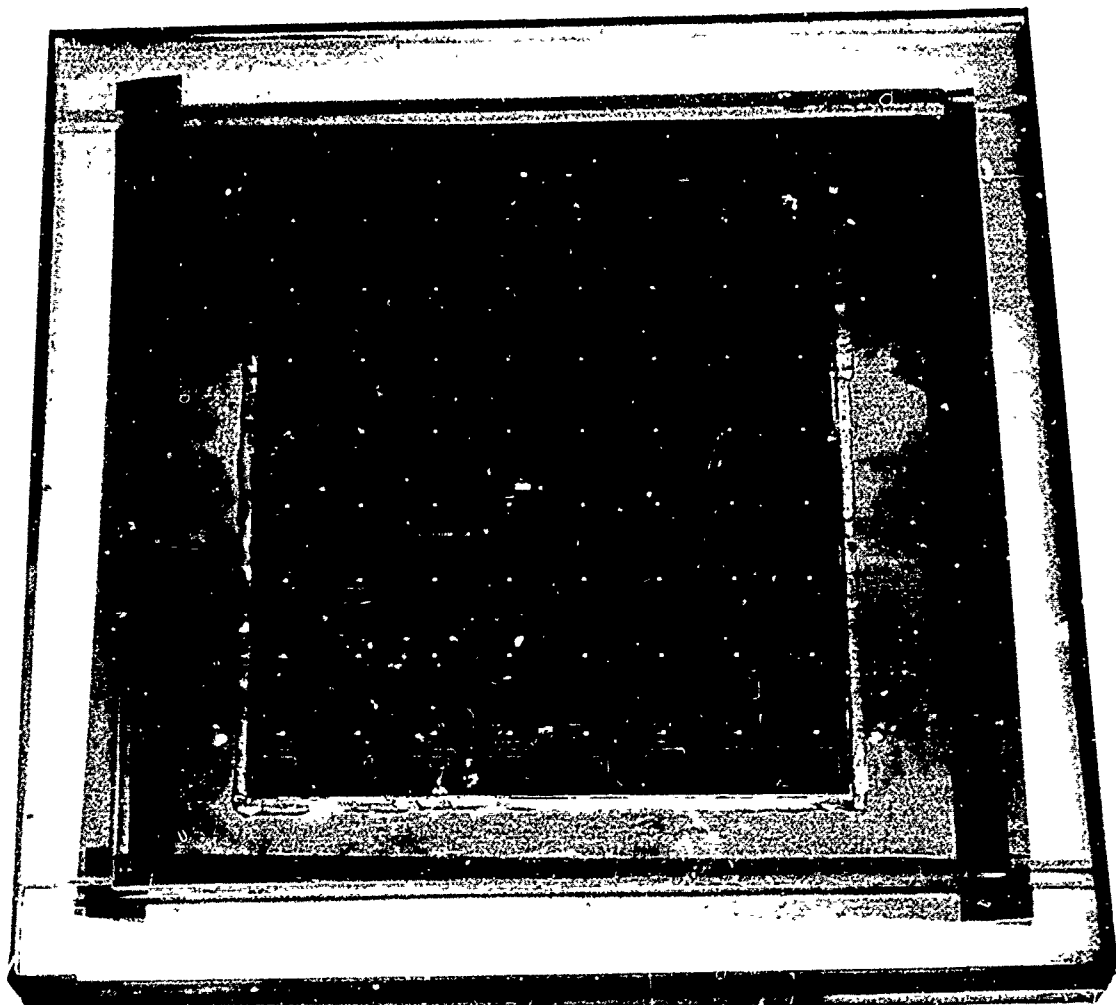
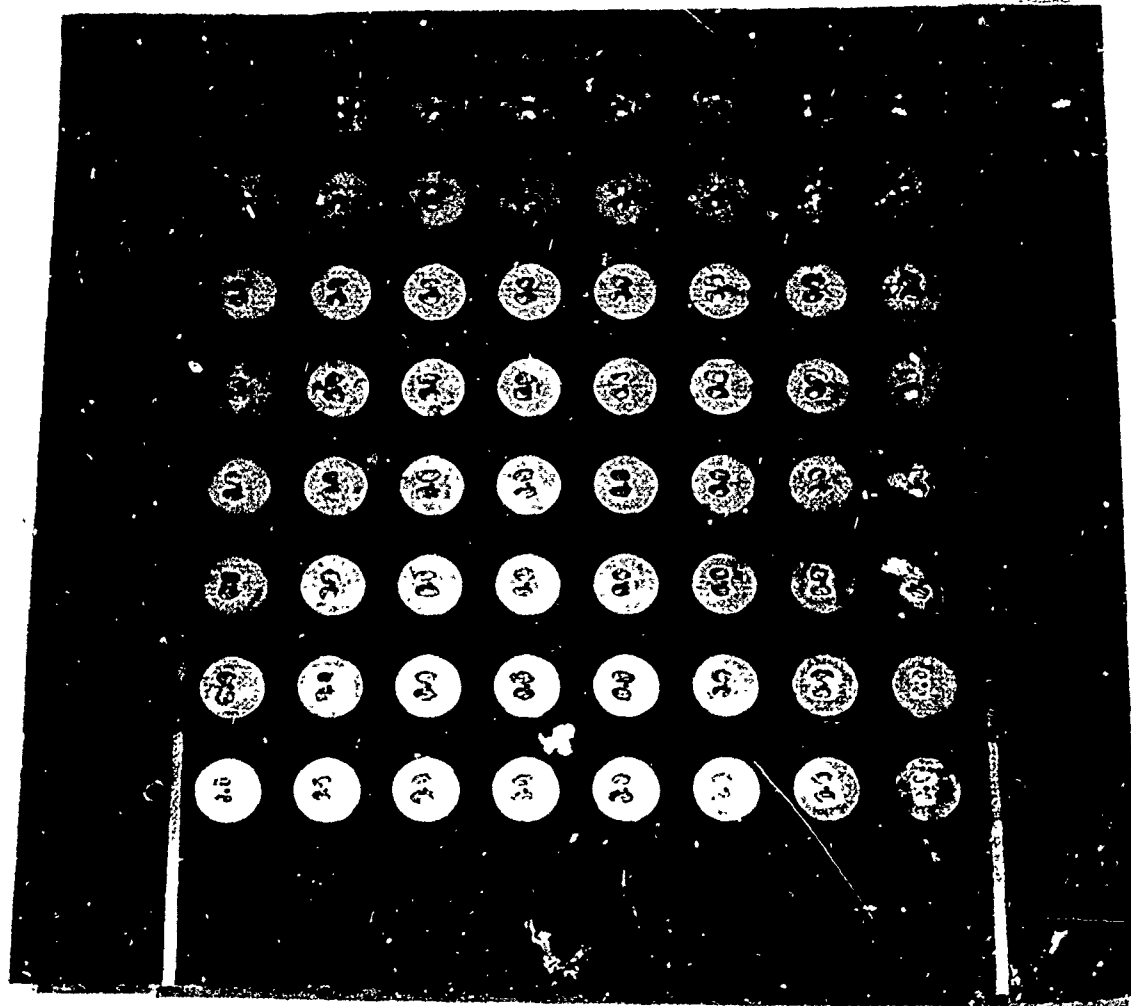


Figure 2. Microstrip 3-Bit Digital Phase Shifter



79-976

Figure 3 Microstrip Corporate and Phase Shifters for SHF Module



79-979

Figure 4. Element Layout of SHF Module

The element circuit board was placed ground plane to ground plane with phase shifter-corporate feed board. Feedthroughs were used to excite the element from the branch line hybrid on the phase shifter-corporate feed board.

D.C. bias was applied to the 3-bit phase shifters through vertical pins soldered to the R.F. chokes on the phase shifter-corporate feed board. Wires with contacts were used to connect these pins with the decoder/driver electronics.

6.0 MICROPROCESSOR CONTROLLER

A TI9900 microprocessor was used to calculate the phase shifter settings for each commanded beam position. This desired beam position is entered on a teleprinter or microterminal in θ , ϕ coordinates (elevation and azimuth) in degrees. The processor uses a simple row-column steering technique to calculate the necessary phase shifter setting for each of the 64 phase shifters. The processor sends this data serially over 22 wires to the decoder/driver electronics which are mounted directly in back of the array. The decoder/driver electronics determine which element gets the corresponding phase shifter setting. The entire system is shown in Figure 5.

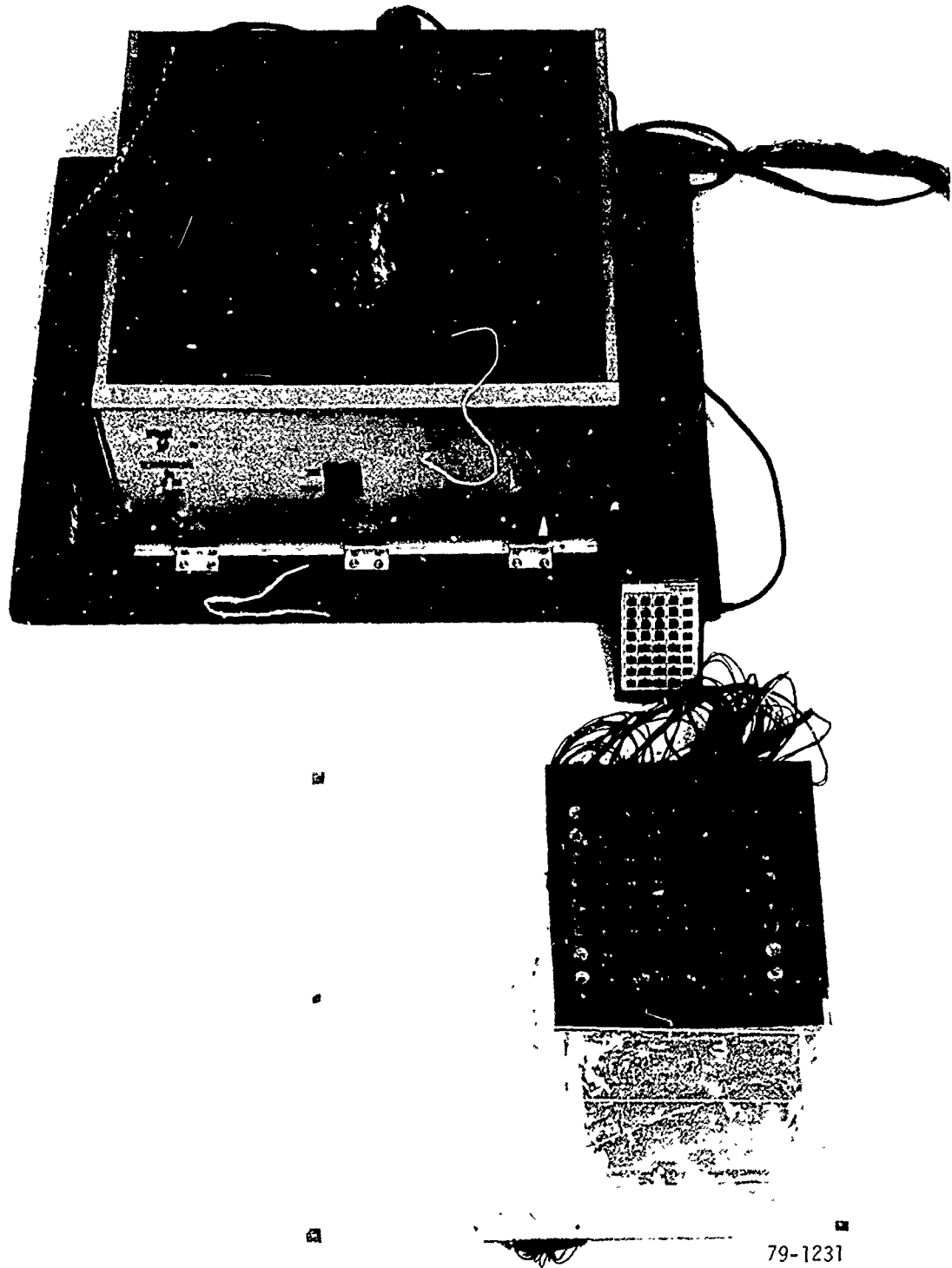
7.0 RESULTS

The 8x8 array module has a theoretical directivity based on its aperture area given by:

$$10 \log (4\pi A/\lambda^2) \quad (1)$$

This is 23 dBi.

Figure 6 shows the element factor and array factor which governs the gain fall-off with steering angle.



79-1231

Figure 5 SHF Microstrip Phased Array and Microprocessor Controller

SHF PHASED ARRAY
THEORETICAL GAIN -vs- STEERING ANGLE.

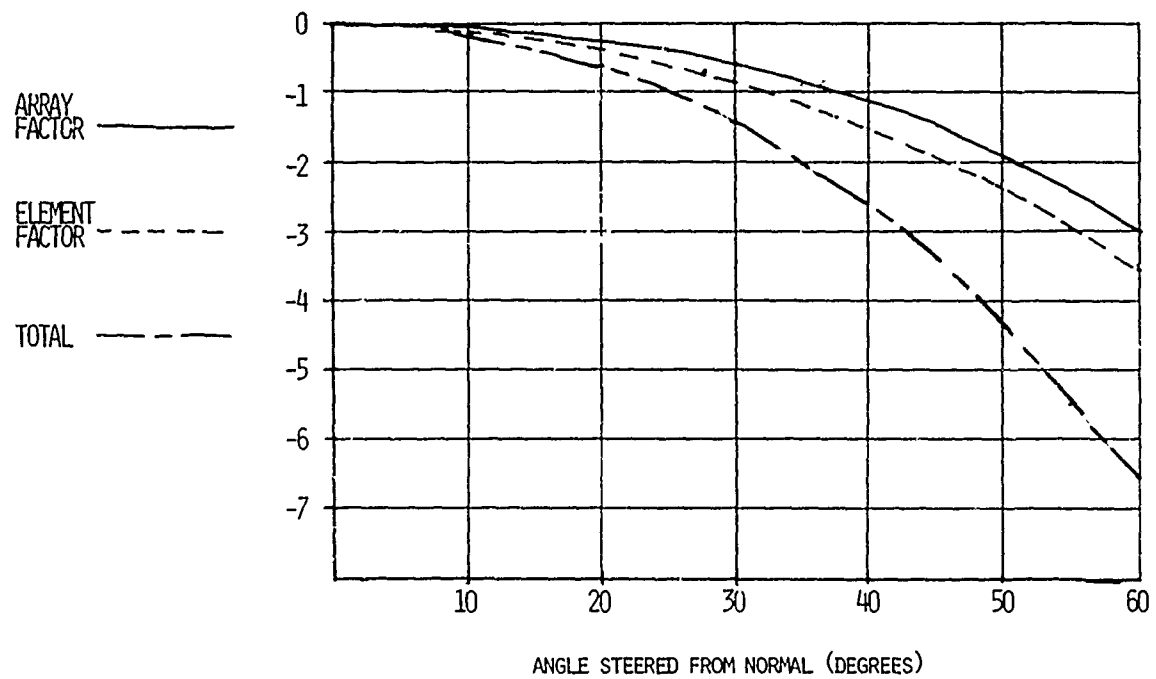


FIGURE 6

Table 1 shows the measured gain at a number of beam positions and the corresponding efficiency. A loss budget for the array module is given in Table 2. Antenna patterns showing axial ratio and scanning are shown in Figures 7 - 11. The axial ratio was ~2-3 dB for the broadside beam over the 500 MHz bandwidth.

8.0 CONCLUSIONS

The overall efficiency of this first 64 element microstrip phased array at 7.5 GHz has proven the feasibility of an all microstrip, conformal phased array.

Further work is necessary to improve the VSWR and axial ratio. This will also help to increase the efficiency from 46% to above 50%.

Major advancements were made in the manufacturing procedures developed in fabricating this antenna. Packaging and environmental protection of the array for the airborne environment is still being improved. With the decode:/driver electronics replaced by hybridized microelectronic circuitry, the total thickness of the array including the electronics can be reduced to ~1.9 cm (.75 in).

9.0 REFERENCES

1. James J. Maune, "An SHF Airborne Receiving Antenna" presented at the 22nd Annual Symposium on USAF Antenna Research and Development, October, 1972.

TABLE 1
SHF MICROSTRIP PHASED ARRAY AVERAGES 46% EFFICIENCY

STEERING ANGLE	THEORETICAL GAIN (DB)	ACTUAL GAIN (DB)	EFFICIENCY %
0	23	19.6	45.7
14.1	22.7	19	42.7
29.2	21.7	18.5	47.9
42	19.7	16.6	49.0
53	17.9	14.4	44.7

THIS CAN BE INCREASED BY IMPROVING THE VSWR.

TABLE 2
LOSS BUDGET FOR THE SHF MICROSTRIP PHASED ARRAY

THEORETICAL GAIN ($4\pi A/\lambda^2$)	,23 dBi
<u>LOSSES</u>	
ELEMENT CAVITY	.6 dB
FEEDLINE	.7
PHASE SHIFTER	1.2
QUADRATURE HYBRID	.2
VSWR (2.2:1)	.7
TOTAL	3.4
EXPECTED GAIN FOR BROADSIDE BEAM	19.6 dBIC

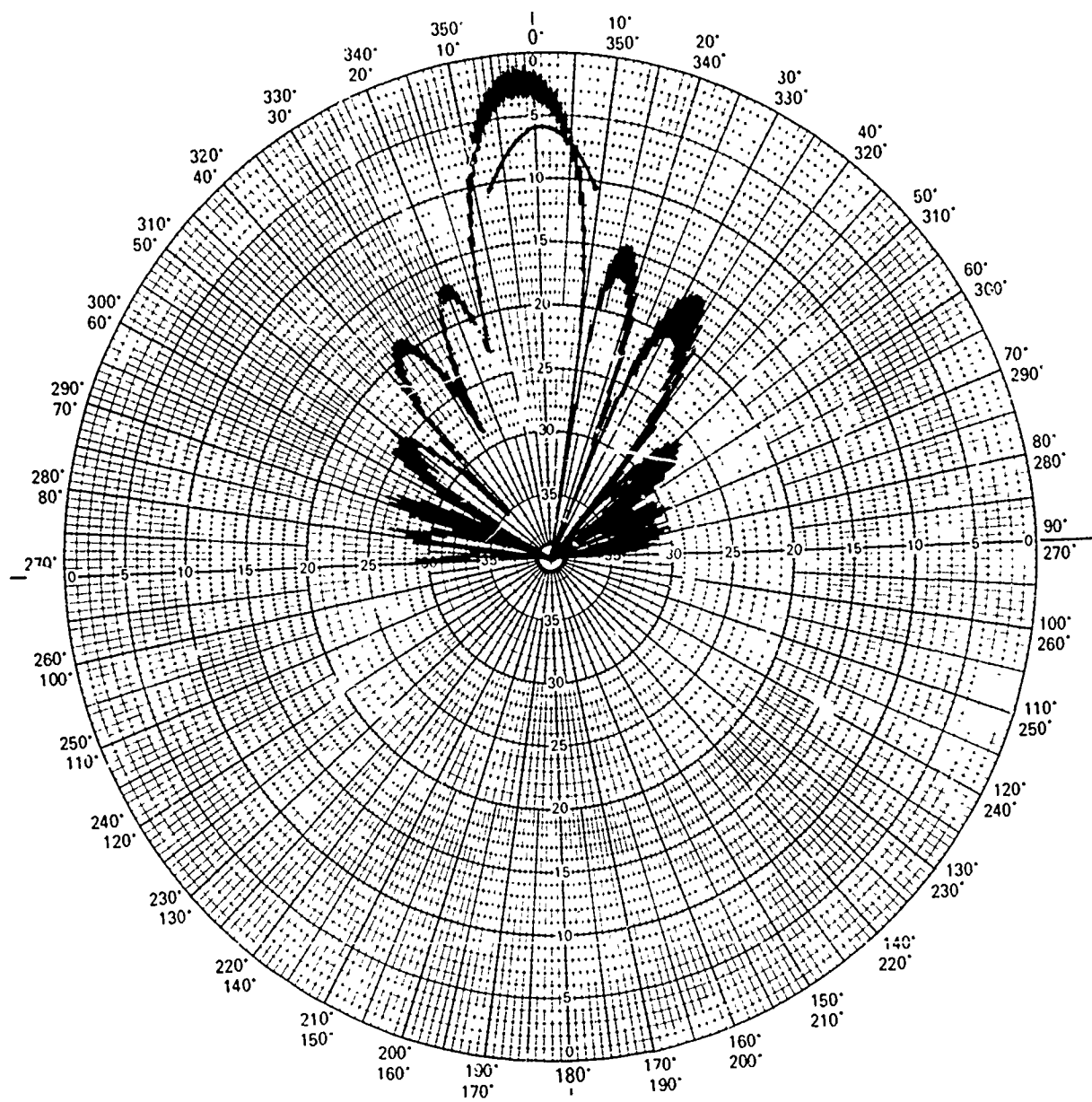


Figure 7 Broadside Beam

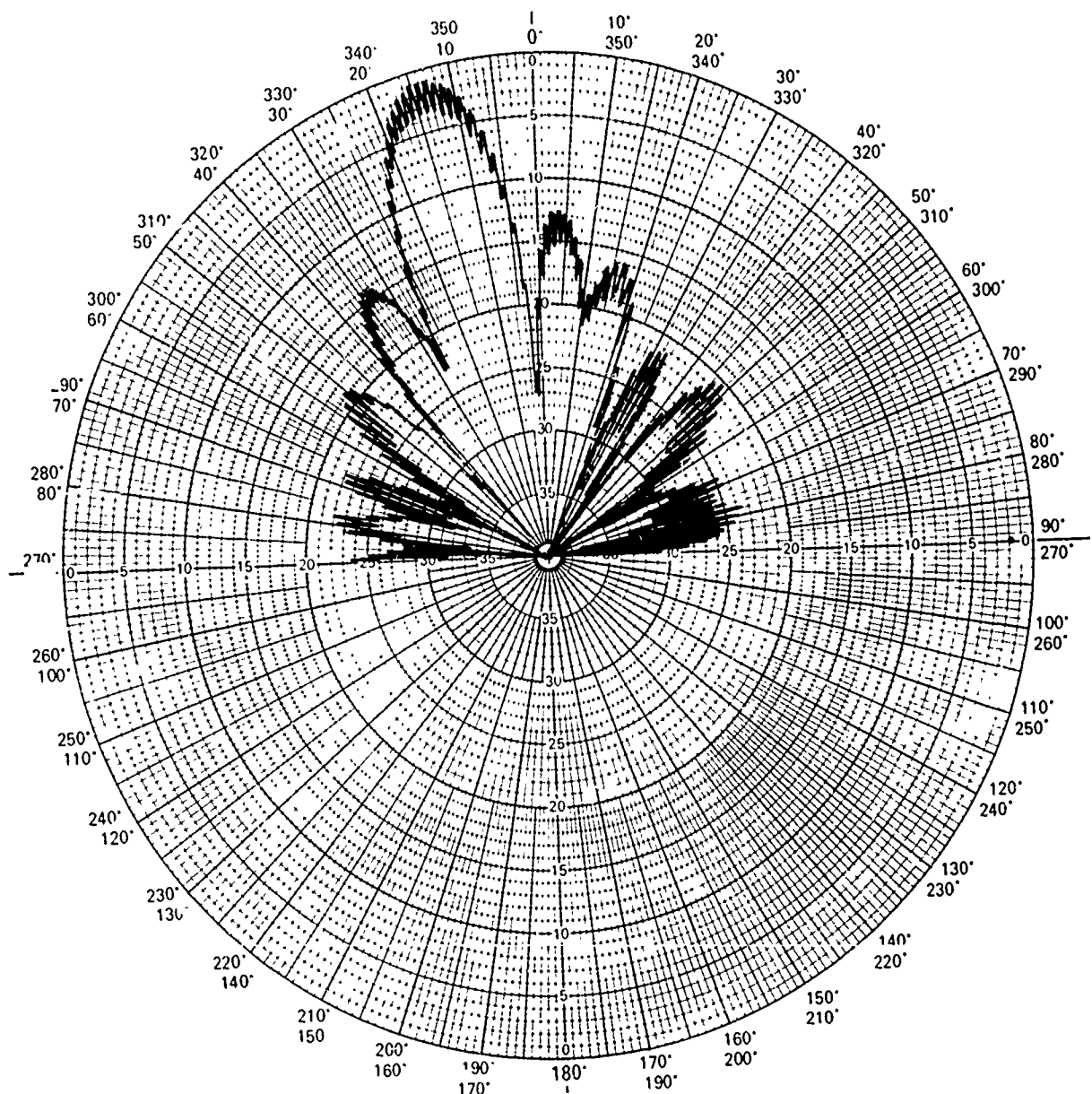


Figure 8 Beam Steered to 13°

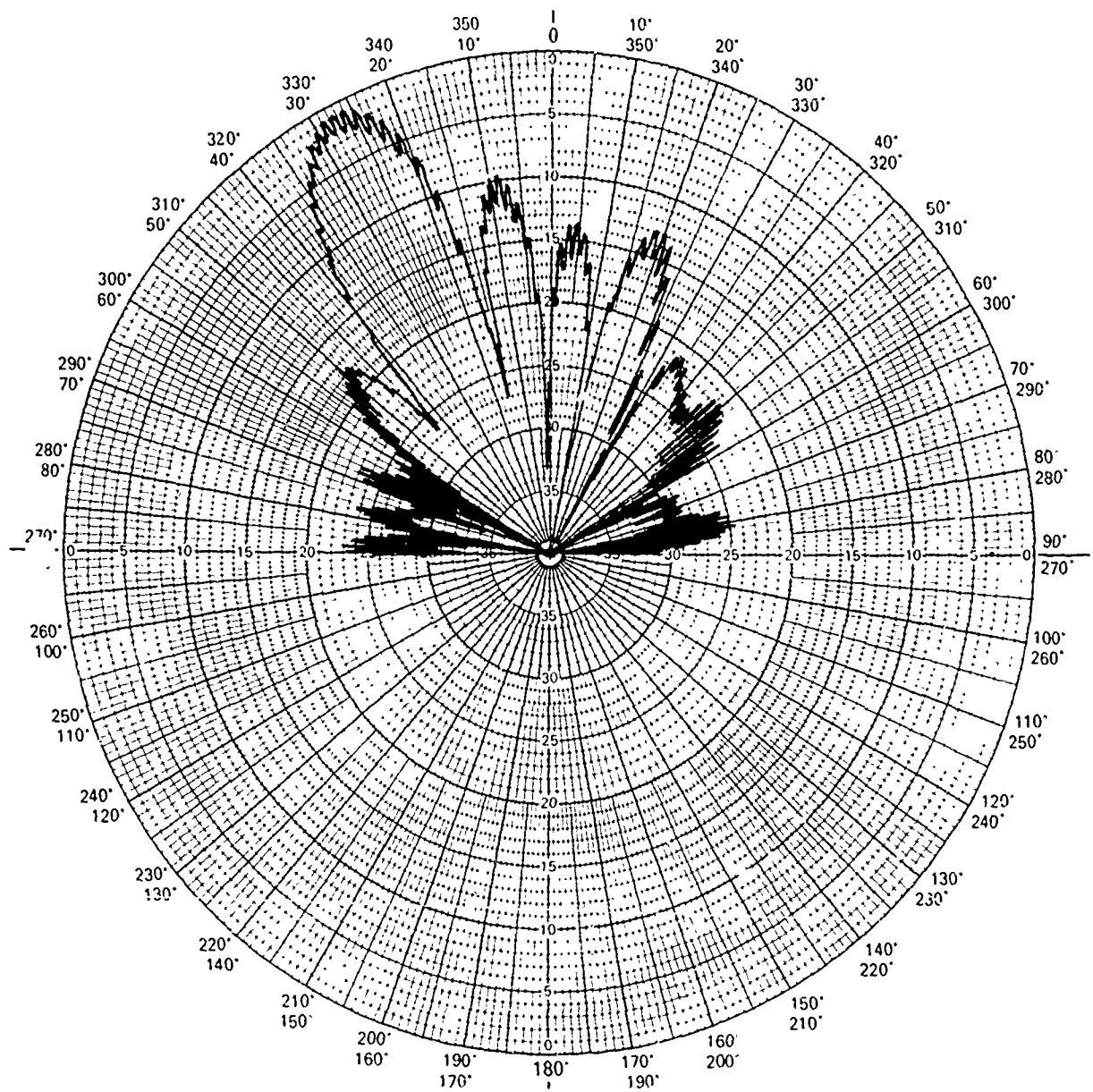


Figure 9 Beam Steered to 26^0

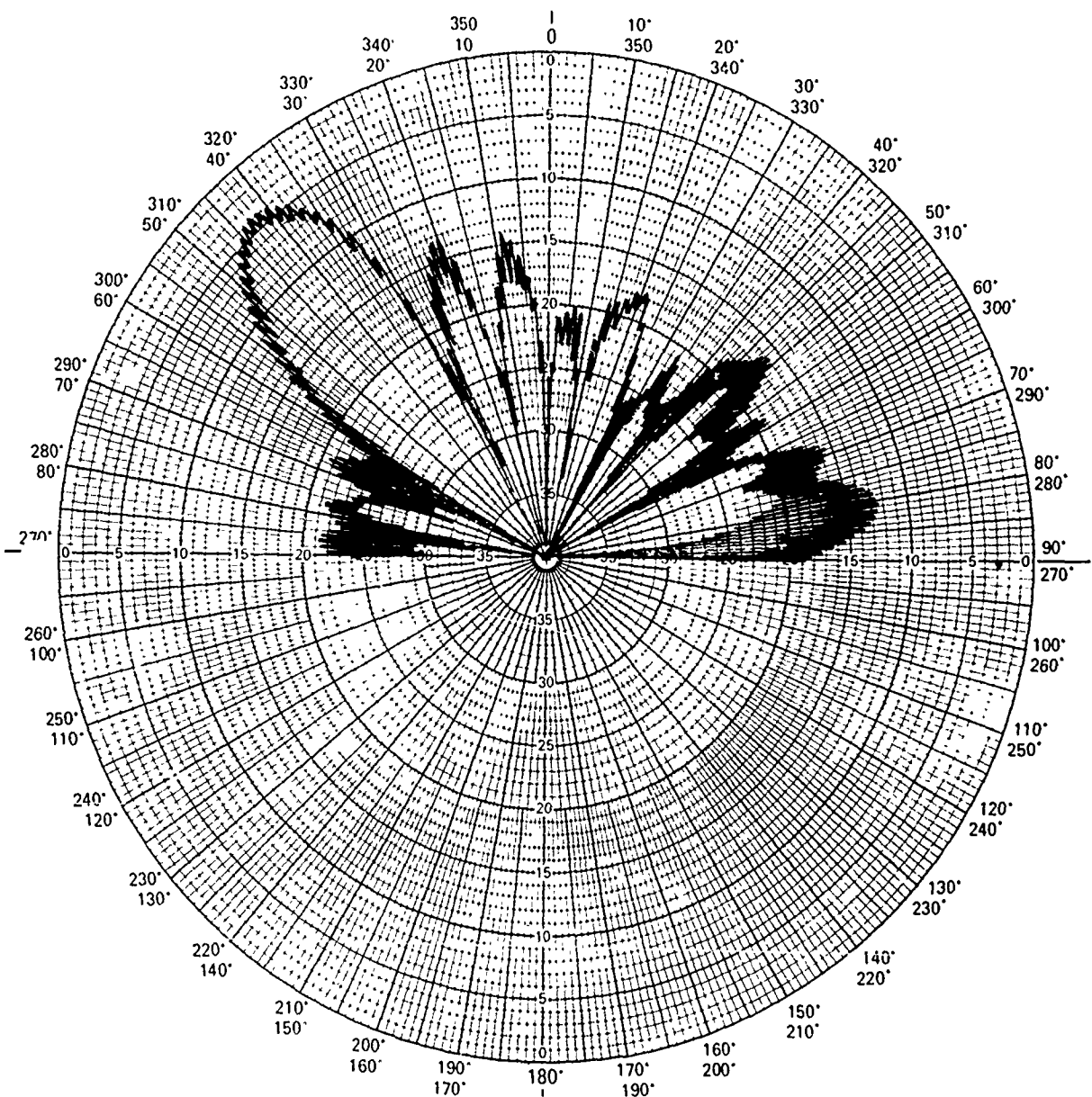


Figure 10 Beam Steered to 42°

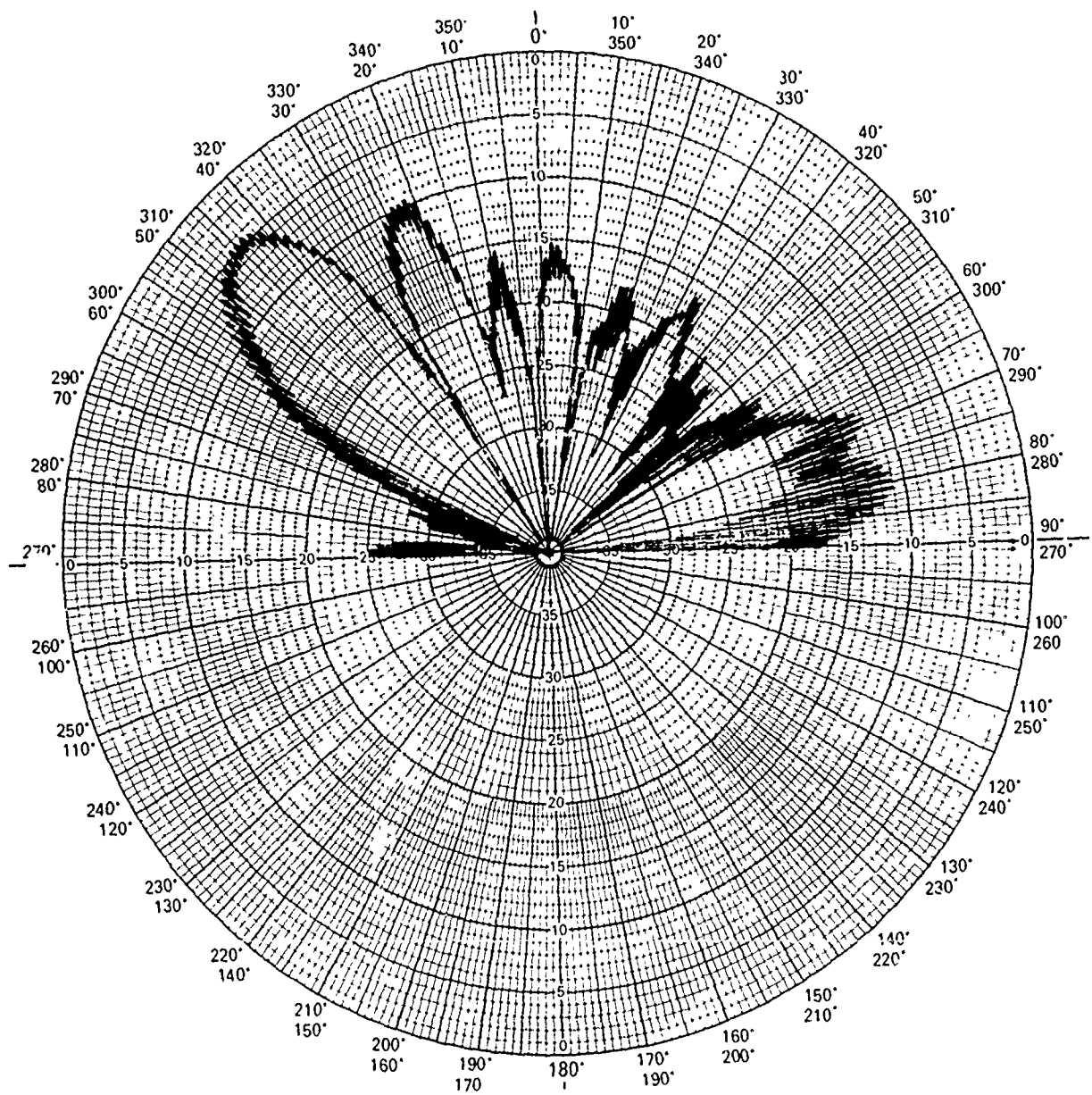


Figure 11 Beam Steered to 45°

MICROSTRIP SERIES ARRAYS

Tom Metzler
BALL AEROSPACE SYSTEMS DIVISION
Boulder, Colorado 80306

SUMMARY

In recent years several theoretical models for microstrip series arrays have been developed which are based on either waveguide [1] or resonant cavity analogies to the microstrip circuit. However, when these models are applied to practical designs, anomalies are observed in the measured patterns such as increased sidelobes and unpredictable beam positions. Using a traveling wave design technique, Ball Aerospace Systems Division has successfully designed both resonant and non-resonant series arrays which have achieved low sidelobes, high efficiency and predictable beam positions.

1.0 BACKGROUND

The development of the arrays discussed in this paper was instigated by a large aperture (10m x 10m) radiometer antenna study funded by Goddard Space Flight Center. The study objective was to design and evaluate a microstrip array which would meet specific radiometer system requirements and be compatible with a Shuttle launch. Figures 1 and 2 depict the proposed antenna mechanical and electrical configurations.

The antenna design was driven by three system requirements. First, effective radiometric mapping of the earth's surface required scanning a narrow pencil beam $\pm 45^{\circ}$ in one plane perpendicular to the orbital flight path. This necessitated dividing the aperture into 84 10m linear arrays with independent phase control of each linear array. Secondly, sidelobes must be suppressed (25 dB below the main beam) in all planes to minimize spurious signals received from targets outside the main beam. Finally, and perhaps most critical to the array design losses must be minimized to

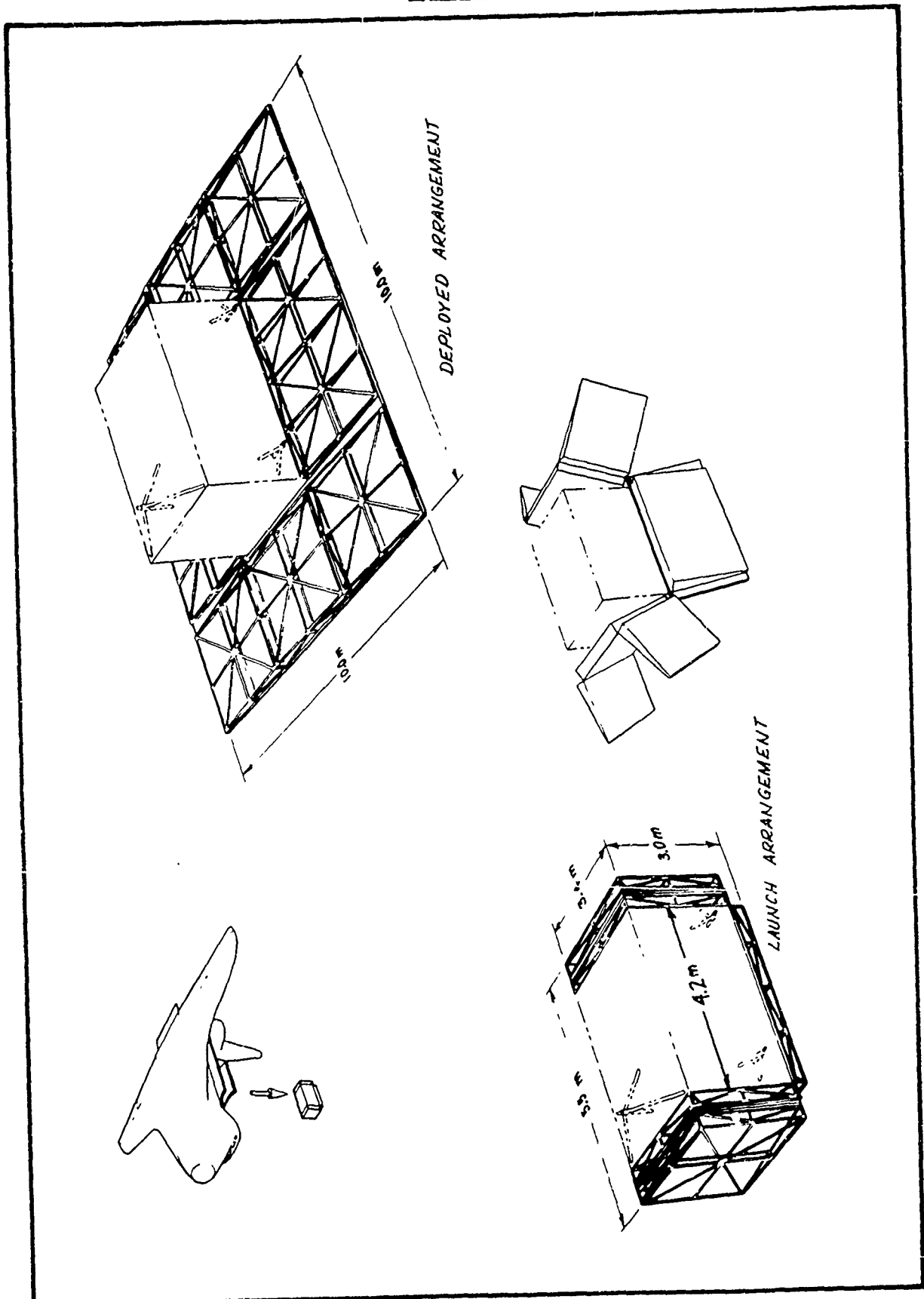


Figure 1 Radiometer Antenna Configuration

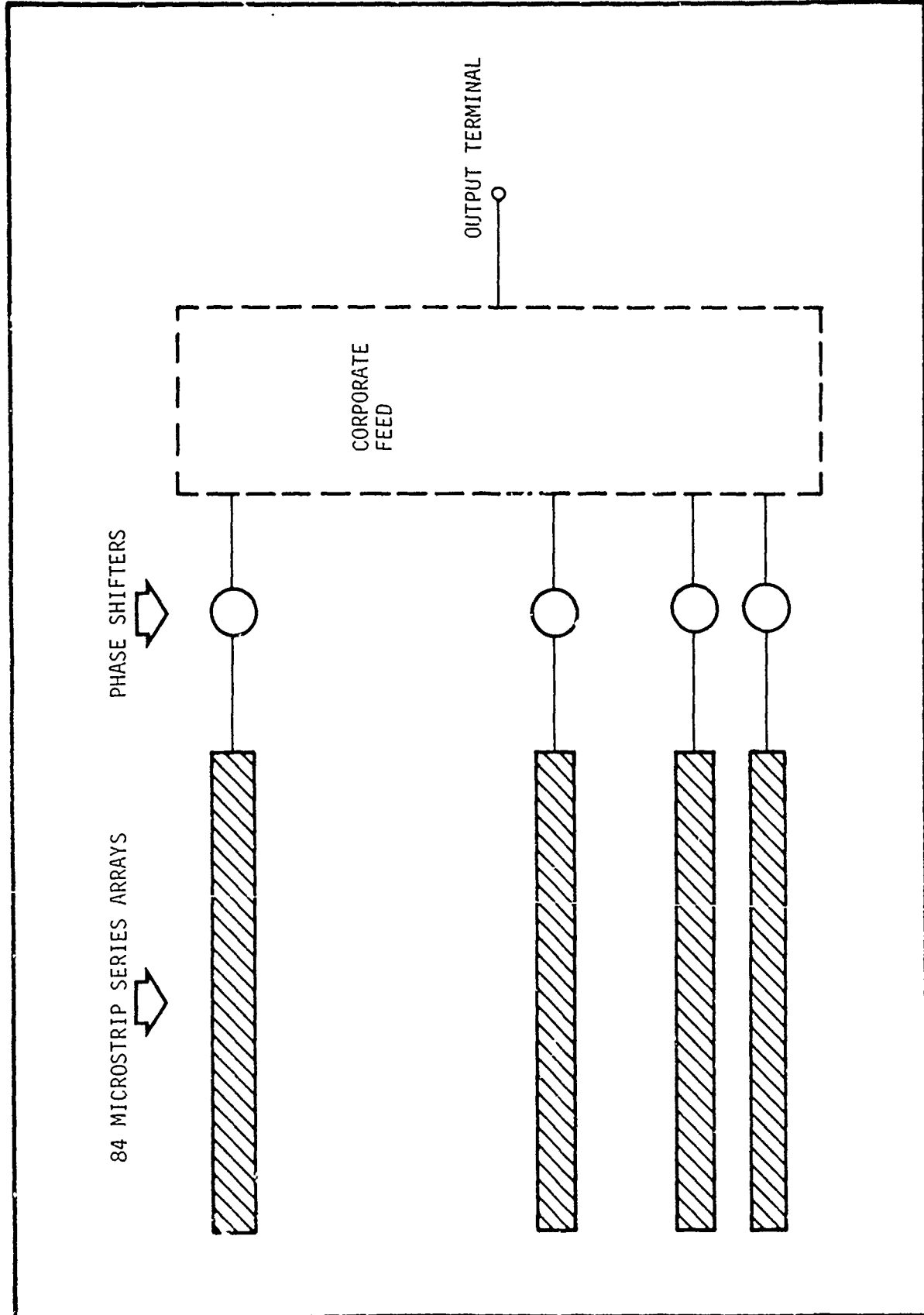


Figure 2 Radiometer Antenna System Configuration

maintain radiometric resolution.

Three potential feed configurations, Figure 3, exist for the linear arrays; corporate, resonant and traveling wave. Corporate feeds are commonly used in microstrip arrays. Each element is fed in phase since equal path lengths (approximately equivalent to half the array length) exist between all elements and the feed point. However, in large linear arrays the losses incurred in the feed become excessive. The series array configurations reduce losses by minimizing the path length between elements. This potential loss reduction makes the series configurations particularly attractive for radiometric applications and motivated our investigation of both resonant and nonresonant (traveling wave) array configurations.

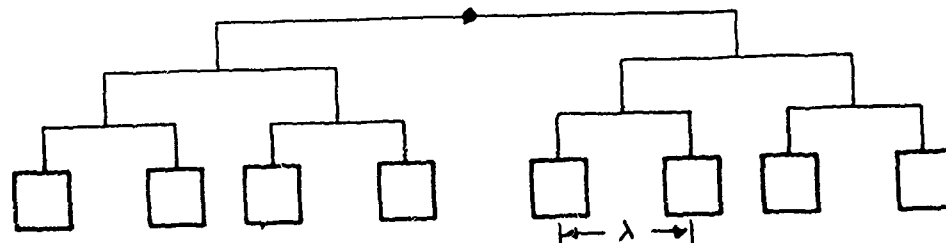
2.0 DESIGN APPROACH

As depicted in Figure 4 the microstrip element is typically modeled as two radiating slots formed by patch edge discontinuities. The radiation conductance is calculated from the equivalent slot of width W and the susceptance is the computed open circuit capacitance of the low impedance line. Initial work at Ball Aerospace and elsewhere attempted to model the series array as cascaded elements interconnected by high impedance lines. In theory all critical parameters (phase velocity and slot conductance) could be calculated and the array designed analytically. This approach was reasonably successful for arrays consisting of a small number of elements, however some anomalies such as moderate beam steering and increased sidelobes were observed. Extending these methods to large arrays proved unsuccessful and it was noted that an unpredicted phase shift was measured across the array. This effect was observed by both near field probing and measured far field patterns of resonant arrays which exhibited steered instead of broadside beams.

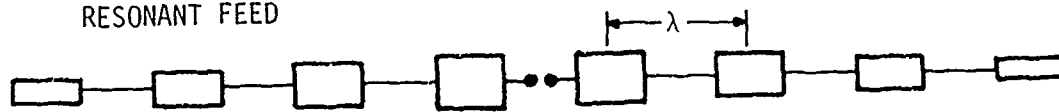
The approach taken during this study was to treat the array as a traveling wave structure and empirical design curves were developed. Figure 5 schematically presents the design procedure. Non resonant test arrays



CORPORATE FEED



RESONANT FEED



TRAVELING WAVE FEED

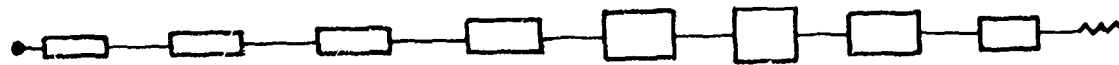


Figure 3 Feed Configurations

Ball

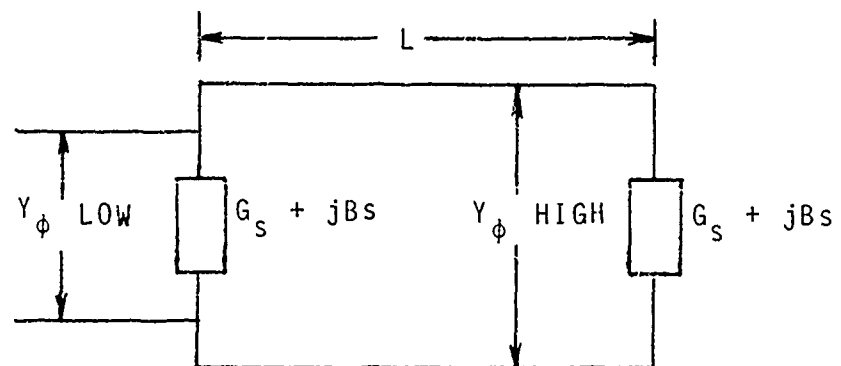
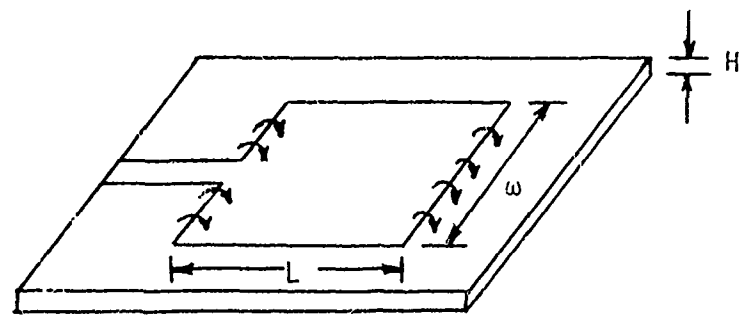


Figure 4 Microstrip Element and Equivalent Circuit

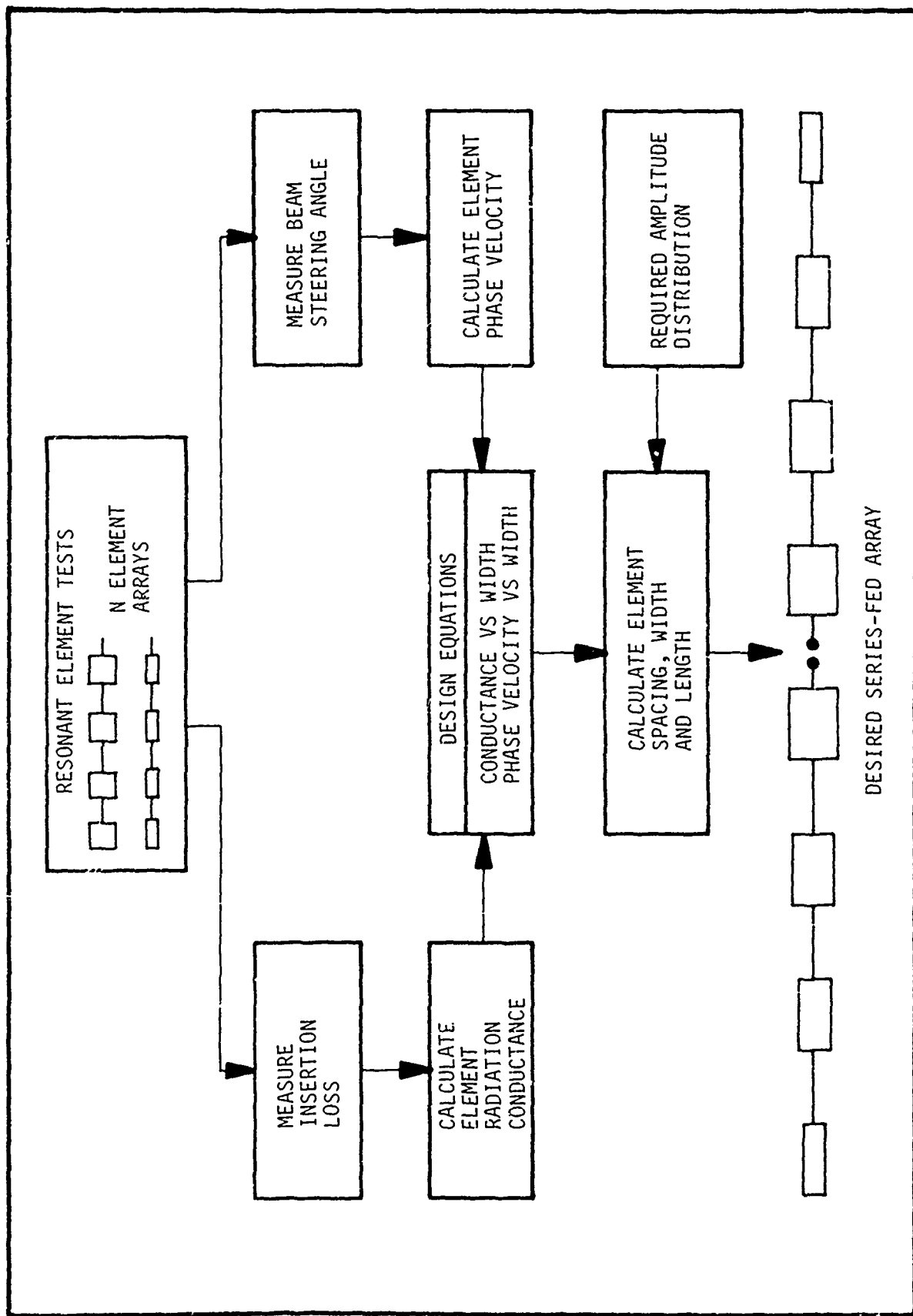


Figure 5 Traveling Wave Array Design Procedure

consisting of 26 similar resonant elements were fabricated on honeycomb substrate. The insertion loss and beam steering angle of each array was measured. Based on this data design curves relating phase velocity and radiation conductance to the element width (W) were formulated and are discussed below.

The measured array insertion loss can be related to the normalized radiation conductance of the element by the following formula [2]:

$$10 \log (1+g) = \frac{\text{insertion loss in dB}}{N} \quad (1)$$

where g = normalized element conductance (normalized to feed line conductance)

N = number of elements in the array

The measured data yielded a design curve given by the following:

$$G = .0162 (W/\lambda_0)^{1.757} \quad (2)$$

where G = element radiation conductance in mhos (not normalized)

W = element width

It has been shown that the theoretical radiation conductance of a resonant microstrip element is given by:

$$G = 2/90 (W/\lambda_0)^2 \quad W/\lambda_0 \ll 1 \quad (3)$$

$$G = 2/120 (W/\lambda_0) \quad W/\lambda_0 \gg 1 \quad (4)$$

The experimental values for (W/λ_0) varied from .033 to .254. The empirically derived curve is in good agreement with the first theoretical curve given above which is valid for small element widths.

In addition, phase velocity in each test array was determined from the measured beam pointing angle. In a traveling wave array the beam position

is given by

$$\cos \theta = \lambda/\lambda_z - \lambda/S \quad (5)$$

where θ = angle measured from end-fire

λ_z = wavelength in substrate

S = element spacing

By measuring the beam steering angle, λ/λ_z (which is directly related to the phase velocity) can be calculated. Two important facts were observed from this measurement. First the phase difference between elements was much larger than could be accounted for by simple line length calculations. This phase difference increased linearly with element width implying that the junction discontinuities introduced an added phase shift proportional to the discontinuity size. This additional phase shift accounts for the failure of the initial analytic models. Secondly, the arrays were dispersive. Again this dispersion was proportional to the discontinuity size with the arrays composed of smaller width elements showing no dispersion over the frequency band of interest. The functional relationship between phase velocity and element width was determined and used to calculate the required element "resonant" width and spacings for a given beam angle.

3.0 RESONANT ARRAY TEST RESULTS

In a resonant array the radiating elements are spaced by one wavelength in the dielectric and radiate in-phase forming a broadside beam. The array may be center fed if a 180° phase difference is introduced between array halves to compensate for their spatial orientation. The input admittance of each array section is simply the sum of the element admittances, and the power radiated by each element is equal to the ratio of the element admittance to the array input admittance. Since the phase velocity differs for elements of different width a non-uniform spatial distribution results.

The resonant array is highly efficient. The length of transmission line connecting each element is inherently minimized by the series configuration. Also in a center fed array, a significant portion of the input power is radiated in the first few elements and does not suffer from extensive line length loss.

A five meter resonant array is shown being tested on a 2,500 ft. mountain range site in Figure 6. The array was designed for 30 dB sidelobes using a Taylor distribution. Integration of the ideal pattern yielded a theoretical directivity of 22.2 dB.

A measured antenna pattern and VSWR plot are shown in Figures 7 and 8. Sidelobes were generally below 26 dB with the exception of one at 22 dB which appeared to be a range reflection. Measured gain was 21.2 dB with a mismatch loss of .3 dB (1.8:1 VSWR) at 1.420 GHz. The antenna gain is .7 dB lower than the theoretical directivity yielding an array efficiency of 85%.

The resonant array is bandwidth limited in terms of both impedance and pattern performance. Sidelobe levels quickly approach 22 dB at 1.400 and 1.430 GHz

4.0 TRAVELING WAVE ARRAY TEST RESULTS

In a traveling wave array the element spacing is other than a wavelength and a linear phase taper exists across the array. The beam is thus scanned off broadside with the scan angle a function of frequency.

A traveling wave array is a broadband configuration. Internal reflections within the array tend to add with random phase at the feed, thus the array input impedance is equivalent to the line impedance connecting the elements. As in the resonant array amplitude tapers are implemented by

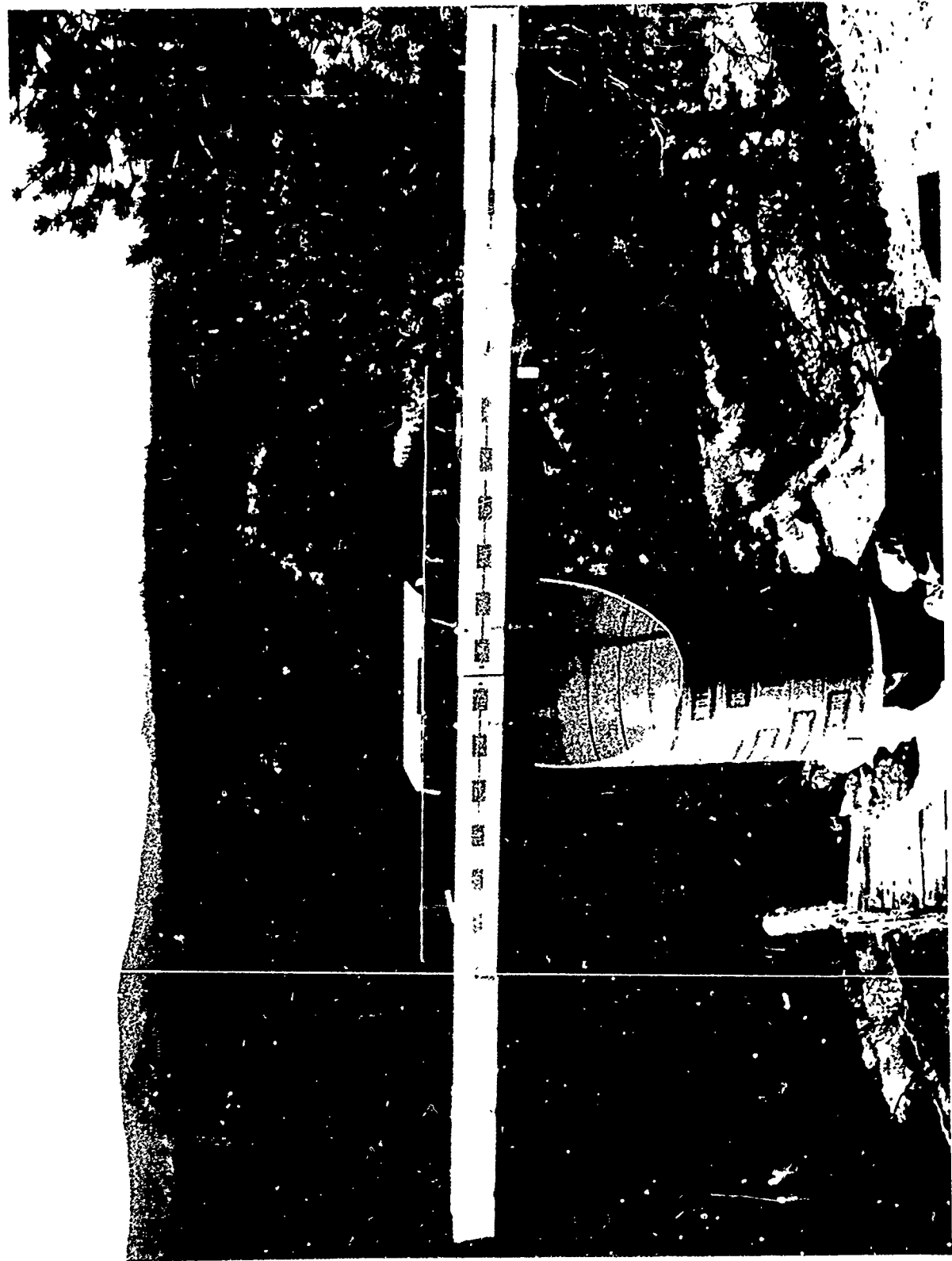


Figure 6 26-Element Series-Fed Array for 1.415 GHz

Ball

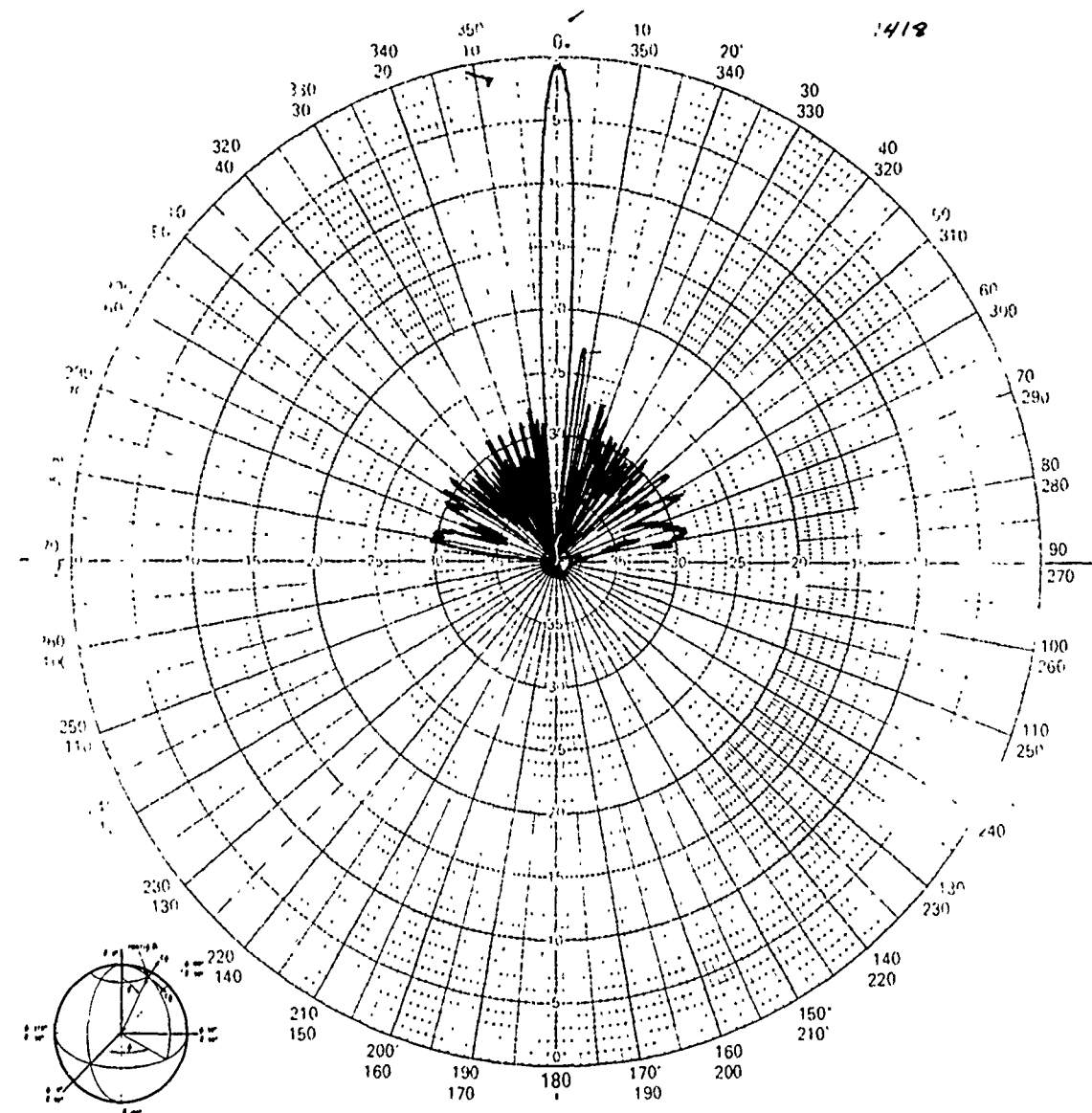


Figure 7 Measured Pattern of Five-Meter Resonant Array

Ball

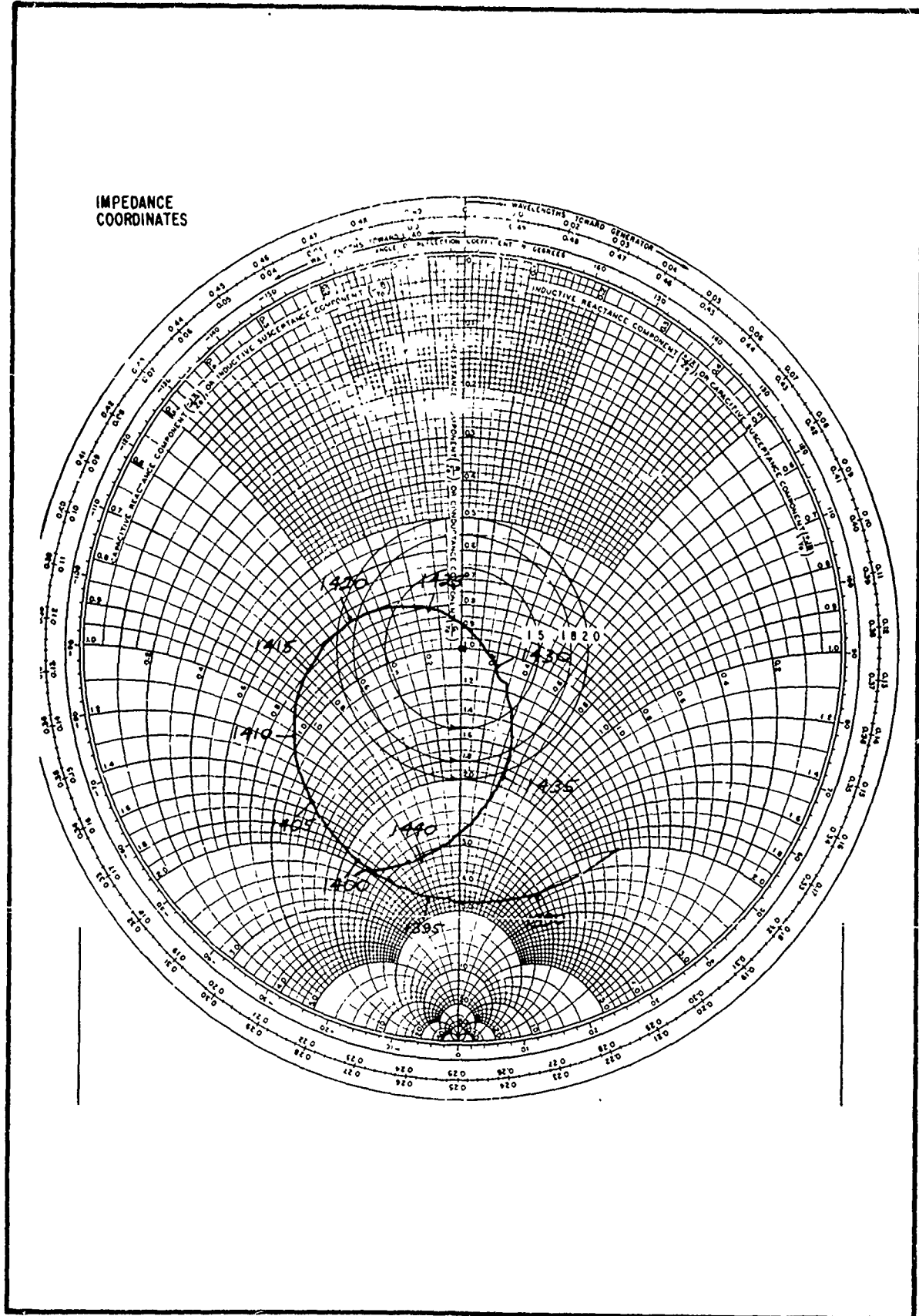


Figure 8 VSWR Plot for 26-Element Series-Fed Array

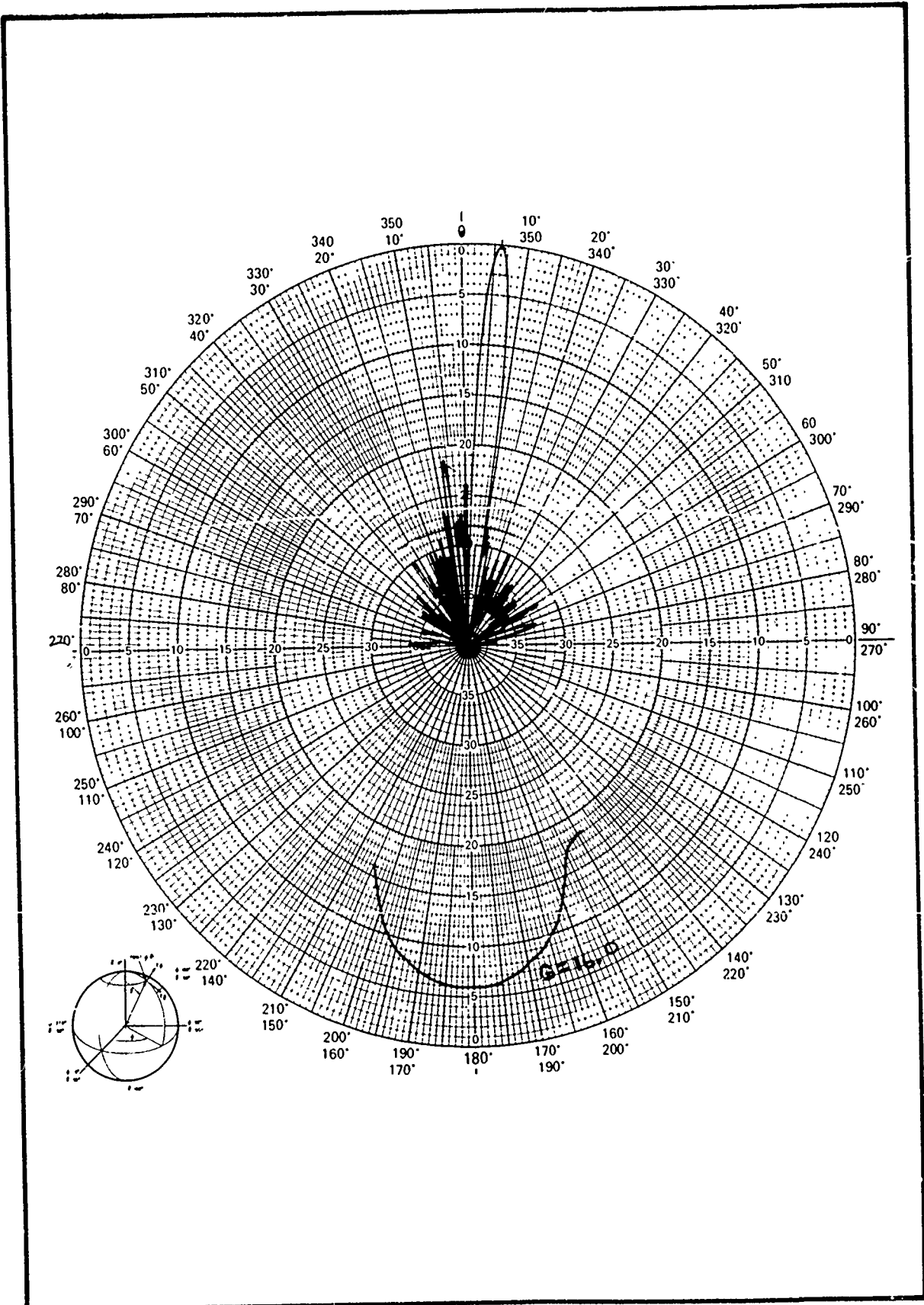


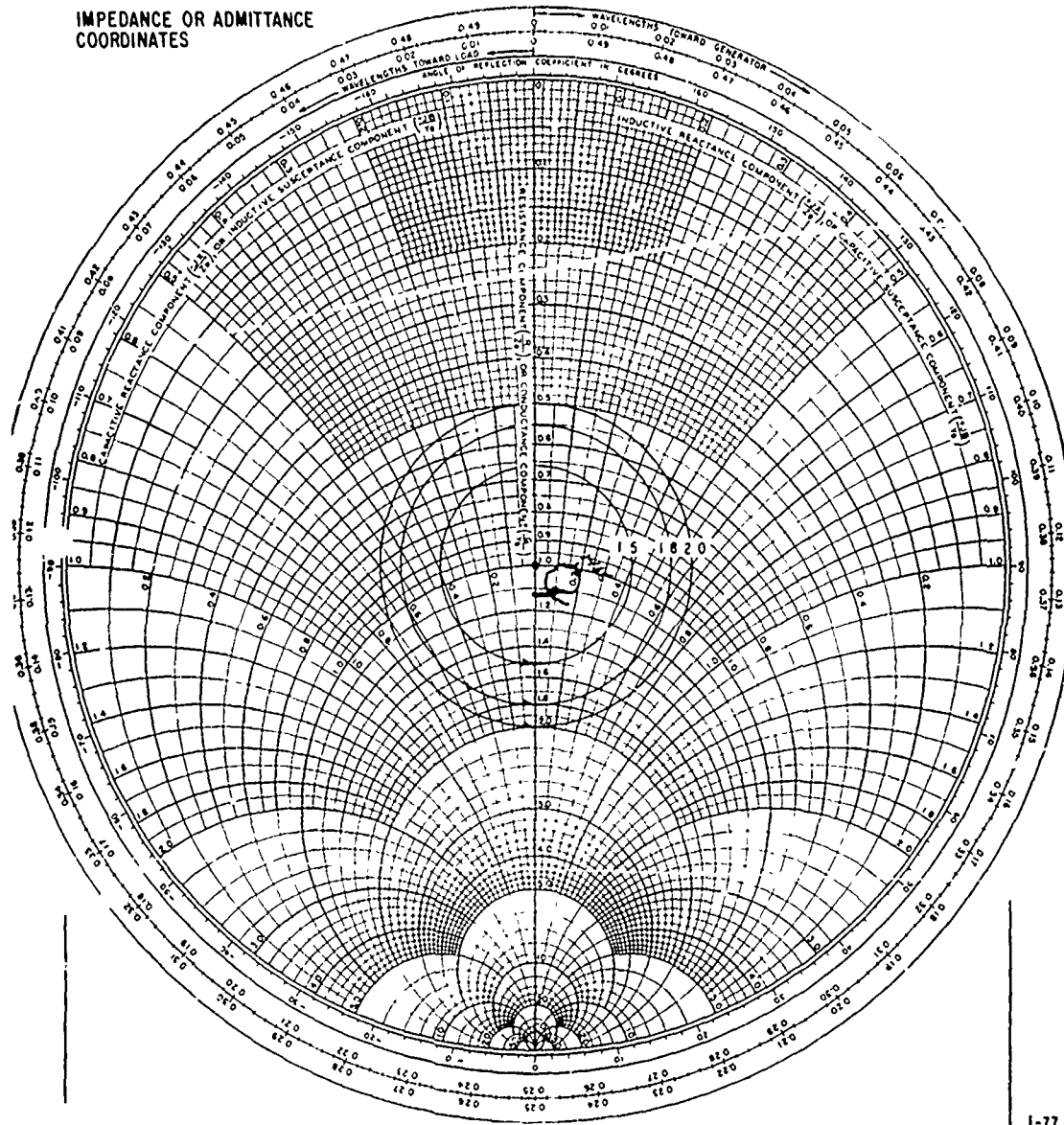
Figure 9 Measured Pattern of Five-Meter Traveling Wave Array

Ball



PROJECT NO.	PROGRAM	RADIOMETER
PART NO.	MODEL NO.	5 M ARRAY
TEST TYPE:	SERIAL NO. 005	
<input type="checkbox"/> DEVELOPMENT		<input type="checkbox"/> PRE
<input type="checkbox"/> IN PROGRESS		<input type="checkbox"/> FINAL
FREQUENCY RANGE 1400 - 1490		SHEET 1 OF 1

IMPEDANCE OR ADMITTANCE COORDINATES



1-77

BALL BROTHERS RESEARCH CORPORATION		
REMARKS _____	OPER <u>BK</u>	WITNESSED _____ DATE <u>2/26/79</u>

Figure 10 Impedance of Five-Meter Traveling Wave Array

varying the non-resonant patch dimensions.

Figures 9 and 10 illustrate a typical radiation pattern and impedance locus of the five meter traveling wave array. An inverted microstrip configuration was utilized in the array construction to reduce dielectric losses.

Measured array gain was 21.5 dB with .2 dB of the input power dissipated in a terminating load. Theoretical directivity is 22.2 dB. Gain and pattern performance was maintained over a 6% bandwidth. With the exception of an image beam sidelobes remained below 23 dB over this bandwidth. From 1400 GHz to 1430 GHz the array scanned 2°.

5.0 CONCLUSION

Microstrip series arrays are efficient radiators and in the traveling wave configuration performance is maintained over a relatively large bandwidth. These arrays represent a monolithic printed circuit design that may find applications not only when high efficiency is required but also in frequency scanned antennas.

6.0 REFERENCES

1. A. Derneryd, "Linearly Polarized Microstrip Antennas," IEEE Trans. on Antennas and Propagation, November 1976, pp 846-850.
2. H. Jasik, ed. Antenna Engineering Handbook, First ed., New York: McGraw Hill, 1961 Chapter 16, pp 28-32.

PRINTED CIRCUIT COLINEAR ARRAY

GARY G. SANFORD
BALL AEROSPACE SYSTEMS DIVISION
BOULDER, COLORADO 80306

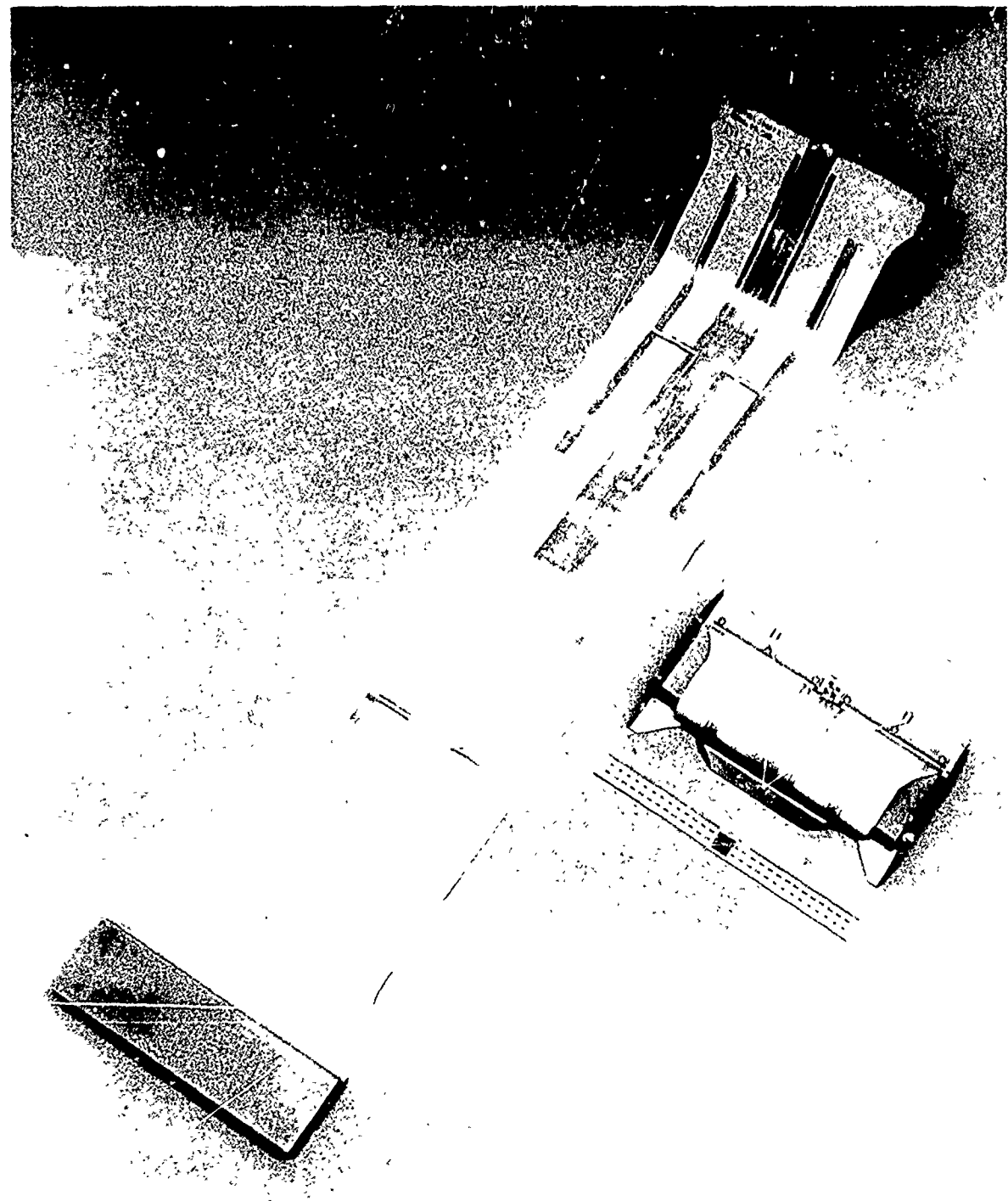
SUMMARY

A UHF communications relay system for naval operations requires a vertically polarized antenna with omnidirectional coverage in azimuth. The antenna must be an array in order to provide the required 4 dB gain at the horizon. It must unfurl from an 18cm x 30cm x 4cm package suspended below a balloon. The antenna and release mechanism must weigh no more than one kg.

The antenna* designed to meet these requirements is a colinear array etched from copper on mylar film, Figure 1. This printed circuit is very flexible so that it can be rolled up on a rectangular tube. The unfurling operation is accomplished by simply releasing the roll and letting it unroll to its full length. The release mechanism is a burn wire actuated by a current pulse.

Three different coplanar structures were investigated in the early stages of the development. A variation of the microstrip traveling wave antenna was found to be predictable and efficient. Like other traveling wave antennas though, the radiation pattern of the array steered with frequency. Over the required 15 percent bandwidth the beam steering was intolerable. Another variation of a microstrip array, a corporate-fed array in this case, was also developed. Although the pattern did not steer with frequency, it became very irregular at the extremes of the bandwidth. Thirdly, a coplanar, corporate-fed dipole array was developed and has proved successful.

*The development of this antenna was supported by Resdel Engineering Corporation and the U. S. Naval Air Development Center



79-1183

Figure 1 Antenna Designed to Unfurl from Compact Package

The dipole array uses folded dipoles to provide control of the element impedance. The coplanar transmission system uses both balanced and unbalanced modes. The entire circuit is etched on one side of the mylar film. Another sheet of film is bonded over the circuit to prevent voltage breakdown and to prevent corrosion of the copper. The measured results demonstrate good efficiency, beam control, and bandwidth. Techniques developed as part of this effort show promise of overcoming some of the limitations typically associated with microstrip arrays.

1.0 MECHANICAL DESIGN

The mechanical design must be compatible with the balloon system. The components of both the balloon system and the relay system are stored inside cylindrical container prior to launch. They are deployed according to the predetermined launch sequence. The relay is deployed approximately 30 seconds after launch, and the antenna must remain furled until this time. The volume allotted for the furled antenna is 18cm x 30cm x 4cm (7 x 12 x 1-1/2 inches). Another requirement imposed by the balloon system is weight; the antenna must weigh no more than one kg. Cost and environment are also critical to the mechanical design.

The antenna circuitry is etched from one-half ounce copper on 0.1mm Mylar film. Conventional printed circuit techniques are used. The film is extremely strong, yet light in weight. Even at the temperature of liquid nitrogen the Mylar retains its strength and flexibility. The actual size of the antenna is 26cm x 104cm, but the mechanical design allows for lengths in excess of six meters. The weight of the antenna circuit with its Mylar backing is less than 0.1 kg.

Prior to deployment, the antenna is wrapped around the outside of a rectangular epoxy-fiberglass spool, as shown in Figure 2. The flexibility of the Mylar film allows it to be easily rolled onto the spool without introducing stresses which would result in crack formation during prolonged storage. The spool also serves as the deployment weight for the antenna. When the antenna/spool combination is released, the antenna unrolls smoothly, borne by the weight of the spool. As the spool reaches the end of its travel, a shock force is generated due to the deacceleration of the mass of the spool. This force is initially carried by the

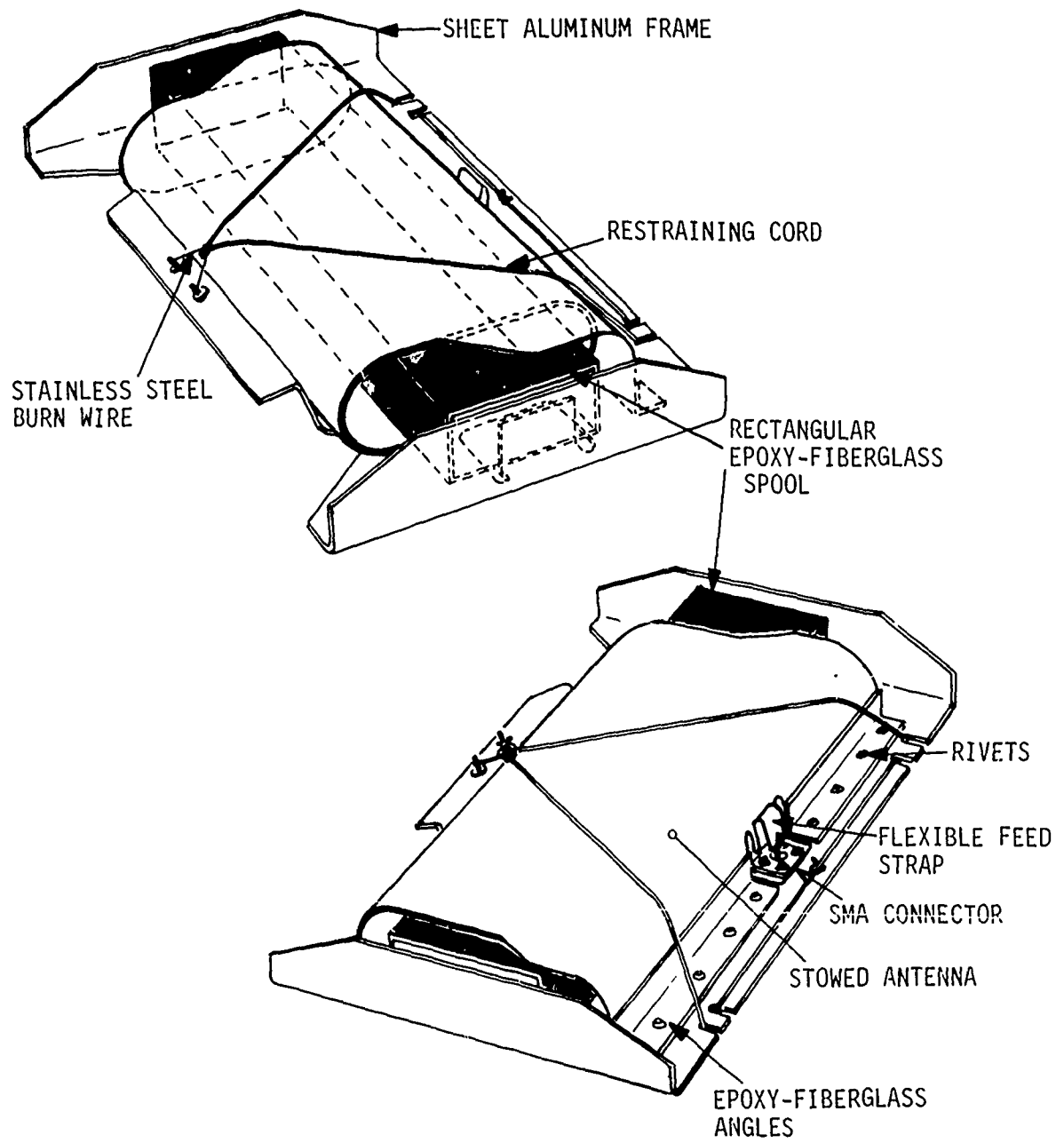


Figure 2 Mechanical Design Keeps the Antenna Simple

Mylar film which elastically deforms and transfers a portion of the stress to the copper antenna circuit. Analysis has shown that even a six-meter long antenna can tolerate this shock with a 50 percent safety margin.

The antenna support structure is formed from sheet aluminum. The Mylar film is secured to the aluminum by means of two epoxy-fiberglass angle brackets riveted through the Mylar to the aluminum. The brackets easily withstand that portion of the antenna deployment shock transferred through the antenna. In the stowed position the rolled-up antenna is held in place by a restraining cord. The cord passes through a loop of fine stainless steel wire which is fastened to two electrical terminals. A current source of no more than 2.5 amperes placed across these terminals will cause the wire to burn in less than 0.25 second.

An SMA connector is fastened to the top of the support structure using machine screws and nuts. Since the support structure is anodized, the antenna ground must be soldered directly to the body of the connector. Similarly, the center conductor is soldered, but a short flexible strap is used to protect the connection from residual deployment shock. Coaxial cable from the electronics package is attached to the SMA connector, and the whole assembly is held together by two machine screws.

Antenna circuitry is protected from corrosion by a 0.3mm Mylar film bonded to the surface. Solder joints are protected by a layer of silicon rubber, and aluminum parts are protected by anodizing.

The antenna and its support structure fit comfortably within the allotted volume. The volume could have been reduced, if necessary, without compromising the performance of the antenna. The complete antenna subsystem weighs less than 50 percent of the specified maximum weight as shown in Table 1.

TABLE 1
TOTAL WEIGHT LESS THAN ONE-HALF KILOGRAM

Antenna Circuit	80g
Antenna Connector and Mounting Fasteners	10g
Frame	140g
Frame Attach Angles	10g
Spool and Weight	175g
Spool Attach Angle	10g
Rivets	5g
Burn Wire Assembly	<u>20g</u>
TOTAL WEIGHT	450g
SPECIFICATION WEIGHT	<u>1,000g</u>
WEIGHT MARGIN	550g

2.0 SELECTION OF ELECTRICAL DESIGN APPROACH

The design approach selected for this antenna was the last of three that were considered. However, the first two are worth mentioning because they may be quite suitable for other applications. The difficulty with these two approaches was simply their limited pattern bandwidth.

The original concept for the antenna, Figure 3, was derived from a traveling wave microstrip antenna design. Instead of the planar ground surface, there was a ground strip running the full length of the array. A narrower conductive strip, lying parallel to the ground strip, formed the other half of an unbalanced transmission system. The line impedance could be controlled by varying the spacing between the two strips and/or by changing the width of the narrower line. Half-wave resonant lengths of low impedance lines formed the radiators. Radiators were connected in series by lengths of high impedance line. Connecting the radiators with half-wavelengths of line provided constant phase radiation from all the elements (a resonant traveling wave array). Other lengths of connecting line could be used to achieve a desired phase taper (a non-resonant traveling wave array).

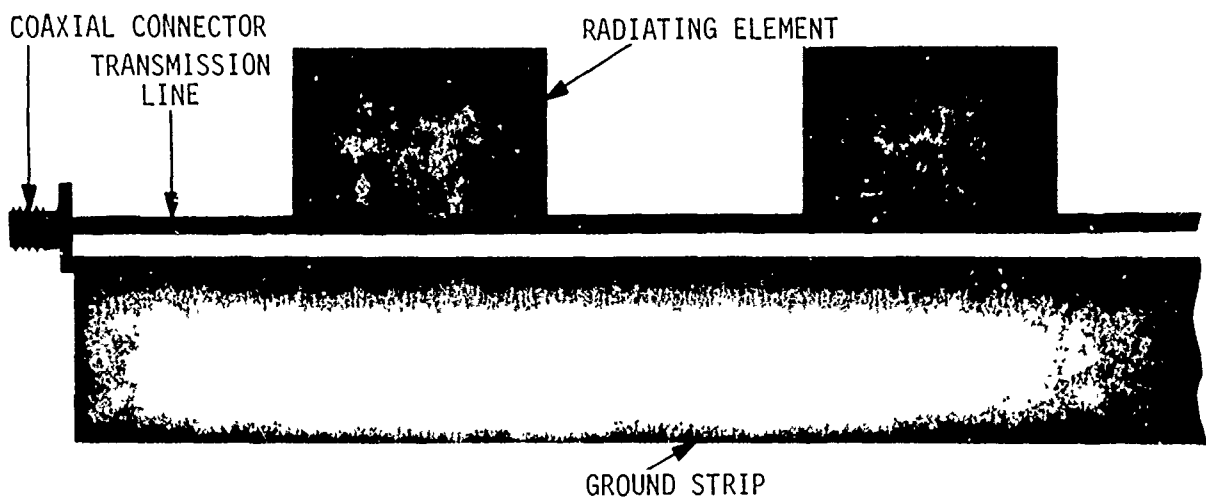


Figure 3 First Approach Based on Microstrip Traveling Wave Antenna

Now the difference between high and low impedance in this transmission system is relatively small. This limits the designer's ability to control the relative amplitude of radiation from each element. The limitation can be overcome by reducing the width of the ground strip adjacent to the low impedance sections of the transmission line, Figure 4. The ground strip begins to look more like a mirror image of the opposite strip, offset by approximately a half wavelength. Indeed, the identification of a ground strip no longer has any meaning. However, this is clearly not an array of horizontal dipoles; resonance is still dependent on dimensions parallel to the transmission line, and the array is polarized parallel to the transmission line.

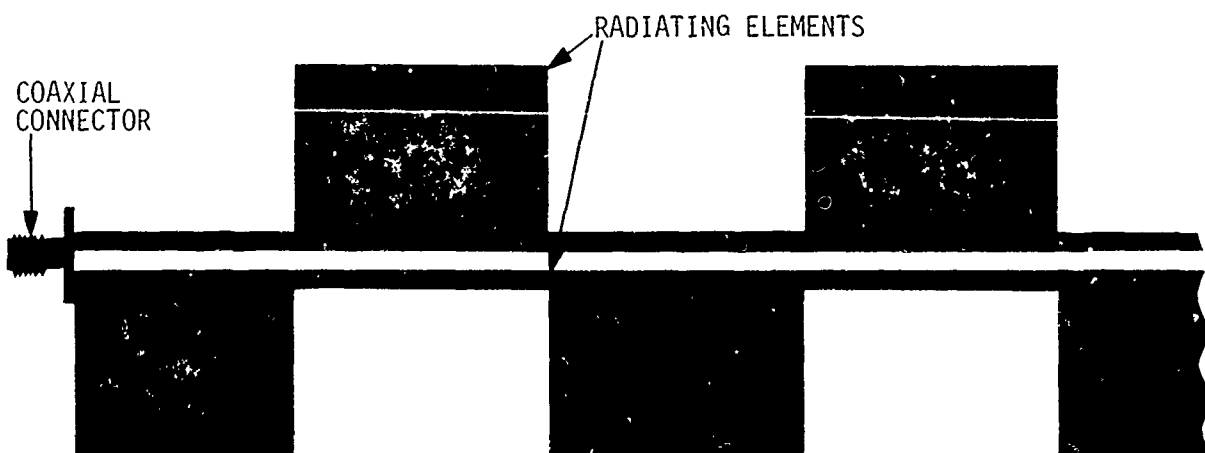


Figure 4 Modified Ground Strip Permits Better Control of Aperture Distribution

Models of this array demonstrated good efficiency and good pattern control. They also demonstrated the characteristic frequency steering associated with all traveling wave antennas. From 345 MHz to 400 MHz the peak of the beam steered 14°. Although the array was not highly directive, the peak of the beam was steered too far to permit meeting the gain specification over the entire bandwidth. The traveling wave approach was wrong for this application.

The more familiar corporate fed microstrip array was the basis for the second design approach. The array was conceived as an array of half-wave resonant strips on both sides of a central ground strip, Figure 5. The half-wave strips were driven against the ground strip just as half-wave microstrip patches are driven against a ground plane. An unbalanced coplanar transmission system was etched in the ground strip to form a corporate feed network. The only disadvantage of this feed network was that it required ground jumpers to cross the center conductor at every power division point. The added complexity was considered to be acceptable and a full-scale model was designed and fabricated. In retrospect it is apparent that this array might have worked if the aperture distribution had been simplified as it was for the final array. As the array was, though, the combination of elements with differing phases and amplitudes caused the array to be sensitive to variations of element impedance. The desired pattern was achieved only over a very narrow bandwidth.

Rather than resort to resistive power dividers, it was determined that a radiating element with less impedance variation over the bandwidth would solve the problem. Therefore, a dipole array as described below, was selected for the final approach. A combination of unbalanced and balanced transmission systems, also described below, eliminated the problem of the ground jumpers.

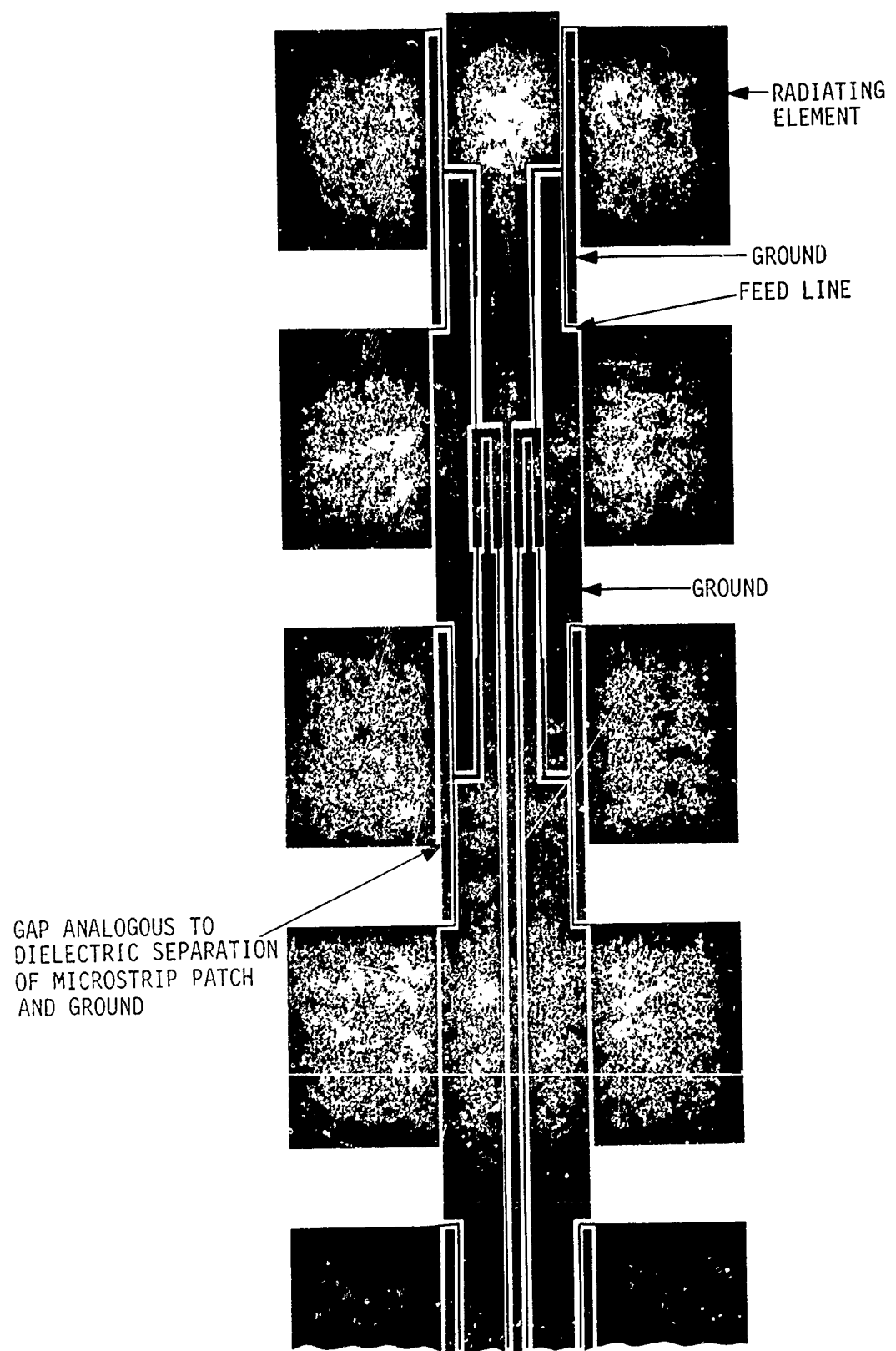


Figure 5 Second Approach Based on Microstrip Corporate-Fed Array

3.0 ELECTRICAL DESIGN

The antenna is an array of two dipole pairs, Figure 6. Dipoles are arrayed in pairs on either side of the feed network in order to maintain azimuthal symmetry. To minimize azimuthal gain variation, the separation between dipoles in each pair is also minimized. With a separation of less than 0.2λ (about 16cm) the dipoles in each pair act very much as one dipole, and the azimuthal variation is less than ± 1 dB.

Vertically, the centers of the dipole pairs are separated by 0.66λ which provides an elevation beamwidth of about 40° . The phase of the lower dipole pair lags that of the upper pair by 20° so that the elevation pattern is steered down 5° . Steering the beam in this way reduces the gain at the horizon by just a small fraction of a dB while increasing the gain at -30° by 4 dB. The result is a compromise that significantly increases the useful coverage of the antenna.

The dipoles are folded in order to make their impedance consistent with the practical range of impedances of the coplanar transmission system. While the basic 70 ohm dipole impedance is too low, the 280 ohm impedance of a standard folded dipole is too high. The proper impedance, about 160 ohms is achieved by making the widths of the parallel conducting strips unequal. The inner strip is 10mm wide and the outer strip is 1mm wide.

The folding of the dipole creates a slot radiator which can radiate in a cross-polarized mode. This unwanted radiation is eliminated by moving the slot resonance out of the operational bandwidth. A higher frequency slot resonance is achieved by shortening the slot, that is, by increasing the size of the band which connects the two parallel strips at the ends of the dipole. This makes a significant improvement in the elevation pattern, and the small change in the dipole reactance is easily corrected in the feed network.

A coplanar transmission line is the only efficient and practical way to feed the antenna. Microstrip on 0.1mm Mylar would be much too lossy. The feed network is actually a combination of unbalanced and balanced coplanar transmission lines. A coaxial connector serves as a launch for

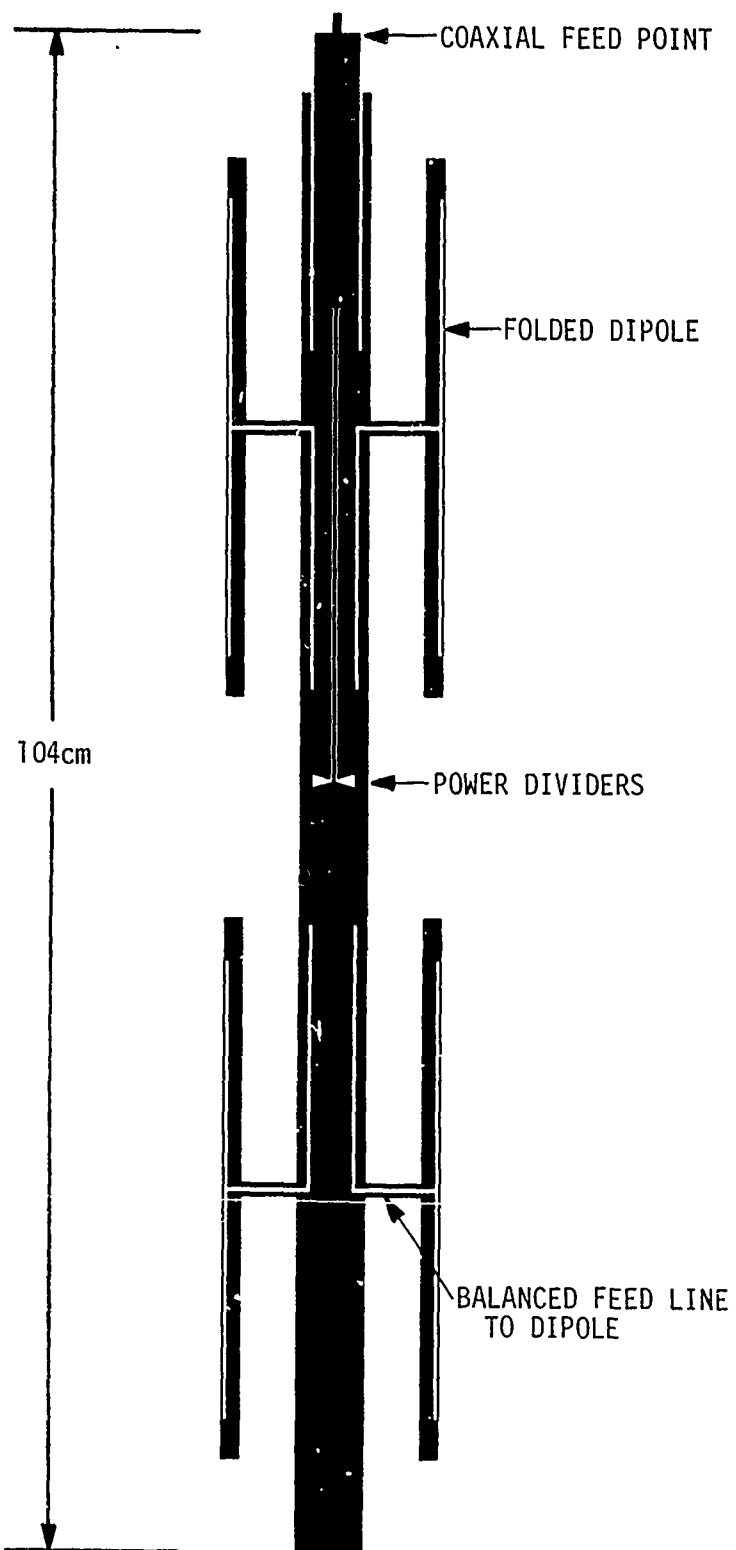


Figure 6 Final Approach Uses Corporate-Fed Dipoles

the unbalanced line. There is a center conductor strip soldered to the coaxial center conductor. On both sides of the center conductor is a ground strip soldered to the coaxial ground. The system is thus unbalanced from the coaxial connector to the first power division. The first quarter-wavelength transforms the 50 ohm coaxial impedance to the higher impedance of the coplanar system. At the power division, two mirror-image balanced transmission systems are fed in parallel. The transition is somewhat like an (unbalanced) coaxial line feeding a (balanced) radial line. By changing to a balanced system at this point, the problem of jumpering grounds at every power division is avoided.

The balanced portion of the feed includes a series-type power divider and a quarter-wavelength section matching the feed to the dipole. The series power divider is analogous to an E-plane waveguide tee, both in the way that impedances add in series and in the way that two opposite phases are generated. It is interesting to trace the phase progression through the feed network to see how the dipoles can be in phase in spite of the phase reversals. In this case of course, the dipoles are not quite in phase because the feed to the lower dipoles is intentionally 4cm longer. This phase lag causes the beam to steer 5° down as already mentioned.

The antenna must handle 60 Watts at altitudes over 25,000m and therefore must be protected from voltage breakdown. For this purpose and for corrosion protection, a self-adhesive Mylar film is laminated to the etched surface of the antenna. As already mentioned, the Mylar cover does not protect the solder connections at the coaxial connector, and this area must be coated with silicon rubber sealant. These cover materials do not effect the performance of the antenna in any measurable way.

4.0 RESULTS

The antenna design has been completed and ten pre-production units, like that shown in Figure 1, have been delivered. All units show remarkable consistency. The maximum VSWR from 345 MHz to 400 MHz was 1.5:1, Figure 7. Radiation patterns, Figure 8, demonstrate minimal variation across the bandwidth. Azimuthal variation at the horizon is less than 2 dB

(total variation); and the minimum gain at the horizon is 4.0 dB or just slightly less in some cases. The gain and beamwidth measurements imply that the antenna efficiency is quite high.

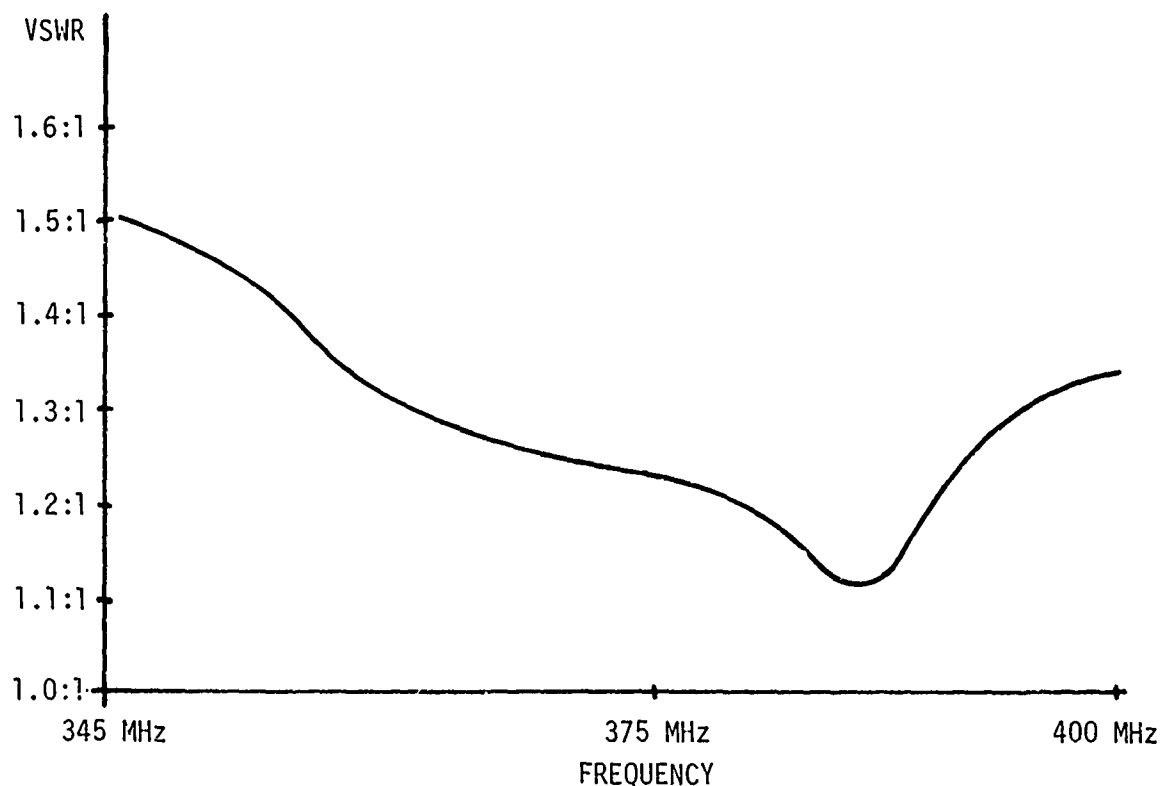
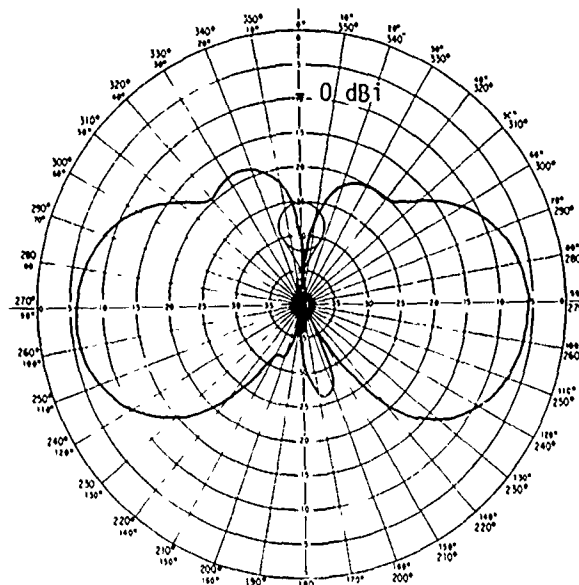


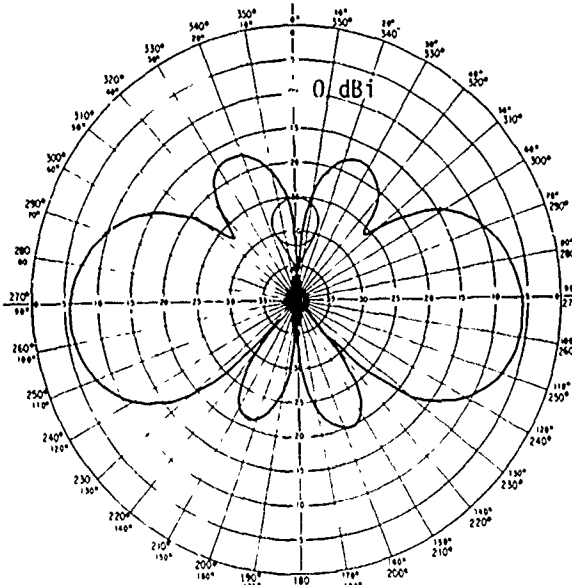
Figure 7 VSWR Less Than 1.5:1 Across Entire Bandwidth

5.0 CONCLUSIONS

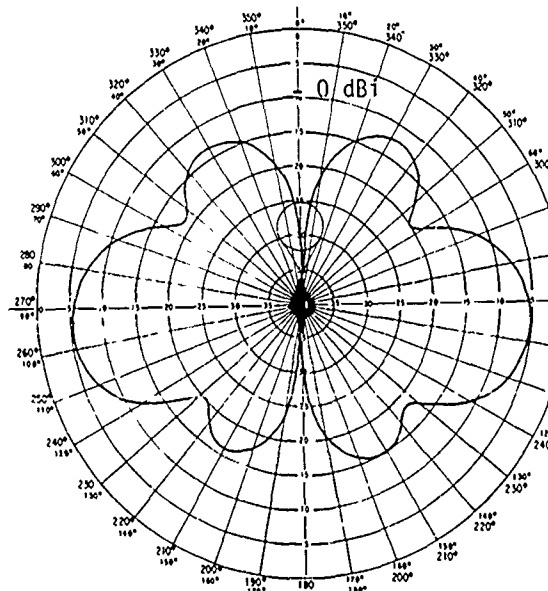
BASD has successfully completed the development of an unfurlable light-weight printed circuit, colinear array. The design represents a significant new departure in printed circuit antennas. Techniques developed during this effort can be applied to many different array configurations and may suggest new solutions to the bandwidth problem associated with most printed circuit antennas.



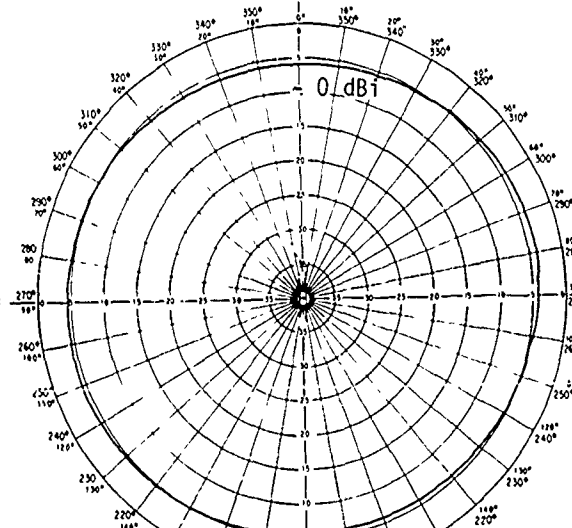
ELEVATION PATTERN AT 345 MHz



ELEVATION PATTERN AT 375 MHz



ELEVATION PATTERN AT 400 MHz



TYPICAL AZIMUTHAL PATTERN

Figure 8 Measured Radiation Patterns Demonstrate Good Pattern Control and Efficiency

PRINTED CIRCUIT ANTENNAS
FOR
SOLVING VARIOUS INSTRUMENTATION PROBLEMS

RAYMOND E. WILTON
SOUNDING ROCKET BRANCH
AEROSPACE INSTRUMENTATION DIVISION
AIR FORCE GEOPHYSICAL LABORATORY
HANSCOM AFB, MASSACHUSETTS

SUMMARY

Printed circuit antenna systems are being used by AFGL on various diameter research sounding rockets. A wide range of frequencies have been encountered as well as have many difficult payload configurations. The printed circuit concepts have provided antenna designs which have been both electrically and mechanically effective in solving various instrumentation problems. The printed circuit antenna has contributed much towards the development of optimum antennas for Air Force sounding rocket applications.

1.0 INTRODUCTION

Since 1946, Air Force Geophysical Laboratory (AFGL) has been instrumenting research sounding rockets. The telemetry, trajectory and command systems carried in these research vehicles have changed significantly over the years and have continually challenged the antenna designer. Antenna systems have evolved with the many changes in airborne instrumentation. Vehicle performance has improved, resulting in higher altitudes, increased heating, more complex payload configurations and an increase in the number of different systems on a payload that requires antennas. The antenna designer has had to solve the problems of changing frequency requirements, such as the moving of telemetry operations from 225 to 260 MHz to the 2.2 to 2.3 GHz UHF S-band. Bandwidth and RF power increases have created problems that have required new approaches to antenna designing. The ultimate problem, however, remains the need to insure that the design of the antenna system satisfies both the electrical requirements of the RF system as well as the mechanical requirements of the aerospace vehicle.

2.0 ANTENNA DESIGN PROBLEMS

Developing antenna systems for research sounding rockets or for any type vehicle, requires an understanding of the payload design problems. As soon as the frequency, power, bandwidth and other electrical parameters have been established, the payload configuration must be considered. Portions of the payload may be ejected or extended during flight which could effect the antenna pattern. It may be difficult to obtain the optimum location or space on a payload for the antenna system. Cost and time will always be a factor. Reliability and survivability will be foremost in the payload designers requirements. An understanding of the vehicle flight path in relation to the ground receiving or tracking sites will be essential to effective antenna systems design. Satisfying the antenna needs of the various types of vehicle payloads that will be encountered, requires a high degree of cooperation between mechanical and electrical engineering activities. Developing an effective antenna system involves much more than solving theoretical problems. A look at some of the instrumentation problems that were solved with printed circuit antenna designs will illustrate the approach used by AFGL.

3.0 NIKE TOMAHAWK TYPE VEHICLE ANTENNAS

A typical research sounding rocket has been the two stage Nike Tomahawk. This is typical of several different vehicles that are instrumented by AFGL. Payloads for these vehicles are often complex, with payload weights of 200 pounds achieving altitudes of over 200 Km. The typical diameter of these payloads today is between 22.86 cm to 30.48 cm (9.0 to 12.0 inches). The initial use of the printed circuit antenna on AFGL payloads was 1970 when telemetry operations moved to the 2.2 to 2.3 GHz band. Several contractors provided prototype telemetry antennas for AFGL at this time. One of the first types flown was from Guide Industries (Figure 1). This design was constructed in different diameter versions. A printed circuit type antenna was installed on a coupling ring so as to be flush with the payload surface. The outside antenna surface was plated to be heat resistant and the entire system was riveted to the coupling ring. This design was both mechanically and electrically effective for the vehicles being instrumented at the time.

Changes in rocket payload design requirements dictated that the number of connecting joints on the payload skin be reduced. This limited the use of the coupling ring concept for these rocket vehicles. The next approach was to fabricate the antenna system as an integral part of the payload skin.

A prototype model was fabricated by New Mexico State University, Physical Science Laboratory (PSL). A stripline antenna was constructed using printed circuit techniques. This was installed on the payload surface but was covered with a fiberglass heatshield. This was electrically effective but was not mechanically or economically satisfactory. An effective technique was developed wherein the payload skin was machined to allow installation of the stripline so as to be flush mounted (Figure 2). This PSL stripline antenna is typical of many that have been successfully used on AFGL vehicles. This stripline antenna has a heat resistant plating and it presents a minimum of outgassing that might effect a scientific experiment. This model includes a 2.2 to 2.3 GHz telemetry system with a 5.4 to 5.9 GHz (C-Band) transponder beacon antenna system. Another version of this design includes a 2.8 to 3.0 GHz (S-Band) beacon antenna in place of the C-Band section. Often, however, the beacon antennas will be small surface mounted blade types and only the telemetry system will require a stripline antenna.

This antenna design has resulted in a nearly omnidirectional pattern which is essential where the vehicle flight path and location of ground receiving stations will vary with different projects.

4.0 RANGING RECEIVER ANTENNAS

At launch site locations where radars are not available for providing trajectory information AFGL has developed a portable tracking system that provides trajectory through telemetry. This system transmits an upleg ranging signal, usually between 430 to 462 MHz, and a return signal is transmitted through the telemetry link. Trajectory data is obtained from the round-trip time for the ranging signal and from the tracking antenna position data. This system is also used for transmitting command signals to a vehicle payload during flight.

The typical antenna used at this frequency was a surface mounted, quadraloop design. A requirement to obtain trajectory data from a series of small diameter, Astrobee D rockets, presented a serious problem in that the aerodynamic drag caused by the surface mounted antenna would limit the altitude of the payload too much.

A stripline antenna was developed for this 15.24 cm (6 inch) diameter payload. (Figure 3). This Astrobee D carried two range receiver antenna systems to support a ground instrumentation test. Note that this payload also included both 2.2 to 2.3 GHz and a 1.68 GHz telemetry antenna systems. Further needs to reduce the size of these range receiver antennas resulted in a reduction from 26.9 cm to 15.0 cm in length (Figure 4). The gain of these flush mounted antennas are more than 10 dB below the quadraloop antenna illustrated, but this was offset by improvements in the ground tracking station.

5.0 AEROBEE ROCKET VEHICLE ANTENNAS

The Aerobee rocket has been a standard vehicle for more than 20 years. This vehicle presents a minimum of aerodynamic problems and was previously the most common sounding rocket used by AFGL. There are also current variations of this vehicle that will have higher performance characteristics.

The Aerobee payload consists of a series of 38.1 cm (15.0 inch) diameter payload skin sections of various lengths. A nose cone section installs on top of these sections. Ball Aerospace Systems developed a 2.2 to 2.3 GHz telemetry antenna for the Aerobee that is exceptionally effective (Figure 5).

Ball Aerospace Systems has provided a number of antennas for AFGL that use printed circuit techniques. The Aerobee antenna incorporates a microstrip design which is built into a configuration that serves as both a coupling ring between payload sections and as a mounting ring for instrumentation components. This type antenna is electrically very effective and mechanically it can survive recovery so as to be suitable for reuse.

As with the smaller diameter rockets, the higher performance follow-on vehicles to the Aerobee, such as the Astrobee F, required limiting the coupling joints. Again, the stripline antenna was considered (Figure 6). Because of the thin walled construction of these payloads, a surface mounted design was selected. Tests indicated that by tapering the edge of the stripline these type vehicles presented no aerodynamic problem for this antenna concept.

The surface mounted technique is the most economical approach to providing telemetry antennas for lower performance vehicles (Figure 7). Installation is easily accomplished at the field location to prevent shipping damage to the antenna. This concept has been used effectively on a number of different diameter rocket vehicle payloads.

6.0 ARCAS SOUNDING ROCKET ANTENNAS

The requirement existed for developing a lightweight, low cost 2.2 to 2.3 GHz telemetry system for this vehicle. The antenna design could not add any aerodynamic drag to the vehicle. This telemetry system design was accomplished by using a small 1.0 watt standard telemetry transmitter, microminiature subcarrier oscillators and a lithium battery pack (Figure 8).

The antenna design was accomplished by cutting radiating slots in the payload skin and then by riveting a stripline antenna section inside the skin to restore the structural strength of the payload (Figure 9). This concept has produced a low cost, effective solution to the requirement to provide a research vehicle for scientific programs that have a limited budget.

7.0 DENSITY SPHERE ANTENNA DEVELOPMENT

AFGL has used the stripline antenna to solve problems associated with instrumenting sphere payloads. For many years AFGL scientists have instrumented sphere payloads and made measurements as the sphere was ejected from a rocket vehicle to descend to impact. In order to improve the value of the data obtained from these flights, a flush mounted antenna system was required as well as a trajectory system within the sphere.

A current payload used by AFGL (Figure 10) that contains an accelerometer experiment, a 2.2 to 2.3 GHz telemetry link and a C-Band transponder beacon. The sphere is installed inside a rocket nose cone where it is ejected at altitudes above 50 Km. The reradiating slots can be viewed in the nose cone sections. These slots allow for enough leakage of signal to assist both the telemetry and radar trackers to maintain tracking lock on the vehicle prior to sphere ejection.

The antenna design was accomplished by installing both the telemetry and stripline antennas on a machined ring (Figure 11). The antenna elements are covered with a foam material in the shape of a sphere. The center section is instrumented and then sealed with the end caps.

A follow-on for this payload is a current investigation to replace the C-Band beacon with a 430 MHz range receiver for remote site trajectory operations.

8.0 ARIES ROCKET ANTENNA DESIGNS

A rocket vehicle that is currently in use at AFGL is the large diameter Aries vehicle. This has been developed from the obsolete Minute Man I system second stage motor (Figure 12). This vehicle is a guided rocket and it typically carries an attitude controlled payload. The large 97.79 cm (38.5 inch) diameter and the large instrumentation capacity of the vehicle have presented new challenges for the development of reliable antenna systems. Several programs using the Aries vehicle have each resulted in unique antenna requirements. Common to all these programs is the reliability requirements of these extremely high cost payloads. A research study was completed by AFGL and PSL to develop telemetry antenna systems for these large diameter vehicles.

The first antenna development was a stripline antenna system that is basically flush mounted. This antenna was to serve a multi-link telemetry system and covered the entire 2.2 to 2.3 MHz frequency band. Omnidirectional coverage was required as well as the ability to withstand severe aerodynamic heating.

The performance of the stripline antenna had been proven on a number of previous payloads, in this design the major concern was heating. Ablative coatings were rejected because particles could affect the scientific sensors. A heat shield and clamp assembly was constructed (Figure 13) which effectively contained the stripline system. Only the radiating portion was left exposed.

Thermal expansion was compensated for by segmenting the clamp assembly. This is a relatively complex assembly but it is a reliable system for high heat applications.

The next antenna design used for one of the Aries payloads was a flush mounted design (Figure 14). This is similar to systems used on smaller diameter payloads and is effective for most Aries flight conditions. The stripline sections are installed using blind holes and are seated in high temperature RTV. This technique allows the vehicle to remain sealed and with the RTV base outgassing contaminants are reduced.

The final type antenna system that was developed for use on the Aries payload has been a surface mounted stripline (Figure 15) similar to those previously described. With surface temperatures of less than 80°C during most of the flight, this design is aerodynamically satisfactory. A significant problem with a surface antenna on a large diameter vehicle is damage during prelaunch handling.

This single antenna section was installed so as to provide radiation coverage in one quadrant only. With the attitude control of the vehicle the antenna position favored a predetermined ground receiving location. This single section with its reduced beamwidth and increased directional gain allowed use of a lower powered transmitter for the telemetry link. Large diameter payloads such as those on the Aries type vehicles will continue to be used by AFGL scientists in the future. The use of stripline antennas has been well tested (Figure 16) on both the PSL antenna range and during flight. The stripline and other printed circuit techniques should prove very useful to develop improved antenna systems for future programs of this nature.

9.0 CONCLUSION

This paper has not considered design details or the quantitative results from tests of the various systems. Each antenna design discussed is an effective system that has provided a solution to a specific instrumentation problem. The intent of this discussion has been to tie together the theoretical considerations of antenna design and the type of applications that must be included as part of the goal for the antenna designer.

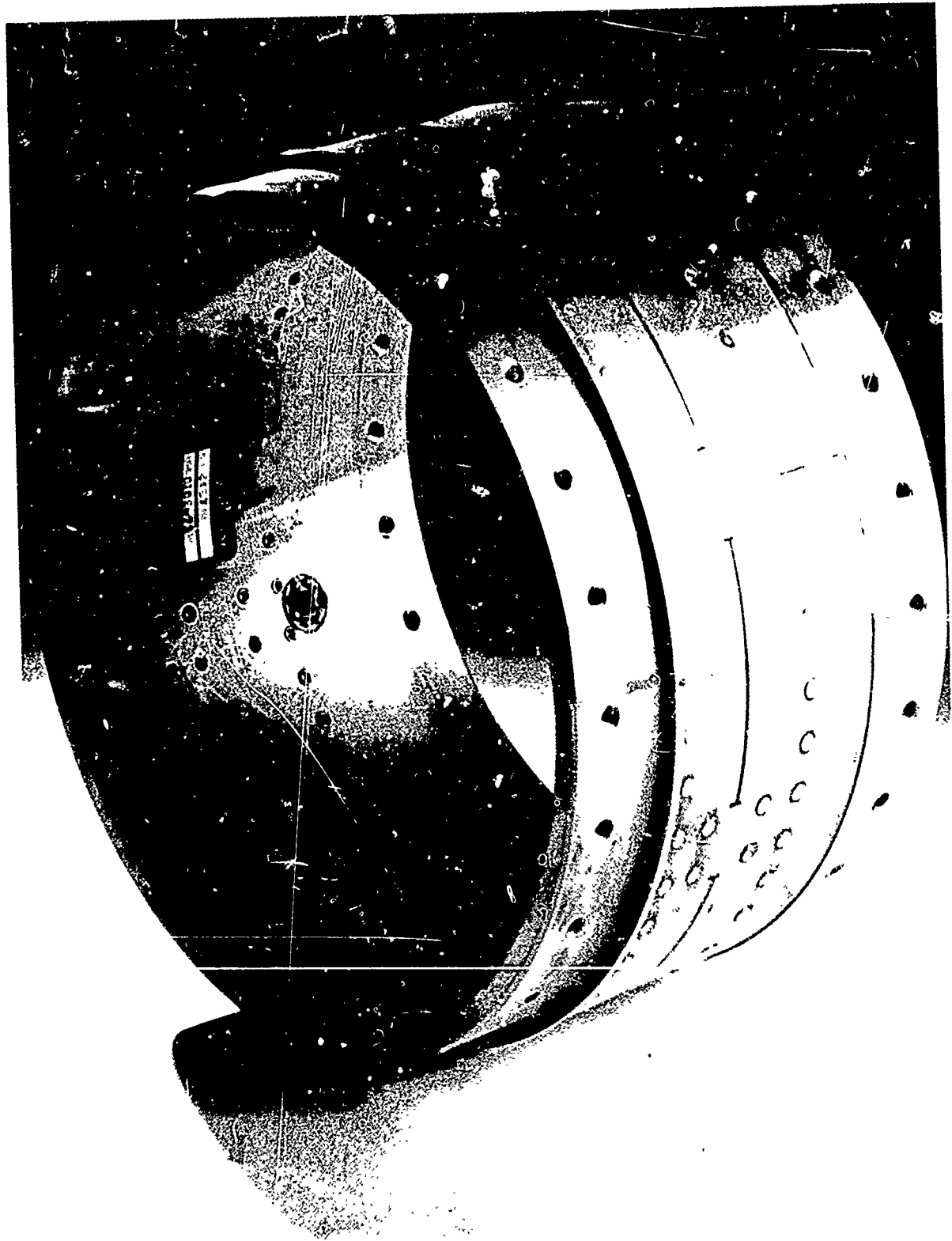


Fig. 1. Guide Industries Telemetry Antenna



Fig. 2. Flush Stripline Telemetry and Beacon Antenna



Fig. 3. Astrobee D Payload

22-11

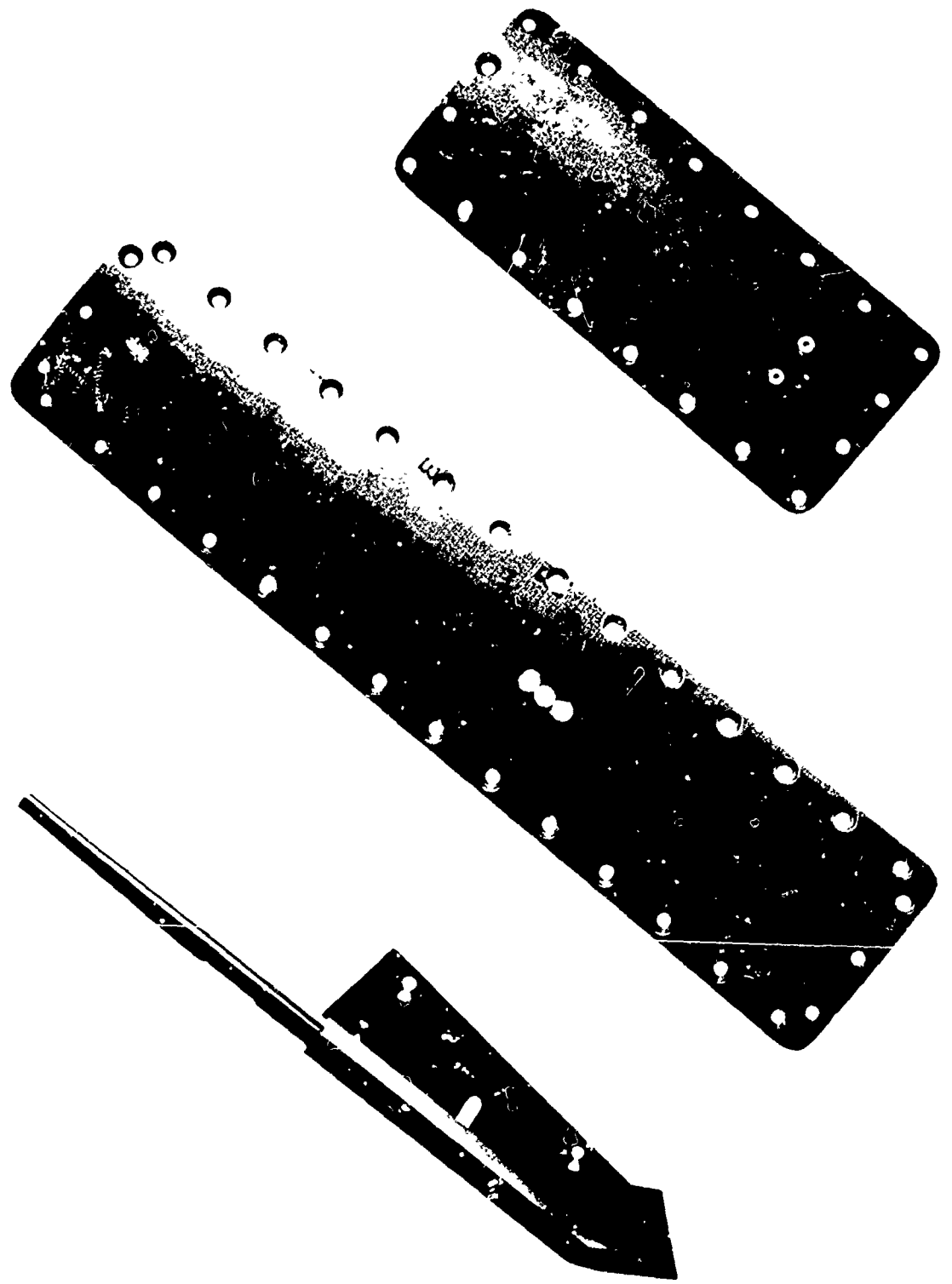


Fig. A Danning Receiver Antenna

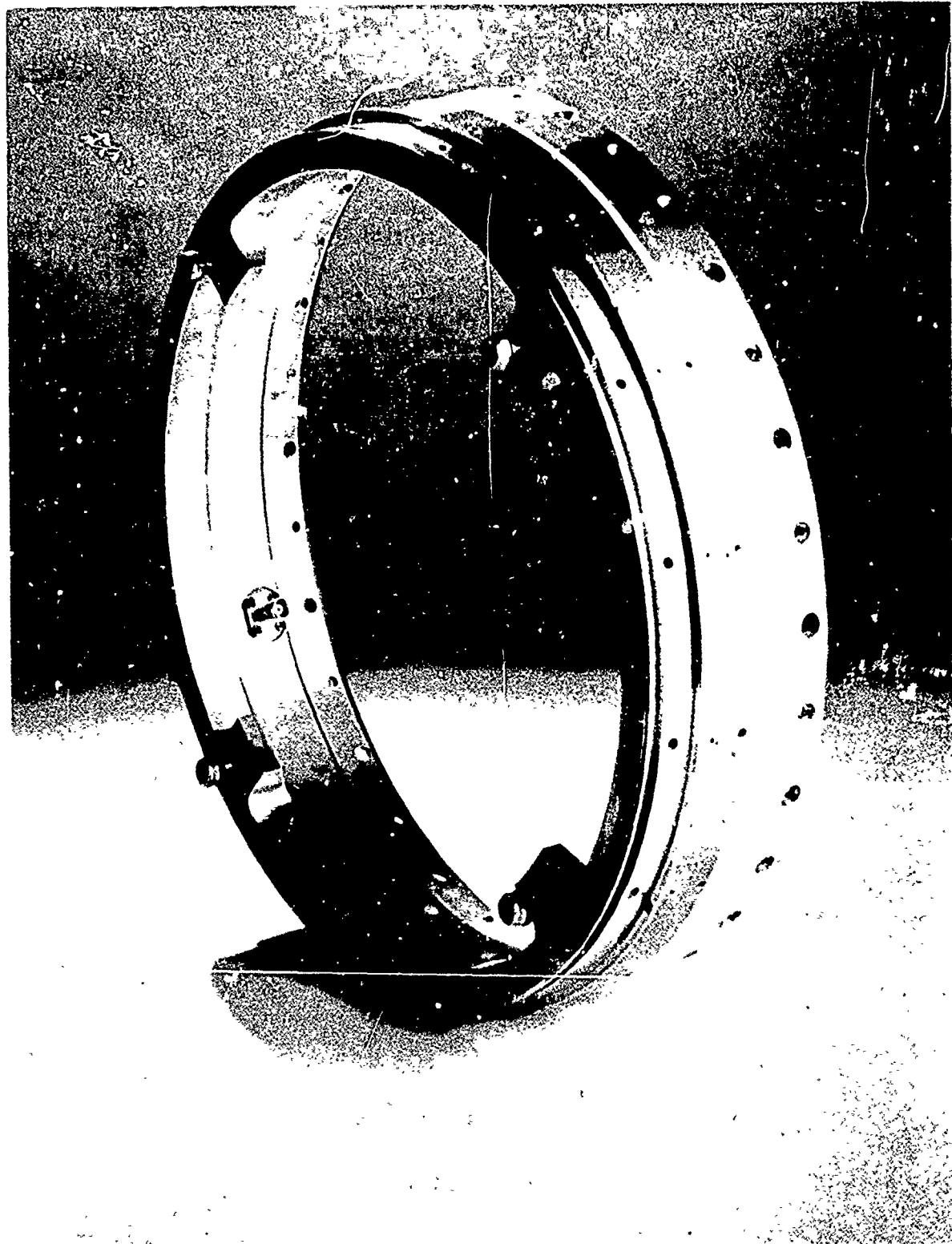


Fig. 5. Aerobee Telemetry Antenna

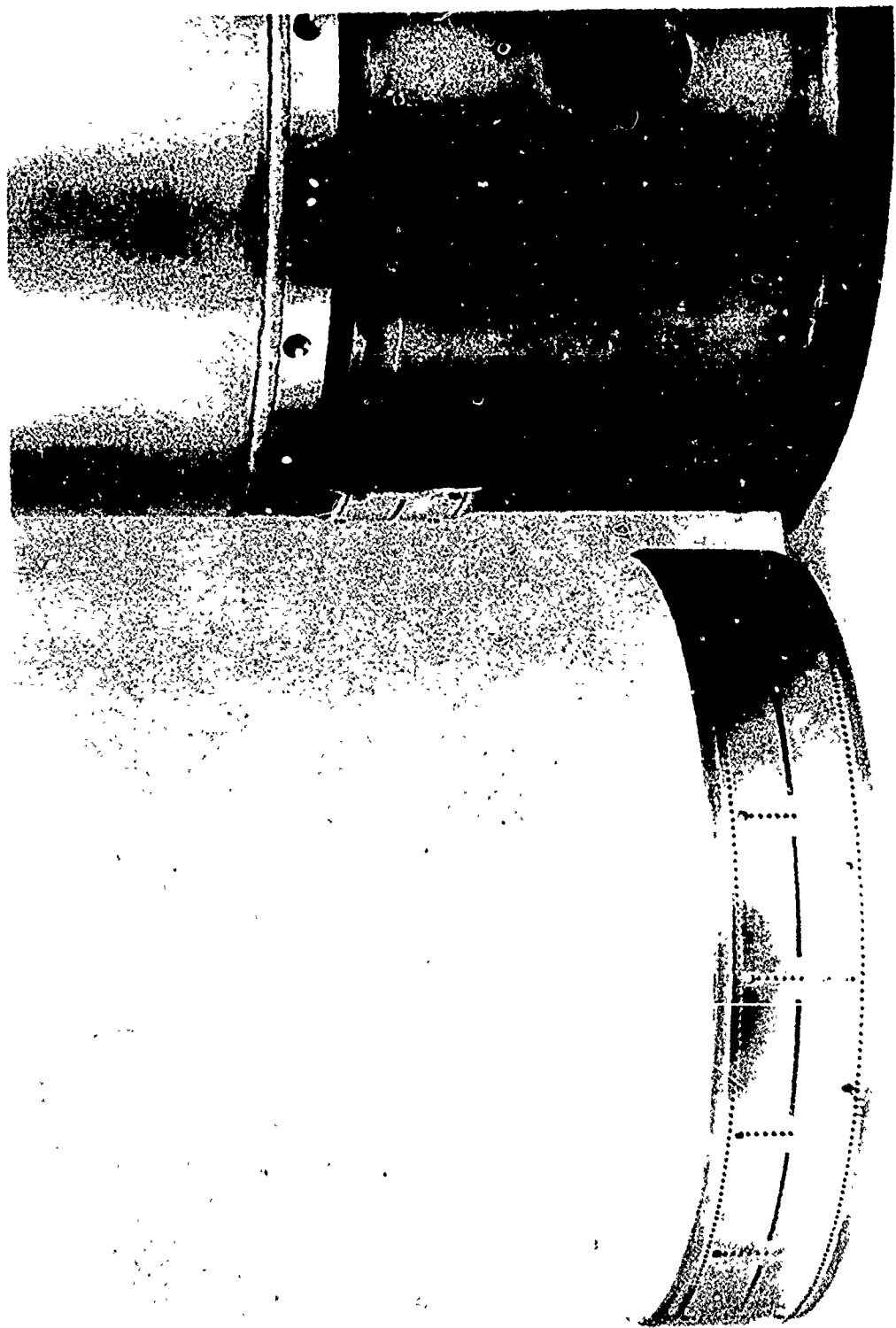


Fig. 6. Stripline Antenna for the Aerobee

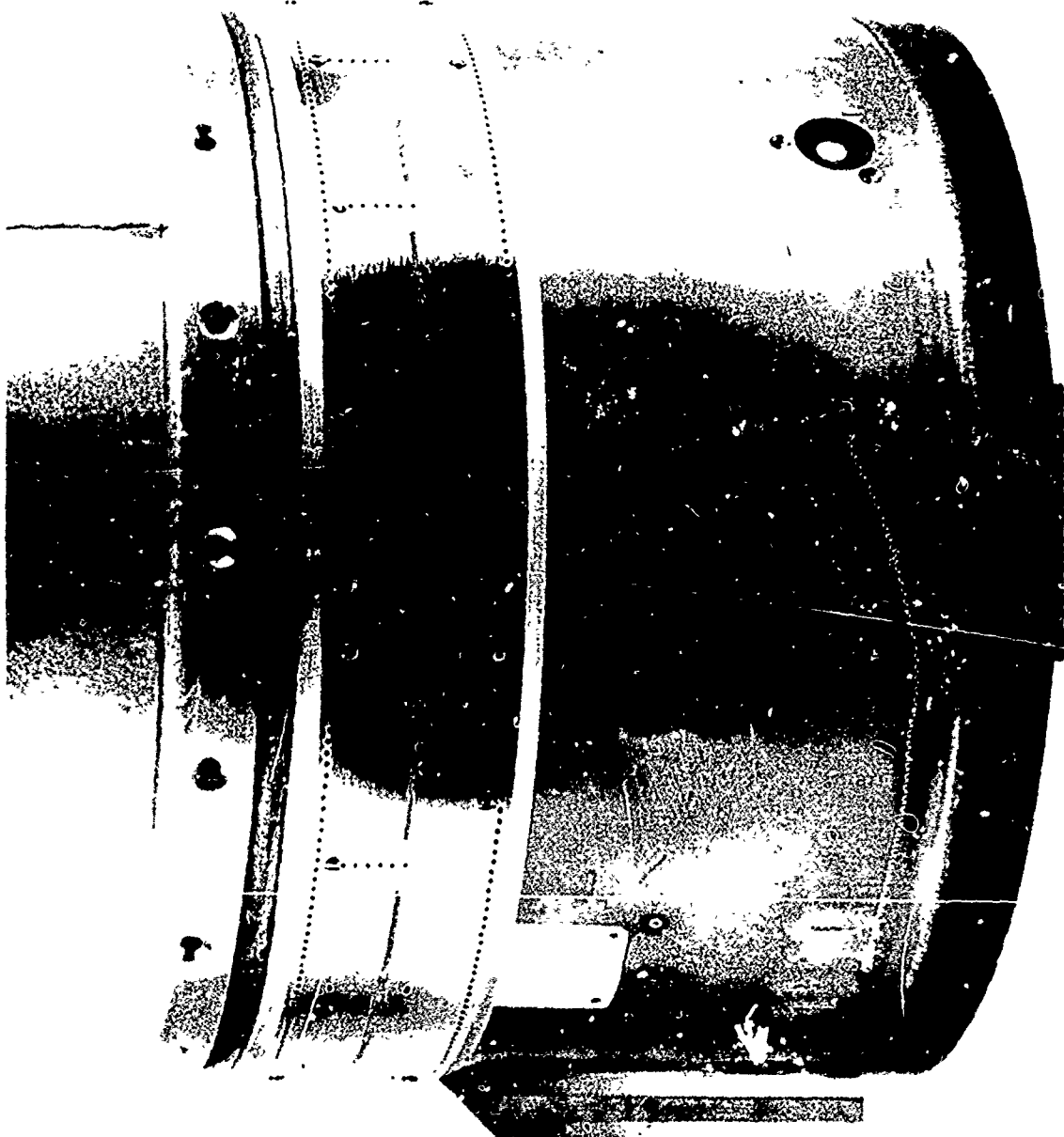
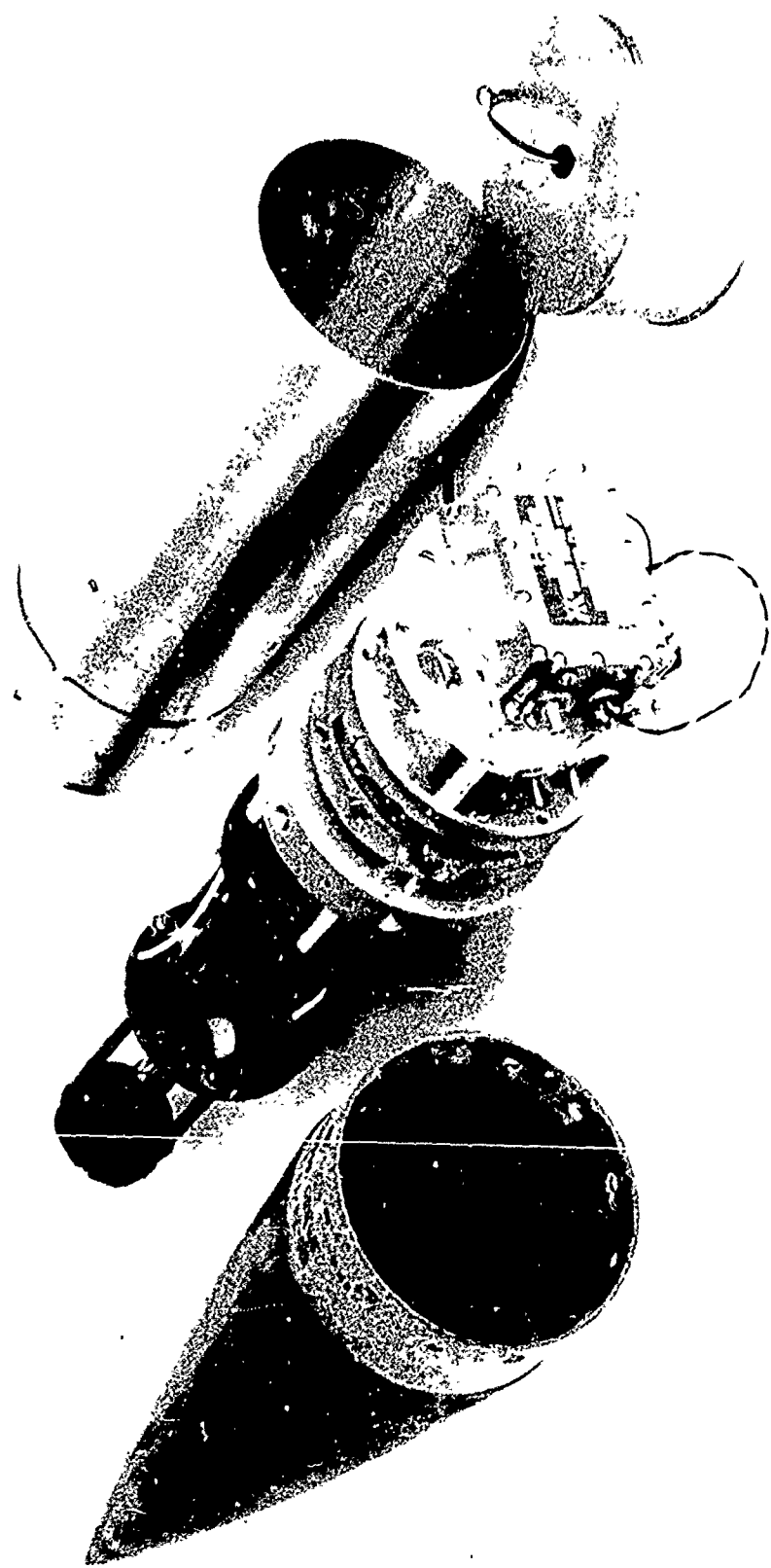


Fig. 7. Surface Aerobee Telemetry Antenna

Fig. 8. Arcas Payload Instrumentation



22-16

Fig. 9. Arcas Telemetry Antenna



22-17

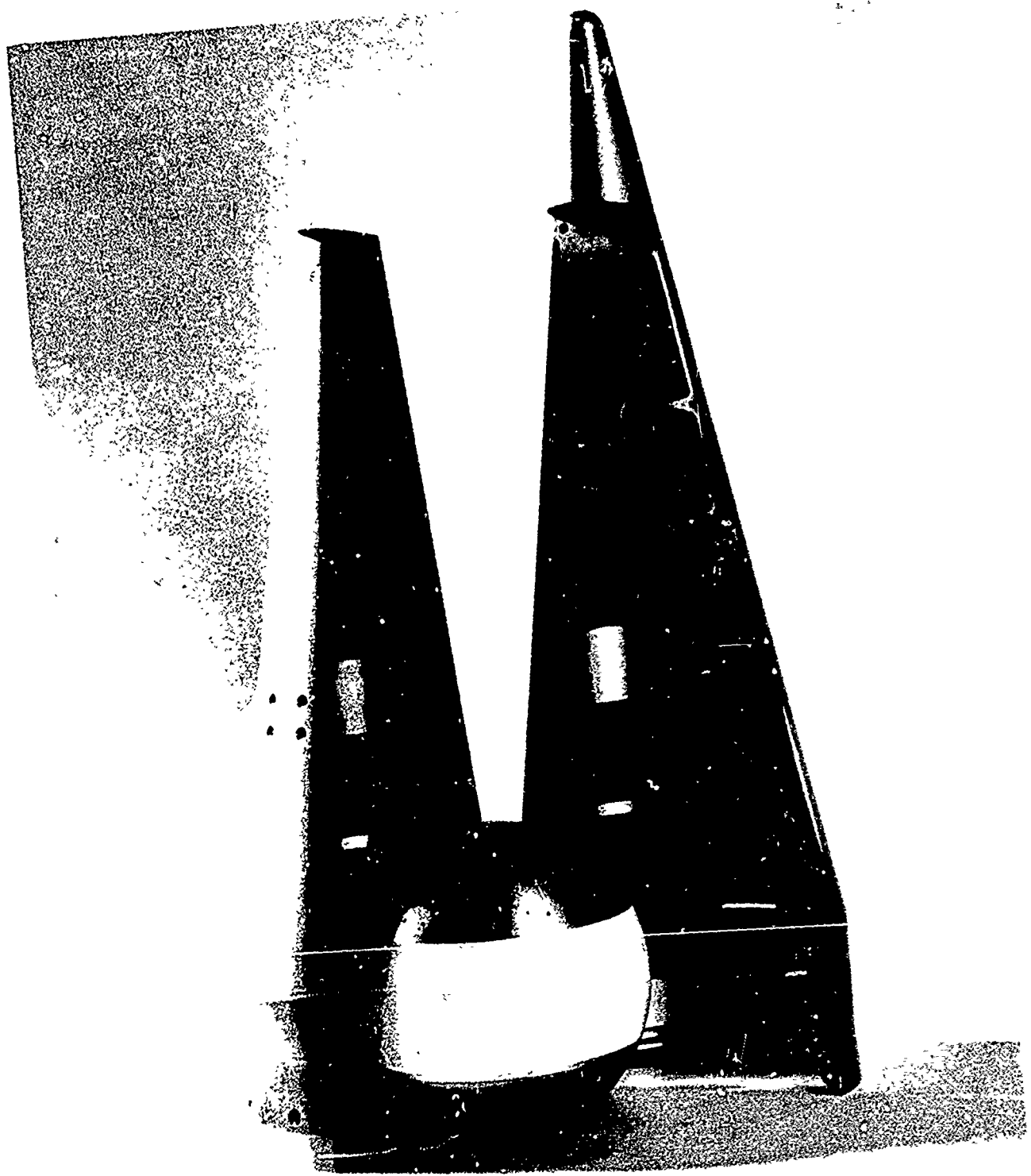


Fig. 10. Ten Inch Sphere and Nose Cone

22-18

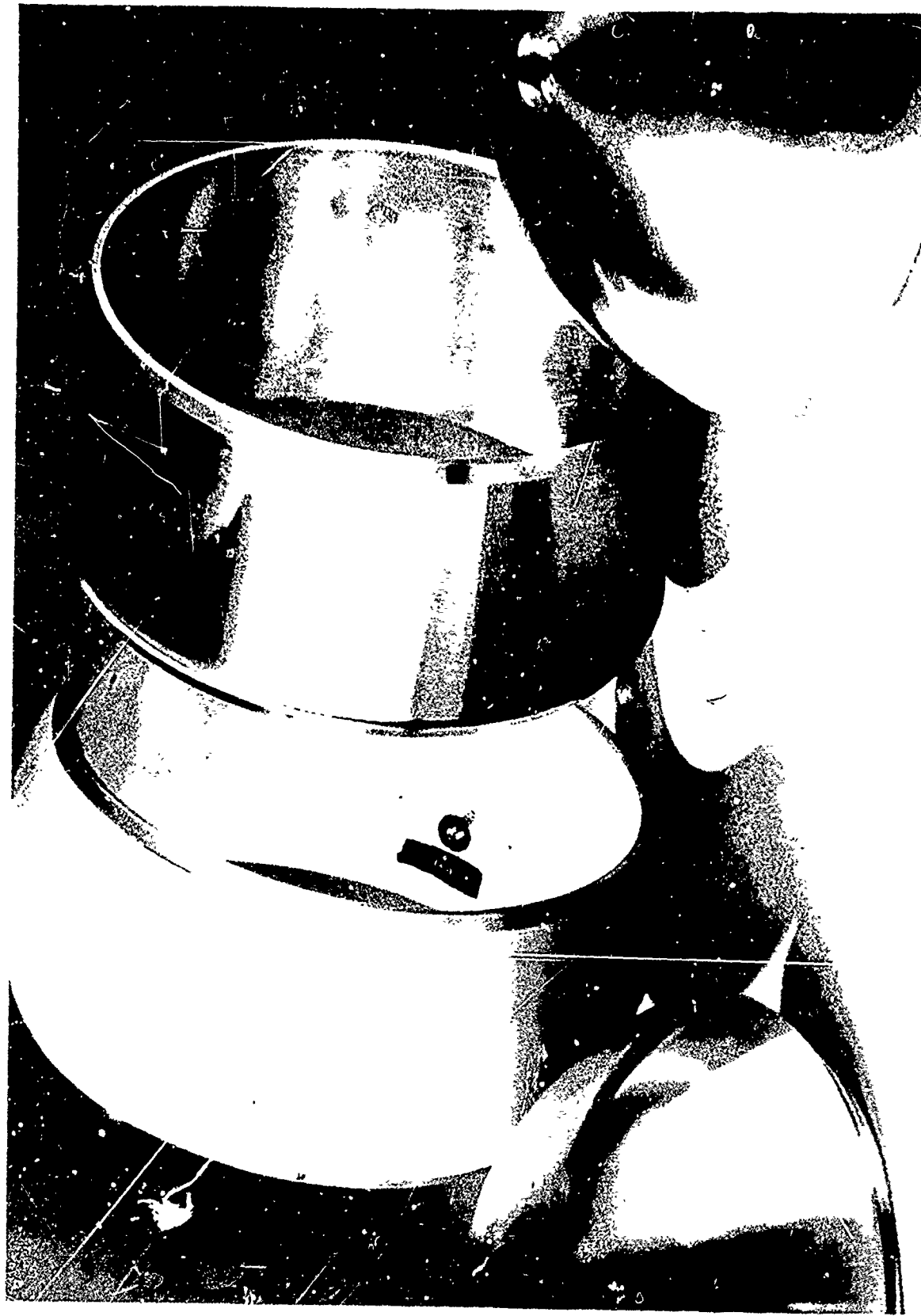


Fig. 11. Ten Inch Sphere Antenna Rings

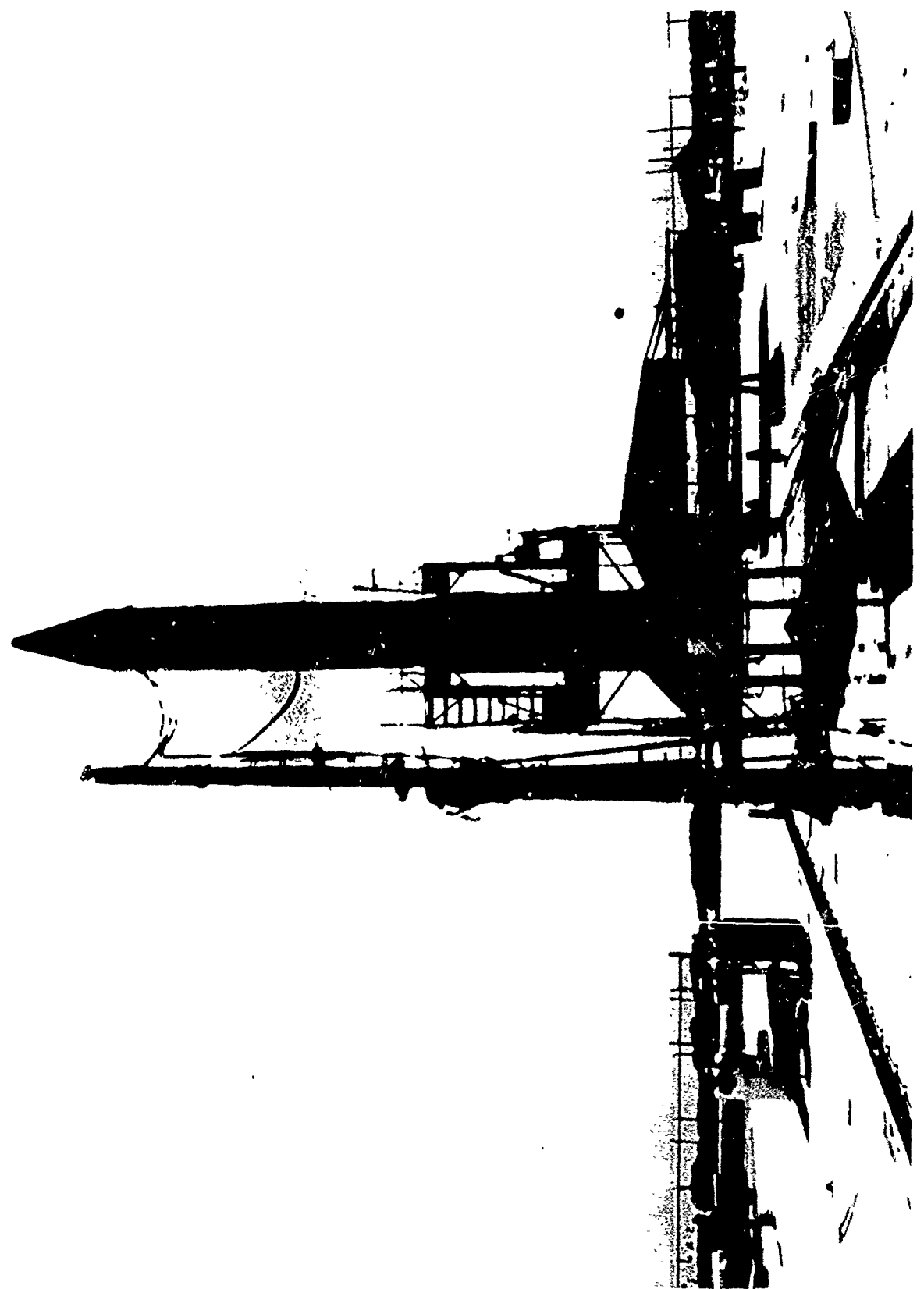
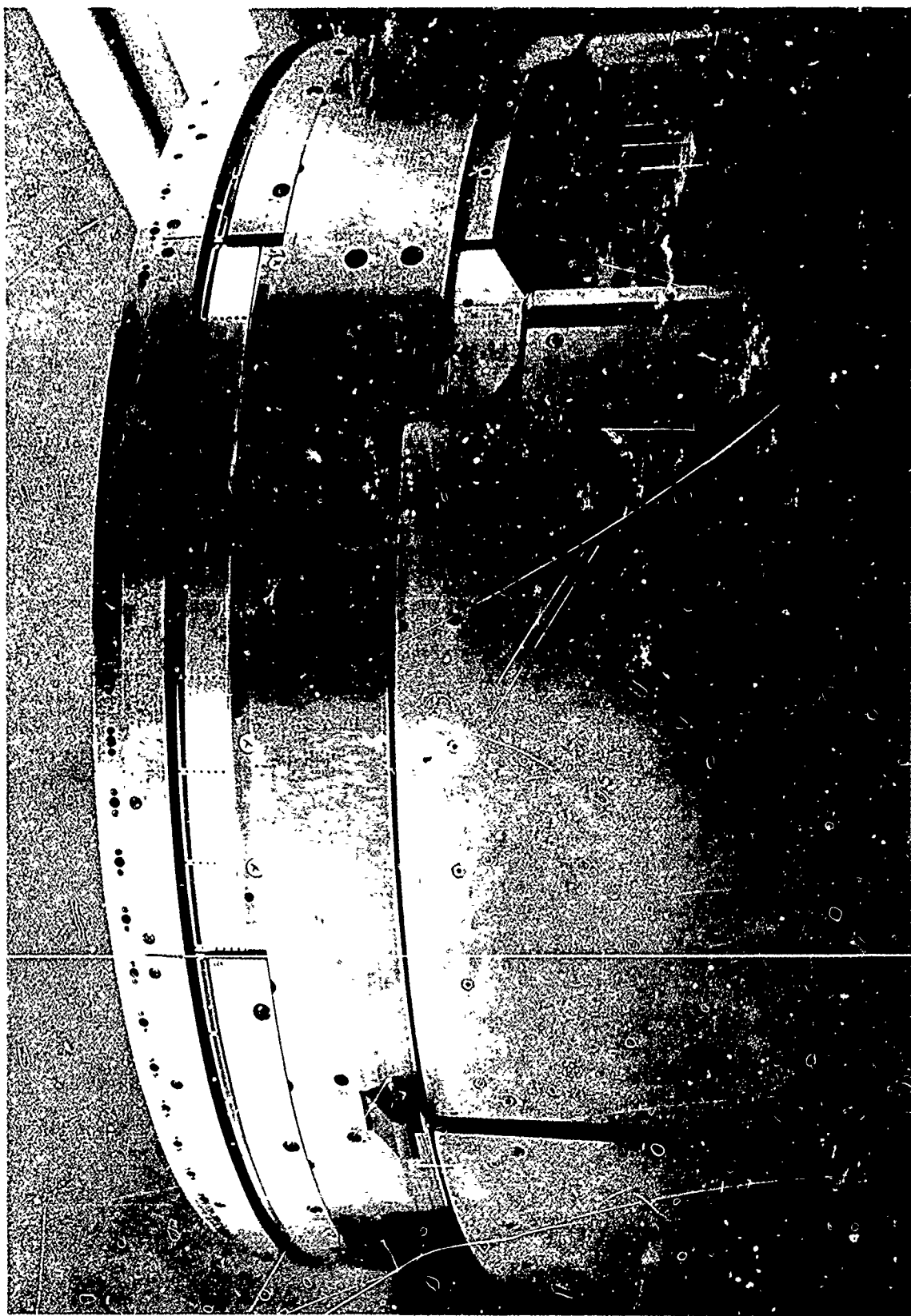


Fig. 12. Aries Rocket Vehicle

Fig. 13. High Temperature Aries Telemetry Antenna



22-21

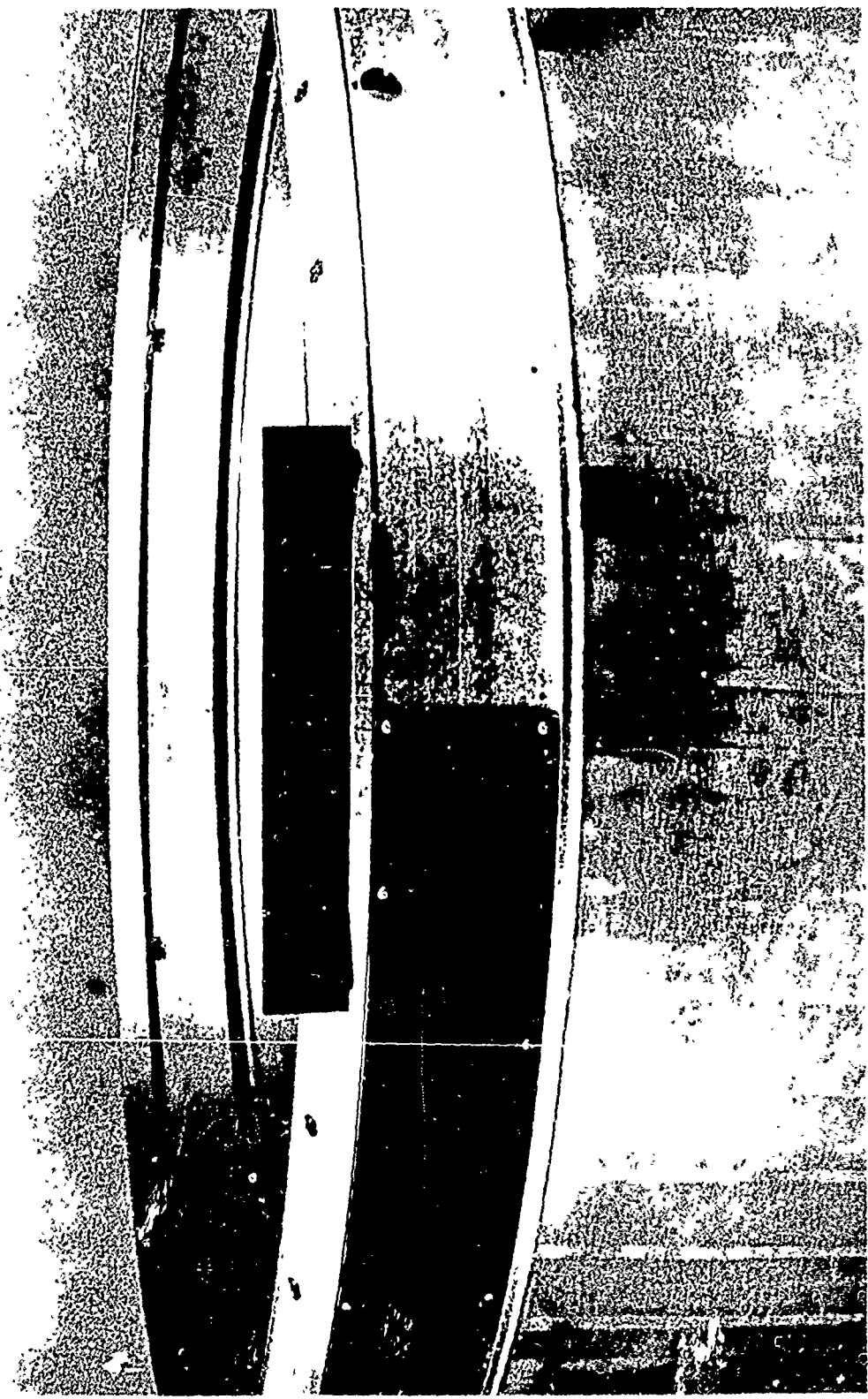


Fig. 14. Flush Aries Telemetry Antenna

22-22

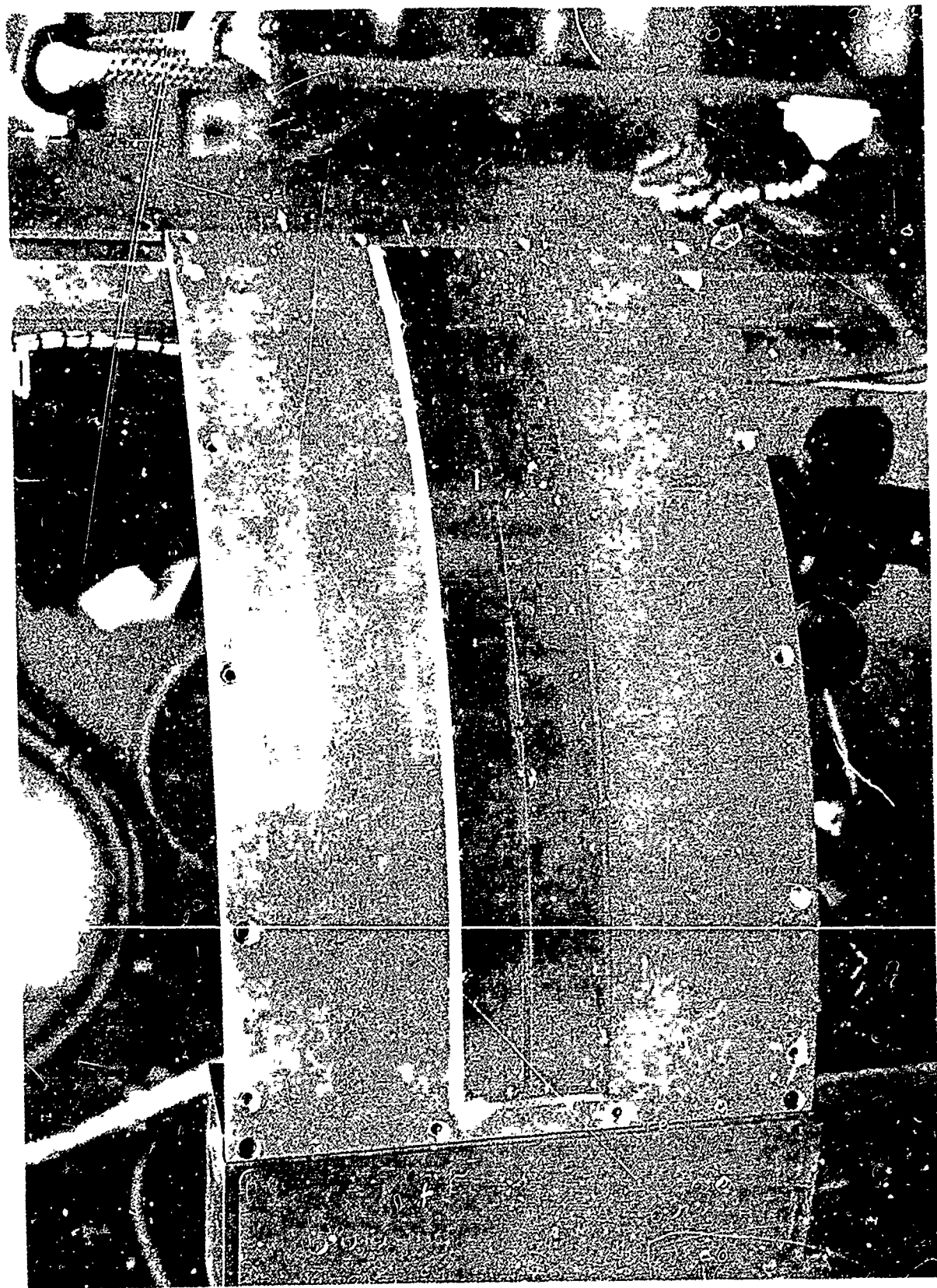


Fig. 15. Surface Aries Telemetry Antenna



Fig. 16. Aries Test on PSL Antenna Range

STRIPPLINE ANTENNA DEVELOPMENT

AL WATERMAN
PHYSICAL SCIENCE LABORATORY
NEW MEXICO STATE UNIVERSITY
LAS CRUCES, NEW MEXICO 88003

SUMMARY

A discussion of the engineering trade offs and design philosophy used to produce repeatable cost effective stripline antennas is presented. The discussion includes various antenna configurations for rockets, satellites and ground units, which have been in use at the Physical Science Laboratory (PSL) since 1970. The presentation shows studies which have led to the development of many stripline and printed circuit antennas in various frequency bands. Included in the paper are some suggestions concerning the design goals for maximum radiation coverage and bandwidth versus the restrictions of minimum size, weight and cost. Data is shown for several typical stripline antennas developed by PSL, and used by the Air Force Geophysics Laboratory, NASA and other organizations.

1.0 INTRODUCTION

Development of printed circuit antennas was greatly stimulated in the late sixties when the U.S. Government decided to shift its telemetry research data from VHF to S-Band. The edict to operate in the 2.2 to 2.3 GHz region added to the antenna designer's usual problems. Interference patterns in the radiation coverage of the usual two element array were grossly affected by the drastic change in the wavelength to diameter ratio. The obvious solution to the problem was a large number of radiating elements [1].

1.1 PRELIMINARY INVESTIGATIONS

The primary goal at PSL in early 1970 was to develop a low profile, light weight, strap-on antenna that utilized a minimum of surface area. Additionally, the antenna system was to provide near omni-directional coverage.

After an intensive literature search, we decided to attempt to fabricate some type of printed circuit antenna. Our first attempt was a stripline type of construction.

Our early experiments started with the typical fabrication and calculations of characteristic impedances[2]. We tested laminates from different manufacturers, and tried various rivet spacings and pressures. Figure 1-a shows the final rivet dimensions, however, the rivets act only as the electrical side walls, and are not relied upon to hold the boards together. The boards are held together by a bonding mylar film. The mylar is set by heating under a uniform external pressure. This technique precludes impedance variations along the line which are usually produced when the rivet or screw pressure is not uniform. Several different line configurations were successfully reproduced, and we proceeded with the next stage.

1.2 UNIT ELEMENT

A linearly polarized cavity backed slot radiator was selected as the simplest approach. The first group of experimental slots used a physical connection from the top of the slot to the feed line. This proved to be very awkward, time consuming, and difficult to reproduce. An easily reproducible technique was developed whereby an open ended quarter wavelength stub was used to couple energy to the slot. Finally, we decided to center feed the slots, since the impedance was high and the slope of the impedance curve was minimal. Both of these conditions held true for a respectable distance, thereby reducing the need for tight tolerance registration between the line and slot. An experimental unit element is shown in Figure 1-b.

An investigation of the resonance and the bandwidth (BW) led us to some obvious conclusions. Several different slot geometries were attempted, but none exhibited any potential for increasing the BW. The slot axial width had only a very minor effect on BW. The circumferential side wall rivet line could be changed drastically with only small changes in resonance. The primary resonance effects were the slot circumferential length and the axial cavity walls. The major BW improvements were made with thicker boards. The problem with thicker boards was that they

would not conform to the vehicle diameter without stress cracks in the copper.

2.0 ARRAY DESIGN

Based on radiation coverage design goals of a small allowable null fore and aft, coverage greater than -10dBi in the H plane with less than a 3dB ripple, the array design was begun. Using the applicable vehicle diameter, we calculated the number of radiating elements needed to satisfy the design goals. A typical sketch for an eight element array on a 15.24 cm (6 in.) diameter vehicle is shown in Figure 2-a. Using eight elements for the array design, the circumferential area was divided into eight equal areas with a small working space at each end for mounting purposes. The slots were centered in each area and the feed line design was begun.

The simplest feeding arrangement turned out to be a constant impedance corporate feed structure. Reliance was placed on line lengths for impedance matching and power division. Using line lengths instead of line widths reduces the need for very precise tolerances. The parallel line combination used in a corporate feed structure rarely requires any matching transformers. Usually an additional quarter wavelength line of the same impedance (nominally fifty ohms) is sufficient to provide the correct matching. This reduces the fringing discontinuities around the feed point. Other techniques for reducing fringing discontinuities include the use of 45° turns whenever possible. Reductions in the axial length can be made by moving the first parallel junction inside the normal cavity area with only minimal disturbance to the array resonance. Coupling effects on the line structures are minimal if a distance of at least four times the line width is maintained between lines. Lines should be no closer to the edge or holes than twice their width.

Using the same design philosophy as previously described, Figure 2-b shows a sketch for a ten element array on a 22.86 cm (9 in.) diameter vehicle. A VSWR curve for this antenna is shown in Figure 3. Figure 4 is a gain reference pattern, and the roll plane pattern is shown in Figure 5. Figure 6 is a typical radiation contour plot for this type of stripline antenna.

This same technique has been used to scale antennas designed for operations on other frequency bands. Omni type coverage has been obtained at L-Band, and adequate beacon coverage at C-band and S-band have been demonstrated. Figures 7 and 8 are views of planar arrays for both airborne and ground use.

2.1 GENERAL INFORMATION

In order to reproduce antennas with minimum tolerance requirements, the following method has proved to be quite satisfactory. A fairly accurate scale drawing is laid out on graph paper and then placed on a light table. Rubylith is then positioned over the drawing, and the lines are stripped out with a double edged adjustable cut and strip tool. The slots and hole locations are handled in the same manner on an overlay piece of rubylith. Both pieces of rubylith are registered in relation to each other and then a double sided copper clad board is placed between them and etched. This method eliminates the drafting and photographic process from the operation, and small arrays can be ready for etching in less than eight hours. A second board is then cleaned of copper on one side and has a feed point access hole drilled through it. Bonding mylar is placed between the boards, and the boards are aligned with the feed point hole in the correct position. The array is then formed in a pressure type clamp with the same radius as the missile. The entire arrangement is then placed in an oven and baked for 2 hours at 425°F; after cooling, the clamps are removed. In this manner the array has been formed to the correct diameter and bonded together; then it is ready to be drilled and machined. The critical portion of the construction is the attachment of the feed point connector. At PSL, we have constructed a centering jig for use while the feed pin is soldered to the array.

The unit is then sent to an in-house plating facility. The antenna is mechanically and chemically cleaned. After the radiating slots have been masked, an electroless copper is deposited on all of the surfaces including the board edges and holes. The slot masking is then removed, and an electroplate copper strike is used to seal the easily removable electroless copper. A final electroplated nickel process is added to give a bright, hard finish.

3.0 CONCLUSION

The methods outlined in this paper have been used successfully since our first flight in May 1971. PSL has developed stripline antennas for rockets and satellites from 11.43 cm (4.5 in.) to 111.76 cm (44 in.) in diameter[3]. We have also used these techniques to construct antennas for planar arrays, and to operate in several bands.

3.1 REFERENCES

1. J. Ricardi, "Directivity of an Array of Slots on the Surface of a Cylinder," Electronic Engineering, September 1967. pp. 578-581.
2. S. B. Cohn, "Characteristic Impedance of a Shielded Strip Transmission Line," Transactions IRE, Vol. MTT-2. July 1954, pp. 52-57.
3. Al Waterman and D. G. Henry, "Research and Development of Antennas for Rocket and Satellite Transmissions, "AFGL-TR-78-0095," March 1978, DDC or NTIS.

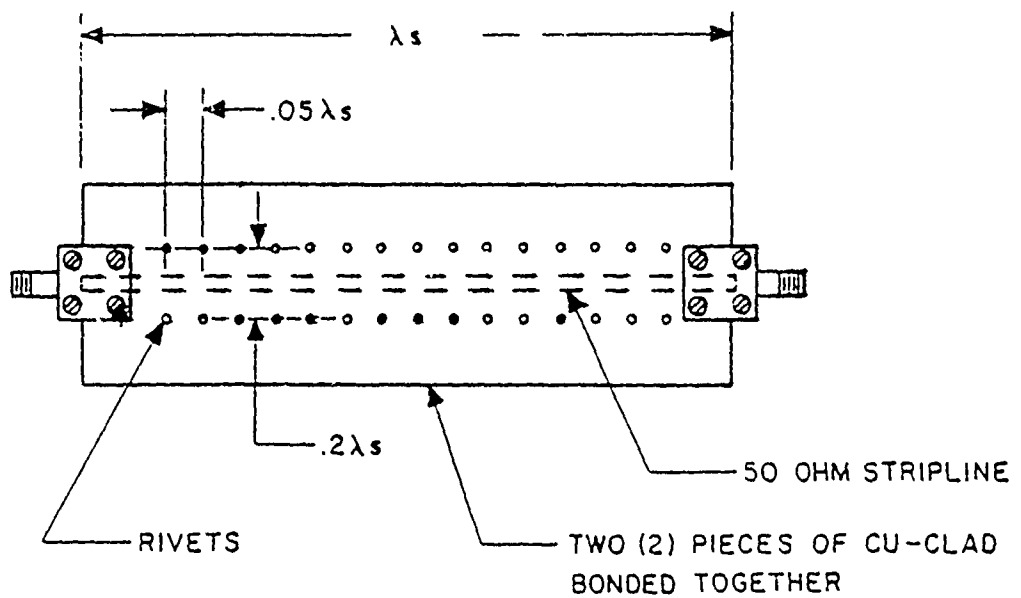


FIGURE 1-a Constant Impedance Line

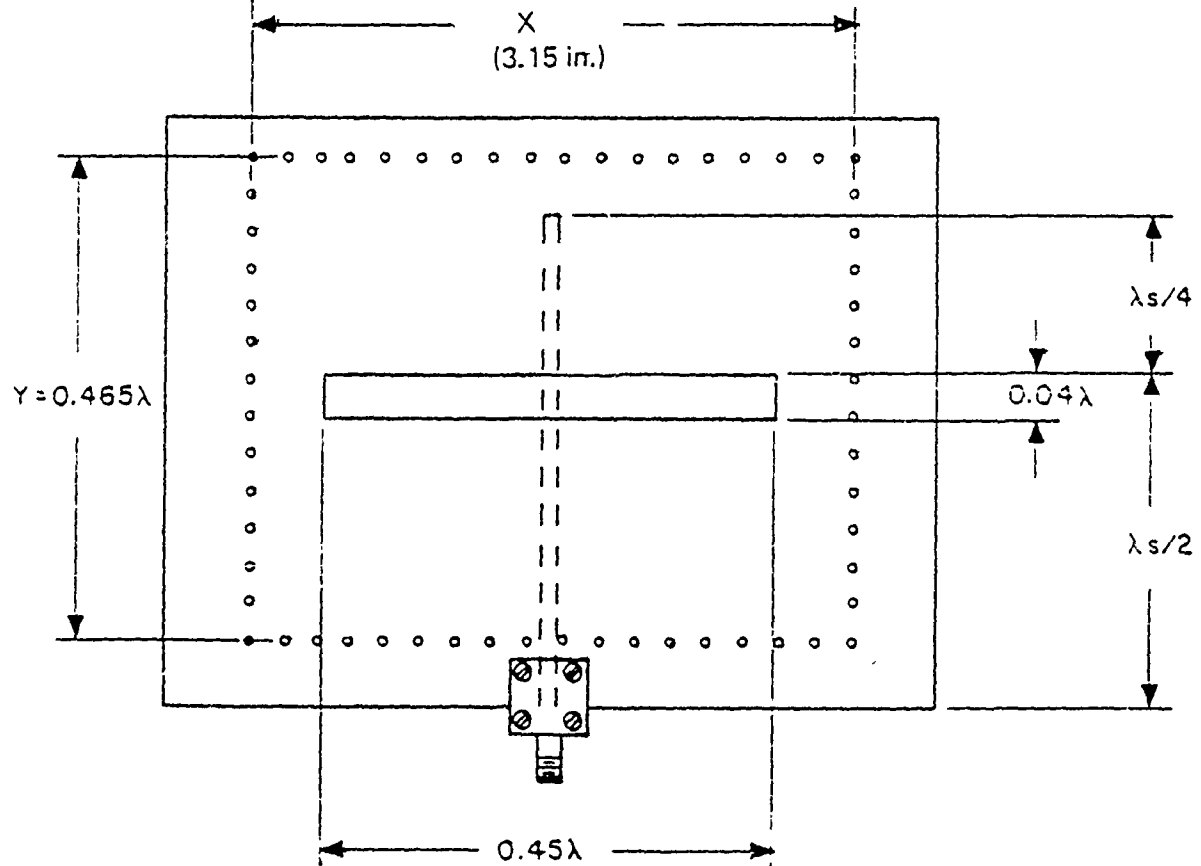


FIGURE 1-b Figure Unit Element

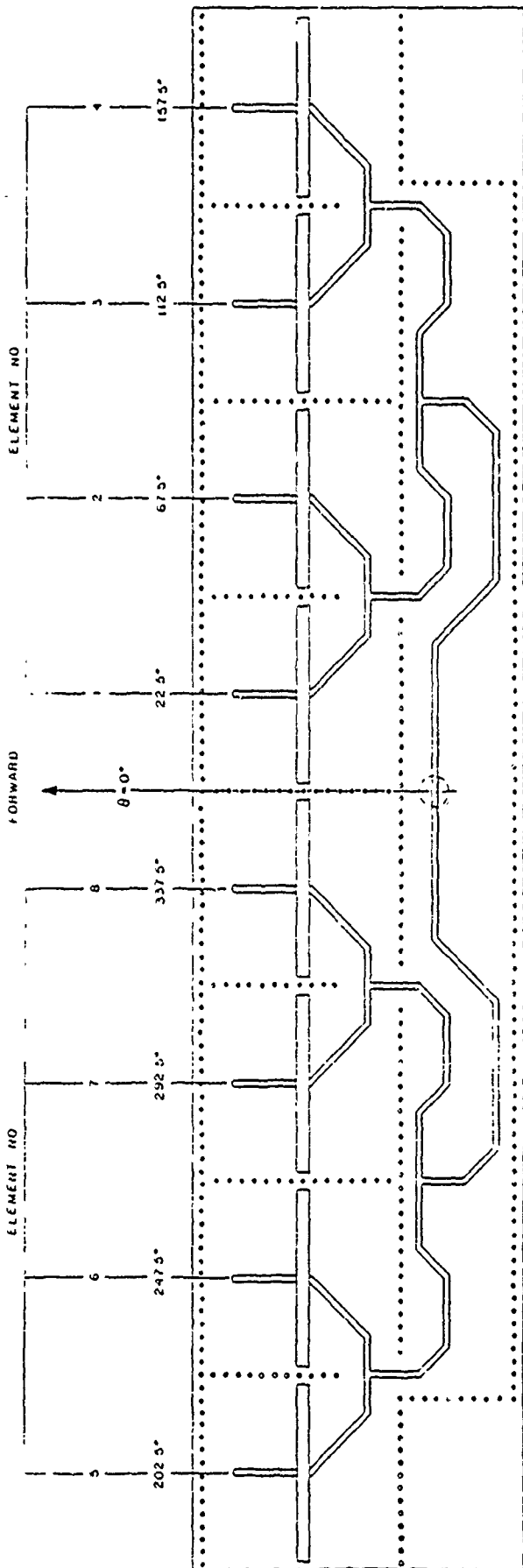


FIGURE 2-a Model 55.003

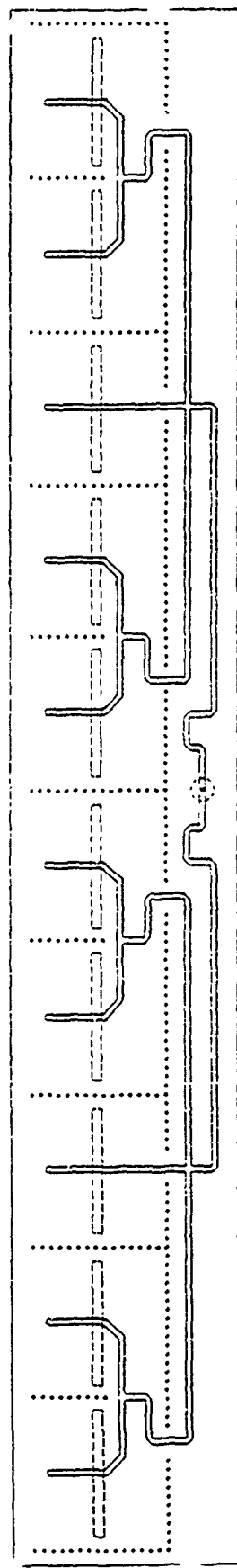


FIGURE 2-b Model 55.005

IMPEDANCE COORDINATES—50-OHM CHARACTERISTIC IMPEDANCE

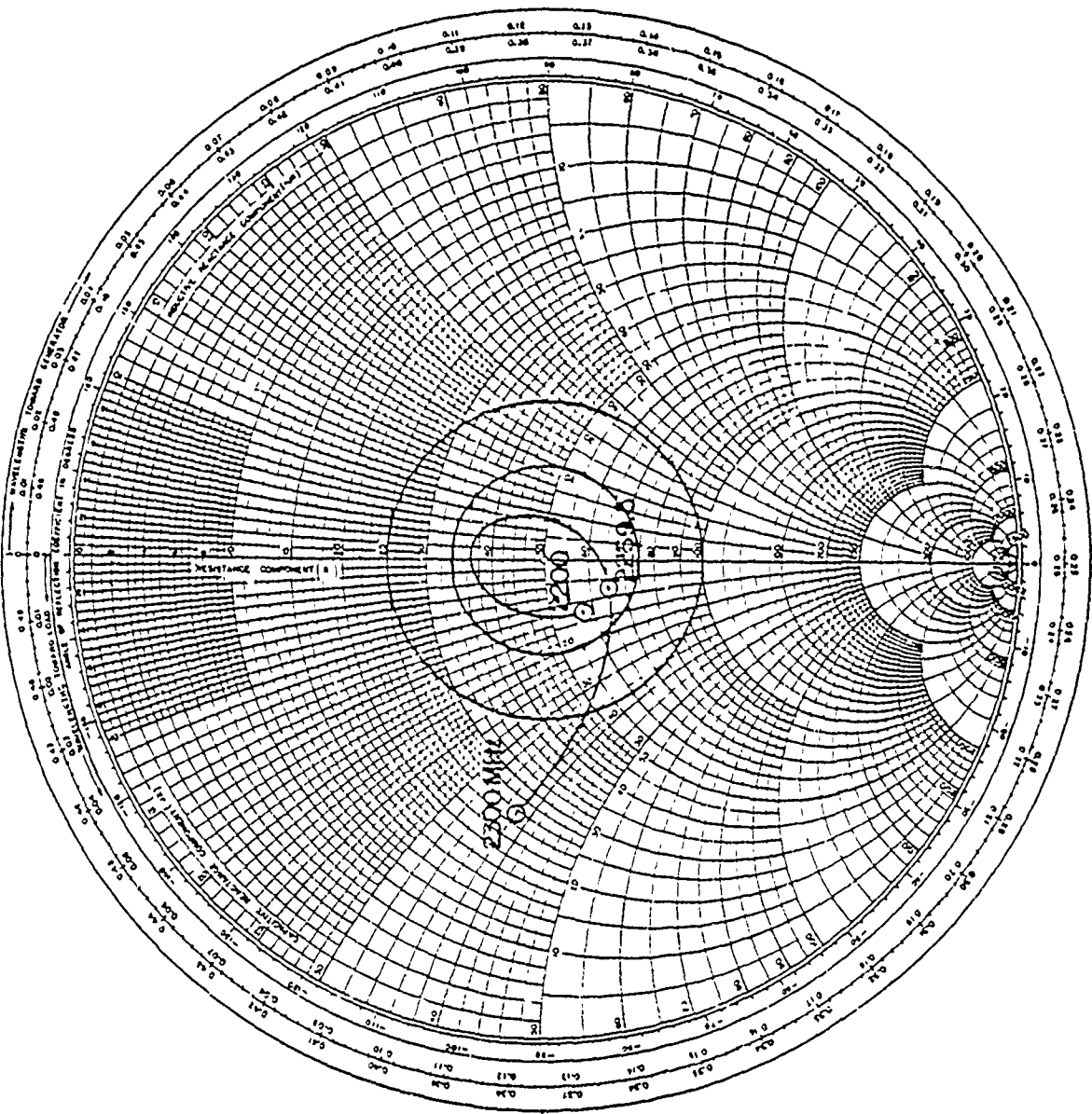


FIGURE 3

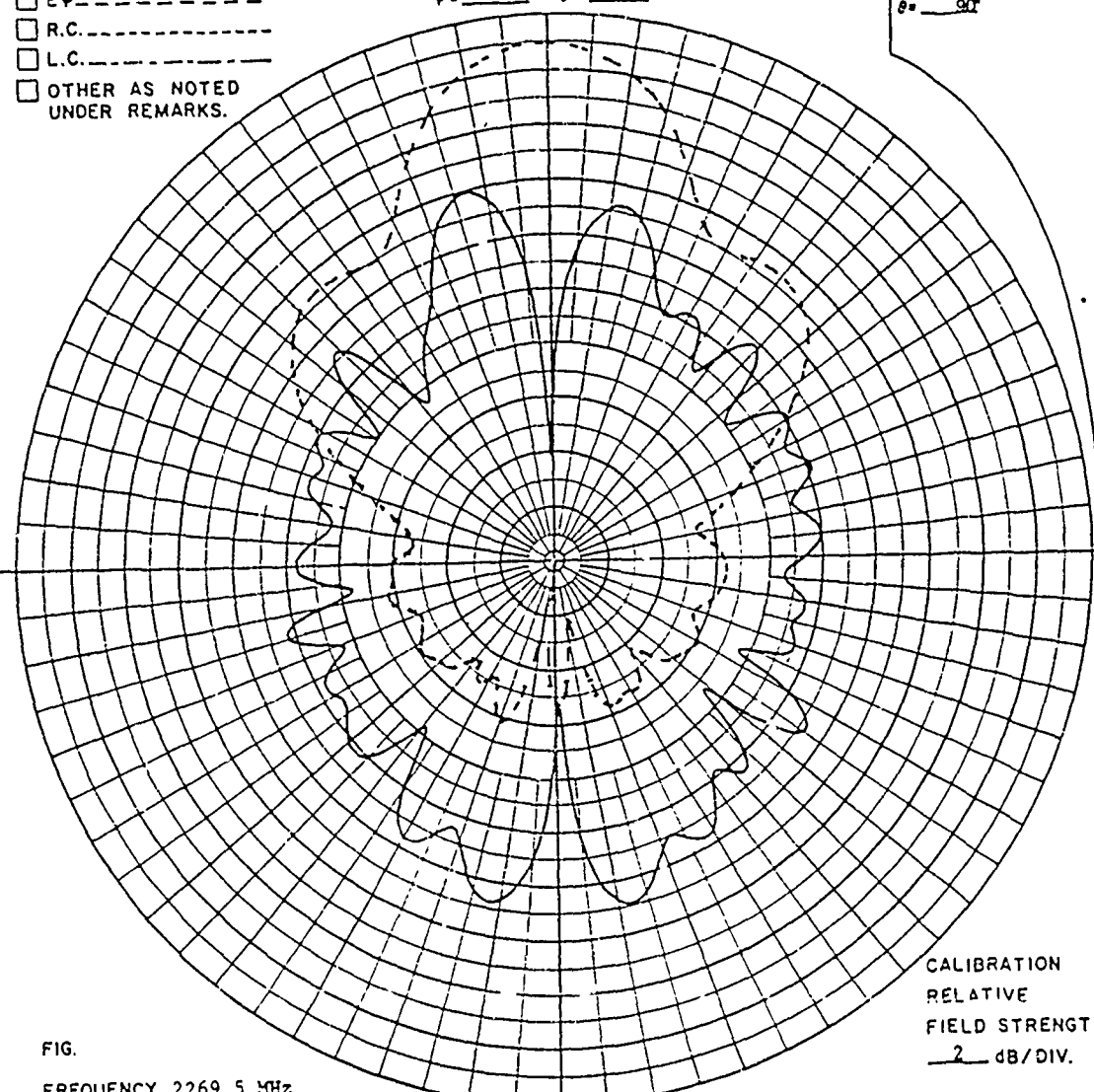
VWSR at Antenna Input

POLARIZATION

- GAIN REF. -----
- E_θ -----
- E_φ -----
- R.C. -----
- L.C. -----
- OTHER AS NOTED
UNDER REMARKS.

COORDINATE
REFERENCE

φ = 0°
θ = 90°



CALIBRATION
RELATIVE
FIELD STRENGTH
2 dB/DIV.

PSL № 110263

FIG.

FREQUENCY 2269.5 MHz
ANTENNA Model 55.505

REMARKS

FIGURE 4 Gain reference

POLARIZATION

- GAIN REF -----
- E_θ -----
- E_φ -----
- R.C. -----
- L.C. -----
- OTHER AS NOTED
UNDER REMARKS.

COORDINATE
REFERENCE

φ = 0° θ = 90°

φ = 90°
θ = 0°

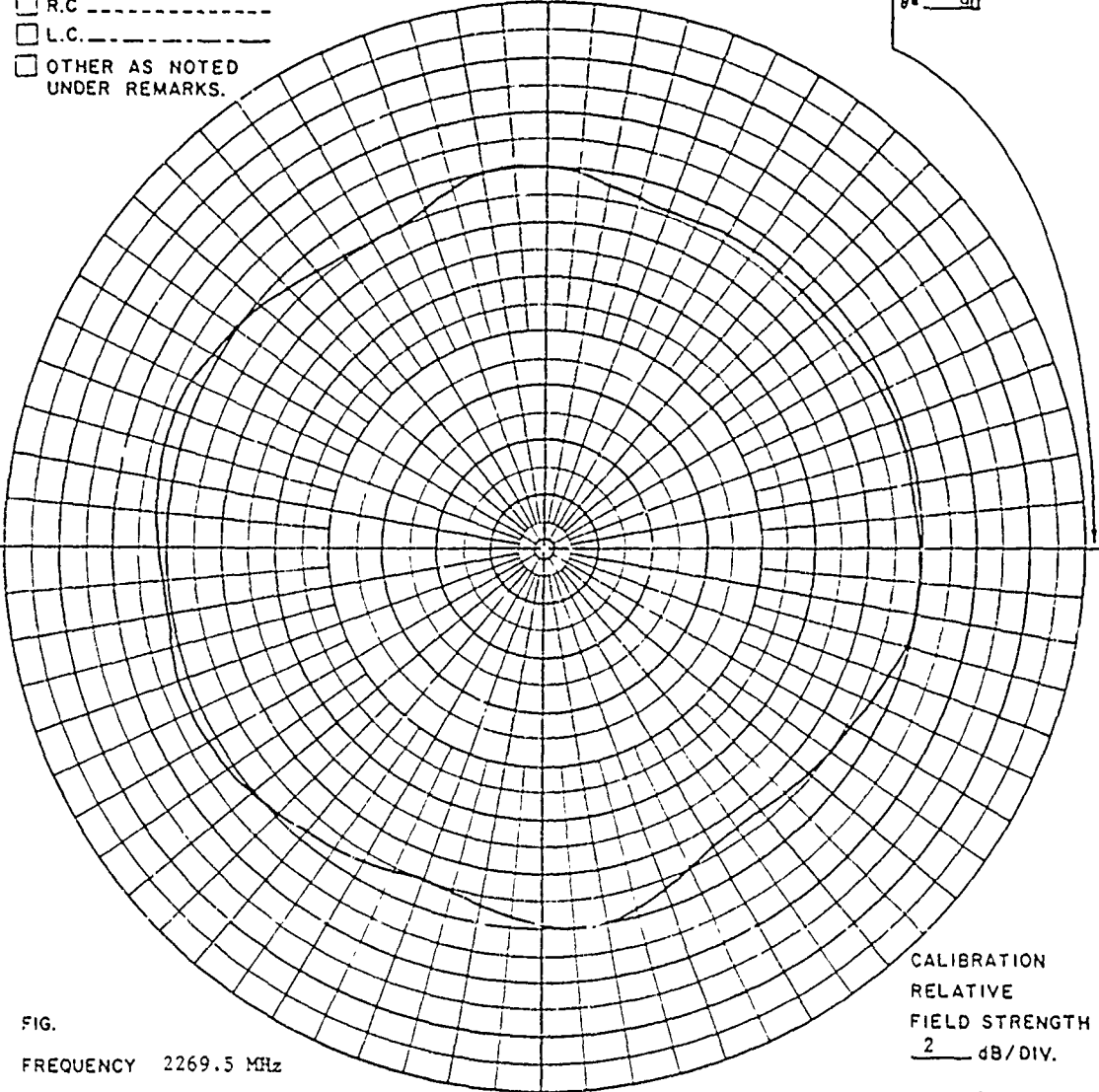


FIG.

FREQUENCY 2269.5 MHz

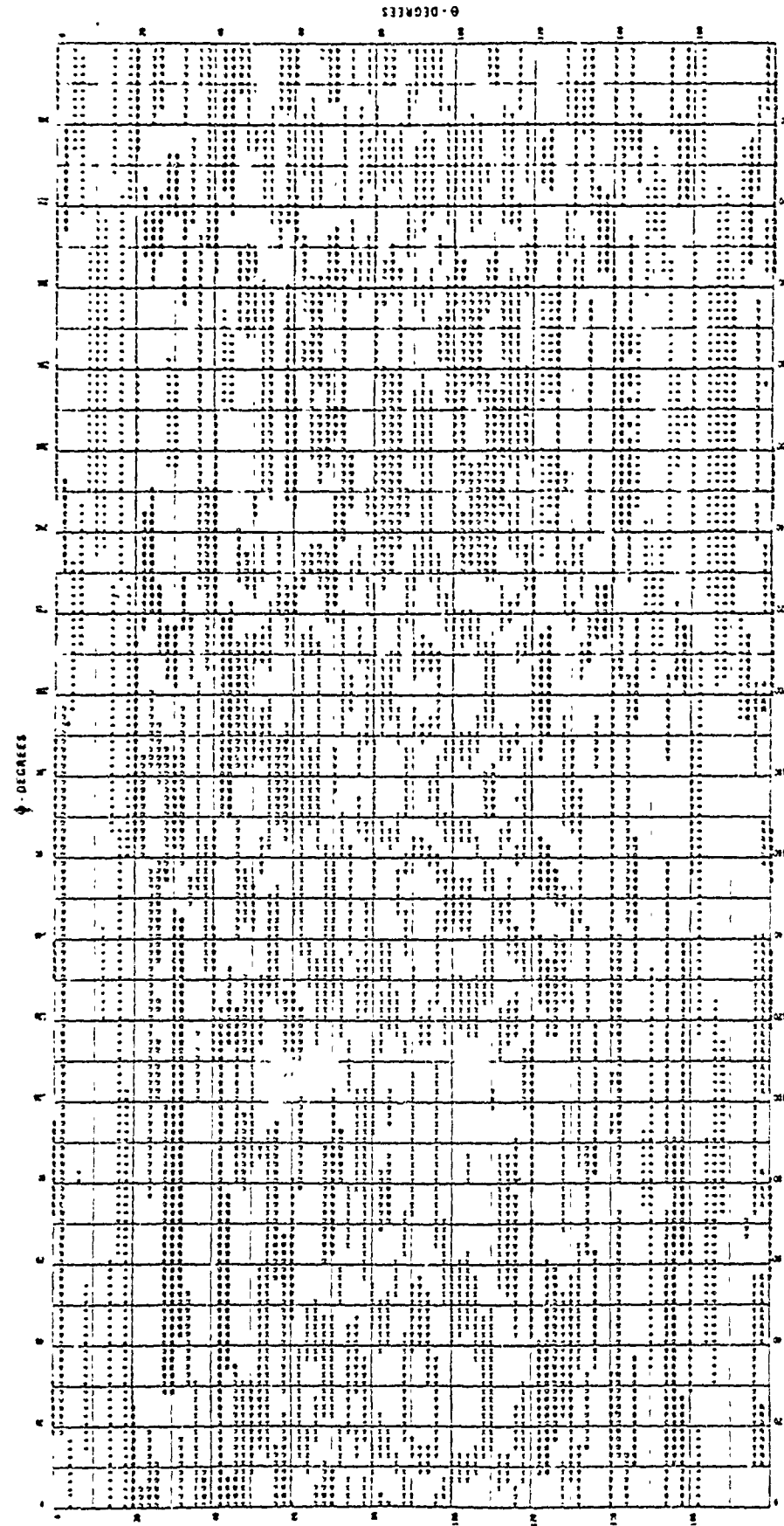
ANTENNA Model 55.505

REMARKS

CALIBRATION
RELATIVE
FIELD STRENGTH
2 dB/DIV.

PSL N° 110259

FIGURE 5 Roll Plane



CONTRACT NO: AF 22628-72-C-0063 RANGE REQUEST NO: 1923 DATE: 18 October 1972
 PATTERN MEASUREMENT FREQUENCY: 1.2695 GHz PSL PHOTO NO: M/A ANTENNA MODEL NO: 111
 POLARIZATION COMPONENT RECORDED: EW ARRAY NO: 111-103 MODEL SCALE: 1:1
 GAIN REFERENCE ANTENNA: TYPE AND S/N: Sun 12 S/N 103 ARRAY PHASING: M/A
 DESCRIPTION OF TEST ANTENNA: 10 ft. dish mounted in the center of a long vehicle with antenna mounted in the center
 DESCRIPTION OF VEHICLE MOCKUP: ¹⁰ ft. long vehicle with antenna mounted in the center
 THE NUMBER ¹⁰ IN THE POWER CONTOUR GRAPH CORRESPONDS TO -16 dB WITH RESPECT TO THE GAIN REFERENCE ANTENNA
 DESCRIPTION OF THE GAIN MEASUREMENT: Reference Pat Gain Reference Number 110287

FIGURE 6 Radiation Contour Plot

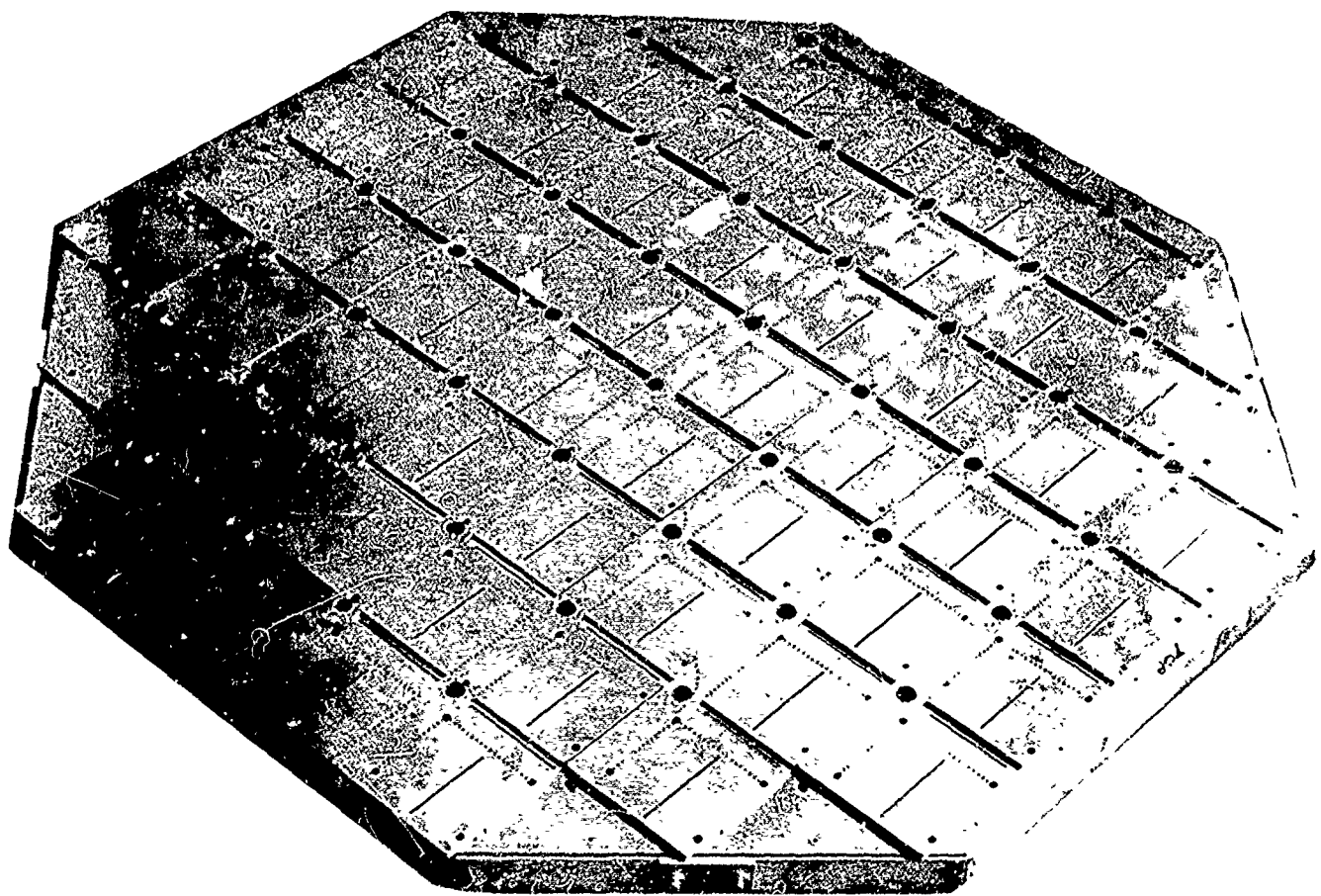
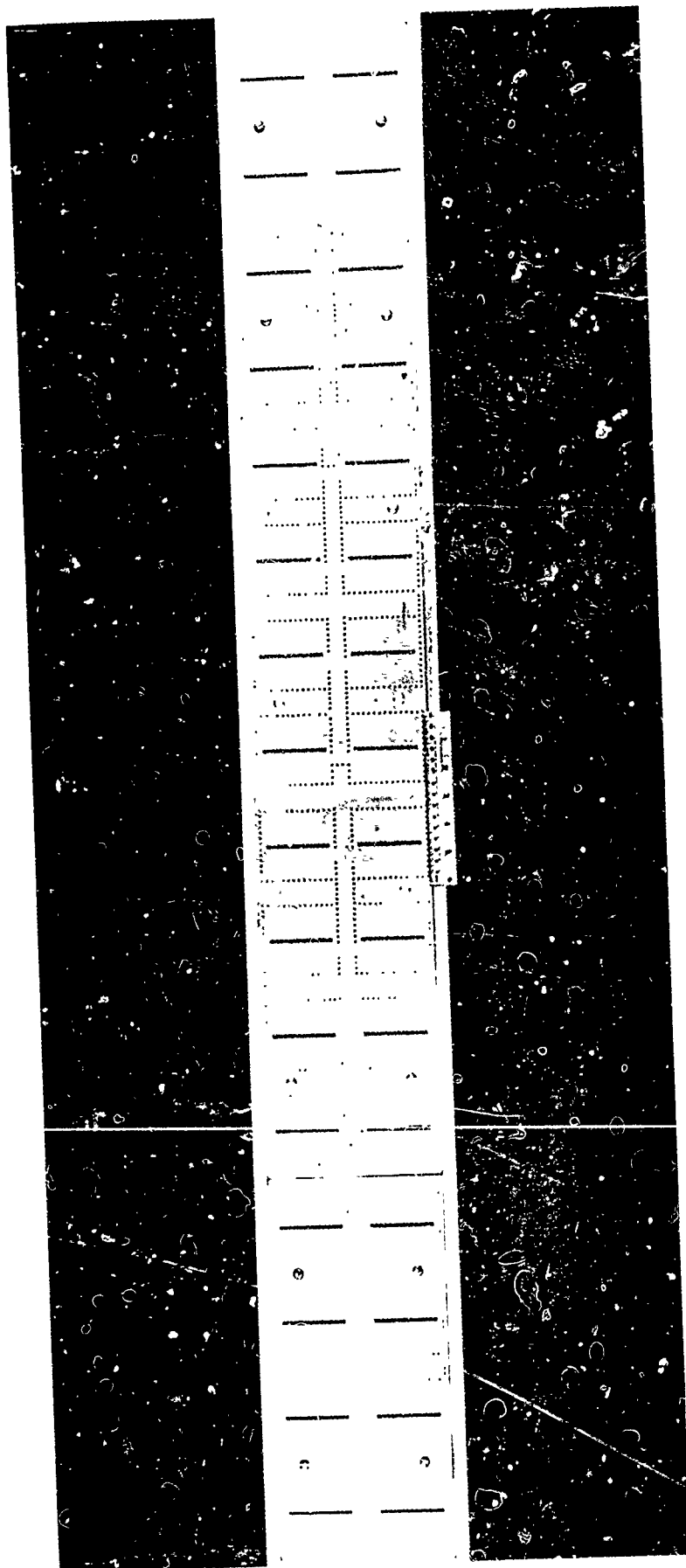


FIGURE 7 Airborne Dual Polarized L-Band Array

FIGURE 8 Ground Shaped Beam S-Band Array -



UHF COPLANAR-SLOT ANTENNA FOR AIRCRAFT-TO-SATELLITE
DATA COMMUNICATIONS

Royce W. Myhre
Applications Division, Communications Technology Branch
NASA Lewis Research Center
21000 Brookpark Road
Cleveland, Ohio

SUMMARY

A lightweight low drag coplanar-slot antenna has been developed for use on commercial jet aircraft that will provide upper hemisphere coverage in the UHF band at receive frequencies of 468 MHz and transmit frequencies of 402 MHz. The antenna, developed under subcontract to the Government, is part of a program for the development of a system to transmit meteorological data from wide-body jet aircraft to ground users via synchronous meteorological data relay satellites. Antennas of this type are presently being flown on international commercial B747 aircraft on an experimental basis for the National Aeronautics and Space Administration (NASA)/National Oceanic and Atmospheric Administration (NOAA), Aircraft-to-Satellite Data Relay (ASDAR) International World Weather Observation Program.

The low profile antenna (23.5 cm wide by 38.1 cm long by 1.9 cm high) is a conformal antenna utilizing the coplanar-slot approach, developed under NASA subcontract by TRANSCO Products, Inc., Venice, California. The coplanar-slot approach is a recent breakthrough in conformal antennas with the advantages over the common stripline antenna of broader frequency bandwidth and improved electrical integrity over wider ranges of temperature. The antenna is circular polarized, has an on axis gain of near +7.5 dB and a HPBW greater than 90°.

1.0 INTRODUCTION

1.1 Need for Weather Data

The United States has been deeply involved in the Global Atmospheric Research Program (GARP) and has assumed responsibility for certain of the activities

which are being coordinated by the National Oceanic and Atmospheric Administration (NOAA). One of the activities is to provide an improved source of meteorological data from aircraft via satellite for long range weather forecasting [1]. The initiative for starting the Aircraft-to-Satellite Data Relay (ASDAR) Program came from a recognition that much of our world's weather originates in the data sparse area of the tropics which are primarily ocean. It was further recognized that these areas are frequently crossed by many of the modern wide-body long-range jet aircraft of the B747, DC-10, and L1011 type. These aircraft contain navigation and air data systems capable of providing the desired weather data, that is, latitude, longitude, wind speed, wind direction, altitude, and outside air temperature. The ASDAR system consists of a data acquisition and control unit to acquire, store and format this data; a clock to time the data sampling and transmission periods; and a transmitter and low-profile upper hemisphere coverage antenna to relay the formatted data via satellite to the National Weather Service (NWS) ground stations as shown in figure 1.

1.2 Prototype Installation

A prototype ASDAR system for automatically transmitting this meteorological observation data from aircraft was developed by the NASA Lewis Research Center, Cleveland, Ohio, during 1975-1976. In late 1976 the NASA, on contract to Pan American World Airways (PAA) Inc., installed the ASDAR system on PAA B747 aircraft No. N657PA, with completion of flight testing, Federal Aviation Administration (FAA) approval, and Supplemental Type Certification in February 1977.

1.3 Additional Installations

In cooperation with the NOAA, ASDAR systems are installed on several B747 world-wide commercial jet aircraft and on an Air Force C141 airplane (Table 1). These systems are installed and operational on an experimental basis during the GARP time period to provide the National Weather Service (NWS) with the desired additional meteorological data. Data is being relayed from these aircraft to ground receiving weather stations around the world via the U.S. Geostationary Operational Environmental Satellites (GOES series) and the European and Japanese Weather Satellites.

TABLE 1
ASDAR INSTALLATIONS AND REPORTING TIMES

Airline	Aircraft tail number	Reporting time (min after hr)
Pan Am	PA001Z	02
KLM	KL002Z	04
SAS	SK003Z	06
Qantas	QF004Z	08
Lufthansa	LH005Z	10
Qantas	QF007Z	34
Qantas	QF008Z	36
Qantas	QF009Z	38
Qantas	QF010Z	40
USAF/MAC	US011Z	12/42
Singapore	S0013Z	16
Singapore	S0014Z	44
Singapore	S0015Z	18
British Air	BA016Z	46
British Air	BA017Z	20
South Africa Air	SA018Z	48
South Africa Air	SA019Z	22

The ASDAR data also provides the unique capability in that the transmitted latitude and longitude information automatically provides the exact location of each ASDAR equipped aircraft in real time, and provides an indication of movement of the aircraft versus flight time along the flight route via satellite to ground receiving stations.

1.4 System Performance

Performance of the systems to date has indicated excellent data coverage of aircraft flights from satellite horizon to horizon, indicating that the low-profile coplanar-slot aircraft antenna does provide acceptable hemisphere coverage at two frequencies (468 MHz RX and 402 MHz TX). A sample formatted data printout

message as received and printed by the National Environmental Satellite Service (NESS) is shown in figure 2. The data transmissions are consistently good and free of errors within the coverage area of each satellite. Figure 3 shows data from two U.S. satellites (GOES-1 at 135° W long and GOES-2 at 75° W long). This data is from six aircraft carrying ASDAR over a 1-month period. Sampling of the data occurs every 7.5 minutes (8 times per hr), with transmission of the blocks of stored data once an hour to the satellite. Figure 3 also shows the contour of constant zero degree elevation to the receive satellites as viewed from the aircraft. The data shown are from ASDAR units equipped with internal precision clocks, allowing continuous data collection and hourly transmissions to all satellites within view above the horizon. Earlier model units using the U.S. satellite time reference had somewhat limited performance near the horizon due to the time required for the ASDAR antenna/receiver to lock onto the satellite time signal, start gathering data and then transmit at the next hourly transmission period.

2.0 SYSTEM DESCRIPTION

2.1 Physical Layout

Figure 4 shows the installation of the ASDAR system in a B747 aircraft. The ASDAR power supply and electronics unit are located in the main electronic equipment area of the lower level of the aircraft. The RF coaxial cable is routed up through the main cabin area to the ceiling of the upper lounge [10.7 m (35 ft)] where it connects to the antenna at station 520. The total system weight including power supply, electronics unit, equipment rack shelves, cabling and antenna is 30.19 kg (66.56 lb).

2.2 Data Source

Data inputs to the ASDAR electronics unit are provided from the aircraft's Inertial Navigation Unit (INS) and Air Data System via the Flight Data Acquisition Unit (FDAU). The INS system provides the latitude, longitude, wind direction and wind speed as serial BCD data. The FDAU system provides altitude and outside static air temperature in the form of PCM serial data. Data is stored in the electronics unit and then transmitted to the satellite once an hour. The ASDAR transmitter ON-TIME is nominally 37 seconds during each reporting period (once per hour) during flight, except for ground testing when

the transmitter can be keyed for 2, 4, 8, and 16 transmissions per hour. The ASDAR transmitter output is 80 watts, with approximately 60 watts input at the antenna after coax losses.

2.3 System Components

The major units of the ASDAR system are shown in figure 5; the power supply, the coplanar-slot antenna and the electronics unit. The power supply and electronics unit were designed and fabricated by the Lewis Research Center and packaged in standard airline radio-rack units. The antenna was developed under contract by TRANSCO Products Inc., Venice, California, and is packaged in an aluminum casting 23.5 cm (9.25 in.) by 38.1 cm (15.0 in.) by 1.9 cm (0.72 in.) thick. The casting is contoured on the underside to fit the aircraft fuselage. The antenna, along with its 0.32 cm (0.125 in.) silicon rubber pressure-seal gasket weighs 3.12 kg (6.88 lb). Figure 6 shows the antenna mounted on the top side of the B474 "hump" at station 520. The only modifications to the aircraft fuselage for mounting the antenna is the installation of a 0.16 cm (0.063 in.) antenna doubler plate, drill one 2.7 cm (1.063 in.) hole for the RF connector feed-through, and eighteen (18) bolt holes for mounting the antenna to the aircraft.

3.0 ANTENNA

3.1 Selection of Candidate Antennas

During development of the ASDAR hardware components, a survey of available aircraft antenna types indicated that no existing antenna would meet the requirements for upper hemisphere coverage and flight qualification for use on commercial jet aircraft. Under a joint NASA/PAA effort with TRANSCO Products Inc., a low-profile, lightweight coplanar-slot antenna was developed, fabricated, and tested that would operate over both the 402 and 468 MHz frequency bands and also would meet the requirements for upper hemisphere coverage and FAA flight qualification. Environmental qualifications as required per Radio Technical Commission for Aeronautics (RTCA) Document DO-160 and Boeing Aircraft Company (BAC) Document D6-16050 were completed by TRANSCO. Flight qualification and FAA approval and certification was completed by PAA under the NASA contract. Table 2 shows the finalized specifications that were submitted for the production model antennas.

TABLE 2
ASDAR ANTENNA SPECIFICATIONS

Frequency	401.7 - 402.1 MHz TX 468.8 - 468.9 MHz RX
Impedance	50 ohm
VSWR	1.5:1 maximum
RF power	90 watts maximum for 37 seconds Maximum duty cycle 37 seconds/3.75 minutes
Axial ratio	5.5 dB maximum (at zenith)
Gain (nominal)	+1.5 dBiC (at zenith)
Beamwidth (3 dB)	90°
Polarization	Right hand circular
RF connector	Type N female

3.2 Physical Characteristics

The physical characteristics of the TRANSCO antenna are summarized in table 3.

TABLE 3
TRANSCO PRODUCTS INC. ASDAR ANTENNA

Model number	213F00100-1
Type	Coplanar slot
Size	23.5 cm (9.25 in.) wide 38.1 cm (15.0 in.) long 1.83 cm (0.72 in.) thick
Weight	3.12 kg (6.88 lb) antenna 0.254 kg (0.56 lb) gasket
Gasket material	0.318 cm (0.125 in.) silicon rubber
Mounting screws	18 each type NAS514P1032-20P

The microcircuit element of the antenna is approximately 20.32 cm (8 in.) by 20.32 cm (8 in.) by 1.27 cm (0.5 in.) thick and is fitted into a milled out cavity in the larger aluminum casting (fig. 7). The casting provides the structure for mounting the antenna to the aircraft, serves as a pressure plate

around the RF connector feed-through, provides an aerodynamic fairing on the aircraft contoured surface and protects the antenna element from weather erosion.

3.3 Antenna Design Considerations

Because of the requirement for low-profile, lightweight and low-cost antennas that could be installed on commercial jet aircraft with minimum rework to the aircraft structure, the large cavity-backed antennas, cross-dipoles and dipole-over-blade antenna types were ruled out. The large protruding antennas were also ruled out since they would create a weight and drag penalty that would not be acceptable to the airlines for carriage over long periods of time. It was also requested by the airlines that a single, dual-frequency type antenna be used in order to minimize the structural rework required to the aircraft. Therefore, the simpler conformal type narrow-band microstrip radiating patch, where two separate antennas would be required, was considered as a secondary approach. Early investigations had indicated that wide band frequency operation would be difficult to achieve with the patch antenna since the input impedance varies rapidly with frequency and temperature changes [2]. Because of the extreme temperature variations due to altitude changes, frequency shift of the ASDAR signal during flight from Doppler shift, and frequency drift of the transmitter output over extended periods of time, verification of operation with the patch antenna would have required extensive development and testing efforts.

3.4 Antenna Construction

The coplanar-slot antenna selected for the ASDAR system is of a multilayer construction as shown in figure 7. The Type N RF connector is mounted on the lower side of the element cavity. The RF connector is mated to a double-stub tuned stripline feed circuit board through a four-port quadrature hybrid. The top insulator board and top ground plane for the feed circuit board also provides the structural assembly (pressure plate) for maintaining overall impedance tolerances and frequency stability. The circuit tuning stubs are pretuned both capacitively and inductively such that they reactively tune the antenna prior to final assembly, eliminating the need for further tuning after assembly and encapsulation is completed. The polycarbonate dielectric material provides the cavity loading, where the dielectric constant uniformity and fabrication

tolerance reproducibility has a significant impact on the antenna performance as to power amplification and bandwidth. The radiating patch over the dielectric cavity is fed by two orthogonally located connector posts to provide the desired circular polarized radiation pattern.

3.5 Antenna Operation

The operational description of the antenna, when considered as a transmitter, is as follows (see fig. 7) [3]: The RF energy is fed into the Type N RF connector Section C-C which transforms the feed from coax to stripline. The stripline input is fed to a 90° hybrid. The feed lines presented to the hybrid output are matched using double stub stripline techniques to a VSWR value of 2:1 or less. The feed lines are again transformed from stripline to coax at the antenna dual feed points by use of IPC connectors, shown in Section A-A. The radiating patch is fed through this arrangement at symmetrical points with a quadrature signal, thus producing circular polarization.

The presenting of a 2:1 or less VSWR at the output of the hybrid allows the isolated port to be terminated in a reactive load versus a resistive load. This method prevents excessive power being distributed in the load if the antenna resonant frequency should slightly change.

3.6 Antenna Qualifications

On completion of assembly, the antenna is encapsulated to inhibit corrosion and is then painted with an outer protective coating of white aircraft-radome ASTRACOAT material. Qualification tests were completed in conformance with airline required specifications per RTCA DO-160 and BAC D6-16050. Input impedance (VSWR) tests were measured at the center frequencies of 401.9 and 468.8 MHz for the operating frequency ranges of 401.7 to 402.9 MHz (transmit) and 468.8 to 468.9 MHz (receive). Radiation distribution plots of the upper hemisphere were made at 2° increments in azimuth and elevation at the center of the transmit and receive frequency bands. Data was taken with the test unit mounted on a large ground plane simulating the installation area on the B747 aircraft. The values were generally uniformly distributed and without deep nulls (figs. 8 and 9).

Polar plots were made at 15° increments in the vertical plane ($\phi = 0$ to 180°) for azimuths of $\theta = 0$ to 360° at the center of the transmit and receive

frequencies. Conic sections were made in planes parallel to the horizon for 0° through 90° elevation in increments of 5°. The gain of the test antenna relative to a $\lambda/4$ stub antenna was +2.5 dBci (401.9 MHz TX) and 1.0 dBci (468.8 MHz RX) at the peak of the elevation beam. A lower gain at the receive frequency was accepted in order to achieve (favor) a higher gain in the transmit mode. The gain at $\pm 45^\circ$ was near 0 dB at each of the two frequencies. The axial ratio was within the 5.5 dB specification at zenith for both frequencies. The temperature and altitude test consisted of a low temperature test at -55° C, a high temperature test at +85° C and an altitude test at the equivalent of 50 000 feet. The power handling capability of the test antenna was measured prior to and during each test by applying 90 watts CW at 401.9 MHz. VSWR measurements were made at each condition, with test results indicating normal operation. Humidity and sinusoidal vibration tests were conducted in accordance with the specified RTCA test requirements. The only exception was minor paint blistering that occurred at high temperature, which was not considered critical.

4.0 CONCLUSIONS

The coplanar-slot antenna developed by TRANSCO Products, Inc. for use on commercial aircraft has operationally demonstrated that a lightweight low-profile conformal antenna can provide consistent and reliable upper hemisphere coverage for data communications between aircraft and satellites. These prototype antenna (and ASDAR systems) have now been operational on B747 international aircraft for over 2 years with a minimum of failures. A few early antennas had experienced increasing VSWR's with time, due to moisture seepage into the cavity area around the antenna mounting screws. This condition was corrected by an improved method of sealing the cavity by TRANSCO, and by sealing around the antenna and its mounting screws during installation on the aircraft. One other antenna had been replaced as a precautionary measure during aircraft overhaul because of hairline surface cracks and leading edge erosion in the protective paint. These problem areas were corrected, and operation to date indicates highly satisfactory performance from these antenna systems.

Because of the successful performance of these prototype systems, the NOAA is now reviewing the desirability and feasibility of making ASDAR a worldwide operational system. To accomplish this effort, the electronics units would be

repackaged for improved reliability and ease of maintenance, and the antenna design would be reviewed for improved performance and lighter packaging to be more compatible for installation on other types of aircraft.

5.0 REFERENCES

1. Bagwell, J. W., and Lindow, B. G., An Airborne Meteorological Data Collection System Using Satellite Relay (ASDAR), NASA Lewis Research Center Technical Memorandum 78992, November 1978.
2. Derneryd, Anders G., Microstrip Disc Antenna Covers Multiple Frequencies, Microwave Journal, Vol. 21, May 1978, pp. 77-79.
3. Greiser, John W., Coplanar Stripline Antenna, Microwave Journal, Vol. 19, October 1976, pp. 47-49.
4. Myhre, R. W., Microstrip Antenna for Aircraft Applications, Interservice Antenna Group Workshop, Point Mugu, California, February 1979.

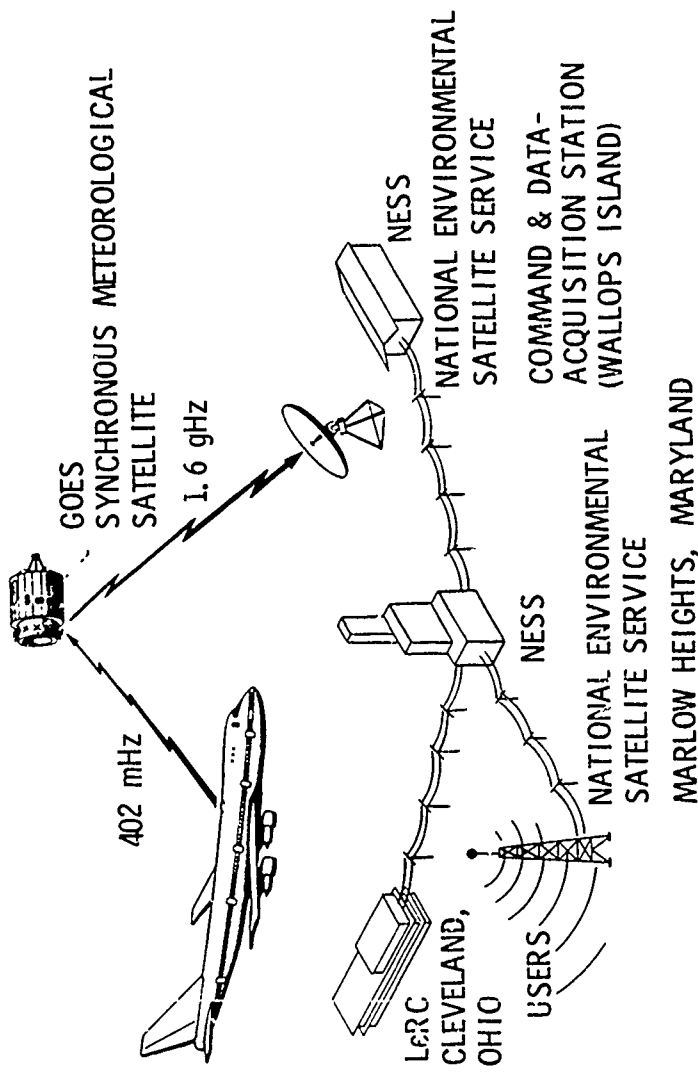


Figure 1. - ASDAR - global weather data gathering system

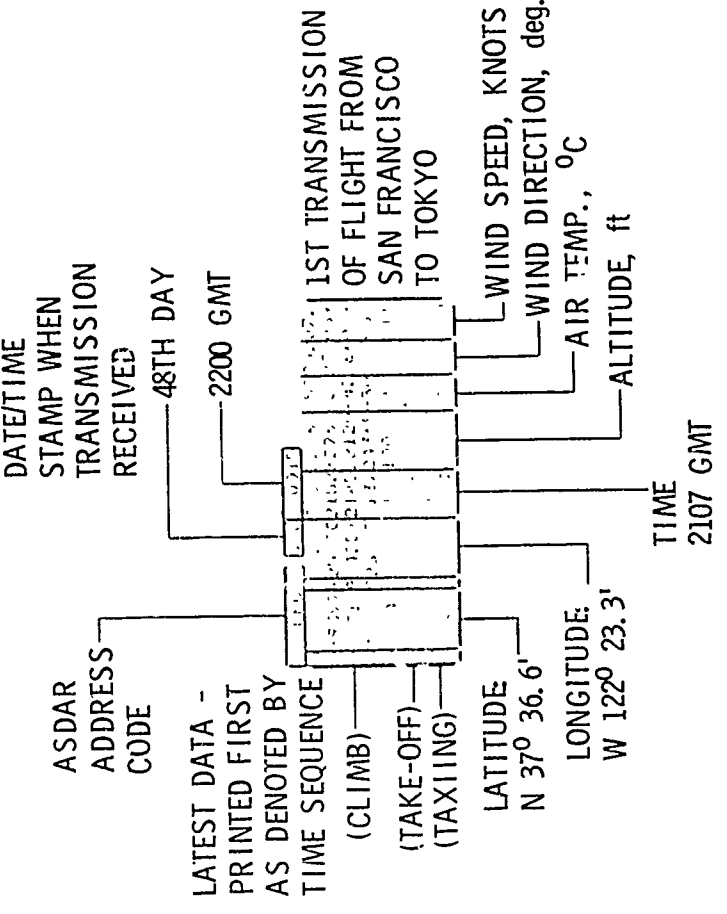


Figure 2 - ASDAR printout obtained, via satellite relay,
from National Satellite Service

ASDAR DATA FROM 01/19/79 TO 02/28/79
ASDAR PLATFORM ID=A0007022

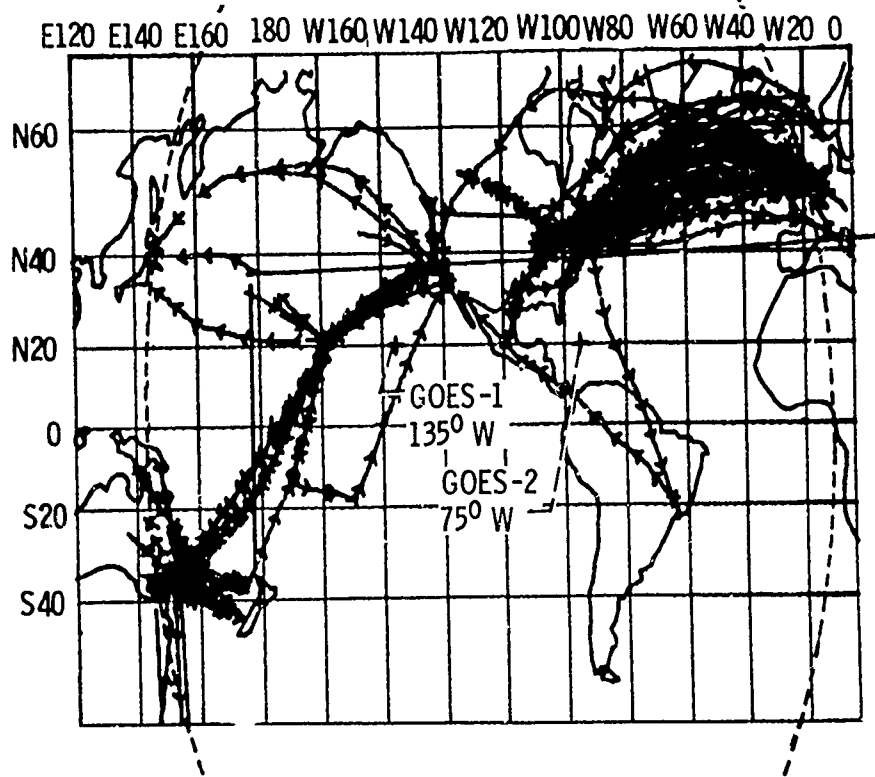


Figure 3. - Aircraft ASDAR flight data record with contour of zero degree elevation to U. S. satellites.

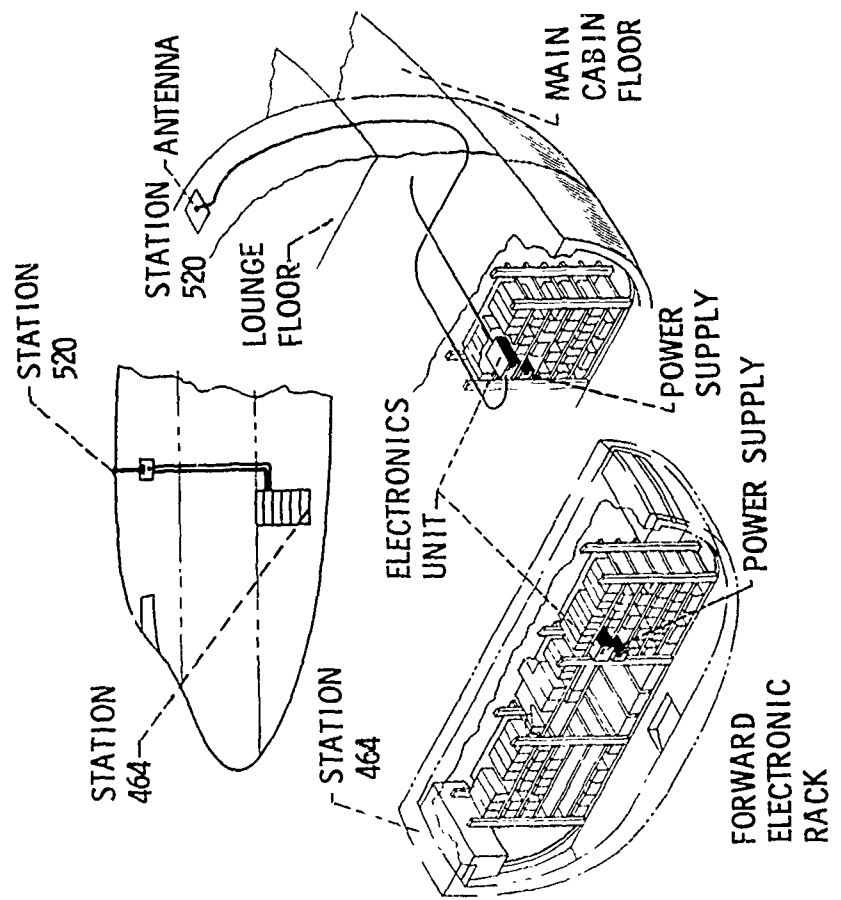
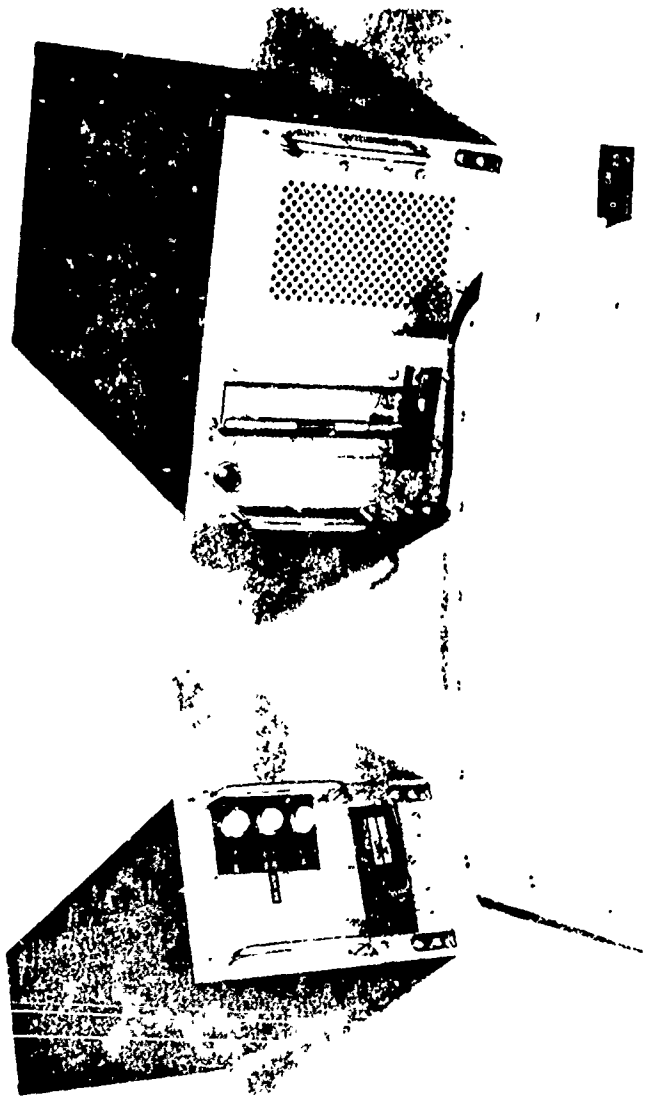


Figure 4. - B747 ASDAR system installation.



NASA
C-78-1047

C-78-1047

Figure 5. - ASDAR power supply antenna, and electronics unit.

Figure 6. - A SSDAR antenna installed on B747 aircraft.



24-16

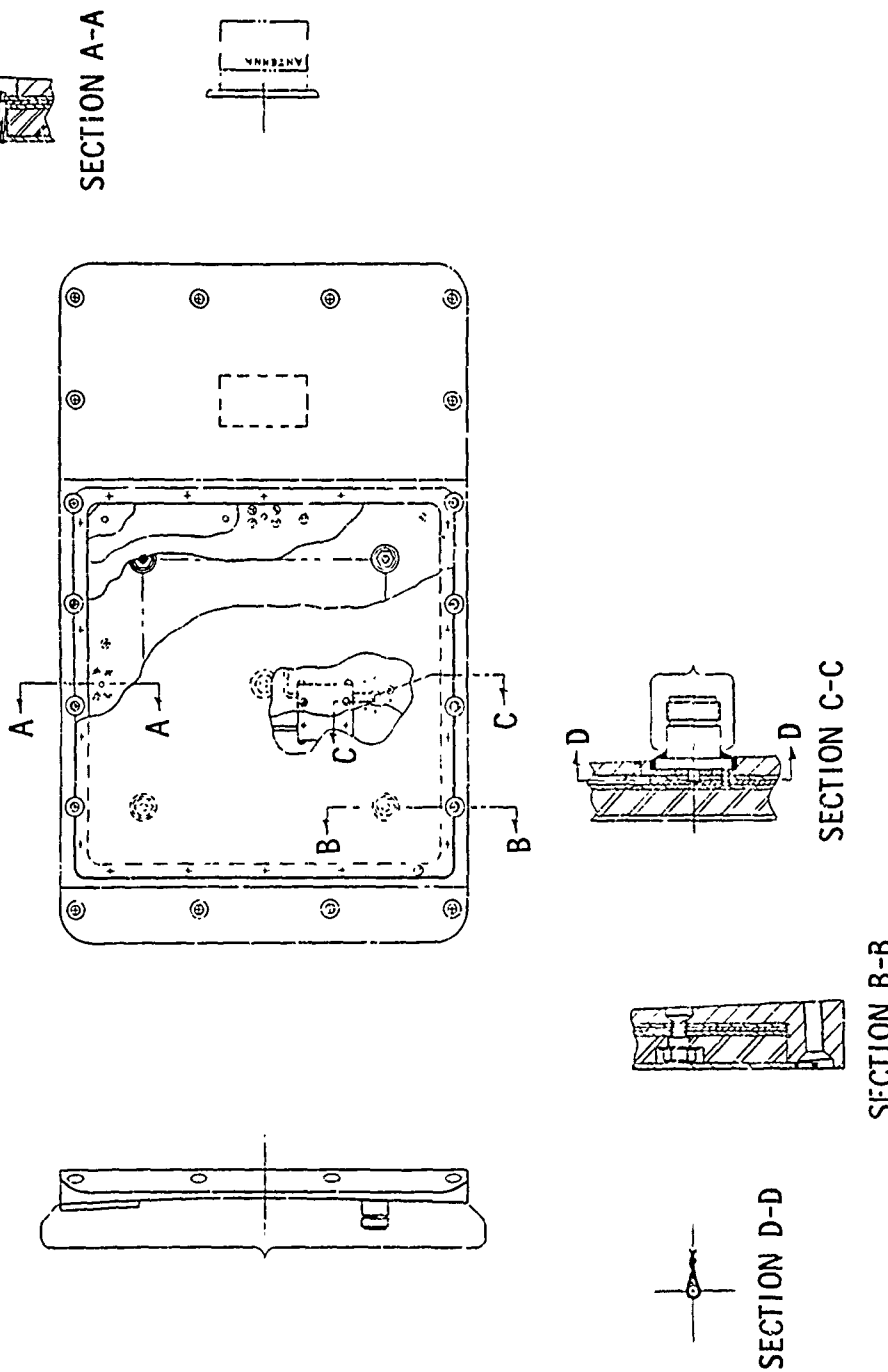


Figure 7. - Transco Products Inc. ASDAR antenna model 213F00100.

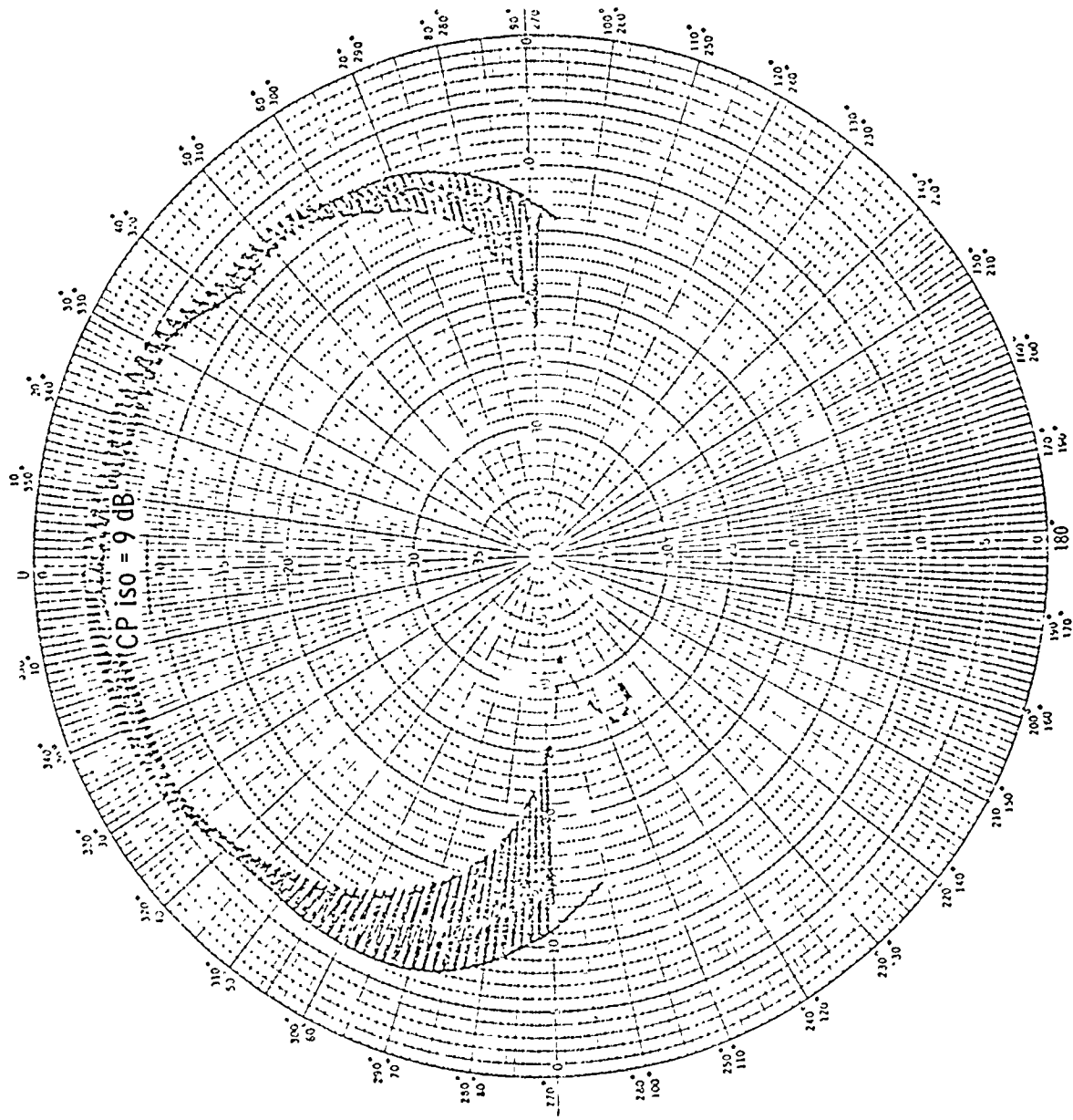


Figure 8. - ASRADAR antenna radiation pattern Transco Products model 213F00100, S/N 11;
ground plane mockup; freq. 401.9 MHz; aircraft pattern; roll plane.

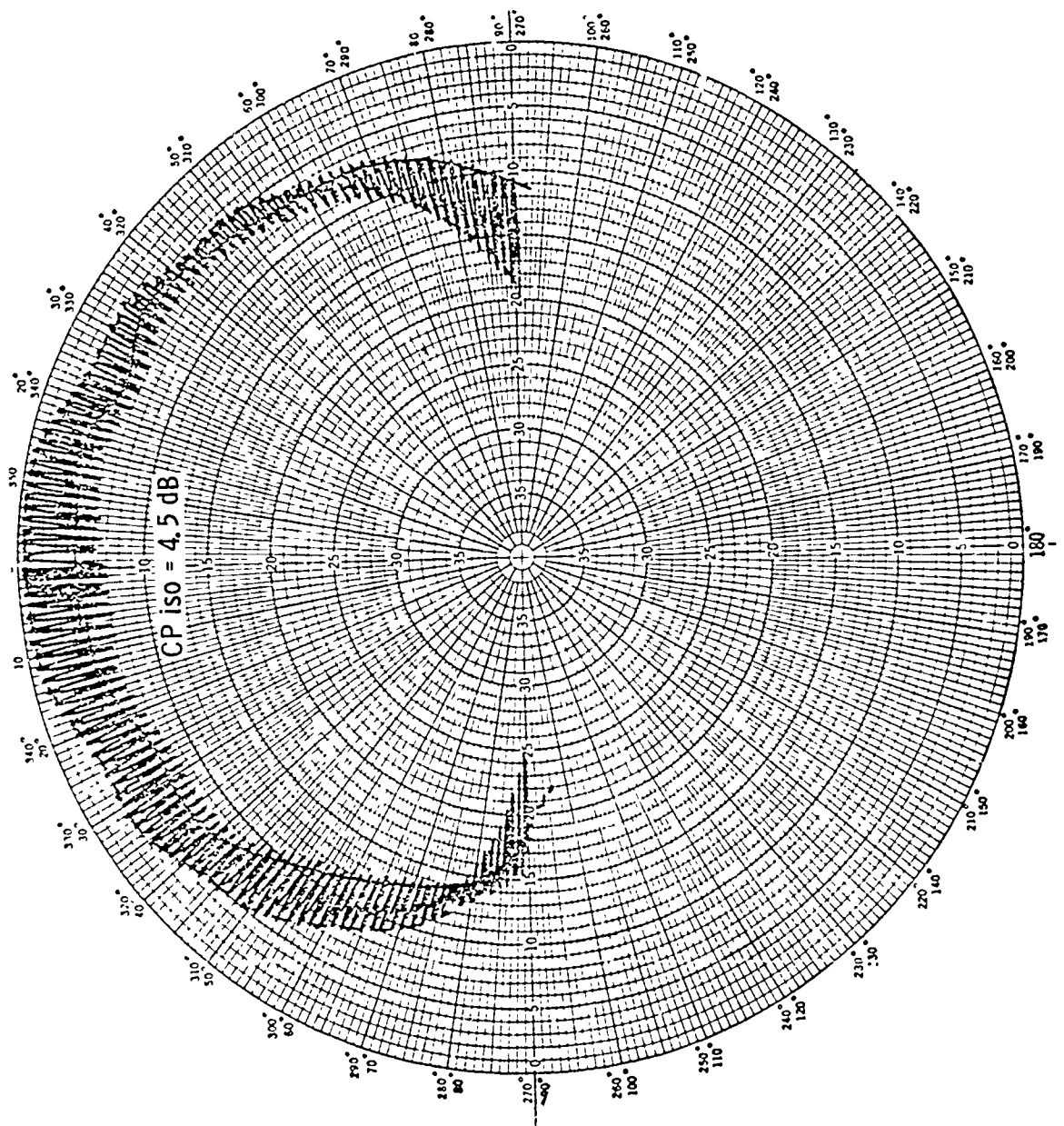


Figure 9. - ASDAR antenna radiation pattern Transco Products model 2135-0100; S/N 11; ground plane mockup; freq. 468.85 MHz; aircraft pattern; roll plane.

VARIATIONS ON THE CIRCULAR MICROSTRIP ANTENNA ELEMENT

JOHN MC ILVENNA and NICHOLAS KERNWEIS
DEPUTY FOR ELECTRONIC TECHNOLOGY
RADC/EEA, HANSCOM AFB
BEDFORD, MA 01731

SUMMARY

Many of the applications for which microstrip antennas are proposed require radiation characteristics that are not inherent in the basic microstrip elements. Recent experiments show however, that circular disc microstrip elements can be easily modified to produce a variety of changes in impedance and radiation pattern. The modification, which consists of adding one or two conducting tabs or strips to the element edges, alters neither the low profile of the disc (a characteristic useful in conformal and flush mounted antenna applications) nor the simplicity of the fabrication process associated with microstrip elements. Depending on the length, width and circumferential location of the strips, (which can be switched in and out electronically), the designer can shift resonant frequency and driving point impedance, or produce nulls in the element radiation pattern, enhance power levels in the angular regions well away from broadside, or produce dual frequency operation.

1.0 ELEMENT MODIFICATIONS FOR HEMISPHERICAL SCAN

1.1 BACKGROUND

Antenna arrays, conformally mounted on an aircraft or satellite surface, suffer various degrees of scanning loss as the main beam is tilted from broadside (1). A single conformal array, mounted on top of an aircraft and capable of scanning electronically down to either horizon, is an attractive but elusive goal for aircraft-to-satellite communication links. Good performance from a scanning array,

especially in the horizon or endfire directions, is difficult. Added to all the scanning losses is the fact that most array elements have radiation patterns that exhibit significant power fall off in the endfire regions. Microstrip disc elements in particular have an endfire pattern fall off that is almost twice as great as comparably sized elements such as slots. The investigation in this section is focused on modifications to microstrip elements that improve their endfire performance. The investigation is experimental and deals exclusively with the circular disc microstrip element.(2)

1.2 SINGLE STRIP DISCS

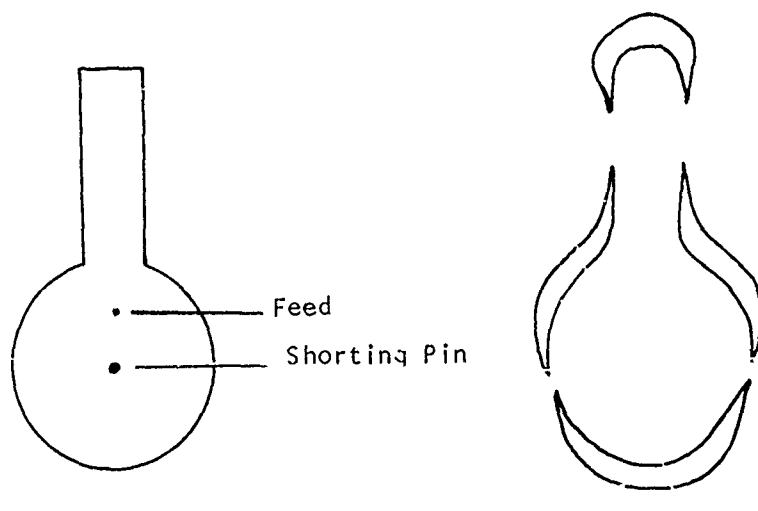
The plain disc element used in these experiments was 1.84 cm in radius and operated in the dominant mode at 2.88 GHz with a VSWR of 1.0. The first and second order resonances were measured at 4.84 and 6.80 GHz and were characterized as expected by radiation patterns with broadside nulls.(3) The disc was fabricated from teflon-fiberglass board, 0.15875 cm thick, with $\epsilon_R = 2.55$. A center shorting pin (0.05 cm diameter) was used and the feed placed on the back of the element at a 50 Ω point determined by experiment to be 0.57 cm out from the center. The measured resonances compare favorably with the 2.86, 4.74 and 6.52 GHz calculated with the formulas available in the literature. (4)

An interesting effect noted early in the experiments was that a small disc (washer, metal piece, etc.) placed on the circumference of the disc caused major changes in the field structure on the disc. (Liquid crystal detectors provided a convenient method for examining these changes (5)). Among the effects produced by the small supplementary

- (1) Mailloux, R., Phased Array Aircraft Antennas for Satellite Communications, Microwave Journal, Oct 1977, pp 38-44.
- (2) Kernweis, N. and McIvenna, J., Microstrip Antenna Elements for Use in Hemispherically Scanned Arrays, RADC-TR-79-43, Feb 1979, AD-A068566.
- (3) Derneryd, A., Analysis of the Microstrip Disk Antenna Element, RADC-TR-77-383, Nov 1977. To be published in IEEE Trans AP, 1979.
- (4) Shen, L.C. et al, Resonant Frequency of a Circular Disc Printed Circuit Antenna, IEEE Trans. Antennas and Propagation, AP-25, July 1977, pp 585-596.
- (5) Kernweis, N. and McIlvenna, J., Liquid Crystal Diagnostic Techniques, An Antenna Design Aid, Microwave Journal, Oct 1977, pp 47-51 or RADC-TR-77-250. Jul 1977, AD-A046231.

discs were: lowering the dominant mode resonant frequency by 6%, increasing the first order resonance by 22% and reducing the second order resonance frequency slightly. The small discs could also be used to excite almost any of the higher order modes simply by changing the circumferential location and overlap with the main disc. The small discs did not significantly alter the endfire behavior of the microstrip element however.

The geometry of the disc was then modified in a systematic manner by replacing the small supplementary discs with radial conducting strips of various lengths and widths. The liquid crystal detectors showed that this modification perturbs the disc surface currents and thus alters the radiation characteristics of the original element. A strip loaded disc element and a sketch of a typical liquid crystal display are shown in Figure 1. The strong fields on the strip are



Single Strip Disc

Sketch of Liquid Crystal
Detector Display

Figure 1

evident. Measurements showed that almost any length and width strip could provide improved endfire performance in the E_θ pattern. (The E_ϕ pattern was not greatly affected by the strip loading.) The endfire improvement was obtained however, only as one of a series of changes in the element behavior. Strip loading caused resonant frequency changes, changes in VSWR and pattern variations in the angular regions about endfire and broadside. Strips ranging in length from $\lambda_\epsilon / 2$ to $\lambda_\epsilon / 8$ (where λ_ϵ is the wavelength in dielectric of the plain disc dominant mode) and in width, from $\lambda_\epsilon / 2$ to $\lambda_\epsilon / 16$, were placed on the edge of the disc, in line with the center pin and feed. Table I summarizes the data collected.

Small strips cause small changes in the resonant frequencies and patterns. For example, a strip $\lambda_\epsilon / 8$ long and $\lambda_\epsilon / 16$ wide produces lowest and first resonant frequencies 10% and 19% below those of a plain disc. These small strips cause a partial fill-in of the broadside null in the first higher order resonant frequency pattern. As the strip length increases, the lowest resonant frequency shifts below 2 GHz and a poor VSWR indicates that this mode is no longer usable without a change in feed position. The first higher order resonance however, continues to alter its pattern as it shifts downward in frequency, completely filling in the broadside null, and becoming for all practical purposes a replacement dominant mode pattern. Using narrow strips, i.e., $\lambda_\epsilon / 16 \leq \text{width} \leq \lambda_\epsilon / 8$, the designer can avail himself of either dominant mode patterns at frequencies below that of a plain disc or dominant mode type patterns (modified first order resonance patterns) with enhanced endfire performance at frequencies above that of a plain disc. The frequency offset is controlled by the strip length.

Typical endfire improvement obtained with a narrow strip is shown in Fig. 2, where the E_θ patterns of a slot, a plain disc and a disc with strip $\lambda_\epsilon / 4$ long and $\lambda_\epsilon / 8$ wide, all placed on identical large ground planes, are compared. Note that the strip element is about as good in the endfire region as a slot and about 5 or 6 dB better than a plain disc element over the entire 70° to 90° sector. The single strip can be relocated somewhat, i.e., $\pm 40^\circ$ off the line connecting center pin and feed, without seriously altering the behavior.

Table 1. Strip Loaded Disc Performance

<u>Plain Disc</u> $f_o = 2.88 \text{ GHz}$ VSWR at $f_o = 1.0$ Pattern Fall-off at 80° - 10 dB 90° - 13 dB Maximum Pattern Ripple - 3.5 dB in $\pm 60^\circ$ Sector about Broadside				
Strip Length Strip Width Δf_o (percent) VSWR Pattern Fall-off Comments:	$\lambda c/2$ $\lambda \epsilon/2$ 0% 1.0 4-6 dB at 80° 7-8 dB at 90° 25 dB Null at Broadside	$3/8 \lambda \epsilon$ $\lambda \epsilon/2$ +13% 1.2 3-4 dB at 80° 8 dB at 90° 19 dB Null at Broadside	$\lambda c/4$ $\lambda \epsilon/2$ +25% 1.1 4 dB at 80° 9 dB at 90° 27 dB Null at Broadside	$\lambda \epsilon/8$ $\lambda \epsilon/2$ + 43% 1.5 4 dB at 80° 9 dB at 90° 13 dB Null at 22°
Strip Length Strip Width Δf_o (percent) VSWR Pattern Fall-off Comments:	$\lambda \epsilon/2$ $\lambda \epsilon/4$ +2% 1.0 4-6 dB at 80° 7-9 dB at 90° 9 dB Null at Broadside	$3/8 \lambda \epsilon$ $\lambda \epsilon/4$ +12% 1.5 3-4 dB at 80° 7-8 dB at 90° 9 dB Null at Broadside	$\lambda \epsilon/4$ $\lambda \epsilon/4$ +24% 1.6 4-5 dB at 80° 8 dB at 90° 7 dB Null at Broadside	$\lambda \epsilon/8$ $\lambda \epsilon/4$ + 35% 1.5 3-4 dB at 80° 7 dB at 90° 15 dB Null at 5°
Strip Length Strip Width Δf_o (percent) VSWR Pattern Fall-off Pattern Ripple	$\lambda \epsilon/2$ $\lambda \epsilon/8$ +3% 1.0 4-5 dB at 80° 8 dB at 90° 5.5 dB	$3/8 \lambda \epsilon$ $\lambda \epsilon/8$ +10% 1.6 4-6 dB at 80° 8 dB at 90° 4.5 dB	$\lambda \epsilon/4$ $\lambda \epsilon/8$ +21% 1.7 3-4 dB at 80° 7-8 dB at 90° 5.5 dB	$\lambda \epsilon/8$ $\lambda \epsilon/8$ -12% 1.7 10 dB at 80° 13 dB at 90°
Strip Length Strip Width Δf_o (percent) VSWR Pattern Fall-off Pattern Ripple	$\lambda \epsilon/2$ $\lambda \epsilon/16$ +3% 1.0 5.5 dB at 80° 8 dB at 90° 3.5 dB	$3/8 \lambda \epsilon$ $\lambda \epsilon/16$ +8% 1.6 5-6 dB at 80° 8.5-10 dB at 90° 3 dB	$\lambda \epsilon/4$ $\lambda \epsilon/16$ +19% 1.5 4 dB at 80° 8 dB at 90° 4.5 dB	$\lambda \epsilon/8$ $\lambda \epsilon/16$ -10% 1.7 10 dB at 80° 13 dB at 90°

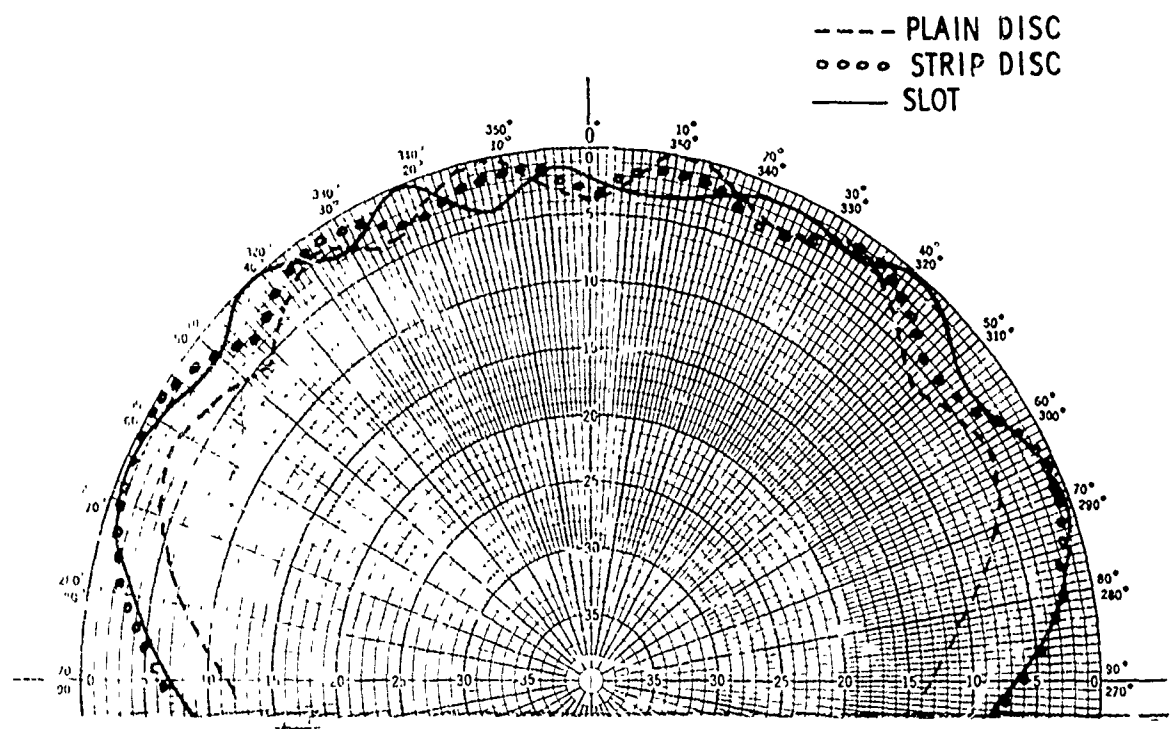


Figure 2. Comparison of Plain Disc, Strip Disc and Slot Radiation Patterns.

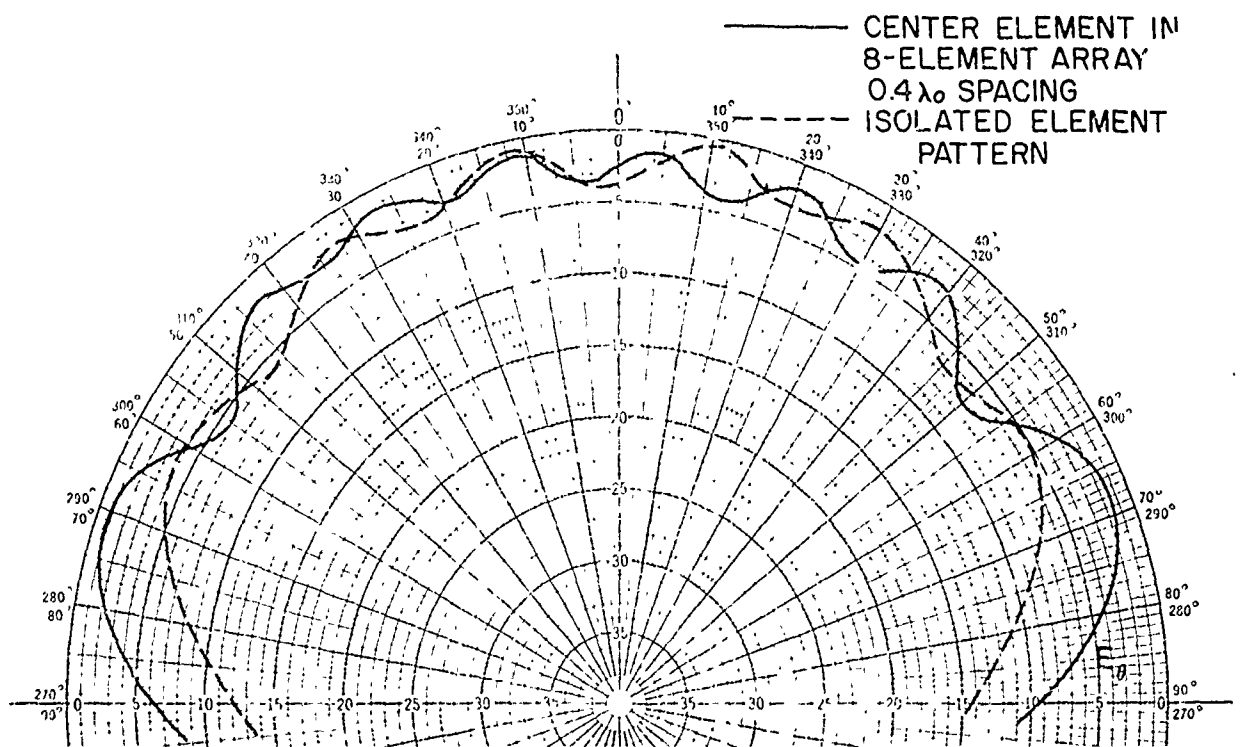


Figure 3. Comparison of Isolated Element with Arrayed Element.

Wide strips, i.e., $\lambda_e/4 \leq \text{width} \leq \lambda_e/2$ behave similarly in that resonant frequencies shift downward, and the dominant mode becomes quickly unusable. In contrast to narrow strips, the null in the first higher order resonance pattern does not completely fill in and becomes characteristic of wide strip radiation patterns. The null depth depends somewhat on the strip width. It is true of course, that large strips substantially change the size and shape of the disc. They do however, provide a simple means to alter both the resonant frequency and the broadside region pattern behavior.

1.3 PINNED DISC ELEMENT

Other modifications to the disc edges are possible. Just as metal pins have been used to short out one entire edge of a rectangular element, (6), the same can be done for the disc. Twenty pins were used around one half of the element edge. The liquid crystal display showed that, indeed, only one of the two field regions originally present on the plain disc exists on the pinned element. When the feed is repositioned to improve the impedance match, the VSWR is about 2.5 to 1, the frequency shift downward is about 22% (compared to the plain element) and the pattern shows about a 4 dB endfire improvement. Placing one or a small number of pins, i.e., less than 6, symmetrically about the center line connecting the shorting pin and the feed, caused no changes in the endfire radiation. Resonant frequency was shifted upward, however, by about 35%, the amount dependent on the number of pins used. In summary, the pinned disc, like the pinned rectangular element, can provide improved element patterns in the endfire sector. Large changes in VSWR, caused by the pin emplacement, can be reduced by proper location of the feed. Small numbers of pins can provide frequency shift and patterns not much changed from the plain element.

1.4 THE PLAIN DISC AND MUTUAL COUPLING

Mutual coupling can seemingly be used to advantage in hemispherical scan disc arrays. Four and eight plain disc elements, linearly arrayed with

(6) Garvin, C., et al., Missile Base Mounted Microstrip Antennas, IEEE Trans. AP, Vol AP-25, No. 5, pp 604-609.

various center-to-center separations ranging from $0.4 \lambda_0$ to $0.8 \lambda_0$ were measured. (λ_0 is the free space wavelength of the frequency corresponding to the lowest resonance in the elements). Comparison of the individual element patterns in the arrays with an isolated disc element pattern indicated that arraying at close distances actually improved the endfire performance of the array element pattern in the $80^\circ - 90^\circ$ angular sector. The array center element was about 5 dB better than the isolated element in this region, while the end element in the array showed less improvement but was still a few dB better than the isolated element. Figure 3 shows the pattern improvement obtained.

1.5 SUMMARY

This section has discussed several experiments aimed at improving the endfire response of the microstrip disc element. The E_ϕ radiation pattern has a deep null at endfire and none of the modifications discussed had any significant effect on this pattern. The E_θ pattern, however, can be changed in the endfire sector. The best of the modifications discussed brought the disc response close to that of a slot in a ground plane. Improvement in the endfire sector was usually obtained only in addition to other modifications in the element characteristics.

2.0 DUAL FREQUENCY DISC ELEMENTS

2.1 BACKGROUND

Several authors have proposed dual frequency schemes for microstrip elements (7) - (11). Designs that use two separate elements, one at each frequency, are versatile and can operate at almost any spread in the two frequencies. Since each element is tailored to its specific

- (7) Long, S. and Walton, M., A Dual Frequency Stacked Circular Disc Antenna, Proc. URSI-IEEE Conference, 1978, University of Maryland, pp 260-263.
- (8) Derneryd, A., Multiple Frequency Microstrip Disc Antenna, Microwave Journal, 1978, 21, pp 77-80. Also: Design of Microstrip Patch Antenna Elements, RADC-TR-78-46, Feb 1978, AD-A053728.
- (9) Sanford, G. and Munson, R., Conformal VHF Antenna for the Apollo - Soyuz Test Project, IEE Conference on Antennas for Aircraft and Spacecraft, 1975, pp 130-135.
- (10) I-Ping Yu, Low Cost Dual-Frequency Microwave Antenna, NASA Tech. Brief MSC-1600, 1976, Technology Utilization Office, P.O. Box 8757, Baltimore/Washington International Airport, MD, 21240.
- (11) Howell, J., Microstrip Antennas, IEEE Trans. AP, Vol AP-23, No. 1 Jan 1975, pp 90-93.

frequency, there are no problems with impedance and pattern deviations. On the other hand, a dual frequency array of such elements can be physically complicated by the abundance of elements and attendant packaging and mutual coupling problems. Operating a single element at two different frequencies is appealing from an array point of view. (12) In order to keep mismatch problems under control the frequency spread is more restricted than in the two separate element design. Almost any microstrip antenna element can be operated at multiple frequencies. Like any resonant cavity, microstrip element resonant modes offer the option of changing frequency, driving point impedance and radiation pattern structure. Differences between dominant and first order resonance radiation patterns are so pronounced as to make their use suited only to special applications however. A better approach is to seek techniques that perturb the dominant mode sufficiently to obtain two similar radiation patterns while providing an acceptable impedance match at the two frequencies.

Kerr (13) has recently reported on a dual frequency rectangular element. He found that adding a narrow strip to the element edge changes the resonant frequency and further, produces a second resonant frequency when the strip end is shorted to ground. The strip length controls the frequency spread. This approach is quite similar to that reported below. It was noticed in our investigations that the small tabs and strips added to the disc element sometimes produced multiple real axis crossings on the network analyzer trace. An investigation of this phenomenon showed that short strips produce good VSWR at several separate frequencies well above the original dominant mode with patterns that are however not very similar. Longer strips induce dual frequency behavior closer to the dominant mode frequency but the two patterns differ by as much as 15 dB in some angular sectors. None of the single strips investigated produced good match and good patterns simultaneously.

- (12) Kernweis, N. and McIlvenna, J., Dual Frequency Microstrip Disc Antenna Elements, RADC-TR-79-74, Mar 1979.
- (13) Kerr, J., Terminated Microstrip Antenna, 1978 Symposium on Antenna Applications, Univ. of Illinois, Sep 1978.

2.2 TWO STRIP DISCS

Placing a second vertical strip on the disc provided two resonant frequencies separated by about 1.2 GHz. The strips were $0.15\lambda_e$ wide and the lengths were varied between $0.6\lambda_e$ and $0.2\lambda_e$. As the strip length changed, the two resonant frequencies varied. The lowest frequency obtained was 28% below the dominant mode of the plain disc, while the highest obtained was 37% above. The two patterns were not similar; the low frequency pattern being characterized by a broadside null and the high frequency pattern displaying a variety of shapes that changed with strip length. Moving the strips to a horizontal position, also produced good VSWR but poor patterns at two frequencies separated by about 0.8 GHz. The lower frequency was in fact the dominant mode frequency of the plain disc and did not change with strip length. The upper frequency varied between 14% and 38% above the dominant mode depending on strip length. Two strips placed $\pm 30^\circ$ from the vertical line joining center and shorting pin provided dual frequency behavior with poor VSWR match and dissimilar patterns.

Relocating the strips to $\pm 60^\circ$ as shown in Figure 4 finally produced acceptable two frequency behavior. Figure 5 shows pattern results for

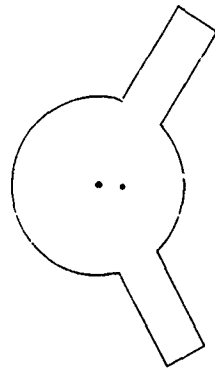


Figure 4. Two-Strip Disc.

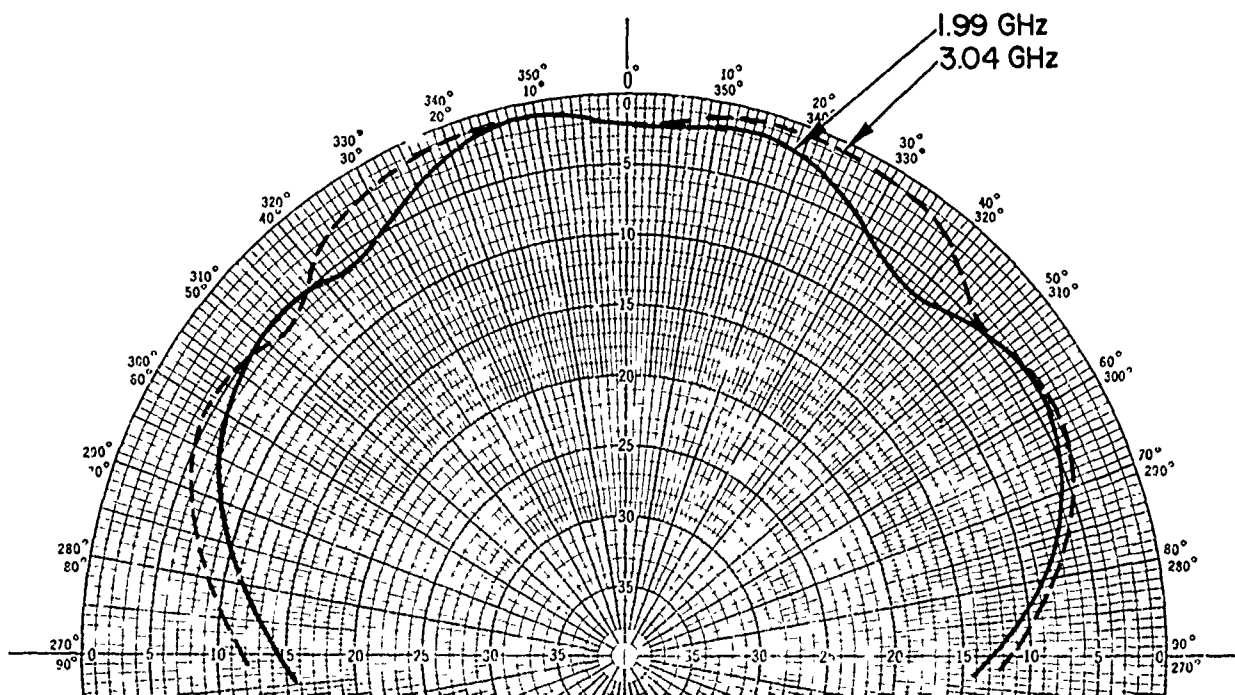


Figure 5. Radiation Patterns for Two Strip Disc ($\pm 60^\circ$)

Table 2. Two Strip Disc Data (Location: $\pm 60^\circ$, Width: 0.15)

Length (λ_e)	Freqs. (GHz)	Freq. Change from Dominant Mode of Plain Disc (%)	VSWR	Max. Pattern Difference (dB)
0.66	2.83	- 1.7	2.5	4
	3.60	+ 25	2.2	
0.62	2.90	+ 0.7	2.0	5
	3.73	+ 29	2.2	
0.55	2.85	- 1	1.0	5
	3.84	+ 33	2.1	
0.46	1.86	- 35	2.8	5
	3.04	+ 6	1.0	
0.38	1.99	- 31	1.5	4
	3.04	+ 6	2.0	
0.31	2.06	- 28	1.5	4.5
	3.11	+ 8	1.6	

strips $0.4 \lambda_e$ long and $0.15 \lambda_e$ wide and is typical of those obtained for other lengths. The two patterns differ at most by about 5 dB and both have the dominant mode shape. Table 2 summarizes the results obtained for two strips at $\pm 60^\circ$. The data shows that strips longer than about $0.5 \lambda_e$ tend to produce one frequency close to the plain disc dominant mode and a second higher frequency. The shorter strips produce one frequency close to the dominant mode and a second lower frequency. Strip lengths shorter than those shown in Table 2 produced two frequencies, one about 65% lower than the plain disc dominant mode, the second anywhere from 20 to 35% above depending on strip length. The VSWR was poor, i.e., 2.5 at the higher frequency and 5.0 at the lower frequency. Moving the two strips to $\pm 75^\circ$ of the center line also produced good dual frequency patterns. The spread in frequencies was somewhat less than that obtained with $\pm 60^\circ$ strips but the difference between patterns was also smaller.

It should be pointed out that each of the strips does not independently control one of the two frequencies. Both strips are required to produce the dual frequency behavior described above. If two unequal length strips are used, the element usually loses its dual frequency characteristics. The second loop in the network analyzer trace degenerates to a "kink" and there is only one resonance indicated. Some adjustment of the VSWR shown in Table 2 is possible by judicious trimming of the strip length. Width adjustments are much less effective in this regard.

The logical extension to the two strip, dual frequency element is the N-strip, M-frequency element. Measurements on 4, 6 and 12-strip elements showed however that even dual frequency behavior was not always obtained and when it was, the element was often very inefficient at one of the two frequencies. A variation of the multistrip element is the "rising sun" element shown in Figure 6, formed by removing sections of the basic disc.

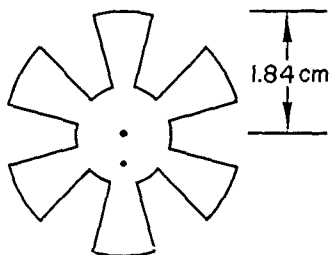


Figure 6. The Multi-Strip Disc.

Although multiple resonances were displayed on the network analyzer trace, only two of resonances provided acceptable patterns. These occurred at 2.195 and 2.29 GHz (a narrow spread in frequency) and were basically dominant mode type patterns. The element was inefficient at the remaining frequencies.

In summary then, the $\pm 60^\circ$ and $\pm 75^\circ$ locations were the only ones found to provide both acceptable VSWR and patterns for a two strip disc. There seemed to be no advantage in using more strips.

2.3 THE DUAL FREQUENCY DISC IN AN ARRAY ENVIRONMENT

In an array environment, with the strips essentially extending the element fringing fields, one could question whether the strips increase mutual coupling effects to the point of altering the dual frequency behavior. This situation was studied with a three-element strip disc array on a large, square ground plane. The outer two elements were moved so that center-to-center distance varied between $0.25\lambda_{01}$ and $0.55\lambda_{01}$ for the lower of the two frequencies ($0.38\lambda_{02}$ to $0.85\lambda_{02}$ at the higher). At the close spacings, the discs were almost touching. Measurements on the center element of the three element array (Fig. 7) showed that the two resonant frequencies were unchanged as the array spacing varied. The center element radiation patterns showed some changes at the closest spacing in the angular sector well away from broadside. It is interesting to note that this type of change, i.e., a decrease in the pattern fall-off close to endfire, is exactly what is desired when designing an element for use in hemispherically scanning arrays. Thus, the strips provide not only dual frequency operation but an improved element pattern when closely arrayed.

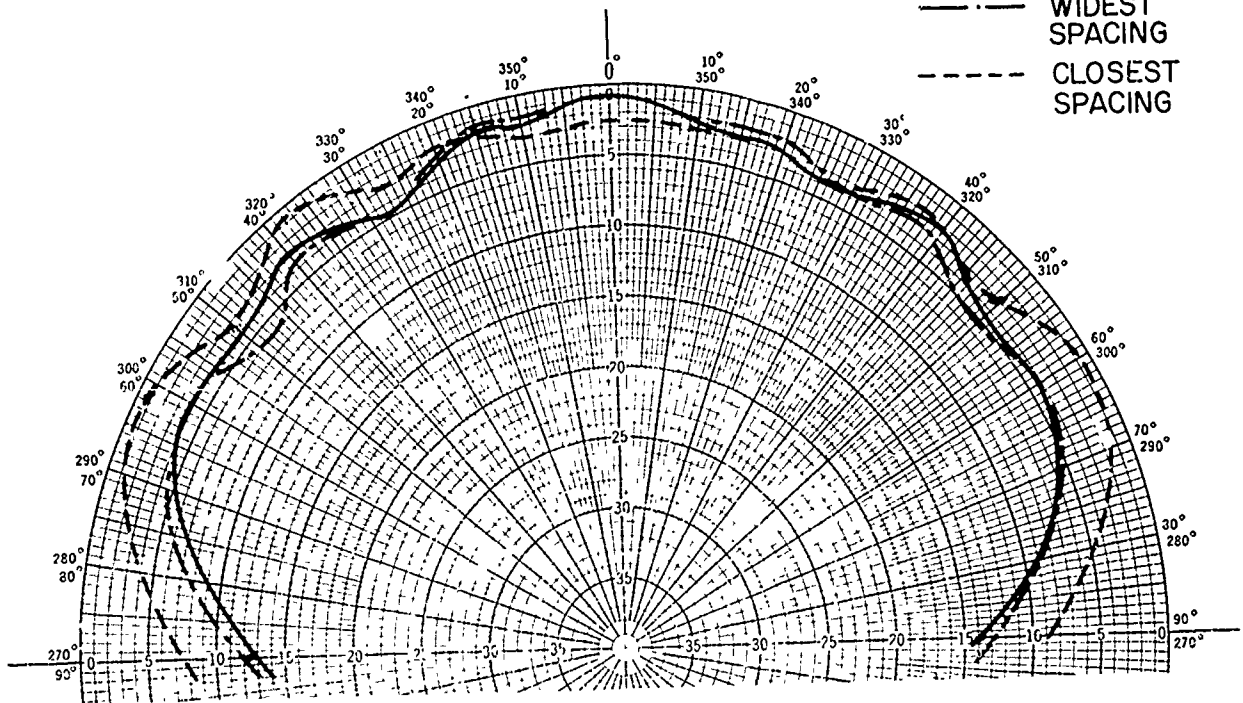
3.0 REFERENCES

Derneryd, A., Analysis of the Microstrip Disc Antenna, Report RADC-TR-77-383, Nov 1977. (To be published in IEEE Trans. AP, 1979.) AD-A051187.

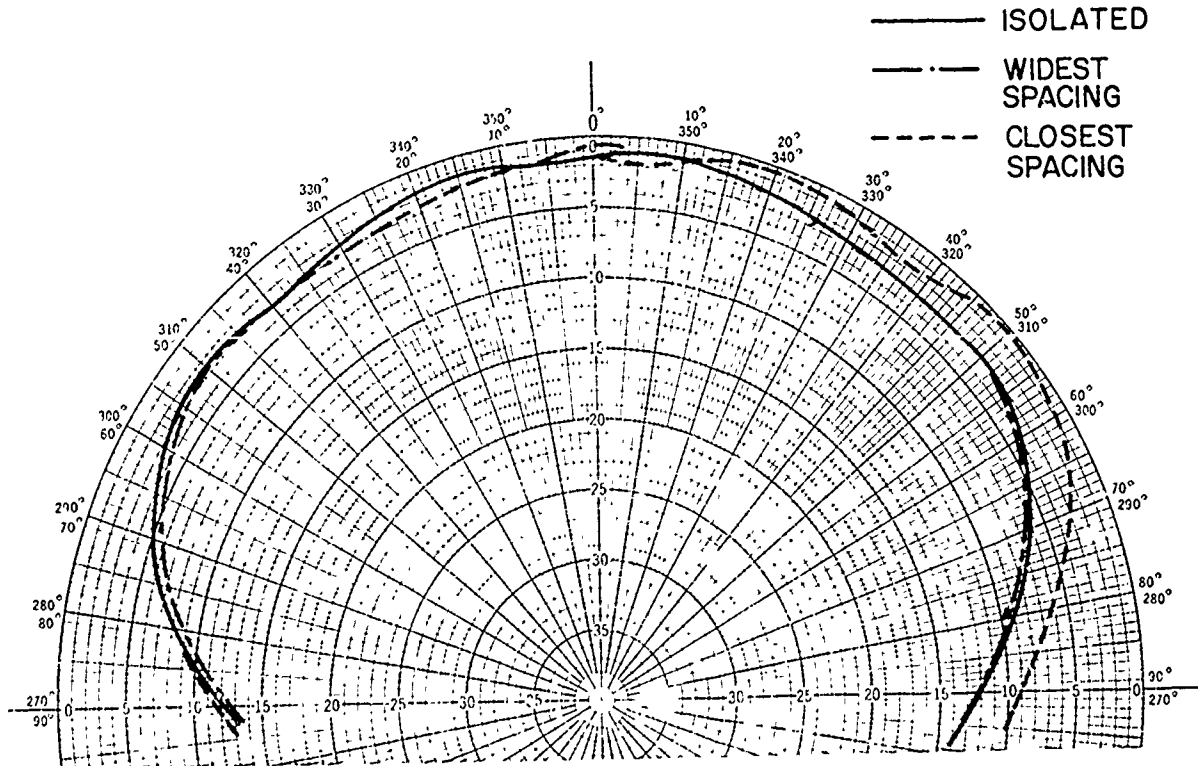
Derneryd, A., Multiple Frequency Microstrip Disc Antenna, Microwave Journal, Vol. 21, May 1978, pp 77-80.

Garvin, C., et al., Missile Base Mounted Microstrip Antennas, IEEE Trans. AP-25, No. 5, pp 604-609.

Figure 7



Comparison of Center Element Radiation Patterns for High Frequency



Comparison of Center Element Radiation Patterns for Low Frequency

Howell, J., Microstrip Antennas, IEEE Trans. Antennas and Propagation, AP-23, Jan 1975, pp 90-93.

Kernweis, N. and McIlvenna, J., Liquid Crystal Diagnostic Techniques: an Antenna Design Aid, Microwave Journal, Vol. 20, Oct 1977, pp 47-51.

Kernweis, N. and McIlvenna, J., Microstrip Antenna Elements for Use in Hemispherically Scanned Arrays, RADC-TR-79-43, Feb 1979, AD-A068566.

Kernweis, N. and McIlvenna, J., Dual Frequency Microstrip Disc Antenna Elements, RADC-TR-79-74, Mar 1979.

Kerr, J., Terminated Microstrip Antenna, Symposium on Antenna Applications, University of Illinois, Sep 1978.

Long, S. and Walton, M., A Dual Frequency Stacked Circular Disc Antenna, Proc. URSI-IEEE Conference, 1978, University of Maryland, pp 260-263.

Mailloux, R., Phased Array Aircraft Antennas for Satellite Communications, Microwave Journal, Vol. 20, Oct 1977, pp 38-44.

Sanford, G. and Munson R., Conformal VHF Antennas for the Apollo - Soyuz Test Project, IEE Conference on Antennas for Aircraft and Spacecraft, 1975, pp 130-135.

Shen, L.C., et al, Resonant Frequency of a Circular Disc Printed Circuit Antenna, IEEE Trans Antennas and Propagation, AP-25, July 1977, pp 595-596.

I-Ping Yu, Low Cost Dual-Frequency Microwave Antenna, NASA Tech. Brief MSC-1600, 1976, Technology Utilization Office, P.O. Box 8757, Baltimore/Washington International Airport, MD, 21240.

MICROWAVE SUBSTRATES PRESENT AND FUTURE

THOMAS E. NOWICKI
TECHNICAL SERVICE ENGINEER
3M ELECTRONIC PRODUCTS DIVISION

SUMMARY

The history of microwave substrates shows a continuous quest for both high and low K products with low loss characteristics. Technological advances in all areas of the microwave industry demand substrates whose tolerances are closely controlled, and the newest additions of these do meet that criteria. New microwave substrate products are keeping pace with today's demands while development work continues on new materials which will meet the increased demands of the future.

1.0 A CAPSULE HISTORY OF PRINCIPAL STRIPLINE LAMINATE FROM 1956 THROUGH 1979

1.1 In the late 1950's, PTFE (Polytetrafluoroethylene) glass cloth was used to manufacture a product with a dielectric constant of 2.73 and a Tan δ of .003. Another substrate popular in that time period was cross linked unfilled styrene with a dielectric constant of 2.55 and a Tan δ of .0005. The glass fiber version of this product has a dielectric constant of 2.62 and a Tan δ of .0010.

3M's early PTFE glass substrate had a dielectric constant of 2.65 and a Tan δ of .0028. During the 1960's, microwave quality glass became available. PTFE woven glass products with dielectric constants of 2.55 and 2.45 with a Tan δ of .0022 and .0018 respectively, were available along with the random fiber PTFE glass substrate having dielectric constants of 2.35 and 2.20; these materials had the corresponding Tan δ of .0013 and .0009.

TABLE 1
CRONOLOGY OF MICROWAVE MATERIALS

<u>TIME PERIOD</u>	<u>MATERIAL</u>	<u>K</u>	<u>TAN "δ"</u>
1950's	PTFE Glass Cloth	2.73	0.003
	Cross Linked Styrene	2.55	0.0005
	Glass Filled Styrene	2.65	0.001
1960's	PTFE Glass Cloth	2.55	0.0022
	PTFE Glass Cloth	2.45	0.0018
	PTFE/Glass Fiber	2.35	0.0013
	PTFE/Glass Fiber	2.20	0.0009
1970's	PTFE Glass Cloth	2.33	0.0013
	PTFE Glass Cloth	2.17	0.0009

2.0 PRINCIPAL SUBSTRATES TODAY

2.1 The principal substrates today are alumina and PTFE glass. Alumina has extremely low loss (.00001) and a dielectric constant of 9.7 to 10.3. PTFE glass substrates have losses in the range of .0008 to .0022 and dielectric constants from 2.17 to 2.70.

Epsilam-10, a new high dielectric constant and low loss PTFE based substrate with a dielectric constant of 10.2 is replacing alumina in many applications. The ability to shrink the dimensions of low frequency board designs by using a high K substrate can give significant reductions in weight, size and cost. Typical cost savings achievable are shown in Table 2. A comparison between thirteen alumina chips and one large Epsilam-10 Aluminum Clad carrier shows a significant cost savings.

TABLE 2
COST OF MATERIALS AND PROCESSING PRIOR TO ASSEMBLY*

<u>Gold on Alumina</u>		<u>Epsilam-10</u>	
Material	\$ 18	Material	\$ 44
Machining	160	Machining	64
Metallizing	<u>30</u>		
	\$208		\$108
Substrates	44		
Material (Gold)	30	Etch Cu	20
Cut & Drill	23	Plate Cu	10
Metallize Holes & Edges	27	RF Terminations	36
Etch Substrates	117		
Inspect	35	Inspect	9
Solder Preforms	10		
Vac Solder	<u>64</u>		
	TOTAL	\$558	TOTAL
			\$183

* These data were supplied by a company using Aluminum Clad Epsilam-10 on a multi-stage 500 watt power amplifier.

2.2 The high dielectric constant conformable substrate also offers other advantages in that entire "mother boards" or systems can be totally designed upon one common ground plane with a minimum of interconnections and, therefore, less impedance matching problems, and reduced handling of parts. Cost reductions up to 60% are not uncommon. [8]

2.3 The impact of these relatively new substrates is just beginning to be felt in the microwave industry. When complex circuits requiring odd shapes and large sizes are required, conformable substrates come into their own. [1], [2] These conformable substrates can be drilled, routed and machined into complex shapes which allows them to be placed into devices where other high K substrates could not economically be used. Their ability to absorb vibration to 45 G's eliminates the need for cushioning and designing to protect the more brittle high K substrates from damage. Sheet sizes available up to 23cm. x 48cm. allow the design engineer more latitude and a shorter fabrication time. Since these substrates are processed like regular printed circuit boards, [1] the cost savings and improved yields more than justify the initial cost of \$0.15/cm².

3.0 AN OVERVIEW OF MICROWAVE SUBSTRATES

3.1 There are many low loss microwave substrates on the market today, but none can provide the overall advantages of woven PTFE glass. (See Table 3) Comparative data on most plastic base substrates follows in Table 4. [7], [9]

TABLE 3
ADVANTAGES OF WOVEN TEFLON GLASS

These advantages are:

- * Excellent Dimensional Stability
- * Closely Controlled Dielectric Constant
- * Good Thermal Expansion Match to Copper
- * Good Copper Etch Resolution and Bond to Copper
- * Negligible Cold Flow
- * Funginert
- * Chemical Resistant
- * Good Mechanical Processability
- * Usable Over a Wide Temperature Range
- * Available in Large Sheet Sizes 91.44cm x 91.44cm

TABLE 4
AN OVERVIEW OF MAJOR MICROWAVE SUBSTRATES

Product	K X-Band	Tan δ X-Band	Dimensional Stability	Chemical Resistance	Temp. Range °C	Cost Range
PTFE Unreinforced	2.10	0.0004	Poor	Excellent	-27 to +260	High
PTFE Glass Woven Web	2.17	.0009	Excellent	Excellent	-27 to +260	Medium
	2.33	.0015	Very Good	Excellent	-27 to +260	Medium
	2.45	.0018	Fair	Excellent	-27 to +260	Medium
	2.55	.0022	Poor	Excellent	-27 to +260	Medium
PTFE Glass Random Fiber	2.17	.0009	Fair	Excellent	-27 to +260	Medium-high
	2.35	.0015	Poor	Excellent	-27 to +260	Medium-high
PTFE Quartz Reinforced	2.47	0.0006	Excellent	Excellent	-27 to +260	High
Cross Linked Poly Styrene/ Woven Quartz	2.65	0.0005	Good	Fair to Poor	-27 to +260	Medium-high
Cross Linked Poly Styrene/Ceramic Powered-Filled	3 to 15	From 0.0005 to 0.0015	Fair	Fair to Poor	-27 to +110	Medium-high
Cross Linked Poly Styrene/ Glass Reinforced	2.62	0.001	Good	Poor	-27 to +110	Low
Irradiated Polyolefin	2.32	0.0005	Poor	Good	-27 to +100	Low

TABLE 4 (cont.)

AN OVERVIEW OF MAJOR MICROWAVE SUBSTRATES

Product	K X-Band	Tan δ X-Band	Dimensional Stability	Chemical Resistance	Temp. Range °C	Cost Range
Irradiated Polyolefin/Glass Reinforced	2.42	0.001	Fair	Good	-27 to +100	Medium
Polyphenylene Oxide (PPO)	2.55	0.0016	Poor	Good	-27 to +193	Medium
Silicone Resin Ceramic Powder-Filled	3 to 25	From 0.0005 to 0.004	Fair to Medium	Good	-27 to +268	High
Sapphire [7]	9.0	0.0001	Excellent	Excellent	-24 to +371	Very high
Alumina Ceramic	9.7 to 10.3	0.0004	Excellent	Excellent	To 1600 unclad	Medium-high
Glass Bonded Mica	7.5	0.0020	Excellent	Good	-27 to +593 unclad	Medium

3.2 PTFE woven glass substrates are available in a variety of claddings to fit many specialized applications. Standard products with copper foil weights of 14 gms., 28 gms., 57 gms., 142 gms., and up, along with heavy ground planes of pure copper, beryllium copper and aluminum allow the user numerous choices for design and packaging

3.3 Epsilam-10 is used mostly in the 3GHz and lower frequency range, but some applications are now up to the 18GHz range. The 2.45 and 2.55 family of PTFE glass applications are mostly 2 to 12 GHz, while 3M's new low loss, low K 2.17 and 2.33 products will see uses to 36GHz or possibly higher depending on the application.

3.4 Most unreinforced or unfilled materials available for stripline or microstrip applications will have a substantial mismatch between the thermal expansion of the substrate and of the copper cladding. The amount of mismatch is substantially reduced by the addition of woven glass or quartz web.

4.0 ANISOTROPY

4.1 There are trade-offs when fill materials are introduced to obtain dimensional stability; one of these is the introduction of anisotropy. Anisotropy is the difference in dielectric constant in the X, Y plane of a substrate compared with the Z direction. A test procedure for measuring the amount of anisotropy is discussed in reference [6].

TABLE 5
DATA FOR DIELECTRIC ANISOTROPY

Material	Description	Thickness cms	K Z	K XY	% Anisot.	K XY/Z
Unfilled PTFE	2 Discs	.522	2.08	2.09	Neg.	1.00
PTFE Glass Cloth	CuClad 2.17	.051	2.15	2.34	Neg.	1.09
	Old CuClad 2.45	.153	2.45	2.89/2.95	2.0	1.19
	New CuClad 2.45	.153	2.43	2.88	Neg.	1.18
Filled PTFE Glass Cloth	CJ, 606	.153	6.24	6.64/5.56	1.29	1.06

5.0 THE BUILDING BLOCK CONCEPT

5.1 In the past, the dielectric constant of PTFE glass substrates varied with thickness. It is no longer necessary to design a stripline package using different dielectric constant. 3M's new "Building Block Concept" allows the designer to select thicknesses with constant K.

5.2 The object is to establish and maintain a fixed dielectric constant for all available thickness in each grade. Thus, the CuClad 2.33 building blocks become multiples of .0127cm (5 mils) all having the same K and the CuClad 2.17 building block becomes .0254cm (10 mils). All multiples of .0254cm (10 mils) have the same 2.17 dielectric constant.

5.3 If there is any doubt as to whether the product is 2.17 or 2.33, simply count the layers of glass. The 2.17 product has one layer of glass for every .0254cm (10 mils) of build and the 2.33 product has one layer of glass for every .0127cm (5 mils) of build.

6.0 CUCLAD 2.17 DIMENSIONAL STABILITY

6.1 Dimensional change in cm before and after etch shows excellent stability as shown by typical data in Table 6.

TABLE 6
DIMENSIONAL STABILITY AFTER ETCH

<u>CuClad 2.17 .0254cm (10 mil)</u>	<u>Before (cm)</u>	<u>After (cm)</u>	<u>cm/cm Change</u>
	21.5176	21.5158	8.4×10^{-5}
	14.6355	14.6256	6.8×10^{-5}
<u>CuClad 2.17 .1524cm (60 mil)</u>	<u>Before (cm)</u>	<u>After (cm)</u>	<u>cm/cm Change</u>
	21.5156	21.5146	4.8×10^{-5}
	14.6339	14.6334	3.1×10^{-5}

7.0 TEMPERATURE EFFECTS ON DISSIPATION FACTOR AND DIELECTRIC CONSTANT

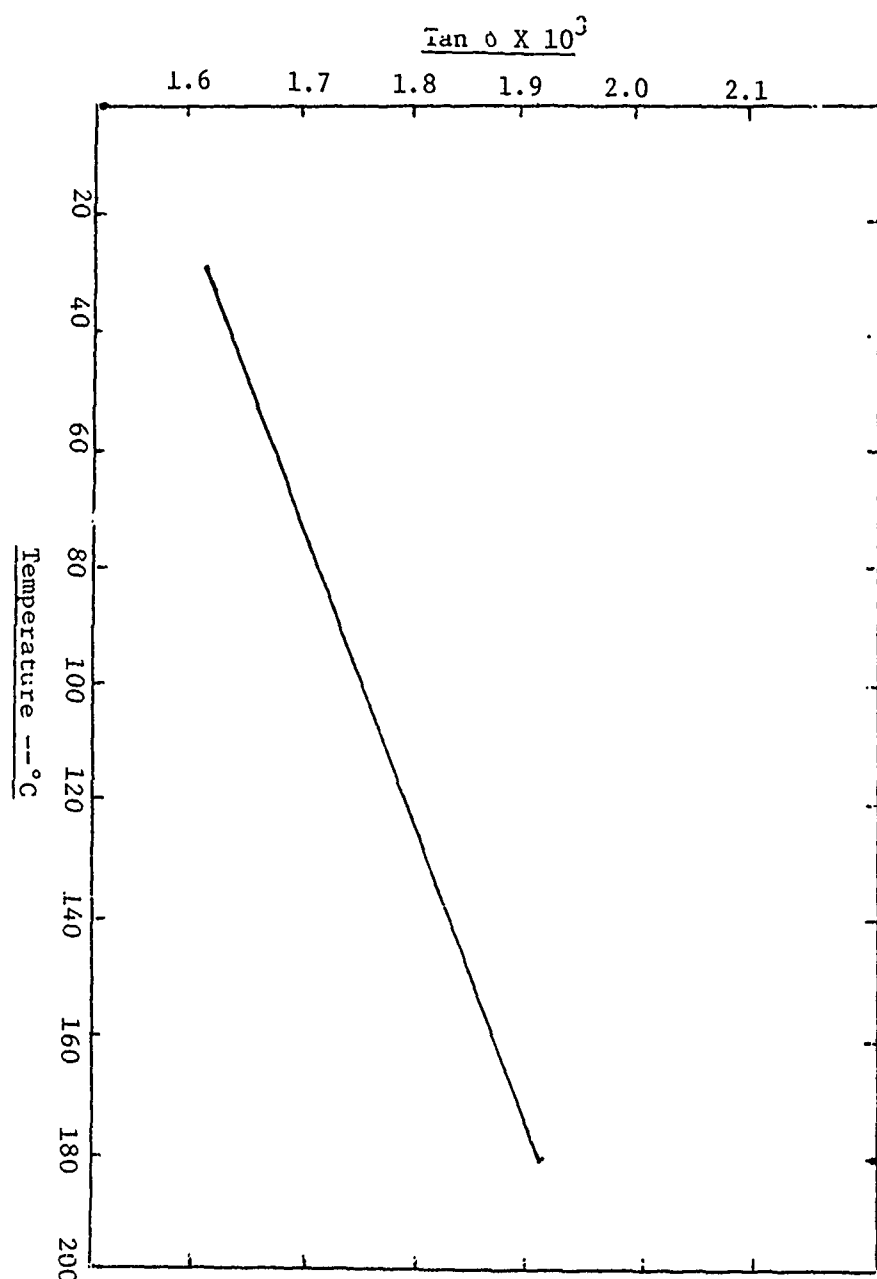
7.1 The dielectric constant of PTFE glass composite substrates decreases with increasing temperature and the dissipation factor increases with increasing temperature (See Table 7 and 8). The data supplied were obtained using the 3M X-Band test method with test fixture mounted in an oven to maintain a constant pressure with a means to monitor the temperature of the test specimen.

The effects of temperature change on electrical response of stripline packages due to change in dielectric constant and dissipation factor with temperature, are negligible for most designs. These data are redrawn from graphs in [4], [5].

TABLE 7 - EFFECT OF TEMPERATURE ON DISSIPATION FACTOR

CUCLAD GX-060-45

K = 2.45

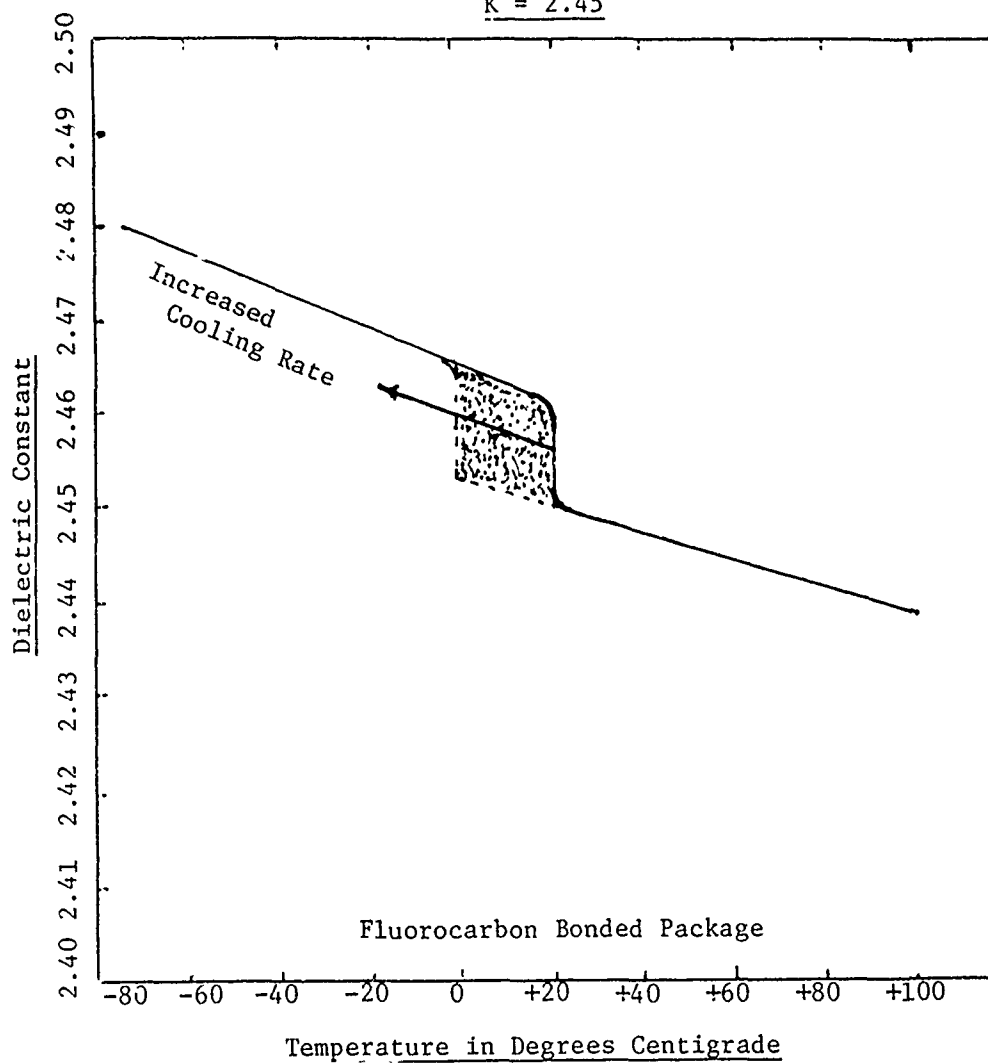


The Tan δ Rate of Increase with Temperature is $2 \times 10^{-6} / ^{\circ}\text{C}$

TABLE 8 - CHANGE IN DIELECTRIC CONSTANT WITH TEMPERATURE

CUCLAD GX-060-45

K = 2.45



The change in K over the temperature range $-75^{\circ}\text{C} + 100^{\circ}\text{C}$ is 96ppm/ $^{\circ}\text{C}$.

The abrupt change from $K = 2.450$ to $K = 2.466$ is caused by the well known room temperature transition which takes place in all PTFE based products.

CONCLUSION

7.0 CONTINUED DOMINANCE OF PTFE SUBSTRATES IN THE FUTURE

We believe the PTFE based substrates will continue to dominate in the future just as they have in the past. Their ease of processing, dimensional stability, low electrical losses, good copper adhesion, large sheet size and cost effectiveness make them very attractive to end users.

With the advent of new technology, especially the burgeoning millimeter wave area, pure PTFE with a suitable ground plane to enhance dimensional stability and perhaps syntactic foams with combinations of bubbles and PTFE are promising approaches to more cost effective millimeter wave substrates.

The new low loss PTFE substrates for use in the millimeter wave technology of today and especially tomorrow, will require thin smooth metallizations contributing a minimum amount of electrical losses.

3M intends, through research and development, to continue to be the leader in microwave substrates, offering the widest selection of low loss products today and tomorrow.

8.0 REFERENCES

- [1] Gregorwitch, W. S. and Kawata, P. K., A Broad Band Conformal Array for Communications Satellites, Proceedings of 1977 Antenna Applications Symposium, 27-29 April, Allerton Park, Monticello, Illinois.
- [2] Hutchins, William D., Microwave Design Utilization With a Non-Ceramic High Dielectric Constant Substrate, IBM Federal Systems Division, Owego, New York.
- [3] Mil-P-13949F
- [4] 3M, CuClad Stripline Laminates, Bulletin Number EL-CSL-1 (175) JPI 3M, Electronic Products Division, St. Paul, Minnesota 55101.
- [5] 3M, Cu Tips #2, Bulletin Number E-LCI/2 (126.3)R, 3M, Electronic Products Division, St. Paul, Minnesota 55101.
- [6] Olyphant, Murray, Jr., Measuring Anisotropy in Microwave Substrates, IEEE-MTT-S-1979 International Symposium Digest, April 30 - May 2, 1979, Orlando, Florida, CAT. NO. 79CH 1439-9MTT-S, pp. 91-4.
- [7] Westphal, W. B. and Sils, A., Dielectric Constant and Loss Data, Massachusetts Institute of Technology, Technical Report AFML-72-39, April, 72 Air Force Materials Lab, Air Systems Command, Wright Patterson Air Force Base, Ohio.
- [8] Woermke, James D., Fellow Engineer Group Leader, Westinghouse Electric, Baltimore, Maryland, Better Your MTC Designs With High K Substrates. Microwaves, March 1979.
- [9] Vossberg, Walter A., Stripping the Mystery From Stripline, 3M Electronic Products Division, Chelmsford, Massachusetts.

CLAD LAMINATES OF PTFE COMPOSITES
FOR MICROWAVE ANTENNAS

G. ROBERT TRAUT
LURIE RESEARCH AND DEVELOPMENT CENTER
ROGERS CORPORATION
ROGERS, CONNECTICUT 06263

SUMMARY

Copper clad or specially backed laminates based on composites of PTFE fluorocarbon polymer with non-woven glass fiber or with high dielectric constant ceramic fillers offer combinations of properties valuable for microwave antennas. Uniformity of dielectric constant, isotropicity, thermal coefficients, stability, low loss tangent, and thickness uniformity are important to the designer. Those building antennas are concerned with such characteristics as chemical resistance, low moisture absorption, strain relief, formability, machineability, and bondability. Conversion techniques to optimize component performance are discussed.

It is important to have convenient test methods for dielectric constant that allow close control of the base material by the producer or close monitoring of dielectric constant so that antenna pattern artwork can be adjusted. A rigid non-destructive test method is summarized.

The situation for producers of microwave printed circuit antennas should improve with laminators working for closer control of critical properties in existing products as well as development of new products better able to meet the demands for antenna applications.

1.0 LAMINATE CHARACTERISTICS IMPORTANT TO ANTENNA DESIGN

In the design of printed circuit antennas of predictable performance certain material characteristics are especially critical to designers.

1.1 UNIFORMITY OF DIELECTRIC CONSTANT

The performance tolerances that may be specified for a given antenna system design probably depend more on uniformity of dielectric constant than on any other material characteristic. Panel to panel uniformity is obviously important for consistent antenna characteristics. At least equally critical is within panel uniformity, particularly where phase relationships for multi-element arrays must be controlled.

Close dielectric constant tolerance, such as the $\pm .02$ currently supplied in the nonwoven fiberglass-PTFE composites in the 2.20-2.35 range, improves predictability. But this may not always be sufficient. In many cases if the fabricator could easily read relative panel to panel differences within the $\pm .02$ range he would have the opportunity to compensate in pattern design for critical applications.

A technique for non-destructively measuring dielectric constant of a small area etched free of foil should be valuable for close tolerance jobs to guide selection of a compensating pattern for the antenna.

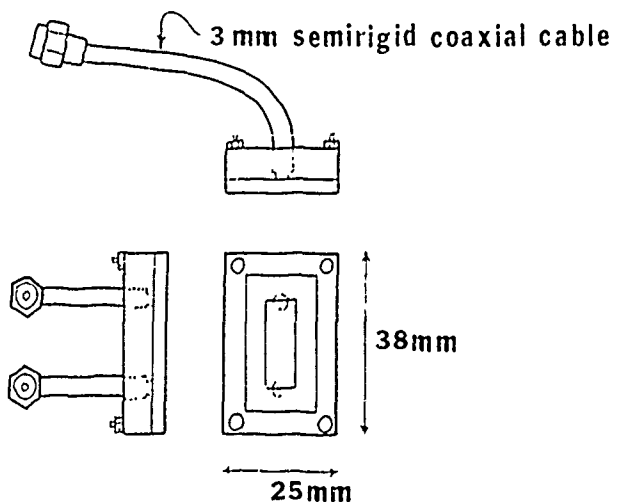


Figure 1. Typical Quick Test Fixture for X-band Non-Destructive Testing of Microwave Circuit Boards for Dielectric Constant

A "Quick Test" fixture has been devised(1) which consists of a one wave length X-band stripline resonator on a dielectric card fastened against a metal block fitted with coaxial probes. When the resonator pattern is pressed against a dielectric sheet with ground plane on the back side to complete the stripline configuration, one may then determine resonant frequency.

The fixture is calibrated by determining the resonant frequency with each of a series of dielectric specimens having a range of known dielectric constant values broader than the range to be encountered. These are machined to a series of thicknesses broader than those expected in testing. A regression analysis procedure is used to convert the frequency-dielectric constant-thickness data to a series of coefficients for a polynomial fit to the data. See Table 1.

The resonant frequency of the fixture is then determined when it is pressed against an unknown test specimen of known dielectric thickness dimension. The polynomial coefficients are used with the frequency-thickness data to compute a dielectric constant. The method is quite precise but not absolutely accurate and may be used in a relative way to detect small panel to panel differences in dielectric constant.

Usually in an antenna circuit pattern an area can be found which may be etched free of foil and used for such a measurement prior to final etching. Thus one may select from a series of patterns to compensate for dielectric constant deviations making possible very precisely tuned antennas.

TABLE 1
CALIBRATION DATA FOR A TYPICAL "QUICK TEST" FIXTURE

Specimen	Thickness mm T	Dielectric constant K	Resonant Frequency in GHz observed F	predicted F
A	3.153	2.2372	9.387	9.392
B	1.551	2.2372	9.735	9.744
C	0.775	2.2372	10.053	10.047
D	0.354	2.2372	10.313	10.315
E	3.132	2.3578	9.257	9.237
F	1.549	2.3578	9.582	9.574
G	0.766	2.3578	9.851	9.853
H	0.370	2.3578	10.054	10.052
I	3.139	2.4891	9.041	9.065
J	1.532	2.4891	9.407	9.397
K	0.776	2.4891	9.610	9.624
L	0.370	2.4891	9.803	9.802
M	3.151	2.5953	8.935	8.925
N	1.539	2.5953	9.242	9.251
P	0.780	2.5953	9.447	9.437
Q	0.377	2.5953	9.614	9.615

Polynomial from regression analysis:

$$\begin{aligned}
 F^2 = & - .019480 + .0055769T + .032089/T - .0099282/T^2 \\
 & + (.023723 - .0047265T - .029210/T + .0087782/T^2)K \\
 & + (-.0046290 + .0010714T + .0064858/T - .0019125/T^2)K^2
 \end{aligned} \quad (1)$$

1.2 ISOTROPICITY OF DIELECTRIC CONSTANT

For synthesis of stripline or microstrip antenna designs, isotropic dielectric constant is usually assumed to avoid further complicating the computations. Composites containing fibrous re-enforcement oriented in the plane of the sheet will show a dependence of dielectric constant on electric field orientation so that the X or Y directions in the plane of the sheet yield a higher value than the Z thickness direction.

The magnitude of this effect is a function of the difference in dielectric constant between fiber and polymer matrix; the degree of fiber orientation, and the volume ratio of fiber to polymer.

Dielectric constant measurements for foil clad polymeric boards for microwave circuitry are usually obtained with a stripline resonator method such as that described in ASTM D3380 "Standard Method of Test for Permittivity (Dielectric Constant) and Dissipation Factor of Plastic Based Microwave Circuit Substrates". The value obtained in such a test is mostly for the Z direction field but the fringing field will contain X or Y components in a manner usually similar to the application.

There can also be anisotropic behavior in the high dielectric constant ceramic-PTFE composites depending on the manner in which the ceramic filler is distributed through the polymer matrix.

To determine the degree to which dielectric constant varies with direction we prepared heavy thickness panels of ceramic-PTFE composite RT/duroid 6010 from which were cut pairs of plates perpendicular to each of the major axes as shown in Figure 2. A stripline resonator method was used to determine dielectric constant values as shown in Table 2.

TABLE 2
X-BAND DIELECTRIC CONSTANT VERSUS MAJOR AXIS
ORIENTATION OF ELECTRIC FIELD IN RT/DUROID 6010

Specimen Identification	Dielectric Constant		
	X direction	Y direction	Z direction
A	10.64	10.69	10.61
B	10.80	10.67	10.24
C	10.60	10.74	10.34
Average	10.68	10.70	10.40

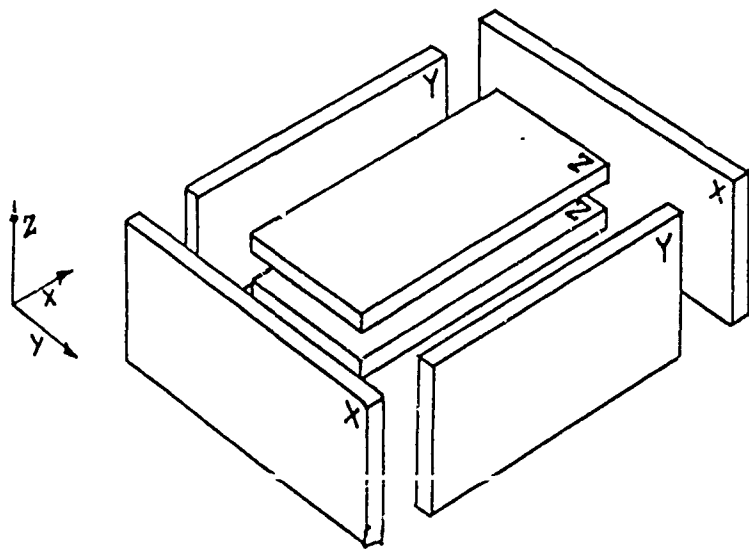


Figure 2. Schematic for Cutting Dielectric Constant Specimens
at Various Orientations from Heavy Thickness Panel

TABLE3
DIELECTRIC CONSTANT VERSUS MAJOR AXIS IN RT/DUROID 5870
NONWOVEN FIBER-PTFE COMPOSITE

Test Method	Dielectric Constant		
	X direction	Y direction	Z direction
1 MHz fluid displacement cell ASTM D1531	2.428	2.430	2.330
10 GHz stripline resonator ASTM D3380	2.452	2.432	2.347

1.3 THERMAL EFFECTS ON DIELECTRIC CONSTANT

The apparent dielectric constant is affected by temperature. Much of the

effect is simply accounted for by the thermal expansion of the material. As the material expands its density and the space concentration of polarizable groups decreases.

PTFE is a very highly crystalline polymer which undergoes several phase transitions over its workable temperature range. At 19 and 30 C there is a two step change in the degree of crystalline order of the polymer that is accompanied by step changes in density and dielectric constant. The rate of change with temperature above and below this step is very nearly the same. However the amorphous portion of the polymer microstructure undergoes a transition from glassy state to rubbery in the temperature region around 130-150 C that is manifest by a gradually increasing rate of change of density with temperature. At the 327 C crystalline melt point there occurs a large step change.

Experiments have been run with nonwoven glass-PTFE and ceramic-PTFE composites to determine the thermal effect on dielectric constant and whether the effect is reversible. For this purpose a stripline two node resonator with capacitively end-coupled 50 ohm probes was prepared from two specimen cards. The assembly was clamped at controlled stress between temperature controlled heating blocks of steel. Resonant frequency and band width at the half power points was determined as the assembly was heated and cooled over a period of several hours.

We found that dielectric constant did decrease with temperature as expected (Figure 3) but that the change was reversible with temperature with no evidence in the range up to 400 C that any permanent impairment of electrical performance occurred. The Q of the circuit did not show the expected peaks at transition points. Individual Q readings showed a lot of scatter but the overall trend was only a slight increase of losses with temperature.

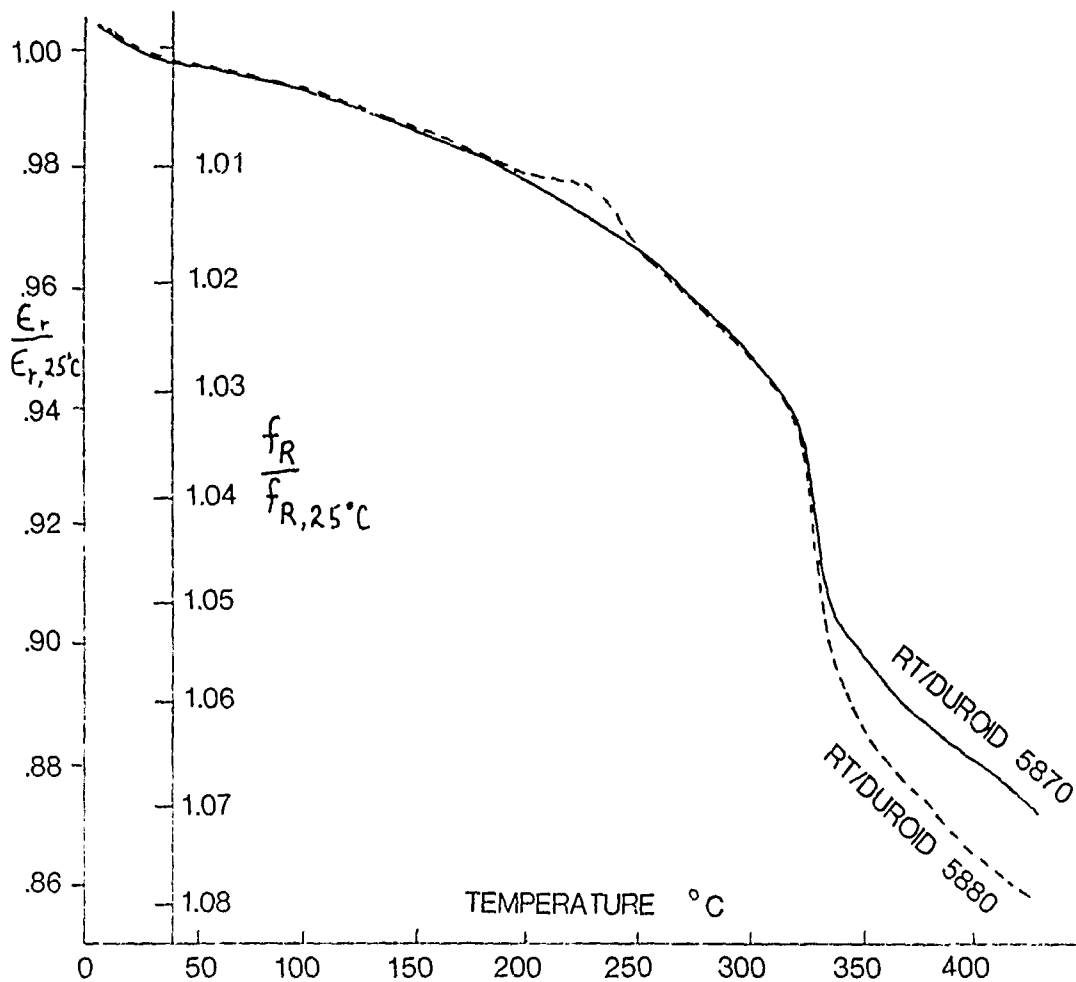


Figure 3. Variation in Stripline of Apparent Dielectric Constant with Temperature

It is expected that the apparent dielectric constant of a microstrip configuration would have been similar. In either case antenna design must take temperature into account. The absence of permanent effects is encouraging.

1.4 COEFFICIENT OF THERMAL EXPANSION

The coefficient of thermal expansion, CTE, of a dielectric material for antennas must be considered for its effect on mechanical behavior of an antenna as well as electricals as discussed in 1.3. The designer must anticipate the range of temperatures in service. While the matrix polymer PTFE possesses many ideal properties it does exhibit a high CTE.

Circuit boards fastened onto a metallic support of different CTE and

greater stiffness will either be stretched or compressed over a temperature excursion. If stretching is great enough it can lead to permanent deformation that will lead to compression upon return of the temperature. Compression could lead to buckling between fastening points.

Fortunately both the nonwoven fiberglass-PTFE and the ceramic-PTFE composites possess a low CTE in the plane of the sheet. This combined with low modulus tends to minimize the stretching and buckling problem.

Effective ways to avoid buckling problems include the use of bonded circuit techniques as discussed in 2.5 or the use of laminated panels produced with a heavy thickness metal, such as aluminum, bonded to one side. It is also feasible to solder plate the ground plane copper on the circuit board and solder reflow bond the board to a supporting metal chassis.

If clamping or riveting is used rather than bonding and thermal excursions are expected, CTE differences can lead to loosening of the assembly. Both nonwoven and woven glass-PTFE composites exhibit a high Z (thickness) direction CTE which is nearly the same as for the neat polymer. The CTE increases with temperature so that upward excursions lead to very high stress levels unless some arrangement in the clamping hardware, such as spring loaded screws, is provided to accomodate the expansion.

1.5 THICKNESS UNIFORMITY

Close tolerance thicknesses are available when needed. From the producer's point of view excessive thickness variations are often early evidence of a problem with the production process and therefore as a matter of practice thickness uniformity within and among panels is subject to continuous monitoring. Every panel is given a thorough thickness survey assuring reliability.

1.6 STABILITY

In considering materials for antenna applications, one must be sure that

the effect of environmental factors such as heat aging, ultraviolet(UV) radiation exposure, weathering, and vibration are too small to impair antenna performance.

PTFE possesses a very high melt point(327 C) and an even higher thermal degradation point (about 440 C). More importantly, prolonged service at temperatures such as 260 C with or without oxygen available make little detectable change in the material.

Unlike many polymers which require UV absorbers and inhibitiors to retard degradation in heat or UV exposure, PTFE with no additives is resistant to UV attack for extended times.

The low permeability to moisture and the low energy surface that resists wetting contribute to the exceptionally good weatherability. The microstructural feature of individual particles of filler or fiber embedded in the polymer matrix with little wicking opportunity retards the effect of prolonged exposure to high moisture.

Low modulus and good extensibility of the composites provide very adequate resistance to vibration, mechanical or thermal shock.

2.0 PROPERTIES IMPORTANT FOR PRODUCTION OF ANTENNAS

It is not enough for a material to have suitable performance characteristics in the final antenna applications. For a design to succeed solutions to production problems must be considered. The following sections deal with some of these:

2.1 CHEMICAL RESISTANCE

For the composites we are discussing, the PTFE continuous matrix has no known solvent or swelling agent. Even fluorinated hydrocarbons are unable to disrupt the polymer. The filler in high dielectric constant composites such as RT/duroids 6010 or 6006 or the microfiber glass in the 2.20, 2.35 dielectric constant materials such as RT/duroid 5880 or 5870 also are insoluble in organic solvents. One might imagine that prolonged

exposure of these materials to very strong inorganic solvents such as the hydrofluoric acid often used to etch back protruding woven glass strands in punched holes would have an adverse effect. It turns out that such materials usually have a superficial effect. Particles or fibers at exposed edges are usually separated from adjacent fiber particles by the continuous polymer matrix so that beyond the surface, attack of composite ingredients is limited by diffusion through the polymer, an extremely slow process.

Chemical resistance of these composites offers some benefits and also some problems for antenna fabrication.

First there is no need to be concerned about selection of materials for cleaning, photo resist, resist removal, etching solutions, or plating solutions.

Then there is little need for concern about entrapping absorbed water or chemicals used in etching or edge plating. Washing to remove superficial adsorption usually is adequate.

The chemically inert PTFE surface poses a problem in that this surface resists being bonded to other materials systems. To apply a potting compound or coating based on, for example, epoxy resin, it is necessary to first prepare the PTFE surface so that such systems can wet and adhere. This is best done by treatment with one of the commercially available sodium complex solutions; often referred to as "sodium etch". The strong chemical reducing potential of sodium is able to degrade the PTFE surface and produce chemical groups on the surface that can be wetted and adhered to.

Excessive exposure to strong aqueous reagents such as plating solutions on etched patterns could cause impairment of the copper-PTFE bond. Where a corrosion resistant plating such as gold is required, the technique of plating a mask of gold followed by etching away the copper foil avoids

the risk of plating solutions damaging the bond.

2.2 STRAIN RELIEF

In the process for lamination of copper foil to the PTFE based substrate, it is necessary to raise temperatures to above 300 C for appreciable periods of time. This necessary thermal history leads to two effects. The copper foil is annealed so that it is quite ductile and soft. There is created a strained condition when the laminate is cooled due to the thermal expansion difference between dielectric and copper. The effect of this strain and in which material the strain is predominant depends on the ratio of the copper foil thickness to dielectric. If this ratio is comparatively low as, for example, in 1.57 mm (.062 inch) thick dielectric with 17 um (0.5 oz/ft²) copper two sides, the bulk of the elastic strain remains in the foil and little change in dimension of the dielectric occurs when foil is removed. When the ratio is high as in a .25 mm (.010 inch) thick dielectric with 68 um(2oz/ft²) copper two sides the dielectric will show greater change as the foil is removed.

In microfiber glass-PTFE composites containing comparatively low levels of glass fiber, it has been found that in the plane of the sheet thermal coefficient is largely controlled by the fiber, to about the same degree as one may observe in woven glass-PTFE composites of considerably higher fiber content. Strain relief presents a problem that is usually quite readily resolved in the generation of printed circuit patterns with precise dimensional control by one of three ways.

2.2.1. The strain relief may be experimentally determined for the particular pattern density, dielectric thickness and foil thickness involved. Artwork for the photo resist etching mask is generated with an adjustment in dimensions to compensate for strain relief anticipated in production. Care should be taken to be sure this strain relief determination method allows time for the viscoelastic response of the polymer composite to occur. This may be accelerated by heat such as an hour or two at 150 to 250 C. In the case of nonwoven fiber-PTFE composites such as RT/duroid 5870 or 5880 the X and Y orientation

differences must not be ignored.

2.2.2. For shorter runs of a given pattern where artwork adjustment is too costly or else where precision is required that is greater than the predictability of strain relief a double mask procedure may be used. In this technique an oversize mask pattern is first used which allows exposure of most of the copper foil to be removed but protects enough to allow for strain relief errors. After the circuit has been etched and strain relieved a second mask is used to get the exact pattern.

2.2.3 The dielectric may be obtained clad on one side with copper foil and on the other side with a heavy aluminum plate. The aluminum plate will control dimensions and also serve as ground plane and chassis. Problems with this solution involve costs of cutting out circuit card shapes and obtaining satisfactory through hole plating when needed. Generally such aluminum plate base circuits are limited to flat surfaces.

2.3 MACHINABILITY

Nonwoven fiberglass-PTFE composites such as RT/duroid 5870-5880 exhibit good machinability with relatively low tool wear. The microfibre glass is considerably lower than tool steel in hardness. This lower hardness, the fine diameter, and the low volume percentage combine to provide a material with tool wear characteristics close to that of neat PTFE.

Nevertheless, it is possible to excessively wear cutting edges by running at high speeds with slow tool feed rate. This combination will tend to scrape material away rather than cut. The relatively low modulus composite will tend to deform and slide around the finite sized radius of the cutting edge rather than be cut. The frictional heat generated, especially due to high speed, further softens the composite making the situation worse. Continued operation in this manner will wear the tool to increase the radius of the edge. Of course carbide tools will maintain a sharp (very fine radius) edge longer than tool steel and should be used for long runs. In either case if excessive tool wear is evident the correction is to slow down the cutting speed and perhaps

increase the tool feed rate.

Unfortunately the ceramic-PTFE composites combine high volume content and relatively high hardness of the filler to result in a material that, in spite of its softness, requires carbide tooling for machining. With carbide tool edges and attention to speed and feed rate good machining results may be obtained.

The above comments apply to machining such as is done by lathe turning, drilling, milling, or even sawing. Both types of material are easily fabricated to desired shapes by shearing or the use of punch and die tooling. Prototypes may be easily cut with a sharp edged model maker's knife.

2.4 FORMABILITY

Where one desires to apply printed circuit antennas to nonplanar surfaces, the ceramic filled or the nonwoven fiber reinforced materials make possible a considerable degree of formability. To form a simple curved shape requires that a sheet material be forced to elongate on the convex surface and compress on the concave surface. The nonwoven fiber structure has an advantage over continuous filament or woven structures in that the discontinuous nature of the fiber in the relatively soft and deformable polymer matrix allows such distortion without permanent stress. The ceramic-PTFE composite offers even more formability. With some effort and a properly designed fixture, compound curvatures should also be feasible.

Forming requires attention be paid to the viscoelastic response of the PTFE matrix and is best done by avoiding exceeding the elastic deformation limit at any given time. Time must then be allowed for the viscous response, observed as stress relaxation. We have found, for example, that curved strips may be formed by wrapping on a mandrel followed by an oven bake to accelerate the stress relaxation.

Care must be taken to avoid breakage or distortion of the copper pattern.

The normally dead soft condition of the foil is some advantage. Work yet needs to be done in the area of successive deformations followed by clamping and heating to anneal the foil and stress relieve the dielectric for extremely sharp radius curvatures.

2.5 BONDABILITY

A cover sheet of dielectric is often employed to protect the printed circuit antenna from environmental damage to the circuit foil pattern and also to provide the proper electrical performance. In many cases a protective cover sheet or a stripline power divider for an antenna requires bonding rather than clamping or riveting to reduce variations in performance. The values and limitations of such bonded assemblies for packaging stripline devices has been discussed (2). A comparatively small range of thermoplastic polymer film types have the combination of electrical characteristics, melting point and adhesion that would be useful for bonding. In some cases a sodium etch treatment as mentioned in 2.1 is used to improve bond.

The more difficult mechanical and thermal environmental stresses of antenna systems make bonding even more desirable. In some cases to obtain bonds that will withstand temperatures in the 300 C region the use of direct bonding by fusion of the exposed PTFE surfaces in the boards themselves becomes necessary. In the case of high dielectric constant ceramic filled composites direct bonding is generally preferred simply to avoid the dielectric constant mismatch of bonding film to base material.

Direct bonding involving the fusion of the polymer in the base material would at first glance appear to be a very risky process since it gives ample opportunity for the printed circuit pattern to move about during the bonding operation. However, the extremely high viscosity of the PTFE polymer combined with the effective restraint of flow afforded by the fiber reinforcement allows one to find pressure-temperature "plateaus" such that fusion will take place without "swimming" of the circuit pattern.

We have had some limited experience with RT/duroid 6010 using 50 x 50 x 1.27 mm cards having 34 um copper on about 3% of the bonding area. First, the cards are assembled with the aid of registration holes and pins between aluminum plates of 10 to 15 mm thickness. If there are etched areas on the ground plane exposing the substrate to contact with the aluminum plate a release sheet of aluminum foil will be required. Second, the assembly should be enclosed in an envelope fashioned from 0.1 mm (.004 inch) aluminum foil crimped around the edges to prevent air exposure during the heating. Third, the assembled enveloped assembly is clamped between steel platens equipped with thermostatically controlled electric heaters at a stress of 0.7 to 1.0 kPa (100 to 140 psi) held constant throughout the cycle. Fourth, the platens are heated to 380 to 390 C (716 to 734 F) over a period of 15 to 16 minutes. This is well above the crystalline melt point of the PTFE and allows the polymer in its amorphous state to fuse without exhibiting excessive sideways flow. Higher temperatures will result in excessive flow. Fifth, the temperature is maintained for about 15 minutes to allow viscosity limited knitting of the surfaces to occur. Sixth, the platens are allowed to cool without thermal shock at about 5 K per minute until below 300 C. Seventh, cooling to 150 C or lower may be accelerated with air flow. Eighth, the clamping stress may be safely released when the temperature is below 150 C.

Quite often press equipment capable of 400 C temperatures is not readily available in a prototype laboratory. Simple steel blocks fitted with cartridge heaters and maintained at temperature with a thermocouple type controller separated from the existing press platens by insulating plates can be set up quite inexpensively for doing such assemblies. Alternately, clamping fixtures can be used in ovens.

3.0 NEW DIRECTIONS FOR MICROWAVE PRINTED CIRCUIT ANTENNAS

New products now available or under development along with new fabrication techniques promise some interesting extensions of the microwave printed circuit antenna field. A few are mentioned here.

3.1 SIZE REDUCTION

The availability of high dielectric constant substrates with the same impact strength and flexibility of the nonwoven glass-PTFE composites should permit reduction of the size of antennas for a given frequency and performance requirement. Additionally it may become feasible to convert some lower frequency applications to printed circuit techniques.

3.2 HIGHER TEMPERATURE CAPABILITY

The direct bonding of circuit boards by PTFE fusion should allow upgrading of bonded microwave antenna assemblies for higher temperature performance. This will, for example, allow formed missile telemetry antennas to withstand the heat generated at higher speeds without failure.

3.3 BEAM FORMING STRUCTURES

The availability of high dielectric constant laminates at various dielectric constants makes feasible the construction of various types of lens antennas incorporating printed circuit elements as a bonded in layer for control of polarization. Techniques for bonding boards to various shapes needs to be developed.

3.4 NON-PLANAR CIRCUIT PATTERNS

Work underway to produce nonwoven glass-PTFE composites in compound curved shapes such as cones or ojive shapes could well lead to printed circuit techniques to form radiating patterns.

4.0 REFERENCES

1. Traut, G. R., Proceedings of the 13th E/EIC, pp39-44, IEEE Pub. No. 77CH1273-2-EI (1977) "Electrical Measurements of Microwave Circuit Board Materials"
2. Traut, G. R., Microwave Journal, 18, No.18 (Aug 1975) "Microwave Stripline Packaging with UMD's"

RESONANCE CHARACTERISTICS OF A RECTANGULAR MICROSTRIP ANTENNA

D.C. CHANG AND E.F. KUESTER
ELECTROMAGNETICS LABORATORY
DEPARTMENT OF ELECTRICAL ENGINEERING
UNIVERSITY OF COLORADO
BOULDER, COLORADO 80309

SUMMARY

A graphical method for determining the size of a resonant, rectangular microstrip patch for a specified frequency is given. Using an expression obtained from the reflection coefficient of a TEM-wave in a semi-infinite microstrip patch, the resonance condition of a given mode for a patch of finite size, is derived in a manner analogous to that of a rectangular, waveguide cavity. Radiation is shown to be in the form of both surface-waves and sky-waves, and is dependent of the angles of incident for waves impinging onto the edges of the patch. By varying the aspect ratio, it is also possible to modify the Q-factor of a resonant patch.

1.0 INTRODUCTION

In the design of a microstrip patch antenna, it is sometimes necessary to consider the trade-offs regarding the aspect ratio of the patch. For instance, to what extent one can enhance the radiation from a patch antenna operating near resonance by adjusting its aspect ratio, is ultimately related to the efficiency of such an antenna. It is our purpose in this paper to provide some physical insights into the radiation mechanism of a microstrip patch antenna by examining in detail the canonical problem of a TEM-wave incident obliquely from inside the region of a semi-infinite patch placed on the surface of a grounded dielectric slab. From an analogy of this type of antenna to that of a resonant rectangular waveguide cavity, condition for the resonance of a given mode is derived. Provided that the edge effect from all four edges can be separated, our method yields

explicitly design criteria for devising a low Q-antenna. In the process, some of the misconceptions regarding the role of surface-wave and sky-wave, the dynamic nature of the end-admittance, etc. also will be clarified.

2.0 ANOTHER LOOK ON THE RESONANCE OF A RECTANGULAR WAVEGUIDE CAVITY

Since the electromagnetic field associated with a microstrip patch antenna typically is concentrated in the region between the patch and the ground plane, it is not unreasonable to expect that such an antenna operating near its resonance is similar to a resonant rectangular waveguide cavity [1-3]. It is well-known that the resonant frequency of the $TE_{q,p,o}$ -mode in a cavity having a dimension of $2h \times 2\ell \times d$ (meters)³, and filled with a lossless dielectric material of permittivity ϵ_1 and permeability μ (Fig.1), is governed by the following equation [4].

$$\omega(\mu\epsilon_1)^{\frac{1}{2}} = \left[\left(\frac{2p-1}{2\ell} \pi \right)^2 + \left(\frac{2q-1}{2h} \pi \right)^2 \right]^{\frac{1}{2}} ; \quad p,q = 1,2,3,\dots \quad (1)$$

where $\omega = 2\pi f$ is the angular frequency of an even mode. (The modes of interest here are restricted to those having no variation in the z-direction). Equation (1) can be used to determine the resonant frequency of a q p th mode once h and ℓ are known, or alternatively, the aspect ratio h/ℓ , if both ω and ℓ are specified. However, it provides no clue as to how the resonance of a cavity can be effected if the boundary condition on one or more waveguide walls are somehow modified.

In order to examine the resonance phenomenon in more detail, we consider first the propagation of individual plane waves in such a cavity. Assuming for the moment a TE-wave of the form

$$E_z^{inc} = E_0 \exp\{-ik_0[\alpha x + (n^2 - \alpha^2)^{\frac{1}{2}}y]\} \exp(iwt) \quad (2)$$

where $k_0 = \omega(\mu\epsilon_0)^{\frac{1}{2}}$ is the free-space wave number and $n = (\epsilon_1/\epsilon_0)^{\frac{1}{2}}$ is the refractive index of the dielectric material, is incident onto the wall on the left in Fig. 1, i.e., $y = 0$; $0 < z < d$, at an angle $\phi = \sin^{-1}(\alpha/n)$ with respect to the y-axis, we can obtain without any difficulty, the form of the reflected wave as

$$E_z^r = E_0 r(\alpha) \exp\{-ik_0[\alpha x - (n^2 - \alpha^2)^{\frac{1}{2}}y]\}$$

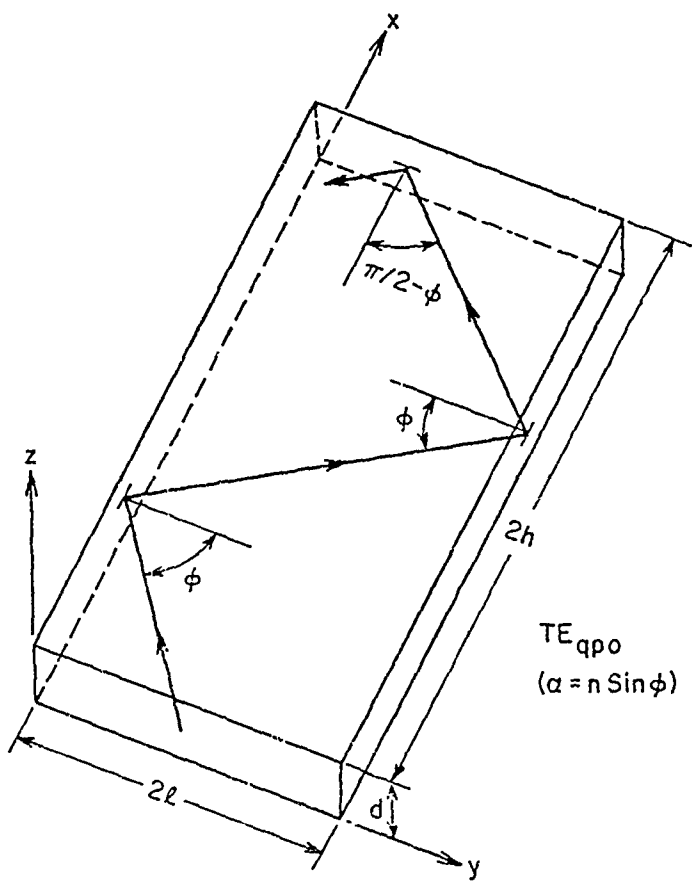


Fig. 1. Geometry of a rectangular waveguide cavity

where $\Gamma(\alpha) = |\Gamma| \exp(i\chi)$ is defined as the Fresnel reflection coefficient of a plane wave incidence. For a perfectly-conducting wall, $\Gamma(\alpha) = -1$ and $\chi(\alpha) = -\pi$, and for a more general case when the wall is lined with some constant impedance surface, the magnitude of Γ , i.e. $|\Gamma|$ is typically equal or less than unity. Thus, for a wave zig-zagging between the two side walls at $y = 0$ and $y = 2\ell$, a constructive interference can occur only if the total phase change after a complete bounce equals to integer multiple of 4π for an even distribution,

$$2k_0\ell(n^2-\alpha^2)^{\frac{1}{2}} - \chi(\alpha) = 2p\pi ; \quad p = 1, 2, \dots . \quad (3)$$

A transverse resonance is said to have been achieved when this condition is met. Alternatively, we can write with a superscript y

$$k_0\ell = j_p^{(y)}, \quad j_p^{(y)}(\alpha) = [2p\pi + \chi^{(y)}(\alpha)]/2(n^2-\alpha^2)^{\frac{1}{2}}; \quad p = 1, 2, \dots \quad (4)$$

Again, $\chi^{(y)} = -\pi$ for a perfectly-conducting wall. Obviously, the same situation exists in the x -direction, with the only exception that the incident angle is now $\pi/2-\phi$ instead of ϕ . Thus, by replacing α with $(n^2-\alpha^2)^{\frac{1}{2}}$, we obtain the transverse resonance in the x -direction as

$$k_0h = j_q^{(x)}, \quad j_q^{(x)}(\alpha) = [2q\pi + \chi^{(x)}(\alpha)]/2\alpha; \quad q = 1, 2, \dots \quad (5)$$

Elimination of α from (4) and (5) yields immediately the governing equation in (1) for a perfectly-conducting cavity where $\chi^{(x)} = \chi^{(y)} = -\pi$. However, it is not possible to achieve this if either $\chi^{(x)}$ or $\chi^{(y)}$ is a function of the incident angle ϕ and hence, α . Instead, we have to resort to graphical methods in that event. As an example, Fig. 2 shows the function $j_p^{(x)}(\alpha)$; $p = 1, 2$ for the case of a lossless waveguide cavity filled with a dielectric material $\epsilon_r = 4\epsilon_0$, as α varies from 0 to 2.

We can now use Fig. 2 to demonstrate how one can determine the acceptable aspect ratios of a cavity, once the desirable resonant frequency is specified. For instance, if our interest is to find the value of h/ℓ for a resonant TE₂₁₀-mode when $k_0\ell$ is chosen to be 1.5, we first determine from the $p=1$ curve that the value of α has to be $\alpha_y = 1.69$ in order to achieve a transverse resonance in the y -direction. The resultant wave then zig-zags

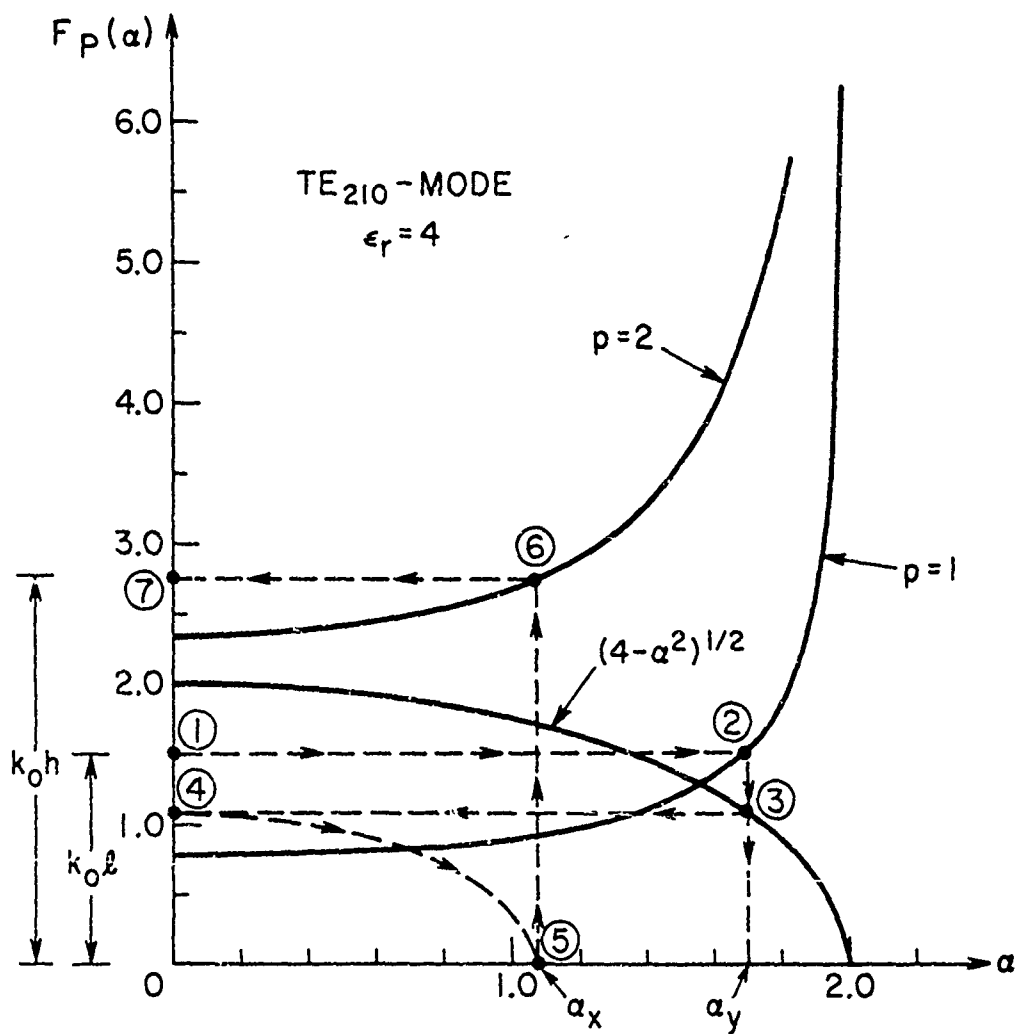


Fig. 2. Characteristic function $F_p(\alpha)$ for a rectangular waveguide cavity, $\epsilon_r = 4$.

between the two walls $y = 0$ and 2ℓ at an angle $\phi = \sin^{-1}(\alpha_y/n) \approx 58^\circ$ with respect to the y -axis, until it hits the wall at $x = 0$ or $x = h$. The angle of incidence at these two walls is 32° , which in turn yields an α value of $\alpha_x = (n^2 - \alpha_y^2)^{\frac{1}{2}} = 1.07$ as plotted in the same graph. For this value, we then determine from the $p=2$ curve that $\mathcal{F}_2(\alpha_x)$ and hence, $k_0 h$ has to be 2.77 in order to achieve a transverse resonance in the x -direction. Consequently, the aspect ratio is given by $h/\ell = 1.85$. Computational procedure for yielding this result is labeled in sequence from (1) to (7) in Fig. 2, and indeed checks with the one obtained directly from (1).

At this point, one may ask what is to be gained from this seemingly more complicated procedure. Clearly, the graphical method can be easily generalized to the case when one or more waveguide walls are lined with a different impedance surface, since the expression for $\chi(\alpha)$ is known explicitly. More important however, is the fact that the two angles of incidence (i.e. α_x and α_y) for waves impinging onto the cavity walls are now built into the solution process. If, for instance, we know certain incidence angles have to be avoided in order to minimize absorption, we can simply block out the undesirable regions in the diagram in searching for the appropriate aspect ratios.

3. RECTANGULAR MICROSTRIP PATCH ANTENNA

As shown in Fig. 3, the structure of a microstrip patch is equivalent to that of a rectangular waveguide cavity, with all the four sides opened up and the dielectric slab together with the bottom plate extended out. Since the dimensions of the patch are typically larger than the slab thickness, the field is mainly confined to the region under the patch. This allows us to view the structure as an open resonator and to determine its resonant condition by considering the bouncing of the waves in the region under the patch. Following the discussion in the previous section, we can immediately conclude that the same computational procedure would apply, provided of course a new reflection coefficient $\Gamma = |\Gamma| \exp(i\chi)$ is derived and used in conjunction with the characteristic equations (4) and (5). We must realize however, because the exterior region consists of a grounded dielectric slab capable of supporting surface-wave mode(s), appropriate physical mechanisms

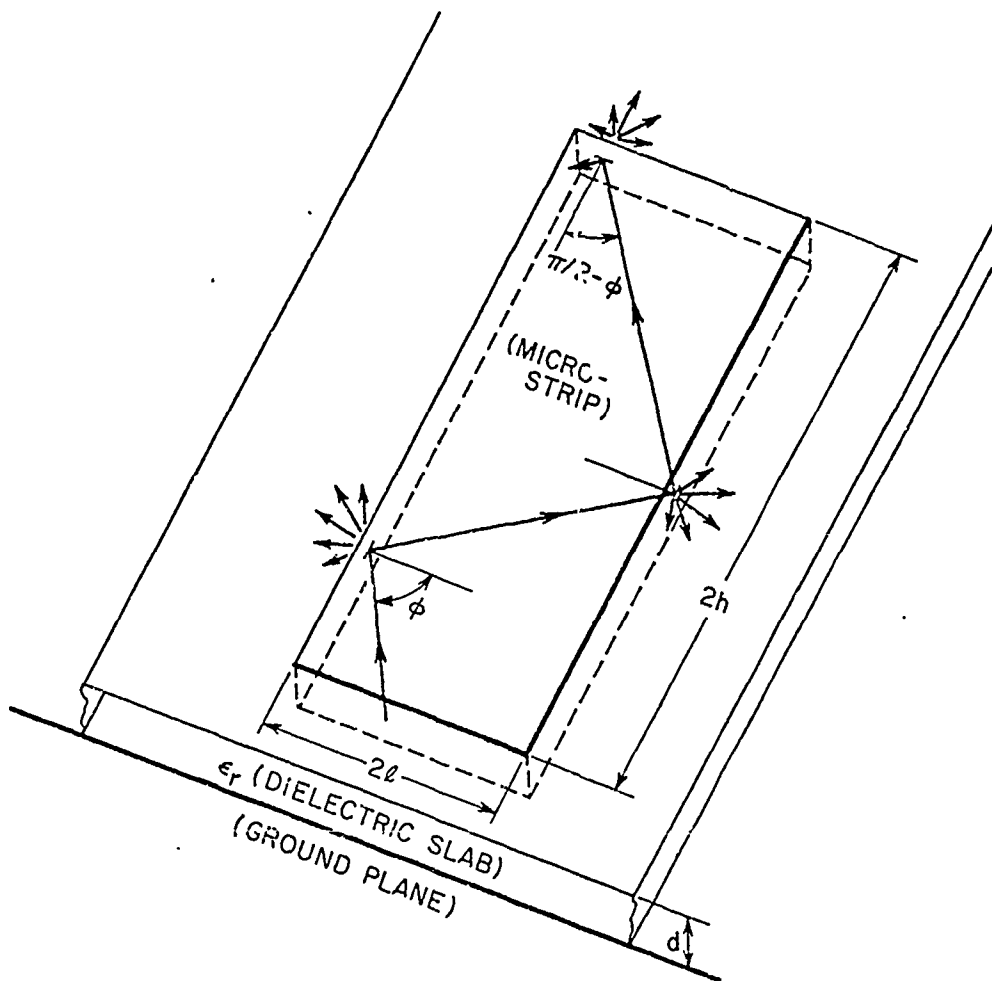


Fig. 3. Geometry of a rectangular microstrip patch

must be built into the solution of $\Gamma(\alpha)$. Thus, before we proceed any further in discussing the resonant condition, we should investigate first the canonical problem of wave propagation in a semi-infinite, perfectly-conducting patch. For the discussion to be followed, we should assume a TEM wave of the same form as (2) is incident obliquely in the parallel-plate region between the patch and the ground plane at an angle $\phi = \sin^{-1}(\alpha/n)$ with respect to the y-axis. This field is then partially reflected from the edge of the patch and partially radiated into the open region external to the patch. As we mentioned before, a grounded dielectric slab in the absence of the conducting patch can support a finite number of surface-waves, the exact number of which depends upon the so-called "numerical aperture" defined as $V = (\mu_r \epsilon_r - 1)^{\frac{1}{2}} k_0 d$ of the structure. Among these, the LSE₁-mode with the electric field polarized in the z-direction actually has no cut-off. This, in addition to the radiation field, one would at least expect the excitation of this wave as a direct result of the TEM-wave incidence. However, unlike a two-dimensional problem where one assumes no variation in the x-direction, both the surface-wave and the radiation field in the open region can propagate in one direction, while exponentially decay in another direction. For instance, since the total solution has to have the same variation of $\exp(-ik_0 \alpha x)$ along the x-direction as the incident wave, the far-field observed at a fixed elevation angle θ in any cross-section has to behave like $f(\theta) \exp(ik_0 [1 - \alpha^2]^{\frac{1}{2}} r)$ in air where r is the radial distance from the parallel-strip waveguide opening. Depending upon the incident wave, the quality $\alpha = n \sin \phi$ can vary from 0 to n . Therefore, for $\alpha < 1$, the "scattered" field indeed propagates radially away from the waveguide opening (Fig. 4a), but for $1 < \alpha < n$, the scattered field decays exponentially instead (Fig. 4b). In a very similar fashion, the field components associated with a surface-wave of wave number α_p must behave like $\exp[-k_0 (\alpha_p^2 - 1) z] \exp\{-ik_0 [\alpha x - (\alpha_p^2 - \alpha^2)^{\frac{1}{2}} y]\}$ in air. Thus, for $\alpha_p < \alpha < n$, an exponential decay of field in both y and z direction, is again observed. We note that the value of α_p is determined from

$$\epsilon_r (\alpha_{p,e}^2 - 1)^{\frac{1}{2}} = (n^2 - \alpha_{p,e}^2)^{\frac{1}{2}} \tan[(n^2 - \alpha_{p,e}^2)^{\frac{1}{2}} k_0 d] \quad (6)$$

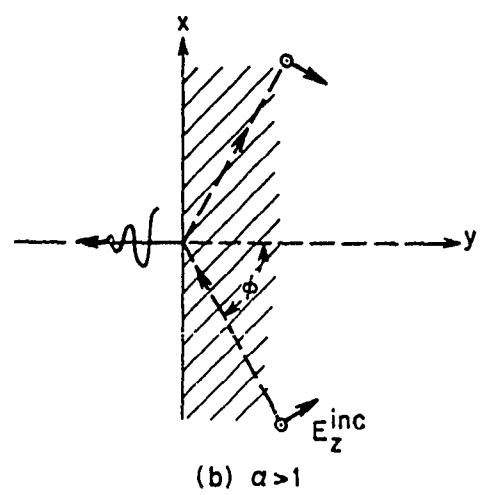
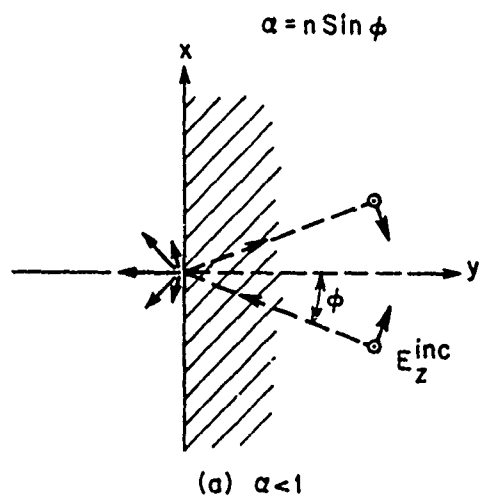


Fig. 4. Transmission and reflection of a TEM-wave obliquely incident onto the edge of a semi-infinite patch.

for LSE surface-waves, and from

$$\mu_r(\alpha_{p,m}^2 - 1)^{\frac{1}{2}} = (n^2 - \alpha_{p,m}^2)^{\frac{1}{2}} \cot[(n^2 - \alpha_{p,m}^2)^{\frac{1}{2}} k_0 d] \quad (7)$$

for LSM surface-waves (if they exist).

The above discussion points to a very important feature, unique to the study of oblique incidence. That is, whether the opening at the end, i.e. $y = 0$, will actually allow the TEM-wave in the parallel plate region to radiate into the open-space or not depends upon the angle of the incident wave. A complete reflection of the wave is therefore entirely possible, if the angle of incidence $\phi = \sin^{-1}(\alpha/n)$ is greater than some critical angle $\phi_c = \sin^{-1}(\alpha_{p,max}/n)$ where $\alpha_{p,max}$ is obtained from the surface-wave mode having the largest value of α_p . Such a phenomenon is certainly not unlike a plane-wave incident obliquely from a lossless medium having a large refractive index to a medium with a smaller refractive index. Beyond critical angle, reflection coefficient has magnitude of unity.

Based upon these observations, an analytical theory involving the use of the Wiener Hopf technique as applied to two coupled integral equations for charge and longitudinal distributions on the patch, is developed in a companion paper. We found that the reflection coefficient is given as [5]

$$\begin{aligned} R(k_0; \alpha) &= |R| e^{i\chi} \\ &= \exp[i[2 \tan^{-1}\left(\frac{\alpha}{[n^2 - \alpha^2]^{\frac{1}{2}}} ; \tanh \Delta\right) - \tan^{-1}\left(\frac{n^2 - 2}{\alpha^2 - 1}\right)^{\frac{1}{2}} + \psi]] \end{aligned} \quad (8)$$

where the functions Δ and ψ are two infinite integrals

$$\Delta(k_0; \alpha) = \frac{2}{\pi} \int_0^\infty \ln \left[\frac{u_0 n^2}{u_n} \left(\frac{u_n + \mu u_0 \tanh u_n k_0 d}{n^2 u_0 + u_n \tanh u_n k_0 d} \right) \right] \frac{d\lambda}{\lambda^2 + \alpha^2} \quad (9)$$

$$\psi(k_0; \alpha) = \frac{2}{\pi} (n^2 - \alpha^2)^{\frac{1}{2}} \int_0^\infty \ln \left[\frac{(1+n^2) u_0^2 \tanh u_n k_0 d}{u_n (n^2 u_0 + u_n \tanh u_n k_0 d)} \right] \frac{d\lambda}{\lambda^2 - (n^2 - \alpha^2)^{\frac{1}{2}}} \quad (10)$$

and $u_0 = (\lambda^2 + \alpha^2 - 1)^{\frac{1}{2}}$, $u_n = (\lambda^2 + \alpha^2 - n^2)^{\frac{1}{2}}$ with the argument of u_0 defined by $\operatorname{Re} u_0 \geq 0$. It is not difficult to show that in the complex λ -plane, the two integrands possess branch cuts of logarithmic nature at $\lambda = \pm i(\alpha^2 - 1)^{\frac{1}{2}}$, and at $\lambda = \pm \lambda_e$ and λ_m where $\lambda_{e,m} = i(\alpha^2 - \alpha_{pe}^2)^{\frac{1}{2}}$ and α_{pe} , α_{pm} are the solutions of (6) and (7) representing the LSE and LSM surface wave modes. Now since the value of α varies according to the incident angle of the TEM wave, location of these singularities and hence, the value of the two integrals can change accordingly. Assuming the thickness of the slab is such that only the LSE₁-mode can propagate, we can consider three possible ranges of incident angle: (i) $1 < \alpha_p < \alpha < n$, (ii) $1 < \alpha < \alpha_p < n$; (iii) $\alpha < 1 < \alpha_p < n$. In the first case, u_0 is real and the integrand is not only real, but smoothly varying (except near $\lambda = \sqrt{n^2 - \alpha^2}$) along the path of integration. Hence, the value of Δ , ψ and consequently, $x(\alpha)$ are all real. The magnitude of Γ is therefore unity, and the incident power is completely reflected back. As we mentioned before, this situation is very similar to a plane-wave incident onto a dielectric interface beyond the critical angle. As in the case of a dielectric waveguide, the phenomenon certainly can be utilized to guide an electromagnetic wave along x -direction when the semi-infinite patch is truncated and a transverse resonance is imposed. On the other hand, for the case (ii) when $1 < \alpha < \alpha_p$, the branch point $\lambda = \lambda_e$ will appear on the positive real axis. The integration from $\lambda = 0$ to λ_e is now complex, as the logarithmic function in the integrands is real and negative. The magnitude of Γ is also less than unity, as part of the power is now used to excite the surface wave.

A similar situation also exists in case (iii) where $\alpha < 1 < \alpha_p$, because the logarithmic singularity associated with u_0 also appears on the real axis. The magnitude of Γ would have to be even smaller, since power can now radiate into the open region in the form of "sky-waves."

From the form of Γ , one can also define the apparent end-admittance of such a structure as

$$Y_a(\alpha) = Y_0 \frac{1-\Gamma}{1+\Gamma} = -iY_0 \tan[x(\alpha)/2] \quad (11)$$

where $Y_0 = (n_1 d)^{-1}$ ohm/m is the characteristic admittance of the TEM-wave in a parallel-plate waveguide. It suffices to note that this admittance is a function of both frequency and angle of incidence, and it is usually not valid to replace it by the value corresponding to the normal incidence.

To further investigate the property of $\Gamma(k_0; \alpha)$ as a function of incident angle, we have included in Fig. 5 the plot of $1 - |\Gamma|^2$ which represents the portion of power radiated into the open region in the form of both sky-waves and surface waves, and the phase of the reflected wave, i.e. $\chi(k_0; \alpha)$ for a dielectric slab of relative permittivity $\epsilon_r = n^2 = 10$ and thickness $d = 1.27$ mm. The frequency of operation is chosen as 8 ghz. As expected, the amount of radiated power reduced to zero when $\alpha > \alpha_p$ which for the present example, has a value of 1.02. The maximum amount of radiated power is about 16% and occurs when the wave is incident normally in the parallel-plate region between the patch and the ground plane. The phase of $\Gamma(k_0; \alpha)$ on the other hand, increases monotonically from a negative value at $\alpha = 0$, to zero at $\alpha = 2.16$, and then to a positive value beyond $\alpha = 2.16$. The rate of increase is more rapid as α increases, i.e., the incidence wave becomes more grazing.

For a microstrip of finite width, the information we obtained from Fig. 5 can now be used in determining the propagation constant of a guided mode along the microstrip structure. As we mentioned earlier, assuming the two edges of the strip can be reasonably separated, a wave can zig-zag along the strip with a propagation constant α along the x-direction, provided a transverse resonance can be established. For the fundamental mode $p = 0$, the requirement is obtained from (3) as

$$k_0 \ell (n^2 - \alpha^2)^{\frac{1}{2}} = \chi(k_0; \alpha) .$$

Now since $\chi(k_0; \alpha)$ in the present example is negative for $\alpha < 2.16$, the propagation constant of the fundamental mode, $p = 0$, has to be greater than 2.16 for any length of $k_0 \ell$. This is actually not surprising, as we know from the theory of a thin-wire, the value of α should approach $[(n^2 + 1)/2]^{\frac{1}{2}}$ ≈ 2.35 as $k_0 \ell \rightarrow 0$ [6]. (Note that the present theory also breaks down

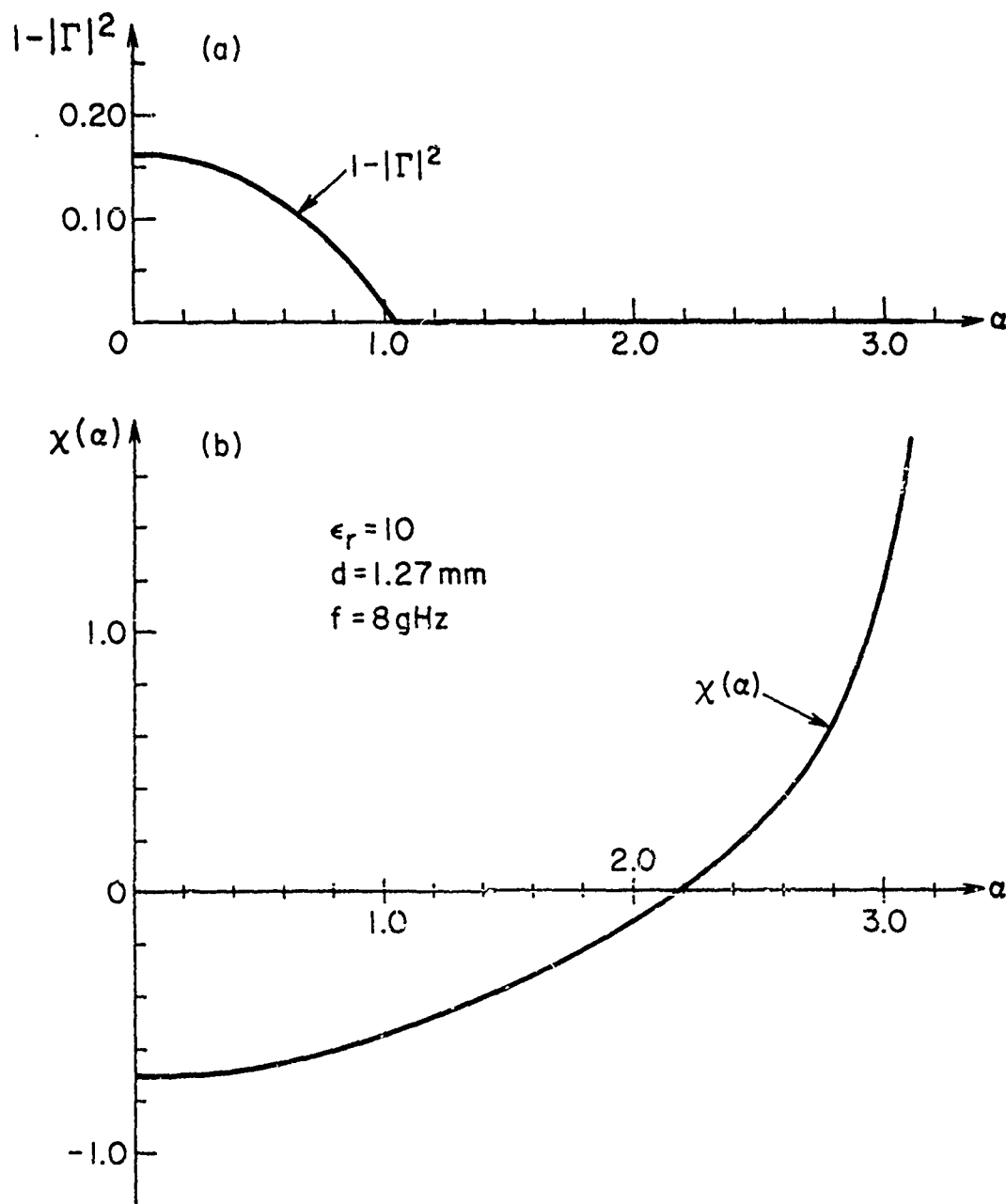


Fig. 5. Amplitude and phase of the reflected wave inside a semi infinite patch, $\epsilon_r = 10$, $d = 1.27 \text{ mm}$ and $f = 8 \text{ GHz}$.

when $(k_0 l)^2 \ll 1$ because the two edges of such a strip can no longer be separated). More important however, is the fact that it is possible to propagate a $p=0$ guided mode along the structure, even when the width of the strip is much smaller than a free-space wavelength. In this sense, the fundamental mode of a microstrip structure acts more like a parallel plate transmission line, rather than a rectangular waveguide which cannot support any $p=0$ mode.

4.0 RESONANT MICROSTRIP PATCH: DESIGN CONSIDERATION

We are now finally in the position to discuss some of the design considerations of a resonant microstrip patch. As in the case of a rectangular waveguide cavity, the aspect ratio of a patch for achieving a qp^{th} resonance at a given frequency can be obtained graphically from the characteristic equation

$$\beta_p(\alpha) = \frac{2p\pi + \chi(\alpha)}{2(n^2 - \alpha^2)^{\frac{1}{2}}} ; \quad p = 0, 1, 2, \dots \quad (4)$$

in the y -direction, and its counterpart, $\tilde{\beta}_q(\sqrt{n^2 - \alpha^2})$ in the x -direction. In Fig. 6, the function β_0 and $\tilde{\beta}_1$ are plotted against α , for a dielectric slab of permittivity $\epsilon_1 = 10 \epsilon_0$ and thickness $d = 1.27 \text{ mm}$ operating at 8 GHz. We note that since the smallest possible α for a guiding mode is $[(n^2+1)/2]^{\frac{1}{2}}$ and since it is not possible to have both α and $(n^2 - \alpha^2)^{\frac{1}{2}}$ to be greater than this value, we can immediately discount the possibility of having a resonant mode where $p=q=0$. For $p=1$ and $q=0$ mode, the procedure is identical to the one we discussed earlier in conjunction with the TE_{210} -mode of a resonant waveguide cavity. Following the sequence of steps from (1) to (7) as demonstrated in Fig. 6, we conclude that for $k_0 l = 2.26$, the corresponding electric length in the x -direction has to be $k_0 h = 1.8$, or an aspect ratio of $h/l \approx 0.8$. Notice that the corresponding angle of incidence is respectively, $\alpha_x = 0.6$ and $\alpha_y = 3.1$. In Fig. 7, the values of $k_0 l$ vs. the corresponding values of $k_0 h$ are shown for the fundamental mode ($p=1, q=0$). We note that, even though $k_0 l$ can vary over a very wide range, the corresponding range of $k_0 h$ is much smaller and in any case cannot be less than 1.73.

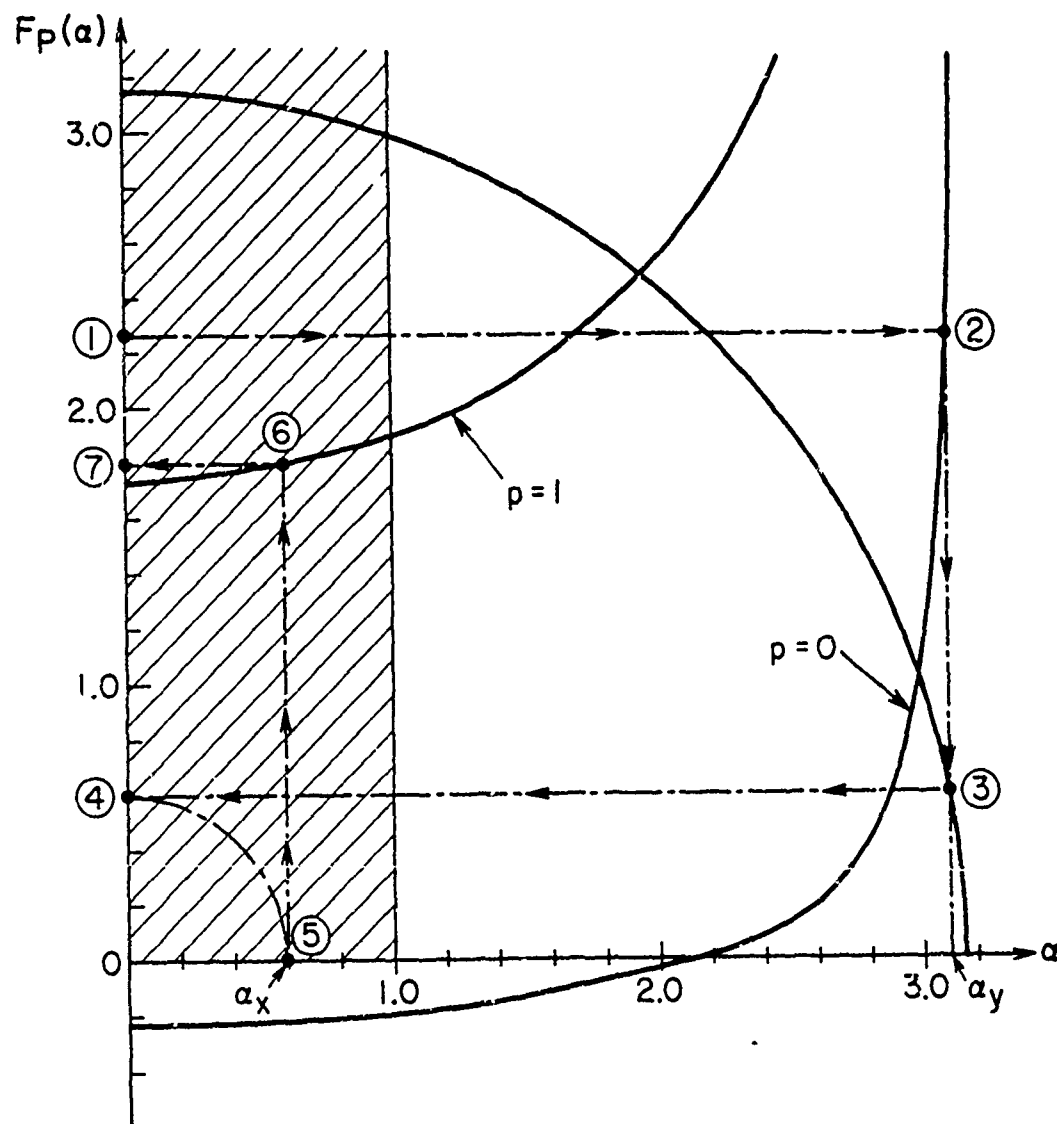


Fig. 6. Characteristic function $F_p(\alpha)$ for a microstrip patch
 $\epsilon_r = 10$, $d = 1.27$ mm and $f = 8$ GHz.

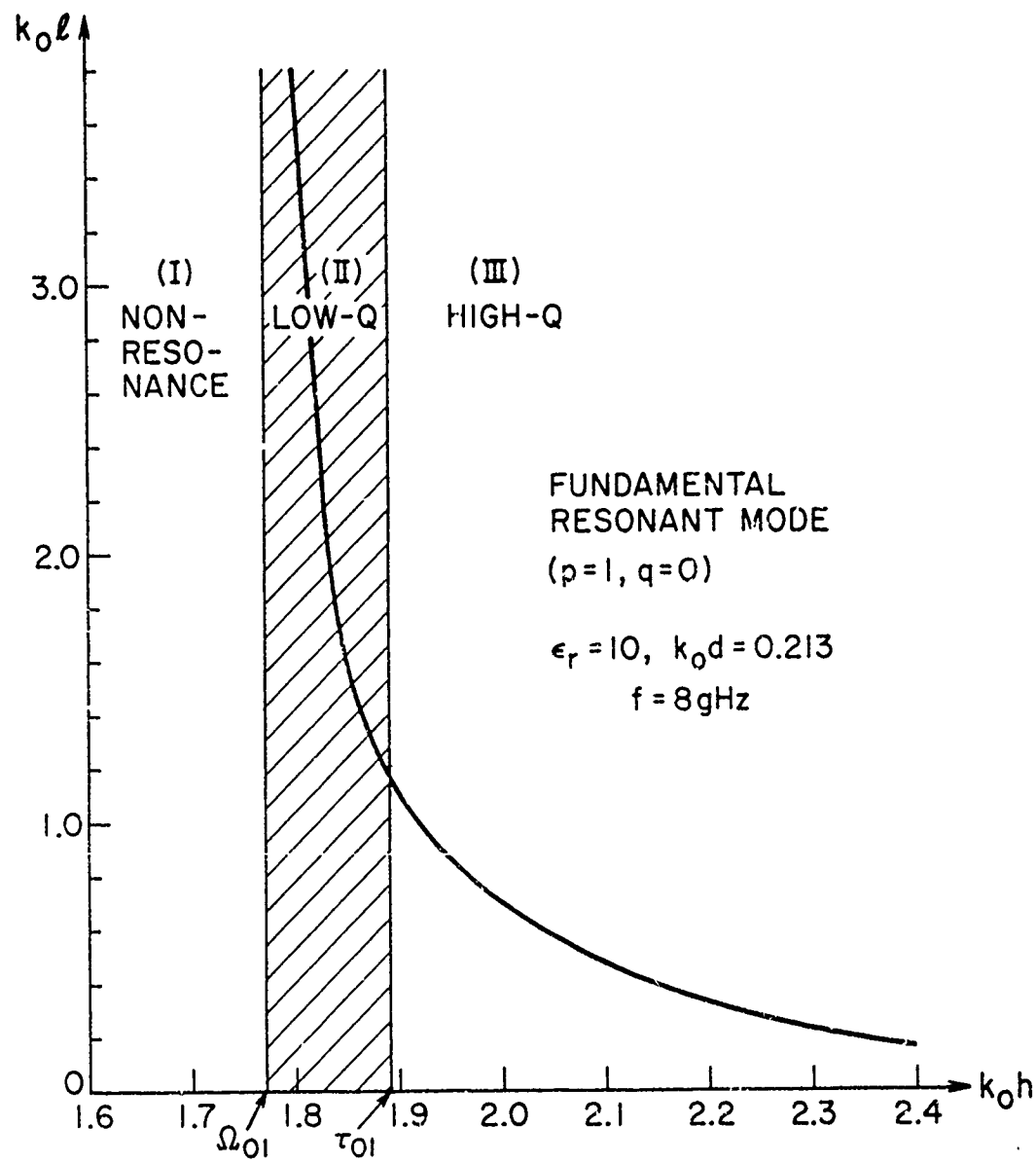


Fig. 7. Acceptable aspect ratio for the fundamental resonance of a rectangular microstrip patch antenna

We may now return to the question of whether we can enhance the radiation of a resonant microstrip path by adjusting its aspect ratio. Recalling from Fig. 5 that radiation of energy occurs only when α is less than $\alpha_p \approx 1.02$, it is apparent in the present example that energy will be radiated from the two edges at $x = 0$ and $x = 2h$, but not at the other two in the y -direction. Thus according to our earlier observation that more energy can be radiated by decreasing the angle of incidence, we would increase the width ℓ at the same time, decrease the length h , although the degree of improvement becomes somewhat marginal as we keep continuing this process. On the other hand, if we decrease $k_0 \ell$ instead of increasing it, we find from Fig. 6 that both the value of α_x and α_y become quickly greater than α_p , and no radiation would occur within the stated limit of the present theory. The microstrip patch in this case acts more like a high Q resonator than a low Q antenna.

5.0 REFERENCES

1. Munson, R.E., "Corner fed microstrip antennas and microstrip phase arrays," IEEE Trans. Ant. & Prop., 74-78, Jan. 1974.
2. Denneryd, A.G., "Linearly polarized microstrip antennas," IEEE Trans. Ant. & Prop., 846-851, Nov. 1974.
3. Carver, K.R., "A modal expansion theory for the microstrip antenna," Proc. Internat. Symp. Ant. & Prop., Seattle, Wash. 101-104, June 1979.
4. Harrington, R.F., Time Harmonic Electromagnetic Fields, Ch. 4, 155-157, McGraw Hill, New York, 1961.
5. Chang, D.C. and E.F. Kuester, "Total and partial reflection from the end of a parallel-plate waveguide with an extended dielectric loading," Scientific Rept. No. 50 Electromagnetics Laboratory, University of Colorado, Sept. 1979.
6. Coleman, B.L., "Propagation of electromagnetic disturbances along a thin-wire in a horizontally stratified medium," Phil. Mag. ser. 7, 41, 276-288, 1950.

ACKNOWLEDGMENT

The authors wish to thank Professor L. Lewin for many useful discussions and suggestions and to Mr. Robert Johnk who diligently read the manuscript and provided the numerical data. The work is supported by National Science Foundation under Grant No. 7809029.

PRINTED WIRE ANTENNAS

I. E. RANA AND N. G. ALEXOPOULOS
ELECTRICAL SCIENCES AND ENGINEERING DEPARTMENT
UNIVERSITY OF CALIFORNIA, LOS ANGELES, CALIFORNIA 90024

SUMMARY

In this paper, the theory of wire antennas, such as dipoles printed on a grounded dielectric substrate, is presented. A Green's function approach has been employed which involves improper Sommerfeld integrals. By considering Pocklington's integral equation with proper choice of expansion and testing functions, the solution for the current distribution and input impedance is obtained, with resulting proper but slowly convergent integrals. The integrals are evaluated by a real axis integration technique which involves analytical and numerical steps.

As an example, the printed wire antenna is analyzed. Numerical results illustrating the effect of substrate thickness and dielectric constant on the current distribution and input impedance are presented herein.

An array of printed wire dipoles is also considered. The pertinent array parameters, such as current distribution, input impedance and mutual impedance are computed. An extensive discussion on the surface waves generation and their role in determining mutual impedance characteristic is undertaken and it has been shown that in collinear configuration mutual coupling is dominantly due to surface waves. Computations for mutual impedance between dipoles in broadside, collinear and echelon arrangements are presented. These results could be used in designing printed dipole arrays.

2.1 GREEN'S FUNCTION

A horizontal Hertzian dipole as shown in Fig. 1, is held at point (x' , y' , z') over a grounded dielectric substrate of thickness B . The substrate

has relative permittivity ϵ_r which may be complex to account for loss. Assuming $e^{-j\omega t}$ time dependence Maxwell's equations can be solved by employing Hertz potentials [1]. After a series of standard manipulations the pertinent components of the Hertz potentials are

$$\pi_x = 2u \int_0^\infty \frac{J_o(\lambda\rho)}{D_e(\lambda)} \cdot e^{-\mu(z+z')} \cdot e^{2\mu B} d\lambda, \quad z > B \quad (1)$$

$$\pi_z = -2(n^2 - 1)u \int_0^\infty \frac{J_1(\lambda\rho) \cdot \cos\phi}{D_e(\lambda) \cdot D_m(\lambda)} \cdot e^{-\mu(z+z')} \cdot e^{2\mu B} \lambda^2 d\lambda, \quad z > B \quad (2)$$

$$\pi_{xe} = \frac{2u}{n^2} \int_0^\infty \frac{J_o(\lambda\rho)}{D_e(\lambda)} \cdot e^{-\mu(z' - B)} \cdot \frac{\sinh\mu_e z}{\sinh\mu_e B} \cdot \lambda d\lambda, \quad 0 < z < B \quad (3)$$

$$\pi_{ze} = -2u \frac{(n^2 - 1)}{n^2} \int_0^\infty \frac{J_1(\lambda\rho) \cdot \cos\phi}{D_e(\lambda) \cdot D_m(\lambda)} \cdot e^{-\mu(z' - B)} \cdot \frac{\cosh\mu_e z}{\cosh\mu_e B} \lambda^2 d\lambda$$

$$0 < z < B \quad (4)$$

where

$$D_e(\lambda) = \mu + \mu_e \coth\mu_e B \quad (5)$$

and

$$D_m(\lambda) = \mu n^2 + \mu_e \operatorname{Tanh}\mu_e B \quad (6)$$

In addition, $\mu = \sqrt{\lambda^2 - k^2}$, $\mu_e = \sqrt{\lambda^2 - \epsilon_r k^2}$, $n^2 = \epsilon_r$, $u = \frac{1}{j\omega 4\pi \epsilon_0}$
and $\rho = \left[(x - x')^2 + (y - y')^2 \right]^{1/2}$

2.2 CURRENT DISTRIBUTION OVER THE PRINTED WIRE ANTENNA

A thin wire dipole of length L and diameter 2a, printed on a grounded substrate, is shown in Fig. 2. It is assumed that the radius of the wire is very small as compared to the free space wavelength ($a < \lambda_0$),

and therefore the thin wire approximation can be used. The current on the wire does not have circumferential symmetry, due to the presence of the grounded substrate. Then antenna current may have circumferential component in addition to the axial component, yet for a thin wire only the axial component is of significance. As shown by Tulyathan and Newman [2], only the axial component is dominant in the determination of the radiation and impedance characteristics. It follows that the thin wire approximation which computes mainly the axial current component is a valid approximation.

The axial component of electric field at any point (x, y, z) due to a source of lineal current density $\tilde{J}(x', y', z')$ is given by, i.e.,

$$E_x(x', y', z') = \int_V J(r') \hat{x} \cdot [k^2 + \nabla \cdot \nabla] \hat{\pi}_x \cdot \hat{x} dv'. \quad (7)$$

For a printed wire dipole, the current density $J(x', y', z')\hat{x}$ can be expressed as,

$$J(x', y', z') = I(x') \cdot \delta(y') \cdot \delta(z' - B), \quad (8)$$

where $I(x')$ is the net dipole current at any point x' on the wire.

Substituting the above equation in (7) and simplifying, one obtains the axial component of electric field, $E_x(x, y, z)$, due to the wire current $I(x')$, as,

$$E_x(x', y, z) = \int_L I(x') \left[k^2 \pi_x + \frac{\partial^2 \pi_x}{\partial x^2} + \frac{\partial^2 \pi_z}{\partial z \partial x} \right] dx', \quad (9)$$

where

$$\pi_x = 2u \int_0^\infty J_0(\lambda\rho) e^{-\mu(z-B)} \frac{\lambda d\lambda}{D_e(\lambda)}, \quad (10)$$

and

$$\pi_z = -2(n^2 - 1)u \int_0^\infty J_1(\lambda\rho) \cos\phi \cdot e^{-\mu(z - B)} \frac{\lambda^2 d\lambda}{D_e(\lambda)D_m(\lambda)} \quad (11)$$

with

$$\rho = \sqrt{(x - x')^2 + y^2}.$$

Equation (9) is known as Pocklington's Equation in which the unknown antenna current $I(x')$ is under the integral sign. The wire antenna is unloaded at the ends, hence the antenna current $I(x')$ must satisfy the following boundary conditions,

$$I(0) = I(L) = 0. \quad (12)$$

In order to solve (9) for the antenna current $I(x')$, Moment methods [3] are used. Accordingly, the wire is divided into N equal segments. As it is usual in the Moment's method, the proper choice of current expansion functions must be made. The sinusoidal expansion functions offer many advantages and have been used by many authors [3], [4]. The advantages are: (1) the current boundary conditions as given by (12) are automatically satisfied, (2) a closed form expression for the fields is obtained, and (3) the impropriety in the Green's function integrals is removed as $z \rightarrow B$. The form of the i th expansion function centered about x_i is simply,

$$I(x') = \begin{cases} \frac{\sin k(d - |x' - x_i|)}{\sin k d} & |x' - x_i| \leq d \\ 0 & \text{otherwise} \end{cases} \quad (13)$$

where d is the length of each wire segment given by

$$d = L/N.$$

Substituting the N-1 term current expansion series into (9), and by making use of $\frac{\partial}{\partial x} = - \frac{\partial}{\partial x'}$, it can be shown that the x component of the electric field E_x is given at any point (x, y, B) on the substrate,

$$E_x(x, y, B) = \frac{k}{\sin kd} \sum_{i=1}^{N-1} I_i \left[\pi_x|_{x_{j-1}} + \pi_x|_{x_{j+1}} - 2 \cos kd \cdot \pi_x|_{x_i} + \right.$$

$$2 \cos kd \cdot \pi|_{x_i} - \pi|_{x_{i+1}} - \pi|_{x_{i-1}} + k \left[\int_{x_{i-1}}^{x_i} \sin[x' - (x' - x_{i-1})] \cdot \pi dx' + \right]$$

$$\left. \int_{x_i}^{x_{i+1}} \sin(k(x_{i+1} - x') - \pi dx' \right] \quad (14)$$

where

$$\pi_x = 2u \int_0^\infty J_0(\lambda\rho) \cdot e^{-\mu[z - B]} \frac{\lambda d\lambda}{D_e(\lambda)} \quad (15)$$

$\lim z \rightarrow B$

$$I_z = \int_{x_{j-1}}^{x_j} \sin(k(x - x_{j-1})) \cdot \left[\int_{x_{i-1}}^{x_i} \sin(x' - x_{i-1}) \cdot \pi dx' + \right.$$

$$\left. \int_{x_i}^{x_{j+1}} \sin(x_{i+1} - x') \pi dx' \right] + \int_{x_j}^{x_{j+1}} \sin(x_{j+1} - x) \cdot$$

$$\left[\int_{x_{i-1}}^{x_i} \sin(x' - x_{i-1}) \cdot \pi dx' + \int_{x_i}^{x_{i+1}} \sin(x_{i+1} - x') \cdot \pi dx' \right], \quad (16)$$

where π_x and π_z are the integrals defined by (15) and (16).

The double integration w.r.t. x and x' is performed very efficiently by a numerical technique which makes use of the overlapping nature of the Green's function and removes redundancy in the calculation of the integrand. The integrals (15) and (16) are Sommerfeld type integrals and they are improper as $z = z' = B$. As such they require a very careful and specialized treatment [5], [6].

2.3 INPUT IMPEDANCE

In Section 2.2, the problem for the current distribution of the printed dipole is formulated. The solution described uses sinusoidal sub-sectional currents and Galerkin's method which is also equivalent to the reaction concept [7]. The dipole is excited by an idealized source, the delta gap model. In actual practice, the excitation is different from the assumed model. In air, it has been found that the input impedance is not critically dependent upon the excitation gap length, as long as the gap length is $< 0.1\lambda_0$. Similarly, neglecting the effect of the incoming exciting line, the input impedance for a small gap between the input terminals will be as seen by the delta gap generator.

In the computation of current distribution, the circumferential variation of the antenna current was neglected. This is due to the fact that whatever device is used to measure the input impedance, it is insensitive to the circumferential variation of the current, provided the wire is very thin. Thus the thin wire approximation is in fact, valid.

The input impedance of the printed dipole is given for a 1.0 volt input excitation by,

$$Z_{in} = 1.0/I_{in} \quad (17)$$

where I_{in} is the input current of the antenna obtained from the knowledge of its current distribution.

2.6 NUMERICAL RESULTS

In this section, numerical results are presented for the printed dipole. Numerical computations have been done for a very thin wire dipole, a typical radius $a = 0.0001\lambda_0$ has been chosen. The dipoles are center-fed

by an in-phase unit voltage delta gap generator. All dimensions presented are normalized with respect to the free space wavelength λ_0 .

The current distribution over a printed dipole of length $0.5 \lambda_0$, printed on a dielectric substrate of thickness $B = 0.1016 \lambda_0$ and dielectric constant $\epsilon_r = 3.25$ is shown in Fig. 3. The $\text{Re}[I]$ and $\text{Im}[I]$ are plotted separately. Due to the presence of the substrate, the electric length of the dipole increases and hence there is a dip in the current distribution curve at the feeding point. For comparison, the current distribution $\epsilon_r = 1.0$ (while the other parameters remain the same), is shown in Fig. 4. Physically this means that substrate has been removed. Due to the proximity of the ground plane, $\text{Im}[I]$ is greater than $\text{Re}[I]$. This shows that the dipole radiates less power in comparison to a dipole in free space. Comparing Fig. (3) and (4), it is obvious that the current level on the printed dipole is about ten times less than the dipole over a grounded plane.

To see the effect of the substrate thickness B , a computation has been carried out for increased substrate thickness; i.e., $B = 0.127\lambda_0$. The current distribution for this case is shown in Fig. 5. In comparing Fig. 5 with Fig. 3, it can be seen that the substrate thickness does not affect the shape of the distribution very much but that current levels are changed. This means that the input impedance of the dipole is changed. It should be noted that in all the above computations only one surface wave modes has been allowed.

The substrate thickness B and dielectric constant ϵ_r has been increased to $0.15 \lambda_0$ and 8.5, respectively, in order to allow two propagating surface wave modes. The current distribution is shown in Fig. 6. The following effects are in order:

- 1) The $\text{Re}[I]$ and $\text{Im}[I]$ both change sign.
- 2) The electrical length increases drastically.

It can be inferred from the above discussion that the impedance level of the printed dipole is higher than the dipole over grounded plane. This higher impedance level is attributed to the fact that the printed

dipole radiates power as space wave and launches a surface wave in the dielectric surface guide. However, this surface wave contributes only to the real part of the input impedance. The higher order nonpropagating modes contribute to the reactive part of the input impedance.

Figures (7) through (9) show the input impedance of the printed dipole versus its length 'L', for different dielectric thickness and dielectric constants. Comparison of the resonant ' L_r ' and the input impedance ' Z_{in} ' for all of the above-mentioned cases is given in Table I.

TABLE I

# of modes	ϵ_r	B	L_r	Z_{in} (resonant)	Z_{in} (for $L=0.5\lambda_0$)
1	3.25	$0.1016\lambda_0$	$0.317\lambda_0$	$34.5 + j0\Omega$	$330 - j880\Omega$
1	3.25	$0.1270\lambda_0$	$0.315\lambda_0$	$60.0 + j0\Omega$	$535 - j788\Omega$
2	8.5	$0.15\lambda_0$	$0.23\lambda_0$	$50 + j0\Omega$	$418 + j664\Omega$

The real part of the Z_{in} is the sum of two terms; namely, the radiation resistance and the surface wave launching resistance. By increasing the substrate thickness from $0.1016\lambda_0$ to $0.127\lambda_0$, the resonant impedance increases from 34.5Ω to 60.0Ω . This is due to the following reasons:

- 1) the surface wave launching efficiency increases, and
- 2) a little reduction in the proximity from the ground plane, increases the radiation efficiency.

The two propagating surface wave modes also effect the impedance characteristics of the printed dipole. The increased dielectric constant ($\epsilon_r = 8.5$) reduces the radiation resistance (efficiency) of the printed dipole. This is due to the fact that electric flux lines have greater affinity for the dielectric medium than for free space. Therefore, a major portion of the input power to the antenna is

guided as two surface wave modes, rather than being power that is radiated. A printed dipole in this case is not a good radiator, but it may be a good surface wave launcher.

3.1 CURRENT DISTRIBUTION OVER TWO PARALLEL PRINTED DIPOLES

In Fig. 10, two printed dipoles are shown at a distance 'S' apart. The dipoles are assumed to have lengths and radii (L_1, a) and (L_2, a). The radius 'a' is assumed very small compared to the free space wavelength λ_0 . Dipole #1 is excited while dipole #2 is short-circuited, and is acting as a parasitic. The current distribution over the pair can be represented as

$$\bar{J}(x', y') = [I_1(x')\delta(y') P_1 + I_2(x')\delta(y' - S) P_2]\delta(z - B)\hat{x} \quad (18)$$

where $I_1(x')$ and $I_2(x')$ are unknown currents, over dipole #1 and dipole #2, respectively. P_1 and P_2 are two unit pulse functions which are zero everywhere except over the lengths of the dipoles L_1 and L_2 . Substituting (18) in (7), the axial component of the electric field E_x at any point over the substrate is given by,

$$E_x = \int_{L_1, y'=0} I_1(x') \cdot \left[k^2 \pi_x + \frac{\partial^2 \pi}{\partial x^2} + \frac{\partial^2 \pi}{\partial x \partial z} \right] dx' + \int_{L_2, y'=s} I_2(x') \cdot \left[k^2 \pi_x + \frac{\partial^2 \pi}{\partial x^2} + \frac{\partial^2 \pi}{\partial x \partial z} \right] dx' \quad (19)$$

Repeating the steps illustrated in Section 2.2; i.e., by dividing the two dipoles in subsections N_1 and N_2 , and making use of the sinusoidal expansion function and Galerkin's method, the following matrix equation is obtained,

$$\begin{bmatrix} V_1 \\ V_2 \\ \vdots \\ V_{N_1 + N_2 - 2} \end{bmatrix} = \begin{bmatrix} Z_{11} & Z_{12} & \cdots & \cdots \\ Z_{21} & Z_{22} & \cdots & \cdots \\ \vdots & \vdots & \ddots & \vdots \\ \vdots & \vdots & \ddots & \vdots \end{bmatrix} \begin{bmatrix} I_1 \\ I_2 \\ \vdots \\ I_{N_1 + N_2 - 2} \end{bmatrix} \quad (20)$$

Depending upon the location of the generator, the corresponding excitation voltage is set to 1. The inversion of the matrix then gives the current distribution on the dipole-parasitic pair. This method can further be extended to any number of printed dipoles parasitic or active. However, the computer storage available does limit the number of elements which can be handled.

3.2 MUTUAL IMPEDANCE COMPUTATION

In Section 3.1, a method is illustrated to compute the current distribution over a pair of printed dipoles which are driven and parasitic. The knowledge of current distribution over the pair will be used in this section to determine the mutual impedance between the printed dipoles. The input impedance of the two dipole printed array is given by,

$$Z_{in} = Z_{11} + Z_{12} I_2 / I_1 \quad (21)$$

where Z_{11} is the self impedance of the driven dipole when the parasitic dipole is open-circuited. Also, Z_{12} is the mutual impedance between the pair, whereas I_1 and I_2 are the input currents which flow into the input terminal of the driven dipole and across the short-circuited input terminals of the parasitic dipole. For unit voltage excitation; i.e., $V_1 = 1.0$ volt, the input impedance of the array is given by,

$$Z_{in} = 1.0 / I_1 \quad . \quad (22)$$

The self impedance Z_{11} of the driven dipole is obtained numerically by deleting the $(N_1 + N_2/2 - 1)$ th row and column of the matrix equation (20) and inverting the resultant $(N_1 + N_2 - 3)$ th order matrix. Physically, this operation means open circuiting the parasitic dipole. The input current of the driven dipole I_1' gives the self impedance of the Z_{11} as

$$Z_{11} = 1.0 / I_1' \quad . \quad (23)$$

When (22) and (23) are inserted in (21) and manipulated, the mutual impedance between the two printed dipoles is given by,

$$Z_{12} = 1.0/I_2 - I_1/(I_1' \cdot I_2) . \quad (24)$$

3.3 NUMERICAL RESULTS

Mutual impedance computations between two printed dipoles have been performed in three configurations,

- 1) broadside, 2) Endfire and, 3) Echelon.

The lowest order surface wave mode has a launching pattern $\sim \cos\phi$. This means when two dipoles are in broadside configuration ($\phi = 90^\circ$), the part of the total coupling due to the surface wave will be minimum. The coupling in this configuration will mainly be due to direct, higher order and leaky waves excited by the antenna.

Figures (11) through (12) show broadside coupling between the two printed dipoles as a function of separation 'S' for different antenna lengths. The rapid fall in the beginning ($S < 0.4\lambda_0$) of the curve confirms that the coupling is mainly due to higher order modes, while for ($S > 0.8\lambda_0$) the direct field wave takes over. In the intermediate zone, leaky wave modes are dominant.

The printed dipole launches a surface wave with maximum efficiency along the axial direction ($\phi = 0$). Also, the radiation pattern of a dipole in free space has nulls along the axial direction ($\phi = 0$ and $\phi = 180$). Therefore, based on these arguments, it can be concluded that in the collinear configuration, the coupling will be mainly due to the surface wave. The surface wave decays as $\frac{1}{\sqrt{\rho}}$. Hence, mutual coupling should decay slowly in this configuration.

Figures 13 - 15 show mutual impedance for the collinear case plotted versus separation 'G', for different dipole lengths. The mutual coupling decays very slowly with 'G'. The period of oscillation of the mutual impedance as obtained from Fig. (13) is $0.88\lambda_0$, while the wavelength of the excited surface wave, as obtained from the computer program, is $0.8811\lambda_0$.

This agreement is excellent and confirms that the mutual coupling for the collinear configuration is due to the TM mode of the surface wave only. The initial behavior for small 'G' is due to the near zone field of the dipoles, as is clear in Fig. (15).

In the echelon configuration, mutual impedance computations versus displacement 'D' are shown in Figs. (16) through (8) for different dipole lengths. For $D = 0$, the dipoles are in broadside configuration, while for 'D' large, the dipoles are approximately collinear. As 'D' increases, Z_{12} decreases drastically from the broadside value and ultimately shows the same behavior as shown by the dipoles in collinearity.

The efficiency of the surface wave excitation depends upon the thickness of the substrate B (i.e., aperture size), for a given dielectric constant ϵ_r . To observe this effect, the substrate thickness is next increased from $0.1016\lambda_0$ to $0.127\lambda_0$, and computations for mutual impedance between the dipoles in collinear arrangement are performed. The results are shown in Figs. (19) and (20). The results shown in Figs. (19) and (20) are compared with the ones shown in Figs. (14) and (15). The comparison indicates that the surface wave efficiency increases with the thickness of the substrate.

Next, two propagating surface wave modes are allowed by increasing the substrate thickness to $0.15\lambda_0$ and the dielectric constant to 8.5. Computations for dipoles in broadside and collinear configuration are performed. The results for linear arrangement and for different dipole lengths are shown in Figs. (21) and (22). The following components are in order:

- 1) The period of oscillation as obtained from the graph is $0.42\lambda_0$, while the wavelength of the TM surface wave mode from the computer program is $0.408\lambda_0$. This agreement is good and proves that the coupling in collinear arrangement is dominantly due to the TM mode of the surface waves.
- 2) Mutual coupling is small. This is due to the fact that most of the surface wave power carried by this mode, flows inside the dielectric substrate.

When (22) and (23) are inserted in (21) and manipulated, the mutual impedance between the two printed dipoles is given by,

$$Z_{12} = 1.0/I_2 - I_1/(I_1' \cdot I_2) . \quad (24)$$

3.3 NUMERICAL RESULTS

Mutual impedance computations between two printed dipoles have been performed in three configurations,

- 1) broadside, 2) Endfire and, 3) Echelon.

The lowest order surface wave mode has a launching pattern $\sim \cos\phi$. This means when two dipoles are in broadside configuration ($\phi = 90^\circ$) the part of the total coupling due to the surface wave will be minimum. The coupling in this configuration will mainly be due to direct, higher order and leaky waves excited by the antenna.

Figures (11) through (12) show broadside coupling between the two printed dipoles as a function of separation 'S' for different antenna lengths. The rapid fall in the beginning ($S < 0.4\lambda_o$) of the curve confirms that the coupling is mainly due to higher order modes, while for ($S > 0.8\lambda_o$) the direct field wave takes over. In the intermediate zone, leaky wave modes are dominant.

The printed dipole launches a surface wave with maximum efficiency along the axial direction ($\phi = 0$). Also, the radiation pattern of a dipole in free space has nulls along the axial direction ($\phi = 0$ and $\phi = 180$). Therefore, based on these arguments, it can be concluded that in the collinear configuration, the coupling will be mainly due to the surface wave. The surface wave decays as $\frac{1}{\sqrt{\rho}}$. Hence, mutual coupling should decay slowly in this configuration.

Figures 13 - 15 show mutual impedance for the collinear case plotted versus separation 'G', for different dipole lengths. The mutual coupling decays very slowly with 'G'. The period of oscillation of the mutual impedance as obtained from Fig. (13) is $0.88\lambda_o$, while the wavelength of the excited surface wave, as obtained from the computer program, is $0.8811\lambda_o$.

This agreement is excellent and confirms that the mutual coupling for the collinear configuration is due to the TM mode of the surface wave only. The initial behavior for small 'G' is due to the near zone field of the dipoles, as is clear in Fig. (15).

In the echelon configuration, mutual impedance computations versus displacement 'D' are shown in Figs. (16) through (8) for different dipole lengths. For $D = 0$, the dipoles are in broadside configuration, while for ' D ' large, the dipoles are approximately collinear. As ' D ' increases, Z_{12} decreases drastically from the broadside value and ultimately shows the same behavior as shown by the dipoles in collinearity.

The efficiency of the surface wave excitation depends upon the thickness of the substrate B (i.e., aperture size), for a given dielectric constant ϵ_r . To observe this effect, the substrate thickness is next increased from $0.1016\lambda_0$ to $0.127\lambda_0$, and computations for mutual impedance between the dipoles in collinear arrangement are performed. The results are shown in Figs. (19) and (20). The results shown in Figs. (19) and (20) are compared with the ones shown in Figs. (14) and (15). The comparison indicates that the surface wave efficiency increases with the thickness of the substrate.

Next, two propagating surface wave modes are allowed by increasing the substrate thickness to $0.15\lambda_0$ and the dielectric constant to 8.5. Computations for dipoles in broadside and collinear configuration are performed. The results for collinear arrangement and for different dipole lengths are shown in Figs. (21) and (22). The following components are in order:

- 1) The period of oscillation as obtained from the graph is $0.42\lambda_0$, while the wavelength of the TM surface wave mode from the computer program is $0.408\lambda_0$. This agreement is good and proves that the coupling in collinear arrangement is dominantly due to the TM mode of the surface waves.
- 2) Mutual coupling is small. This is due to the fact that most of the surface wave power carried by this mode, flows inside the dielectric substrate.

For the broadside situation the results are shown in Figs. (23) and (24). The following points are noted:

- 1) The mutual impedance plot oscillates with a period of $0.566\lambda_0$ which is close to the wavelength of the TE surface wave mode, i.e., $0.553\lambda_0$. This proves that mutual coupling in the broadside case is mainly due to TE surface wave mode.
- 2) The decay in coupling is rather rapid as compared to the collinear case.

CONCLUSION

In this paper, the radiation properties of dipoles printed on a grounded substrate have been derived. It has been demonstrated that mutual coupling is a significant problem in printed antenna technology.

ACKNOWLEDGEMENTS

This work was performed under U.S. Army contract 4-482521-25507-3.

- [1] A. Sommerfeld, Partial Differential Equations of Physics, Academic Press, New York.
- [2] P. Tulyathan and P. K. Newman, "The Circumferential Variation of the Axial Component of Current in Closely Spaced Thin Wire Antennas", IEEE Trans. Antennas Propag. Vol. AP-27, Jan. 1979.
- [3] R. F. Harrington, Field Computations by Moment Methods, MacMillan, Co., New York, 1968.
- [4] J. H. Richmond, "Radiation and Scattering by Thin Wire Structures in a Homogeneous Conducting Medium", IEEE Trans. Antennas Propagat. Vol. AP-22, Mar. 1975.
- [5] I. E. Rana and N. G. Alexopoulos, "On the Theory of Printed Wire Antennas", 9th European Microwave Conference, Brighton, England, September, 1979.
- [6] N. K. Uzunoglu, N. G. Alexopoulos and J. G. Fikioris, "Radiation Properties of Microstrip Dipoles" to be published IEEE Transactions AP-S, November 1979 issue.
- [7] V. H. Ramsey, "The Reaction Concept in Electromagnetic Theory", Phys. Rev. sec. 2. Vol. 94, pp. 1483-1491, June 15, 1954.

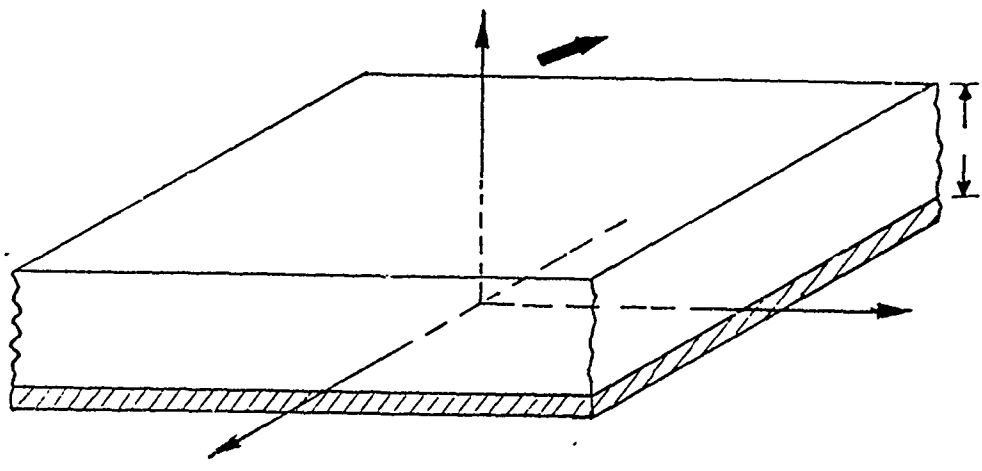


Figure 1. Coated perfect conductor geometry.

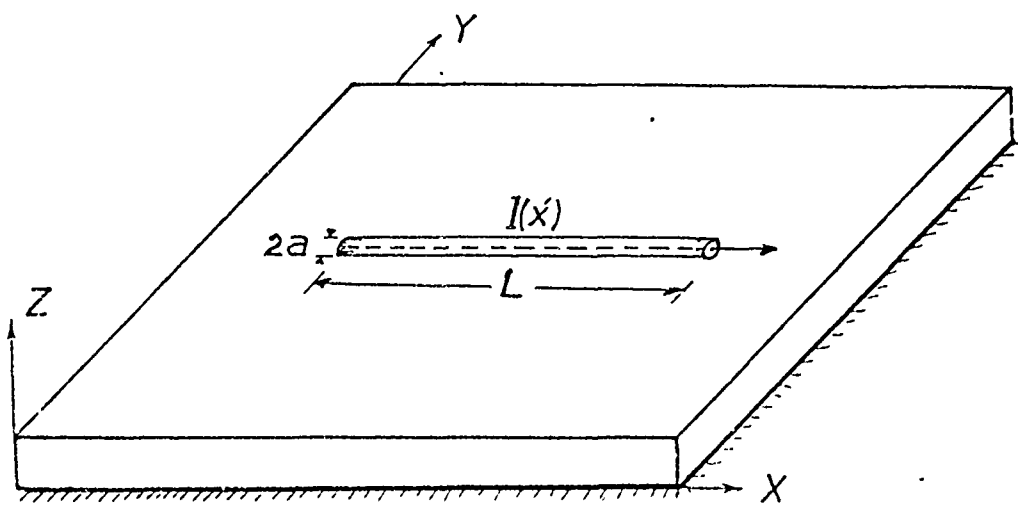


Figure 2. Printed Wire Dipole geometry.

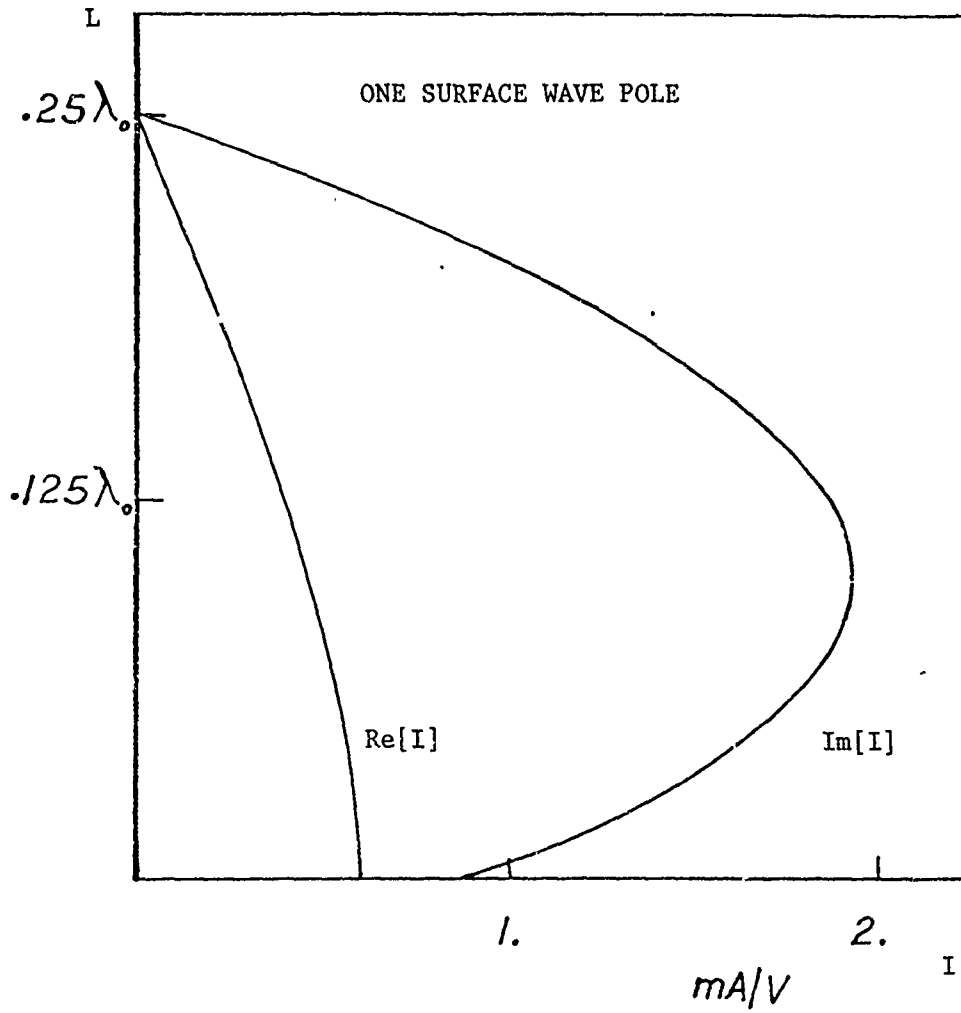


Figure 3. Current distribution on Printed Wire Dipole,
 $\text{Re}[I]$ and $\text{Im}[I]$ vs L (in λ_0), ($B=0.1016\lambda_0$, $\epsilon_r = 3.25$)

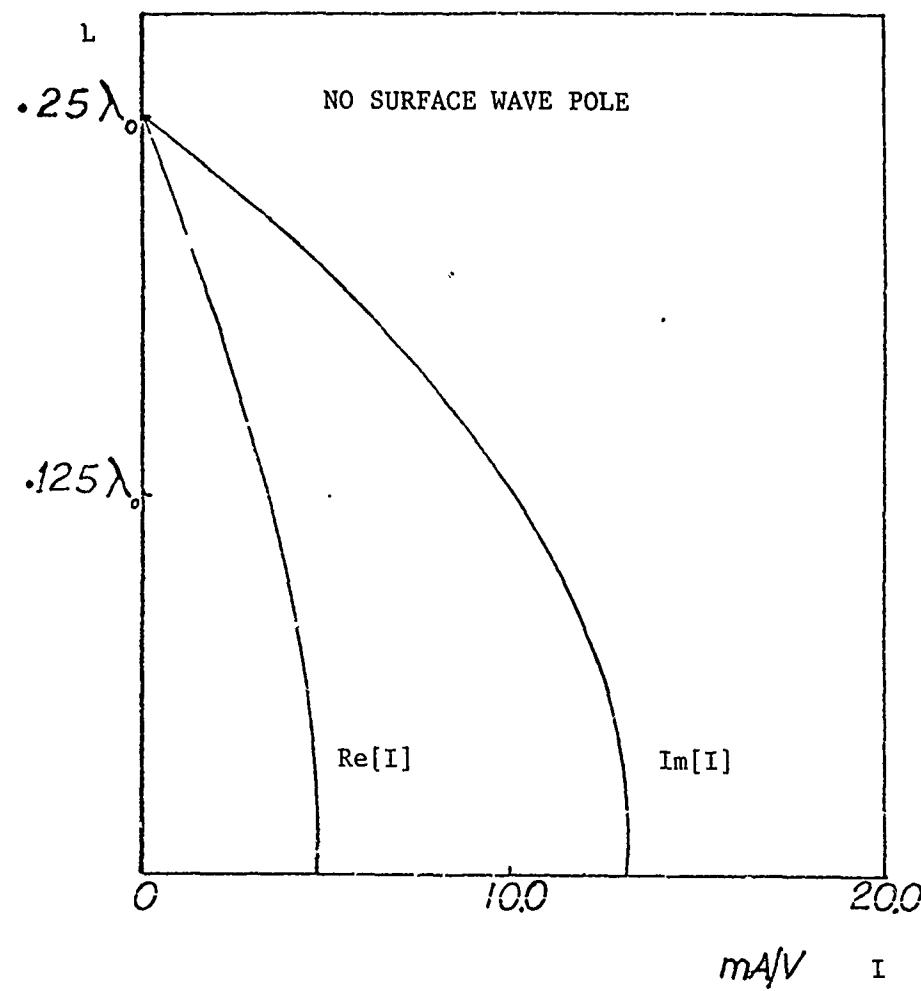


Figure 4. Current distribution on a Printed Dipole,
 $\text{Re}[I]$ and $\text{Im}[I]$ vs L ($\text{in } \lambda_0$), ($B=0.1016\lambda_0$, $\epsilon_r=1.0$)

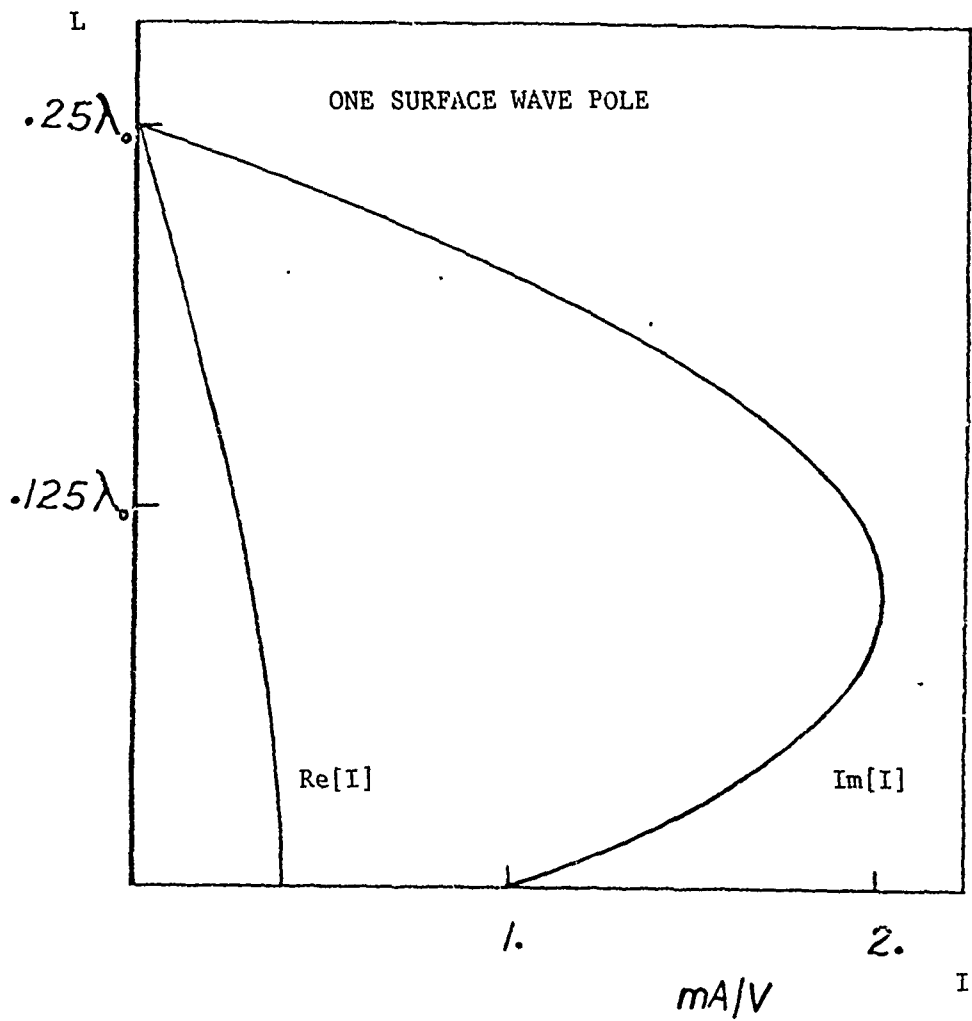


Figure 5. Current distribution on a Printed Wire Dipole,
 $Re[I]$ and $Im[I]$ vs L (in λ_0), ($B=0.127\lambda_0$, $\epsilon_r=3.25$)

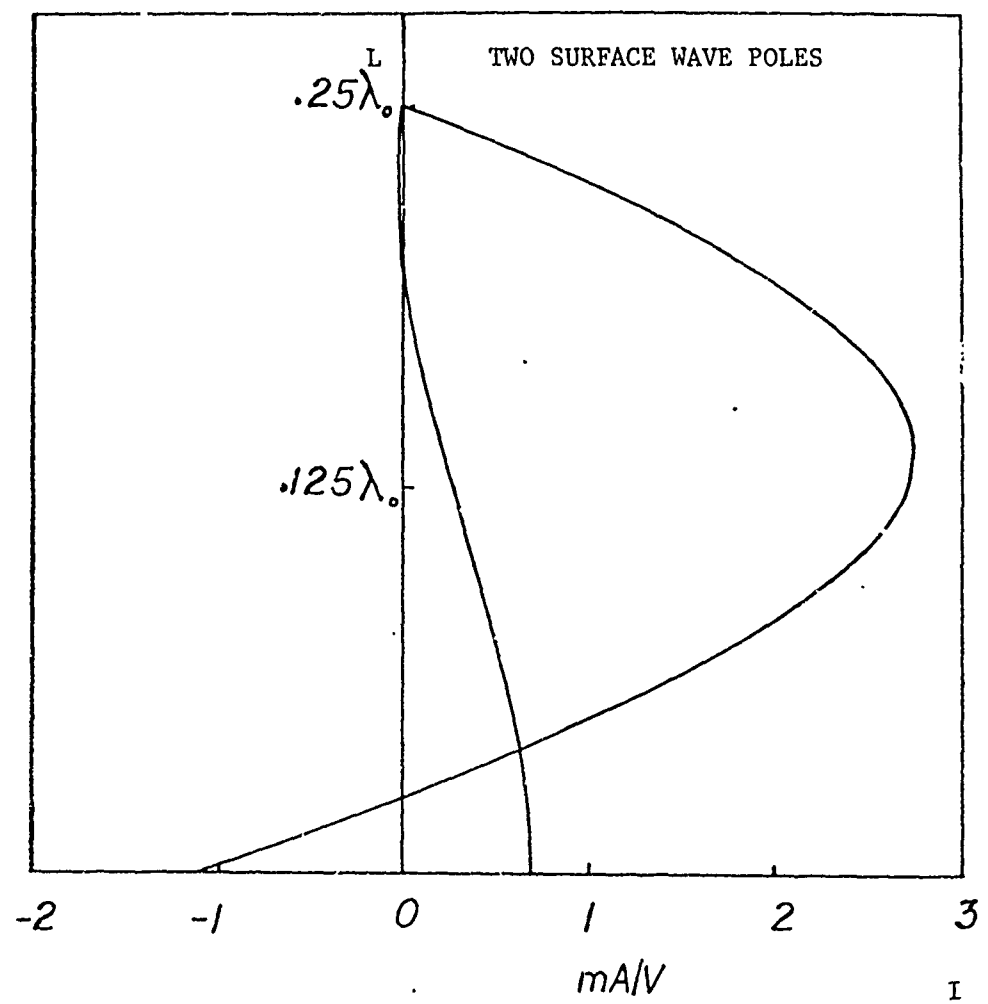


Figure 6. Current distribution on a Printed Wire Dipole,
 $\text{Re}[I]$ and $\text{Im}[I]$ vs L (in λ_0), ($B=0.15\lambda_0$, $\epsilon_r=8.5$)

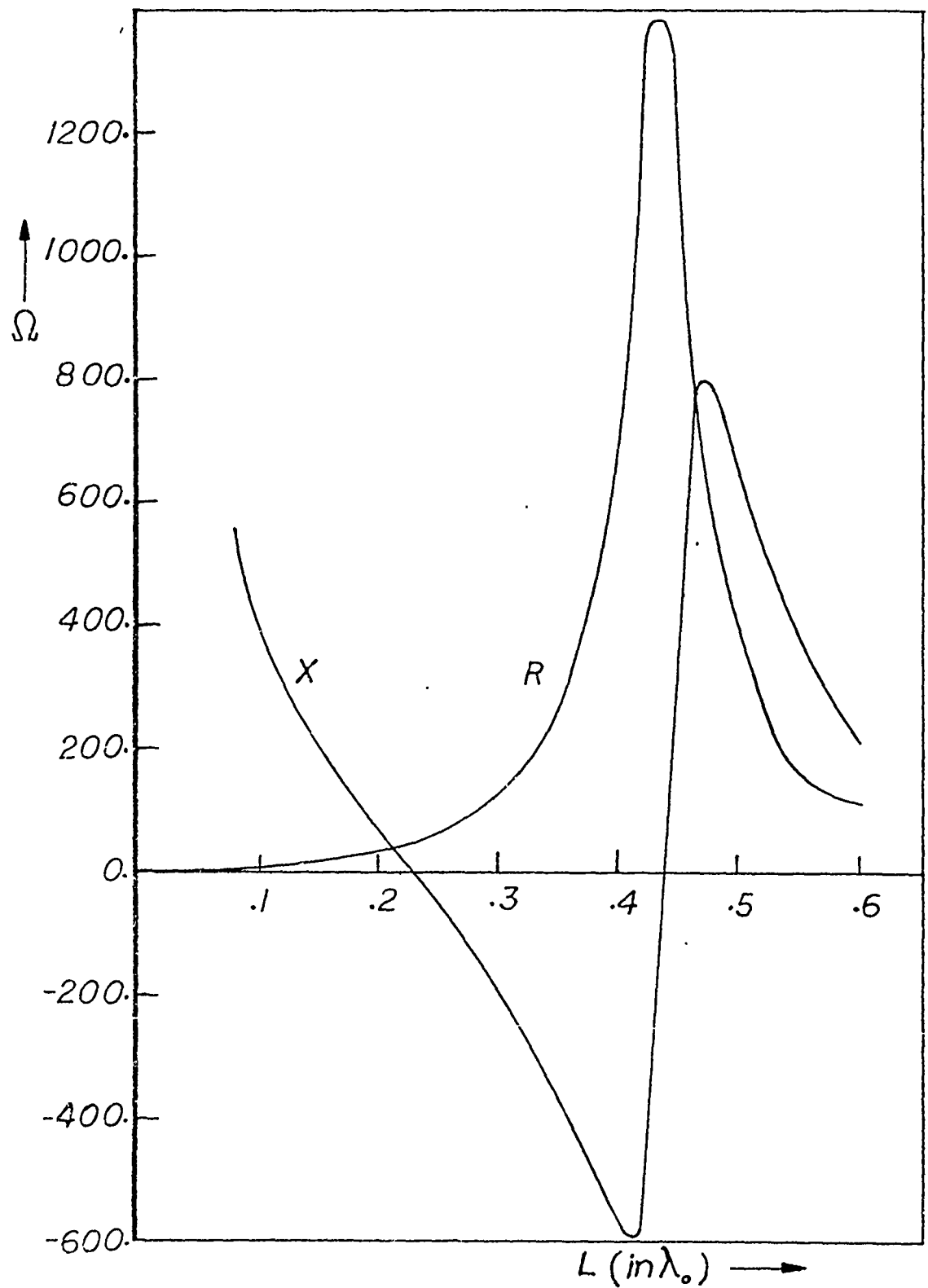


Figure 7. Input impedance vs antenna length L (in λ_0),
 $(B=0.1016\lambda_0, \epsilon_r=3.25, D=0.0001\lambda_0)$.

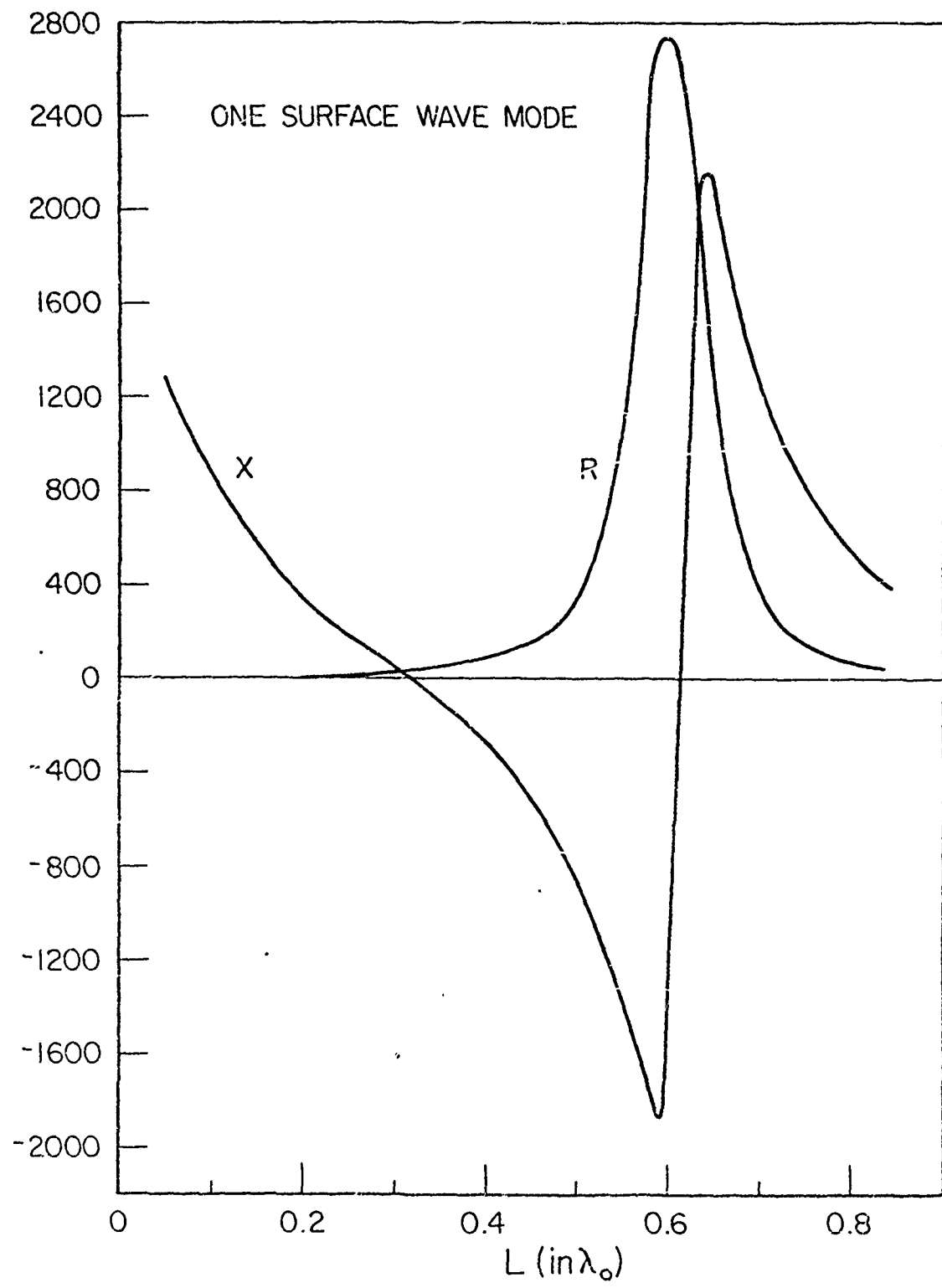


Figure 8. Input Impedance vs Antenna Length L (in λ_0), ($B = 0.1016 \lambda_0$, $\epsilon_r = 3.25$, $D = 0.0001 \lambda_0$).

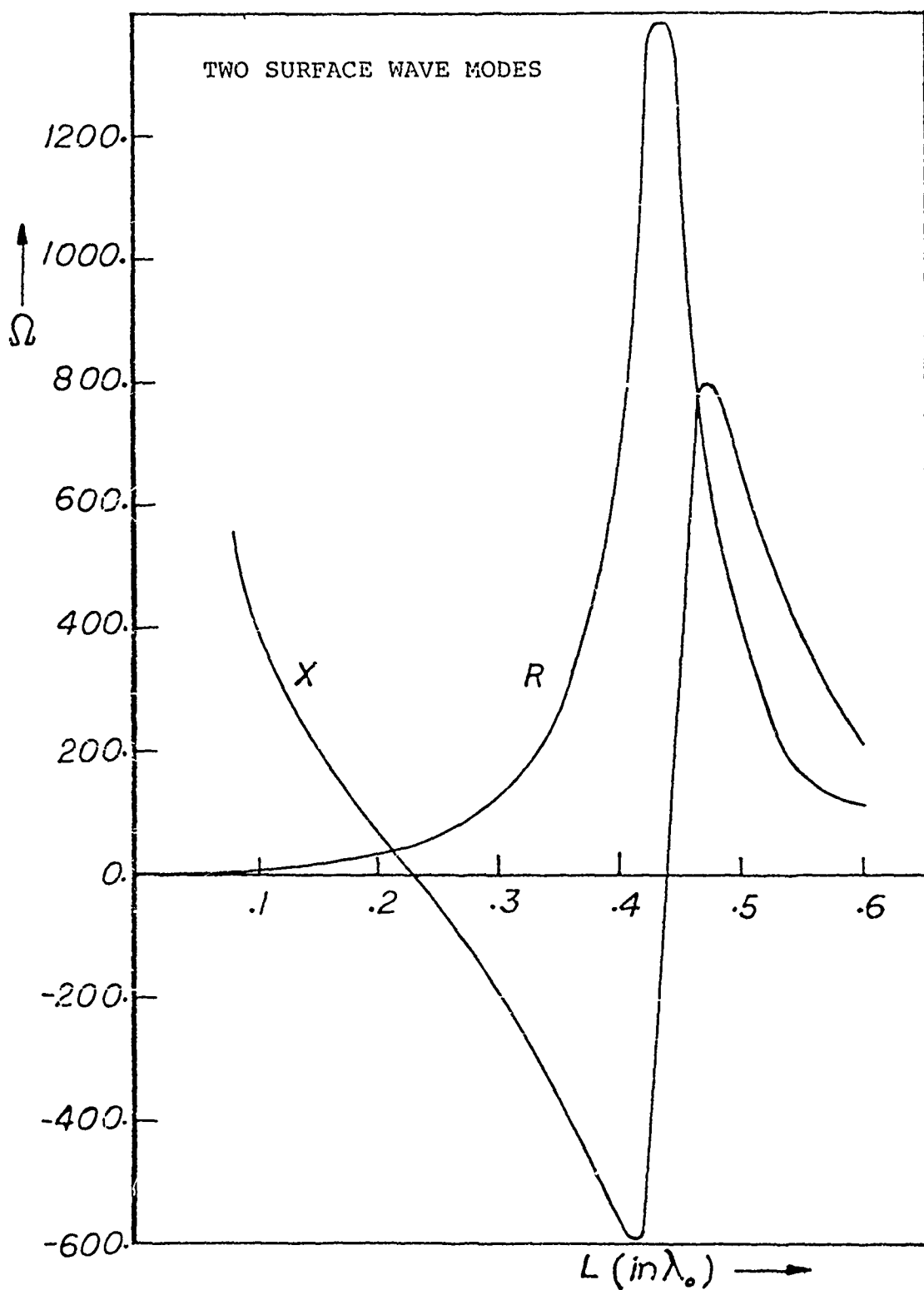


Fig. 9. Input Impedance of a Printed Wire Dipole vs
 L (in λ_0), ($B=0.15\lambda_0$, $\epsilon_r=8.5$, $a=0.000025\lambda_0$)

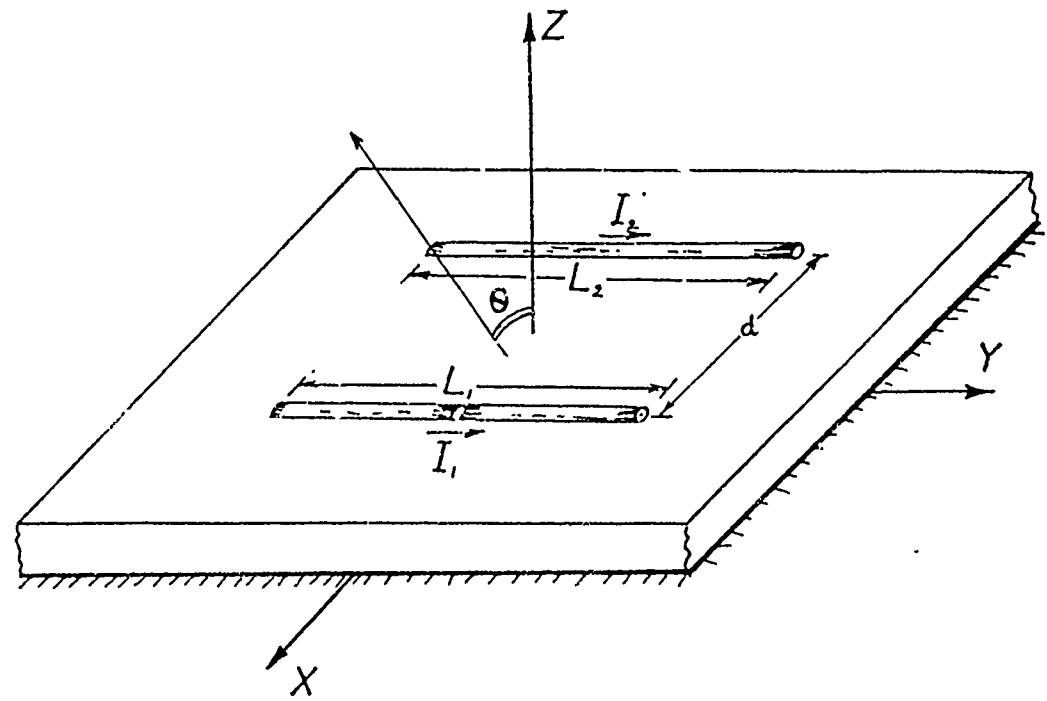


Figure 10. Two Printed Wire Dipoles (Driven & Parasitic)

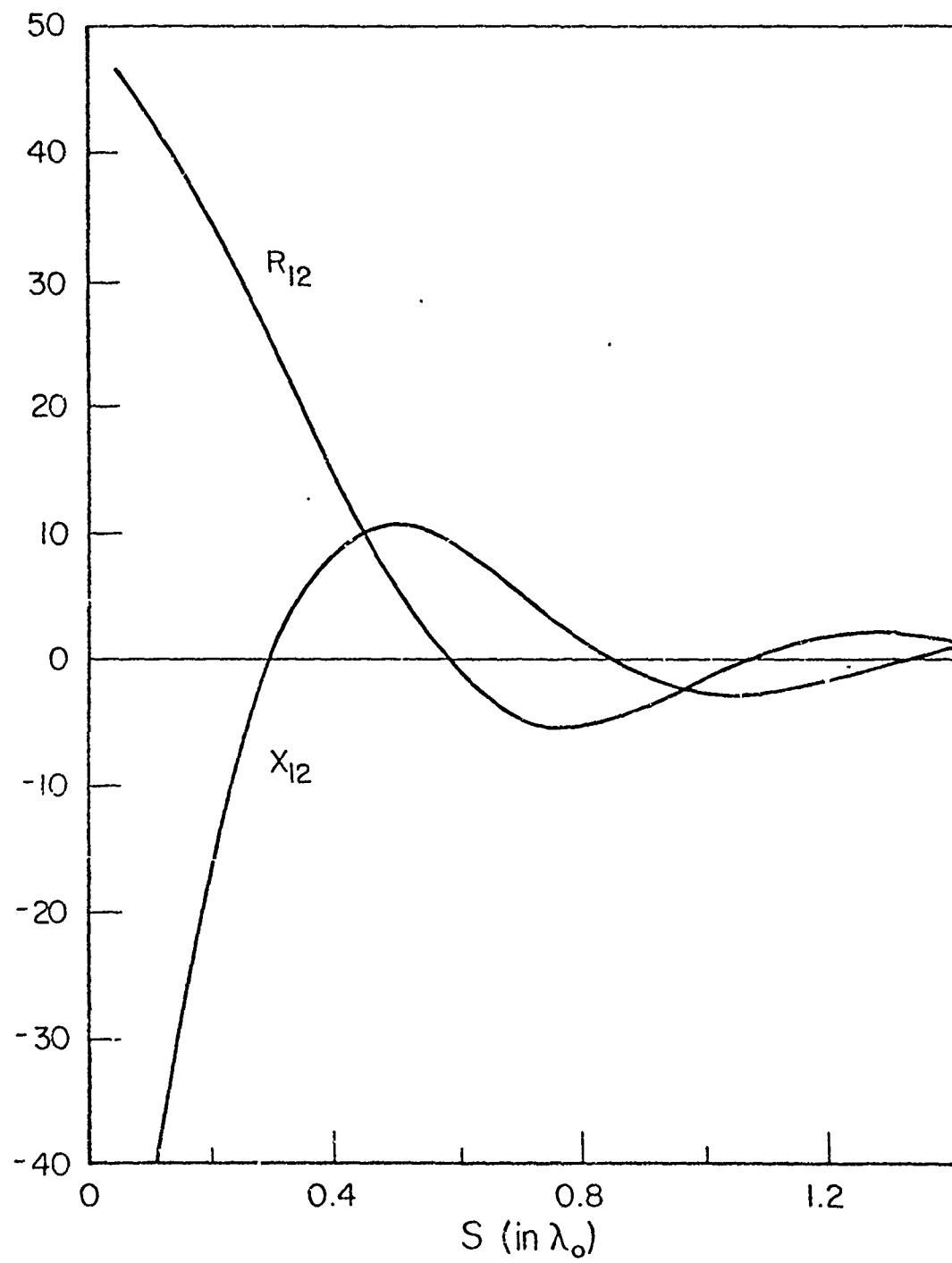


Figure 11.

Mutual Impedance Between Two Broadside Dipoles vs Separation S (in λ_0), ($B = 0.1016 \lambda_0$, $\epsilon_r = 3.25$, $L = 0.333 \lambda_0$).

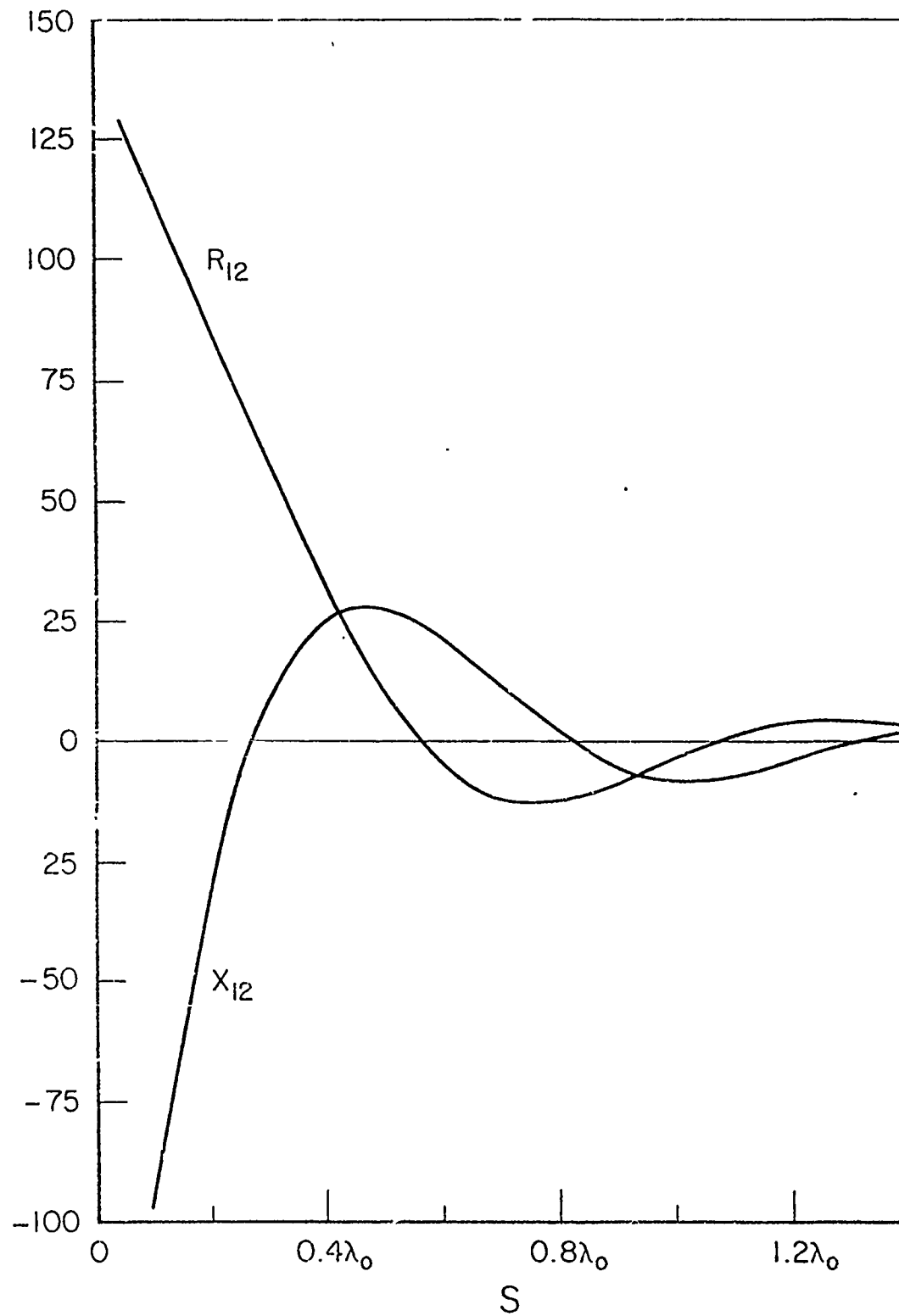


Figure 12. Mutual Impedance Between Two Broadside Dipoles vs.
Separation S (in λ_0) ($B = 0.1016 \lambda_0$, $\epsilon_r = 3.25$, $L = 0.5 \lambda_0$).

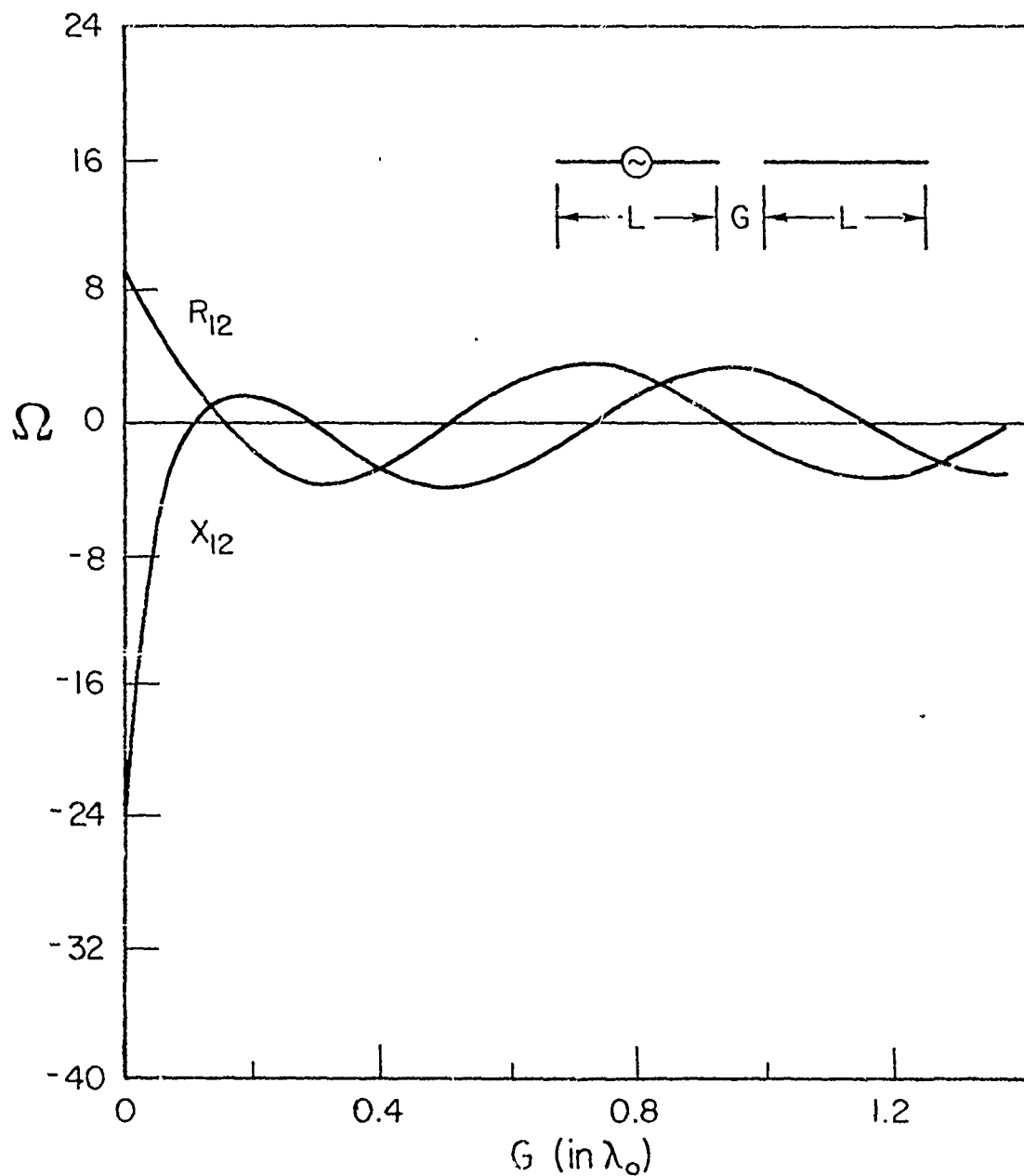


Figure 13.

Mutual Impedance Between Two Colinear Dipoles vs Spacing G (in λ_0), ($B = 0.1016 \lambda_0$, $\epsilon_r = 3.25$, $L = 0.25 \lambda_0$).

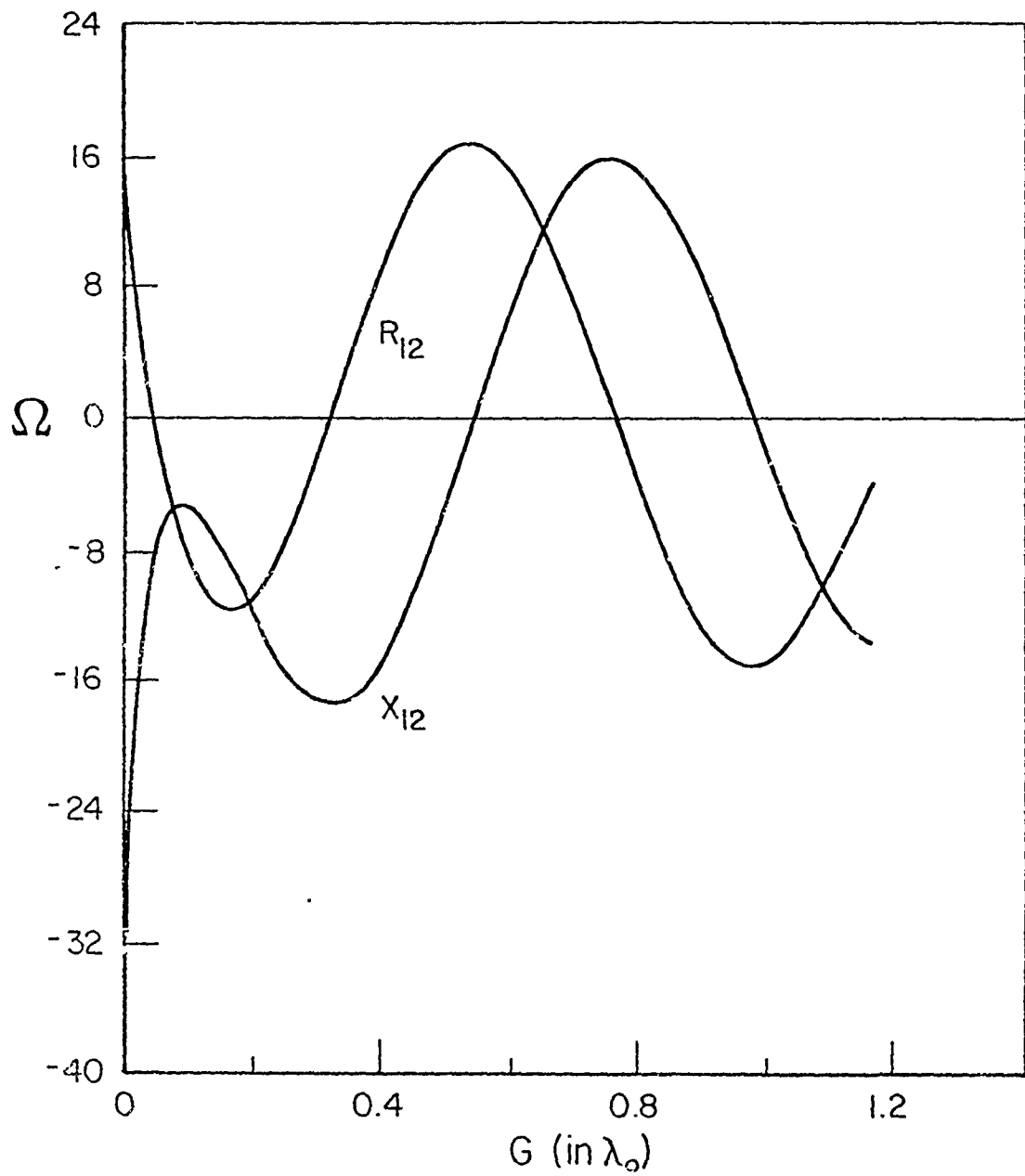


Figure 14.

Mutual Impedance Between Two Colinear Dipoles vs Spacing G (in λ_0), ($B = 0.1016 \lambda_0$, $\epsilon_r = 3.25$, $L = 0.4167 \lambda_0$).

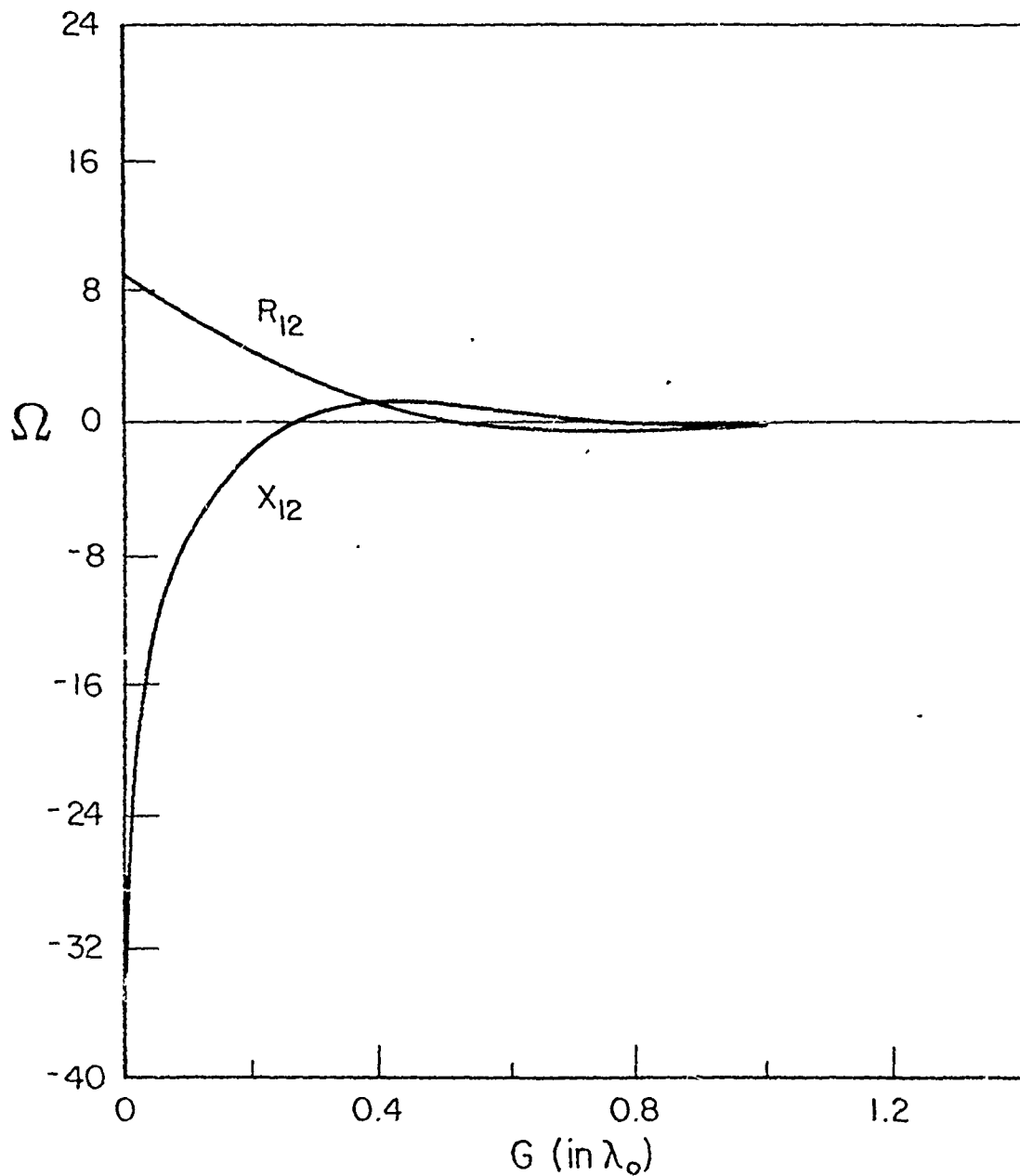


Figure 15.

Mutual Impedance Between Two Colinear Dipoles vs Spacing G (in λ_0), ($B = 0.1 \lambda_0$, $\epsilon_r = 1.00$, $L = 0.4167 \lambda_0$).

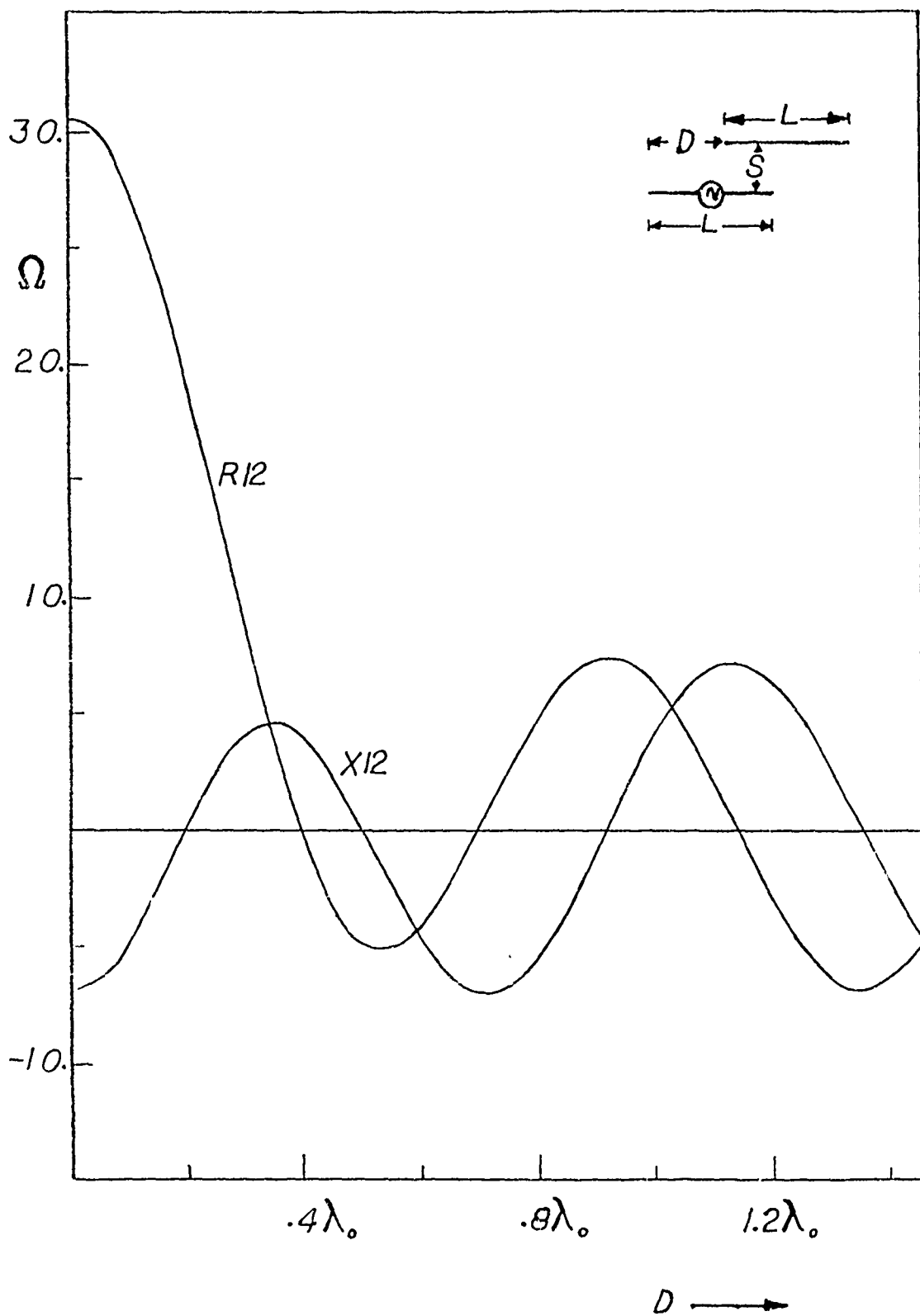


Figure 16. Mutual Impedance between two Dipoles in Echelon vs. Displacement D (in λ_0), ($B=0.1016\lambda_0$, $\epsilon_r=3.25$, $L=0.333\lambda_0$, $S=0.25\lambda_0$)

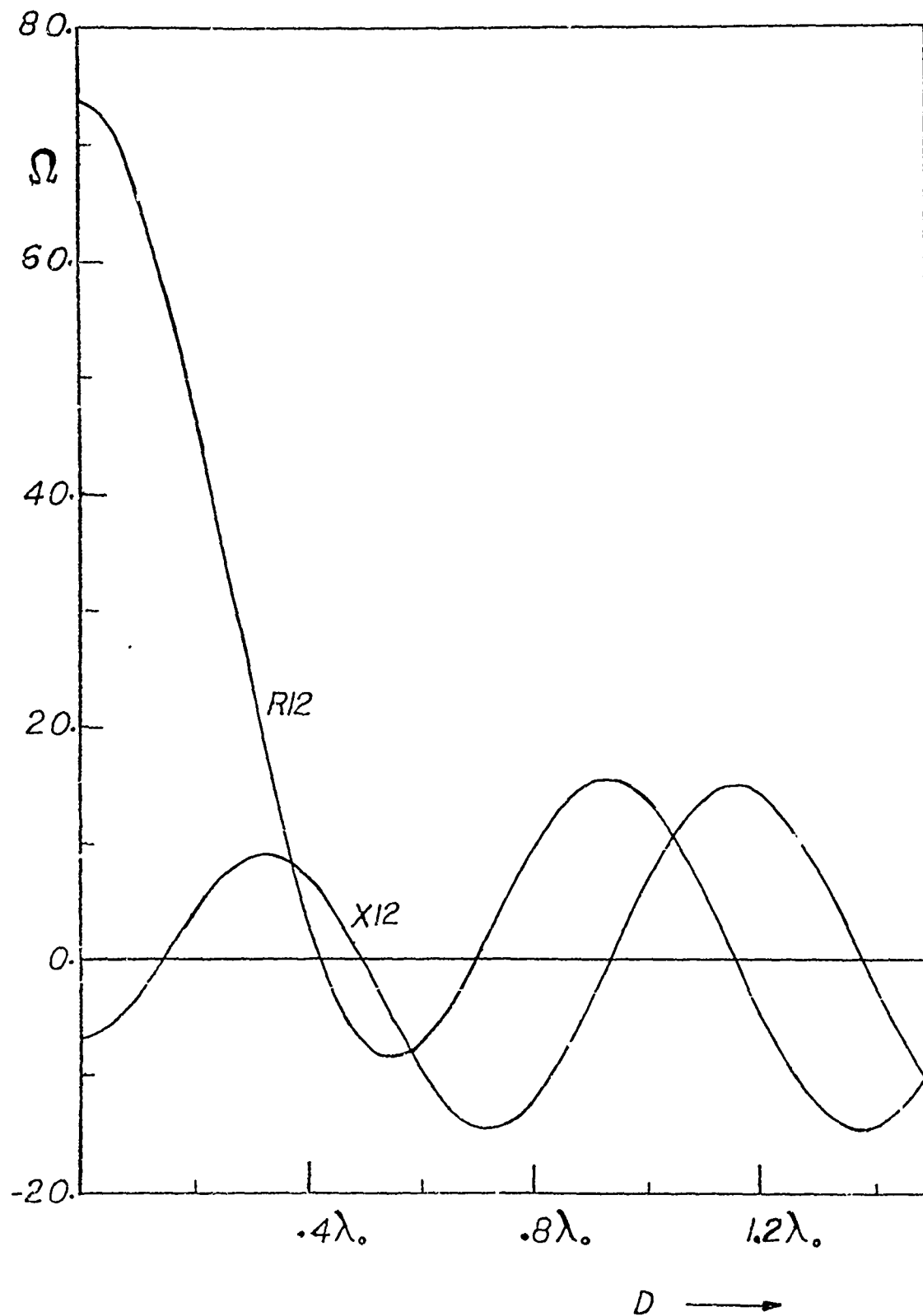


Figure 17. Mutual Impedance between two Dipole in Echelon vs Displacement D (in λ_0), ($B=0.1016\lambda_0$, $\epsilon_r=3.25$, $L=0.4167\lambda_0$, $S=0.25\lambda_0$)

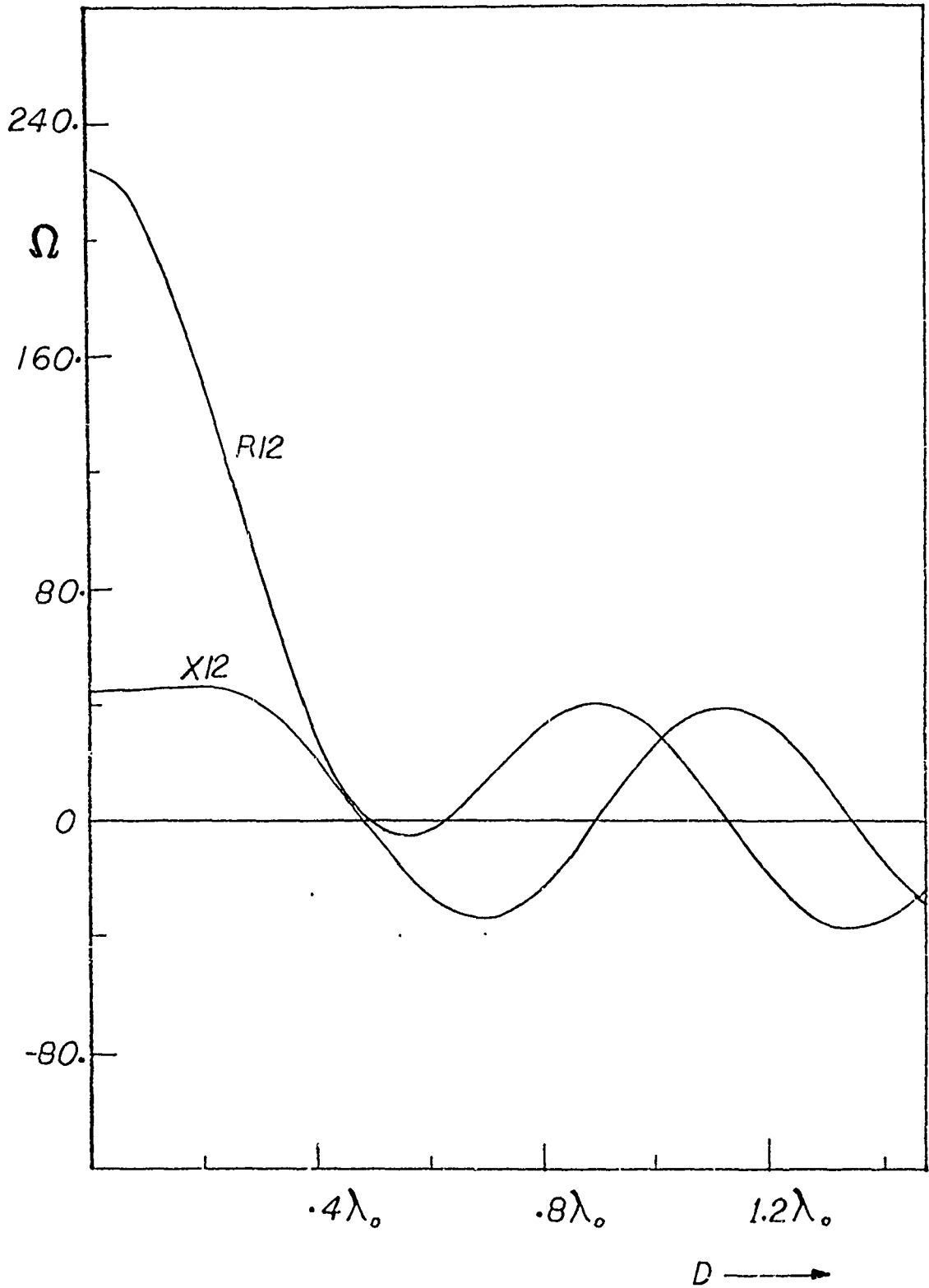


Figure 18. Mutual Impedance between two Dipoles in Echelon vs Displacement D (in λ_0), ($B=0.1016\lambda_0$, $\epsilon_r=3.25$, $L=0.5\lambda_0$, $S=0.25\lambda_0$)

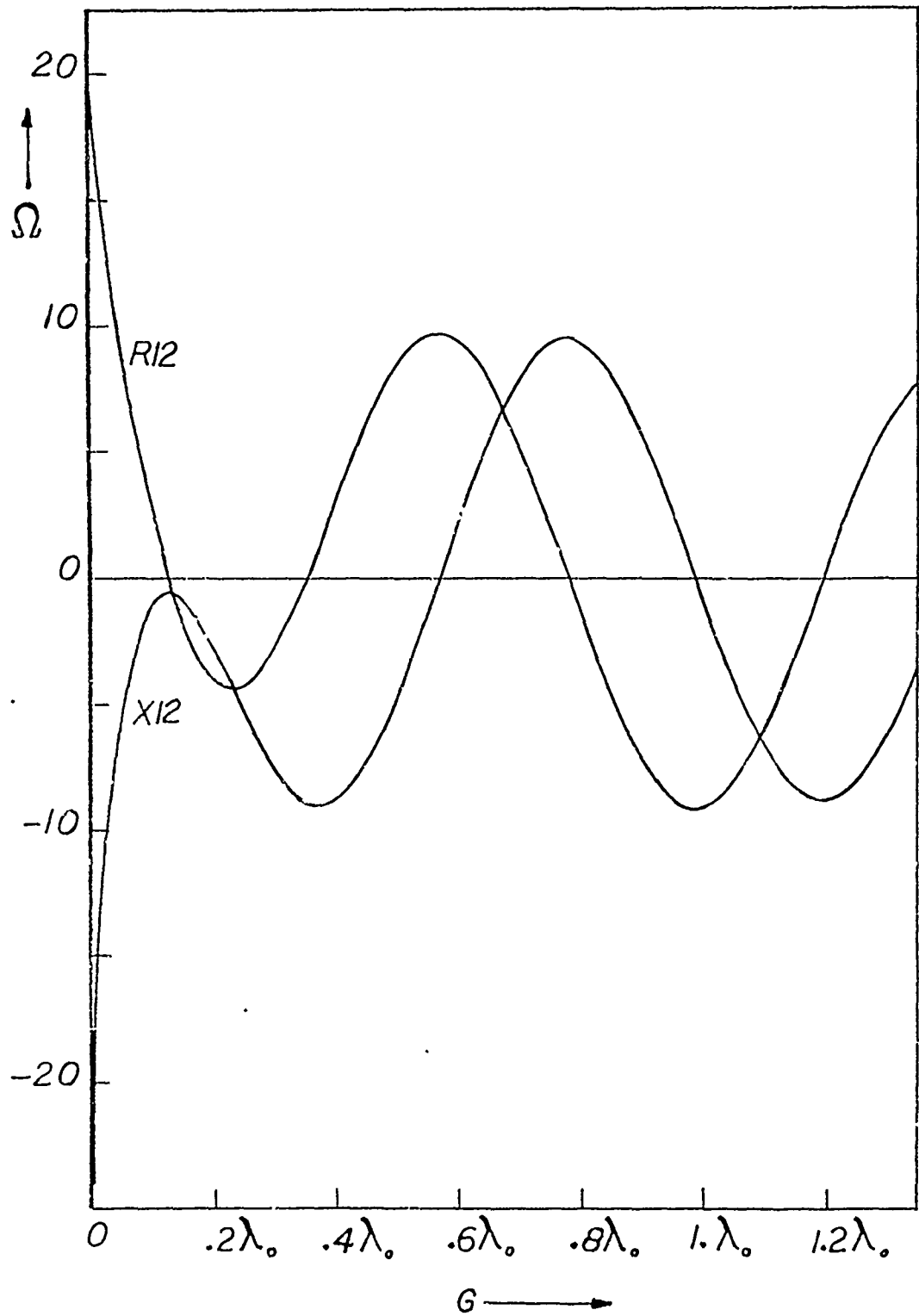


Figure 19. Mutual Impedance between two Collinear Dipoles vs Spacing G (in λ_0), ($B=0.127\lambda_0$, $\epsilon_r=3.25$, $L=0.3\lambda_0$)

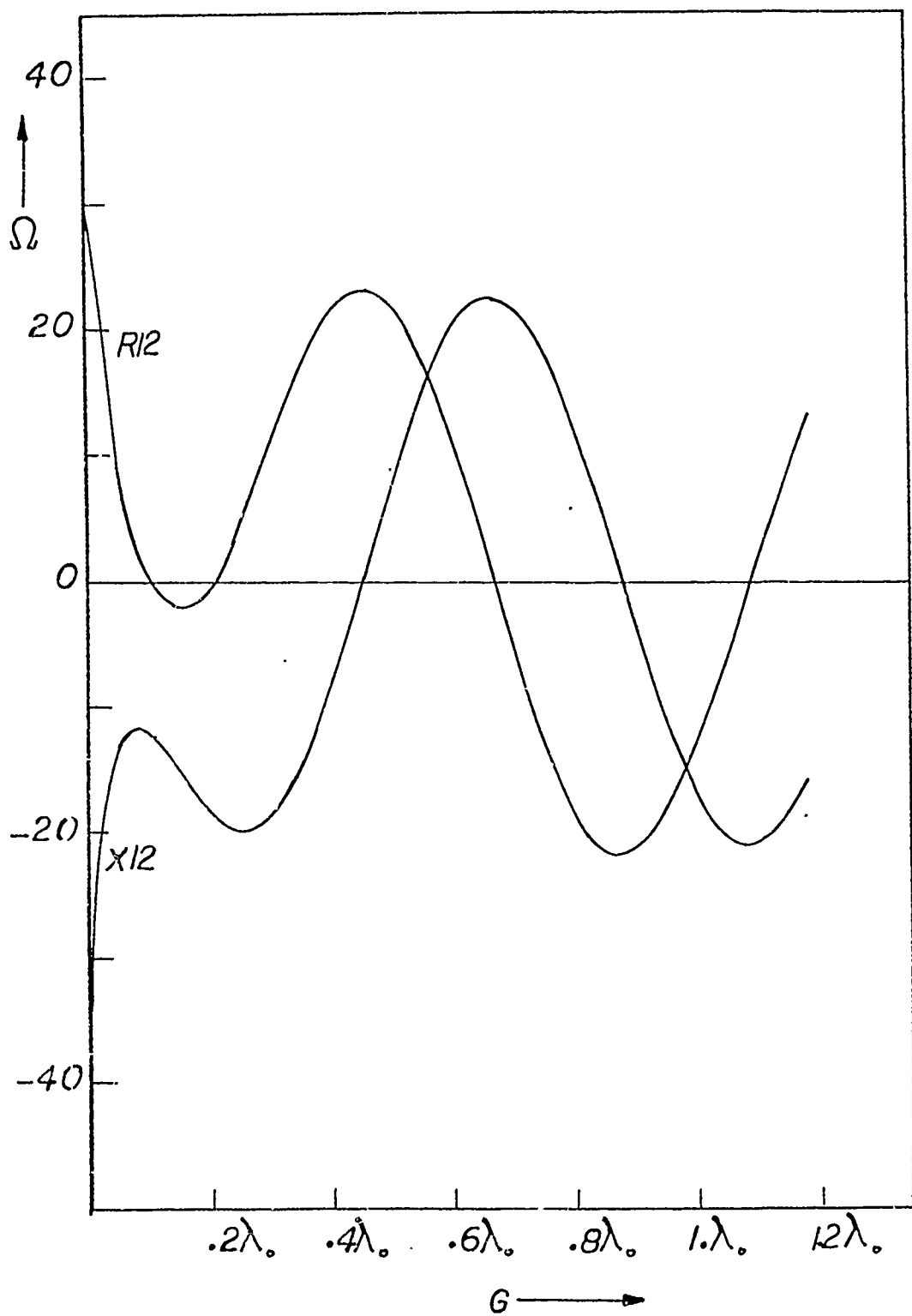


Figure 20. Mutual Impedance between two Collinear Dipoles vs Spacing S (in λ_0), ($B=0.127\lambda_0$, $\epsilon_r=3.25$, $L=0.4\lambda_0$)

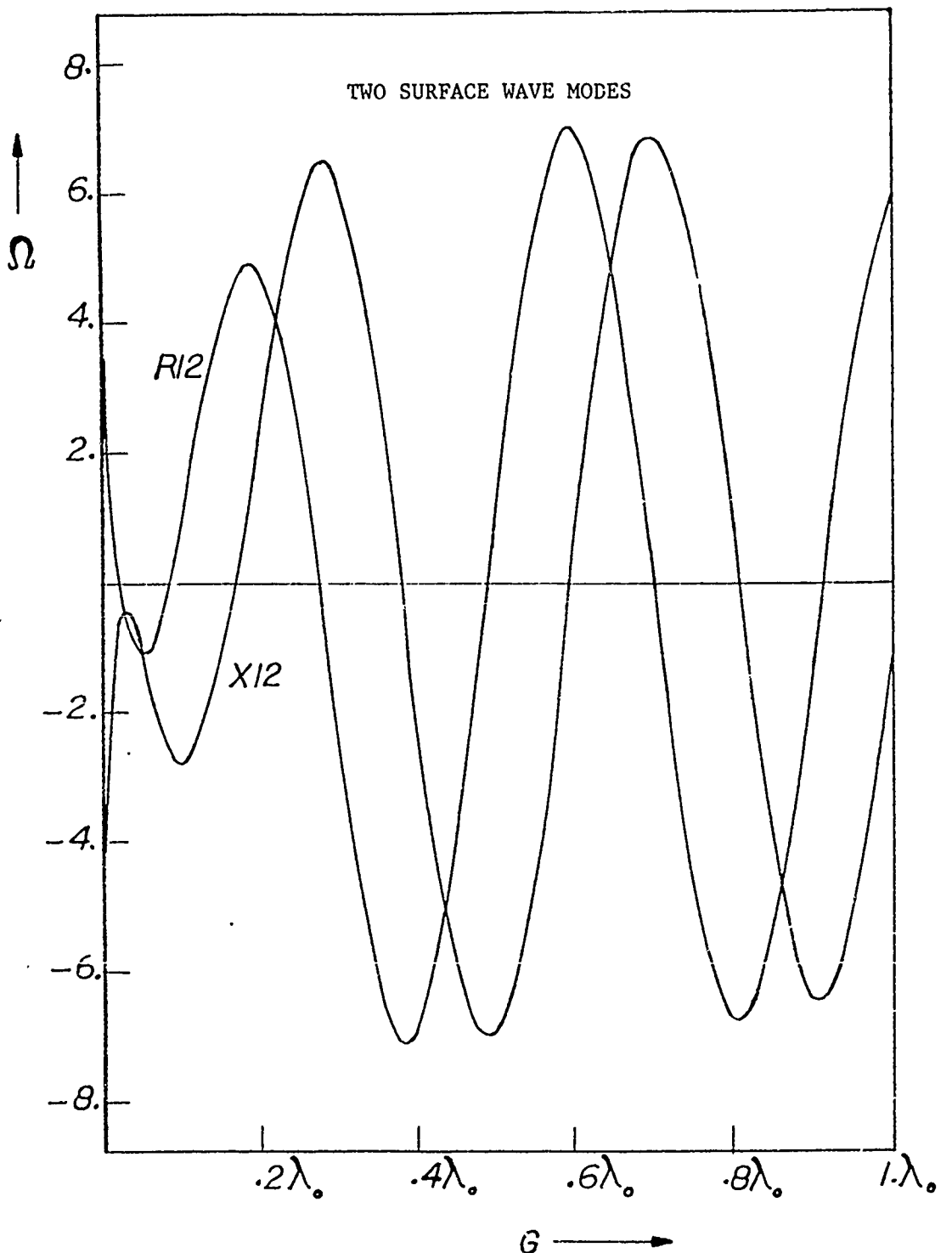


Figure 21. Mutual Impedance between two Collinear Dipoles vs Separation G (in λ_0), ($B=0.15\lambda_0$, $\epsilon_r=8.5$, $L=0.25\lambda_0$)

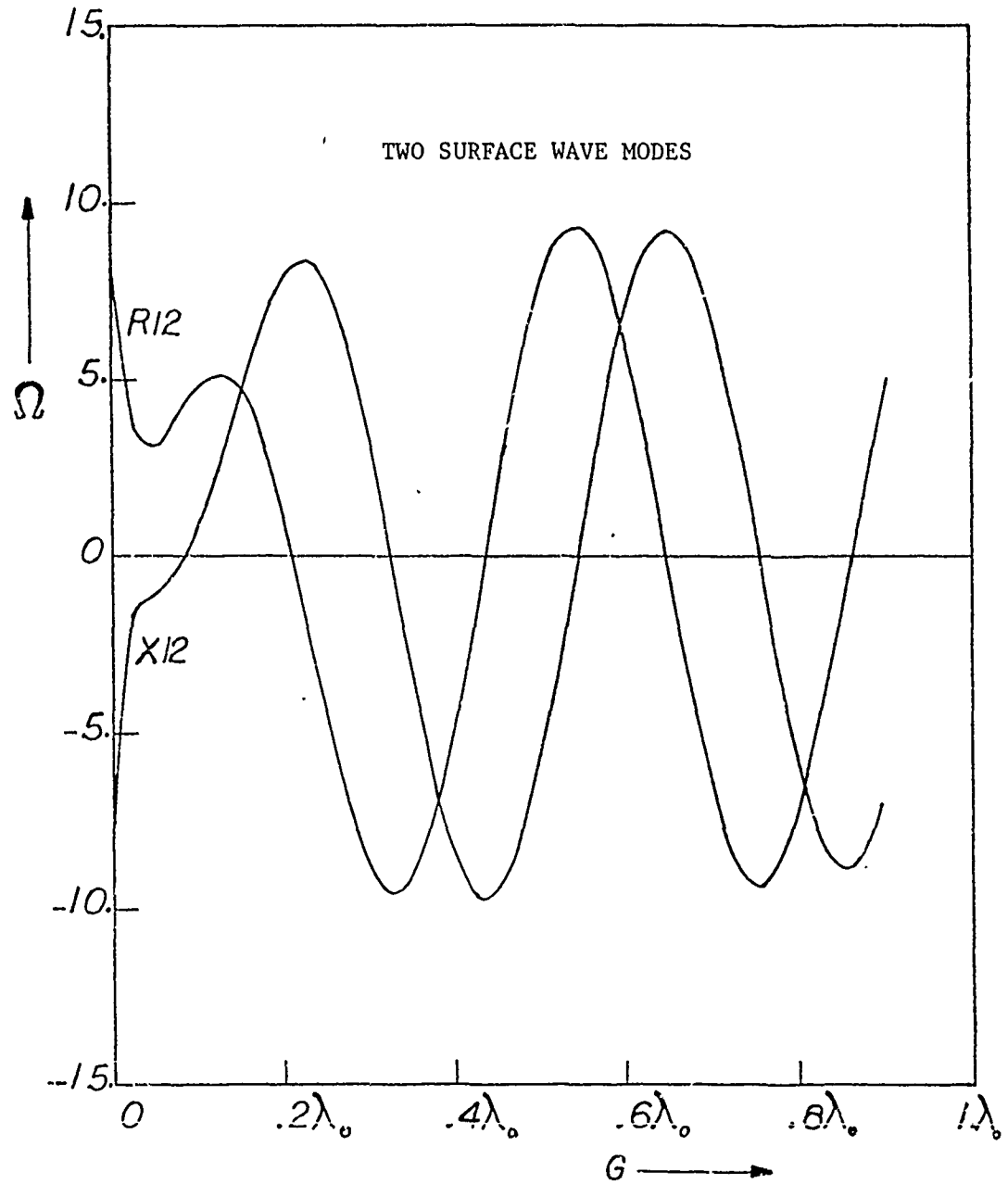


Figure 22. Mutual Impedance between two Collinear Dipoles vs Separation G (in λ_0), ($B=0.15\lambda_0$, $\epsilon_r=8.5$, $L=0.3\lambda_0$)

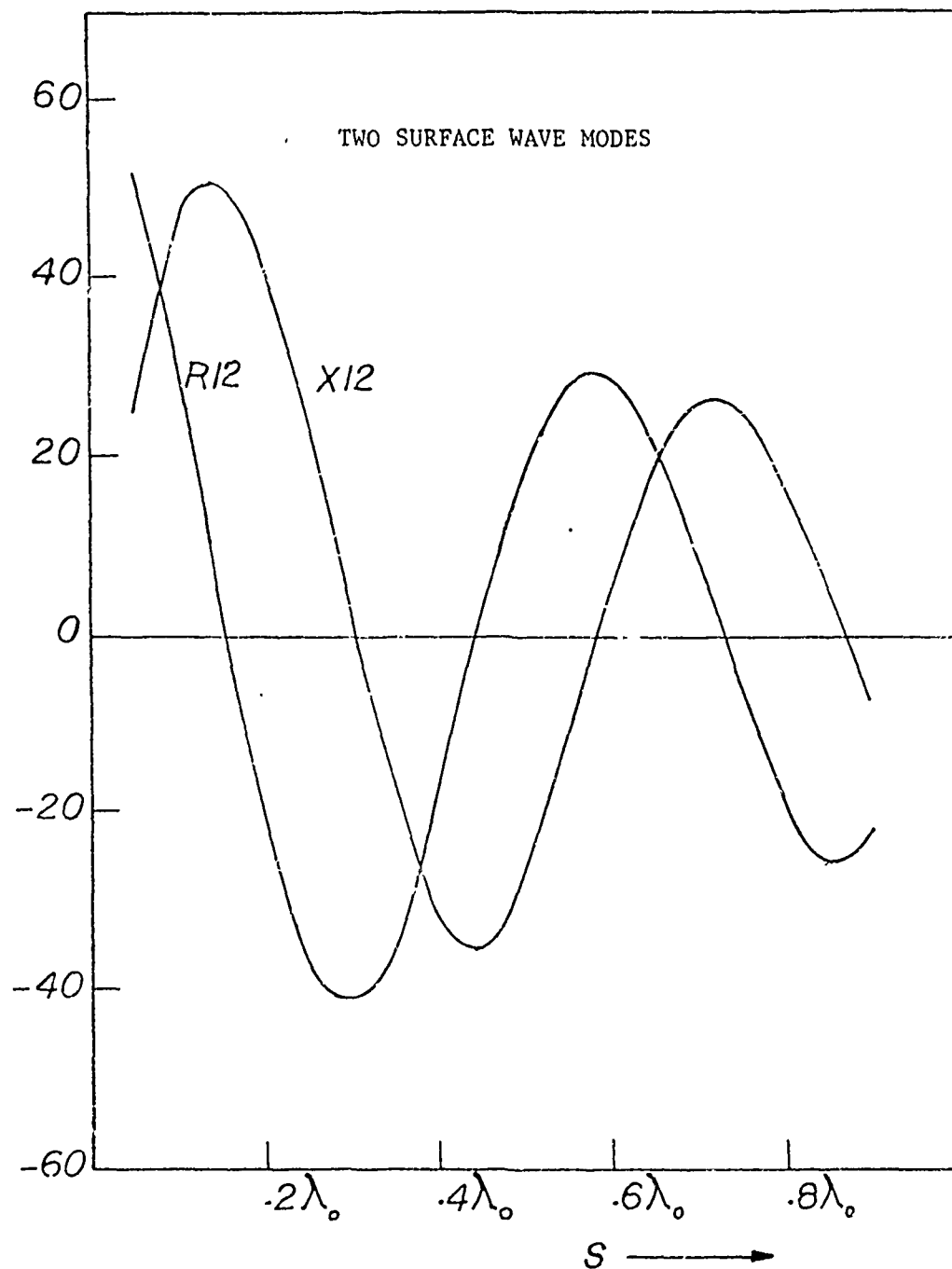


Figure 23. Mutual Impedance between two Broadside Dipoles
 Separation S (in λ_0), ($B=0.15\lambda_0$, $\epsilon_r=8.5$, $L=0.25\lambda_0$)

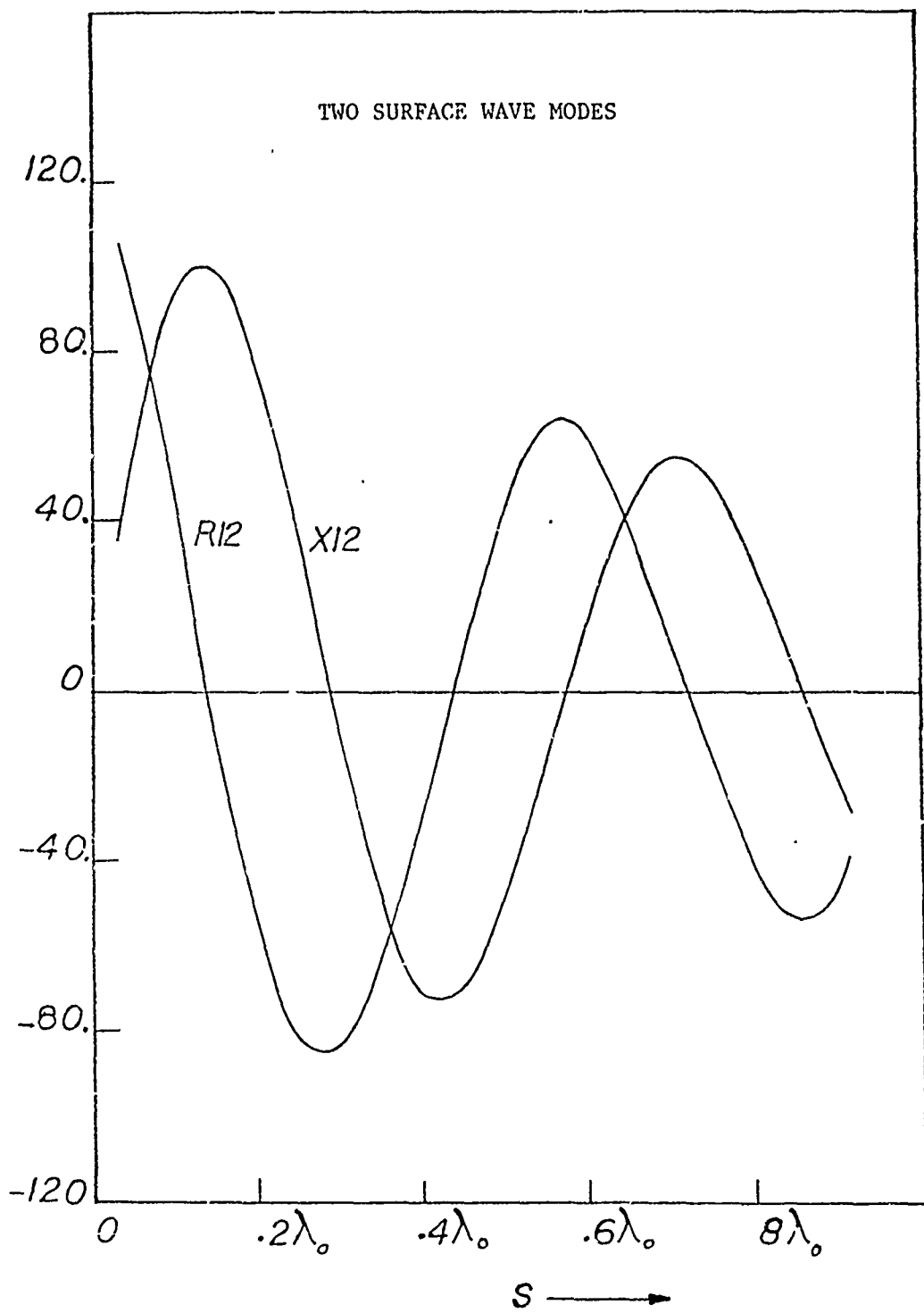


Figure 24. Mutual Impedance between two Broadside Dipoles vs Separation S (in λ_0), ($B=0.15\lambda_0$, $\epsilon_r=8.5$, $L=0.3\lambda_0$)

A NEW ANALYSIS TECHNIQUE FOR CALCULATING THE SELF
AND MUTUAL IMPEDANCE OF MICROSTRIP ANTENNAS

EDGAR L. COFFEY, III
T. H. LEHMAN
THE BDM CORPORATION
2600 YALE BLVD S.E.
ALBUQUERQUE, NEW MEXICO 87106

SUMMARY

The Direct Form of Network Analog (DFNA) method is developed for arbitrarily shaped microstrip patch antennas with impedance boundary conditions and lossy dielectrics. This method is capable of determining the self and mutual impedance of microstrip antennas in nearly any configuration, stacked or planar. Furthermore, it is trivial to interface the electromagnetic radiation problem with its associated transmission line or electronics problem. The bulk of this paper addresses the formulation of the impedance boundary condition as it is from this consideration that mutual coupling is addressed.

1.0 INTRODUCTION

A requirement for the rapid solution of large scale algebraic and differential systems, such as those required to obtain the input impedance and coupling coefficients of a microstrip array, has led to the development of a new analysis technique which (1) is mathematically sound, (2) is capable of interfacing easily with other system components, and (3) can handle arbitrary patch geometries, dielectric constants, wall impedance, and the stacking of multiple antennas above a single ground

This work was supported in part by the Army Research Office, ARO Grant DAAG 29-78-G-0082, while the first author was with the Physical Science Laboratory, New Mexico State University, Las Cruces.

plane. The method, called the Direct Form of Network Analogs (DFNA), is grounded solidly upon fundamental physics, and all parameters and variables are directly traceable to \vec{E} - and \vec{H} -fields, ϵ , μ , and σ . (The IFNA, or Indirect Form of Network Analogs is a complementary analysis technique based on a time-domain formulation of the Electric Field Integral Equation. Its value is in the study of scattering, not radiation, problems and, hence, will not be discussed here.)

2.0 DFNA: DIRECT FORM OF NETWORK ANALOGS

2.1 HISTORY OF CIRCUIT ANALOG MODELING

Electromagnetic modeling by circuit analogs was first investigated in the mid 1940's by Kron [7], who published a series of papers on circuit models for a variety of physical phenomena. Kron, of course, had no digital computer, and his work could not be put to any practical use. One of Kron's three-dimensional electromagnetic models is shown in Figure 1. Later Branin [1] attacked the same problem from a graph theoretic viewpoint and pointed the way toward understanding how network analogs could be derived for many physical processes. However, he offered no circuits of his own. In 1958, Karplus [6] discussed finite difference analogs on squares and triangles, but like the later finite element techniques of the 1960's and 1970's, these derivations were based on numerical considerations, not the underlying physics.

The most familiar network analog model is the one-dimensional L-C transmission line model, which is usually derived from the finite difference approximations of the transmission line equations. However, this is a very special case of a much more general technique. It should be noted that DFNA is not network synthesis. While network synthesis is a viable modeling tool for many electromagnetic problems [10,13], it has the disadvantage that the circuit component values are not directly related to any physical process.

2.2 THE DFNA TECHNIQUE

Following the method of Branin, the electromagnetics problem is divided

into topology operators (Maxwell's equations) and algebraic relations (constitutive relations). This is represented pictorially in Figure 2. The circuit elements are derived from the algebra, and the interconnection of elements is determined by topology. This division allows the physics to be described within a small region, which is called a "unit cell." Then all unit cells are connected together by the topological operators.

For example, consider a triangular unit cell as shown in Figure 3. A two-dimensional TM_z transmission line (E_z , H_x , H_y) has been superimposed on the drawing. Notice that there are intra-cell elements and inter-cell elements. The intra-cell connections can be deduced from

$$\oint \bar{H} \cdot d\bar{\ell} = \iint \dot{D} \cdot d\bar{S} \quad (1)$$

If ℓ describes the perimeter of the triangle, then S must indicate the triangular area bounded by the perimeter. Equation (1) states that the line integral of \bar{H} around the perimeter (represented by the currents in the three inductors) equals the time derivative of the electric flux (displacement current) through the triangular area. In terms of the circuit analog, the capacitor current is equal to the sum of the three inductor currents. Hence, from Kirchoff's current law, we deduce that the intra-cell connection is at a node. We also see that the current in each inductor is $I_l d\ell$ and that the capacitor current is $\epsilon E_z dA_z$.

The inter-cell connection is derived from

$$\oint \bar{E} \cdot d\bar{\ell} = - \iint \dot{\bar{B}} \cdot d\bar{S} \quad (2)$$

The magnetic flux in equation (2) must be that flux which passes through the area which is bounded by the two capacitors and interconnecting inductor. Equation (2) is a network loop equation since $d\bar{\ell}$ must traverse the boundary of $d\bar{S}$. Hence the difference in capacitor voltages ($E_z dz$) equals the inductor voltage ($\mu H_z dA_z$).

In summary, we now know the following quantities:

$$\text{Inductor current: } H_\ell d\ell = I_\ell$$

$$\text{Capacitor current: } \epsilon E_z dA_z = I_c$$

$$\text{Capacitor voltage: } E_z dz = V_c$$

$$\text{Inductor voltage: } \mu H_\ell dA_\ell = V_\ell$$

The circuit component values may now be calculated:

$$C = \frac{I_c}{dV_c/dt} = \frac{\epsilon E_z dA_z}{E_z dz} = \frac{\epsilon dA_z}{dz} \quad (3)$$

$$L = \frac{V_\ell}{dI_\ell/dt} = \frac{\mu H_\ell dA_\ell}{H_\ell d\ell} = \frac{\mu dA_\ell}{d\ell} \quad (4)$$

Similar relationships can be derived for TE_z (E_x, E_y, H_z) modes. Higher order TM and TE modes may be simulated by "stacking" the circuits already derived.

Notice that this two-dimensional analog requires a three-dimensional circuit just as a one-dimensional transmission line requires a two-dimensional circuit. It can be shown that a three-dimensional analog requires a "four-dimensional" circuit. This can be visualized by interlaced three-dimensional cubes of capacitors (E-field) and inductors (H-field) with dependent sources coupling the two problems together, not unlike Kron's circuit of Figure 1.

No assumptions concerning linearity or time-independence have been made. In fact, one of the most powerful applications of the method is to time-varying, non-linear problems.

3.0 APPLICATION TO MICROSTRIP ANTENNA MODELING

The microstrip antenna problem may be divided into three parts:

- (1) Modeling of the feed
- (2) Modeling of the cavity itself
- (3) Modeling of the cavity wall impedance

This partition is illustrated in Figure 4. Each of these models will be discussed separately first. Then the model interfaces will be identified and discussed.

3.1 DFNA MODELING OF THE FEED

A microstrip antenna may have two types of feed: (1) a microstrip transmission line (fed from the edge) or (2) coaxial probe (fed from underneath). The microstrip transmission line feed does not enter into the impedance calculation, unless feed line radiation and coupling effects need to be included. Once the antenna impedance is found, the impedance presented to the source may be determined by using standard transmission line theory.

When one or more antennas are interconnected by a transmission line network, then the feed network S-parameters or Z-parameters must be included in the composite model. This is because there are now two coupling paths: (1) through electromagnetic radiation and (2) through the feed network. S-parameters are easiest to measure directly, but Z-parameters work best with network models.

A probe-fed antenna requires additional consideration. For simple cases, Carver and Coffey found that the probe requires the addition of a series inductance [2] which, for thin dielectrics, is proportional to the dielectric thickness. When the probe is close to a conducting wall, a more complex model is necessary, such as the one of Newman and Pozar [11], in order to account for the coupling between the probe and wall.

One frequently uses shorted probes (posts) in patch antennas for tuning [14] or beam shaping [12]. These posts can be modeled as mutually

coupled inductors attached between the patch and the ground plane in the same way that feed probes are modeled.

3.2 DFNA MODEL OF THE CAVITY

The cavity itself can be thought of as supporting a TM_z (E_z , H_x , H_y) field and therefore can be modeled exactly as described in section 2.2 using unit cells of appropriate geometry (triangles, rectangles, etc.). Losses are accounted for in the same fashion as in L-C transmission lines: dielectric losses are represented by conductances in parallel with electric field capacitors, and copper losses are represented by resistances in series with magnetic field inductors.

It can be shown that the circuits obtained when the cells of section 2.2 are interconnected are the same as the circuits obtained by the method finite differences (piecewise constant approximation) and therefore reduce to standard L-C transmission lines in one dimension. Higher order approximations require more circuit elements, but not as many cells are needed to model a particular object. Piecewise constant and piecewise linear transmission line segments are illustrated in Figure 5. Even though twice as many circuit elements per unit length are needed for the higher order model, it has been shown that only 22% as many segments are needed to obtain the same spectral error (a measure of dispersion) [15].

3.3 DFNA MODEL OF THE WALL IMPEDANCE

Carver and Coffey obtained an expression for wall admittance for separable patches and low-order modes [2]. This parallel RC network represents the power radiated from the slot and the fringing capacitance associated with the fields at the slot. Unfortunately, this model breaks down when the fields are not uniform across the slot. Hence, complicated geometries and higher order modes present a more difficult modeling problem. Furthermore, no measure of mutual coupling can be obtained with a localized network.

If one were not interested in the mutual coupling problem, a more rigorous network could be developed quite simply after the method of Derneryd [4]. If the field in a slot is not uniform, perhaps the slot can be partitioned into several cells in each of which the field is approximately constant. Then, for co-linear cells, the total power radiated could be written as

$$P_{\text{rad}} = \sum_i \sum_j P_{ij} \quad (5)$$

$$P_{ij} = \frac{V_i V_j^*}{240} \left[\frac{w_i}{\lambda} \right] \left[\frac{w_j}{\lambda} \right] \left[\frac{4 \sin \alpha}{\alpha^3} - \frac{4 \cos \alpha}{\alpha^2} \right] \quad (6)$$

where V_n = voltage across the nth cell

w_n = width of nth cell

$\alpha = \beta_0 \Delta d_{ij} = 2\pi/\lambda \times$ cell separation distance

From this expression a mutual conductance matrix can be deduced, which describes the coupling among all the cells which make up one slot. In a similar manner a capacitance coupling matrix can be derived from a method of moments formulation of the magnetic line source radiation problem.

3.4 INTERCONNECTION OF THE MODEL COMPONENTS

The strongest feature of DFNA is that the various "pieces" of the micro-strip problem may be formulated separately and interconnected trivially. This is illustrated in Figure 4. The feed inductance (if needed) is directly connected to the circuit node analogous to the physical feed point location. The wall impedances are impedance matrices are connected directly to the patch circuit nodes which represent physically the location of the walls. It is not necessary to understand the numerics of the solution algorithm to formulate the problem.

3.5 A SIMPLE EXAMPLE

An edge-fed rectangular patch is shown in Figure 6. The DFNA method agrees almost exactly with the theoretical work of Carver and Coffey [7], as well as the experimental results of Lo [8]. This is to be expected, since for the dominant mode, the DFNA two-dimensional model reduces to a one-dimensional transmission line. The wall impedance is the same and thus the only discrepancy in the results would be due to numerical error in the DFNA method.

4.0 MICROSTRIP ANTENNA MUTUAL COUPLING

In considering the mutual coupling between two arbitrarily-shaped and positioned antennas, the above formulation is not sufficient. The rigorous solution must consider radiation, surface waves, edge diffraction, and currents on the upper side of the copper patch. The DFNA method can be used directly to simulate all of the above phenomena, and this will be discussed first. However, much simplification of the circuit can be had by judicious use of the unimoment method [9].

4.1 APPLICATION OF DFNA TO UNBOUNDED PROBLEMS

The microstrip antenna mutual coupling problem is essentially an unbounded problem since coupling occurs through radiation and surface wave mechanisms. DFNA can be used in unbounded problems with two related restrictions: (1) the problem must be electrically small enough so that the number of circuit elements is no more than several thousand, and (2) some assumption must be made of field behavior as $r \rightarrow \infty$ so that equivalent impedances may be used to terminate the problem.

Condition 1 is satisfied for most microstrip antennas in that their maximum dimension D is on the order of a half wavelength. In order to be in the far field the distance R from the patch must be

$$R \geq \frac{2D^2}{\lambda} \quad (7)$$

If $D = 0.5\lambda$, then $R \approx 0.5\lambda$ also. Hence the volume required for the unbounded problem is that of a hemisphere whose radius is 0.5λ , or

$$\text{Volume} = 0.262\lambda^3 \quad (8)$$

If 0.1λ spacing is used, then the volume of a unit cell is $0.001\lambda^3$. Therefore 262 cells are required to model the problem. Twelve circuit elements are required for each cell, giving a total of 3144 inductors, capacitors, and resistors in the model.

Condition 2 is made trivial by condition 1. In the far field, the radiation condition is valid, and a terminating impedance of 376.7Ω is used for cells with equal $r\delta\theta$ and $r\sin\theta\delta\phi$ lengths.

4.2 UNIT CELL FOR THREE-DIMENSIONAL PROBLEMS

Circuit analogs outside the patch must be able to support any arbitrary electromagnetic field propagating in any arbitrary direction. The networks needed for three dimensional modeling are more complicated than those derived in section 2.2. The rigorous development of such a network is beyond the scope of this paper, but some guidelines are given for the interested reader.

Consider the static fringing pattern of a parallel plate capacitor as shown in Figure 7a. One might model this device with a network of capacitors as shown in Figure 7b. Of course, the capacitors parallel to the equipotentials need not be included for the static case since these capacitors store no charge. (They are necessary for time-harmonic modeling.) A more regular grid of capacitors is shown in Figure 7c. Both Figures 7b and 7c are valid models for the static behavior of the capacitor. (Figure 7c is easier to implement, while Figure 7b more closely represents the true field structure.)

The circuits in Figures 7b and 7c are inadequate for the time-harmonic case unless each capacitor junction is modified by the ring of inductors

in Figure 7d. This is because the contribution of the time derivative of the magnetic flux must be considered in writing the loop equation about each ring of capacitors, as demanded by equation (2). The interconnection of three-dimensional cells is shown in Figure 1. There are 18 elements to each unit cell. (A cell which uses only 12 elements can be derived using dependent voltage and current sources.)

4.3 USE OF UNIMOMENT METHOD TO REDUCE SIZE OF NETWORK

A full DFNA solution of the unbounded problem requires a large number of elements to model the volume in Figure 8a. Considerable savings may be obtained by using the unimoment method [9] to reduce the hemispherical three-dimensional problem to an "almost" two-dimensional planar problem. Such a technique was proposed two years ago for the hybrid computer solution of microstrip antenna radiation problems [3] but was not formulated in an equivalent impedance form which could be used in network modeling. The savings in computer time and storage is most dramatic in mutual coupling modeling, as shown in Figure 9.

4.4 THE MUTUAL COUPLING FORMULATION

By using the unimoment technique to reduce the size of the problem, the mutual coupling problem may be divided into three regions (Figure 9).

- (1) The microstrip patch interiors: this is modeled with two-dimensional cells exactly as discussed in section 2.2. The patches need not have the same shape and, in fact, may be stacked.
- (2) The unimoment equivalent impedance of a half space: this model consists of a dense impedance matrix which couples the fields properly at the unimoment boundary.
- (3) The region exterior to the patch but inside the unimoment boundary: here, three-dimensional cells must be used since the fields will, in general, be combinations of TM and TE modes.

The circuit for each region is formulated separately and then interconnected as before. The mutual impedance between the two antennas is the

same as the mutual impedance of the network model. (The entire network problem need not be worked at once if the method of Diakoptics [5] is also incorporated into the solution algorithm.)

If near or far field strengths are required, they can be obtained as follows. First connect the feed line and source to the antenna or array. Then compute the mutual coupling between the source node and unimoment boundary nodes. This allows one to calculate the tangential electric field at the unimoment boundary. The field at any point above this boundary may be obtained by integrating the tangential unimoment field with the standard diffraction integral.

5.0 NUMERICAL RESULTS

Numerical results using this method will be presented for several different shapes of microstrip radiators. Results will be compared with available analytical calculations and measurements of actual antennas.

6.0 REFERENCES

1. F. H. Branin, Jr., "The Algebraic-Topological Basis For Network Analogies and the Vector Calculus," Proc. Symposium on Generalized Networks, Polytechnic Institute of Brooklyn, pp. 453-491, April 1966.
2. K. R. Carver and E. L. Coffey, "Theoretical Investigation of the Microstrip Antenna" (Semi-Annual Progress Report), Physical Science Laboratory, New Mexico State University, Las Cruces; PSI Technical Report PT-00929, January 23, 1979.
3. E. L. Coffey and K. R. Carver, "Towards the Theory of Microstrip Antenna Patterns," Proc. 1977 Allerton Antenna Applications Symposium, University of Illinois, Urbana, April 1977.
4. A. G. Derneryd, "Mutual Coupling in Array Antennas," School of Electrical Engineering, Chalmers University of Technology, Göteborg, Sweden, Technical Report 60, 1976.
5. H. H. Happ, Diakoptics and Networks, Academic Press, 1971.
6. W. J. Karplus, Analog Simulation, McGraw-Hill Book Co. (New York: 1958).

7. G. Kron, "Equivalent Circuit of the Field Equations of Maxwell," Proc. IRE, pp. 289-299, May 1944.
8. Y. T. Lo, D. Solomon, F. R. Ore, D. D. Harrison, and G. A. Deschamps, "Study of Microstrip Antennas, Microstrip Phased Arrays, and Microstrip Feed Networks," Dept. of Electrical Engineering, Univ. of Illinois, Urbana; Rome Air Development Center report RADC-TR-77-406, 21 October 1977.
9. K. K. Mei, "Unimoment Method of Solving Antenna and Scattering Problems," IEEE Trans. on Antennas and Propagation, Vol. AP-22, pp. 750-766, November 1974.
10. M. A. Messier, Coupling to Antennas (DNA Handbook Revision, Ch. 10) prepared for Harry Diamond Laboratories, Contract DAAG 39-73-C-0010, Appendix 10.B.
11. E. H. Newman and D. M. Pozar, "Electromagnetic Modeling of Composite Wire and Surface Geometries," IEEE Trans. Antennas and Propagation, Vol. AP-26, pp. 784-788, November 1978.
12. F. G. Parks and M. C. Bailey, "Mutual Coupling Between Microstrip Disk Antennas," 1976 AP-S International Symposium Digest, University of Massachusetts, Amherst, pp. 399-402, October 1976.
13. D. H. Schaubert, "Application of Prony's Method to Time-Domain Reflectometer Data and Equivalent Circuit Synthesis," IEEE Trans. on Antennas and Propagation, Vol. AP-27, pp. 180-184, March 1979.
14. D. H. Schaubert, H. S. Jones, and F. Reggia, "Conformal Dielectric-Filled Edge-Slot Antennas for Bodies of Revolution," Harry Diamond Laboratories, Adelphia, MD, HDL-TR-1837, September 1977.
15. R. Vichnevetsky and F. DeSchutter, "A Frequency Analysis of Finite Difference and Finite Element Methods For Initial Value Problems," Rutgers University, New Brunswick, N.J., DCS-TR-36, July 1975.

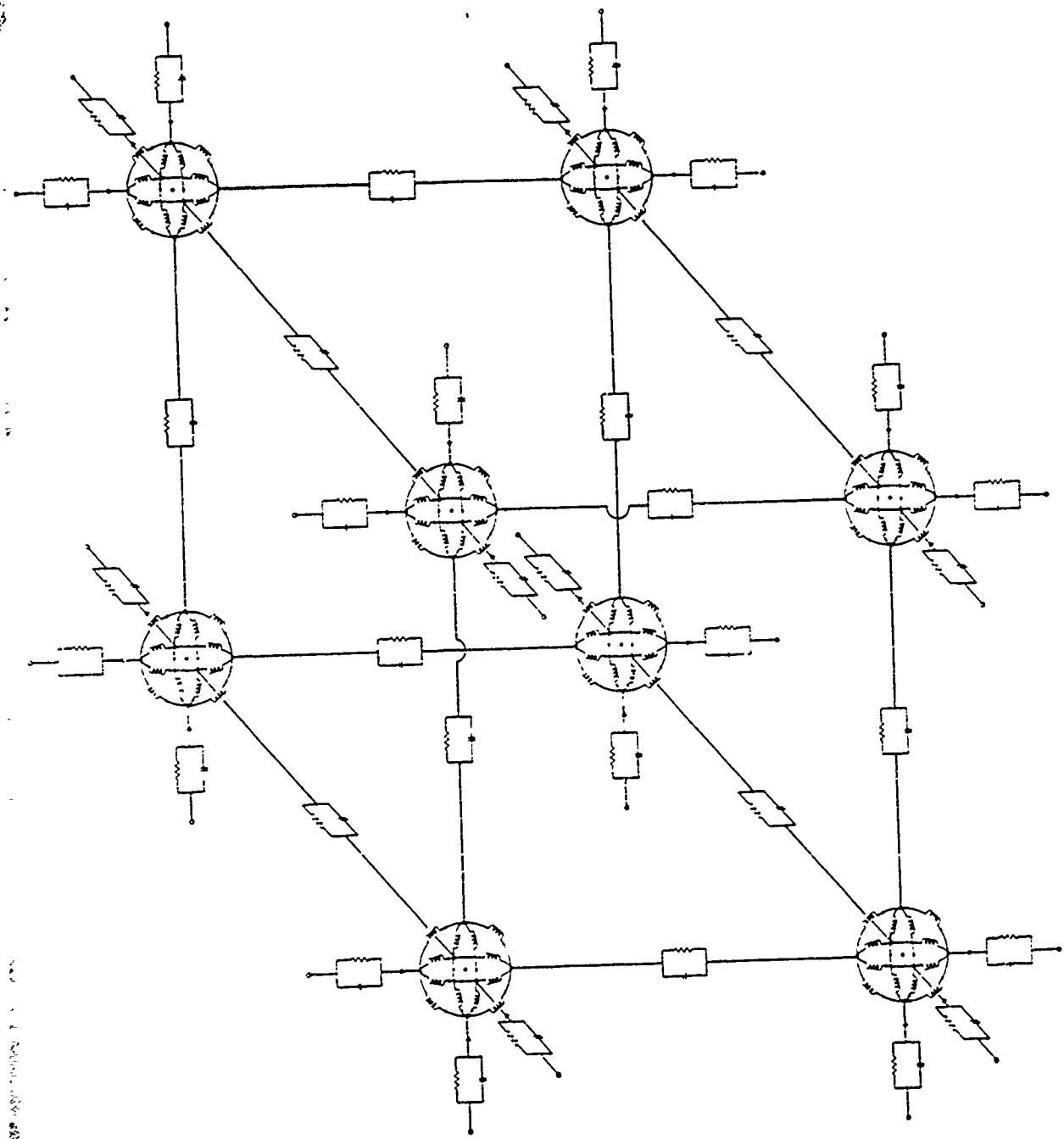
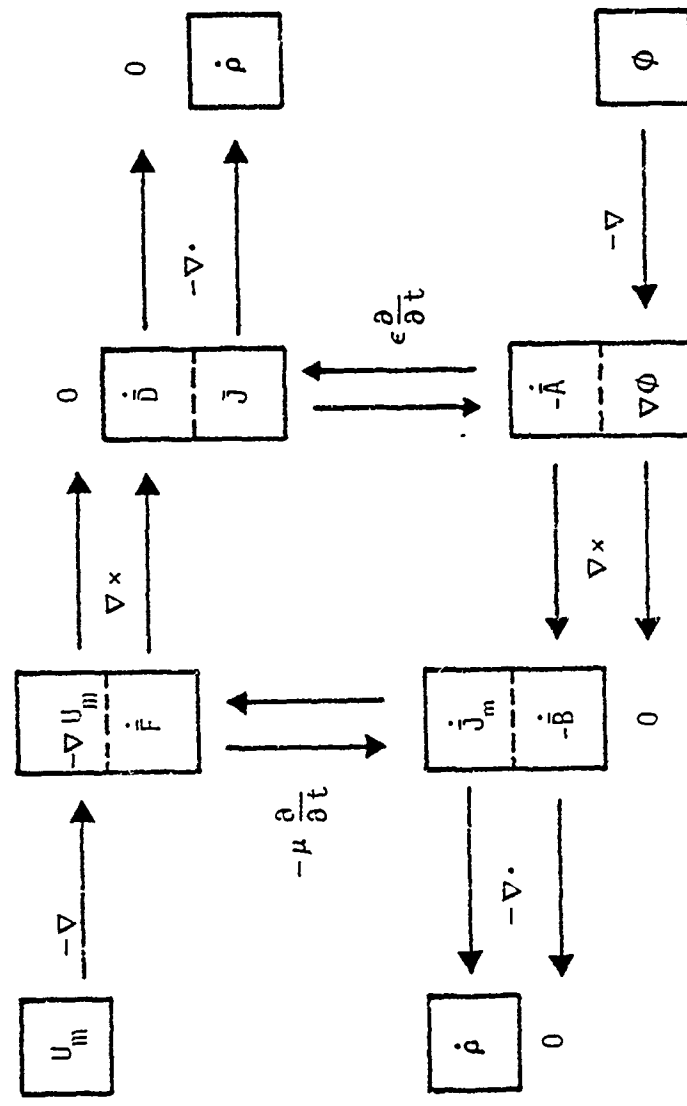


Figure 1. Interconnection of eight three-dimensional unit cells (After Kron [7]).

Figure 2. Graph theoretic statement of Maxwell's equations in which the topology and algebra have been separated (After Brannin [1]).



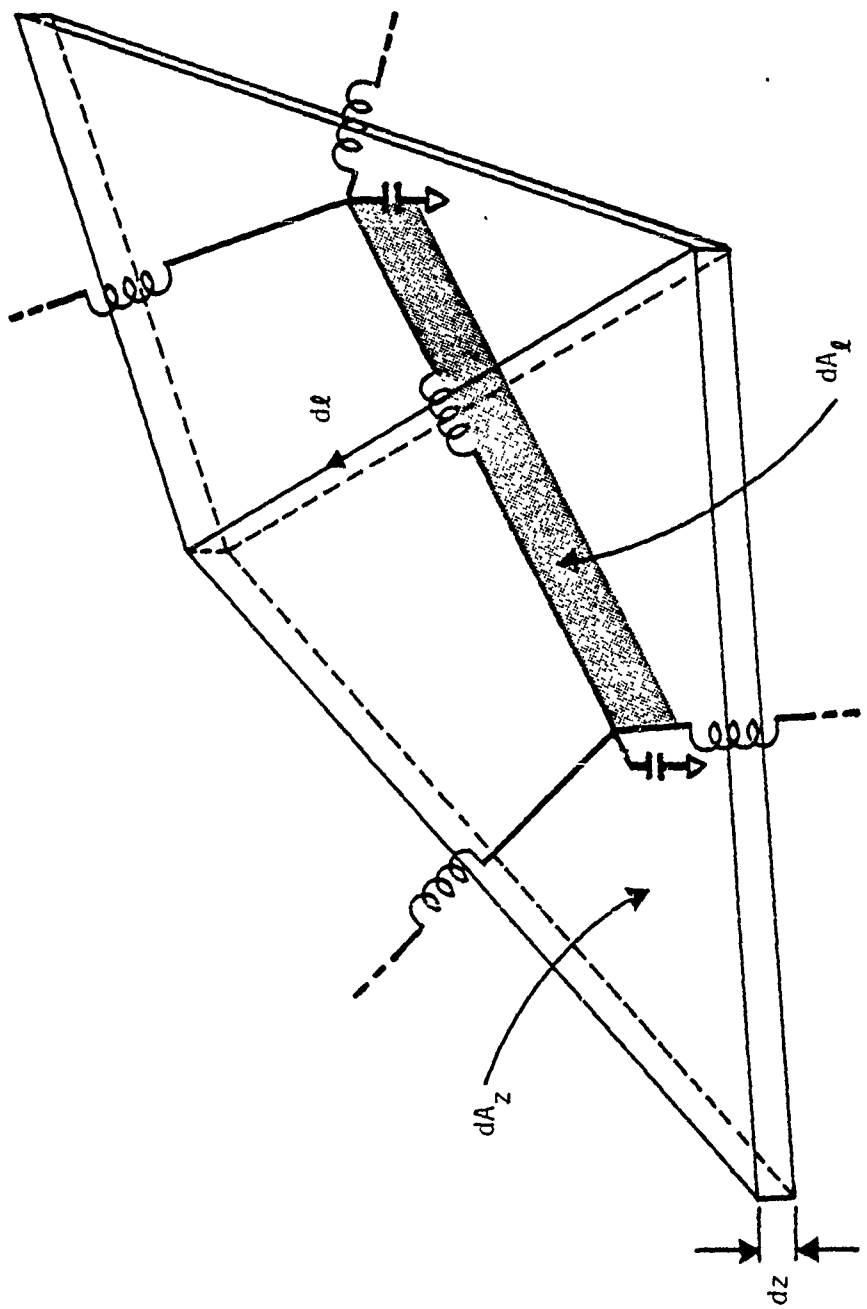


Figure 3. Two triangular unit cells. The dimensions dz , dA_z , dA_t , and A_t' are discussed in the text.

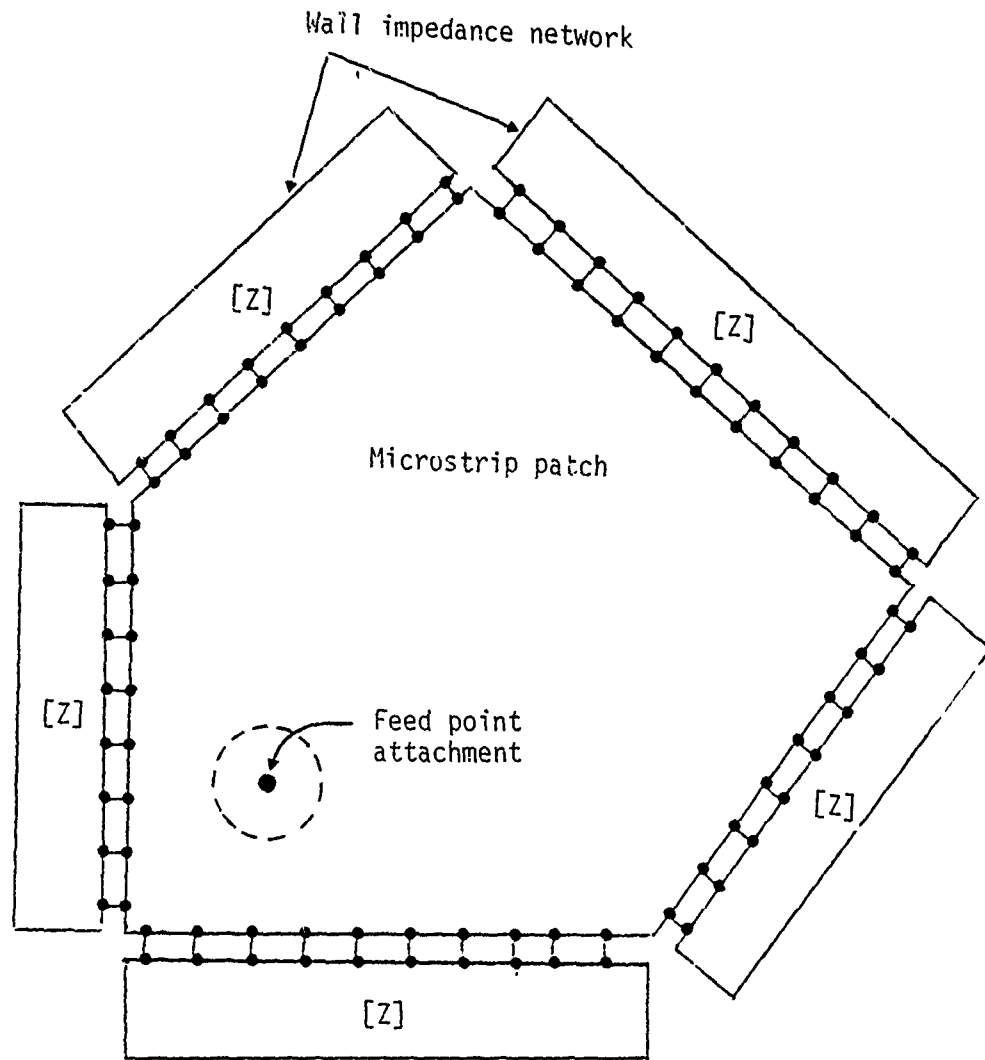
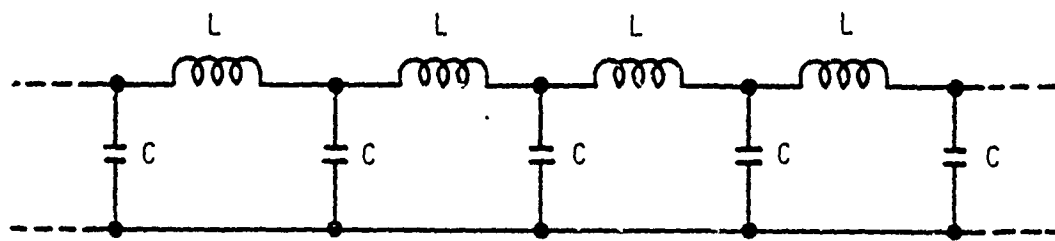
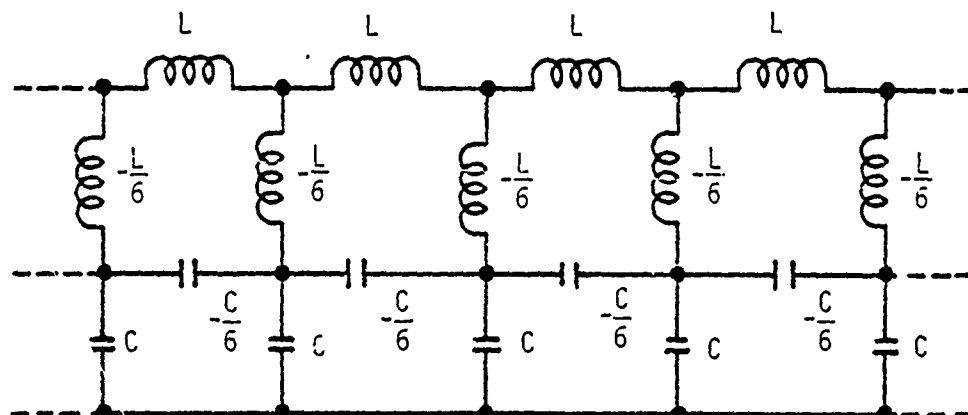


Figure 4. Partitioning of the microstrip antenna problem into (1) cavity, (2) feed attachment, and (3) wall impedance.



(a)



(b)

Figure 5. Circuit analog models of a one-dimensional transmission line.
 (a) finite difference model, (b) finite element (piecewise linear) model.

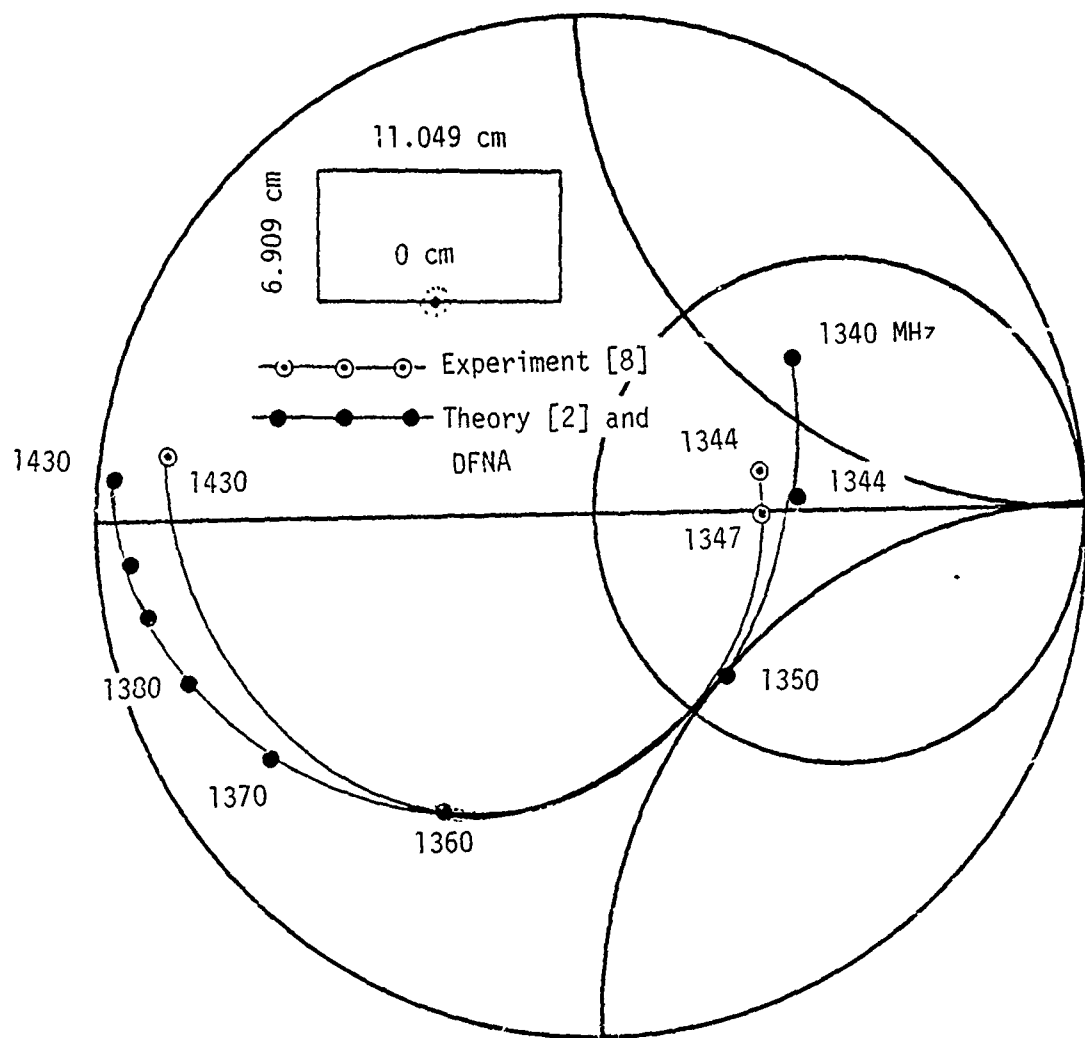
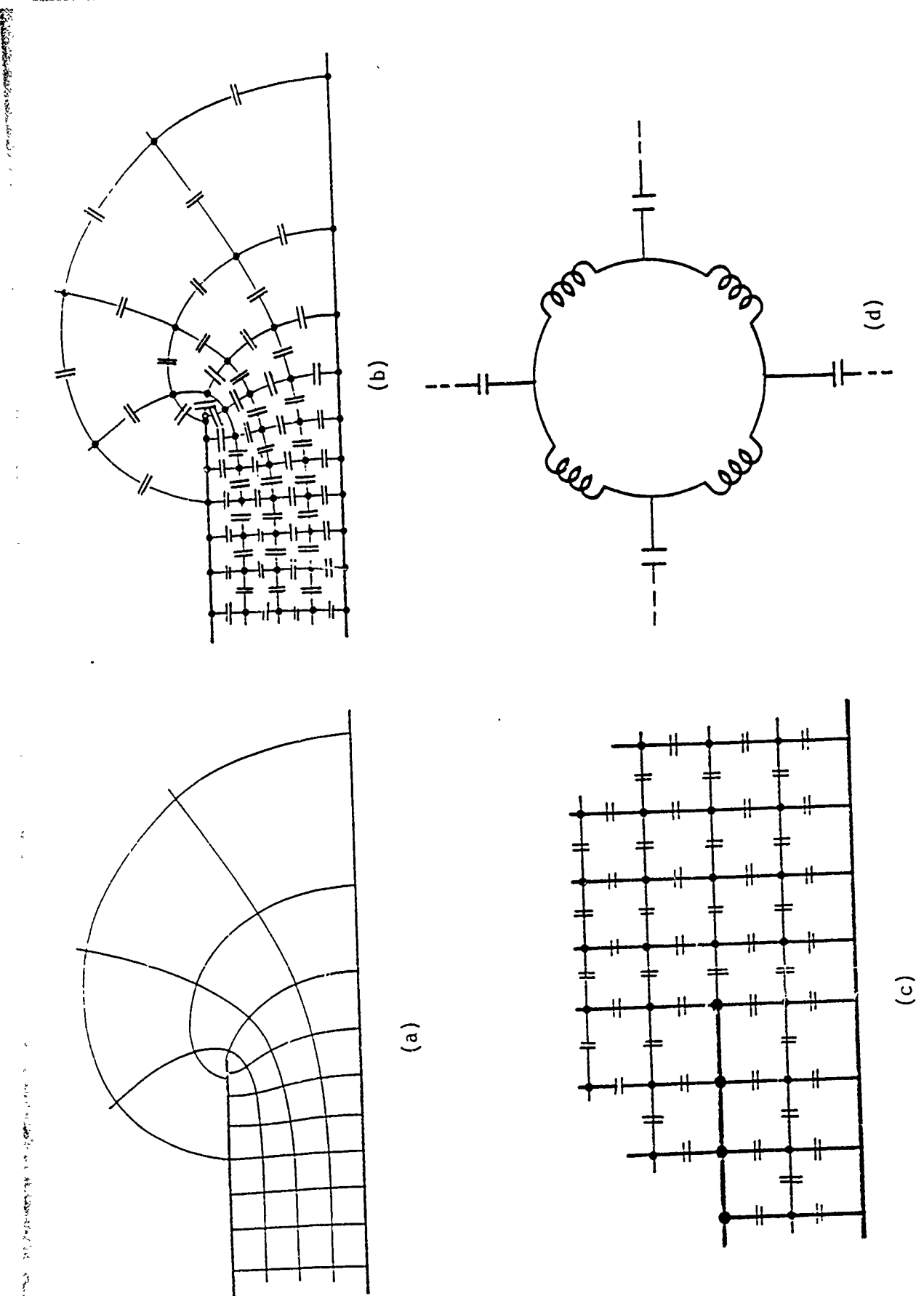
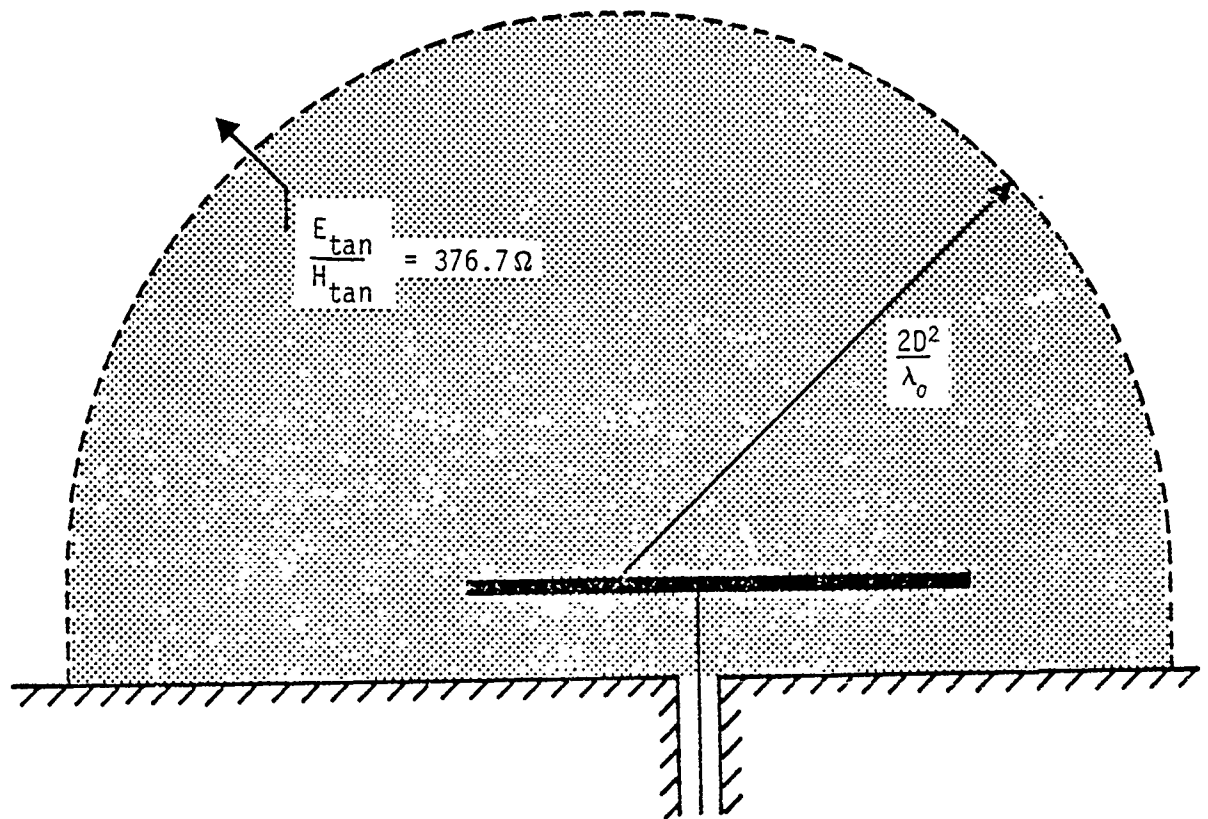


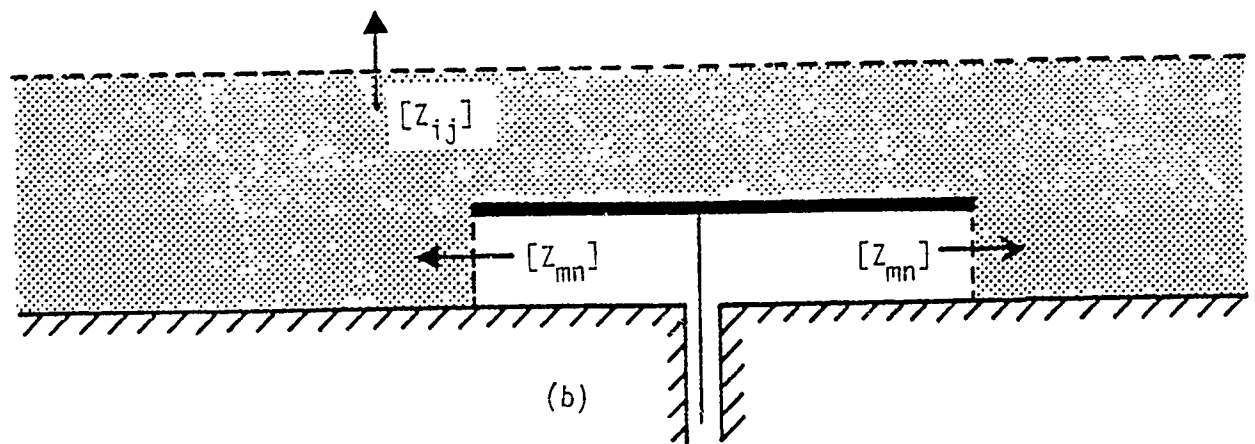
Figure 6. Comparison between experimental and DFNA values of impedance for L-band patch fed at edge.

Figure 7. Development of circuit analog for the parallel plate capacitor:
 (a) static fields, (b) conformal capacitor grid, (c) rectangular capacitor grid, (d) capacitor attachment for time-harmonic fields.



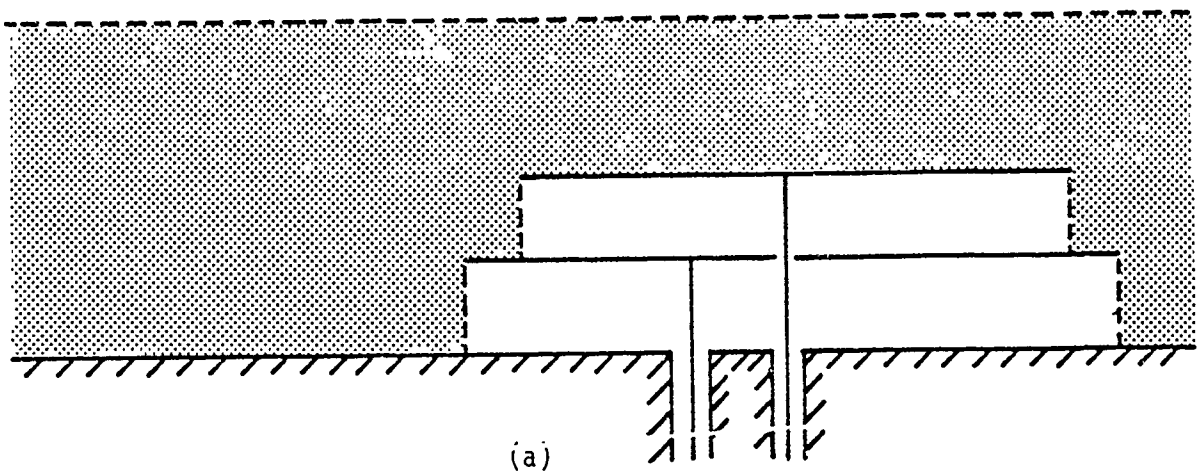


(a)

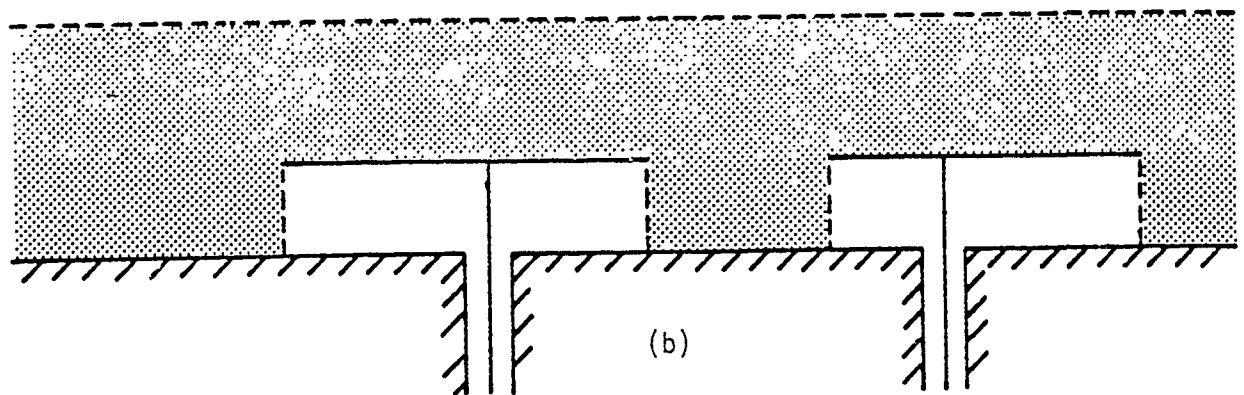


(b)

Figure 8. DFNA modeling domains. (a) far-field hemisphere, (b) Unimoment planar boundary.



(a)



(b)

Figure 9. Mutual coupling solution domains for (a) stacked antennas, (b) co-planar antennas.

THEORY AND EXPERIMENTS OF A BROADBAND
SHORT-CIRCUITED MICROSTRIP DIPOLE AT RESONANCE

G. DUBOST
LABORATOIRE ANTENNES ET RAYONNEMENT
UNIVERSITE DE RENNES 35000 FRANCE

SUMMARY

The behavior of a short-circuited, flat dipole and outside resonance has already been described, when placed parallel to a reflector plane. The object of this paper is to provide, within the resonance area, an approximate theory of the short-circuited, flat half-dipole, based on the hypothesis that the current is distributed sinusoidally, and which can be justified by experiment. Literal formulas are then reached which enable one to understand how the antenna functions radioelectrically and to evaluate the influence of the geometric parameters without difficulty.

The antenna's dimensions are equal, in relation to the wavelength and especially its thickness, and as such, it is extremely efficient having a bandwidth which is wider than other different antennas which have already been described. Its conception is such that it may be realised using a double printed circuit.

1.0 INTRODUCTION.

We have previously [1], [2] performed an experimental parametric study of a linearly polarised microstrip antenna, consisting of a flat, broad-folded dipole, parallel to, and at a short distance from a reflector plane. The bandwidth was sufficient for various applications despite the antenna being very thin.

A broadband, circularly polarised, flat source has also been described [3], [4], which is used in an array wrapped around a perfectly conducting cylinder [6].

A theoretical method has been proposed to explain the previously measured

bandwidth [5]. Given a sinusoidal current, the open-circuited symmetrical dipole was then compared with a lossy transmission line. It was then possible to express the bandwidth in terms of simple formulas which concurred with the experiments. It then seemed possible to increase the bandwidth using a short-circuited model, whose measurements have been given [7]. The bandwidth and radiation impedance were then expressed in terms of simple formulas obtained from an approximate theory, with the resonance strictly excluded [8].

Recently [10], this approximate theory was confirmed by means of the integral equation method, outside the resonance state. The object of this paper is to provide an approximate theory of the behavior of a broadband short-circuited microstrip half-dipole, acting at resonance, and which will be justified by experiment.

2.0 BEHAVIOR.

2.1 DESCRIPTION.

Figure 1 shows the arrangement of the short-circuited flat half-dipole placed in air. The radiating element, disposed on a double-sided printed circuit, is situated at a height H opposite a perfectly conducting reflector plane, and upon which it is short-circuited. Its length is h , and its width W . It is fed by a stripline, through a high impedance adaptation transformer. Two non-radiating, short-circuited striplines of low characteristic impedance, arranged in parallel at the entrance of the transformer, are used to partially compensate the susceptance. Last, a small metal cylinder is used to ensure the linkage between the stripline and the reflector so that the high impedance adaptation transformer is closed in upon the impedance of the radiation of the flat, short-circuited, radiating half-dipole.

2.2 APPROXIMATE THEORY.

The radiating half-dipole (fig. 1) is assimilated to a short-circuited line, length h , whose impedance characteristic R_c for low frequencies is a function of W/H ratio, the attenuation constant per unit of length being α . A simple calculation, assuming axial sinusoidal distribution of the current, will give the radiation impedance $Z_r = R_r + j X_r$ with :

$$\frac{R_r}{R_c} = \frac{\sinh 2\alpha H' + (\alpha/k) \sin 2kH'}{\cosh 2\alpha H' + \cos 2kH'} \quad (1)$$

$$\frac{X_r}{R_c} = \frac{\sin 2kH' - (\alpha/k) \sinh 2\alpha H'}{\cosh 2\alpha H' + \cos 2kH'} \quad (2)$$

k is the wave number and $H' = h + H$.

The resonance frequency f_r is such that :

$$f_r = \frac{c}{4(H+h)}$$

where c is the speed of the electromagnetic waves in air.

The main problem lies in determining the attenuation constant α . In order to do this, for $H' \ll \lambda$ and $W \ll \lambda$, the radiation resistance of the flat half-dipole is identified with half of that of the loop constituted by the flat half-dipole and its electrical image in relation to the reflector plane. The following is thus obtained :

$$\tanh \alpha H' = \frac{1}{3\pi} \cdot \frac{1}{R_c} \sqrt{\frac{\mu_0}{\epsilon_0}} \cdot (kh \cdot kh)^2 \quad (3)$$

On the basis of formulas (1) (2) and (3), we clearly obtain, close to resonance ($H' = \lambda/4$) :

$$(R_r)_{\text{res}} = \frac{3\pi R_c^2}{[(\frac{\pi}{2} - kh)kh]^2} \cdot \sqrt{\frac{\epsilon_0}{\mu_0}} \quad (4)$$

$$(X_r)_{\text{res}} = - \frac{2R_c}{\pi} \quad (5)$$

that is to say with the S.I. units the resistance R_c being expressed in ohms :

$$(R_r)_{\text{res}} = \frac{R_c^2}{40} \cdot \frac{1}{[(\frac{\pi}{2} - kh)kh]^2} \quad (6)$$

Now let us evaluate the half-dipole's Q factor close to resonance, that is to say for $H' = \lambda/4$, using the following expression :

$$(Q_r)_{res} = \frac{f_r}{2(R_r)_{res}} \cdot \left| \left(\frac{\partial X_r}{\partial f} \right)_{f_r} \right| \quad (7)$$

By means of the formulas (2) (3) and (4) and with the S.I. units, we obtain, without difficulty, the following approximate formula which is valid for H/λ values which are small in relation to the wavelength :

$$(Q_r)_{res} = \frac{\pi \cdot R_c}{160[(\frac{\pi}{2} - kH)kH]^2} \quad (8)$$

N.B. - In practice, in order to determine the bandwidth for H/λ heights, which are not negligible in relation to the wavelength, it is better to calculate the variations of R_r and X_r given by (1) and (2) in function of the frequency, in order to deduce $(Q_r)_{res}$ according to (7).

2.3 INTERPRETATION.

Fig. 2 shows the variation of the theoretical resistance $(R_r)_{res}$ according to (6), as a function of the height H/λ of the half-dipole at resonance, in relation to the reflector plane for different widths W/λ . The resistance decreases as the width increases. Fig. 3 presents, as a function of the height H/λ and for different widths W/λ , both the Q factor of the half-dipole at resonance in accordance with the approximate formula (8), and also the relative bandwidth $(B)_{res}$, expressed as a percentage, and corresponding to a V.S.W.R. lower than 3, such that :

$$(B)_{res} = \frac{130}{(Q_r)_{res}} \quad (9)$$

The bandwidth increases as the height and width, in relation to the wavelength, increase.

Compared with different sources, which have already been described, and whose dimensions are of a similar size [9], [11], [12], our model has a wider bandwidth. Thus for $H/\lambda = 0.008$, $W/\lambda = 0.25$ and $h/\lambda = 0.242$ with $R_c = 11$ ohms, our model corresponds to $(R_r)_{res} = 518$ ohms (6), $(Q_r)_{res} = 37$ (8) and $B = 3.5\%$ (9). However, for the antenna [11] shown on table II, for a wavelength in air with : $H/\lambda = 0.008$, $a/\lambda = 0.31$ and $b/\lambda = 0.30$ the Q factor is equal to 93. It should be noted that our flat short-circuited half-dipole is in air, whereas microstrip antennas

mentioned above are all built on a dielectric substrate. It would be possible to realize our model on a substrate, the antenna and its feed supply would then be printed on two superposed circuits.

3.0 EXPERIMENTAL JUSTIFICATION.

Recently [10], we successfully compared the experimental and theoretical results obtained using the "integral equation method" for a short-circuited symmetrical cylindrical dipole with $2a$ diameter.

The parameters of the cylindrical dipole were the following :

$h = 75 \text{ mm}$, $H = 11.3 \text{ mm}$, $2a = 12 \text{ mm}$ ($W = 24 \text{ mm}$).

The width of the equivalent strip is taken to equal to twice the diameter. Table I compares the Q factor and bandwidth, and the resonance frequencies.

TABLE I

RESULTS SHOWING BEHAVIOR OF A FINE
SHORT-CIRCUITED HALF DIPOLE AT RESONANCE

Parameter	Integral Equation method [10].	Experiment [10]	Approximate Theory
$(Q)_{\text{res}}$	34	33	22 [according to (7)]
$B \%$ [according to (9)]	3.82	3.94	5.9
$f_r (\text{GHz})$	0.905	0.805	0.869
$(R_r)_{\text{res}} (\Omega)$	1550	1650	2290 [according to (6)]
H/λ	0.034	0.030	0.032
W/λ	0.072	0.064	0.069

Despite the difficulties encountered during the course of taking measurements and the uncertainty in the choice of the number of cuts necessary to resolve the integral equation numerically, it would seem that for this fine half-dipole, the calculation of the bandwidth according to the approximate theory (7) and (9) is a little high. It should be noted that the relative bandwidth B shown in Table I is small because of the

small width W/λ of the half-dipole.

Still more recently a model was built more especially for television reception. It was much wider and corresponded to the following parameter values (fig. 1) : $H = 20.6 \text{ mm}$, $h = 82.2 \text{ mm}$, $W = 94.5 \text{ mm}$. From these values $R_C = 54 \text{ ohms}$ can be deduced. The resonance frequency had to be 730 MHz. ($\frac{H}{\lambda} = 0.05$, $\frac{h}{\lambda} = 0.20$, $\frac{W}{\lambda} = 0.23$).

The circuit on which the radiating element and the feed supply circuits are printed is 0.8 mm thick and has a relative dielectric constant of : $\epsilon_r = 2.6$. Before the short-circuited compensation lines were inserted, different quarter-wave matching transformers, each 64 mm long and with a high impedance characteristic Z_C , were tested. Table II shows, for several Z_C , the transformed resistance values R_t , from which the value of the half-dipole's radiation resistance $(R_r)_{\text{res}}$ at resonance can be deduced, as well as the Q factor $(Q_r)_{\text{res}}$.

TABLE II
RADIATION RESISTANCE AND Q FACTOR DEDUCED FROM MEASUREMENT

Z_C (ohms)	R_t (measured) ohms	$(Q_r)_{\text{res}}$ measured	$(R_r)_{\text{res}}$ ohms
120	29	8.70	496
144	48	8.25	432
184	77	9.80	440

According to fig. 2, and for the above parameter values, the theoretical value of $(R_r)_{\text{res}}$ is close to 450 ohms. The theoretical Q factor defined by (7) and rigorously calculated on the basis of (1), (2), (3) (c.f. note to paragraph 2.2) has a value of 8.6. When this value is compared to those deduced from the experiment shown on Table II, and whose mean value is equal to 8.9, it can be concluded that the impedance transformer has a wide band and does not modify in any significant way the antenna's bandwidth. When there is no reactive compensation of the susceptance, the relative bandwidth of the antenna (8) and (9) without transformer is

therefore close to 15 %.

Table III shows the half-dipole's bandwidth, matched with the high impedance transformer, with or without partial reactive compensation, given by experiment or by theory.

TABLE III
RELATIVE BANDWIDTH (IN PERCENT) IN TERMS OF V.S.W.R.

V.S.W.R.	≤ 2	≤ 3
Theory without reactive compensation	8 %	13.5 %
Theory with reactive compensation (fig. 4)	11 %	14.5 %
Experiment fig. 1 and fig. 4	12 %	16 %

For the crossed and principal components, the directivity diagrams has been measured in the "E and H planes" of the half-dipole arranged on a circular counterweight.

In the E plane, which is the dipole's symmetrical plane, the principal component has a wider directivity diagram than that of the "H plane" due to the radiation of the short circuit's current. In the "H plane", the crossed component, which is nil on the axis of the principal radiation, has a symmetrical diagram, which can be ascribed to the short circuit's current and the symmetrical deformation o. the field strength lines on the radiating plate.

4.0 CONCLUSION.

We have described, by means of an approximate theory based on a sinusoidal distribution of current, the radioelectric behavior at resonance of a flat, short-circuited, half-dipole, working in the air, and translated

into literal expressions, which allow the influence of the antenna's geometric parameters to be examined without difficulty. This theory was moreover justified by experiment. Given that the width of the radiating plate is not negligible in relation to the wavelength, it is possible, despite the thickness of the antenna being a hundredth of that of the wavelength, to obtain a bandwidth which is relatively wide and greater than that obtained from others different models.

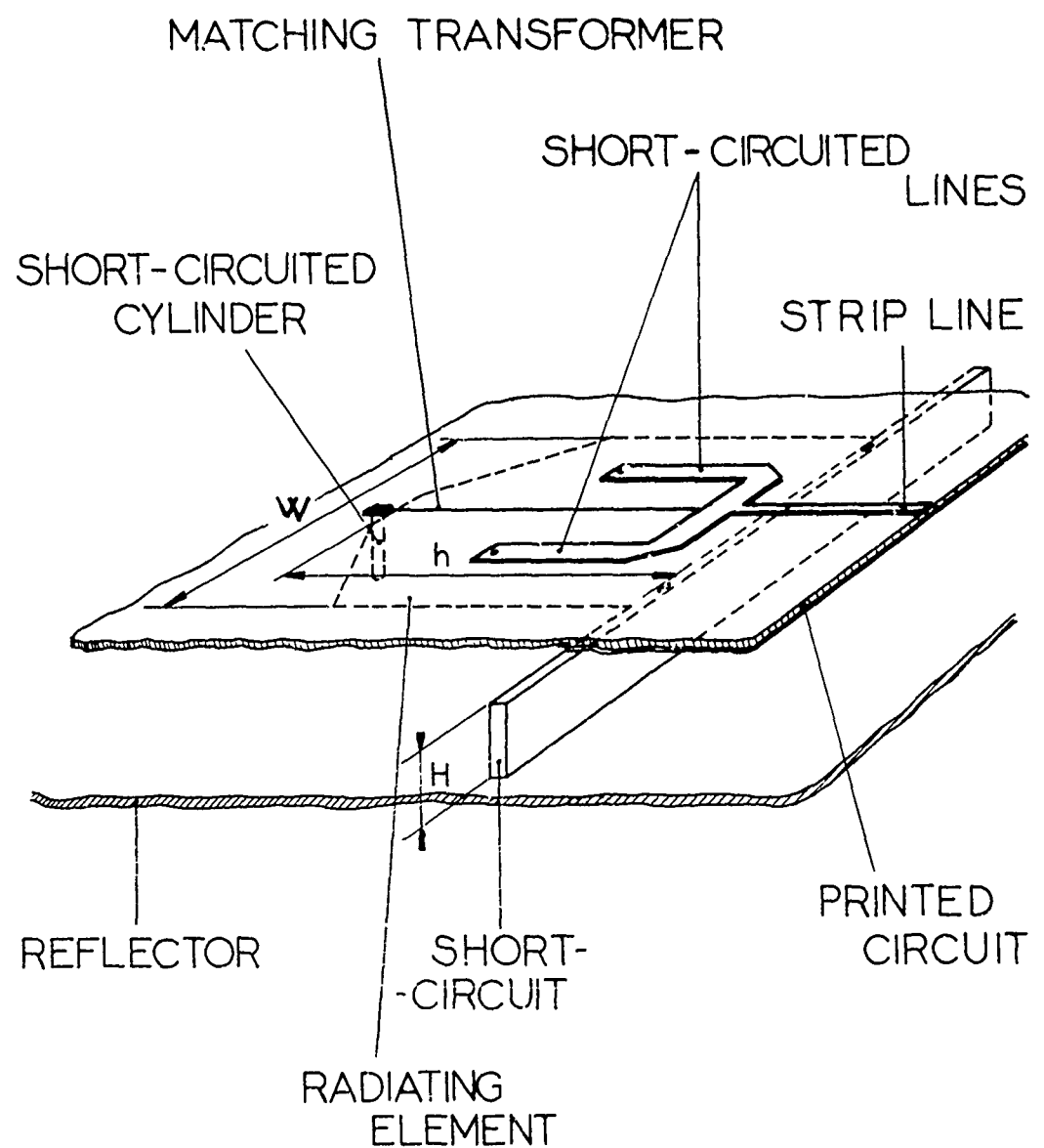
An approximately square $0.2 \lambda \times 0.23 \lambda$ experimental model, with a thickness of 0.05λ has been studied for the television. It has a relative bandwidth of about 16 %, and has an excellent efficiency. With this theory, and with a thickness equal to 0.008λ , one can hope for a bandwidth of 3.5 %.

Lastly, for small thicknesses, the antenna can be built by means of two superposed printed circuits, one bearing the supply stripline, and the other the radiating plate.

5.0 REFERENCES.

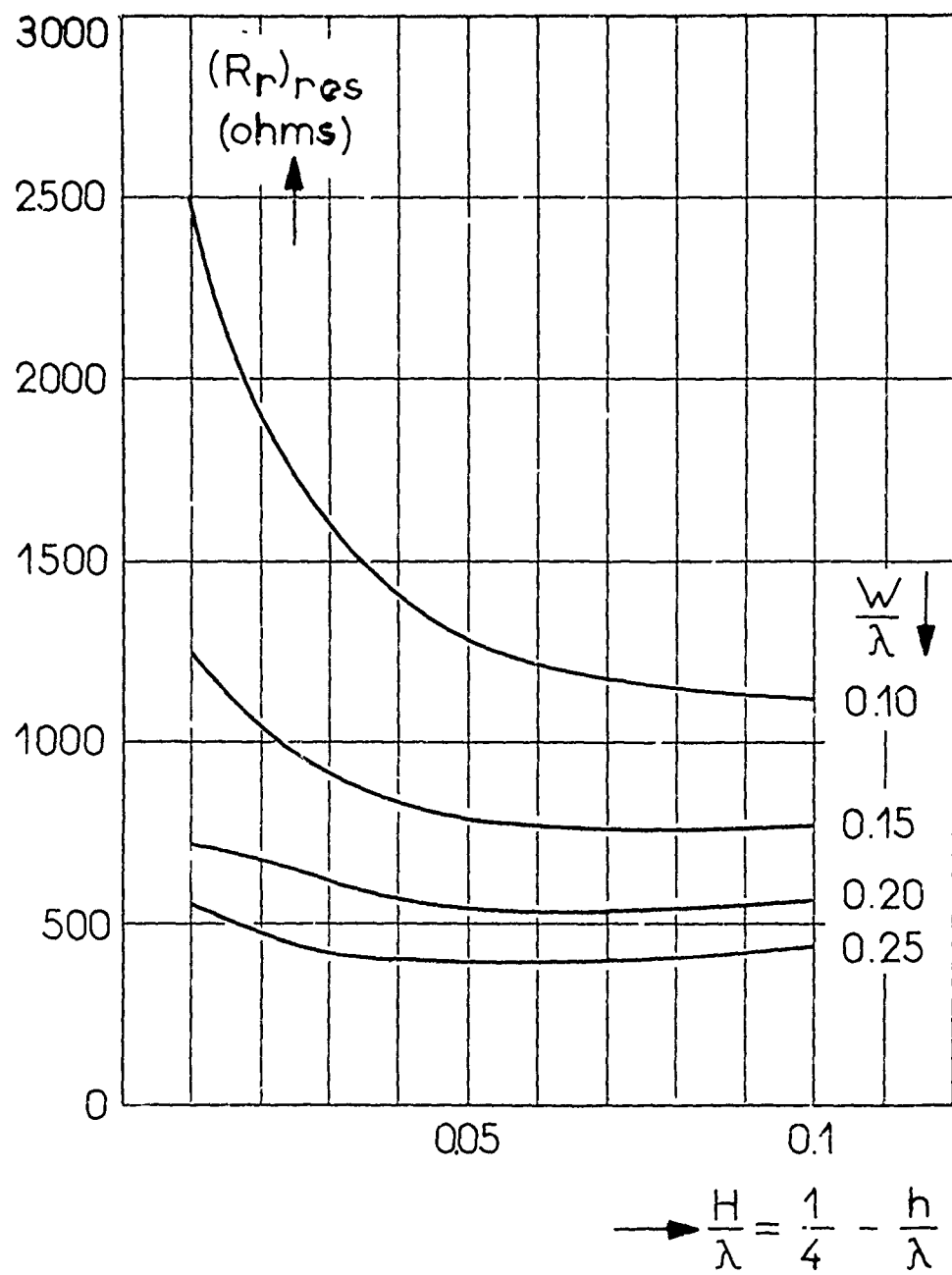
1. Dubost G., Havot H. : Doublet replié en plaques.
Brevet d'invention délivré :
en France n° 2.311.422 le 29.11.1977
en G.B. n° 15.307.03 le 07.02.1979
en R.F.A. n° P 26. 21452.8 le 14.05.1976
aux U.S.A. n° 4.084.162 le 11.04.1978.
2. Dubost G., Nicolas M., Havot H. : Theory and applications of broadband microstrip antennas.
6th E.M.C., Rome, 1976, pp. 275-279.
3. Dubost G., Frin R., Samson J. : Doublet et antenne en plaques à polarisation circulaire.
Brevet d'invention n° 78.18.196 du 19.06.1978.
4. Dubost G., : Broadband circularly polarized flat antenna.
I.S.A.P., Sendai, Japan, August 1978, pp. 89-92.
5. Dubost G., : Bandwidth of a dipole near and parallel a conducting plane.
Electr. Letters 9th November 1978, vol. 14, n° 23, pp. 734-736.
6. Dubost G., Samson J., Frin R. : Large bandwidth flat cylindrical array with circular polarisation and omnidirectional radiation.
Electr. Letters 15th Feb. 1979, vol. 15, n° 4, pp. 102-103.
7. Dubost G., Frin R. : Certificat d'addition au brevet d'invention n° 78.18.196, déposé le 5 mars 1979 sous le n° 79.05.580.

8. Dubost G. : Justification d'une théorie approchée du rayonnement de doublets plaques court-circuités.
C.R. Acad. Sci. Paris, t. 288 (07.05.1979) série B 273-276.
9. Howell J.Q. : Microstrip antennas.
IEEE Transactions on Antennas and Propagation. Jan. 1975,
pp. 90-93.
10. Khellaf A. : Contribution à l'étude d'antennes plaques symétriques à polarisation rectiligne.
Thèse de 3^e cycle soutenue le 22.06.1979 devant l'Université de Rennes.
11. Lo Y.T., Solomon D., Richards W.F. : Theory and experiment on microstrip antennas.
IEEE Transactions on Antennas and Propagation. Vol. AP 27,
N° 2, March 1979.
12. Munson R.E. : Conformal Microstrip Antennas and Microstrip Phased Arrays.
IEEE Transactions on Antennas and Propagation. Vol. AP 22,
Jan. 1974, pp. 74-78.



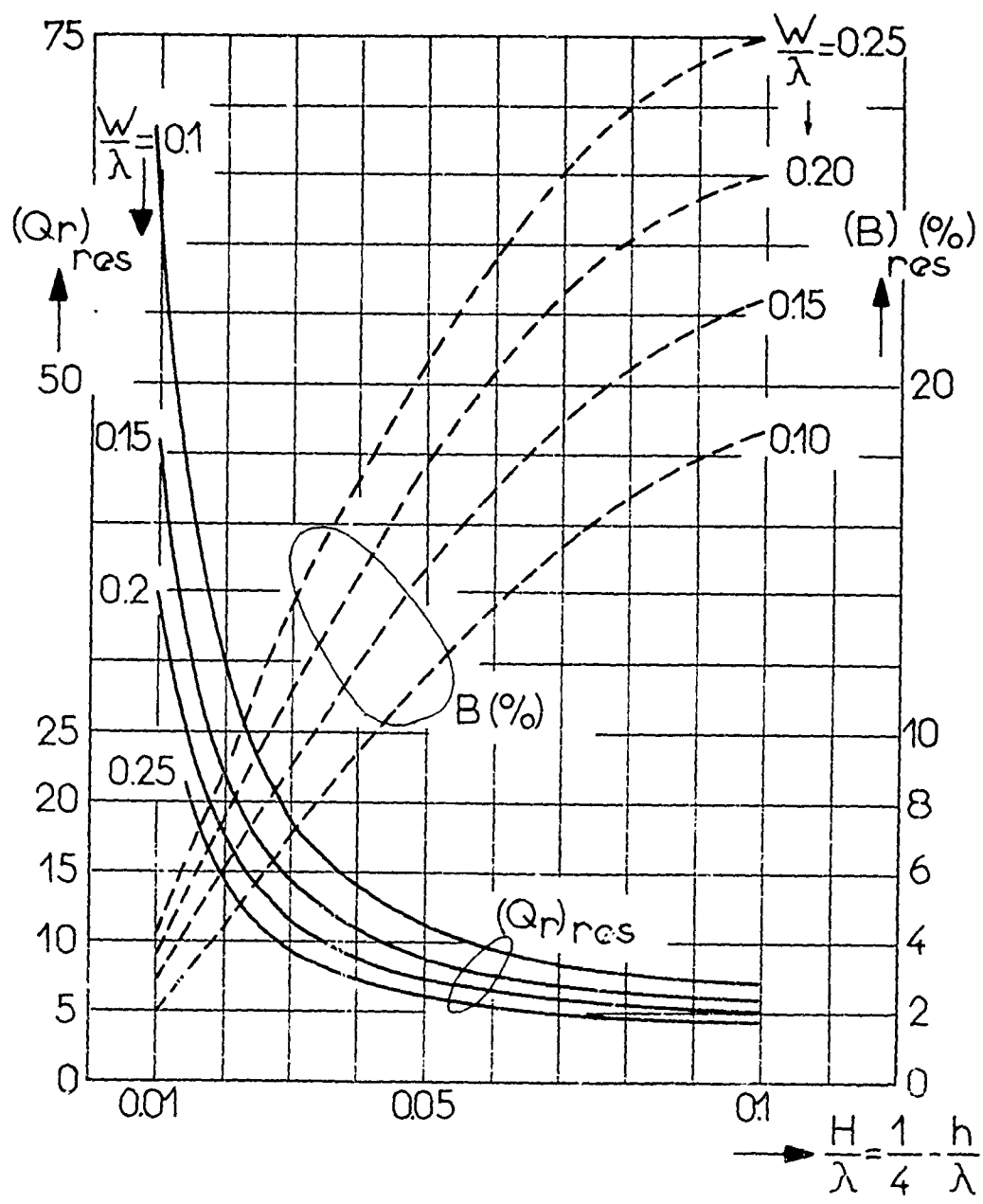
SHORT-CIRCUITED HALF DIPOLE.

FIG. 1



RADIATION RESISTANCE OF HALF FLAT
DIPOLE ACTING AT RESONANCE IN
TERMS OF H/λ AND W/λ . (THEORY)

FIG. 2

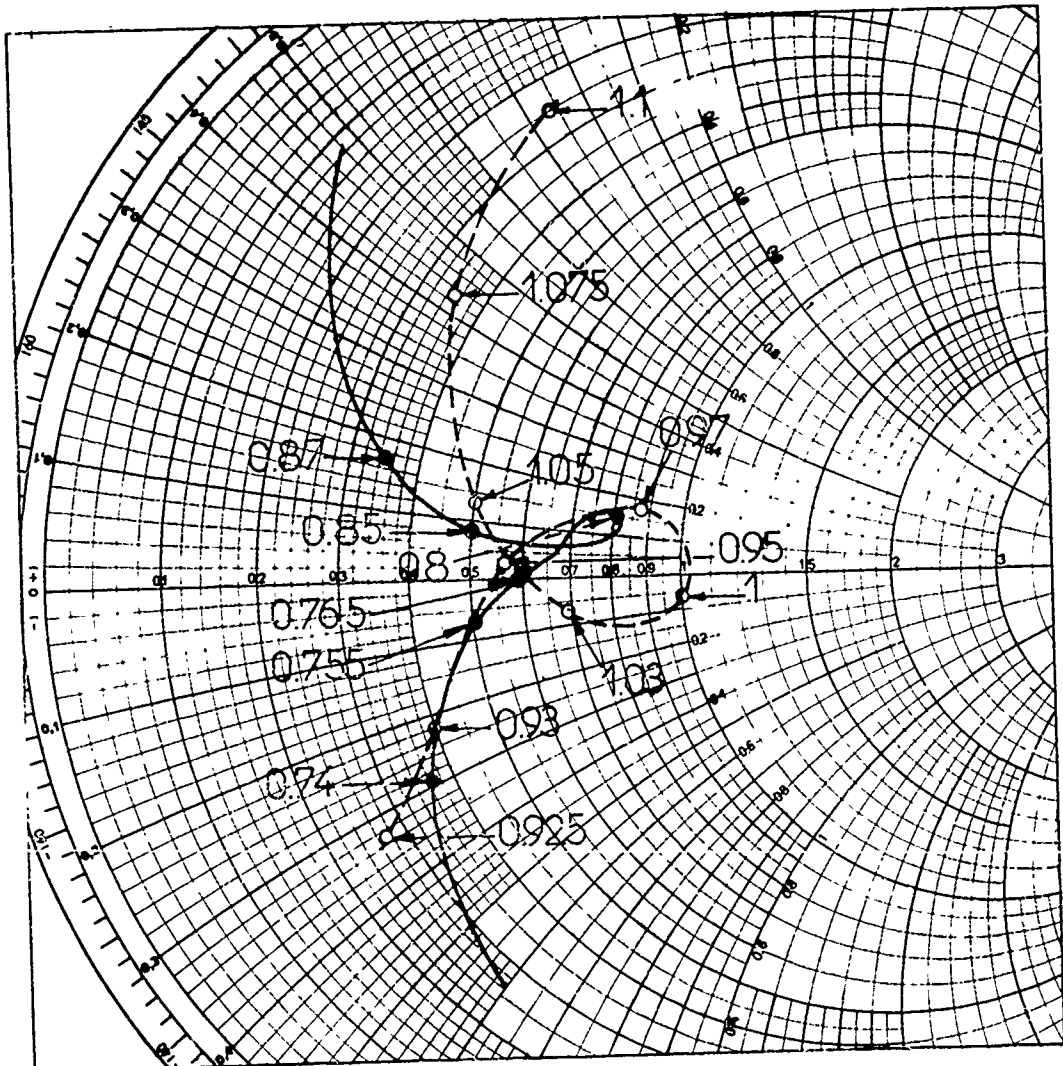


Q FACTOR AND BANDWIDTH (3 to 1 VSWR)
OF HALF FLAT DIPOLE ACTING AT RESONAN-
CE IN TERMS OF H/λ AND W/λ .(THEORY).

FIG.3

— EXPERIENCE
GHz

- - - THEORETICAL
RESULTS. (RELATIVE
FREQUENCY).



1 ≈ 20 MMHOS

FIG. 4.

AUTHOR INDEX

ALEXOPOULOS, N. G.	30-1	NELSON, C.	16-1
BUTLER, C. M.	13-1	NEWMAN, E. H.	9-1
CARVER, K. R.	4-1, 7-1	NOWICKI, T. E.	26-1
CHANG, D. C.	28-1	RANA, I. E.	30-1
CIPOLLA, F. W.	19-1	RICHARDS, W. F.	8-1
COFFEY, E. L.	31-1	SANFORD, G. G.	21-1
DERNERYD, A. G.	12-1	SCHAUBERT, D. H.	5-1
DUBOST, G.	32-1	SHEN, L. C.	14-1
FARRAR, F. G.	5-1	SIMON, P.	8-1
FURLONG, W. J.	15-1	TRAUT, G. R.	27-1
HALL, P. S.	1-1	TULYATHAN, P.	9-1
HARRISON, D. D.	8-1	VAN DE CAPELLE, A. R.	11-1
HENDERSON, A.	1-1	WATERMAN, A.	23-1
HUISJEN, M. A.	15-1	WEINSCHEL, H. D.	2-1
HUEBNER, D. A.	17-1	WILTON, R. E.	22-1
ITOH, T.	10-1	WOOD, C.	1-1
JAMES, J. R.	1-1	YEE, J. S.	15-1
JEDLICKA, R. P.	4-1		
KALOI, C. M.	6-1		
KERNWEIS, N.	25-1		
KUESTER, E. F.	28-1		
KERR, J. L.	3-1		
LEHMAN, T. H.	31-1		
LIND, A. G.	12-1		
LO, Y. T.	8-1		
LONG, S. A.	14-1		
McILVENNA, J.	25-1		
MENZEL, W.	10-1		
METZLER, T.	20-1		
MURPHY, L. R.	18-1		
MYHRE, R. W.	24-1		

SUPPLEMENTARY

INFORMATION

Unclassified

SECURITY CLASSIFICATION OF THIS PAGE (When Data Entered)

REPORT DOCUMENTATION PAGE		READ INSTRUCTIONS BEFORE COMPLETING FORM
1. REPORT NUMBER 16626.1-EL	2. GOVT ACCESSION NO. <i>A104404</i>	3. RECIPIENT'S CATALOG NUMBER
4. TITLE (and Subtitle) Printed Circuit Antenna Technology		5. TYPE OF REPORT & PERIOD COVERED Final Report Proceedings
7. AUTHOR(s) Keith Carver		6. PERFORMING ORG. REPORT NUMBER DAAG29 79 M 0091
9. PERFORMING ORGANIZATION NAME AND ADDRESS New Mexico State University Las Cruces, NM		10. PROGRAM ELEMENT, PROJECT, TASK AREA & WORK UNIT NUMBERS
11. CONTROLLING OFFICE NAME AND ADDRESS U. S. Army Research Office Post Office Box 12211 Research Triangle Park, NC 27709		12. REPORT DATE Sep 81
14. MONITORING AGENCY NAME & ADDRESS (if different from Controlling Office)		13. NUMBER OF PAGES 509
		15. SECURITY CLASS. (of this report) <u>Unclassified</u>
		16a. DECLASSIFICATION/DOWNGRADING SCHEDULE
16. DISTRIBUTION STATEMENT (of this Report) Approved for public release; distribution unlimited.		
17. DISTRIBUTION STATEMENT (of the abstract entered in Block 20, if different from Report)		
18. SUPPLEMENTARY NOTES The view, opinions, and/or findings contained in this report are those of the author(s) and should not be construed as an official Department of the Army position, policy, or decision, unless so designated by other documentation		
19. KEY WORDS (Continue on reverse side if necessary and identify by block number) printed circuit antennas technology microstrip antenna striplines		
20. ABSTRACT (Continue on reverse side if necessary and identify by block number) This Proceedings is the first major volume to deal exclusively with the technology of printed circuit antennas, and will serve as a useful reference on microstrip and stripline radiators and arrays. The thirty-one papers herein have been contributed by forty-eight authors from universities, industrial research groups and governmental agencies in Belgium, England, France, Sweden, the United States and West Germany and are a permanent record of this first Workshop on Printed Circuit Antenna Technology. The intent of this workshop, which has been co-sponsored by (CONT.)		

UNCLASSIFIED

SECURITY CLASSIFICATION OF THIS PAGE(When Data Entered)

ABSTRACT CONT.

the U.S. Army Research Office and the NMSU Physical Science Laboratory, has been to survey the state of printed circuit antenna technology as it exists at present and to focus on specific needs for future R&D emphasis.

UNCLASSIFIED

SECURITY CLASSIFICATION OF THIS PAGE(When Data Entered)